



ISSN 1580-3155

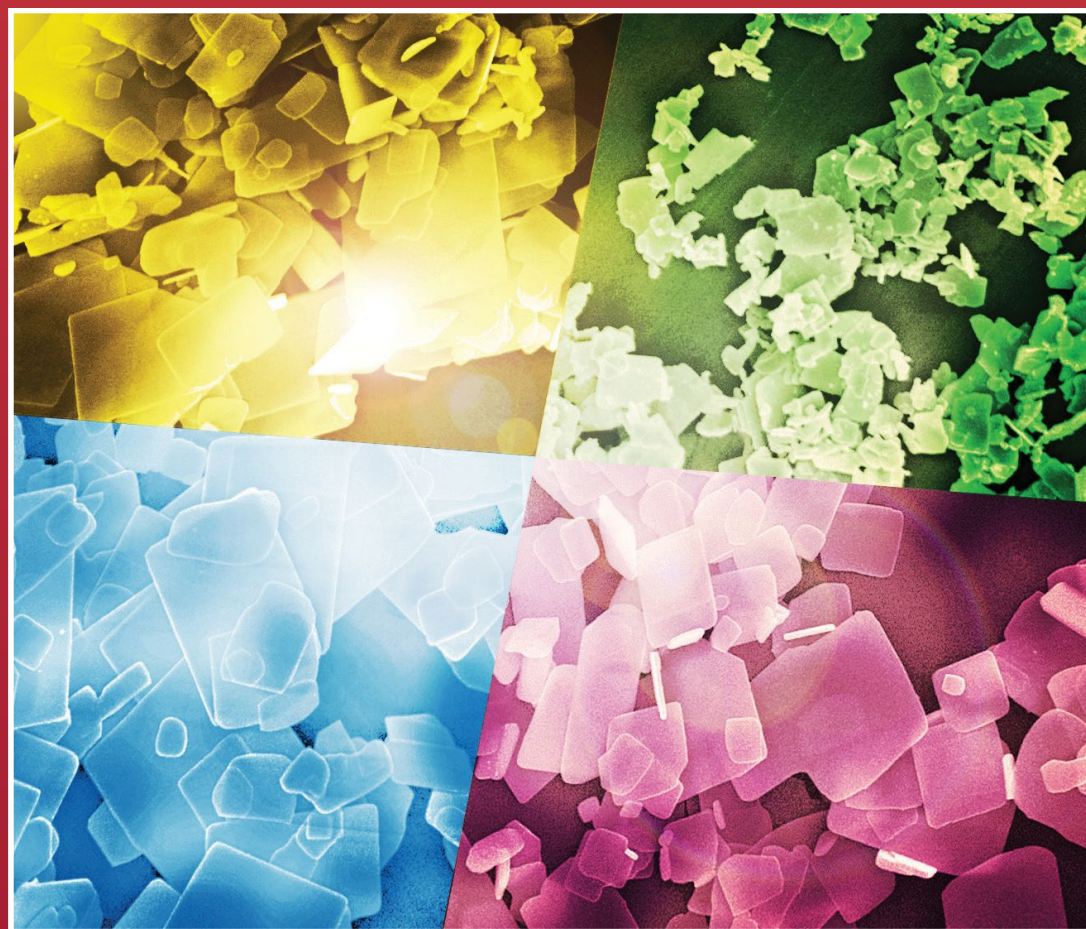
Pages 483–768 ■ Year 2018, Vol. 65, No. 3

Slovensko kemijsko društvo
Slovenian Chemical Society



Acta Chimica Slo Acta Chimica Slo Slovenica Acta C

3



65/2018

EDITOR-IN-CHIEF

KSENİJA KOGEJ

Slovenian Chemical Society, Hajdrihova 19, SI-1000 Ljubljana, Slovenija,

E-mail: ACSi@fkt.uni-lj.si, Telephone: (+386)-1-479-8538

ASSOCIATE EDITORS

Janez Cerkovnik, University of Ljubljana, Slovenia
Krištof Kranjc, University of Ljubljana, Slovenia
Ksenija Kogej, University of Ljubljana, Slovenia
Franc Perdih, University of Ljubljana, Slovenia
Aleš Podgornik, University of Ljubljana, Slovenia
Helena Prosen, University of Ljubljana, Slovenia
Damjana Rozman, University of Ljubljana, Slovenia

Melita Tramšek, Jožef Stefan Institute, Slovenia
Irena Vovk, National Institute of Chemistry, Slovenia

ADMINISTRATIVE ASSISTANT

Marjana Gantar Albreht, National Institute of Chemistry, Slovenia

EDITORIAL BOARD

Wolfgang Buchberger, Johannes Kepler University, Austria
Alojz Demšar, University of Ljubljana, Slovenia
Stanislav Gobec, University of Ljubljana, Slovenia
Marko Goličnik, University of Ljubljana, Slovenia
Günter Grampp, Graz University of Technology, Austria
Wojciech Grochala, University of Warsaw, Poland
Danijel Kikelj, Faculty of Pharmacy, Slovenia
Janez Košmrlj, University of Ljubljana, Slovenia
Blaž Likozar, National Institute of Chemistry, Slovenia
Mahesh K. Lakshman, The City College and
The City University of New York, USA

Janez Mavri, National Institute of Chemistry, Slovenia
Friedrich Sreinc, University of Minnesota, USA
Walter Steiner, Graz University of Technology, Austria
Jurij Svete, University of Ljubljana, Slovenia
Ivan Švancara, University of Pardubice, Czech Republic
Jiri Pinkas, Masaryk University Brno, Czech Republic
Gašper Tavčar, Jožef Stefan Institute, Slovenia
Christine Wandrey, EPFL Lausanne, Switzerland
Ennio Zangrando, University of Trieste, Italy

ADVISORY EDITORIAL BOARD

Chairman

Branko Stanovnik, Slovenia

Members

Josef Barthel, Germany
Udo A. Th. Brinkman, The Netherlands
Attilio Cesaro, Italy
Dušan Hadži, Slovenia
Vida Hudnik, Slovenia
Venčeslav Kaučič, Slovenia

Željko Knez, Slovenia
Radovan Komel, Slovenia
Janez Levec, Slovenia
Stane Pejovnik, Slovenia
Anton Perdih, Slovenia
Slavko Pečar, Slovenia
Andrej Petrič, Slovenia
Boris Pihlar, Slovenia
Milan Randić, Des Moines, USA

Jože Škerjanc, Slovenia
Miha Tišler, Slovenia
Đurđa Vasić-Rački, Croatia
Marjan Veber, Slovenia
Gorazd Vesnaver, Slovenia
Jure Zupan, Slovenia
Boris Žemva, Slovenia
Majda Žigon, Slovenia

Acta Chimica Slovenica is indexed in: *Chemical Abstracts Plus*, *Current Contents (Physical, Chemical and Earth Sciences)*, *PubMed*, *Science Citation Index Expanded* and *Scopus*. Impact factor for 2017 is IF = 1.104.



Articles in this journal are published under Creative Commons Attribution 3.0 License

<http://creativecommons.org/licenses/by/3.0/>

Izdaja – Published by:

SLOVENSKO KEMIJSKO DRUŠTVO – SLOVENIAN CHEMICAL SOCIETY

Naslov redakcije in uprave – Address of the Editorial Board and Administration

Hajdrihova 19, SI-1000 Ljubljana, Slovenija

Tel.: (+386)-1-476-0252; Fax: (+386)-1-476-0300; E-mail: chem.soc@ki.si

Izdajanje sofinancirajo – Financially supported by:

Slovenian Research Agency, Ljubljana, Slovenia

National Institute of Chemistry, Ljubljana, Slovenia

Jožef Stefan Institute, Ljubljana, Slovenia

Faculty of Chemistry and Chemical Technology at University of Ljubljana, Slovenia

Faculty of Chemistry and Chemical Engineering at University of Maribor, Slovenia

Faculty of Pharmacy at University of Ljubljana, Slovenia

University of Nova Gorica, Nova Gorica, Slovenia



Acta Chimica Slovenica izhaja štirikrat letno v elektronski obliki na spletni strani <http://acta.chem-soc.si>. V primeru posvečenih števil izhaja revija tudi v tiskani obliki v omejenem številu izvodov.

Acta Chimica Slovenica appears quarterly in electronic form on the web site <http://acta.chem-soc.si>. In case of dedicated issues, a limited number of printed copies are issued as well.

Transakcijski račun: 02053-0013322846 Bank Account No.: SI56020530013322846-Nova Ljubljanska banka d. d., Trg republike 2, SI-1520 Ljubljana, Slovenia, SWIFT Code: LJBA SI 2X

Oblikovanje ovitka – Design cover: KULT, oblikovalski studio, Simon KAJTNA, s. p. Grafična priprava za tisk: Majanafin, d. o. o.

Tisk-Printed by: Tiskarna Stušek, Ljubljana

© Copyright by Slovenian Chemical Society

Graphical Contents



Acta Chimica Slovenica Acta Chimica Slovenica Slovenica Acta Chimica Slovenica

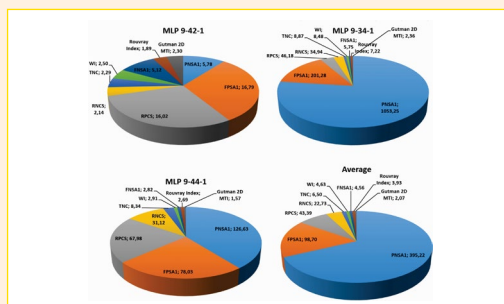
Year 2018, Vol. 65, No. 3

SCIENTIFIC PAPER

483–491 Biomedical applications

Electrostatic and Topological Features as Predictors of Antifungal Potential of Oxazolo Derivatives as Promising Compounds in Treatment of Infections Caused by *Candida albicans*

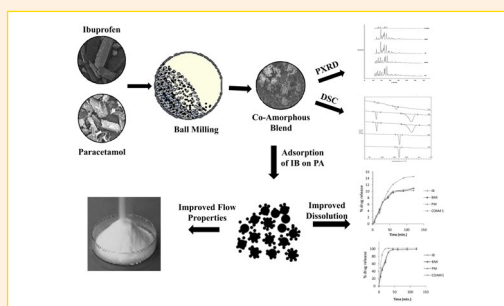
Strahinja Kovačević, Milica Karadžić, Sanja Podunavac-Kuzmanović, Lidija Jevrić, Evica Ivanović and Matilda Vojnović



492–501 Materials science

Co-Amorphization of Ibuprofen by Paracetamol for Improved Processability, Solubility, and *In vitro* Dissolution

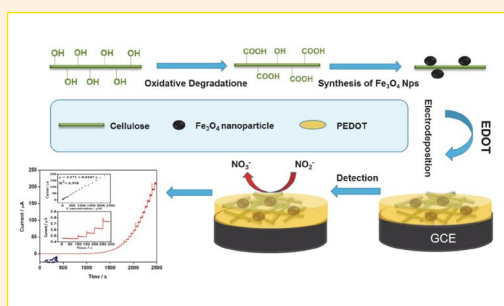
Mayuri S. Bhandari, Sarika M. Wairkar, Udaykumar S. Patil and Namdeo R. Jadhav



502–511 Analytical chemistry

Electrochemical Detection of Nitrite in Food Based on Poly (3,4-ethylenedioxythiophene) Doped with Fe_3O_4 Nanoparticles Loaded Carboxylated Nanocrystalline Cellulose

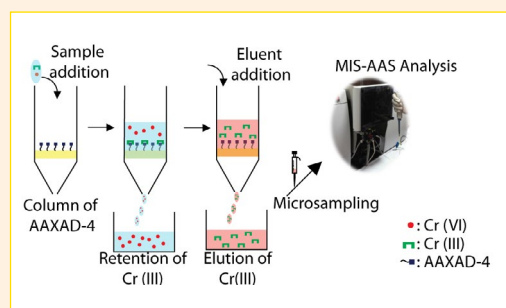
Guiyun Xu, Mingming Zhang and Xijuan Yu



512–520 Analytical chemistry

Chromium Speciation Using an Aminated Amberlite XAD-4 Resin Column Combined with Microsample Injection-Flame Atomic Absorption Spectrometry

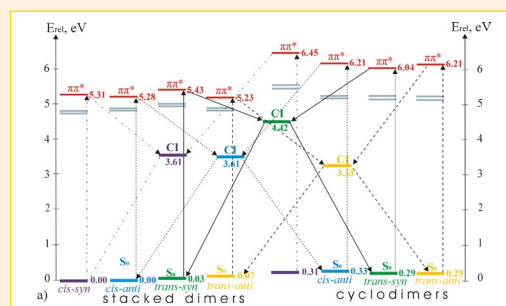
Erkan Aksoy, Şükrü Gökhan Elçi, Ali N. Siyal and Latif Elçi



521–530 Physical chemistry

Comparative Study of the Gas-phase Cyclodimer Formations of Uracil and 6-azauracil in Excited State and through Conical Intersections S_0/S_1

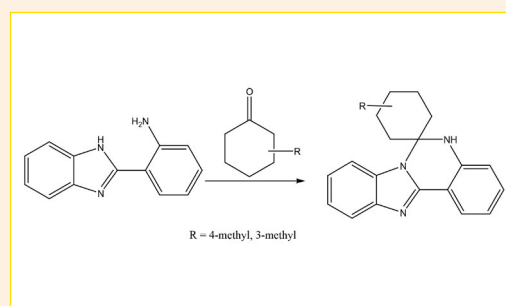
Pavlina Bogomilova Kancheva and Vassil Borissov Delchev



531–538 Organic chemistry

Synthesis, Characterization and Computational Studies of Two Triazaspiro Tetracycles

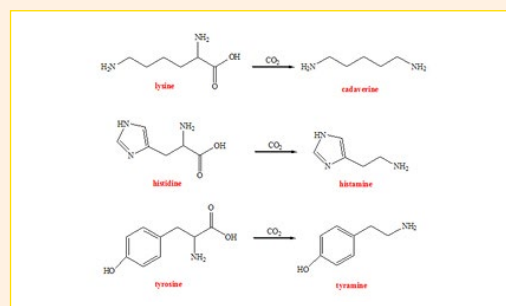
Felix Odame and Eric C. Hosten



539–546 Analytical chemistry

Determination of Biogenic Amines at Low $\mu\text{g L}^{-1}$ Levels as Acetylacetonone Derivatives by RP-HPLC with UV-Visible Detection in Expired Apple Juice Samples

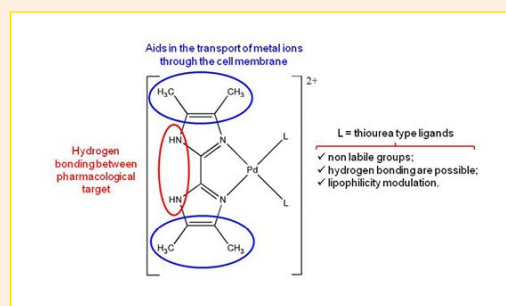
Bediha Akmeses and Adem Asan



547–553 Inorganic chemistry

Synthesis, Characterization and Cytotoxicity Evaluation of New Biimidazole Palladium(II) Complexes with Thioureas

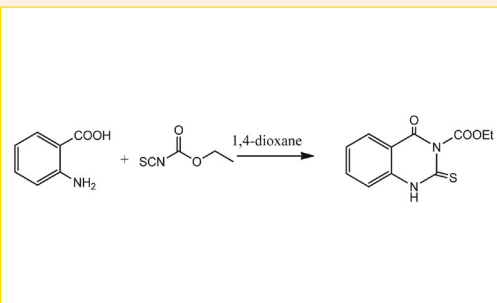
Silmar José Spinardi Franchi, Rodrigo Alves de Souza, Antonio Eduardo Mauro, Iracilda Zeppone Carlos, Livia Carolina de Abreu Ribeiro, Fillipe Vieira Rocha and Adelino Viera de Godoy-Netto



554–568 Organic chemistry

Uses of Anthranilic Acid for the Synthesis of Dihydroquinazolin Derivatives with Antitumor, Antiproliferative and Pim-1 kinase Activities

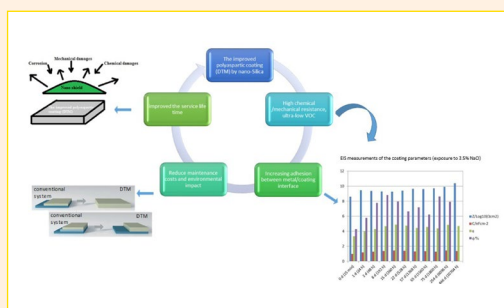
Rafat M. Mohareb and Peter A. Halim



569–577 Materials science

Improving Polyaspartic Anti-Corrosion Coating Protective Properties with the use of Nano-silica

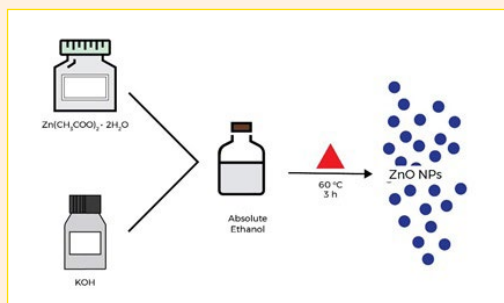
Arezoo Assarian and Sanja Martinez



578–585 Physical chemistry

Synthesis and Characterization of Zinc Oxide Nanoparticles with Small Particle Size Distribution

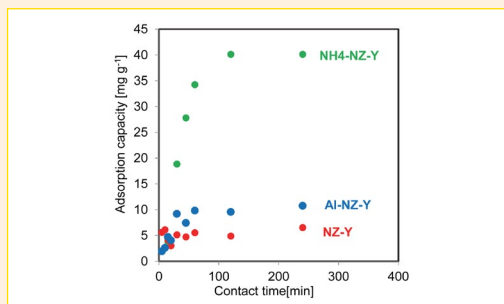
Nuraqeelah Mohammad Shamhari, Boon Siong Wee, Suk Fun Chin and Kuan Ying Kok



586–598 Chemical, biochemical and environmental engineering

Role of Modification of Natural Zeolite in Removal of Arsenic from Aqueous Solutions

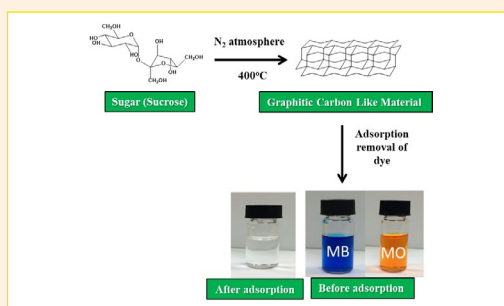
Ayten Ates, İnci Özkan and Gamze Topal Canbaz



599–610 Chemical, biochemical and environmental engineering

Adsorptive Removal of Selected Anionic and Cationic Dyes by Using Graphitic Carbon Material Prepared from Edible Sugar: A Study of Kinetics and Isotherms

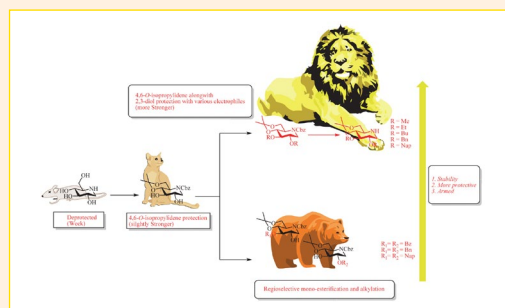
Lakshmi Prasanna Lingamdinne, Jong-Soo Choi, Jae-Kyu Yang, Yoon-Young Chang, Janardhan Reddy Koduru and Jiwan Singh



611–620 Organic chemistry

Selective Protection/Deprotection in 1-Deoxynojirimycin Scaffold: Regioselective Mono-Benzylation and Alkylation using TBAB-NaOH Catalytic System

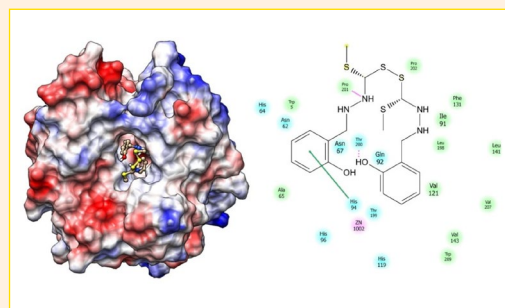
Mehwish Iftikhar and Zhijie Fang



621–629 Organic chemistry

Synthesis, Characterization, Crystal Structure and Molecular Docking Studies of a S-methyldithiocarbamate Derivative: Bis[2-hydroxy- benzylidenehydrazono) ...

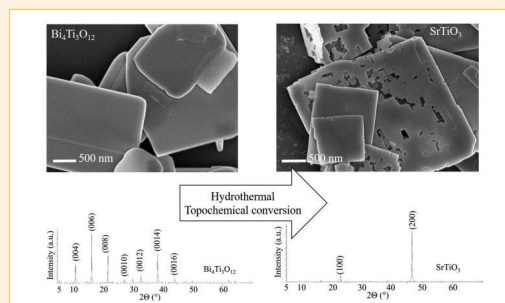
Winaki P. Sohtun, Arunachalam Kannan, K. Hari Krishna, Dhandayutham Saravanan, Muthuvel Suresh Kumar, and Marappan Velusamy



630–637 Materials science

Plate-Like $\text{Bi}_4\text{Ti}_3\text{O}_{12}$ Particles and their Topochemical Conversion to SrTiO_3 Under Hydrothermal Conditions

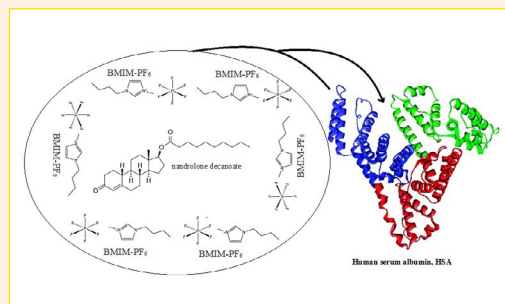
Alja Čontala, Marjeta Maček Kržmanc and Danilo Suvorov



638–654 Physical chemistry

Enhanced Transport of Nandrolone Decanoate Drug by Human Serum Albumin in Presence of [BMIM]PF₆ and [BMIM]BF₄

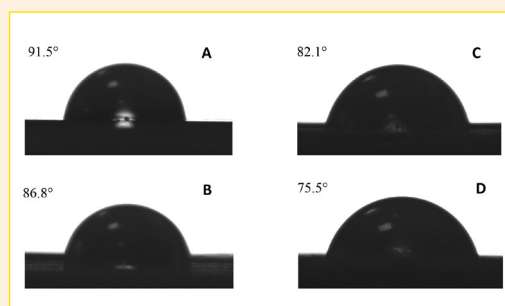
Zeyad J. Yasseen, Salman M. Saadeh and Hazem M. Abu Shawish



646–651 Materials science

Effects of Magnesia Incorporation on Properties of Polystyrene/Magnesia Composites

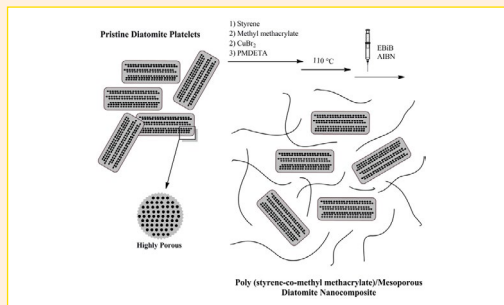
Salah Eddine Hachani, Abdulmounem Alchekh wis, Zelikha Necira, Nadia Nebbache, Ahmed Meghezzi and Guralp Ozkoc



652–611 Materials science

SR&NI Atom Transfer Radical Random Copolymerization of Styrene and Methyl Methacrylate: Incorporation of Diatomite Platelets

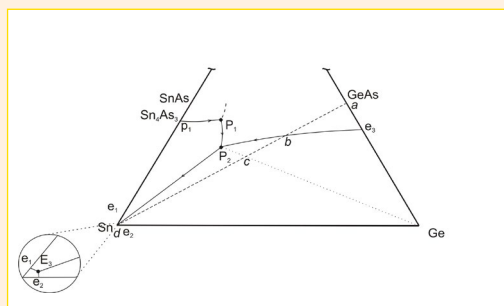
Khezrollah Khezri, Hassan Alijani and Yousef Fazli



662–669 Materials science

Phase Diagram of the Sn–As–Ge System

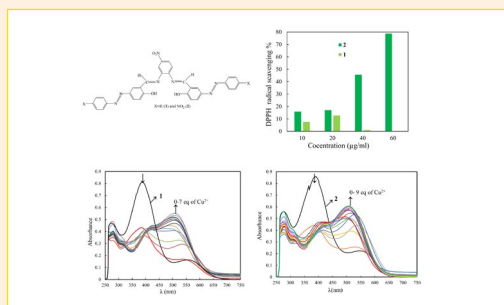
Galina V. Semenova, Elena Yu. Proskurina, Tatiana P. Sushkova and Victor N. Semenov



670–678 Inorganic chemistry

Optical Response of Two Azo Ligands Containing Salicyaldimine-based Ligand as Side Chains Towards Some Divalent Metal Ions and Their Antioxidant Behavior

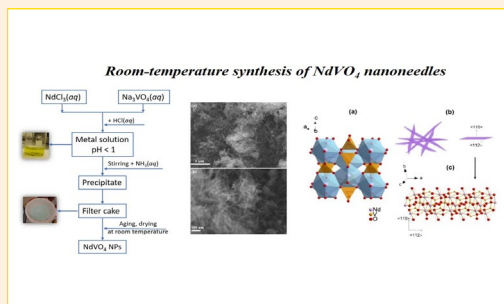
Zohreh Shaghghi and Gholamreza Dehghan



679–686 Materials science

Room-Temperature Synthesis and Optical Properties of NdVO₄ Nanoneedles

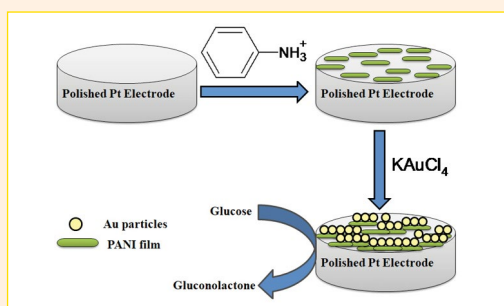
Mirela Dragomir and Matjaž Valant



687–697 Applied chemistry

Amperometric Enzyme-Free Glucose Sensor Based on Electrodeposition of Au Particles on Polyaniline Film Modified Pt Electrode

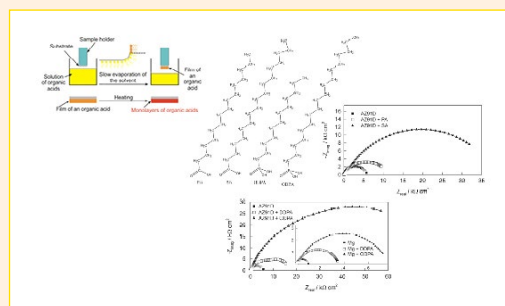
Shveta Malhotra, Yijun Tang and Pradeep K. Varshney



698–708 Materials science

Surface Modifications of the Biodegradable Magnesium Based Implants with Self-Assembled Monolayers Formed by T-BAG Method

Ivana Škugor Rončević, Nives Vladislavić and Marijo Buzuk



709–717 Applied chemistry

Adsorptive Removal of Cationic and Anionic Dyes from Aqueous Solutions by Using Eggshell Household Waste as Biosorbent

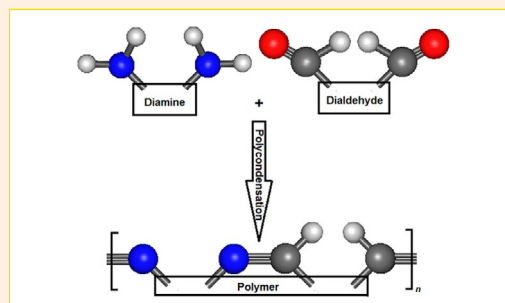
Eszter Rápó, Robert Szép, Ágnes Keresztesi, Maria Suciú and Szende Tonk



718–729 Materials science

Synthesis and Characterization of New Photoresponsive, Ortho and Para Oriented Azomethine Polymers

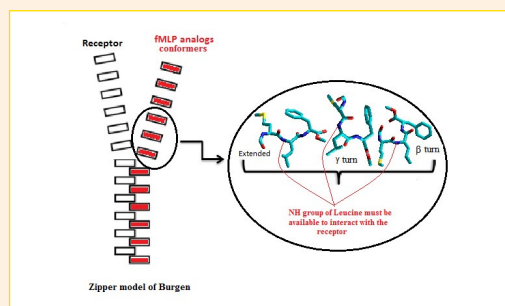
Farah Qureshi Muhammad Yar Khuhawar and Taj Muhammad Jahangir



730–738 Physical chemistry

Structural Requirements for Molecular Recognition by fMLP Analogs Receptors: Comparative Conformational Analysis of (for-Met-Leu-Phe-OMe) and its Thioamide Analog (for-Met-Leuψ[CSNH]Phe-OMe)

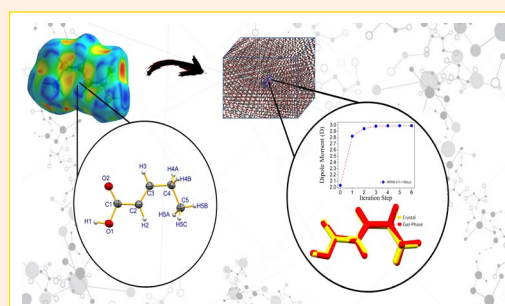
Chakib Ameziane Hassani, Mourad Houssat, Jamal Eddine Hazm and Ahmed Harrach



739–749 Physical chemistry

Third-Order Nonlinear Optical Properties of a Carboxylic Acid Derivative

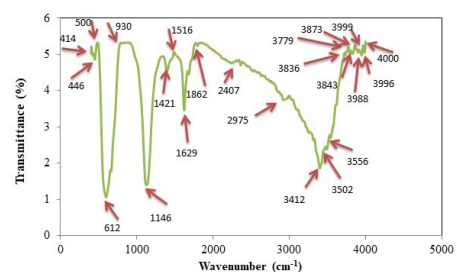
Clodoaldo Valverde, Sizelizio Alves de Lima e Castro, Gabriela Rodrigues Vaz, Jorge Luiz de Almeida Ferreira, Basílio Baseia, and Francisco A. P. Osório



750–756 Chemical, biochemical and environmental engineering

Synthesis of Fe₃O₄ Nanoparticles Modified by Oak Shell for Treatment of Wastewater Containing Ni(II)

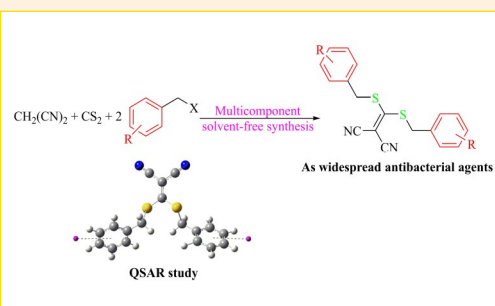
Seyyed Mojtaba Mousavi, Seyyed Alireza Hashemi, Hossein Esmaeili, Ali Mohammad Amani and Fatemeh Mojoudi



757–767 Organic chemistry

Multicomponent Solvent-Free Synthesis, Antibacterial Evaluation and QSAR Study of 2-(Bis(benzylthio)methylene)malononitriles

Hamid Beyzaei, Parviz Baranipour, Reza Aryan, Pouya Karimi, Mahmood Sanchooli and Hojat Samareh Delarami



Scientific paper

Electrostatic and Topological Features as Predictors of Antifungal Potential of Oxazolo Derivatives as Promising Compounds in Treatment of Infections Caused by *Candida albicans*

Strahinja Kovačević,^{1,*} Milica Karadžić,¹ Sanja Podunavac-Kuzmanović,¹ Lidija Jevrić,¹ Evica Ivanović² and Matilda Vojnović³

¹ University of Novi Sad, Faculty of Technology Novi Sad, Bulevar cara Lazara 1, 21000 Novi Sad, Serbia

² University of Belgrade, Faculty of Agriculture, Nemanjina 6, 11080 Belgrade-Zemun, Serbia

³ University of Novi Sad, Faculty of Medicine, Hajduk Veljkova 3, 21000 Novi Sad, Serbia

* Corresponding author: E-mail: strahko@uns.ac.rs,
phone: +381214853666, fax: +38121450413

Received: 15-05-2017

Abstract

The results presented in this study include the prediction of the antifungal activity of 24 oxazolo derivatives based on their topological and electrostatic molecular descriptors, derived from the 2D molecular structures. The artificial neural network (ANN) method was applied as a regression tool. The input data for ANN modeling were selected by stepwise selection (SS) procedure. The ANN modeling resulted in three networks with the outstanding statistical characteristics. High predictivity of the established networks was confirmed by comparisons of the predicted and experimental data and by the residuals analysis. The obtained results indicate the usefulness of the formed ANNs in precise prediction of minimum inhibitory concentrations of the analyzed compounds towards *Candida albicans*. The Sum of Ranking Differences (SRD) method was used in this study to reveal possible grouping of the compounds in the space of the variables used in ANN modeling. The obtained results can be considered to be a contribution to development of new antifungal drugs structurally based on oxazole core, particularly nowadays when there is a lack of highly efficient antimycotics.

Keywords: Artificial neural networks; Antifungal activity; Molecular topology; Electrostatic descriptors; QSAR; Sum of Ranking Differences

1. Introduction

Quantitative structure-activity relationship (QSAR) approach is an attempt to remove the trial-and-error element from drug design by using high-quality mathematical relationships which relate measurable physicochemical parameter(s) as independent variable(s) and a biological response (a dependent variable).¹ These variables have been correlated in many QSAR studies applying various chemometric regression methods, as linear regression (LR), multiple linear regression (MLR), polynomial regression (PR), artificial neural networks (ANN), partial least squares regression (PLS), principal component regression (PCR), etc.^{2–8} Any high-quality model obtained

by aforementioned chemometric techniques may be used by the chemist in order to facilitate the synthesis of more effective drugs. A high-quality QSAR model must be based on reasonable number of tested compounds, characterized by good values of statistical parameters, defined for particular application domain and suitably validated by internal and external validation approaches. Using these QSAR models, it is possible to precisely calculate the theoretical activity of compounds prior to their synthesis, and thus decrease financial expenses and time needed for the experimental work.

The selection of appropriate regression method depends on nature of the variables. ANN method is suitable for correlation analysis when there is a complex relation-

ship between the variables, as in the case of biological systems. The complex relationships between biological activity and molecular characteristics are not unusual, since there are many factors which have certain influence on biological effect of a compound, such as lipophilicity, dissociation, molecular weight, presence of polar/non-polar functional groups, conformation, etc. In the present paper, the electrostatic and topological characteristics of benzoxazoles and oxazolo[4,5-*b*]pyridines were used as predictors of their antifungal activity against *Candida albicans*. Topological descriptors of a compound can be calculated based on molecular graphs that are hydrogen-suppressed. In these graphs the bonds are presented by edges and atoms by vertices.⁹ Simple topological descriptors are based on the counting of some specific graph elements (Kier shape descriptors, Hosoya Z index, pat/walk shape indices, self-returning walk counts), but the most common topological descriptors are obtained by using some algebraic operators.⁹ In QSAR and quantitative structure–property relationship (QSPR) modeling, the graph-invariants have been effectively used in characterization of the structural similarity and dissimilarity of compounds.⁹ There is no need for energy minimization of the molecular structure for calculation of topological descriptors. Electrostatic descriptors describe many of the electrical characteristics of molecules, such as polarity, dipole moment, polarizability, ionization energy, etc. These characteristics certainly have an influence on interactions between the molecule and its surroundings, in example interactions with cell membranes, extra- and intercellular molecules.

The most popular classes of molecules that are used in treatment of infections caused by *Candida* species are polyenes, azoles, analogs of nucleosides, allylamines, etc. In treatment of *Candida albicans* infections, fluconazole, as one of the members of azoles, is definitely one of the most popular antifungals. According to previous studies, *Candida* has developed high-level resistance toward some azole antifungal drugs.¹⁰ However, some oxazole analogs, such as oxazolo[4,5-*b*]pyridines and benzoxazoles expressed significant antifungal activity and are considered to be a very good basis for development of new antifungal therapeutics. This study presents our efforts to define sophisticated QSARs that would be limited on prediction of antifungal activity of structurally similar oxazolo[4,5-*b*]pyridines and benzoxazoles toward *Candida albicans*. The existing QSARs have been defined on the basis of MLR, PCR and PLS regression methods applying lipophilicity and some physicochemical descriptors.^{11–14} The ANN method with absorption, distribution, metabolism and excretion (ADME) descriptors was applied for the same purpose as well.¹⁴ However, this study explores the importance of topological and electrostatic characteristics of a series of benzoxazoles and oxazolo[4,5-*b*]pyridines in prediction of their antifungal activity toward *Candida albicans*.

2. Material and Methods

2. 1. The Studied Series of Oxazolo[4,5-*b*]pyridines and Benzoxazoles

Structural formulae of the analyzed benzoxazoles and oxazolo[4,5-*b*]pyridines are presented in Figure 1. The

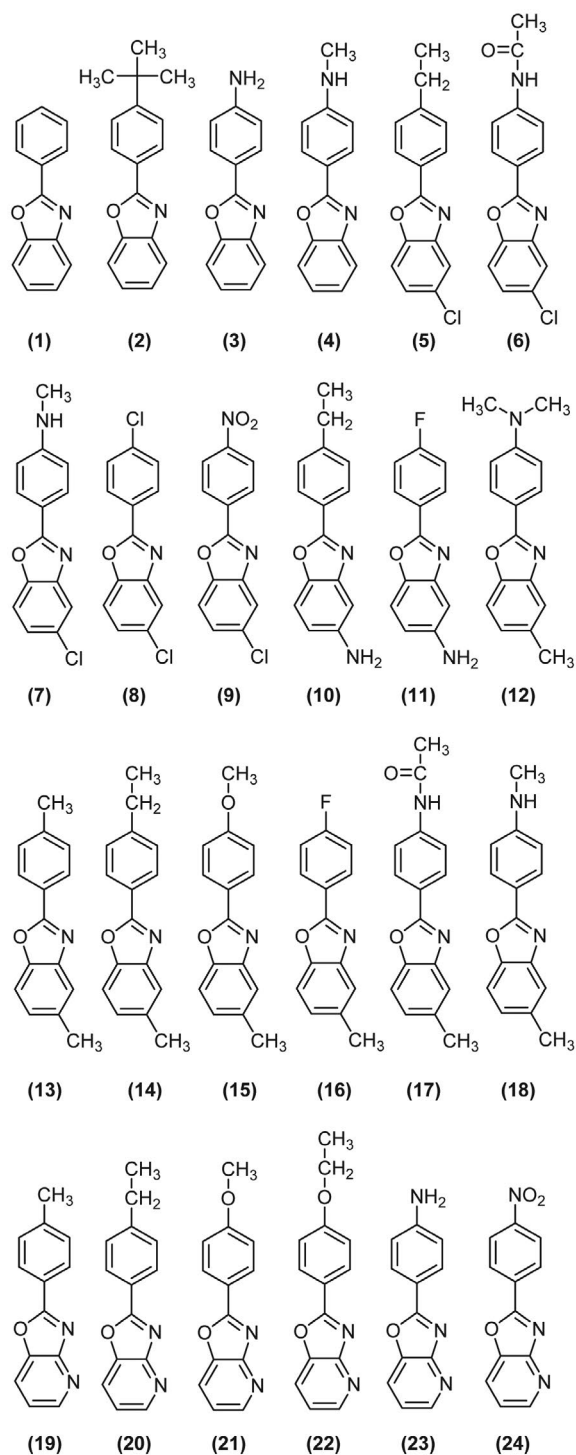


Figure 1. The molecular structures of the analyzed oxazole derivatives

analyzed compounds possess various types of substituents/functional groups, including *tert*-butylphenyl, ethylphenyl, dimethyl, chlorophenyl, nitrophenyl, fluorophenyl, methoxyphenyl, ethoxyphenyl and acetamide groups. The experimental results of determination of the antifungal activity of studied derivatives against *Candida albicans* MTCC 183 are given in literature.¹⁵ Antifungal activity in the form of minimum inhibitory concentration (MIC), that was used in further QSAR–ANN modeling, was mathematically transformed in the form of logarithm of the MIC reciprocal value, $\log(1/c_{MIC})$.

2. 2. Electrostatic and Topological Descriptors Calculation

The set of 35 electrostatic and 10 topological descriptors was calculated by using PreADMET online software.¹⁶ The structural optimization and energy minimization were not required since the molecular descriptors were calculated on the basis of 2D structures. The values of the calculated descriptors are shown in Supplementary data (Table S1).

2. 3. Chemometric Methods

The first step in chemometric analysis was the selection of the most appropriate descriptors which will be used as inputs in ANN modeling. For this purpose, stepwise selection (SS) procedure was applied by using NCSS statistical software.¹⁷ In the SS procedure minimum change in the root mean square error (*RMSE*) was used as a measure for removing or adding variables. In the present analysis, the limit of *RMSE* change was set at 0.05.

Artificial neural networks are a non-linear chemometric tool. They have been widely applied in modeling of complex relationships between different type of variables, which is usually the case in prediction of biological activity of many biologically active compounds. An ANN consists of several layers: the input layer, one or more hidden layers, and one output layer.¹⁸ The ANNs were trained applying the feedforward multilayer perceptron (MLP) ANN function with Broyden–Fletcher–Goldfarb–Shanno (BFGS) learning algorithm in Statistica 10.0 software.¹⁹ The data normalization was carried out by *min-max* normalization method.^{20, 21}

Prior to ANN modeling, the analyzed compounds were divided into the training set (compounds **1**, **2**, **3**, **4**, **5**, **6**, **8**, **9**, **11**, **13**, **15**, **17**, **18**, **19**, **20**, **21**, **22** and **23**), validation set (compounds **12**, **14** and **24**) and test set (compounds **7**, **10** and **16**).

The estimation of the contribution of every input variable in a network was done by calculation of Global sensitivity analysis (GSA) coefficients.²² A GSA coefficient describes the ANN's outputs changes that are caused by variations in the parameters that affect the ANN. If the GSA index is higher than 1, the greater change in ANN's

performance is achieved with minor variation in the input variable.^{22, 23}

The ANN models' validity was estimated on the basis of the following statistical parameters: *R* (correlation coefficient), *R_{tr}* (correlation coefficients of training set), *R_t* (correlation coefficients of test set), *R_v* (correlation coefficients of validation set), *RMSE* (root mean square error), *RMSE_{tr}* (root mean square error of training set), *RMSE_t* (root mean square error of test set), *RMSE_v* (root mean square error of validation set), *F*-test, variation coefficient (*VC*) and significance level (*p*). Also, the analysis of residuals and the graphical comparison of predicted and experimental data were carried out in order to estimate predictive ability of ANN models.

SRD method was used as relatively new approach in comparison of samples, compounds, models.²⁴ The purpose of the SRD analysis in this study was to reveal possible similarities or dissimilarities among the analyzed molecules on the basis of their topological and electrostatic descriptors used in ANN modeling. In the SRD analysis the row average values were used as the reference ranking. It is substantially different than hierarchical cluster analysis (HCA) and principal component analysis (PCA) approaches. The SRD methodology, its algorithms and practical uses are described in details in literature.^{24–26} The validation of SRD analysis was done by comparison of ranks by random numbers (CRRN) and 7-fold cross-validation.²⁴

3. Results and Discussion

3. 1. The Selection of Suitable Variables – SS Procedure

SS analysis was conducted after the descriptors calculation procedure. The significance level of 0.05 was required for a variable to enter the equation, while the significance level of 0.20 was used as a criterion for removal of variables from the model. The iterations number was set at

Table 1. The results of stepwise selection procedure.

Iteration number	Action	Variable	R ²	Sqrt(MSE)
0	Unchanged		0.0000	0.1253
1	Added	RPCS	0.2914	0.1078
2	Added	PNSA1	0.5010	0.0926
3	Added	RNCS	0.5764	0.0874
4	Added	FNSA1	0.6175	0.0853
5	Added	Rouvray_Index	0.6963	0.0780
6	Added	FPSA1	0.8093	0.0636
7	Added	WI	0.8990	0.0477
8	Added	Gutman_2D_MTI	0.9150	0.0452
9	Added	TNC	0.9240	0.0443
10	Unchanged		0.9240	0.0443

500. As a result of SS analysis, the subset of 9 calculated descriptors was formed (Table 1).

The selected descriptors, suggested by SS analysis, are the following: RPCS (relative positive charge surface area), PNSA1 (partial negative surface area 1st type), RNCS (relative negative charge surface area), FNSA1 (fractional charged partial negative surface area 1st type), Rouvray index, FPSA1 (fractional charged partial positive surface area 1st type), WI (Wiener index), Gutman 2D MTI (Gutman 2D molecular topological index) and TNC (total negative charge). This subset of 9 descriptors was used as the input variables for further ANN modeling.

3. 2. ANN Modeling and Validation of Models

The ANN modeling resulted into three statistically very good models, whose activation functions and statisti-

Table 2. The results of ST-ANN procedure.

Network architecture	MLP 9-7-1	MLP 9-13-1	MLP 9-14-1
R_{train}	0.9701	0.9759	0.9726
R_{test}	0.9534	0.9909	0.9786
R_{val}	0.9986	0.9997	0.9986
$RMSE_{train}$	0.002930	0.002456	0.002875
$RMSE_{test}$	0.001077	0.000669	0.000082
$RMSE_{val}$	0.005169	0.013497	0.003369
F -test	350.7	295.6	431.6
$VC(\%)$	0.79	0.84	0.68
p -value	0.000000	0.000000	0.000000
Hidden activation	Tanh	Tanh	Tanh
Output activation	Exponential	Exponential	Exponential
Training algorithm	BFGS 20	BFGS 20	BFGS 19

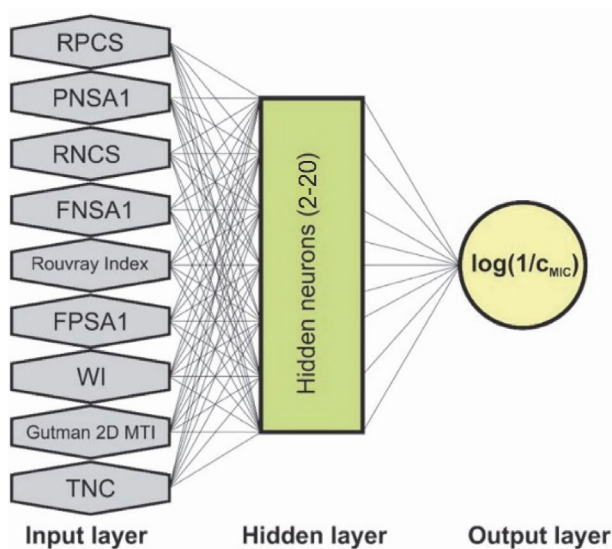


Figure 2. The general architecture of the established QSAR-ANN models.

cal parameters are presented in Table 2. The comparison of statistical quality of the obtained ANNs was done based on these parameters. Exponential (*Exp*) and tangent (*Tanh*) functions were used as MLP activation functions for hidden and output neurons. The total number of 150 ANNs was obtained, but only three ANNs were chosen as the best ones. During the training of the networks, the number of neurons in the hidden layer varied in the range of 2–20. The architecture of the obtained ANNs is presented in Figure 2.

Based on the data given in Table 2 it can be seen that the statistical quality of selected ANNs is very similar. The comparison of the ANNs quality was estimated by comparing their R and $RMSE$ values (Figure 3). The comparisons of $RMSE$ and R indicate that the network MLP 9-14-1 make the best concurrence of the data (the highest R) with the lowest $RMSE$ values (Figure 3).

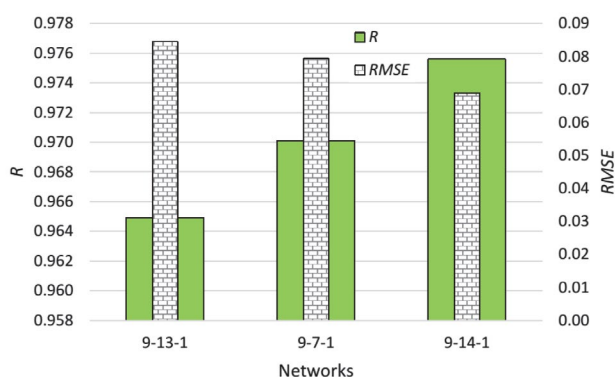


Figure 3. Comparisons of R and $RMSE$ values of the established networks.

The prediction ability of the established networks is tested by the graphical comparison of the predicted and experimental $\log(1/c_{MIC})$ values (Figure 4). The outstanding concurrence between the predicted and experimental values and small scattering of the points around linear relationship indicate high quality of the obtained models. Also, the slope of this linear relationship is very close to 1 and the intercept is very close to zero. This is another proof of the outstanding predictive ability of the ANNs. The residuals *versus* predicted $\log(1/c_{MIC})$ values plots for the established networks are presented in Figure 5. The presented ANN models fit the data well since the residuals behave randomly, which is obvious from the presented plots. The amplitude of the residuals is in acceptable range. The application of the external test set confirmed the quality of the established networks.

Other confirmation of reliability of the obtained networks is individual percentage deviations (IPD%) for experimental–predicted values pairs. Figure 6 shows that all three ANNs have almost all IPD% values lower than 2.0% which indicates acceptable differences between predicted and experimental $\log(1/c_{MIC})$ values.

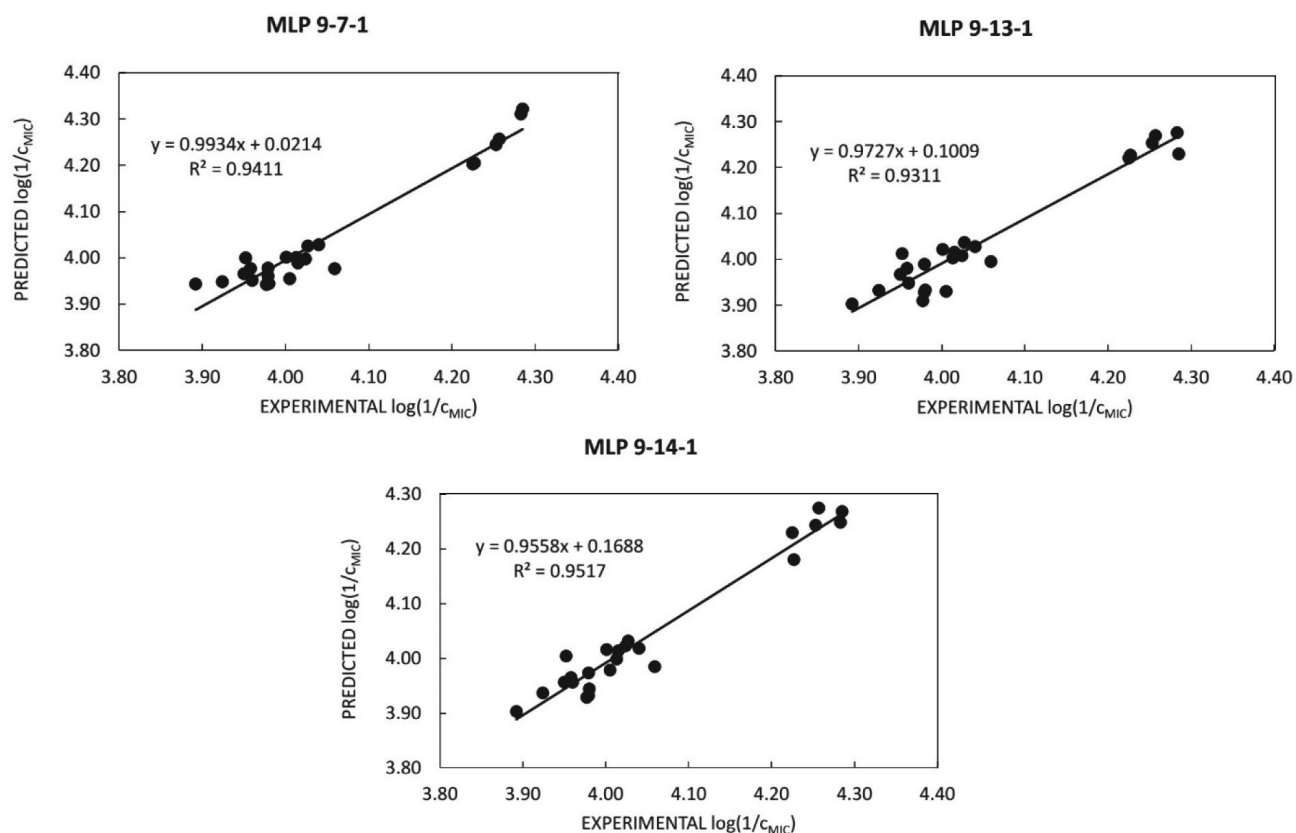


Figure 4. Correlations between the experimental and predicted antifungal activity of the analysed compounds.

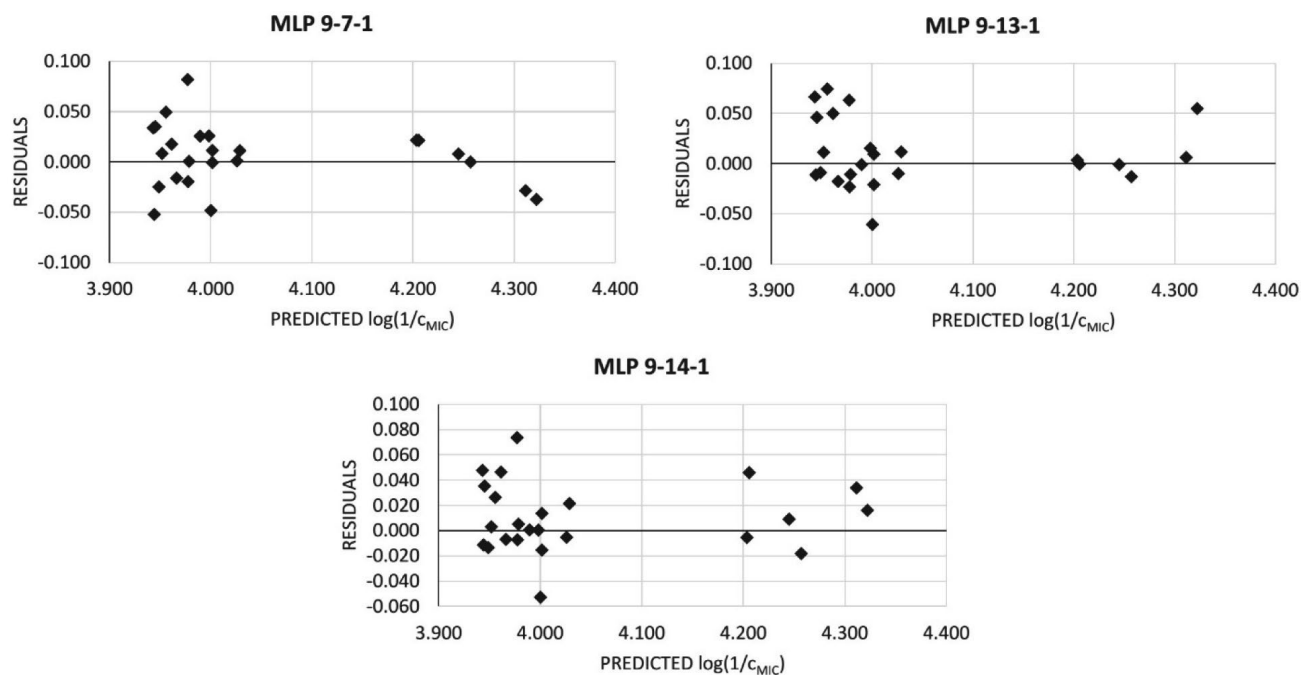


Figure 5. Predicted vs. residual values plots.

3. 3. Global Sensitivity Analysis

As the result of global sensitivity analysis, the GSA coefficients were calculated by the applied software for ev-

ery input variable. A GSA coefficient is presented in the following form:

$$GSA = \frac{ERR_o}{ERR_p} \quad (1)$$

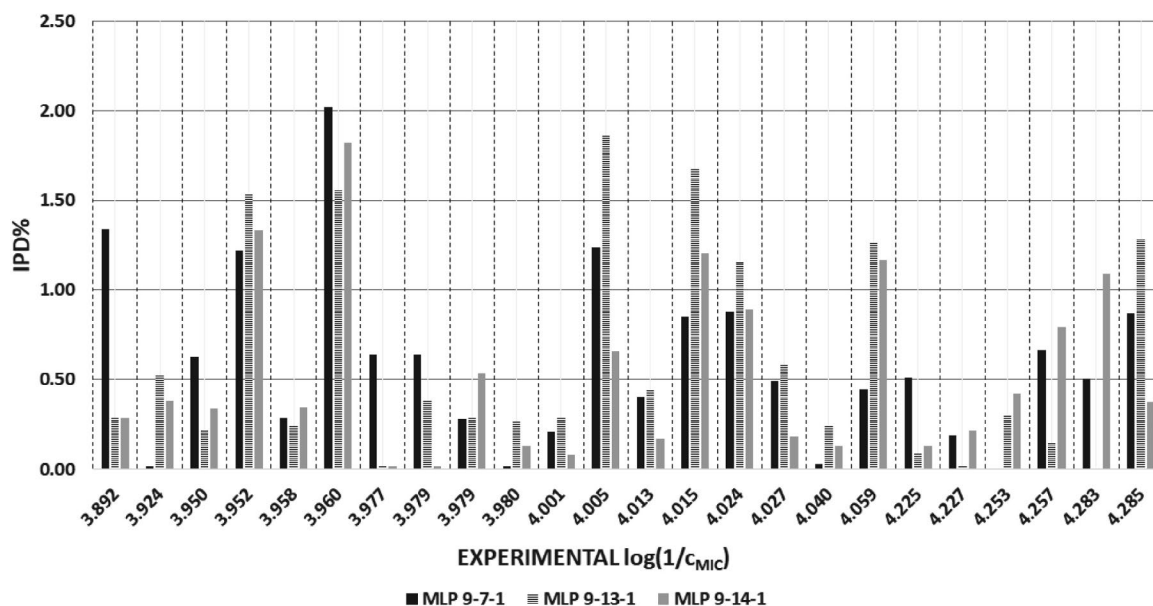


Figure 6. Individual percentage deviations (IPD%) of predicted values compared with the experimental values.

where ERR_o is the network error when the observed input variable is omitted and ERR_p is the network error when the observed input variable is included in the model. The GSA coefficients for MLP 9-7-1, MLP 9-13-1 and MLP 9-14-1 networks are given in Figure 7. As it is shown in the pie charts, each input variable is described by GSA coefficient higher than 1. This indicates a significance of each input variable, particularly the significance of RPCS, FPSA1 and PNSA1 descriptors (the highest average GSA coefficients).

In comparison with the results of QSAR analysis of oxazolo[4,5-*b*]pyridines and benzoxazoles previously published in literature,^{13,14} the results described in the present paper are based on non-linear prediction of their antifungal activity based on topological and electrostatic descriptors, while in the previous studies¹³ the linear modeling (PCR and PLS) of the antifungal activity have been carried out on the basis of some physicochemical and lipophilicity descriptors, as well as non-linear prediction (ANN) of antifungal activity based on some ADME descriptors.¹⁴ The presented results emphasized the influence of electrostatic and topological molecular features on the antifungal activity based on the established non-linear models. These models can be considered slightly statistically better than the models presented in literature.^{13,14}

3. 4. Sum of Ranking Differences Analysis of Oxazolo[4,5-*b*]pyridines and Benzoxazoles

SRD analysis was carried out on the basis of average row values as the reference value of the variables included in the ANN models (consensus ranking). The results of the SRD analysis (Figure 8) indicate the separation of the compounds into three main groups and detection of one outlier.

The first group (the compounds 2, 10, 13, 17, 19, 20, 21, 22 and 23) is characterized by the ranking number 0, which means that these compounds have the same ranking as the reference one. The second group (the compounds 1, 3, 4, 5, 7, 8, 11, 12, 14, 15 and 16) has the ranking number 2 and third group (the compounds 6, 9 and 24) the ranking number 4. The second and third group are considered to be very close to the reference ranking and contain most of the benzoxazole derivatives. However, the compound 18, with the ranking number 6, is separated from the other compounds, but still can be considered relatively close to the reference ranking in the variable space (since it fits very well in the established QSAR models, it is not considered to be an outlier in the QSAR models). This compound has most of the molecular descriptors that are significantly different from the molecular descriptors of other compounds. Generally, oxazolo[4,5-*b*]pyridines are placed in the first group, indicating their distinctiveness regarding RPCS, PNSA1, RNCS, FNSA1, Rouvray index, FPSA1, WI, Gutman 2D MTI and TNC molecular features. The compounds 9 and 24 from the third group are specific due to the presence of $-NO_2$ functional group in their structures. The presented results of SRD analysis of oxazolo[4,5-*b*]pyridines and benzoxazoles revealed particular similarities/dissimilarities among the analyzed derivatives. This fact could be particularly interesting for further 3D-QSAR and 4D-QSAR modeling and molecular docking studies of antifungal activity of oxazolo[4,5-*b*]pyridines and benzoxazoles toward *Candida albicans*.

4. Conclusions

The conducted variable selection procedure and artificial neural network modeling resulted in three reliable

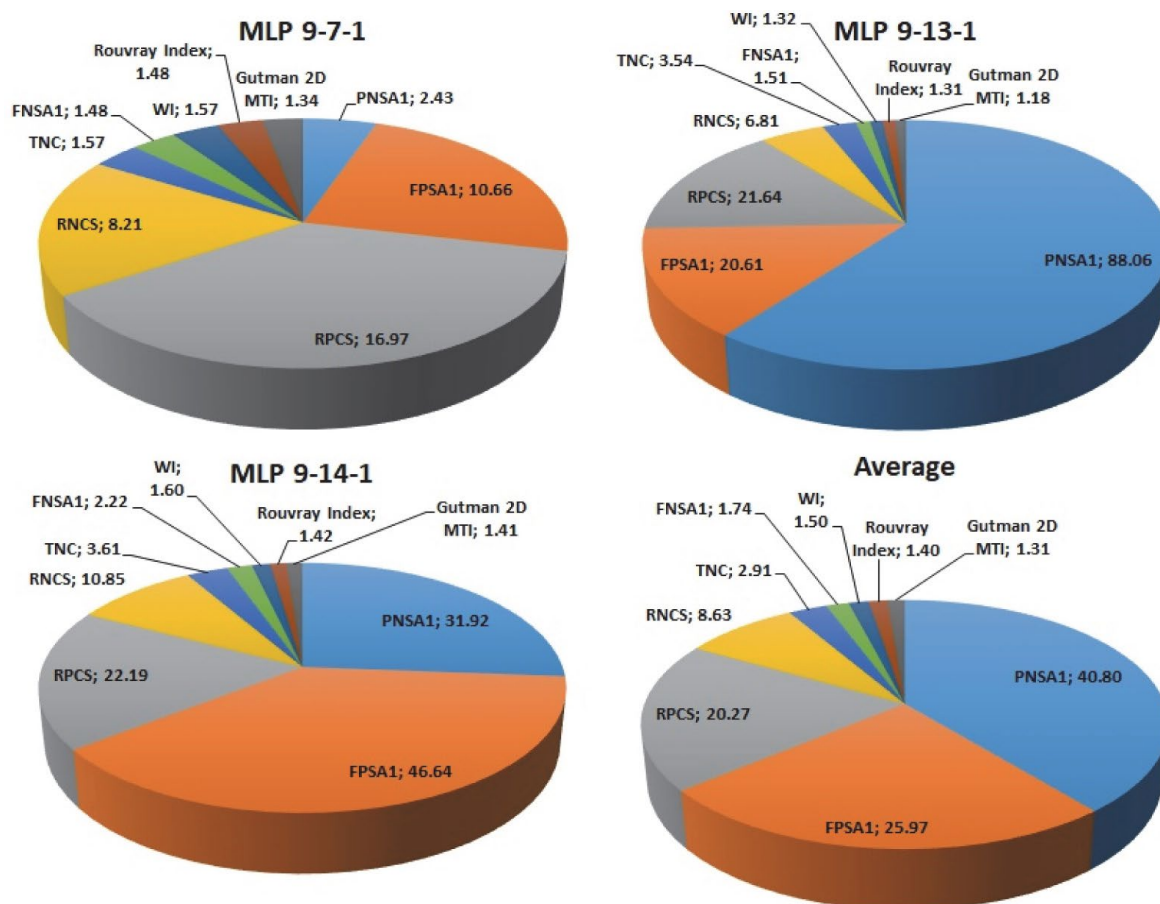


Figure 7. The GSA coefficients of the established ANNs and their average values.

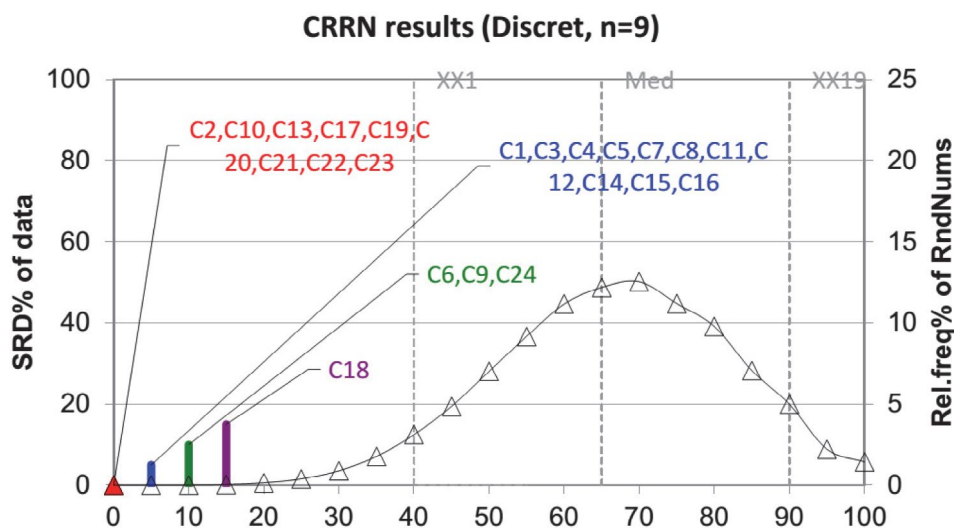


Figure 8. The result of SRD-CRRN analysis of oxazolo[4,5-*b*]pyridines and benzoxazoles. The statistical properties of theoretical distribution function are: first icosale (5%), XX1 = 16; first quartile, Q1 = 22; median, Med = 26; last quartile, Q3 = 32; last icosale (95%), XX19 = 36.

neural networks which can be used in prediction of anti-fungal potential of structurally similar oxazolo[4,5-*b*]pyridines and benzoxazoles. The prediction ability of the obtained networks has been confirmed by adequate statistical

measures, by comparisons of the experimental and predicted data including the residuals analysis. Applying stepwise selection procedure, the most important electrostatic and topological descriptors were determined: RPCS,

PNSA1, RNCS, FNSA1, Rouvray index, FPSA1, WI, Gutman 2D MTI and TNC. These descriptors can be used as predictor variables in assessment of minimum inhibitory concentrations of novel oxazolo[4,5-*b*]pyridine and benzoxazole derivatives prior to their synthesis, and in that way, facilitate synthesis of more effective antifungal agents. The SRD-CRRN analysis, which was based on the molecular descriptors included in the ANN models and average row values as a reference ranking, detected certain structural similarities in the applied variable space.

5. Acknowledgement

The research presented in this paper is financially supported by the Project No. 172012 of the Ministry of Education, Science and Technological Development of the Republic of Serbia.

6. Abbreviations

ADME – Absorption, Distribution, Metabolism and Excretion
 ANN – Artificial Neural Networks
 BFGS – Broyden–Fletcher–Goldfarb–Shanno algorithm
 CRRN – Comparison of Ranks with Random Numbers
 GSA – Global Sensitivity Analysis
 HCA – Hierarchical Cluster Analysis
 LR – Linear Regression
 MIC – Minimum Inhibitory Concentration
 MLP – Multi Layer Perceptron
 PCA – Principal Component Analysis
 PCR – Principal Component Regression
 PLS – Partial Least Squares
 PR – Polynomial Regression
 QSAR – Quantitative Structure–Activity Relationship
 QSPR – Quantitative Structure–Property Relationship
 RMSE – Root Mean Square Error
 SRD – Sum of Ranking Differences

7. References

- G. Thomas (Ed.), *Fundamentals of Medicinal Chemistry*, 1st edn, John Wiley and Sons, New York, **2003**, pp 71–93.
- S. O. Podunavac-Kuzmanović, D. D. Cvetković, D. J. Barna, *Int. J. Mol. Sci.* **2009**, *10*, 1670–1682. DOI:10.3390/ijms1004167
- B. Hemmateenejad, *J. Chemometr.* **2004**, *18*, 475–485. DOI:10.1002/cem.891
- O. Farkas, J. Jakus, K. Heberger, *Molecules* **2004**, *9*, 1079–1088. DOI:10.3390/91201079
- A. Puratchikody, G. Nagalakshmi, M. Doble, *Chem. Pharm. Bull.* **2008**, *56*, 273–281. DOI:10.1248/cpb.56.273
- S. O. Podunavac-Kuzmanović, D. D. Cvetković, L. R. Jevrić,

- N. J. Uzelac, *Acta Chim. Slov.* **2013**, *60*, 26–33.
- S. Z. Kovačević, S. O. Podunavac-Kuzmanović, L. R. Jevrić, E. A. Djurendić, J. J. Ajduković, *Eur. J. Pharm. Sci.* **2014**, *62*, 258–266. DOI:10.1016/j.ejps.2014.05.031
- I. N. Weaver, D. F. Weaver, *J. Math. Chem.* **2013**, *51*, 811–816. DOI:10.1007/s10910-013-0143-x
- R. Todeschini, V. Consoni (Eds.), *Handbook of molecular descriptors*, Wiley-VCH, Dusseldorf, Germany, 2000, pp 50–58. DOI:10.1002/9783527613106
- S. G. Whaley, E. L. Berkow, J. M. Rybak, A. T. Nishimoto, K. S. Barker, P. D. Rogers, *Front. Microbiol.* **2017**, *7*, 2173, 1–12.
- S. O. Podunavac-Kuzmanović, S. D. Velimirović, *APTEFF* **2010**, *41*, 177–185. DOI:10.2298/APT1041177P
- S. O. Podunavac-Kuzmanović, L. R. Jevrić, S. Z. Kovačević, N. D. Kalajdzija, *APTEFF* **2012**, *43*, 273–282. DOI:10.2298/APT1243273P
- S. Z. Kovačević, S. O. Podunavac-Kuzmanović, L. R. Jevrić, *Acta Chim. Slov.* **2013**, *60*, 756–762.
- S. Z. Kovačević, S. O. Podunavac Kuzmanović, L. R. Jevrić, N. D. Kalajdzija, *APTEFF* **2013**, *44*, 249–258. DOI:10.2298/APT1344249K
- O. Ursu, A. Costescu, M. V. Diudea, B. Parv, *Croat. Chem. Acta* **2006**, *79*, 483–488.
- PreADMET software, URL: <http://preadmet.bmdrc.org/> (Assessed on April 4, 2017)
- Hintze J, NCSS and GESS, NCSS, LLC, Kaysville, Utah, <http://www.ncss.com/>
- S. B. Gadzuric, S. O. Podunavac Kuzmanovic, A. I. Jokic, M. B. Vranes, N. Ajdukovic, S. Z. Kovacevic, *Aust. J. Forensic. Sci.* **2014**, *46*, 166–179. DOI:10.1080/00450618.2013.825812
- StatSoft Inc., 2300 East 14th Street, Tulsa, Oklahoma, USA: <http://www.statsoft.com/>
- T. Jayalakshmi, A. Santhakumaran, *IJCTE* **2011**, *3*, 89–93. DOI:10.7763/IJCTE.2011.V3.288
- A. I. Jokić, J. A. Grahovac, J. M. Dodić, S. N. Dodić, S. D. Popov, Z. Z. Zavargo, D. G. Vučurović, *Hem Ind* **2012**, *66*, 211–221. DOI:10.2298/HEMIND110805085J
- R. Therón, J. F. De Paz, Visual sensitivity analysis for artificial neural networks: Intelligent Data Engineering and Automated Learning – IDEAL, 7th International Conference, Conference Proceeding, Burgos, Spain, **2006**. DOI:10.1007/11875581_23
- M. H. Shojaeefard, M. Akbari, M. Tahani, F. Farhani, *Adv. Mater. Sci. Eng.* **2013**, *2013*, 1–7.
- K. Héberger, K. Kollár-Hunek K, *J. Chemometr.* **2011**, *25*, 151–158. DOI:10.1002/cem.1320
- K. Kollár-Hunek, K. Héberger, *Chemom. Intell. Lab. Syst.* **2013**, *127*, 139–146. DOI:10.1016/j.chemolab.2013.06.007
- S. Z. Kovačević, S. O. Podunavac-Kuzmanović, L. R. Jevrić, E. A. Djurendić, J. J. Ajduković, S. B. Gadžurić, M. B. Vraneš, *J. Iran. Chem. Soc.* **2016**, *13*, 499–507. DOI:10.1007/s13738-015-0759-9

Povzetek

Rezultati, predstavljeni v tej študiji, vključujejo napoved protiglivične aktivnosti 24 derivatov oksazola, ki temeljijo na njihovih topoloških in elektrostatskih molekularnih deskriptorjih, ki izhajajo iz 2D molekularnih struktur. Metoda umetnega nevronskega omrežja (ANN) je bila uporabljena kot regresijsko orodje. Vhodni podatki za modeliranje ANN so bili izbrani s postopnim izbiranjem (SS). Modeliranje ANN je privedlo do treh mrež z izjemnimi statističnimi značilnostmi. Visoka predvidljivost vzpostavljenih omrežij je bila potrjena s primerjavami predvidenih in eksperimentalnih podatkov ter s preostalo analizo. Dobljeni rezultati kažejo na koristnost nastalih ANN pri natančni napovedi minimalnih inhibitornih koncentracij analiziranih spojin proti *Candida albicans*. V tej študiji je bila uporabljena metoda vsote razvrstitvenih razlik (SRD), da bi razkrili možno združevanje spojin v prostoru spremenljivk, uporabljenih pri modeliranju ANN. Dobljene rezultate lahko štejemo kot prispevek k razvoju novih protiglivičnih zdravil, ki strukturno temeljijo na oksazolnem jedru, še posebej v današnjih časih, ko primanjkuje visoko učinkovitih antimikotikov

Scientific paper

Co-Amorphization of Ibuprofen by Paracetamol for Improved Processability, Solubility, and *In vitro* Dissolution

Mayuri S. Bhandari,¹ Sarika M. Wairkar,² Udaykumar S. Patil¹
and Namdeo R. Jadhav^{1,*}

¹ Department of Pharmaceutics, Bharati Vidyapeeth College of Pharmacy, Kolhapur Maharashtra-416013, India.

² Shobhaben Pratapbhai Patel School of Pharmacy & Technology Management, SVKMs NMIMS, Vile Parle (W), Mumbai. Maharashtra – 400 056, India.

* Corresponding author: E-mail: nrjadhav18@rediffmail.com
Tel: +91-9823751579; Fax: +91-231-2638833

Received: 03-09-2017

Abstract

Co-amorphous (COAM) systems of ibuprofen (IB) and paracetamol (PA), in clinical dose ratios, were prepared by ball milling to enhance solubility and dissolution of IB. Subsequently, COAM were characterized by solubility, processability, XRPD, DSC, ATR-FTIR, SEM, *in-vitro* dissolution and accelerated stability studies. Maximum increase in aqueous solubility of IB was seen in 500:200 mg dose ratio (COAM 1) with 6.7 fold rise from 78.3 ± 1.1 to 522.6 ± 1.29 $\mu\text{g/ml}$. COAM 1 exhibited $99.80 \pm 0.58\%$ dissolution of IB at 20 min in phosphate buffer, significantly high ($P < 0.05$) compared to plain IB. Thus saturation solubility and dissolution rate of IB was found significantly improved unlike PA. The flowability/processability of COAM system was remarkably improved compared to pure IB, speculated due to as formation of miniscular forms of PA-IB, having strong adhesive interactions. XRPD and DSC results confirmed amorphization of IB. ATR-FTIR results evidenced hydrogen bonding interactions between both the drugs. In accelerated stability studies, flowability, XRPD, DSC and *in-vitro* dissolution studies demonstrated insignificant changes, thus confirming successful stabilisation of IB by PA.

Keywords: Ibuprofen; co-amorphism with paracetamol; improved processability; solubility and dissolution of ibuprofen

1. Introduction

Ibuprofen (2-(4-(2-methylpropyl) phenyl) propionic acid) is a widely used non-steroidal anti-inflammatory drug having poor solubility and high permeability (BCS II), and limited bioavailability.¹ However, it has a poor processability due to its low glass transition temperature (T_g), thus, enunciating difficulty in the design of solid dosage forms.²

So as to overcome its aforesaid problems, solid dispersions (SDs) using polyethylene glycol, polyvinyl pyrrolidone, microcrystalline cellulose, colloidal silicon dioxide, HPMC, soluplus, employing techniques like spray drying, freeze drying, electro-spinning, hot melt extrusion, ball milling etc. have been attempted.^{3–9} These SDs demonstrated solubility and dissolution enhancement by amorphization, solid solution formation, non-covalent interactions like hydrogen bonding etc. However, ibuprofen

due to its low melting temperature devitrifies rapidly and post process residual crystallites act as nuclei for further crystallisation. Additionally, a large quantity of polymer increases the bulk of the final dosage form.¹⁰ Hence, commercial applications of SDs have been limited due to their stability, reproducibility, and scale up constraints.^{11,12} Unlike SDs, micronization of Ibuprofen has been found to be of limited significance due to a slight reduction in its crystallinity. When processed alone, its *in-situ* homodimer formation impedes crystallinity reduction and vitrification, and consequently results into poor solubilisation.¹³ Relatively, crystal habit change and co-crystallisation have been found to be promising crystal engineering techniques aiming aforesaid improvements.¹⁴ Use of ionic liquids and self assembled mixed micelles of surfactant have also been reported for solubility enhancement of ibuprofen.^{15–16} But, safety and toxicity of solvent, surfactant, and co-crystal

former are prime concerns. Recently, a new technique using mesoporous silica has been introduced to overcome the solubility and stability problems of ibuprofen.¹⁷ Use of mesoporous SBA-15, modified SBA-16, and MCM-41 has been attempted to stabilise amorphous state and enhance its dissolution. However, it possesses high manufacturing costs due to expensive silica sources and surfactants used in the fabrication.¹⁸ To alleviate cost, its stabilization has also been attempted using inexpensive mesoporous magnesium carbonate.¹⁹ Recently, co-processing of Ibuprofen-magnesium trisilicate has been carried out by ball milling and freeze drying for imparting amorphism and improved drug release of former.²⁰

Two decades ago, the concept of co-amorphism was introduced, demonstrating potential binary amorphous system, comprising two or more small molecules instead of polymers.^{21–22} Studies have shown that small molecules like amino acids, sugar, urea, citric acid, kaolin, aluminium hydroxide²³ or other API can improve physical stability of the amorphous drugs more effectively than polymers.^{24–26} The main reason for the stability of the co-amorphous system was attributed to molecular interactions between the drugs/excipient in the system. It was reported that unstable drug like Naproxen could be stabilized by Indomethacin and Cimetidine, and dissolution rates of these systems were also enhanced.²⁷ Löbmann et al. have reported improvement in both stability and solubility of Glipizide when combined with Simvastatin.²⁸ Further, ball milled Nateglinide-Metformin hydrochloride co-amorphous system has demonstrated improved dissolution of Nateglinide.²⁹ Interestingly, carbamazepine, citric acid and L-arginine ternary system was ball milled for inducing coamorphism, to enhance Tg and solubility/dissolution.³⁰

Keeping in view benefits reaped from appropriate co-amorphous combinations of two drugs, we have attempted to improve processability, solubility and *in vitro* dissolution, and amorphous state stability of Ibuprofen using Paracetamol, which is a BCS class III drug. Clinically relevant combinations of both drugs are available in the market and have been widely recommended for analgesic, antipyretic, and anti-inflammatory conditions. Predominantly available three clinical dose combinations viz; 500 mg: 200 mg, 500 mg: 400 mg and 325 mg: 400 mg of Paracetamol: Ibuprofen were ball milled for coamorphism. The simplicity, versatility and green nature of ball milling technique has compelled us to employ same. Eventually, prepared coamorphous mixtures (COAM) were characterized by solubility, micromeritic properties, flowability, ATR-FTIR, DSC, XRPD and *In-vitro* dissolution studies.

2. Experimental

2.1. Materials

Ibuprofen and Paracetamol were provided as a gift samples by Wintech Pharmaceuticals, Nashik, India and

Sanofi India Ltd., Mumbai, India respectively. All other reagents used in the study were of analytical grade.

2.2. Methods

2.2.1. Preparation of COAM and Saturation Solubility Studies

Paracetamol (PA) and Ibuprofen (IB) were ball milled (Lab Hosp, Mumbai, India) together in clinically available dose ratios 500 mg: 200 mg (COAM 1), 500 mg: 400 mg (COAM 2) and 325 mg: 400 mg (COAM 3) of PA: IB respectively. The COAM of PA and IB were ball milled using 8 mm stainless steel balls at critical speed of 120 rpm for 2 h. The milling speed and time was optimised after taking trials, based on increase in solubility of COAM. Also, both pure drugs were ball milled separately, PA (BMP) and IB (BMI) at same milling parameters. Physical mixtures (PM) of pure PA and IB were prepared, and all aforementioned samples were stored in desiccators until further use.

Subsequently, saturation solubility of PA and IB was determined by adding excess amount of each drug in 10 mL distilled water separately. The dispersions were kept on an orbital shaker (Remi Instruments Ltd., Mumbai, India) for 72 h at 37 °C and further centrifuged at 7000 rpm for 10 min. The supernatant was filtered through 0.45 µm syringe filter and the concentration of each drug was determined by simultaneous UV-spectrophotometric analysis (Jasco V 530, India) at absorption maxima 243 nm (λ_1) for PA and 219 nm (λ_2) for IB.

$$C_x = \frac{A_2 a_{y_1} - A_1 a_{y_2}}{a_{x_2} a_{y_1} - a_{x_1} a_{y_2}} \quad (1)$$

$$C_y = \frac{A_1 a_{x_2} - A_2 a_{x_1}}{a_{x_2} a_{y_1} - a_{x_1} a_{y_2}} \quad (2)$$

Where, C_x and C_y = Concentration of PA and IB respectively in COAM
 A_1 and A_2 = Absorbance of PA at λ_1 and IB at λ_2 respectively
 a_{x_1} and a_{y_1} = Absorptivity of PA and IB respectively at λ_1
 a_{x_2} and a_{y_2} = Absorptivity of PA and IB respectively at λ_2

The saturation solubility of PA and IB at various pH viz. 1.2, 4.5, 6.8 and 7.2 was also determined using the same procedure. The experiments were performed in triplicate.

2.2.2. Micromeritics

The particle size analysis of PA, IB, BMP, BMI and COAM 1 was performed by ImageJ software using scanning electron microphotographs taken.

Flowability of PA, IB, BMP, BMI, PM and COAM 1 was assessed from angle of repose (θ). The value of θ was determined using fixed funnel free-standing cone method, performing measurement in triplicate, using the formula,

$$\theta = \tan^{-1} \left(\frac{H}{R} \right) \quad (3)$$

Where, H (cm) is height between lower tip of funnel and base of sample, and R (cm) is the radius of the base of heap formed.³¹

The samples were also evaluated for Carr's compressibility index (CCI) and Hausner's ratio (HR) using the following formula,

$$\text{CCI} = \left(\frac{\text{TD} - \text{BD}}{\text{TD}} \right) \times 100 \quad (4)$$

$$\text{HR} = \frac{\text{TD}}{\text{BD}} \quad (5)$$

Where, TD and BD are tapped density and bulk density.³²

2. 2. 3. X-ray Powder Diffraction (XRPD)

XRPD patterns of PA, IB, BMP, BMI and COAM 1 were recorded at room temperature on X-ray diffractometer (Philips analytical XRPD, PW 3710, Holland) with CuK α radiation (1.54 Å), at 30 kV, 10 mA and passing through a nickel filter. Samples were scanned between 10⁰ and 70⁰ 2 θ with a step time of 16.5 sec and step size of 0.02⁰.

2. 2. 4. Differential Scanning Calorimetry (DSC)

Differential scanning calorimetry was used to assess thermal changes in PA, IB, BMP, BMI, and COAM 1. The study was carried out on model SDT Q600 V20.9 Build 20 (TA Instruments, USA). The DSC instrument was calibrated for temperature and heat flow using high-purity standards of indium. The samples (3–5 mg) were heated 30 °C to 300 °C at the rate of 10 °C/min. under dry nitrogen purge (80 mL/min) in crimped and pin-holed aluminium pans. The melting points were determined using TA-Universal Analysis software (version 4.7A).

The percent crystallinity of all samples was calculated using an equation given by Rawlinson et al.³³

$$\text{Crystallinity} = \frac{\delta H_{\text{mCOAM}}}{\delta H_{\text{mDrug}} \times w} \times 100 \quad (6)$$

Where, δH_{mCOAM} is the melting enthalpy of the co-amorphous sample (J g^{-1}), δH_{mDrug} is the melting enthalpy of drug (J g^{-1}), and W is the weight fraction of drug in co-amorphous system ($W = 2/7 = 0.285$ for IB and $W = 5/7 = 0.714$ for PA).

2. 2. 5. Attenuated Total Reflectance- Fourier Transform Infrared Spectroscopy (ATR-FTIR)

ATR-FTIR spectra of PA, IB, BMI, BMP and COAM 1 were recorded using attenuated total reflectance infra red spectrophotometer (Bruker Alpha-T, India) to study the possible interactions between both drugs. About 3–4 mg of powdered sample was directly placed onto the ATR crystal and the spectrum was recorded over the wave number 400–4000 cm^{-1} on spectrophotometer.

2. 2. 6. Scanning Electron Microscopy (SEM)

Scanning electron microphotographs of PA, IB, BMP, BMI, and COAM 1 were taken using SEM coupled EDAX (Model-JEOL-SEM 6360 A, Tescan, Brno-Czech Republic). An accelerating voltage of 12 kV for PA and 18 kV for IB and COAM was used. Before taking microphotographs, the samples were coated with gold using Gold coating machine JEOL JFC-1600.

2. 2. 7. In-vitro Dissolution Studies

The in-vitro dissolution study for PA, IB, BMI, BMP and COAM 1 was carried out in USP type-II dissolution test apparatus (Electrolab Ltd., TDT 08L, Mumbai, India). Quantities equivalent to 500 mg of PA and 200 mg of IB were placed in the dissolution medium. The study was carried out for 2 h in 0.1 N HCl and 2 h in phosphate buffer (pH 7.2) with a rotation speed of 100 rpm and dissolution media of 900 ml at 37 °C ($n = 3$). Five ml of samples were withdrawn and immediately replaced with same volume of fresh dissolution media. The filtered samples were analysed on UV-spectrophotometer (Jasco V-530, Japan) using simultaneous equation method.

2. 2. 8. Accelerated Stability Studies

The COAM 1 samples were stored at 40 °C/75% RH for 3 months for accelerated stability studies. The samples were withdrawn after 0, 30, 60, 90 days and analyzed for angle of repose, XRPD, DSC and *in-vitro* dissolution.

3. Result and Discussion

3. 1. Preparation of COAM and Saturation Solubility Studies

The saturation solubility of PA in distilled water, pH 1.2, pH 4.5, pH 6.8, pH 7.2, was found to be 17790.6 ± 1.8 , 18616 ± 2.4 , 18726.3 ± 2.1 , 18022.2 ± 1.9 , 18092.5 ± 2.5 $\mu\text{g/mL}$ respectively. And, for IB in distilled water, pH 1.2, pH 4.5, pH 6.8, pH 7.2 was 78.3 ± 1.1 , 47.1 ± 1.2 , 65.2 ± 1.6 , 128.9 ± 0.9 , 181.1 ± 1.0 $\mu\text{g/mL}$ respectively. These values indicated that, PA solubility at various pH was invariably same, however, IB showed pH-dependent solubility. The reason for pH dependent solubility is its weak acidic nature, which enhances solubility at higher pH values and reduces solubility at lower pH.^{34,35} The water solubility of BMP and BMI was found to be 18050.4 ± 1.6 and 90.4 ± 1.3 $\mu\text{g/mL}$ respectively (solubility data for other pH values not shown). Which indicated that, although size reduction was noted (particle size data given under micromeritics) for BMP and BMI, significant increase in solubility was not demonstrated.

A combination of PA and IB was successfully ball milled in different clinical dose ratios to form COAM. The

method involved mechanical activation of both the drugs using a ball mill and optimisation of milling time and speed after taking many trials in the view of conversion of a crystalline drug into amorphous counterpart and particle size reduction enhancing solubility and dissolution.^{36–39} In COAM, saturation solubility of IB in distilled water was altered after ball milling and was different for all dose combinations with PA, whereas, it was invariably same for PA, as depicted in Table 1. Maximum increase in aqueous solubility of IB was seen in 500 mg: 200 mg dose ratio (COAM 1), indicating role of PA and coamorphism towards solubility enhancement of IB, even if its solubility is pH dependent. Rise in aqueous saturation solubility of IB in COAM 1 from $78.3 \pm 1.1 \mu\text{g/ml}$ to $522.6 \pm 1.29 \mu\text{g/ml}$, confirmed 6.7 fold increase.

All the three clinical combinations showed increase in solubility of IB, but amongst them, COAM 1 showed maximum increase in solubility of IB. Thus, COAM 1 was selected for further characterization.

Table 1. Saturation solubility of PA and IB in COAM in various dose combinations

Dose combination (mg) (PA + IB)	Saturation solubility in water ($\mu\text{g/ml}$)	
	PA	IB
500 + 200 (COAM 1)	17798.9 ± 2.05	522.6 ± 1.29
500 + 400 (COAM 2)	17794.9 ± 0.74	387.7 ± 3.24
325 + 400 (COAM 3)	17791.3 ± 1.11	83.9 ± 1.93

3. 2. Micromeritics

The average particle size of IB, BMI, PA, BMP and COAM 1 was found to be $191.07 \pm 12.69 \mu\text{m}$, $143.30 \pm 4.51 \mu\text{m}$, $17.06 \pm 2.11 \mu\text{m}$, $15.23 \pm 0.87 \mu\text{m}$ and $4.75 \pm 0.37 \mu\text{m}$ respectively. Which indicated the complimentary role of PA and IB towards size reduction in COAM during ball milling.

Studies have revealed poor flowability parameters for PA, IB, BMP, BMI and PM as given in Table 2. Both drugs possess poor flow properties, especially IB has very poor flow and processability problems due to its sticky nature.^{40–42} However, PA and IB in COAM 1 form demonstrated excellent flowability as indicated from CCI ($19.2 \pm$

0.08) and HR (1.25 ± 0.04). Noteworthy, θ value, $30.3 \pm 0.51^\circ$ has clearly enunciated free flowing nature of COAM 1. Statistically, improvement in θ value of COAM 1 was significant ($P < 0.05$), compared to rest all samples. Moreover, aforementioned flow parameters were also not satisfactory for BMP and BMI, although improved a bit with size reduction. Thus, remarkably improved flow property of IB in COAM is an indicator of reduced stickiness, uniform and size reduced particles, which divulges pivotal role of PA in improving flow, especially in COAM, unlike PM. In tableting, addition of glidant has been recommended to improve flow properties by reducing strong interparticulate interactions. Herein, both PA and IB in COAM1 seem to perform the role of glidants. Newly generated fines of PA and IB during ball milling undergo strong adhesive interactions and deposits on energetic surfaces of PA crystals, thereby overcoming cohesive interactions. The deposit of PA-IB on paracetamol crystals may resemble miniscular form of solids designed, in which bigger but distorted PA crystals acts a carrier on which fine particulates of PA-IB deposit.⁴³ Thus, such non-sticky particulates having improved processability, may increase its speed of production, reduces risk of stoppage and improves blend quality, filling procedures and end product quality. Conclusively, micromeritic properties have clearly unveiled, a new form of IB in COAM 1 which has resolved poor processability associated with its stickiness.

3. 3. X-ray Powder Diffraction (XRPD)

X-ray diffractograms of PA, IB, BMP, BMI and COAM 1 have been depicted in Fig. 1. Crystalline peaks of PA have been noted at 2θ values 23.2, 24.1, 26.3. Similarly, distinct and intense peaks of IB have been observed at 12.3, 16.7, 20.1, and 22.4. Powder X-ray diffractogram of individually ball milled drugs, BMP and BMI showed high intensity peaks revealing partial amorphism in PA and IB. This limited reduction in crystallinity of IB might be attributed to homodimer formation impeding crystallinity disruption. As anticipated, remarkable reduction in crystallinity of both PA and IB was divulged from diffractogram of COAM 1. The XRPD of COAM 1 shows some peaks of PA and two very low intensity peaks of IB which suggests almost complete amorphization of IB and outweighs role of PA, along with milling force, in disruption

Table 2. Data for micromeritic properties of PA and IB (API, separately ball milled API, physical mixture, COAM 1)

Drug/s	Bulk density (g/ml)	Tapped density (g/ml)	Carr's compressibility index (%)	Hausner's ratio	Angle of repose (θ)
PA	0.216 ± 0.01	0.284 ± 0.07	23.90 ± 0.14	1.31 ± 0.06	39.8 ± 0.80
IB	0.231 ± 0.09	0.324 ± 0.12	28.70 ± 0.22	1.40 ± 0.03	43.4 ± 1.21
BMP	0.271 ± 0.05	0.355 ± 0.03	23.66 ± 0.18	1.31 ± 0.10	37.7 ± 0.53
BMI	0.246 ± 0.01	0.333 ± 0.20	26.12 ± 0.13	1.35 ± 0.08	40.9 ± 0.80
PM	0.321 ± 0.05	0.431 ± 0.06	25.52 ± 0.31	1.34 ± 0.13	40.0 ± 0.67
COAM 1	0.353 ± 0.02	0.437 ± 0.04	19.20 ± 0.08	1.25 ± 0.04	30.3 ± 0.51

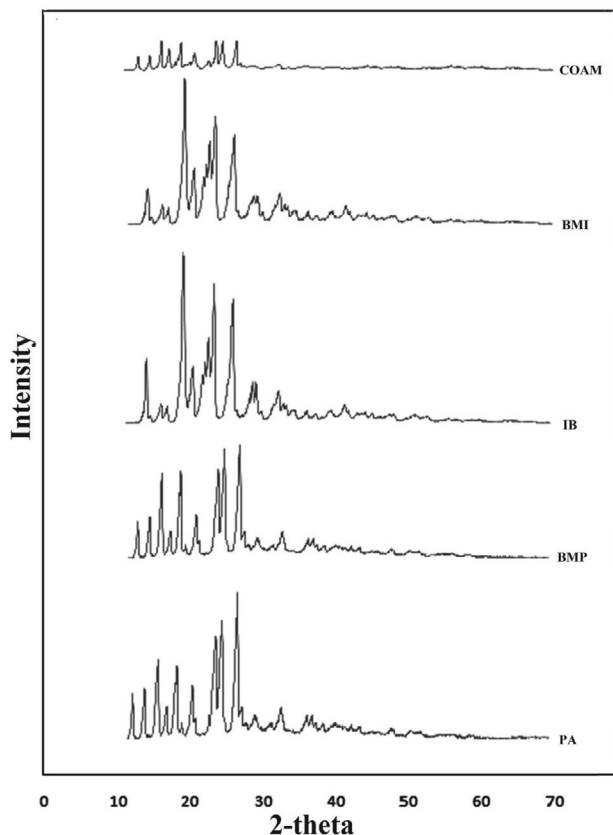


Figure 1. XRPD diffractogram of plain PA and IB, ball milled PA and IB, and COAM 1 samples

of IB geometry. The conversion of IB in co-amorphous form was responsible for increase in its aqueous solubility, although it has pH dependent solubility.^{44, 45}

3. 4. Differential Scanning Calorimetry (DSC)

The DSC thermogram (Fig. 2) of PA and IB showed sharp endothermic transitions at 170.05 °C (Fig. 2a) and 77.9 °C (Fig. 2c) respectively, corresponding to their melting points. A second endothermic peak seen in thermogram of IB at 223 °C, was corresponding to its boiling point.⁴⁶ The figure depicts slight changes in the crystallinity of BMP (Fig. 2b) and BMI (Fig. 2d), whereas, in COAM 1, significant transformation of both crystalline PA and IB to amorphous form. Interestingly, shift in melting point of PA from 170.05 °C (in PA) to 159.6 °C (in COAM 1) has been noted (Fig. 2e) and boiling point of IB at 223 °C was also not observed in DSC of COAM 1, indicating strong solid state interactions between PA and IB, and partial dissolution of PA in molten IB.²⁸ The details of % crystallinity of both the drugs have been given in Table 3. The % crystallinity of PA and IB in COAM 1 sample was found to be 44.37% and 9.63% respectively. Whereas, % crystallinity of BMP was 77.44%, and 91.42% for BMI, which was quiet high, compared to COAM 1.

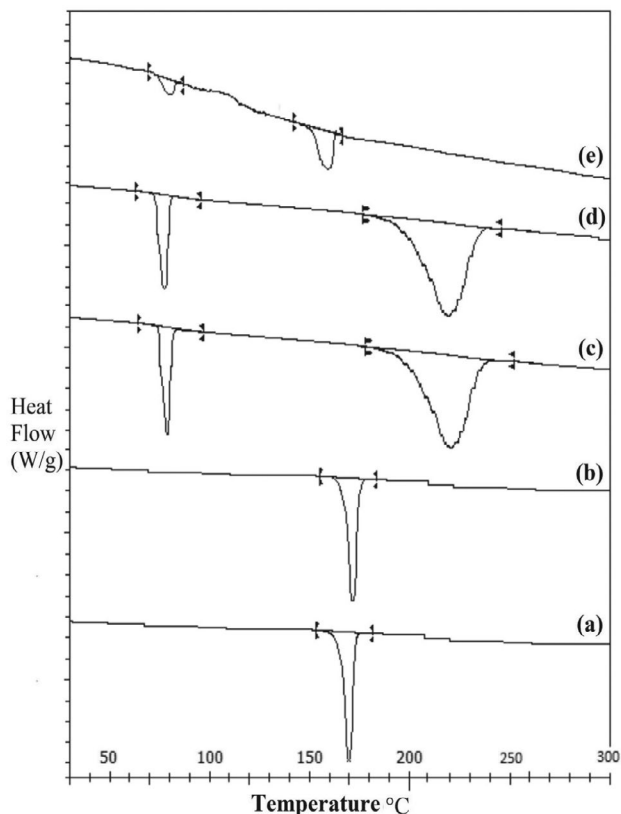


Figure 2. DSC thermogram of (a) PA, (b) BMP, (c) IB, (d) BMI and (e) COAM 1

Table 3. Enthalpy and % crystallinity of COAM 1 after a) 0 days, b) 30 days, c) 60 days and d) 90 days (accelerated stability samples)

COAM 1	Enthalpy (J/g)		% Crystallinity	
	PA	IB	PA	IB
0 days	79.87	12.40	44.37	9.63
30 days	83.94	12.90	46.63	10.01
60 days	86.45	13.80	48.02	10.71
90 days	88.54	14.20	49.18	11.03

3. 5. Attenuated Total Reflectance- Fourier Transform Infrared Spectroscopy (ATR-FTIR)

Till date, ATR-FTIR has been considered as a work-horse for studying drug-drug interactions. The ATR-FTIR spectra of COAM 1 (Fig. 3c) reveals shift in phenolic C=O stretch of PA (1372.1 cm^{-1}) to higher wave number 1396.84 cm^{-1} . Similarly, N-H stretch of amide in PA at 3162.69 cm^{-1} was also shifted to higher wave number. For IB, C=O stretch of carboxylic acid (1714.41 cm^{-1}) was shifted to lower wave number at 1647.77 cm^{-1} . And, O-H stretch of carboxylic acid of IB at 2953.45 cm^{-1} was shifted to higher wave number (2980.20 cm^{-1}). The ATR-FTIR spectra (Fig. 3) shows shift in wave numbers sug-

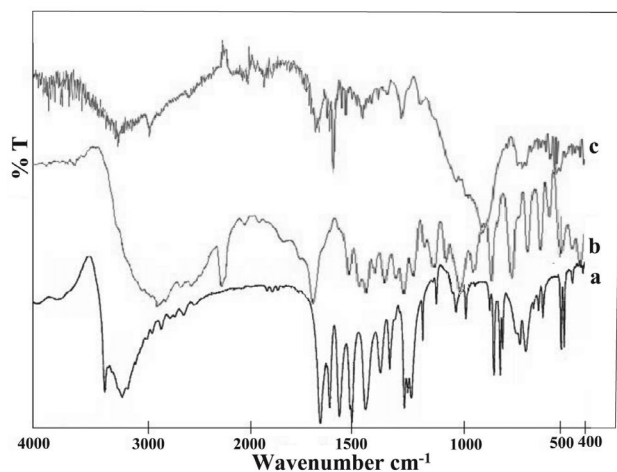


Figure 3. ATR-FTIR spectra of (a) PA, (b) IB, and (c) COAM 1

gesting strong hydrogen bonding interactions between PA and IB.

As mentioned previously, increased solubility and dissolution of IB in COAM 1 system was due to molecular

interactions between PA and IB.^{21,22} Even, adsorption of PA-IB fine particulates on PA, might have generated a miniscular form as discussed earlier. Such strong adhesive molecular interactions might have lead to band shifts in the IR spectra.^{47,48} These shifts are also observed when a crystalline drug is converted into its amorphous form.⁴⁸ Here, molecular interaction between PA and IB were confirmed due to shift of phenolic C=O stretch, N-H stretch (amide) of PA and C=O stretch, O-H stretch (carboxylic acid) of IB.

3. 6. Scanning Electron Microscopy (SEM)

The microphotographs taken using SEM showed long, slender, needle shaped crystals of IB (Fig. 4a and 4b), and Fig. 4c shows irregular shaped crystals of PA. Distorted crystal morphology and extensively reduced grain size along with congregated PA and IB clearly indicated partial transformation of crystal form of PA to its amorphous state, and almost complete crystallinity loss for IB in COAM 1 (Fig. 4d).

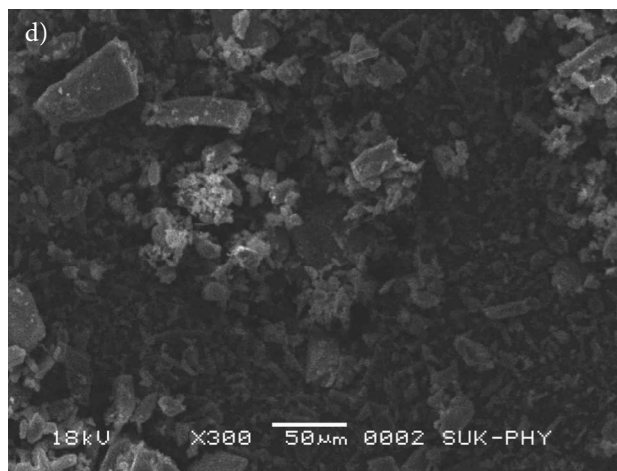
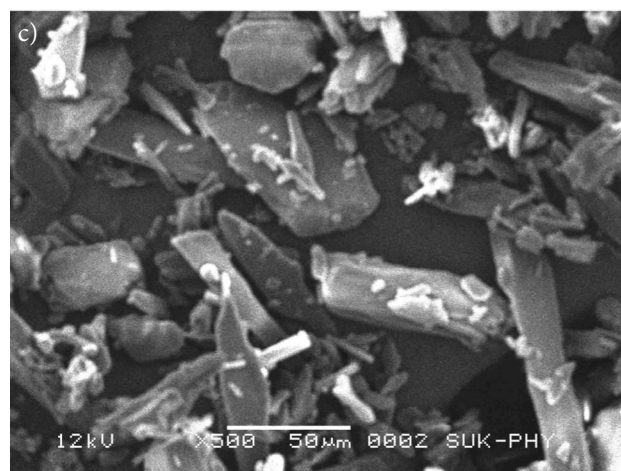
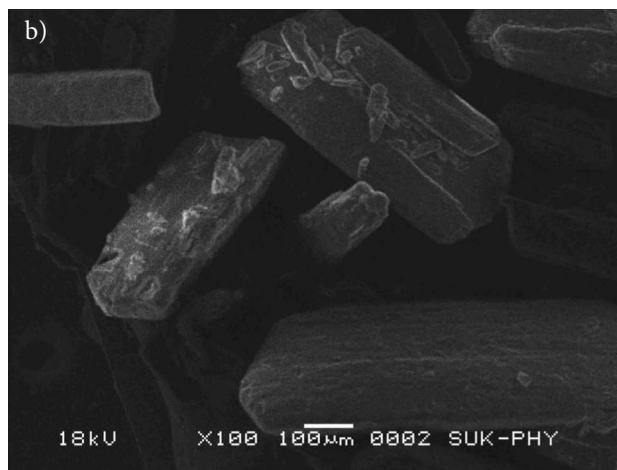
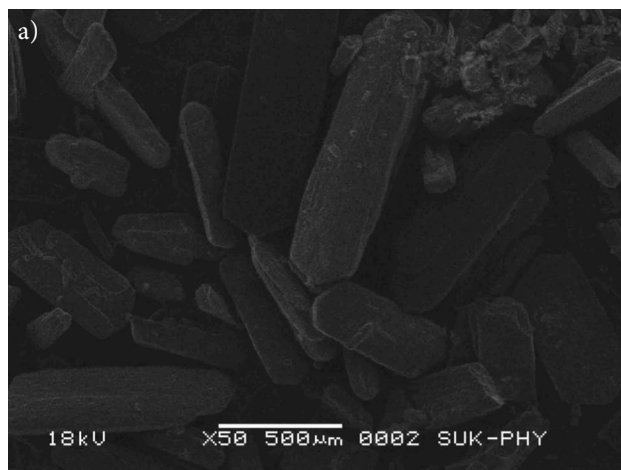


Figure 4. Scanning electron microphotograph of (a) IB [50x], (b) IB [100 x], (c) PA [500x] and (d) COAM 1 [300x]

3. 7. *In-vitro* Dissolution Studies

In-vitro dissolution profile of PA, IB, BMP, BMI, and COAM 1 in 0.1 N HCl and phosphate buffer pH 7.2 is depicted in Fig. 5. It is known that particle size reduction enhances dissolution of drugs^{36–40} but, is not a sole reason for improved dissolution. This can be explained by the dissolution profile of BMP and BMI, in which the dissolution of individually milled drug was not improved. It has also been reported in previous studies that both ball milling at room temperature and cryogenic ball milling of IB only slightly reduced its crystallinity.⁴⁹ For plain PA to dissolve in phosphate buffer pH 7.2, it took 40 min (Fig. 5c; data not shown in table), and in co-amorphous form showed 80% dissolution in 0.1 N HCl, in 20 min (Fig. 5a). There was a insignificant difference ($P < 0.05$) found in the dissolution of PA, BMP, and PA in its co-amorphous form in both dissolution media.

On the contrary, IB in co-amorphous form showed improved dissolution in both the dissolution media. In 0.1 N HCl, dissolution of IB, BMI, and IB in PM was poor ($10.26 \pm 0.41\%$ in 2 h for plain IB) which can be seen in Fig. 5b, whereas, remarkable improvement was noted in dissolution of IB in COAM 1 ($14.55 \pm 0.45\%$ in 2 h), which was 1.5 times more. Interestingly, in phosphate buffer pH 7.2, COAM 1 showed $99.80 \pm 0.58\%$ dissolution of IB in 20 min (Table 4), which was significantly high ($P < 0.05$) compared to plain IB ($63 \pm 0.27\%$). Moreover, at 5 and 10 minute time points, the dissolution of IB in COAM was double to that of plain IB, highlighting likely rapid onset of action. For plain IB to be completely dissolved it took 90 min ($98.3 \pm 0.69\%$), and similar were observations for dissolution of IB from BMI and PM (Fig. 5d).

3. 8. Stability Studies

Angle of repose of COAM 1 demonstrated an insignificant change for stability samples (data not shown). Diffractometric analysis demonstrated slight increase in intensity of the peaks of COAM 1, as seen in Fig. 6. Similarly, slight increase in enthalpy and % crystallinity was observed in DSC thermogram of COAM 1. Percent crystallinity of IB after three months was raised to 11.03% from initial 9.63% and of PA was increased to 49.18% from initial 44.37%. Slight increase in crystallinity of IB has been reflected in its *In vitro* dissolution profiles. With slight increase in crystallinity and reduction in amorphism, % IB dissolved has been slightly reduced (Table 4).

Accelerated stability studies suggested that the COAM 1 samples were stable up to 3 months. Neither the flowability, XRPD, DSC results nor the *in-vitro* dissolution studies showed significant change thus confirming stability of the product. Inhibition of propensity of amorphous material to devitrify was evident from these findings. Eventually, PA not only assisted in disruption of IB crystallinity, but, also stabilised its amorphous form at molecular level.

Table 4. *In-vitro* dissolution data of IB in COAM 1 sample in 0.1 N HCl and phosphate buffer pH 7.2 after a) 0 days, b) 30 days, c) 60 days and d) 90 days (accelerated stability samples)

Time (min.)	% cumulative IB dissolved in 0.1 N HCl				% cumulative IB dissolved in phosphate buffer pH 7.2			
	Plain IB	COAM 1	COAM 1	COAM 1	Plain IB	COAM 1	COAM 1	COAM 1
5	0.5 ± 0.06	1.21 ± 0.03	1.18 ± 0.24	1.02 ± 0.44	23.8 ± 0.47	48.28 ± 0.97	46.90 ± 1.10	46.17 ± 0.49
10	2.1 ± 0.19	2.43 ± 0.11	2.35 ± 0.39	2.22 ± 0.59	42.8 ± 0.88	82.43 ± 0.72	80.14 ± 0.88	79.52 ± 0.82
20	4.23 ± 0.27	3.79 ± 0.02	3.65 ± 0.49	3.57 ± 0.31	63.0 ± 0.27	98.91 ± 0.91	98.22 ± 0.84	98.11 ± 1.03
30	6.81 ± 0.29	6.76 ± 0.31	6.61 ± 0.42	6.53 ± 0.56	89.7 ± 0.49	99.29 ± 1.21	99.06 ± 0.90	98.57 ± 0.79
45	7.94 ± 0.48	10.11 ± 0.23	9.98 ± 0.53	9.84 ± 0.41	97.9 ± 0.54	99.68 ± 0.69	99.15 ± 1.05	98.80 ± 0.61
60	9.99 ± 0.39	12.14 ± 0.76	11.79 ± 0.48	11.57 ± 0.27	98.1 ± 0.11	99.94 ± 1.02	99.57 ± 0.50	99.15 ± 0.44
90	10.18 ± 0.20	14.08 ± 0.84	12.94 ± 0.36	12.72 ± 0.66	98.3 ± 0.69	100.16 ± 0.87	99.78 ± 0.84	99.53 ± 0.38
120	10.26 ± 0.41	14.55 ± 0.45	13.37 ± 0.83	12.92 ± 0.73	99.1 ± 0.37	100.12 ± 0.59	99.86 ± 1.32	99.64 ± 1.05

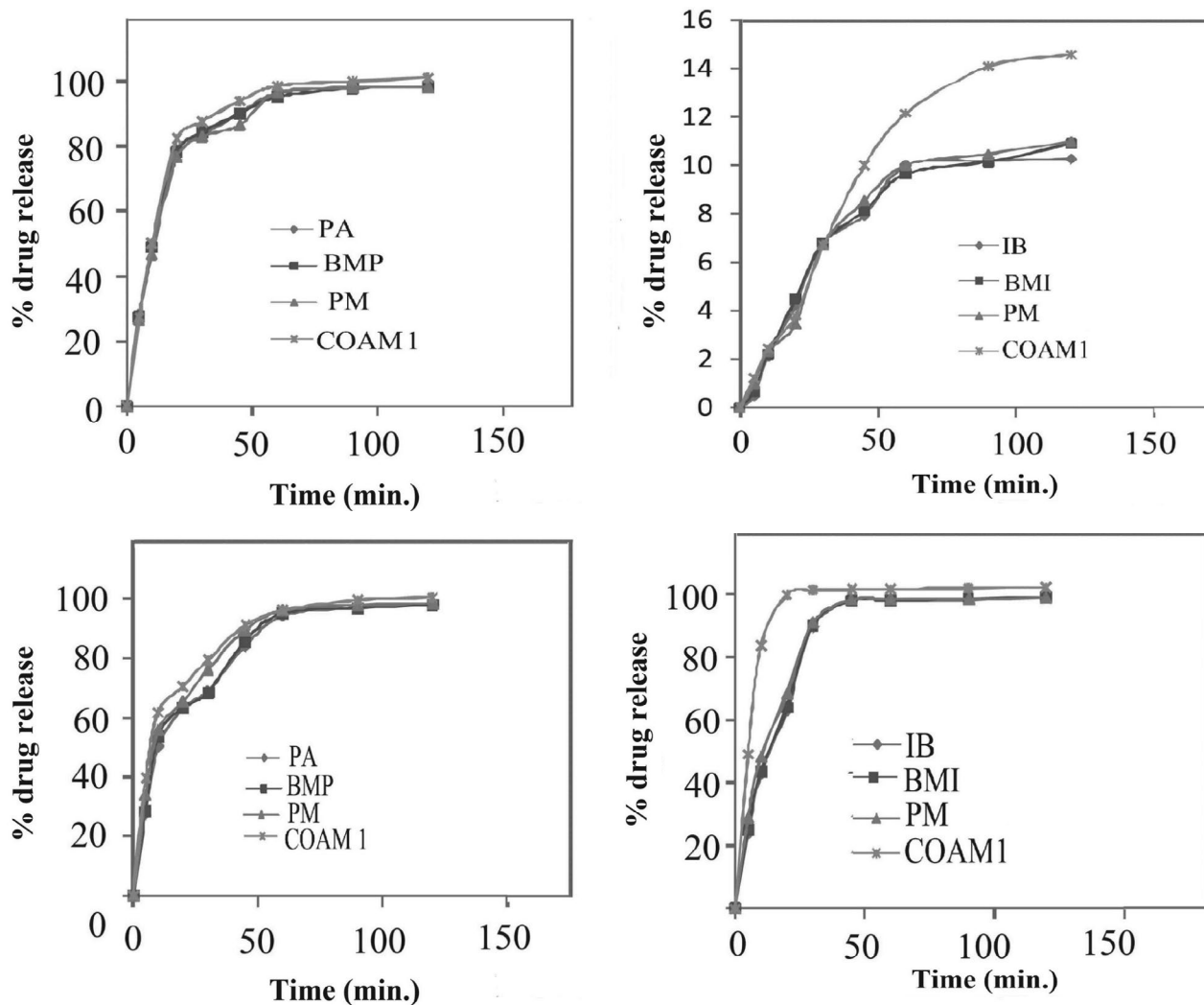


Figure 5. In-vitro dissolution profile of (a) PA in 0.1 N HCl, (b) IB in 0.1 N HCl, (c) PA in phosphate buffer (pH 7.2) and (d) IB in phosphate buffer (pH 7.2)

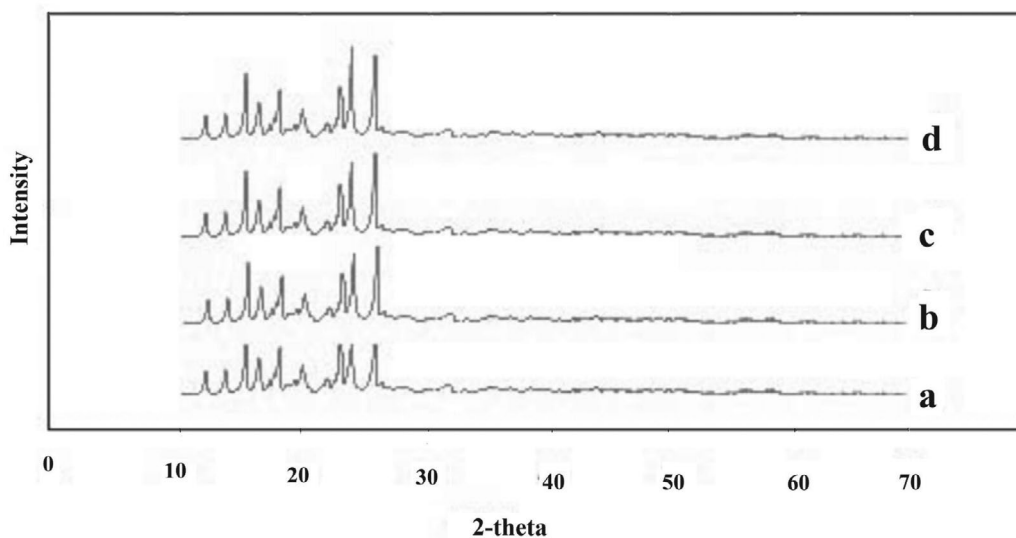


Figure 6. XRPD of COAM 1 after a) 0 days, b) 30 days, c) 60 days and d) 90 days at accelerated stability conditions

4. Conclusion

Paracetamol-Ibuprofen co-amorphous system was successfully generated by ball milling technique. Flow properties of IB were satisfactorily improved in co-amorphous form, thus overcoming its problem of stickiness, processability and homodimer formation during sizing down. Diffractometric studies have revealed amorphism/reduced crystallinity of IB and its subsequent stabilisation by PA. Amorphization and subsequent adsorption of IB on PA can speculate generation of a particulate system similar to miniscular dosage form. As a consequence, the COAM I form of IB demonstrated approximately seven fold solubility enhancement and threefold increase in dissolution of IB. Since, individually ball milled drugs did not show any significant increase in solubility and dissolution, the role of coamorphism for IB and essential role of PA has been unveiled. The presence of PA with IB in COAM could outweigh over the role of particle size of both in solubility and dissolution enhancements. Hence, work has demonstrated generation of COAM form of PA and IB in clinical dose ratio 500 mg: 200 mg, which may overcome poor processability, solubility and dissolution, and bioavailability constraints of IB. The method being simple, green, cost effective, and novel for PA-IB combination, holds great industrial potential.

Acknowledgements

Authors are thankful to AICTE, New Delhi, India for Providing Junior Research Fellowship to Mayuri Bhandari.

Declaration of Interest section

The authors report no declarations of interest.

5. References

- H. Potthast, J. B. Dressman, H. E. Junginger, K. K. Midha, H. Oeser, V. P. Shah, *J. Pharm. Sci.* **2005**, *94*, 2121–2131. DOI:10.1002/jps.20444
- E. Dudognon, F. Danède, M. Descamps, T. Correia, *Pharm. Res.* **2008**, *25*, 2853–2858. DOI:10.1007/s11095-008-9655-7
- Md. A. A. Masum, F. Sharmin, S. M. A. Islam, Md. S. Reza, *Dhaka Univ. J. Pharm. Sci.* **2012**, *11*, 1–6.
- M. Newa, K. H. Bhandari, D. X. Lee, J. H. Sung, J. A. Kim, B. K. Yoo, J. S. Woo, *Drug Dev. Ind. Pharm.* **2008**, *34*, 1013–21. DOI:10.1080/03639040701744095
- M. M. Gupta, M. G. Patel, N. S. Patel, M. Kedawat, *Int. J. Pharm. Pharm. Sci.* **2011**, *3*, 204–206.
- S. Mallick, S. K. Pradhan, M. Chandran, M. Acharya, T. Digdarsini, R. Mohapatra, *Results Pharma Sci.* **2011**, *1*, 1–10. DOI:10.1016/j.rinphs.2011.05.003
- M. Dixit, P. K. Kulkarni, S. Panner, *Int. Res. J. Pharm.* **2011**, *2*, 250–256.
- K. A. Bodek, *Acta Pol. Pharm.* **2002**, *59*, 105–108.
- A. Ousset, P. Chavez, J. Meeus, F. Robin, M. A. Schubert, P. S. and K. Dodou, *Pharmaceutics*. **2018**, *10*, pii: E29. DOI:10.3390/pharmaceutics10010029.
- A. T. Serajuddin, *J. Pharm. Sci.* **1999**, *88*, 1058–1066. DOI:10.1021/js980403l
- J. Vijay, J. T. Sahadevan, R. M. Gilhotra, *Chron. Young Sci.* **2012**, *3*, 95–105. DOI:10.4103/2229-5186.98668
- G. Z. Papageorgiou, S. Papadimitriou, E. Karavas, E. Georgarakis, A. Docoslis, D. Bikiaris, *Curr. Drug. Deliv.* **2009**, *6*, 101–112. DOI:10.2174/156720109787048230
- D. Kayrak, U. Akman, O. Hortacsu, *The J. Supercrit. Fluids.* **2003**, *26*, 17–31. DOI:10.1016/S0896-8446(02)00248-6
- A. Nokhodchi, A. Homayouni, R. Araya, W. Kaialy, W. Obeidat, K. Asare-Addo, *RSC Adv.* **2015**, *5*, 46119–46131. DOI:10.1039/C5RA06183K
- T. E. Sintra, K. Shimizu, S. P. M. Ventura, S. Shimizu, J. N. Canongia Lopes and J. A. P. Coutinho, *Phys. Chem. Chem. Phys.* **2018**, *3*, 2094–2103.
- Katerina Stoyanova, Zahari Vinarov, Slavka Tcholakova, Improving ibuprofen solubility by surfactant-facilitated self-assembly into mixed micelles, *J Drug Deliv Sci Technol.* **2016**, *36*, 208–215 DOI:10.1016/j.jddst.2016.10.011
- A. Hillerström, J. Stam, M. Andersson, *Green Chem.* **2009**, *11*, 662–667. DOI:10.1039/B821281C.
- C. Gerardin, J. Reboul, M. Bonne, B. Lebeau, *Chem. Soc. Rev.* **2013**, *42*, 4217–4255.
- P. Zhang, J. Forsgren, M. Stromme, *Int. J. Pharm.* **2014**, *472*, 185–191. DOI:10.1016/j.ijpharm.2014.06.025
- M. Acharya, S. Mishra, R. N. Sahoo, S. Mallick, *Acta Chim. Slov.* **2017**, *64*, 45–54. DOI:10.17344/acsi.2016.2772
- N. Chieng, J. Aaltonen, D. Saville, T. Rades, *Eur. J. Pharm. Biopharm.* **2009**, *71*, 47–54. DOI:10.1016/j.ejpb.2008.06.022
- M. Allesø, N. Chieng, S. Rehder, J. Rantanen, T. Rades, J. Aaltonen, *J. Controlled Release* **2009**, *136*, 45–53. DOI:10.1016/j.jconrel.2009.01.027
- T. Masuda, Y. Yoshihashi, E. Yonemochi, K. Fujii, H. Uekusa, K. Terada, *Int. J. Pharm.* **2012**, *422*, 160–169. DOI:10.1016/j.ijpharm.2011.10.046
- K. Grzybowska, M. Paluch, P. Włodarczyk, A. Grzybowski, K. Kaminski, L. Hawelek, *Mol. Pharmaceutics.* **2012**, *9*, 894–904. DOI:10.1021/mp200436q
- E. Kaminska, K. Adrjanowicz, M. Tarnacka, K. Kolodziejczyk, M. Dulski, E. Mapesa, *Mol. Pharmaceutics.* **2014**, *11*, 2935–2947. DOI:10.1021/mp500286b
- S. Yamamura, H. Gotoh, Y. Sakamoto, Y. Momose, *Int. J. Pharm.* **2002**, *241*, 213–221. DOI:10.1016/S0378-5173(02)00195-3
- K. Löbmann, R. Laitinen, H. Grohgan, K. C. Gordon, C. Strachan, T. Rades, *Mol. Pharmaceutics.* **2011**, *8*, 1919–1928. DOI:10.1021/mp2002973
- K. Löbmann, C. Strachan, H. Grohgan, T. Rades, O. Korhonen, R. Laitinen, *Eur. J. Pharm. Biopharm.* **2012**, *81*, 159–169. DOI:10.1016/j.ejpb.2012.02.004
- S. Wairkar, R. Gaud, *AAPS PharmSciTech.* **2016**, *17*, 673–681. DOI:10.1208/s12249-015-0371-4
- H. Ueda, W. Wu, K. Loebmann, H. Grohgan, A. Müllertz,

- and T. Rades, *Mol. Pharm.* **2018**, *15*, 2036–2044
DOI:10.1021/acs.molpharmaceut.8b00174
31. D. Train, *J. Pharm. Pharmacol.* **1958**, *10*, 127 T-135 T.
32. R. L. Carr, *J. Chem. Eng.* **1965**, *72*, 163–168.
33. C. F. Rawlinson, A. C. Williams, P. Timmins, I. Grimsey, *Int. J. Pharm.* **2007**, *336*, 42–48.
DOI:10.1016/j.ijpharm.2006.11.029
34. I. E. Shohin, J. I. Kulinich, G. F. Vasilenko, G. V. Ramenskaya, *Indian J. Pharm. Sci.* **2011**, *73*, 443–446.
35. A. Anil Kumar, T.E. Gopala Krishna Murthy, A. Prameela Rani, *World j. pharm. pharm. sci.* **2014**, *3*, 311–324.
36. Z H Loh, A. K. Samanta, P. W. S. Heng, *Asian J. Pharm. Sci.* **2015**, *10*, 255–274. DOI:10.1016/j.ajps.2014.12.006
37. P. Khadka, J. Ro, H. Kim, I. Kim, J. T. Kim, *Asian J. Pharm. Sci.* **2014**, *9*, 304–316. DOI:10.1016/j.ajps.2014.05.005
38. J. Sun, F. Wang, Y. Sui, Z. She, W. Zhai, C. Wang, Y. Deng, *Int. J. Nanomed.* **2012**, *7*, 5733–5744. DOI:10.2147/IJN.S34365
39. J. Jinno, N. Kamada, M. Miyake, K. Yamada, T. Mukai, M. Odomi, *J. Controlled Release* **2006**, *111*, 56–64.
DOI:10.1016/j.jconrel.2005.11.013
40. N. Rasenack, B. W. Muller, *Int. J. Pharm.* **2002**, *245*, 9–24.
DOI:10.1016/S0378-5173(02)00294-6
41. A. Nada, B. W. Mueller, S. M. Al-Saidan, *Pharm. Technol.* **2005**, *29*, 1–8
42. H. Ehlers, H. Rääkkönen, O. Antikainen, J. Heinämäki, J. Yli-ruusi, *Int. J. Pharm.* **2009**, *368*, 165–170.
DOI:10.1016/j.ijpharm.2008.10.013
43. N. Jadhav, A. Pawar, A. Paradkar, *AAPS Pharm Sci Tech* **2007**, *8*, Article 59, E1-E7.
44. S. B. Murdande, M. J. Pikal, R. M. Shanker, R. H. Bogner, *Pharm. Dev. Technol.* **2011**, *16*, 187–200.
DOI:10.3109/10837451003774377
45. M. A. Czarnecki, Y. Morisawa, Y. Futami, Y. Ozaki, *Chem. Rev.* **2015**, *115*, 9707–9744. DOI:10.1021/cr500013u
46. S. Ramukutty, E. Ramachandran, *J. Cryst. Process Technol.* **2014**, *4*, 71–78. DOI:10.4236/jcpt.2014.42010
47. S. Shen, P. S. Chow, F. Chen, R. B. H. Tan, *Chem. Pharm. Bull.* **2007**, *55*, 985–991. DOI:10.1248/cpb.55.985
48. A. Heinz, C. J. Strachan, K. C. Gordon, T. Rades, *J. Pharm. Pharmacol.* **2009**, *61*, 971–988. DOI: 10.1211/jpp.61.08.0001
49. S. M. Lee, H. J. Park, S. S. Kim, T. H. Choi, E. Kim, K. H. Na, H. K. Cho, K. Y. Rhee, *Materials Science Forum.* **2005**, *475–479*, 2403–2406.
DOI:10.4028/www.scientific.net/MSF.475-479.2403.

Povzetek

Material (oznaka COAM) sestavljen iz amorfega paracetamola (PA) in ibuprofena (IB) smo pripravili z mletjem v krogličnem mlinu. Namen raziskave je bil pripraviti material z višjo topnostjo in boljšim raztapljanjem ibuprofena. Tako pripravljeno amorfnno mešanico paracetamola in ibuprofena smo karakterizirali z rentgensko praškovo difrakcijo (XRPD), diferencialno dinamično kalorimetrijo (DSC) infrardečo spektroskopijo (ATR-FTIR), vrstično elektronsko mikroskopijo (SEM) in opravili *in vitro* študije raztapljanja in stabilnosti. Največje povečanje (6,7-kratno) topnosti ibuprofena v vodi smo opazili v vzorcu, ki smo ga pripravili v odmerkih 500 (PA) : 200 (IB) mg (oznaka COAM 1). Topnost se je povečala iz $78,3 \pm 1,1$ µg/ml na $522,6 \pm 1,29$ µg/ml. V vzorcu (COAM 1) smo določili $99,80 \pm 0,58$ % raztapljanje ibuprofena v dvajsetih minutah v fosfatnem pufri, kar kaže na znatno povečanje v primerjavi s samim ibuprofenom. Tako je bila za razliko od paracetamola ugotovljena bistveno izboljšana topnost in hitrost raztapljanja ibuprofena. V vzorcu (COAM 1) je bila tudi izjemno izboljšana pretočnost v primerjavi s čistim ibuprofenom. Le-ta je najverjetneje posledica močnih adhezivnih interakcij v sistemu PA-IB. Rezultati XRPD in DSC so potrdili amorfnno obliko ibuprofena. Rezultati ATR-FTIR spektroskopije kažejo na prisotnost interakcij preko vodikovih vezi med obema učinkovinama. Pospešeni testi stabilnosti, rezultati meritev pretočnosti, XRPD, DSC in testi *in vitro* raztapljanja so potrdili uspešno stabilizacijo ibuprofena s paracetamolom.

Scientific paper

Electrochemical Detection of Nitrite in Food Based on Poly (3,4-ethylenedioxythiophene) Doped with Fe₃O₄ Nanoparticles Loaded Carboxylated Nanocrystalline Cellulose

Guiyun Xu, Mingming Zhang and Xijuan Yu*

Key Laboratory of Sensor Analysis of Tumor Marker, Ministry of Education, College of Chemistry and Molecular Engineering, Qingdao University of Science and Technology, Qingdao 266042, China

* Corresponding author: E-mail: xjuanyu@qust.edu.cn

Tel: + 86 532 84022681; Fax: + 86 532 84023927

Received: 08-11-2017

Abstract

Carboxylated nanocrystalline cellulose (CNCC) was prepared by oxidation degradation of microcrystalline cellulose (MCC) using ammonium peroxydisulfate and modified with Fe₃O₄ nanoparticles to form Fe₃O₄-CNCC nanocomposite via simple refluxing process. The Fe₃O₄-CNCC nanocomposite doped poly(3,4-ethylenedioxythiophene) (PEDOT) was successfully decorated on the glassy carbon electrode (GCE) by electrochemical deposition. The PEDOT/Fe₃O₄-CNCC modified GCE with enlarged real electrochemical surface area was used to determine nitrite with high selectivity, sensitivity and outstanding reproducibility. Using amperometric current-time (i-t) curve, the proposed sensor provided a wider linear range (0.5–2500 μM) and a lower detection limit (0.1 μM) towards nitrite compared with the method of differential pulse voltammetry (DPV). This analytical method gave good selectivity in the practical measurement of nitrite in pickles.

Keywords: Carboxylated nanocrystalline cellulose; Fe₃O₄ nanoparticle; Poly(3, 4-ethylenedioxythiophene); Amperometric sensor; Nitrite

1. Introduction

Nanocellulose (NCC), one kind of sustainable functional nanomaterials, is derived from native cellulose.^{1–5} Their morphology mainly depends on the source of precursor cellulose and the conditions of preparation. NCC exhibits remarkable properties, such as high surface area, thermally stable, renewable, biodegradable, non-toxic^{6–8} and accessible industrially in large scale.⁹ NCC has been extensively researched as key components in the design of super capacitors,^{10–12} aerogels,¹³ sensors,¹⁴ pharmaceuticals,¹⁵ chiral materials¹⁶ and catalysts.¹⁷ They are generated by the removal of amorphous regions of different sources of cellulose using acid hydrolysis, enzymatic or mechanical treatments. As a functional derivative of NCC, carboxylated nanocrystalline cellulose (CNCC) possesses better dispersibility and stability compared to NCC because of high density of carboxyl groups on its surface. In this work, CNCC was prepared using a strong

oxidant, ammonium peroxydisulfate, instead of conventional acid hydrolysis.¹⁸

As an important magnetic nanomaterial, Fe₃O₄ magnetic nanoparticle received much attention and extensive investigation in the past years for its excellent electrocatalytic activity, biocompatibility and absorption ability.^{19–23} For example, a sensitive electrochemical biosensor for the detection of H₂O₂ from living cells has been developed based on graphene blended with Fe₃O₄ nanoparticles.²⁴ Fe₃O₄ nanosphere decorated with Au nanoparticles was used as a kind of catalyst for the detection of As(III) in water.²⁵ However, Fe₃O₄ nanoparticles are thermodynamically unstable and tend to aggregate to form bulk particle. To overcome this problem, Fe₃O₄-CNCC was synthesized by dispersing Fe₃O₄ nanoparticles on the surface of CNCC in this work. Fe₃O₄-CNCC can be doped into poly(3,4-ethylenedioxythiophene) (PEDOT) to enhance its electrical conductivity.²⁶ Electrochemically polymerized PEDOT composites with differ-

ent dopant have been widely used in various kinds of electrochemical sensors.^{27–30}

Nitrite, a kind of food additive, is widely used in the food industry. However, excessive nitrite is detrimental to human health.^{31,32} In human body, nitrite can lead to the irreversible oxidation reaction of hemoglobin to methemoglobin and also can be converted into nitrosamine, which would cause hypertension and cancer.³³ Therefore, the accurate detection of nitrite becomes a pressing issue both in the human body and food industries. Till now, various analytical techniques have been used to detect nitrite. For example, Zhang used chemiluminescence to detect nitrite with the detection limit of 0.024 μM .³⁴ Huang adopted spectrofluorimetry to determine nitrite in human saliva with the detection limit of 0.5 μM .³⁵ However, most of these methods are lengthy, expensive, require complicated procedure and expert knowledge that make them unsuitable for routine analysis. To the contrary, electrochemical techniques^{36,37} provided a highly sensitive and rapid nitrite determination. Besides, the electrochemical approach was an environmentally friendly method because no extra chemical loading is required.

In this paper, Fe_3O_4 -CNCC was synthesized through a simple refluxing process and then doped PEDOT onto a glass carbon electrode by electrochemical deposition. Combining the advantages of CNCC, Fe_3O_4 , and PEDOT, the fabricated sensor can determine nitrite with high selectivity, sensitivity and outstanding reproducibility. This method gave good selectivity in the practical measurement of nitrite in pickles.

2. Experimental

2.1. Materials

Microcrystalline cellulose with the length of 20–30 μm , ammonium peroxydisulfate (APS), 3,4-ethylenedioxythiophene (EDOT), ferrous sulfate ($\text{FeSO}_4 \cdot 7\text{H}_2\text{O}$), ferric chloride ($\text{FeCl}_3 \cdot 6\text{H}_2\text{O}$), ammonia solution ($\text{NH}_3 \cdot \text{H}_2\text{O}$), sodium nitrite (NaNO_2) were obtained from Aladin Ltd. (Shanghai, China). All chemicals used in this research were analytical grade. The 0.2 M phosphate buffer solutions (PBS, pH 7.4, containing 0.9% NaCl) was prepared by mixing stock solutions of 0.2 M NaH_2PO_4 and 0.2 M Na_2HPO_4 and it was used as supporting electrolyte in the detection of nitrite. Deionized water from a Milli-Q water purifying system was used throughout.

2.2. Apparatus and Measurements

All electrochemical experiments were performed using a conventional three-electrode system containing a bare or PEDOT/CNCC, PEDOT/ Fe_3O_4 -CNCC modified glassy carbon working electrode (3 mm diameter), a platinum wire counter electrode and a saturated calomel reference electrode on a CHI660D (Shanghai CH Instruments

Co., China) electrochemical work station. The structure and morphology of the samples were characterized by transmission electron microscopy (TEM; Hitachi High-Technology Co., Ltd., Japan) and field emission scanning electron microscopy (SEM; Hitachi High-Technology Co., Ltd., Japan). XRD spectra were recorded on an X-ray diffractometer (Shimadzu7000S, Shimadzu Analytical, Japan) equipped with CuK α radiation ($\lambda = 0.154 \text{ nm}$). Zeta potentials of samples were measured with the Malvern Zetasizer Nano ZS90 (Malvern Instruments Ltd., UK).

2.3. Synthesis of CNCC

CNCC was prepared by a one-pot green procedure treatment of the mixture of MCC and APS. In brief, 2.5 g MCC and 57.05 g APS were dissolved in 250 mL of deionized water to form white suspension. The mixture was heated at 70 $^\circ\text{C}$ under stirring for 12 h to give a suspension of CNCC and then cooled to room temperature naturally. The suspension was centrifuged and washed with deionized water for several times until the pH of the suspension was close to that of deionized water. Finally, the product was lyophilized to yield a white powder.

2.4. Synthesis of Fe_3O_4 -CNCC Composite

Fe_3O_4 -CNCC was synthesized through a simple refluxing process. Typically, 100 mL of the as-synthesized CNCC (8 mg mL^{-1}), 0.1127 g of $\text{FeSO}_4 \cdot 7\text{H}_2\text{O}$ and 0.1918 g $\text{FeCl}_3 \cdot 6\text{H}_2\text{O}$ were added to the three-necked flask. Then the pH value of solution was buffered close to 10 using 25 % $\text{NH}_3 \cdot \text{H}_2\text{O}$, and the solution was heated at 60 $^\circ\text{C}$ in flow of N_2 for 2 h. The prepared reaction products were put into the reaction still and heated at 80 $^\circ\text{C}$ for 2 h. The obtained solution was isolated in a centrifugal machine at the rate of 10000 rpm for 5 min and then washed thoroughly and dispersed with deionized water. Eventually, the Fe_3O_4 -CNCC was composed following the processes discussed previously.

2.5. Preparation of the PEDOT/ Fe_3O_4 -CNCC Modified Electrode

Before the modification, GCE was polished with 0.3 μm , 0.05 μm alumina slurries in sequence and then cleaned by ultrasonication in deionized water, ethanol and deionized water for 3 min, respectively. For preparation of PEDOT/ Fe_3O_4 -CNCC modified electrodes, CNCC- Fe_3O_4 nanocomposites were first decorated on the GCE by electrochemical deposition in a solution containing 1 mg mL^{-1} CNCC- Fe_3O_4 and 0.02 M EDOT. The electrodeposition was performed at a potential of 1.2 V (vs. SCE) for 180 s.

As control, PEDOT/CNCC modified electrode was prepared under the same conditions without the presence of Fe_3O_4 . GCEs modified with the PEDOT/ Fe_3O_4 -CNCC and PEDOT/CNCC were denoted as PEDOT/ Fe_3O_4 -CNCC/GCE and PEDOT/CNCC/GCE, respectively.

2. 6. Electrochemical Measurements

Electrochemical impedance spectroscopy (EIS) measurements were recorded in 5.0 mM $[\text{Fe}(\text{CN})_6]^{3-/4-}$ solution containing 0.1 M KCl within a frequency range of 1–100,000 Hz. The amplitude of the applied sine wave was 5 mV, and the direct current potential was set at 0.80 V. Both cyclic voltammetry (CV) and differential pulse voltammetry (DPV) used to study the electrochemical reaction of nitrite were carried out in 0.2 M phosphate buffered saline (PBS, pH 7.4, containing 0.9% NaCl) containing 5 mM nitrite. The CV was recorded from 0.4–1.1 V at a scan rate of 100 mV s^{-1} , while the DPV was performed from 0.4–1.4 V with the following parameters: pulse amplitude 50 mV; pulse width 0.2 s and pulse period 0.5 s. Amperometric current-time (i-t) curve was performed in stirring PBS (0.2 M, pH 7.4) with the potential set at 0.80 V. All experiments were conducted at ambient temperature.

2. 7. HPLC Measurements

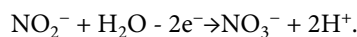
The HPLC technique was employed as a reference method to measure nitrite in real samples. The measurement was based on the national standards of China (GB 5009.33–2016 [38]).

3. Results and Discussion

3. 1. Working Mechanism of PEDOT/ Fe_3O_4 -CNCC Modified Electrode

The electrode modification and electrocatalytic mechanism are shown in Fig 1. CNCC was prepared by degradation of MCC using ammonium peroxydisulfate, and then Fe_3O_4 -CNCC was synthesized by a simple refluxing process. The obtained Fe_3O_4 -CNCC nanocomposite doped poly(3,4-ethylenedioxythiophene) (PEDOT) was

successfully decorated on the GCE by electrochemical deposition. The PEDOT/ Fe_3O_4 -CNCC modified electrode was used to determine nitrite in PBS. Based on the following results of the electrochemical tests, the corresponding transformation is shown as follows:



3. 2. Characterization of the Fe_3O_4 -CNCC

Fig S1 shows the zeta potentials of different materials. The zeta potentials of NCC and CNCC were measured as -20.46 mV and -30.05 mV , which were ascribed to the high density of the carboxyl groups on the CNCC surface. Therefore hydrophilic CNCC has good dispersiveness and stability. The zeta potential of Fe_3O_4 -CNCC was -34.05 mV , which made it easily to be doped in the polymerizing EDOT to neutralize the positive charges on the backbone of PEDOT.

The XRD patterns of CNCC and Fe_3O_4 -CNCC composite are shown in Fig S2. The diffraction peaks at $2\theta = 16.5^\circ$, 22.5° and 34.5° (labeled by the star) correspond to (110), (200) and (004) planes of CNCC respectively.³⁹ In the case of CNCC- Fe_3O_4 composite, the emerging diffraction peaks were from the (022), (400), (333) and (044) crystallographic planes of cubic structure of Fe_3O_4 ,²⁵ indicating that Fe_3O_4 has been successfully modified on CNCC.

The TEM images of the CNCC and Fe_3O_4 -CNCC are shown in Fig 2. Clearly, the CNCC was rod-like and the average diameter of CNCC was about 10 nm (Fig 2a). When modified on CNCC, Fe_3O_4 nanoparticles formed uniformly on the surface of CNCC (Fig 2b). PEDOT/CNCC (Fig 2c) exhibited a network-like wrinkled surface morphology. Compared to PEDOT/CNCC, the obtained PEDOT/ Fe_3O_4 -CNCC (Fig 2d) showed different morphology and the diameter of the PEDOT/ Fe_3O_4 -CNCC was significantly wider than that of the PEDOT/CNCC.

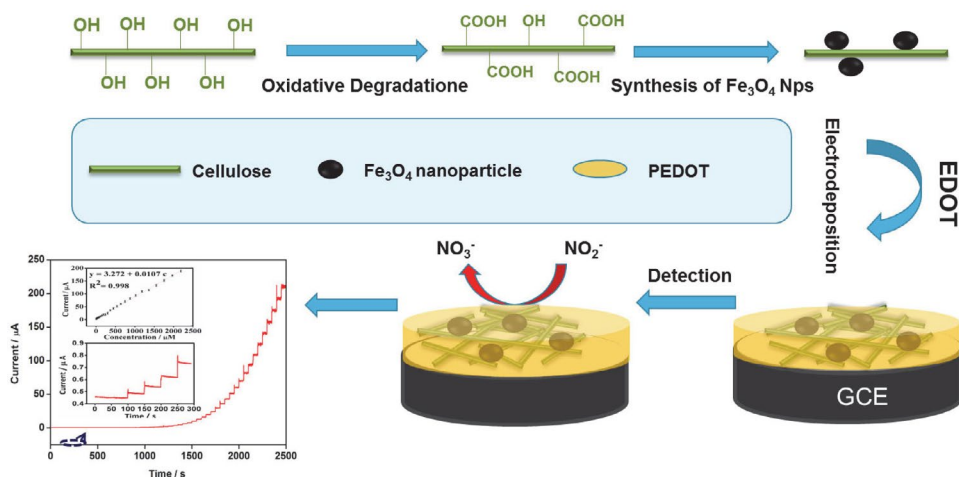


Fig 1. Schematic illustration of the preparation of the PEDOT/ Fe_3O_4 -CNCC/GCE and the proposed mechanism for the nitrite detection.

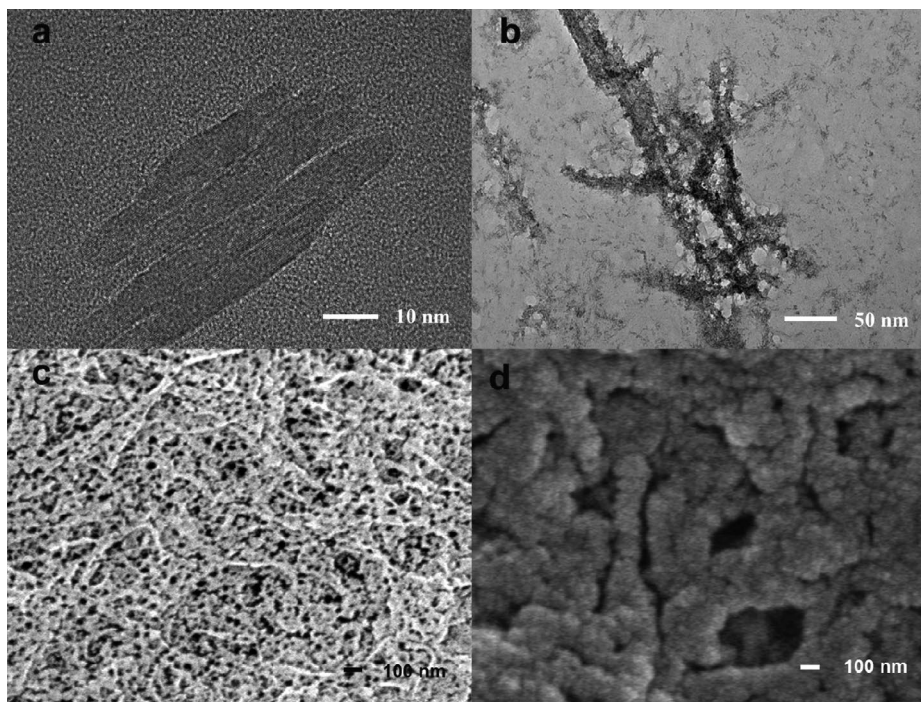


Fig 2. TEM images of CNCC (a), Fe_3O_4 -CNCC (b). SEM images of PEDOT/CNCC (c) and PEDOT/ Fe_3O_4 -CNCC (d).

3. 3. Electrochemical Characterization of PEDOT/ Fe_3O_4 -CNCC/GCE

CV and EIS were useful tools to research the nature of the modified electrodes and the influence of nanoparticles on electron-transfer kinetics.⁴⁰ Fig 3A shows CVs recorded in a 0.1 M KCl aqueous solution containing 5 mM $\text{Fe}(\text{CN})_6^{3-/4-}$. The bare GCE (curve a) showed poor electron-transfer kinetics for the $\text{Fe}(\text{CN})_6^{3-/4-}$ redox couple with an obvious peak-to-peak separation (ΔE_p). Both the

PEDOT/CNCC/GCE (curve b) and PEDOT/ Fe_3O_4 -CNCC/GCE (curve c) exhibited a reversible redox response. The reversible redox peak currents at PEDOT/ Fe_3O_4 -CNCC/GCE (curve c) was larger than that at bare GCE and PEDOT/CNCC/GCE, indicating that the introduction of Fe_3O_4 could markedly increase the electron transfer ability of the electrode. The EIS for $\text{Fe}(\text{CN})_6^{3-/4-}$ at different electrodes are shown in Fig 3B. The diameter of semicircle could be used to estimate the electron-transfer resistance (Ret) [37]. The Ret value obtained at bare GCE

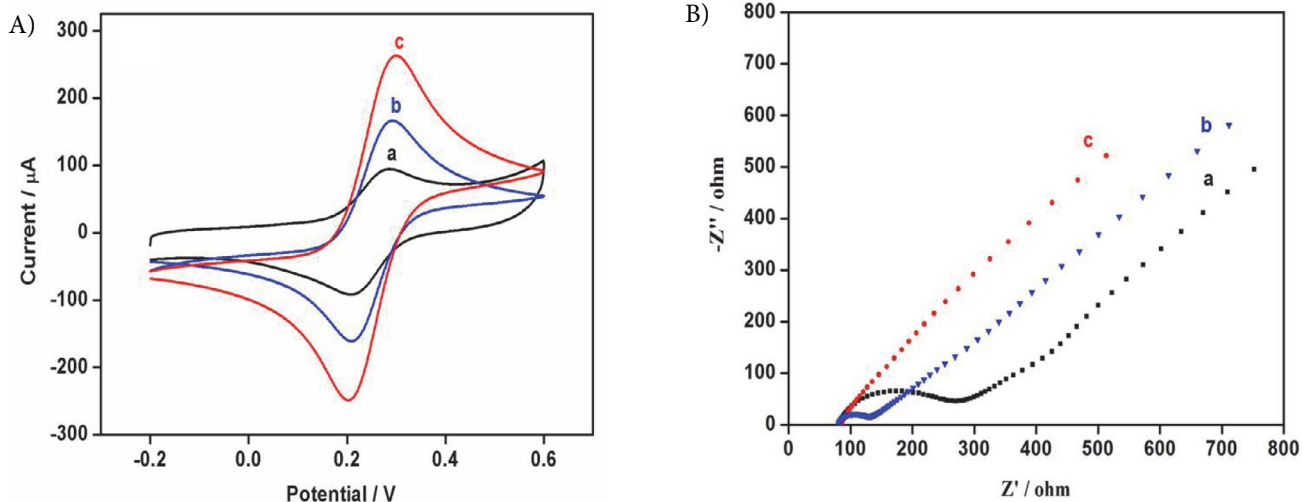


Fig 3. Cyclic voltammograms (A) and electrochemical impedance spectroscopy (B) of 5.0 mM $[\text{Fe}(\text{CN})_6]^{3-/4-}$ on bare GCE (a), PEDOT/CNCC/GCE (b), PEDOT/ Fe_3O_4 -CNCC/GCE (c) in 0.1 M KCl solution. The scan rate is 100 mV s^{-1} .

(curve a, 197.8 Ω) was significantly higher than that of the PEDOT/CNCC/GCE (curve b, 53.54 Ω). The PEDOT/Fe₃O₄-CNCC/GCE (curve c) was linear curve, implying that the Ret was close to zero, which may be ascribed to PEDOT/Fe₃O₄-CNCC composite film being highly conductive and the unique microstructure of the PEDOT/Fe₃O₄-CNCC can increase the effective surface area of the

modified electrode. The PEDOT/Fe₃O₄-CNCC/GCE showed much lower electron-transfer resistance than PEDOT/CNCC/GCE and bare GCE, which was quite in agreement with the results obtained from CV.

The real electrochemical surface areas of different electrodes (Fig 4) were characterized by CV in 5 mM Fe(CN)₆^{3-/4-} containing 0.1 M KCl at various scan rates.

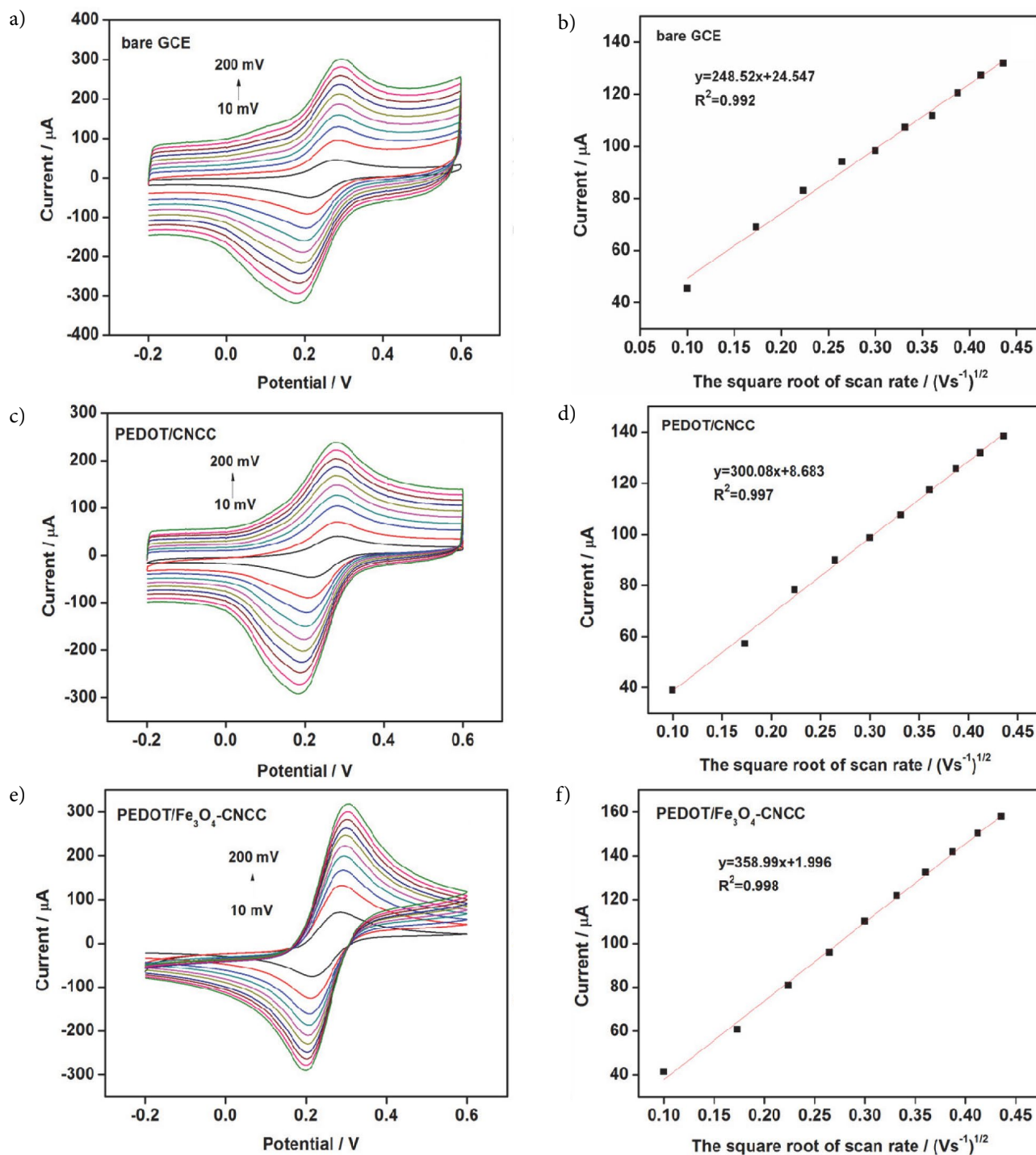


Fig 4. Cyclic voltammograms of 5 mM Fe(CN)₆^{3-/4-} at bare GCE (a), PEDOT/CNCC/GCE (c), PEDOT/Fe₃O₄-CNCC/GCE (e) with different scan rate, and (b), (d), (f) the corresponding plots of current at a, c, e versus the square root of the scan rate, respectively.

According to the Randles–Sevcik equation [24], $i_p = (2.69 \times 10^5) n^{3/2} A C D^{1/2} \nu^{1/2}$, the real electrochemical surface areas of the bare GCE, PEDOT/CNCC/GCE, PEDOT/Fe₃O₄-CNCC/GCE were calculated to be 0.0145, 0.0175, and 0.0209 cm², respectively. These results further revealed that the introduction of CNCC and Fe₃O₄ nanoparticles could enlarge the electrochemical active electrode surface.

3. 4. Electrochemical Detection of Nitrite at the PEDOT/Fe₃O₄-CNCC/GCE

The electrochemical response of the different electrodes toward nitrite was examined by CV, as shown in Fig 5. The voltammetric peaks observed at 0.7–1.05 V were ascribed to the oxidation of NO₂⁻ to NO₃⁻. The bare GCE showed no obvious anodic peak after the addition of nitrite (curve a). The oxidation currents and peak potentials of nitrite on the PEDOT/CNCC/GCE (curve b) and PEDOT/Fe₃O₄-CNCC/GCE (curve c) were measured to be 130 μA, 237 μA and 0.88 V, 0.76 V, respectively. More negative oxidation peak potential (~ 0.1 V) confirmed that Fe₃O₄ nanoparticles could notably increase the catalytic activity of the PEDOT/Fe₃O₄-CNCC/GCE.

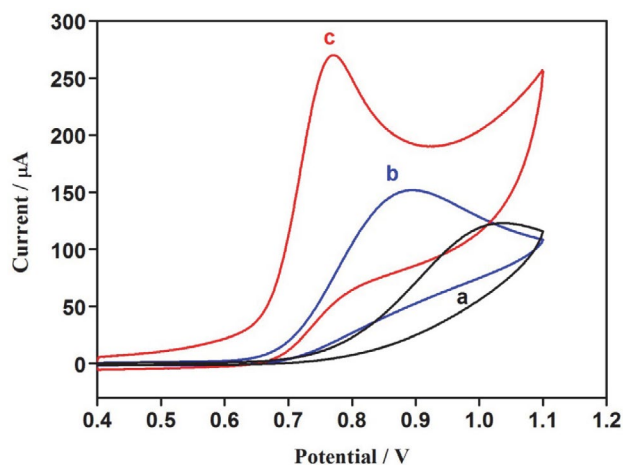


Fig 5. CV curves of different electrodes in PBS (0.2 M, pH 7.4) in the presence of 5.0 mM nitrite at 100 mV s⁻¹: bare GCE (a), PEDOT/CNCC/GCE (b), PEDOT/Fe₃O₄-CNCC/GCE (c).

As shown in S3, DPV detection gave similar results. 5 mM nitrite showed a peak current (I_p) of 38.96 mA with the peak potential of 1.05 V at the bare GCE (a). The I_p of 5 mM nitrite was 100.42 μA at the PEDOT/CNCC/GCE with the peak potential of 0.87 V (b), and 142.2 μA at the PEDOT/Fe₃O₄-CNCC/GCE with the peak potential of 0.80 V (c). Significantly improved peak current and more negative peak potential were obtained for nitrite oxidation at the PEDOT/Fe₃O₄-CNCC/GCE.

The effect of scan rate on the anodic current from nitrite oxidation on the PEDOT/Fe₃O₄-CNCC/GCE was

also investigated. As shown in Fig S4A, the oxidation current increased with the increasing of the scan rate and a liner relationship can be obtained between the peak current versus square root of scan rate in the range from 0.05 to 0.19 V/s ($R^2 = 0.997$). The diffusion-controlled irreversible electrochemical process of nitrite oxidation on the PEDOT/Fe₃O₄-CNCC/GCE was determined. Fig S4B also confirmed that sodium nitrite did not adsorb to the electrode surface and therefore did not affect the subsequent experimental determination.

3. 5. Amperometric Response to Nitrite Detection

For better nitrite detection, the effect of deposition time was investigated. As exhibited in Fig 6, when the deposition time reached 180 s, the oxidation peak current of nitrite reached the maximum. With a shorter deposition time, the deposited PEDOT/Fe₃O₄-CNCC was not sufficient, and with a longer deposition time, the thicker PEDOT/Fe₃O₄-CNCC composite will peel off during the reaction. Therefore, 180 s was selected as the optimal deposition time.

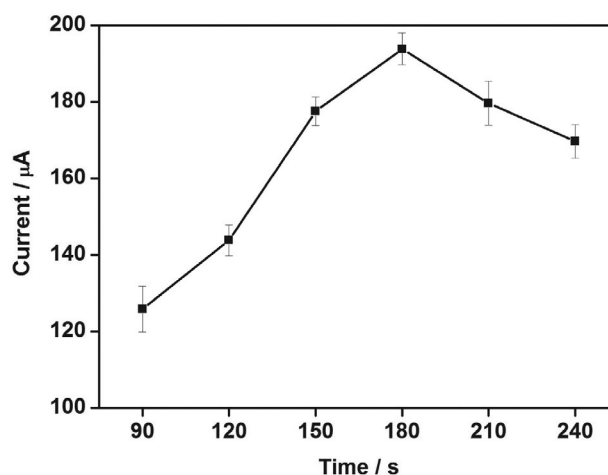


Fig 6. Effects of deposition time on the oxidation peak current of 5.0 mM nitrite at the prepared PEDOT/Fe₃O₄-CNCC/GCE.

The impact of pH on the electro-oxidation behavior of nitrite was analyzed in the pH range from 4.0–8.0 in 0.2 M PBS by DPV technique (Fig 7). The maximum peak current was obtained at pH 7 and then decreased slowly. We chose pH 7.4 for further studies because it was closely related to our physiological pH ranges.

The detection of nitrite with different concentrations at PEDOT/Fe₃O₄-CNCC/GCE was performed under the optimized deposition time. A well-defined anodic peak was observed at about 0.8 V (vs SCE), and the peak current increased with the increase of nitrite concentration (Fig 8). Moreover, the peak current (I_p) has good linear relationship with the concentration (c) of nitrite in a wide range of

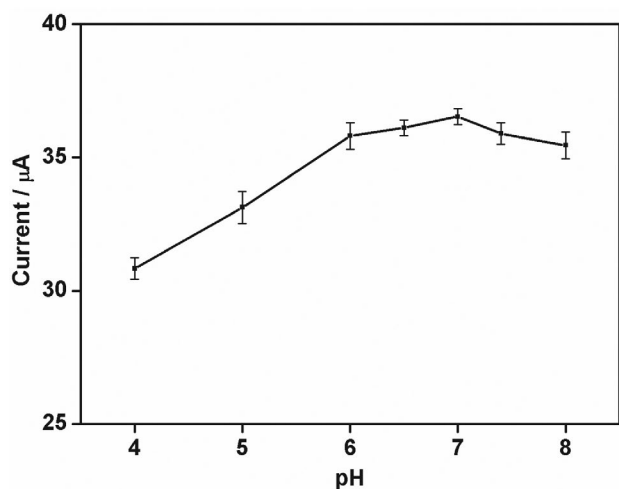


Fig 7. The influence of pH on the oxidation peak current (DPV) of 0.5 mM nitrite at the prepared PEDOT/ Fe_3O_4 -CNCC/GCE.

15 μM to 993 μM . The linear regression equation was determined to be $I_p/\mu\text{A} = 0.074 c + 1.637$ with a coefficient of $R^2 = 0.999$, and the limit of detection (LOD) was 15 μM .

In addition, amperometric (i-t) technique was also employed to detect nitrite. From Fig 9, the amperometric current response of the oxidation of nitrite on PEDOT/ Fe_3O_4 -CNCC/GCE at an applied potential of 0.8 V and the rotation speed of 1200 rpm with successive addition of varying concentrations of nitrite in 0.2 M PBS solution (pH 7.4). The sensor responded quickly to the change of nitrite concentration and achieved a steady state current within 2 s after the injection of nitrite. The linear range for the nitrite electrocatalysis was 0.5–2500 μM with linear regression equation of $I_p/\mu\text{A} = 0.079 c + 0.495$ (0.5–270.8 μM , $R^2 = 0.999$) and $I_p/\mu\text{A} = 0.074 c + 2.83$ (270.8–2500

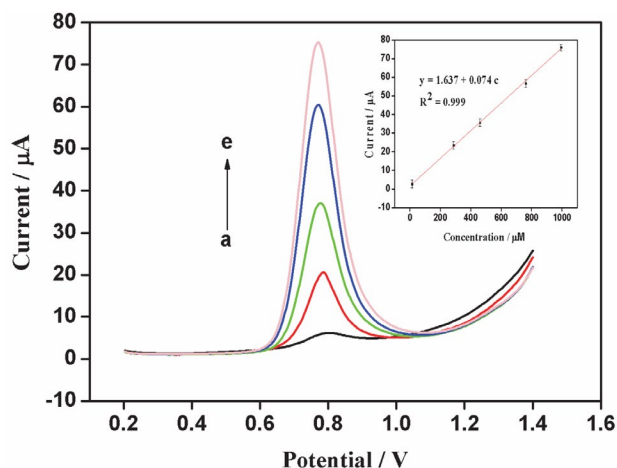


Fig 8. DPVs of nitrite with different concentrations on PEDOT/ Fe_3O_4 -CNCC/GCE in PBS (0.2 M, pH 7.4) at a scan rate of 100 mV s^{-1} . The inset is the linear relationship between peak currents and concentrations of nitrite.

μM , $R^2 = 0.996$) The LOD was calculated to be 0.1 μM . We achieved to develop a nitrite sensor with low LOD and wide liner range that is superior to previously reported sensors, as listed in Table 1.

3. 6. Selectivity, Stability, Repeatability, and Reproducibility

The selectivity of a sensor is a crucial factor for its practical application. Some possible interfering substances in electrochemical detection of nitrite, such as ascorbic acid (AA), dopamine (DA), uric acid (UA), sodium citrate and sodium benzoate were added to nitrite solution (Fig 10). Clearly, a large oxidation peak current was obtained in

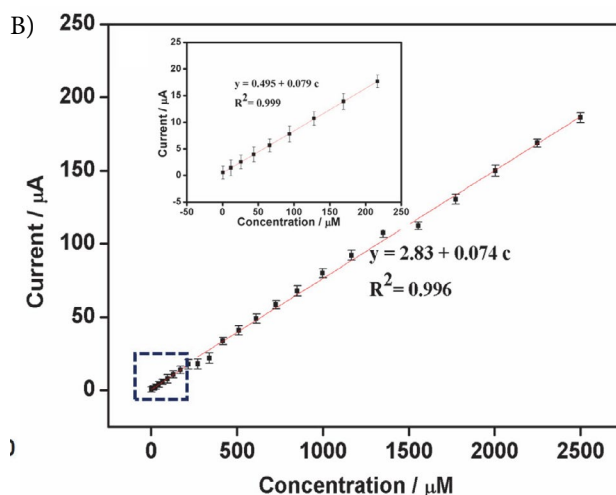
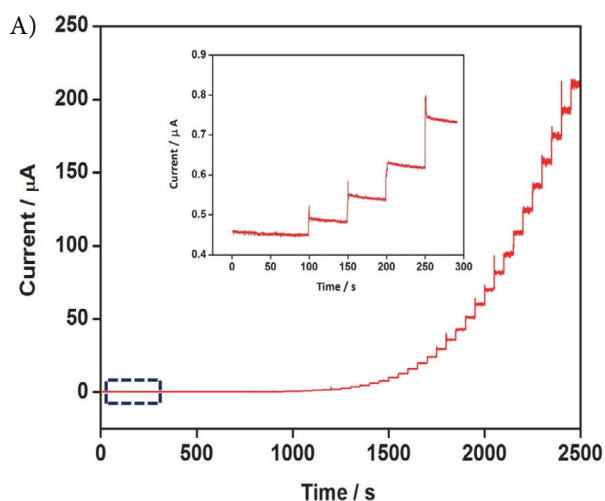


Fig 9. (A) Amperometric responses of the PEDOT/ Fe_3O_4 -CNCC/GCE in stirring PBS (0.2 M, pH 7.4) at an applied potential of 0.8 V to various concentrations of nitrite from 0.5 mM to 2500 mM. Inset shows the magnified amperometric response to the low nitrite concentration (0.5–5 μM). (B) The corresponding calibration plot for the PEDOT/ Fe_3O_4 -CNCC/GCE (the nitrite concentrations were 0.50, 11.7, 25.6, 43.7, 65.9, 93.6, 128.0, 216.7, 270.8, 337.7, 417.2, 508.9, 612.1, 726.4, 851.2, 997.9, 1165.2, 1351.2, 1554.2, 1772.4, 2003.9, 2246.9 and 2500.0 μM in sequence). Inset shows the corresponding calibration plot for the low nitrite concentration (0.5–270.8 μM).

Table 1. Comparison of the performances of different electrochemical sensors for the determination of nitrite.

Analysis methods	Material used	Analytical Range [μM]	LOD [mM]	Reference
Amperometric	CeOrGo	0.7–385	0.18	41
Amperometric	PANI-MoS ₂	4–4834	1.5	42
DPV	Au-RGO/PDDA	0.05–8.5	0.04	43
DPV	<i>N</i> -acetyl- <i>L</i> -methionine	1–500	0.75	44
Square-wavevoltammetry	Cu/MWCNT/RGO	0.1–75	0.03	45
Square-wavevoltammetry	AgPs-IL	50–1000	3	46
Cyclic voltammetry	CNT-PPy-Pt	0.5–2000	0.5	47
Amperometric	PEDOT/AuNPs	3–300	0.1	48
Amperometric	poly(1,3-DAB) film	10–1000	2	49
Amperometric	cellulose acetate membrane	1–100	0.5	50
Amperometric	PEDOT/Fe ₃ O ₄ -CNCC	0.5–2500	0.1	This work

PBS (0.2 M, pH 7.4) containing 0.1 mM nitrite (Fig 10a). After 0.5 mM AA, 0.5 mM DA, 1 mM UA, 1 mM sodium citrate and 1 mM sodium benzoate were added into 0.1 mM nitrite solution, the nitrite oxidation peak current declined by 4% but oxidation peak potential was not changed (Fig 10b). These electroactive species and food additives have no obvious interference on the determination of nitrite. The developed sensor can easily distinguish DA, AA, UA, and nitrite. The results suggested that the PEDOT/Fe₃O₄-CNCC exhibited high selectivity for nitrite detection.

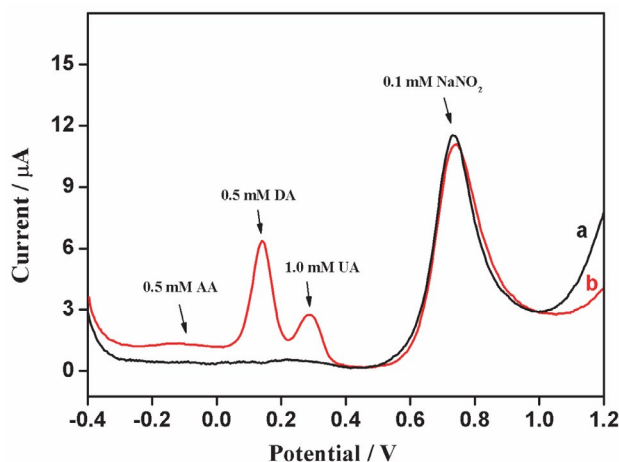


Fig 10. DPVs of the PEDOT/Fe₃O₄-CNCC/GCE in the absence (a) and presence (b) of 0.5 mM AA, 0.5 mM DA, 1.0 mM UA, 1 mM sodium citrate and 1 mM sodium benzoate in PBS (0.2 M, pH 7.4) containing 0.1 mM nitrite.

The selectivity of proposed sensor was also evaluated by amperometric method at the potential of 0.8 V. A 0.1 mM amount of nitrite, 0.5 mM AA, 0.5 mM DA, 1.0 mM UA, 1.0 mM sodium citrate, 1.0 mM sodium benzoate, and a second injection of 0.1 mM nitrite were added into PBS (pH 7.4) to investigate the selectivity of the PEDOT/

Fe₃O₄-CNCC/GCE. Figure S5 displays that the addition of AA, DA, and UA exhibited measurable current responses. DPV method should be used when nitrite coexists with AA, DA, and (or) UA in biological samples to avoid the interferences.

The stability of PEDOT/Fe₃O₄-CNCC/GCE was investigated by amperometric (i-t) technique in 0.2 M PBS with the presence of 200 μM nitrite. The current response of nitrite oxidation was recorded over a long operational period of 2500 s and retained about 96.7% of its original current. Furthermore, the PEDOT/Fe₃O₄-CNCC/GCE was fabricated and the nitrite oxidation response monitored for 2 weeks. The prepared sensor achieved 95.3% of efficiency towards the detection of nitrite, revealing the excellent long-term stability. The repeatability was observed for 10 consecutive measurements with one modified electrode in the presence of 200 μM nitrite with relative standard deviation (RSD) of 4.6%, suggesting an acceptable repeatability of the PEDOT/Fe₃O₄-CNCC modified electrode. In addition, three independent PEDOT/Fe₃O₄-CNCC modified electrodes were chosen for the determination of nitrite with an RSD of 3.7% that displayed a good reproducibility.

3. 7. Determination of Nitrite in Pickles

To demonstrate the practical feasibility of such an electrochemical sensor, the PEDOT/Fe₃O₄-CNCC/GCE was used to detect nitrite in pickles. The pickle samples were purchased from the local market in Qingdao, Shandong, and were pretreated as follows. The samples were ground adequately in a juicer, a portion of 10 g of puree was mixed with 50 mL of water, followed by sonication for 30 min in a beaker. Then the resulting mixture was centrifuged for 10 min at 4000 rpm. Finally, the supernatant was diluted to 100 mL using 0.2 PBS (pH 7.4). The recovery of nitrite was calculated using the standard addition method. The standard HPLC method was employed for the comparison. Table 2 lists the results obtained by these two

Table 2. Results of the determination of nitrite in pickles (n = 4).

Samples	The proposed electrochemical method					HPLC method	
	Detected [mg kg ⁻¹]	Added [μM]	Found [μM]	Recovery [%]	RSD [%]	Detected [mg kg ⁻¹]	Relative error[%]
1	3.48	10	9.65	96.5	3.01	3.62	3.87
2	3.57	20	19.54	97.7	2.86	3.47	-2.88
3	3.73	30	30.60	102	2.71	3.92	4.85
4	4.21	40	39.76	99.4	2.94	4.32	2.55

methods. The recoveries from 96.5% to 102% suggest that results from the proposed method are comparable with those from HPLC. Noticeably, without the use of extraction columns which are required for HPLC, the simple and rapid pretreatment of the proposed method is suitable for on-site detection. These results imply the good accuracy, reliability, and feasibility of PEDOT/Fe₃O₄-CNCC/GCE for the detection of nitrite in pickle samples.

4. Conclusions

A simple electrochemical sensor was developed based on PEDOT/Fe₃O₄-CNCC composite and used to determine nitrite. It is confirmed that rod-like CNCC works as a substrate and the Fe₃O₄ magnetite nanoparticles grow on the surface of CNCC. The prepared Fe₃O₄-CNCC nanocomposite can be doped into PEDOT to enhance its electrical conductivity. As a key element of the nitrite sensor, the PEDOT/Fe₃O₄-CNCC nanocomposite combines the advantages of CNCC and Fe₃O₄, as well as PEDOT, and can enhance the measurement of nitrite. The PEDOT/Fe₃O₄-CNCC/GCE has been applied to determine nitrite with high selectivity, low detection limit (0.1 mM), large linear range (0.5–2450 μM) and outstanding stability and reproducibility. More importantly, the electrochemical sensor based on PEDOT/Fe₃O₄-CNCC has shown great potential application for nitrite detection in food safety analysis.

5. Acknowledgements

This research was supported by the National Natural Science Foundation of China (21675093), the Natural Science Foundation of Shandong Province of China (JQ201406, ZR2016BM05), and the Science and Technology Project of Shandong Province (J15LC14).

6. References

1. S. J. Eichhorn, A. Dufresne, M. Aranguren, N. E. Marcovich, J. R. Capadona, S. J. Rowan, C. Weder, W. Thielemans, M. Roman, S. Renneckar, W. Gindl, S. Veigel, J. Keckes, H. Yano, K.

- Abe, M. Nogi, A. N. Nakagaito, A. Mangalam, J. Simonsen, A. S. Benight, A. Bismarck, L. A. Berglund, T. Peijs, *J. Mater. Sci.* **2010**, *45*, 1–33. DOI:10.1007/s10853-009-3874-0
2. Y. Habibi, L. A. Lucia, O. J. Rojas, *Chem. Rev.* **2010**, *110*, 3479–3500. DOI:10.1021/cr900339w
3. R. J. Moon, A. Martini, J. Nairn, J. Simonsen, J. Youngblood, *Chem. Soc. Rev.* **2011**, *40*, 3941–3994. DOI:10.1039/C0CS00108B
4. N. Lin, J. Huang, A. Dufresne, *Nanoscale.* **2012**, *4*, 3274–3294. DOI:10.1039/C2NR30260H
5. C. Salas, T. Nypelö, C. Rodriguez-Abreu, C. Carrillo, O. J. Rojas, *Curr. Opin. Colloid Interface Sci.* **2014**, *19*, 383–396. DOI:10.1016/j.cocis.2014.10.003
6. B. L. Peng, N. Dhar, H. L. Liu, K. C. Tam, *Can. J. Chem. Eng.* **2011**, *89*, 1191–1206. DOI:10.1002/cjce.20554
7. J. K. Jackson, K. Letchford, B. Z. Wasserman, L. Ye, W. Y. Hamad, H. M. Burt, *Int. J. Nanomed.* **2011**, *6*, 321. DOI:10.2147%2FIJN.S16749
8. A. C. W. Leung, E. Lam, J. Chong, S. Hrapovic, J. H. T. Luong, *J. Nanopart. Res.* **2013**, *15*, 1636. DOI:10.1007/s11051-013-1636-z
9. M. Kaushik, A. Moores, *Green Chem.* **2016**, *18*, 622–637. DOI:10.1039/C5GC02500A
10. A. Kafy, A. Akther, L. Zhai, H. C. Kim, J. Kim, *Synth. Met.* **2017**, *223*, 94–100. DOI:10.1016/j.synthmet.2016.12.010
11. R. Liu, L. Ma, S. Huang, J. Mei, J. Xu, G. Yuan, *New J. Chem.* **2017**, *41*, 857–864. DOI:10.1039/C6NJ03107B
12. Y. Liu, Z. Shi, Z. Gao, W. An, Z. Cao, J. Liu, *ACS Appl. Mater. Interfaces.* **2016**, *8*, 28283–28290. DOI:10.1021/acsami.5b11558
13. X. Wei, T. Huang, J. Yang, N. Zhang, Y. Wang, Z. Zhou, *J. Hazard. Mater.* **2017**, *335*, 28–38. DOI:10.1016/j.jhazmat.2017.04.030
14. A. Jasim, M. W. Ullah, Z. Shi, X. Lin, G. Yang, *Carbohydr. Polym.* **2017**, *163*, 62–69. DOI:10.1016/j.carbpol.2017.01.056
15. M. G. Bekaroğlu, Y. İşçi, S. İşçi, *Mater. Sci. Eng.* **2017**, *78*, 847–853. DOI:10.1016/j.msec.2017.04.030
16. M. Han, X. Jin, H. Yang, X. Liu, Y. Liu, S. Ji, *Carbohydr. Polym.* **2017**, *172*, 223–229. DOI:10.1016/j.carbpol.2017.05.049
17. A. M. El-Nahas, T. A. Salaheldin, T. Zaki, H. H. EI-Maghrabi, A. M. Marie, S. M. Morsy, N. K. Allam, *Chem. Eng. J.* **2017**, *322*, 167–180. DOI:10.1016/j.cej.2017.04.031
18. E. Lam, A. C. W. Leung, Y. Liu, E. Majid, S. Hrapovic, K. B.

- Male, J. H. T. Luong, *ACS Sustainable Chem. Eng.* **2012**, *1*, 278–283. DOI:10.1021/sc3001367
19. C. T. Yavuz, J. T. Mayo, W. W. Yu, A. Prakash, J. C. Falkner, S. Yean, L. Cong, H. J. Shipley, A. Kan, M. Tomson, D. Natelson, V. L. Colvin, *Science* **2006**.
20. X. Z. Yao, Z. Guo, Q. H. Yuan, Z. G. Liu, J. H. Liu, X. J. Huang, *ACS Appl. Mater. Interfaces* **2014**, *6*, 12203–12213. DOI:10.1021/am501617a
21. J. Zhu, S. A. Baig, T. Sheng, Z. Lou, Z. Wang, X. Xu, *J. Hazard. Mater.* **2015**, *286*, 220–228. DOI:10.1016/j.jhazmat.2015.01.004
22. J. Giménez, M. Martínez, J. de Pablo, M. Rovira, L. Duro, *J. Hazard. Mater.* **2007**, *141*, 575–580. DOI:10.1016/j.jhazmat.2006.07.020
23. W. Yang, A. T. Kan, W. Chen, M. B. Tomson, *Water Res.* **2010**, *44*, 5693–5701. DOI:10.1016/j.watres.2010.06.023
24. L. Wang, Y. Zhang, C. Cheng, X. Liu, H. Jiang, X. Wang, *ACS Appl. Mater. Interfaces* **2015**, *7*, 18441–18449. DOI:10.1021/acsami.5b04553
25. J. Wei, S. S. Li, Z. Guo, X. Chen, J. H. Liu, X. J. Huang, *Anal. Chem.* **2015**, *88*, 1154–1161. DOI:10.1021/acs.analchem.5b02947
26. G. Xu, S. Liang, J. Fan, G. Sheng, X. Luo, *Microchim. Acta* **2016**, *183*, 2031–2037. DOI:10.1007/s00604-016-1842-3
27. W. Wang, G. Xu, X. T. Cui, G. Sheng, X. Luo, *Biosens. Bioelectron.* **2014**, *58*, 153–156. DOI:10.1016/j.bios.2014.02.055
28. M. Cui, Z. Song, Y. Wu, B. Guo, X. Fan, X. Luo, *Biosens. Bioelectron.* **2016**, *79*, 736–741. DOI:10.1016/j.bios.2016.01.012
29. G. Xu, B. Li, X. Luo, *Sens. Actuators, B* **2013**, *176*, 69–74. DOI:10.1016/j.snb.2012.09.001
30. Z. T. Zhu, J. T. Mabeck, C. Zhu, N. C. Cady, C. A. Batt, G. G. Malliaras, *Chem. Commun.* **2004**, *13*, 1556–1557. DOI:10.1039/B403327M
31. L. Jiang, R. Wang, X. Li, L. Jiang, G. Lu, *Electrochem. Commun.* **2005**, *7*, 597–601. DOI:10.1016/j.elecom.2005.04.009
32. R. Ojani, J. B. Raoof, E. Zarei, *Electrochim. Acta* **2006**, *52*, 753–759. DOI:10.1016/j.elecom.2005.04.009
33. R. Yue, Q. Lu, Y. Zhou, *Biosens. Bioelectron.* **2011**, *6*, 4436–4441. DOI:10.1016/j.bios.2011.04.059
34. H. Zhang, L. Zhang, C. Lu, L. Zhao, Z. Zheng, *Spectrochimica Acta, Part A* **2012**, *85*, 217–222. DOI:10.1016/j.saa.2011.09.063
35. K. J. Huang, W. Z. Xie, H. S. Zhang, H. Wang, *Microchim. Acta* **2008**, *161*, 201–207. DOI:10.1007/s00604-007-0784-1
36. Y. Wang, J. Qu, R. Wu, R. Wu, P. Lei, *Water Res.* **2006**, *40*, 1224–1232. DOI:10.1016/j.watres.2006.01.017
37. M. A. Kamyabi, F. Aghajanaloo, *J. Electroanal. Chem.* **2008**, *614*, 157–165. DOI:10.1016/j.jelechem.2007.11.026
38. Ministry of Health of the People's Republic of China, National Food Safety Standard, Determination of Nitrite and Nitrate in Foods, GB 5009.33–2016, 2016.
39. H. Wang, F. Wen, Y. Chen, T. Sun, Y. Meng, Y. Zhang, *Biosens. Bioelectron.* **2016**, *85*, 692–697. DOI:10.1016/j.bios.2016.05.078
40. D. Wang, J. Wang, Z. Liu, X. Yang, X. Hu, J. Deng, N. Yang, Q. Wan, Q. Yuan, *ACS Appl. Mater. Interfaces* **2015**, *8*, 28265–28273. DOI:10.1021/acsami.5b08294
41. D. M. Stanković, E. Mehmeti, J. Zavašnik, K. Kalcher, *Sens. Actuators, B* **2016**, *236*, 311–317. DOI:10.1016/j.snb.2016.06.018
42. Y. Zhang, P. Chen, F. Wen, C. Huang, H. Wang, *Ionics* **2016**, *22*, 1095–1102. DOI:10.1007/s11581-015-1634-5
43. S. Jiao, J. Jin, L. Wang, *Sens. Actuators, B* **2015**, *208*, 36–42. DOI:10.1016/j.snb.2014.11.020
44. A. Kannan, A. Sivanesan, G. Kalaivani, *RSC Adv.* **2016**, *6*, 96898–96907. DOI:10.1039/C6RA18440E
45. J. Dai, D. Deng, Y. Yuan, J. Zhang, F. Deng, S. He, *Microchim. Acta* **2016**, *183*, 1553–1561. DOI:10.1007/s00604-016-1773-z
46. E. Menart, V. Jovanovski, S. B. Hočevar, *Electrochem. Commun.* **2015**, *52*, 45–48. DOI:10.1016/j.elecom.2015.01.017
47. S. Rajesh, A. K. Kanugula, K. Bhargava, G. Llavazhagan, S. Kotmrāju, C. Karunakaran, *Biosens. Bioelectron.* **2010**, *26*, 689–695. DOI:10.1016/j.bios.2010.06.063
48. O. Zhang, Y. Wen, J. Xu, L. Lu, X. Duan, H. Yu, *Synth. Met.* **2013**, *164*, 47–51. DOI:10.1016/j.synthmet.2012.11.013
49. V. Biagiotti, F. Valentini, E. Tamburri, M. L. Terranova, D. Moscone, G. Palleschi, *Sens. Actuators, B* **2007**, *122*, 236–242. DOI:10.1016/j.snb.2006.05.024
50. M. Badea, A. Amine, G. Palleschi, D. Moscone, G. Volpe, A. Curulli, *J. Electroanal. Chem.* **2001**, *509*, 66–72. DOI:10.1016/S0022-0728(01)00358-8

Povzetek

Karboksilirano nanokristalinično celulozo (CNCC) smo pripravili z oksidativnim razkrojem mikrokristalinične celuloze (MCC) z amonijevim peroksidisulfatom in jo modificirali z Fe_3O_4 nanodelci ter pridobili Fe_3O_4 -CNCC nanokompozitni material s preprostim postopkom z refluksom. Z Fe_3O_4 -CNCC nanokompozitom dopirani poli(3,4-etilendioksitiofen) (PEDOT) smo uspešno nanесли na elektrodo iz steklastega ogljika (GCE) z elektrokemično depozicijo. GCE modificirana z PEDOT/ Fe_3O_4 -CNCC je imela večjo elektrokemično-aktivno površino in smo jo uporabili za določitev nitrita z visoko selektivnostjo, občutljivostjo in izjemno obnovljivostjo. Ob uporabi amperometrične tokovno-časovne (i-t) krivulje je predlagani senzor imel širše linearno območje (0,5–2500 μM) in nižjo mejo zaznave (0,1 μM) za nitrit v primerjavi z metodo diferencialne pulzne voltometrije (DPV). Predlagana analizna metoda je pokazala dobro selektivnost pri praktičnem določanju nitrita v vloženi zelenjavi.

Chromium Speciation Using an Aminated Amberlite XAD-4 Resin Column Combined with Microsample Injection-Flame Atomic Absorption Spectrometry

Erkan Aksoy,¹ Şükrü Gökhan Elçi,¹ Ali N. Siyal² and Latif Elçi^{1,*}

¹ Chemistry Department, Faculty of Science and Arts, University of Pamukkale, 20020, Denizli, Turkey

² Institute of Advance Research Studies in Chemical Science, University of Sindh, Jamshoro, Pakistan

* Corresponding author: E-mail: elçi@pau.edu.tr

Received: 10-11-2017

Abstract

Amberlite XAD-4 resin (AXAD-4) was chemically modified to an aminated Amberlite XAD-4 (AAXAD-4) resin and characterized by infrared spectroscopy. AAXAD-4 resin was used as an efficient solid phase for the preconcentration and speciation of Cr(III) and Cr(VI) ions by column technique. The concentration of chromium species was determined by microsample injection system-flame atomic absorption spectrometer (MIS-FAAS). Selective retention of Cr(III) ions was achieved at pH 8.0 and eluted using 1.0 mL of 3.0 mol L⁻¹ HCl and 1.0 mL of 2.0 mol L⁻¹ NaOH, successively, at the flow rate of 5.0 mL min⁻¹. The maximal sorption capacity of AAXAD-4 resin for Cr(III) ions was found to be 67.0 mg g⁻¹. The limit of detection (LOD) and limit of quantitation (LOQ) for Cr(III) ions were found to be 0.041 and 0.131 µg L⁻¹, respectively, with preconcentration factor (PF) of 375 and relative standard deviation (RSD) of 3.75% (n = 11). The method was validated using certified reference materials (CRMs) and successfully applied to the real samples, spiked with Cr(III) and Cr(VI) ions.

Keyword: Aminated Amberlite XAD-4 resin; column; solid-phase; chromium speciation; MIS-FAAS

1. Introduction

Speciation of chromium is still one of most important long-standing analytical challenges due to its impact on environmental chemistry, ecotoxicology, clinical toxicology and food industry. Among several redox states, chromium exists mostly in the trivalent Cr(III) and hexavalent Cr(VI) redox states with contrasting chemical, biological and toxicological properties. While water insoluble Cr(III) is an essential ion for mammals, water soluble Cr(VI) is a human carcinogen, mutagen and toxin due to its high oxidation potential and relatively small size. Compounds of Cr(VI) are 10 to 100 times more toxic than those of Cr(III).^{1,2} Cr(III) and Cr(VI) also cause dermatologic allergy during contact. Thus, US EPA and WHO recommend the threshold value for total chromium as 100 µg L⁻¹ for drinking water and 50 µg L⁻¹ Cr(VI) as tolerance level, respectively.^{3,4}

The toxicity of metals strongly depends on their oxidation states rather than their total concentrations.⁵ Therefore, metallic species have become a prime task for analytical chemists for years.⁶ Various techniques, such as flame atomic absorption spectrometry (FAAS), graphite furnace

atomic absorption spectrometry (GF-AAS), inductively coupled plasma mass spectrometry (ICP-MS), inductively coupled plasma atomic emission spectrometry (ICP-AES), inductively coupled plasma optical emission spectrometry (ICP-OES), thermospray flame furnace atomic absorption spectrometry (TS-FF-AAS) and electrothermal atomic absorption spectrometry (ET-AAS), have been routinely used for the determination of total chromium.⁷ Unfortunately these techniques cannot differentiate Cr(III) from Cr(VI) ions. For the speciation and preconcentration of chromium species, several methods based on solid-phase extraction (SPE),^{8–11} coprecipitation,^{12–14} cloud point extraction¹⁵ and liquid phase microextractions^{16–18} have been developed. Among these, SPE has advantages such as easy operation, smallest consumption of toxic solvents, recycling of solid phases and high selectivity.^{19,20} For speciation of chromium species, activated carbon,²¹ silica gel,²² sawdust,²³ chelating resins^{11–18,23–25} and Amberlite XAD resin series have been used as solid phase.^{25–27} Amine group was incorporated on the polymeric matrix of Amberlite XAD-4 resin. This modified resin was used as effective solid phase for SPE speciation and preconcentration of chromium species.

2. Experimental

2. 1. Apparatus

A Perkin-Elmer flame atomic absorption spectrometer (AAAnalyst 200) equipped with a chromium hollow cathode lamp, an air-acetylene flame atomizer and hand-made microinjection system was used for chromium determination. The instrumental parameters were established as recommended by manufacturer: wavelength, 357.9 nm; lamp current, 30.0 mA; slit width, 0.7 nm; acetylene flow, 2.0 L min⁻¹ and air flow, 17.0 L min⁻¹. As reported in the previous study, a 100 µL volume (for all sample and standard solutions) was injected manually into a micropipette tip of the microinjection system connected to the nebulizer of FAAS.¹³ The pH of solution was carefully measured using a digital pH meter (Hanna 211, Germany). ATR-IR spectrometer (UATR Spectrum Two from PerkinElmer) was used for recording ATR spectra. The reverse osmosis system (Human Corp., Seoul, Korea) was used to obtain ultrapure (UP) quality water (resistivity, 18.2 MΩ cm⁻¹).

2. 2. Reagents and Solutions

Analytical grade chemicals and UP water were used throughout the study. Stock solutions of Cr(III) and Cr(VI) were prepared using high-purity Cr(NO₃)₃ · 9H₂O (Sigma-Aldrich, St. Louis, MO, USA) and K₂Cr₂O₇ (Merck, Darmstadt, Germany), respectively. The working and reference solutions were prepared daily by diluting the stock solutions. Amberlite XAD-4 resin was purchased from Alfa Aesar (Germany). The pH was adjusted using CH₃COOH/CH₃COONa buffer to pH 3–6, a solution of equal volume of 1.0 mol L⁻¹ HCl and 1.0 mol L⁻¹ NaOH solutions for pH 7 and NH₄NO₃/NH₃ buffer for pH 7.5–10.

2. 3. Sampling

The bottled drinking and mineral water samples were purchased from a local market in Denizli, Turkey. The waste water samples were collected from outlet of the wastewater treatment plant in Denizli, Turkey. The fountain water was taken from Incilipinar, Denizli, Turkey. The waste water samples were immediately transported to the laboratory and filtered with 0.45 µm cellulose nitrate membrane (Sartorius, GmbH, Germany) under vacuum to remove suspended materials and then analysed by the proposed procedure within 24 h.

2. 4. Chemical Modification of Amberlite XAD-4 resin

Amberlite XAD-4 resin (polystyrene divinyl benzene) was chemically modified by the reported procedure.^{26,27} 5.0 g of Amberlite XAD-4 resin was put into 250

mL round bottom flask and a nitrating mixture of 10 mL of concentrated HNO₃ and 25 mL of concentrated H₂SO₄ was added. The system was stirred for 1 h at 60 °C. Reaction mixture was poured into an ice-cold water and filtered. The nitro derivative was washed repeatedly with cold water until acid was rinsed out and air-dried. The nitro group was reduced to amino derivative by refluxing with 40 g of SnCl₂ and 60 mL of 2.0 mol L⁻¹ HCl in 100 mL of ethanol. The amino product (AAXAD-4) was treated thoroughly with 2.0 mol L⁻¹ sodium hydroxide to decompose the tin-amine complex, followed by 1.0 mol L⁻¹ HCl in order to remove the excess stannous chloride. Finally, the product was washed with excess water and dried at 75 °C in drying oven for 24 h. The final resin product was confirmed by infrared spectroscopy.

2. 5. Preparation of SPE Column

A purchased empty Chromabond column SPE cartridge tube (3 mL) from Macherey-Nagel, Düren, Germany, was packed with 185 mg of aminated resin (ground). Glass wool was used to pack both ends of the column to avoid the loss of the resin during experiments. The flow rate of the sample solution was controlled with Chromabond vacuum manifold. The SPE column was decontaminated by washing with acetone, 1.0 mol L⁻¹ HCl, 1.0 mol L⁻¹ NaOH and water, respectively. For adjusting pH of the resin to 8, NH₄NO₃/NH₃ buffer was passed through the column.

2. 6. Speciation and Preconcentration Procedure

The model solutions in the range of 10–750 mL including 5–10 µg Cr(III) or Cr(VI) were adjusted to pH 8 and passed through the column. Cr(III) ions were retained on the resin and Cr(VI) ions were passed as effluent. Cr(III) ions were eluted by sequential use of 1.0 mL of 3.0 mol L⁻¹ HCl and 1.0 mL of 2.0 mol L⁻¹ NaOH at the flow rate of 5.0 mL min⁻¹. The Cr(III) ions in the eluent were determined by MIS-FAAS. The recovery of Cr(III) ions was quantitatively achieved. The total concentration of chromium was determined by the same procedure after the reduction of Cr(VI) to Cr(III) ions using reported reducing mixture of 0.5 mL of ethanol and 0.5 mL of concentrated H₂SO₄.²⁹

3. Results and Discussion

3. 1. Characterization

The modification of Amberlite XAD-4 resins was characterized by infrared spectroscopy. In supporting information, ATR-IR spectra of unmodified Amberlite XAD-4 resin (Figure S1), nitro derivative (Figure S2) and amino derivative (Figure S3) are given. By comparing

spectra (Figure S1 and S2), the additional strong peaks in Figure S1 spectrum at 1525 and 1347 cm^{-1} , respectively, correspond to the asymmetric and symmetric stretching vibrations of N=O bond in nitro derivative.²⁸ By comparing spectra in Figure S2 and Figure S3, appearance of two characteristic peaks at 3359 and 3217 cm^{-1} in Figure S3 spectrum corresponds to N-H bond in amino derivative (primary amine). The spectral information revealed that Amberlite XAD-4 resin was successfully converted to amino derivative.

3. 2. Effect of pH

The pH is an important parameter that strongly influences the retention of metal species on the surface of the resin. Thus, the effect of pH between 2 and 9 on the adsorption of Cr(III) and Cr(VI) ions was studied separately. For optimization, 50 mL of model solutions at pH from 2 to 9 was passed through the column individually. The adsorbed Cr(III) and Cr(VI) ions were eluted by sequential use of 2.5 mL of 3.0 mol L^{-1} of HCl and 2.5 mL of 2.0 mol L^{-1} of NaOH and determined by MIS-FAAS. At pH

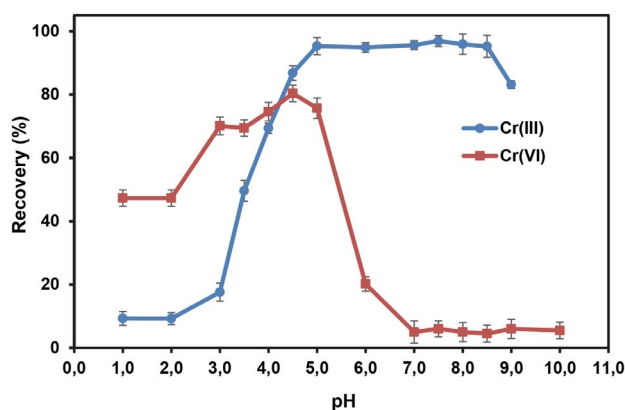


Figure 1. Effect of pH on recoveries of 1.0 $\mu\text{g L}^{-1}$ Cr(III) and 1.0 $\mu\text{g L}^{-1}$ Cr(VI) ions from 50 mL sample solution ($n = 3$).

7 through 9, the recoveries of Cr(III) and Cr(VI) ions were $\geq 95\%$ and $\leq 10\%$, respectively, as shown in Figure 1. Therefore, pH 8 was selected as the best point for the separation of Cr(III) and Cr(VI) ions. Very low uptake of Cr(VI) ions at pH 7 through 10 can be explained as amino group of AAXAD-4 resin became negatively charged in alkaline medium and possessed electrostatic repulsion with CrO_4^{2-} ions that caused a decrease in the uptake of Cr(VI) ions. At low pH values, Cr(III) exists as its kinetically non-reactive aqua-complex $\text{Cr}(\text{H}_2\text{O})_3^{3+}$ that leads to its low uptake due to possible electrostatic repulsion between $\text{Cr}(\text{H}_2\text{O})_3^{3+}$ and protonated amino group of AAXAD-4 resin. As pH was increasing, the coordinated water molecules were replaced by the more reactive hydroxide ions, transforming the former complex ($\text{Cr}(\text{H}_2\text{O})_3^{3+}$) to a more active form ($\text{Cr}(\text{H}_2\text{O})_2(\text{OH})^{2+}$ or $\text{Cr}(\text{H}_2\text{O})(\text{OH})_2^+$), which leads to comparatively better interaction with amino group ($-\text{NH}_2$) of AAXAD-4 resin.³¹

3. 3. Effect of Eluents

The effects of type, volume and concentration of eluents were tested for the quantitative desorption of Cr(III) ions from the column. Figure 1 clearly indicates the percentage decrease in recoveries below pH 3 for the uptakes of Cr(III) ions by AAXAD-4 resin. Thus, 5.0 mL of HCl with concentration range from 1.0 through 7.0 mol L^{-1} was tested to elute the Cr(III) ions. The recovery of Cr(III) was not achieved quantitatively up to 7.0 mol L^{-1} HCl as shown in Table 1. At $\text{pH} > 8.5$ (Figure 1) the uptake of Cr(III) ions decreased due to the conversion of $\text{Cr}(\text{OH})_3$ to highly soluble tetrahydroxo complex ($\text{Cr}(\text{OH})_4^-$). Thus, 5.0 mL of NaOH with concentration range from 1.0 through 4.0 mol L^{-1} was tested to elute the Cr(III) ions. The quantitative recovery of Cr(III) ions was not achieved until up to 4.0 mol L^{-1} NaOH (Table 1). Based on these results, a consecutive use of 2.5 mL of 3.0 mol L^{-1} HCl and 2.5 mL of 2.0 mol L^{-1} NaOH solutions was tested for desorption of Cr(III) ions and resulted in quantitative recovery

Table 1. Effect of type, concentration and volume of eluents on the recovery of 1.0 $\mu\text{g L}^{-1}$ Cr(III) ions in 100 mL sample from the column ($n = 4$)

Eluents	Recovery \pm RSD, %
5.0 mL 1.0 mol L^{-1} HCl	44.7 \pm 0.8
5.0 mL 3.0 mol L^{-1} HCl	51.7 \pm 2.1
5.0 mL 5.0 mol L^{-1} HCl	67.2 \pm 1.0
5.0 mL 7.0 mol L^{-1} HCl	69.1 \pm 1.2
5.0 mL 1.0 mol L^{-1} NaOH	26.2 \pm 1.4
5.0 mL 2.0 mol L^{-1} NaOH	38.4 \pm 1.3
5.0 mL 4.0 mol L^{-1} NaOH	40.2 \pm 1.1
2.5 mL 3.0 mol L^{-1} HCl and then 2.5 mL 2.0 mol L^{-1} NaOH	97.9 \pm 1.2
2.0 mL 3.0 mol L^{-1} HCl and then 2.0 mL 2.0 mol L^{-1} NaOH	95.1 \pm 1.2
1.0 mL 3.0 mol L^{-1} HCl and then 1.0 mL 2.0 mol L^{-1} NaOH	96.3 \pm 2.1
0.5 mL 3.0 mol L^{-1} HCl and then 0.5 mL 2.0 mol L^{-1} NaOH	78.7 \pm 1.1
0.25 mL 3.0 mol L^{-1} HCl and then 0.25 mL 2.0 mol L^{-1} NaOH	48.5 \pm 1.1

ery. The volume of eluent solutions was further decreased to 1.0 mL of 3.0 mol L⁻¹ HCl and 1.0 mL of 2.0 mol L⁻¹ NaOH (to obtain high preconcentration factor) and resulted in quantitative recovery of Cr(III) ions (Table 1). Thus, a consecutive use of 1.0 mL of 3.0 mol L⁻¹ HCl and 1.0 mL of 2.0 mol L⁻¹ NaOH solutions was selected as the best elution solvent for the desorption of Cr(III) ions in further experiments.

3. 4. Effect of Sample Volume

Another strategy to concentrate analyte at very low concentration is to increase the volume of sample. Therefore, the effect of sample volume on the retention of Cr(III) was studied. The recovery of Cr(III) ion was achieved quantitatively ($\geq 95\%$) up to the sample volume of ≤ 750 mL as shown in Figure 2. Thus, the PF was calculated to be 375 as the ratio of maximal sample volume (750 mL) to minimal eluent volume (2.0 mL). Considering time factor, the volume of real samples for analysis was fixed to 100 mL.

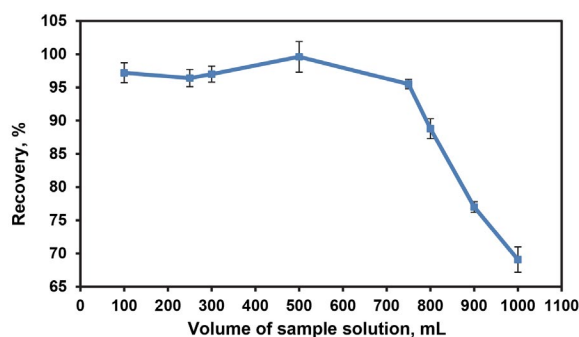


Figure 2. Effect of sample volume on retention of 1.0 µg L⁻¹ Cr(III) ions by the column at pH 8 (n = 4).

3. 5. Effect of Flow Rate of Eluent and Sample Solution

In order to decrease the preconcentration time, the flow rates of sample and eluent solutions were optimised

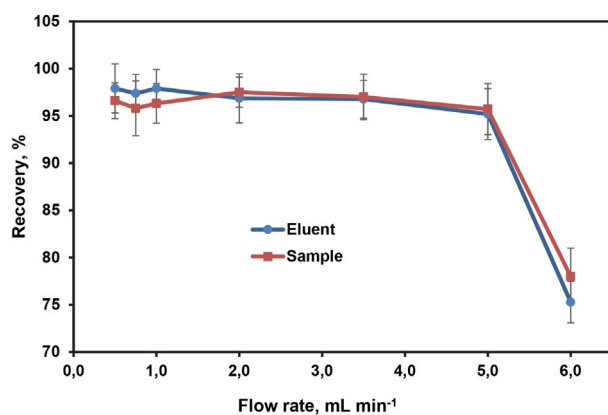


Figure 3. Effect of flow rate of eluent and sample solutions on the recovery of 1.0 µg L⁻¹ Cr(III) ions from 25.0 mL samples (n = 4).

in the range of 0.5–6.0 mL min⁻¹. The results (Figure 3) demonstrated that the quantitative retention and percentage recovery of Cr(III) ions were achieved at the flow rate of 5.0 mL min⁻¹ of sample solution and eluent as well.

3. 6. Adsorption Capacity

The adsorption capacity of the resin is a significant parameter that determines the minimal quantity of adsorbent required for quantitative uptake of analyte from a sample solution. Based on a previous report in reference³¹, the capacity experiments were conducted. Buffered at pH 8.0 in room temperature, 10 mL of model solutions containing Cr(III) in the concentration range of 0.5–400 mg L⁻¹ were equilibrated with 10 mg AAXAD-4 up to 24 h to saturate amino groups. The adsorption isotherm (Figure 4) was plotted as concentrations of Cr(III) ions against adsorbed amount of Cr(III) ions per gram of AAXAD-4 resin. The adsorption capacity of Cr(III) ions was found to be 67.0 mg g⁻¹ as a value at which the adsorbed amount of Cr(III) ions remained constant although the concentration of Cr(III) was increased.

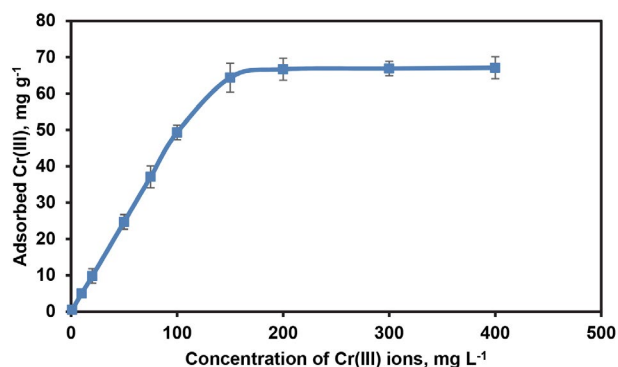


Figure 4. Adsorption isotherm for Cr(III) ions. Conditions: 10 mg adsorbent, 0.5–400 mg L⁻¹ Cr(III), Saturation time: 24 h and pH = 8.0 (n = 3).

3. 7. Sorption Competition of Coexisting Ions with Cr(III) Ions

Environmental water samples contain many heavy metal ions and some common alkali and alkaline earth metals as coexisting ions. For this reason, the effect of present coexisting ions on the preconcentration of Cr(III) needs to be evaluated at optimal conditions. For this purpose, 20 mL of model solution containing 1.0 µg L⁻¹ of Cr(III) ions was spiked with possible interfering ions and subjected to the column according to the proposed method. The Cr(III) ions were quantitatively recovered in the presence of coexisting ions at tolerance limits, taken as a relative error $\leq \pm 5\%$. It can be seen from Table 2 that the presence of main cations and anions cause an insignificant

Table 2. The influence of the common coexisting ions on recovery of 1.0 $\mu\text{g L}^{-1}$ Cr(III)

Coexisting ions	Tolerance limits of the ions, mg L^{-1}
Na ⁺ & K ⁺	40000
Ca ²⁺ & Mg ²⁺	250
CH ₃ COO ⁻	8000
Cl ⁻	60 000
H ₂ PO ₄ ⁻	10 000
SO ₄ ²⁻	1000
CO ₃ ²⁻	3000
Zn ²⁺ , Ni ²⁺ , Mn ²⁺ & Pb ²⁺	50
Cu ²⁺ , Hg ²⁺ , Fe ²⁺ & Fe ³⁺	10

influence on the retention of Cr(III) ions onto AAXAD-4 resin. This shows us that AAXAD-4 resin is highly selective for Cr(III) ions for the analysis of various real water samples.

3. 8. Cr(III) Determination in Presence of Cr(VI) and Determination of Total Chromium Amount

The applicability of the proposed method was tested in presence of Cr(VI) ions for the determination of Cr(III) ions. For testing, the synthetic aqueous solutions including various mixtures of Cr(III) and Cr(VI) ions at different concentration levels were passed through the column at optimal conditions. Cr(III) ions were quantitatively separated and retained while Cr(VI) ions were almost completely passed through the column. This was observed by analyzing the effluent. The recoveries of Cr(III) ions were achieved quantitatively as shown in Table 3. In further study, the usability of the method for the determination of total chromium amount was also tested. Total chromium was determined after the reduction of Cr(VI) ions to Cr(III) ion by adding a mixture of 0.5 mL of concentrated H₂SO₄ and 0.5 mL of ethanol to 50 mL of sam-

ple solution containing Cr(VI) and Cr(III) ions at different concentration levels (Table 3).²⁹ The recovery of total chromium was also achieved quantitatively as shown in Table 3.

3. 9. Analytical Performance of the Proposed Method

The accuracy and validation of proposed method was confirmed by analysing different CRMs such as industrial wastewater (BCR-715), drinking water (TMDW-500) and lyophilised water (BCR-544) for the determination of Cr(III) ions and total chromium. It was checked by Student's t-test whether the difference between the certified value and the found value was significant. The results shown in Table 4 indicated that there is not a significant difference between certified and found values.

After preconcentration of Cr(III) ions, the linear equation was $A = 5.5259X + 0.0008$ and $r^2 = 0.9995$ for 600 mL with concentration range of 2–12 $\mu\text{g L}^{-1}$ of Cr(III) ions. Before preconcentration, the linear equation was $A = 0.0191X + 0.0021$ and $r^2 = 0.998$ within the concentration range of 0.2–5.0 $\mu\text{g mL}^{-1}$ of Cr(III) ions. Theoretical PF was calculated to be 289 as the ratio of slope of linear equation after preconcentration to the slope of linear equation before preconcentration close to the experimental PF of 300, indicating the retention and elution of the analyte was quantitative with recovery of 96%. The sensitivity was found to be 5.53 $\mu\text{g L}^{-1}$ from the slope of the calibration curve.³² The reproducibility of the overall preconcentration method in terms of RSD was calculated to be 3.75% ($n = 11$) at the concentration of 0.5 $\mu\text{g L}^{-1}$ Cr(III) ions. LOD (blank + 3 σ) and LOQ (blank + 10 σ , where σ is RSD of blank analysis, $n = 20$) are defined by IUPAC and were calculated accordingly.^{33,34} The LOD and LOQ of Cr(III) ions were found to be 0.041 and 0.131 $\mu\text{g L}^{-1}$, respectively. AAXAD-4 resin was successfully reused more than 250 times without significant loss in its performance.

Table 3. Test of proposed method for the determination of 1.0 $\mu\text{g L}^{-1}$ Cr(III) in presence of Cr(VI) ions and determination of total chromium (Sample volume: 50 mL & $n = 4$)

Added, μg Cr(III)	Cr(VI)	Found, μg , mean \pm SD			Recovery, %			
		Cr	Cr(III) ^a	Cr(VI) ^b	Cr ^c	Cr(III)	Cr(VI)	Cr
5	5	10	4.74 \pm 0.5	4.85 \pm 0.06	9.48 \pm 0.16	95 \pm 10	97 \pm 1	95 \pm 2
5	10	15	4.79 \pm 0.14	9.86 \pm 0.30	14.28 \pm 0.13	95 \pm 3	99 \pm 3	95 \pm 1
5	20	25	5.25 \pm 0.12	19.64 \pm 0.24	24.15 \pm 0.41	105 \pm 2	98 \pm 1	97 \pm 2
5	30	35	5.01 \pm 0.06	30.07 \pm 0.37	33.37 \pm 0.34	100 \pm 1	100 \pm 1	95 \pm 1
10	5	15	9.40 \pm 0.33	5.05 \pm 0.10	14.49 \pm 0.24	94 \pm 3	101 \pm 2	97 \pm 2
20	5	25	18.97 \pm 0.34	4.88 \pm 0.13	23.85 \pm 0.52	95 \pm 2	98 \pm 3	95 \pm 2
30	5	35	28.39 \pm 0.68	5.03 \pm 0.10	33.84 \pm 0.84	95 \pm 2	101 \pm 2	97 \pm 2

Cr(III)^a: Found amount of Cr(III) ions in presence of Cr(VI) ions.

Cr(VI)^b: Total amount of Cr(VI) ions by subtracting Cr(III) amount from total amount of Cr added.

Cr^c: Total amount of Cr determined after reducing Cr(VI) to Cr (III) ions in sample solutions

Table 4. Analysis of some certified reference materials (n = 3, final vol.: 2 mL)

Analytes		Certified reference materials/sample volume/concentrations		
		BCR-715 industrial waste water/5mL/ $\mu\text{g mL}^{-1}$	CRM TMDW-500 drinking water/ 50mL/ $\mu\text{g L}^{-1}$	BCR-544 Lyophilised water, 50mL/ $\mu\text{g L}^{-1}$
Total Cr	Certified	1.00 ± 0.09	20.0 ± 0.1	49.6 ± 1.4 ^b
	Found	1.05 ± 0.02	19.1 ± 0.4	47.5 ± 1.4
	Recovery,%	105	95.5	95.6
	t _{test} value	4.3(ns)	3.9(ns)	2.6(ns)
Cr(III)	Certified	–	–	26.8 ± 1.0
	Found	0.56 ± 0.02	9.7 ± 0.1	25.4 ± 1.1
	Recovery,%	–	–	94.8
	t _{test} value	–	–	2.2(ns)
Cr(VI)	Certified	–	–	22.8 ± 1.0
	Found	0.49 ± 0.02 ^a	9.4 ± 0.3 ^a	22.1 ± 0.9 ^a
	Recovery,%	–	–	96.9
	t _{test} value	–	–	1.4(ns)

^a Calculated from found total Cr and Cr(III) concentrations. ^b Calculated from the certified Cr(III) and Cr(VI),

^c Significance of t-test (n = 3) at 95% confidence level, t_{critical} = 4.30; ns: Not Significant.

3. 10. Application of the Developed Method

The proposed method was applied successfully on different real water samples for the determination of Cr(III) ions and total chromium. The samples were analysed before and after spiking with Cr(III) ions and

Cr(VI) ions. The recoveries of Cr(III) ions from the samples were achieved quantitatively as shown in Table 5. The total chromium levels of Incilipınar drinking fountain water and outlet water of waste water plant (Denizli, Turkey) samples do not pose a risk for public health.

Table 5. Determination of Cr(III) and Cr(VI) in various water samples (sample volume: 100 mL, n = 4).

Samples	Added, $\mu\text{g L}^{-1}$		Found, $\mu\text{g L}^{-1}$			Recovery,%	
	Cr(III)	Cr(VI)	Cr(III)	Cr(VI) ^a	Total Cr ^b	Cr (III)	Cr(VI)
Nestle bottled drinking water	–	–	n.d.	n.d.	n.d.	–	–
	20	20	20.72 ± 0.79	19.29 ± 2.02	40.01 ± 1.86	104 ± 4	96 ± 10
	40	20	40.81 ± 1.75	20.31 ± 1.81	61.12 ± 0.46	102 ± 4	102 ± 9
	20	40	21.18 ± 1.39	38.11 ± 1.74	58.29 ± 1.05	106 ± 7	93 ± 4
Pure bottled drinking water	–	–	n.d.	n.d.	n.d.	–	–
	20	20	19.10 ± 0.22	20.59 ± 1.14	39.69 ± 1.12	96 ± 1	103 ± 6
	40	20	39.36 ± 1.21	20.49 ± 1.42	59.85 ± 0.76	98 ± 3	102 ± 7
	20	40	19.55 ± 0.76	39.74 ± 1.20	59.29 ± 0.93	98 ± 4	99 ± 3
Mineral water	–	–	n.d.	n.d.	n.d.	–	–
	40	40	42.13 ± 1.99	37.21 ± 3.29	79.34 ± 4.90	105 ± 5	93 ± 8
	80	40	79.48 ± 2.66	41.22 ± 3.24	120.70 ± 3.05	99 ± 3	103 ± 8
	40	80	41.40 ± 0.31	78.45 ± 4.58	119.85 ± 4.57	104 ± 1	98 ± 6
İncilipınar drinking fountain water	–	–	1.14 ± 0.07	0.79 ± 0.11	1.93 ± 0.08	–	–
	20	20	21.22 ± 0.63	19.69 ± 1.11	40.91 ± 0.91	106 ± 3	98 ± 6
	40	20	41.11 ± 1.39	19.89 ± 1.74	61.00 ± 1.05	103 ± 4	99 ± 9
	20	40	20.91 ± 1.00	40.26 ± 1.44	61.17 ± 1.04	105 ± 5	101 ± 3
Outlet water of waste water plant (Denizli)	–	–	6.45 ± 0.12	1.22 ± 0.54	7.67 ± 0.53	–	–
	20	20	19.60 ± 0.65	21.26 ± 1.08	40.86 ± 0.86	98 ± 3	106 ± 5
	40	20	40.90 ± 0.97	20.25 ± 1.58	61.15 ± 1.25	102 ± 2	101 ± 8
	20	40	20.02 ± 0.87	41.10 ± 1.26	61.12 ± 0.91	101 ± 4	103 ± 3

^a Calculated from found total Cr and Cr(III) concentrations.

^b Total amount of Cr determined after reducing Cr(VI) to Cr (III) ions in sample solutions

3.10. Comparison

Analytical performance of the proposed method was compared with recently reported methods. In comparison, LOD and PF of reported method are better than those of reported methods shown in Table 6.

4. Conclusion

In this work, a modified AAXAD-4 resin column was evaluated for the speciation of Cr(III) and Cr(VI) ions, providing for selective preconcentration of Cr(III) at high pH. Besides its good selectivity between Cr(III) and Cr(VI) ions, it also has some characteristics such as good stability under working conditions, fast sorption and desorption kinetics, large adsorption capacity and good tolerance to coexisting ions. The used SPE system could recover more than 95% of Cr(III) from aqueous solution at pH=8. The feasibility of speciation at $\mu\text{g L}^{-1}$ levels make it an efficient sorbent for Cr(III). By com-

paring AAXAD-4 minicolumn SPE with MIS-FAAS, the developed method was successfully applied for chromium speciation in various water samples with low LOD, high PF, good accuracy and repeatability. Because of its simplicity, low cost and safety, it could be adopted for routine use for the speciation of Cr(III) and Cr(VI) ions.

5. Conflict of Interest

Authors declare that they do not have any conflict of interest with anyone.

6. Acknowledgement

The authors would like to acknowledge the scientific research projects unit of Pamukkale University which is the fund to this study (No. 2014 FEF 011).

Table 6. Comparison of proposed method with reported methods for speciation of Cr(III) and Cr(VI) ions based on SPE

Resins/Techniques	Speciation Modality	Sample V, mL	LOD, $\mu\text{g L}^{-1}$	PF	RSD, %	Refs #
Amberlite XAD-16 loaded with salicylic acid/on-line column	Cr(III) sorption/ Cr(VI) reduction	10	0.10	79	1.2	11
Silica gel modified by <i>N,N'</i> -bis-(α -methyl salicylidene)-2,2-dimethyl-1,3-propa- nediimine/ column	Cr(III) sorption/ Total Cr By GFAAS	0.024 500	50	3.1	22	
Amberlite XAD-16 modified with α -benzoin oxime/on-line column	Cr(III) sorption/ Cr(VI) reduction	10	0.14	76	1.03	24
Maleic acid-functionalized XAD sorbent/column	Cr(III) sorption/ Cr(VI) reduction/	6000	150	300	0.2	35
Cr(VI) reduction C-18 bonded phase silica/ SPE disks	Cr(VI) sorption/ Cr(III) oxidation	1500	20	150	11.2	36
Dowex M 4195 chelating resin/column	Cr(VI) sorption/ Cr(III) oxidation	250	1.94	31	<10	37
MWCNTs-D2EHPA/ batch	Cr(III) sorption Cr(VI) reduction	300	50	60	<10	38
(MAD) chelating resin/column	Cr(III) sorption/ Cr(VI) reduction	2000	0.01	200	1.2	39
Poly(1,3-thiazol-2-yl-methacrylamide)-co-4-vinyl pyridine-co-divinyl benzene / column	Cr(VI) sorption/ Cr(III) oxidation	150	2.4	30	3.2	40
Chromium(III)-cochineal red A chelate/filter	Cr(III) sorption/ Cr(VI) reduction	800	1.4	94	<5	41
Diphenylcarbazone-incorporated resin/column	Cr(III) sorption/ Total Cr by GFAAS	–	30	–	3.2–3.7	42
Aminated XAD-4 / column	Cr(III) sorption/ Cr(VI) reduction	750	0.041	375	3.75	This work

7. References

1. J. Namiesnik, A. Rabajczyk. *Crit. Rev. Environ. Sci. Technol.*, **2012**, *42*, 327–377. DOI:10.1080/10643389.2010.518517
2. J. O. Nriagu, E. Nieboer (Eds.), *Chromium in the Natural and Human Environment*, Wiley, New York, 1998.
3. US EPA. Report No. EPA/570/9-76/003; Washington, DC, 1976.
4. Code of Federal Regulation. Protection of Environment. Section 141, 80, p. 425, 2011.
5. P. Quevauviller, E. A. Maier, B. Griepink, *Fresenius J. Anal. Chem.*, **1993**, *3459* (2-4), 282–286. DOI:10.1007/BF00322611
6. N. Ozdemir, M. Soylak, L. Elci, M. Dogan, *Anal. Chim. Acta*, **2004**, *505*(1), 37–41. DOI:10.1016/S0003-2670(03)00353-2
7. A. N. Siyal, S. Q. Memon, A. Elci, A. Akdogan, A. Hol, A. Arslan Kartal, L. Elci, *Int. J. Environ. Anal. Chem.*, **2014**, *94*(14-5), 1463–1477.
8. S. Chen, S. Zhu, Y. He, D. Lu. *Food Chem.*, **2014**, *150*, 254–259. DOI:10.1016/j.foodchem.2013.10.150
9. C. Cui, M. He, B. Chen, B. Hu. *Anal. Methods*, **2014**, *6*, 8577–8583. DOI:10.1039/C4AY01609B
10. S. Tiwari, N. Sharma and R. Saxena. *Anal. Sci.*, **2016**, *32*, 1321–1325. DOI:10.2116/analsci.32.1321
11. R. Ansari. *Acta Chim. Slov.*, **2006**, *53*, 88–94.
12. J. A. Baig, L. Elci, M. I. Khan, T. G. Kazi. *J. AOAC Int.*, **2014**, *97*(5), 1421–1425. DOI:10.5740/jaoacint.12-139
13. J. A. Baig, A. Hol, A. Akdogan, A. Arslan Kartal, U. Divrikli, T. G. Kazi, L. Elci. *J. Anal. At. Spectrom.*, **2012**, *27*, 1509–1517. DOI:10.1039/c2ja30107e
14. A. Karatepe, E. Korkmaz, M. Soylak, L. Elci. *J. Hazard. Mater.*, **2010**, *173*(1-3), 433–437. DOI:10.1016/j.jhazmat.2009.08.098
15. L. Zhang, L. Xuelei, X. Wang, W. Wang, X. Wang, H. Han. *Anal. Methods*, **2014**, *6*(15), 5578–5583. DOI:10.1039/C4AY00922C
16. E. Yilmaz and M. Soylak. *Talanta*, **2016**, *160*, 680–685. DOI:10.1016/j.talanta.2016.08.001
17. S. Kapitány, E. Sóki, J. Posta, Á. Béni. *Acta Chim. Slov.*, **2017**, *64*, 248–255. DOI:10.17344/acsi.2017.3137
18. Z. Bahadır, V. N. Bulut, M. Hidalgo, M. Soylak, E. Marguí. *Spectrochim. Acta B*, **2016**, *115*, 46–51. DOI:10.1016/j.sab.2015.11.001
19. R. K. Sharma and P. Pant. *Int. J. Environ. Anal. Chem.*, **2009**, *89*, 503–514. DOI:10.1080/03067310802691680
20. E. Molaakbari, A. Mostafavi, and D. Afzali, *Int. J. Environ. Anal. Chem.*, **2013**, *93*, 365–376. DOI:10.1080/03067319.2012.663753
21. R. A. Gil, S. Cerutti, J. A. Gasquez, R. A. Olsina, L. D. Martinez. *Talanta*, **2006**, *68*, 1065–1070. DOI:10.1016/j.talanta.2005.06.069
22. A. Bartyzel and E. M. Cukrowska. *Anal. Chim. Acta*, **2011**, *707*, 204–209. DOI:10.1016/j.aca.2011.09.023
23. S. Q. Memon, M. I. Bhangar and M. Y. Khuhawer. *Anal. Bioanal. Chem.*, **2005**, *383*, 619–624. DOI:10.1007/s00216-005-3391-1
24. S. Tiwari, N. Sharma and R. Saxena. *New J. Chem.*, **2016**, *40*(2), 1412–1419. DOI:10.1039/C5NJ02283E
25. R. K. Sharma and P. Pant. *J. Hazard. Mater.*, **2009**, *163*(1), 295–301. DOI:10.1016/j.jhazmat.2008.06.120
26. H. A. Panahi, H. S. Kalal, E. Moniri, M. N. Nezhati, M. T. Menderjani, S. R. Kelahrodi, F. Mahmoudi. *Microchem. J.*, **2009**, *93*, 49–54. DOI:10.1016/j.microc.2009.04.007
27. I. B. Solangi, S. Memon and M. I. Bhangar. *J. Hazard. Mater.*, **2009**, *171*, 815–819. DOI:10.1016/j.jhazmat.2009.06.072
28. A. A. Bhatti, S. Memon, N. Memon, A.A. Bhatti, I. B. Solangi. *Arab. J. Chem.*, **2017**, *10*, S1111–S1118. DOI:10.1016/j.arabjc.2013.01.020
29. V. N. Bulut, D. Ozdes, O. Bekircan, A. Gundogdu, C. Duran, M. Soylak, *Anal. Chim. Acta*, **2009**, *632*, 35–41. DOI:10.1016/j.aca.2008.10.073
30. D. L. Pavia, G. M. Lampman and G. S. Kriz. *Introduction to Spectroscopy*, Third Ed., Cengage Learning, 2001.
31. H. Peng, N. Zhang, M. He, B. Chen, B. Hun. *Talanta*, **2015**, *131*, 266–272. DOI:10.1016/j.talanta.2014.07.054
32. B. Welz, *Atomic Absorption Spectrometry*, 2nd ed., VCH, New York, 1985, p. 108.
33. Analytical Methods Committee, *Analyst*, **1987**, *112*, 199–204. DOI:10.1039/an9871200199
34. IUPAC, Analytical Chemistry Division, *Spectrochim. Acta Part B*, **1978**, *33*, 241–245. DOI:10.1016/0584-8547(78)80044-5
35. S. Yalcin and R. Apak. *Anal. Chim. Acta*, **2004**, *505*, 25–35. DOI:10.1016/S0003-2670(03)00498-7
36. M. S. Tehrani, A. A. Ebrahimi and F. Rastegar. *Annali di Chimica*, **2004**, *94*(5-6), 429–435. DOI:10.1002/adic.200490052
37. K. O. Saygi, M. Tuzen, M. Soylak, L. Elci. *J. Hazard. Mater.*, **2008**, *153*, 1009–1014. DOI:10.1016/j.jhazmat.2007.09.051
38. S. Vellaichamy and K. Palanivelu. *Indian J. Chem.*, **2010**, *49A*, 882–890.
39. S. Sacmaci, S. Kartal, Y. Yilmaz, M. Sacmaci, C. Soykan. *Chem. Eng. J.*, **2012** (181-182), 746–753. DOI:10.1016/j.cej.2011.11.057
40. O. Hazer and D. Demir. *Anal. Sci.*, **2013**, *29*, 729–734. DOI:10.2116/analsci.29.729
41. M. Habila, Y. E. Unsal, Z. A. Alothman, A. Shabaka, M. Tuzen, M. Soylak. *Anal. Lett.*, **2015**, *48*(14), 2258–2271. DOI:10.1080/00032719.2015.1025278
42. B. Lesniewska, A. Jeglikowska, B. Godlewska-Zylkiewicz. *Water Air Soil Pollut.*, **2016**, *227*, 291. DOI:10.1007/s11270-016-2974-0

Povzetek

S kemično modifikacijo smo Amberlite XAD-4 smolo (AXAD-4) pretvorili v aminirano Amberlite XAD-4 (AAXAD-4) smolo in jo okarakterizirali z infrardečo spektroskopijo. AAXAD-4 smolo smo uporabili kot učinkovito trdno fazo za predkoncentracijo in speciacijo Cr(III) in Cr(VI) ionov s kolonsko tehniko. Koncentracijo kromovih zvrsti smo določili z mikrovzorčevalnim injekcijskim sistemom in plamenskim atomskim absorpcijskim spektrometrom (MIS-FAAS). Selektivno retencijo Cr(III) ionov smo dosegli pri pH 8,0 in elucijo z 1,0 mL 3,0 mol L⁻¹ HCl ter 1,0 mL 2,0 mol L⁻¹ NaOH zaporedoma pri pretoku 5,0 mL min⁻¹. Maksimalna sorpcijska kapaciteta AAXAD-4 smole za Cr(III) ione je bila 67,0 mg g⁻¹. Meja zaznave (LOD) za Cr(III) ione je bila 0,041 µg L⁻¹, meja določitve (LOQ) 0,131 µg L⁻¹, medtem ko je bil predkoncentracijski faktor (PF) 375 in relativni standardni odklik (RSD) 3,75% (n = 11). Metodo smo validirali s certificiranimi referenčnimi materiali (CRM) in jo uspešno uporabili za analizo realnih vzorcev z dodanimi Cr(III) in Cr(VI) ioni.

Scientific paper

Comparative Study of the Gas-phase Cyclodimer Formations of Uracil and 6-azauracil in Excited State and through Conical Intersections S_0/S_1

Pavlina Bogomilova Kancheva* and Vassil Borissov Delchev

University of Plovdiv Paisii Hilendarski, Dept. Physical Chemistry, 24 Tzar Asen, 4000 Plovdiv, Bulgaria

* Corresponding author: E-mail: pkancheva@uni-plovdiv.net
Tel.: 00359 896545727

Received: 28-11-2017

Abstract

The photocyclodimerization mechanisms of two oxo tautomers of uracil and 6-azauracil were studied at the CC2 level of theory and cc-pVDZ basis functions. Uracil was explored in three orientations of the monomers - *cis-anti*, *trans-syn* and *trans-anti*, while 6-azauracil - in all four orientations. Conical intersections S_0/S_1 were found at the CASSCF(2,2)/6-31G* theoretical level. The study propose a photophysical mechanisms of photoformation and photodestruction of cyclodimers (CDs), which occur through the $^1\pi\pi^*$ electron excited states (spectroscopically bright states). The photophysical relaxations (internal conversions) to the ground states are mediated by conical intersections S_0/S_1 , which we found and discussed in the current paper.

Keywords: *Ab initio* calculations; CASSCF optimizations; Conical intersections S_0/S_1 ; Pyrimidine cyclodimers; Uracil; 6-azauracil

1. Introduction

The photostability of nucleobases has a fundamental role in the protection of living organisms from the damaging UV light.¹ The nucleic acid bases are main UV chromophores in cells. They absorb UV radiation under 300 nm and participate in a number of photoreactions - in particular internal conversions to ground states. These processes are connected with ring deformations and they are responsible for the photostability of nucleobases.^{2,3} The competitive [2+2] cyclodimerizations through excited states are the second most common response of the pyrimidine nucleobases exposed to UV irradiation.^{2,4}

The cyclodimers (CDs), formed by two adjacent pyrimidine bases are considered to be the most prevailing lesions of cellular DNA induced by the UV radiation. They can cause death of cells and skin cancer.^{4–11} The yield of formation of the CDs with a four-membered cyclobutane ring is larger than other photoadducts.^{7,12–17} The recognition and the repair of such DNA lesions is possible through different enzyme pathways. For example, the DNA photolyase catalyzes the cleavage of the cyclobutane bonds formed between the monomers. Thus the pyrimidine CD turns back in the initial stacked dimer.^{18,19}

The found possible orientations of pairs of pyrimidines to form CD are four: *cis-syn*, *trans-syn*, *cis-anti* and *trans-anti*. Such structures are shown in Fig. 1.²⁰

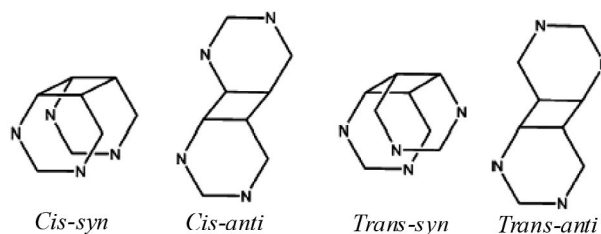


Fig. 1. Four CDs of pyrimidine nucleobases

After irradiation of frozen water solution of uracil (U) the *cis-syn* and *cis-anti* CDs are predominantly formed.^{21–23} The *trans-syn* and *trans-anti* isomers are also present but in significantly lower amounts.²³ The analysis (NMR, chromatography, etc.) has shown that the *cis-syn* CD is the major photoproduct.^{21–24} All four CDs are formed after irradiation of a fluid solution (water or acetonitrile) and when the aqueous solution is acetone sensitized.^{23–26} The *trans-syn* cyclodimers of U can be formed

also by irradiation of denaturated DNA.²⁷ The molecular and crystal structure of *cis-syn* photodimer of U has been proposed by Adman.²⁴

6-Azauracil (6-AU) is a close analogue to U. The compound has an extra nitrogen atom in the aromatic ring. With respect to the biological effects, 6-AU has been shown to inhibit animal tumors,²⁸ human acute leukemia²⁹ and growth of a large number of microorganisms^{30,31}. The compound is also used as an antiviral drug.³² The IR absorption spectrum of 6-AU in low temperature matrix has shown that the diketo tautomer is predominant.³³ In the UV absorption spectra of 6-AU in acetonitrile; two peaks are registered – at 200 nm and 260 nm.³⁴ The last one has been assigned to a $\pi \rightarrow \pi^*$ electron transition as in U. Some authors claimed that the main relaxation process of 6-AU is the intersystem crossing (ISC) mechanism involving a triplet state ($^3\pi\pi^*$).^{34–36} Irradiation with a wavelength of 308 nm has confirmed that the ISC process is predominant in 6-AU but it is accompanied with weak fluorescence.³⁴

The mechanisms of formation of the *cis-syn* cyclophotodimer of thymine^{37–39} uracil^{40–42} and cytosine^{43,44} have been proposed also by theoretical computations. It has been concluded that these processes are ultrafast and barrierless photoreactions in which the driving state is the

first $^1\pi\pi^*$ excited state which relaxes through a conical intersection (CI) S_0/S_1 .⁴⁵ The triplet states have been also suggested to play a role in the photodimerizations of pyrimidine bases.^{12,46,47} It has been found that upon 266 nm radiation the CDs are formed via the singlet channel which is 30 times more efficient than the triplet one. By increasing the irradiation wavelength, the importance of the singlet channel is also increased.⁴⁸

The aim of this study is to investigate theoretically the two close analogues U and 6-AU in order of their ability to form CDs through the bright $^1\pi\pi^*$ excited states in the gas phase. It is interesting to see whether the extra nitrogen atom in the ring of 6-AU as compared to U would influence the photophysics of the compound.

2. Theoretical Methods

The structures of the stacked dimers (SDs), conical intersections S_0/S_1 , and CDs of U and 6-AU were optimized with the Complete-active-space self-consistent field (CASSCF) method and 6-31G* basis functions. The active space was constructed by two electrons on two orbitals: HOMO and LUMO – they are shown in Fig. 2 (the remaining MOs are given in the electronic supplementary

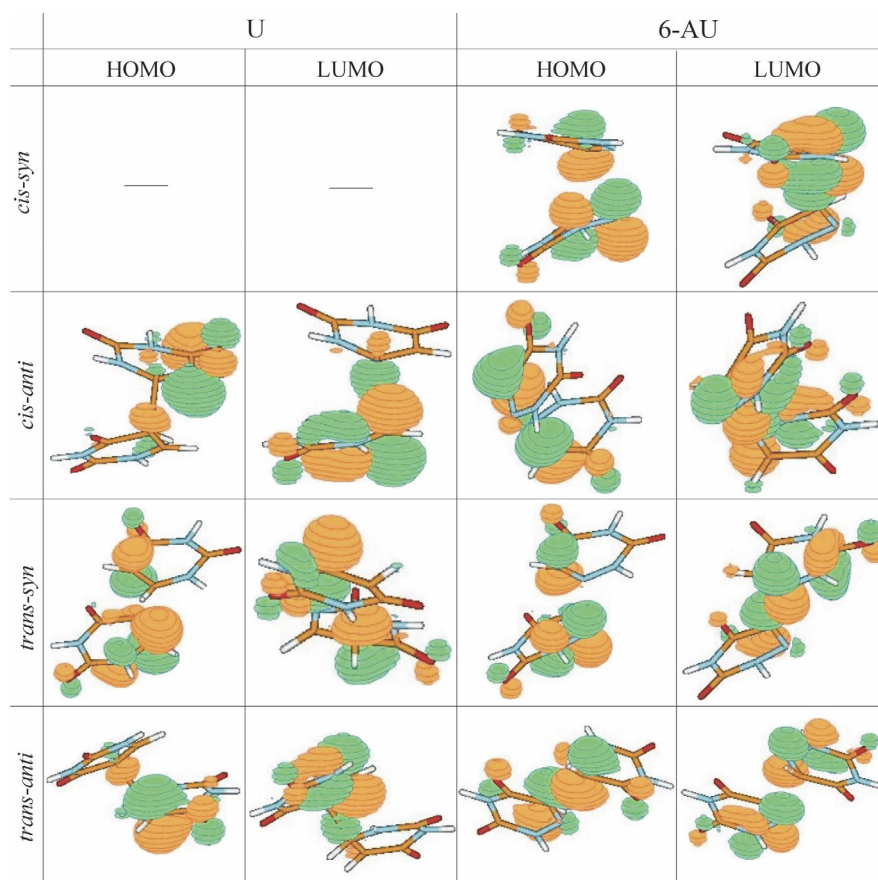


Fig. 2. HOMO and LUMO molecular orbitals of the conical intersections S_0/S_1 included in the active space (2,2)

information). Since the structures under study are rather complicated – including valent and non-valent bonds – we applied a limited active space for the optimizations. Our experience imposes this because the extension of the active space usually leads to serious troubles with the configuration wavefunction. – In other words a large active space includes a great many excited states and thus leads to a location of wrong conical intersections S_0/S_1 . In order to be consistent with the level of computation, the branching space vectors (the gradient difference and derivative coupling vectors) were computed at the same theoretical level. Subsequently, we reoptimized the structures of the geometries-minima at the CC2 level (approximate second-order coupled-cluster method)⁴⁹ with cc-pVDZ basis functions. Additional computations of the CC2-vertical excitation energies of the CDs and SDs of U and 6-AU were performed at this level either. No symmetry and geometry restrictions were applied for the optimizations of CBDs and the conical intersections S_0/S_1 .

All SDs were optimized by freezing of one or two distances between the monomers forming the four-membered ring (see electronic supplementary information). The freezing of one of the distances is required since the structures lie in very shallow minima on the *hyper*PESs and the fully relaxed optimizations lead to planar Watson-Crick dimers. To find the distance(s) for freezing we performed preliminary SCAN computations of the CDs with respect to the responsible distance(s). We located the minimal distance(s) at which only Van der Waals forces start to act between the two monomers.

The excited-state reaction paths connecting the SDs and the CDs through conical intersections S_0/S_1 were found by the linear-interpolation-in-internal-coordinates approach (LIIC). It was performed in two steps: 1) interpolation between the SD and the conical intersection S_0/S_1 , and 2) interpolation between the conical intersection S_0/S_1 and the CD. The internal coordinates of the interpolated structures (q_i) along the reaction paths were generated by equation (1):

$$q_i = q_r + \varepsilon (q_p - q_r), \quad (1)$$

where q_r – internal coordinate of the reactant (one of the minima in this case); q_p – internal coordinate of the product (the conical intersection S_0/S_1 in this case); ε – interpolation parameter, which varies from 0 (at the reactant) to 1 (at the product).

In each LIIC-step several intermediate structures were generated and their CC2-excitation energies were computed for the construction of the excited-state reaction paths. The proposed mechanisms concern the reactions in the gas phase.

The geometry optimizations of the conical intersections S_0/S_1 , the calculations of the branching space vectors, and the equilibrium structures of the minima were carried out with the GAUSSIAN 03 program package.⁵⁰ The reac-

tion paths (CC2) were studied with the Turbomole program.⁵¹ The programs MOLDEN⁵² and Chemcraft⁵³ were used for the visualization of the results.

3. Results and Discussion

The CASSCF equilibrium geometries of the CDs, SDs as well as the conical intersections S_0/S_1 of U and 6-AU are shown in Fig. 3. The frontier MO included in the active space (HOMO and LUMO) of the conical intersections S_0/S_1 , depicted in Fig. 2 are of π -type. The typical $\pi \rightarrow \pi^*$ charge transfer states are those in *cis-anti* and *trans-anti* conical intersections S_0/S_1 of U and in *cis-syn* and *trans-syn* conical intersections S_0/S_1 of 6-AU.

The aromatic rings of the CDs of U are nonplanar. The nonplanarity is a result of the repulsion between the π -electron clouds of the rings and of the lone electron pairs of the oxygen atoms. The C–C' bonds between the monomers are about 1.55 Å long. The rings have envelope conformations, mutually twisted one to another (see electronic supplementary information). In contrast to the CDs, the SD structures of U have planar aromatic rings. In the *anti*-configurations, the C–C' distances have close lengths, whereas in the *trans-syn* structure they differ with about 0.62 Å. In the *cis-syn* structure, obtained by Domcke et al.³⁸ the corresponding difference is about 0.16 Å. In the SDs, the aromatic rings of the *cis-anti* U are slightly twisted one to another. In the *trans-syn* isomer, the rings are highly twisted which means that the formation of the cyclodimer includes a reorientation of the aromatic rings of the SD (see the electronic supplementary information). In the *trans-anti* SD, instead twisting of both rings there is a parallel translation of the monomers and they form a “sandwich”-like structure.

The CDs of 6-AU and U are with nonplanar aromatic rings and “envelope” conformations. In the *syn*- 6-AU structures, the four-membered ring has one N–N' and one C–C' bond, which show difference about 0.075 Å. In the *anti*-orientations, these bonds are of N–C' (or C–N') type and they are equal in length. The SDs of 6-AU are generally very similar to the corresponding structures of U. The aromatic rings of the *syn*- structures are highly twisted one to another, while the structure of *trans-anti* is a “sandwich”-like; analogous to U. The SDs of 6-AU are with almost planar aromatic rings, like those of U and the single monomers.

3. 1. Conical Intersections S_0/S_1

All conical intersections S_0/S_1 of U (Fig. 3) are structurally closer to the cyclodimers than to the SDs and have nonplanar aromatic rings. Only the hydrogen atoms from the four-membered rings deviate considerably from the planarity. The C–C' distances between the two pyrimidine monomers are shorter than those of the SDs and differ in

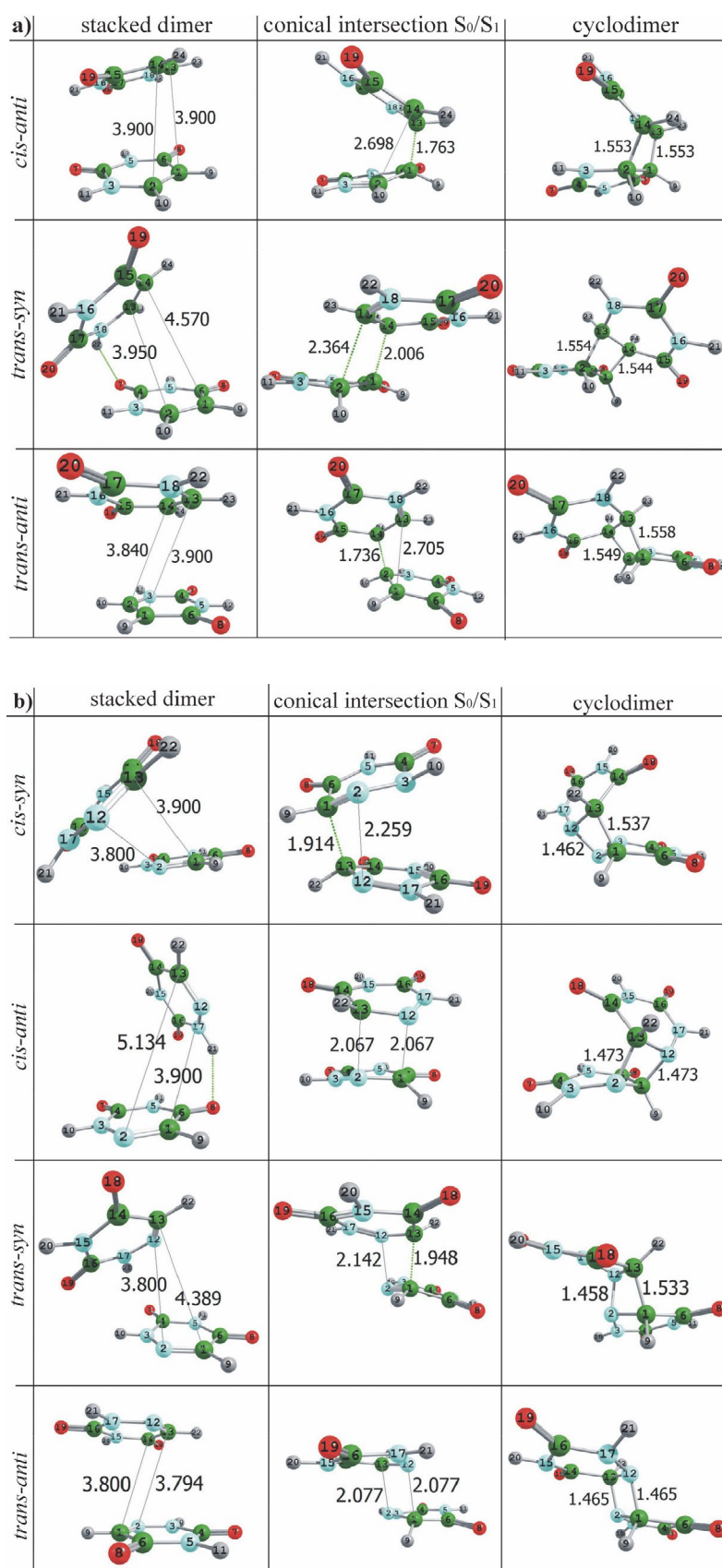


Fig. 3. CASSCF-optimized structures of CDs, conical intersections S_0/S_1 and SDs of a) U and b) 6-AU

lengths. The *anti*- structures are with mutually twisted rings. The conical intersections S_0/S_1 of U exhibit a twisting of the ring C=C bond, typical for the single pyrimidine conical intersections S_0/S_1 ^{2,3,54–59} which have found to be the main channel for internal conversions in nucleobases.

All conical intersections S_0/S_1 of 6-AU have nonplanar aromatic rings, similar to those of U. The two closest distances between the two monomers depend on the orientation of the rings. In the *syn*-isomers we have different in length distances C–C' and N–N'. In the *anti*-isomers these are the two C–N' distances which are equidistant. The conical intersections S_0/S_1 of 6-AU, like those of U, are structurally closer to the cyclodimers than to the SDs. The conical intersections S_0/S_1 of 6-AU are in general similar to those of U, but their aromatic rings are not as much twisted one to another as in U.

The calculated branching space vectors of the conical intersections S_0/S_1 are illustrated in the electronic supplementary information. They indicate clearly the trend of the systems to form four-membered rings. We believe that the found conical intersections S_0/S_1 mediate the photocyclodimerizations of U and 6-AU via internal conversions.

3. 2. Vertical Excitation Energies

The CC2/cc-pVDZ vertical excitation energies of the systems SDs and CDs of the two compounds are listed in Table 1. One can see that for U the *cis*- and *trans-anti* CDs have higher vertical excitation energy of the bright $^1\pi\pi^*$ excited states than the *trans-syn* CD. The first two excited states of all isomers of U (for SDs and CDs) are the spectroscopically dark $^1n\pi^*$ states.

Comparing the vertical excitation energies of the CDs of U with the UV absorption maximum of uracil in the gas phase – 4.79 eV (259 nm),^{60,61} it can be seen that the

cyclodimerization of two U monomers leads to a blue shift of the UV absorption maximum. This tendency is also theoretically supported, since for all CDs of U we found higher $^1\pi\pi^*$ vertical excitation energies (more than 6 eV) than the calculated value of the uracil monomer (5.54 eV). The SDs of U have lower vertical excitation energies of the $^1\pi\pi^*$ excited state in comparison to the monomer.

The CDs of 6-AU have two low-lying $^1\pi\pi^*$ excited states. The *cis-syn* isomer has the lowest vertical excitation energy of the first $^1\pi\pi^*$ excited state while the *trans-syn* isomer has the highest. The calculated (CC2/cc-pVDZ) vertical excitation energy of the low-lying $^1\pi\pi^*$ excited state of the monomer of 6-AU is 5.19 eV. This value is higher than the vertical excitation energies of the first bright $^1\pi\pi^*$ excited state of the CD structures and lower than those of the SDs. Therefore, in contrast to U, a red shift of the calculated UV absorption spectra should be expected for 6-AU in the course of the photocyclodimerization. Opposite to the computed data, according to the experimental $^1\pi\pi^*$ absorption maximum of 6-AU monomer (4.779 eV), a blue shift is expected in the course of the cyclodimerizations to *cis-anti*, *trans-syn* and *trans-anti* isomers and no shift for the formation of the *cis-syn* isomer (4.774 eV).

The SDs of U have lower $^1\pi\pi^*$ vertical excitation energy than the corresponding CDs. The *trans-syn* isomer has higher $^1\pi\pi^*$ vertical excitation energy than *cis-anti* and *trans-anti* systems. In the SDs of 6-AU, similar to U, the two low-lying excited states are of $^1n\pi^*$ character. In contrast to U, the $^1\pi\pi^*$ excited-state energy of the *cis-syn*, *cis-anti* and *trans-anti* SDs of 6-AU is higher than that of the corresponding CDs, although that difference is very small in the *cis-anti* and *trans-anti* isomers – about 0.076 eV and 0.003 eV, respectively. The *trans-syn* SD of 6-AU has higher $^1\pi\pi^*$ vertical excitation energy than the CD, like U.

Table 1. Vertical excitation energies (CC2) of the SDs and CDs of U and 6-AU, all in eV. In brackets are given the oscillator strengths

	CDs							
	<i>cis-syn</i>		<i>cis-anti</i>		<i>trans-syn</i>		<i>trans-anti</i>	
U	5.204(0.0006)	$^1n\pi^*$	5.223(0.0016)	$^1n\pi^*$	5.176(0.0006)	$^1n\pi^*$	5.193(0.0006)	$^1n\pi^*$
	5.271(0.0015)	$^1n\pi^*$	5.232(0.0017)	$^1n\pi^*$	5.227(0.00008)	$^1n\pi^*$	5.218(0.0007)	$^1n\pi^*$
	6.177(0.0148)	$^1\pi\pi^*$	6.207(0.0119)	$^1\pi\pi^*$	6.046(0.0710)	$^1\pi\pi^*$	6.213(0.0043)	$^1\pi\pi^*$
6-AU	4.774(0.0417)	$^1\pi\pi^*$	4.942(0.0166)	$^1\pi\pi^*$	5.157(0.0276)	$^1\pi\pi^*$	4.929(0.00000001)	$^1\pi\pi^*$
	4.955(0.0060)	$^1\pi\pi^*$	4.996(0.00002)	$^1\pi\pi^*$	5.200(0.0239)	$^1\pi\pi^*$	5.184(0.0052)	$^1n\pi^*$
	5.176(0.0166)	$^1n\pi^*$	5.503(0.0044)	$^1n\pi^*$	5.241(0.00002)	$^1n\pi^*$	5.647(0.00000003)	$^1\pi\pi^*$
	SDs							
	<i>cis-syn</i>		<i>cis-anti</i>		<i>trans-syn</i>		<i>trans-anti</i>	
U	4.785(0.0002)	$^1n\pi^*$	4.874(0.0001)	$^1n\pi^*$	4.911(0.0002)	$^1n\pi^*$	4.866(0.00005)	$^1n\pi^*$
	4.813(0.0002)	$^1n\pi^*$	4.875(0.0006)	$^1n\pi^*$	4.912(0.0001)	$^1n\pi^*$	4.867(0.0005)	$^1n\pi^*$
	5.386(0.0883)	$^1\pi\pi^*$	5.283(0.0368)	$^1\pi\pi^*$	5.426(0.1107)	$^1\pi\pi^*$	5.226(0.0004)	$^1\pi\pi^*$
6-AU	4.373(0.0001)	$^1n\pi^*$	4.387(0.0001)	$^1n\pi^*$	4.381(0.0004)	$^1n\pi^*$	4.381(0.0003)	$^1n\pi^*$
	4.406(0.0001)	$^1n\pi^*$	4.399(0.0002)	$^1n\pi^*$	4.385(0.000002)	$^1n\pi^*$	4.384(0.000002)	$^1n\pi^*$
	5.043(0.0685)	$^1\pi\pi^*$	5.015(0.0549)	$^1\pi\pi^*$	4.915(0.0040)	$^1\pi\pi^*$	4.912(0.00008)	$^1\pi\pi^*$

3.3. Excited-state Reaction Paths

In Figs. 4–7 are given the excited-state reaction paths of the proposed gas-phase mechanisms of CD formation of U. The relative energies are referred to the ground-state equilibrium geometries of the SDs, calculated at the CC2/cc-pVDZ level of theory. In Fig. 4 includes only the cyclodimerization mechanism of *cis-syn* 6-AU since it has been already investigated for U.^{40–42}

The excited-state reaction paths show that after UV-irradiation of the SDs the $^1\pi\pi^*$ excited states can reach the conical intersections S_0/S_1 without barriers along the excited-state reaction paths. An exception is the *trans-syn* (U) mechanism where small energy barrier is estimated (Fig. 6). After the conical intersections S_0/S_1 the systems can relax non-radiatively (internal conversion) to the ground states S_0 of SD or CD. The low-lying $^1\pi\pi^*$ excited states in the Frank-Condon region of *cis-anti* (Fig. 5a), *trans-syn* (Fig. 6a) and *trans-anti* (Fig. 7a) CDs of U have higher energies than those of the corre-

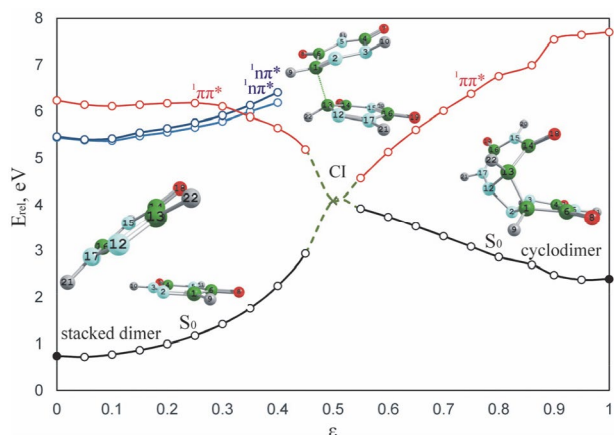


Fig. 4. Excited-state reaction paths (CC2/cc-pVDZ) of the photodimerization of *cis-syn* 6-AU. The full circles (●) correspond to optimized structures (CASSCF(2,2)/6-31G*), while the open circles (○) correspond to linearly-interpolated structures. The conical intersection is designated with x. The relative energy E_{rel} is referred to the optimized CC2 energy of the SD (−859.439819 a.u.)

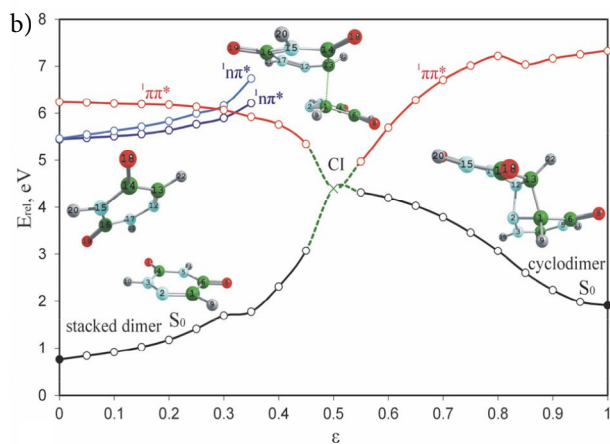
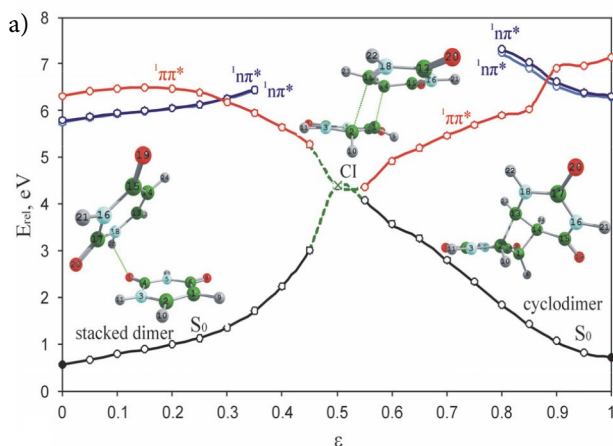


Fig. 5. Excited-state reaction paths (CC2/cc-pVDZ) of the photodimerization of a) *cis-anti* U and b) *cis-anti* 6-AU. The full circles (●) correspond to optimized structures (CASSCF(2,2)/6-31G*), while the open circles (○) correspond to linearly-interpolated structures. The conical intersection is designated with x. The relative energy E_{rel} is referred to the optimized CC2 energy of the SD (−827.454581 a.u. for U and −859.440401 a.u. for 6-AU)

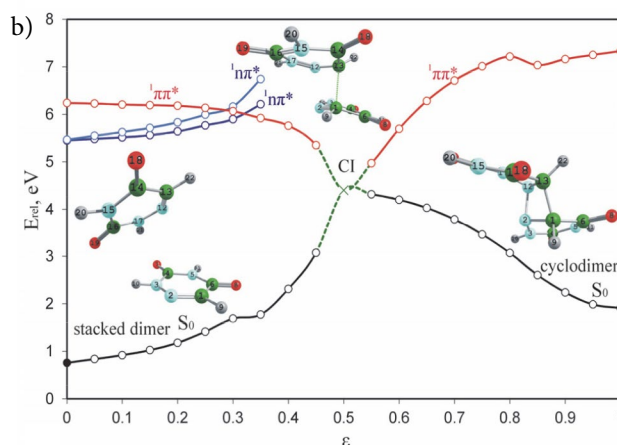
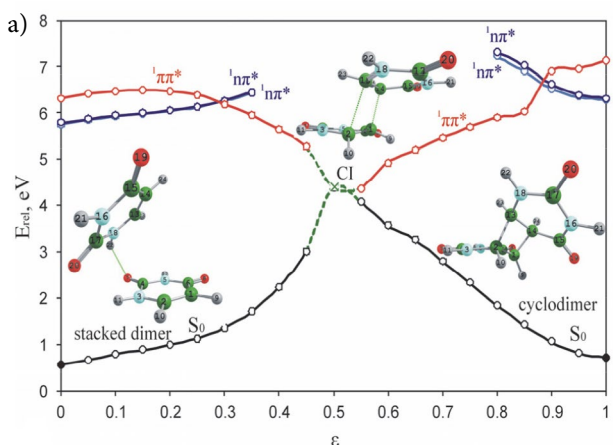


Fig. 6. Excited-state reaction paths (CC2/cc-pVDZ) of the photodimerization of a) *trans-syn* U and b) *trans-syn* 6-AU. The full circles (●) correspond to optimized structures (CASSCF(2,2)/6-31G*), while the open circles (○) correspond to linearly-interpolated structures. The conical intersection is designated with x. The relative energy E_{rel} is referred to the optimized CC2 energy of the SD (−827.453428 a.u. for U and −859.439129 a.u. for 6-AU)

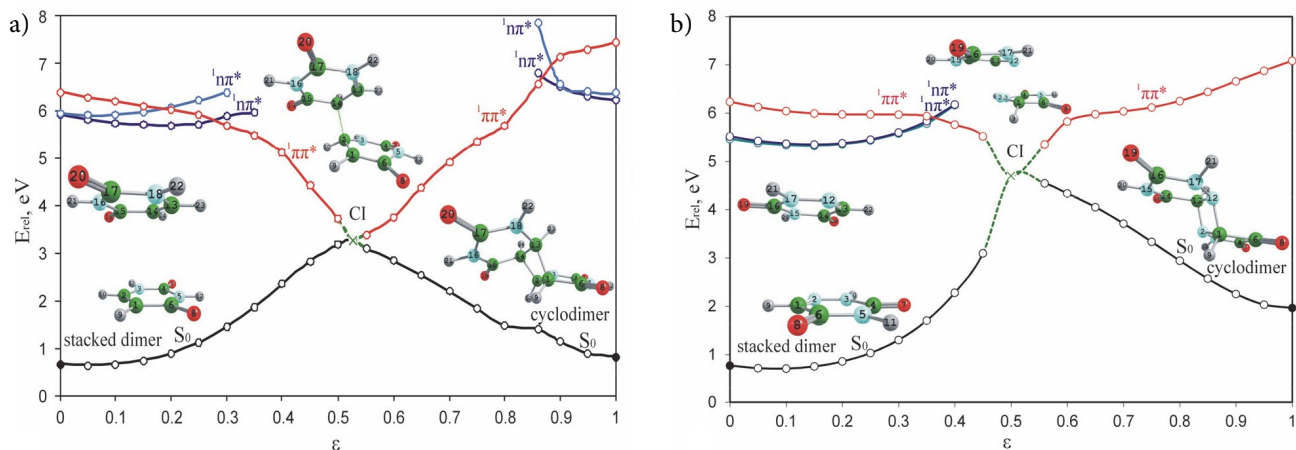


Fig. 7. Excited-state reaction paths (CC2/cc-pVDZ) of the photodimerization of a) *trans-anti-U* and b) *trans-anti-6-AU*. The full circles (●) correspond to optimized structures (CASSCF(2,2)/6-31G*), while the open circles (○) correspond to linearly-interpolated structures. The conical intersection is designated with ×. The relative energy E_{rel} is referred to the optimized CC2 energy of the SD (−827.452068 a.u. for U and −859.438461 a.u. for 6-AU)

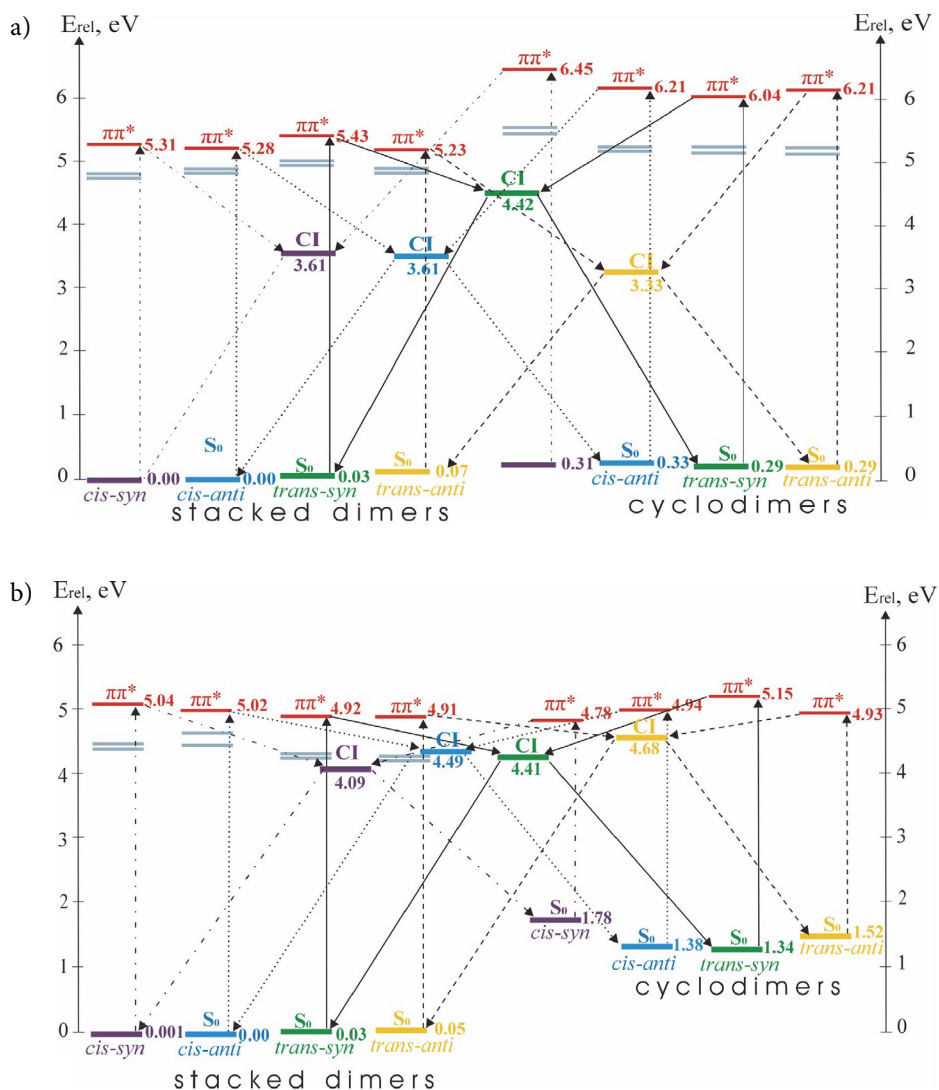


Fig. 8. Energy-level diagrams of the possible relaxation pathways of the $1\pi\pi^*$ excited states of the SDs and CDs of a) U and b) 6-AU. The relative energy E_{rel} was referred to the CC2 energy of the optimized *cis-anti* SD (−827.4545801 a.u. of U and −859.440401 a.u. of 6-AU). The data for U *cis-syn* is taken from Ref. [41].

sponding SDs. Therefore for the photodestruction of the CDs of U by these mechanisms is required higher energy than the energy required for their formation. 6-AU shows opposite effect – for the photodestruction of the CDs are required lower energies than for their formation.

Conical intersections S_2/S_1 ($^1\pi\pi^*/^1n\pi^*$) are found along all reaction paths of U as well as along the reaction paths of 6-AU starting from the SDs. They are channels through which the excited system can be trapped to the dark $^1n\pi^*$ excited state. As a result, low intensive fluorescent transitions could be expected as competitive reactions to the cyclodimerizations. On the other hand as competitive mechanisms the reactions can occur through the dark $^1n\pi^*$ excited states but these reactions will be objects of our special future attention.

All non-radiative mechanisms of photocyclodimerization of U and 6-AU studied here are summarized in two energy-level diagrams illustrated in Fig. 8. (The data for *cis-syn* U is taken from Ref. 41). The driven excited state of the reactions is of $^1\pi\pi^*$ type. The excited-state reaction paths of the $^1\pi\pi^*$ excited states connect the SDs and the CDs through the conical intersections S_0/S_1 . The relative energies of the ground states of the SDs and their $^1\pi\pi^*$ vertical excitation energies are similar for U and 6-AU. The CDs of U have lower relative energies of the ground states and higher $^1\pi\pi^*$ vertical excitation energies than the corresponding structures of 6-AU. All conical intersections S_0/S_1 of 6-AU have energies higher than 4 eV, similar to the *trans-syn* isomer of U. The *cis-syn*,⁴⁰ *cis-anti* and *trans-anti* conical intersections S_0/S_1 of U have lower energies which indicates that they could be accessed easily with smaller energy gradient in the course of the reactions in comparison to those of 6-AU.

4. Conclusion

The theoretical study (CC2/cc-pVDZ) on the relaxation mechanisms of the photo-induced cyclodimerization reactions of uracil and 6-azauracil to *cis-syn*, *cis-anti*, *trans-syn* and *trans-anti* cyclodimers proposes gas-phase mechanisms through $^1\pi\pi^*$ excited-state reaction paths as one of the possible reactions. The mechanisms indicate that the formation of CDs as well as their destruction is a non-radiative reaction passing through conical intersection S_0/S_1 , which is in accordance with recent studies.^{40–42} The destruction of the CDs of U requires much higher excitation energies than their formation. Opposite to U, the formation of the CDs of 6-AU requires higher energies than the energies for their destruction. In other words, according to the proposed mechanisms, the cyclodimerization of two U molecules to CD would provoke a blue-shift of the UV absorption maximum, while the formation of CD of 6-AU leads to a corresponding red-shift.

5. Acknowledgment

The authors thank Prof. Petko Ivanov (Institute of Organic Chemistry, Bulgarian Academy of Sciences) for the computational resource (Linux-cluster MADARA, project RNF01/0110), where the TURBOMOLE computations were performed. We are also thankful to the Department for scientific research at the University of Plovdiv for the financial support (project MU15-HF-012) for the dissemination and popularization of the results.

The investigations are not in conflicts of interest with other researches and do not disturb any ethical rules.

6. References

1. A. Downes, Th. P. Blunt, *Proc. R. Soc. Lond.* **1877**, 26, 488–500. DOI:10.1098/rspl.1877.0068
2. L. Serrano-Andrés, M. Merchán in: M. K. Shukla, K. Leszczynski (Eds.): Radiation induced molecular phenomena in nucleic acids, Springer **2008**, p. 435. DOI:10.1007/978-1-4020-8184-2_16
3. M. Merchán, R. Gonzalez-Luque, T. Climent, L. Serrano-Andrés, E. Rodriguez, M. Reguero, D. Pelaez, *J. Phys. Chem. B* **2006**, 110, 26471–26476. DOI:10.1021/jp066874a
4. J. Cadet, E. Sage, T. Douki, *Mutat. Res.* **2005**, 571, 3–17. DOI:10.1016/j.mrfmmm.2004.09.012
5. E. Sage, *Photochem. Photobiol.* **1993**, 57, 163–174. DOI:10.1111/j.1751-1097.1993.tb02273.x
6. G. P. Pfeifer, *Photochem. Photobiol.* **1997**, 65, 270. DOI:10.1111/j.1751-1097.1997.tb08560.x
7. S. Mouret, C. Baudouin, M. Charveron, A. Favier, J. Cadet, T. Douki, *Proc. Nat. Acad. Sci* **2006**, 103, 13765–13770. DOI:10.1073/pnas.0604213103
8. Y-T. Kao, C. Saxena, L. Wang, A. Sancar, D. Zhong, *Proc. Nat. Acad. Sci.* **2005**, 102, 16128–16132. DOI:10.1073/pnas.0506586102
9. F. R. de Gruijl, *Methods Enzymol.* **2000**, 319, 359–366. DOI:10.1016/S0076-6879(00)19035-4
10. J. C. van der Leun, F.R. Gruijl de, *Photochem. Photobiol. Sci.* **2002**, 1, 324–326. DOI:10.1039/b201025a
11. Y. Matsumura, H. N. Ananthaswamy, *Toxicol. Appl. Pharmacol.* **2004**, 195, 298–308. DOI:10.1016/j.taap.2003.08.019
12. J. Cadet, P. Vigny in: H. Morrison (ed.): Bioorganic Photochemistry Vol. 1, J. Wiley & Sons, New York, **1990**.
13. T. Douki, J. Cadet, *Biochem.* (2001), 40, 2495–2501. DOI:10.1021/bi0022543
14. E. C. Friedberg, G. C. Walker, W. Siede, R. D. Wood, R. A. Schultz in: T. Ellenberger (ed): DNA Repair and mutagenesis, ASM Press, Washington, **2006**.
15. S. Mouret, C. Phillipe, J. Garcia-Chantegrel, A. Banyasz, S. Karpati, D. Markovitsi, T. Douki, *Org. Biomol. Chem.* **2010**, 8, 1706–1711. DOI:10.1039/b924712b
16. S. Courdavault, C. Baudouin, M. Charveron, A. Favier, J. Cadet, T. Douki, *Mutat. Res.* **2004**, 556, 135–142. DOI:10.1016/j.mrfmmm.2004.07.011

17. S. Kim, S. Jin, G. Pfeifer, *Photochem. Photobiol. Sci.* **2013**, *12*, 1409–1415. DOI:10.1039/c3pp50037c
18. A. Sancar, *Biochem.* **1994**, *33*, 2–9.
19. L. Joubert-Doriol, T. Domratheva, M. Olivucci, A. F. Izmaylov, **2016**, arXiv:1602.05044 [physics.chem-ph].
20. E. Adman, L. H. Jensen, *Acta Cryst. B* **1970**, *26*, 1326–1334. DOI:10.1107/S0567740870004077
21. A. J. Varghese, *Biochem.* **1971**, *10*, 4283–4290. DOI:10.1021/bi00799a020
22. B. H. Jennings, S. Pastra-Landis, J. W. Lerman, *Photochem. Photobiol.* **1972**, *15*, 479–491. DOI:10.1111/j.1751-1097.1972.tb06259.x
23. M. D. Shetlar, V. J. Basus, *Photochemistry and Photobiology* **2011**, *87*, 82–102. DOI:10.1111/j.1751-1097.2010.00826.x
24. E. Adman, M. P. Gordon, L. H. Jensen, *Chem. Commun.* **1968**, *17*, 1019–1020. DOI:10.1039/C19680001019
25. C. H. Krauch, D. M. Kramer, P. Chandra, P. Mildner, H. Feller, A. Wacker, *Angew. Chem. Int. Ed. Engl.* **1967**, *6*, 956. DOI:10.1002/anie.196709561
26. C. L. Greenstock, H. E. Johns, *Biochem. Biophys. Res. Commun.* **1968**, *30*, 21–27. DOI:10.1016/0006-291X(68)90706-7
27. L. A. Frederico, T. A. Kunkel, B. R. Shaw, *Biochem* **1990**, *29*, 2532–2537. DOI:10.1021/bi00462a015
28. R. Schinder, A. D. Welch, *Science* **1957**, *125*, 548–549. DOI:10.1126/science.125.3247.548
29. B. I. Schinder, E. Frei, J. H. Tuohy, J. Gorman, E. Freireich Jr., J. Clements, *Cancer Res.* **1960**, *20*, 28–33.
30. R. E. Handschumacher, A. D. Welch, *Cancer Res.* **1956**, *16*, 965.
31. F. Exinger, F. Lacroute, *Curr. Genet.* **1992**, *22*, 9–11. DOI:10.1007/BF00351735
32. E. De Clercq, *Antiviral Res.* **2005**, *67*, 56–75. DOI:10.1016/j.antiviral.2005.05.001
33. J. Fulara, M. J. Nowak, L. Lapinski, A. Leś, L. Adamowicz, *Spectrochim. Acta.* **1991**, *47*, 595–613. DOI:10.1016/0584
34. T. Kobayashi, Y. Harada, T. Suzuki, T. Ichimura, *J. Phys. Chem. A* **2008**, *112*, 13308–13315. DOI:10.1021/jp803096j
35. J. P. Gobbo, A. C. Borin, L. Serrano-Andés, *J. Phys. Chem. B* **2011**, *115*, 6243–6251. DOI:10.1021/jp200297z
36. M. Etinski, C. Marian, *Phys. Chem. Chem. Phys.* **2010**, *12*, 15665–15671. DOI:10.1039/c0cp00106f
37. M. Boggio-Pasqua, G. Groenhof, L. V. Schaefer, H. Grubmüller, M. A. Robb, *J. Am. Chem. Soc.* **2007**, *129*, 10996–10997. DOI:10.1021/ja073628j
38. L. Blancafort, A. Migani, *J. Am. Chem. Soc.* **2007**, *129*, 14540–14541. DOI:10.1021/ja074734o
39. J. J. Serrano-Pérez, I. González-Ramírez, P. B. Coto, M. Merchán, L. Serrano-Andrés, *J. Phys. Chem. B* **2008**, *112*, 14096–14098. DOI:10.1021/jp806794x
40. V. B. Delchev, W. Domcke, *High performance computing in science and engineering Garching/Munich* **2009**, *7*, 709.
41. I. González-Ramírez, D. Roca-Sanjuán, T. Climent, J. José Serrano-Pérez, M. Merchán, L. Serrano-Andrés, *Theor. Chem. Acc.* **2011**, *128*, 705–711. DOI:10.1007/s00214-010-0854-z
42. V. B. Delchev, W. Domcke, *J. Photochem. Photobiol. A* **2013**, *271*, 1–7. DOI:10.1016/j.jphotochem.2013.07.015
43. D. Roca-Sanjuán, G. Olaso-González, I. González-Ramírez, L. Serrano-Andrés, M. Merchán, *J. Am. Chem. Soc.* **2008**, *130*, 10768–10779. DOI:10.1021/ja803068n
44. P. Kancheva, V. B. Delchev, *J. Mol. Model.* **2016**, *22*, 230. DOI:10.1007/s00894-016-3087-9
45. R. Improta, F. Santoro, L. Blancafort, *Chem. Rev.* **2016**, *116*, 3540–93. DOI:10.1021/acs.chemrev.5b00444
46. J. Eisinger, R. G. Shulman, *Science* **1968**, *161*, 1311–1319. DOI:10.1126/science.161.3848.1311
47. M. Merchán, L. Serrano-Andrés, M. A. Robb, L. Blancafort, *J. Am. Chem. Soc.* **2005**, *127*, 1820–1825. DOI:10.1021/ja044371h
48. L. Liu, B. M. Pilles, J. Gontcharov, D. B. Bucher, W. Zinth, *J. Phys. Chem. B* **2015**, *120*, 292–298. DOI:10.1021/acs.jpcc.5b08568
49. O. Christiansen, H. Koch, P. Jørgensen, *Chem Phys. Lett.* **1995**, *243*, 409–418. DOI:10.1016/0009-2614(95)00841-Q
50. M. J. Frisch et al., GAUSSIAN 03, Gaussian, Inc., Wallingford, CT **2004**.
51. R. Ahlrichs, M. Baer, M. Haeser, H. Horn, C. Koelmel, *Chem Phys Lett* **1989**, *162*, 165–169. DOI:10.1016/0009-2614(89)85118-8
52. G. Schaftenaar, J. H. Noordik, *J. Comput.-Aided Mol. Design* **2000**, *14*, 123–134. DOI:10.1023/A:1008193805436
53. Chemcraft program 1.6 (built 338), Programming: GA Zhurko, Design, additional support: D A Zhurko
54. L. Serrano-Andrés, M. Merchán, *J. Photochem. Photobiol. C* **2009**, *10*, 21–32.
55. C. E. Crespo-Hernández, B. Cohen, P. M. Hare, B. Kohler, *Chem. Rev.* **2004**, *104*, 1977–2019. DOI:10.1021/cr020677o
56. K. A. Kistler, S. Matsika, *J. Phys. Chem. A* **2007**, *111*, 2650–2661. DOI:10.1021/jp0663661
57. M. Merchán, R. González-Luque, T. Climent, L. Serrano-Andrés, E. Rodríguez, M. Reguero, D. Peláez, *J. Phys. Chem. B* **2006**, *110*, 26471–26476. DOI:10.1021/jp066874a
58. Z. Lan, E. Fabiano, W. Thiel, *J. Phys. Chem. B* **2009**, *113*, 3548–3555. DOI:10.1021/jp809085h
59. M. Barbatti, A. J. A. Aquino, J. J. Szymczak, D. Nachtigallova, P. Hobza, Hans Lischka, *Proc. Nat. Acad. Sci.* **2010**, *107*, 21453–21458. DOI:10.1073/pnas.1014982107
60. L. B. Clark, G. G. Peschel, I. Tinoco, *J. Phys. Chem.* **1965**, *69*, 3615–3618. DOI:10.1021/jj100894a063
61. M. K. Shukla, J. Leszczynski, *J. Biomol. Struct. Dyn.* **2007**, *25*, 93. DOI:10.1080/07391102.2007.10507159

Povzetek

Z uporabo cc-pVDZ baznih funkcij smo na CC2 teorijskem nivoju preučevali fotociklodimerizacijske mehanizme dveh okso tautomerov uracila in 6-azauracila. Uracil smo raziskovali pri treh orientacijah monomerov – cis-anti, trans-sin in trans-anti, medtem ko so bili za 6-azauracil računi izvedeni za vse štiri orientacije. Na CASSCF(2,2)/6-31G* teorijskem nivoju smo ugotovili stožčasta presečišča S_0/S_1 ter predlagali fotofizikalne mehanizme fotoformacije in fotodestrukcije ciklodimerov, ki nastajajo preko $^1\pi\pi^*$ elektronsko vzbujenih stan.

Scientific paper

Synthesis, Characterization and Computational Studies of Two Triazaspiro Tetracycles

Felix Odame^{1,*} and Eric C. Hosten¹¹ Department of Chemistry, Nelson Mandela Metropolitan University, P.O. Box 77000, Port Elizabeth 6031, South Africa

* Corresponding author: E-mail: felixessah15@gmail.com

Tel.: +27415042684, Fax: +2741 504 4236.

Received: 12-12-2017

Abstract

Two new triazaspiro tetracycles have been synthesized, the compounds have been characterized using spectroscopy, microanalysis and single crystal X-ray diffractometry. The single crystal X-ray crystallography of 4-methyl-8I,10I,17I-triazaspiro[cyclohexane-1,9I-teracyclo[8.7.02,7.011,16]heptadecane]-1I(17),2I(7I),3I,5I,11I,13I,15I-heptaene (compound I) has been discussed. The DFT computed bond angles have been obtained for both compounds and contrasted with experimental results for compound I. The atoms that make up the frontier orbitals which contribute to the reactivity of the compounds have been discussed.

Keywords: Aminophenylbenzimidazole; Triazaspirotetracyclics; 3-methylcyclohexanone; 4-methylcyclohexanone; Frontier molecular orbitals.

1. Introduction

The conversion of 2-(2'-aminophenyl)-1H-benzimidazoles to triazatetracycles provides a backbone on which to construct different tetracyclic compounds that are also biologically active. It is well known that amines undergo condensation reactions with aldehydes and ketones but utilization of this transformation in the formation of cyclic amines often requires a more intricate procedure. Thus, cyclic amines have been accessed *via* a sequence of deprotection followed by intermolecular reductive amination of Boc-protected amino ketones (Boc is *tert*-butyloxycarbonyl group) under asymmetric transfer hydrogenation conditions.¹ Cyclizations of diamines and ketones have also been catalyzed by HY zeolite at 50 °C under solvent-free conditions yielding benzodiazepines.² Benzodiazepine formation has also been reported to occur in the absence of a catalyst.³ A three-component allylation and cyanation reactions utilising a ketone and *N*-methoxyamine have been reported, and the high nucleophilicity of the *N*-methoxyamine and high electrophilicity of the corresponding iminium ion enable the concise synthesis of *X*-trisubstituted amines in a single step.⁴ A fourth method reported in the literature, the treatment of *N*-tosylaldimines with acetophenone at room temperature has been reported to give the corresponding *N*-tosyl β -amino ketones in high yields within 6–9 h. Subsequent reduction and cyclization of the

compounds in this case afforded 2,4-disubstituted *N*-tosylazetidines, comprising a three step high-yielding synthesis from aldimines.⁵

Twelve *N*-glycosyl amines were synthesized using 4,6-*O*-benzylidene-*D*-glucopyranose and different substituted aromatic amines, including some diamines that resulted in *bis*-glycosyl amines. Another set of six *N*-glycosyl amines was synthesized using different hexoses and pentoses with 2-(*o*-aminophenyl)benzimidazole. In these reactions only the 2-amino group reacted with the hydroxyl groups of 2-(*o*-aminophenyl)benzimidazole.⁶ Reactions of substituted aldehydes with 2-(*o*-aminophenyl)benzimidazole have been reported to yield Schiff's bases.⁷ The syntheses of 2-(2-nitrophenyl)-1-benzoyl-1H-benzimidazole derivatives and their reduction to the corresponding 2-benzimidazolylbenzamides have been reported. The compounds were cleanly and efficiently converted to the corresponding 6-arylbenzimidazo[1,2-*c*]quinazolines by microwave activation using SiO₂-MnO₂ as a solid inorganic support.⁸ In our case the products were accessed *via* a solvent-free method. Some triazatetracycles have been synthesized heating 2-(2-aminophenyl)benzimidazole and aryl aldehydes under reflux in ethanol for 5 h.⁹ Also triazatetracyclic compounds with substituents on the aryl ring have been synthesized from aminophenylbenzimidazole and substituted aryl aldehydes at room temperature in mixtures of ethanol and acetic acid.¹⁰ The synthesis of

1,3,8-triazaspiro[4.5]decane-2,4-diones (spirohydantoin) as a structural class of pan-inhibitors of the prolyl hydroxylase (PHD) family of enzymes for the treatment of anemia has also been reported.¹¹

This work presents the synthesis and characterization of two new triazaspiro tetracycles, their characterization with IR, NMR, GC-MS and microanalysis. The bond angles of compounds **I** and **II** computed using the functionals B3LYP, B3PW91 and wB97XD have been compared with experimental bond angles of compounds **1**.

2. Experimental

2.1. Materials and Instruments

Analytical grade reagents and solvents for the synthesis, such as 2-(2'-aminophenyl)-1*H*-benzimidazole were obtained from Sigma Aldrich (USA), whilst 4-methylcyclohexanone, tetrahydrofuran, ethanol and 3-methylcyclohexanone were obtained from Merck Chemicals (SA). The chemicals were used as received (*i.e.* without further purification). ¹H and ¹³C NMR spectra were recorded on a Bruker Avance AV 400 MHz spectrometer operating at 400 MHz for ¹H and 100 MHz for ¹³C using deuterated dimethyl sulfoxide as the solvent and tetramethylsilane as the internal standard. Chemical shifts are expressed in ppm. FT-IR spectra were recorded on a Bruker Platinum ATR Spectrophotometer Tensor 27. Elemental analyses were performed using a Vario Elementar Microcube ELIII. Melting points were obtained using a Stuart Lasec SMP30 whilst the mass spectra were determined using an Agilent 7890A GC System connected to a 5975C VL-MS with electron impact as the ionization mode and detection by a triple-axis detector. The GC was fitted with a 30 m × 0.25 mm × 0.25 μm DB-5 capillary column. Helium was used as the carrier gas at a flow rate of 1.63 mL·min⁻¹ with an average velocity of 30.16 cm s⁻¹ and a pressure of 63.73 kPa.

2.1.1. 4-Methyl-8¹,10¹,17¹-triazaspiro[cyclohexane-1,9¹-teracyclo[8.7.0^{2,7}.0^{11,16}]heptadecane]-1¹(17),2¹(7¹),3¹,5¹,11¹,13¹,15¹-heptaene (**I**)

2-(2'-Aminophenyl)-1*H*-benzimidazole (3.14 g, 0.015 mol) was heated under reflux with 10 mL of 4-methylcyclohexanone for 6 h. The reaction mixture was dissolved in ethanol and allowed to stand overnight. The white solid obtained was recrystallized as a white crystal from ethanol:THF (1:1), yield 72%; mp 192–193 °C. IR (ν_{\max} , cm⁻¹): 3300 (N–H), 2941 (C–H), 1615 (C=N), 1530 (C=C), 1479 (C–N), ¹H NMR (400 MHz) δ (ppm): 7.91 (d, $J = 7.6$ Hz, 1H, ArH), 7.82 (d, $J = 7.6$ Hz, 1H, ArH), 7.64 (d, $J = 6.8$ Hz, 1H, ArH), 7.26 (t, $J = 7.6$ Hz, 1H, ArH), 7.18 (q, $J = 6.8$ Hz, 2H, ArH), 7.12 (t, $J = 8.0$ Hz, 1H, ArH), 6.80 (t, $J = 7.6$ Hz, 1H, ArH), 6.74 (s, 1H, ArH), 2.50 (s, 3H), 2.09

(d, $J = 12.8$ Hz, 2H, CH₂), 1.59 (dd, $J_1 = 12.8$ Hz, $J_2 = 12.0$ Hz, 2H, CH₂), 1.00 (m, 2H, CH₂). ¹³C NMR (100 MHz) δ (ppm): 148.2 (C), 144.8 (C), 142.7 (C), 132.9 (CH), 132.1 (C), 125.3 (CH), 122.4 (CH), 122.2 (C), 119.6 (CH), 118.6 (CH), 115.9 (CH), 113.1 (CH), 113.0 (C), 74.4 (C), 34.8 (CH), 31.2 (CH₂), 30.0 (CH), 22.2 (CH₂). Anal. calcd. for: C₂₀H₂₁N₃: C, 79.17; H, 6.98; N, 13.85. Found: C, 79.05; H, 6.84; N, 13.78. LRMS (m/z , M⁺): Found for C₁₇H₁₇N₃ 303.23, calcd. mass 303.40.

2.1.2. 3-Methyl-8¹,10¹,17¹-triazaspiro[cyclohexane-1,9¹-teracyclo[8.7.0^{2,7}.0^{11,16}]heptadecane]-1¹(17),2¹(7¹),3¹,5¹,11¹,13¹,15¹-heptaene (**II**)

2-(2'-Aminophenyl)-1*H*-benzimidazole (3.14 g, 0.015 mol) was heated under reflux with 10 mL of 3-methylcyclohexanone for 6 h. The reaction mixture was dissolved in ethanol:diethyl ether (1:1). A white solid was obtained which was recrystallized as white crystals from ethanol:THF (1:1), yield 84%; mp 164–166 °C. IR (ν_{\max} , cm⁻¹): 3315 (N–H), 2948 (C–H), 2922 (C–H), 1619 (C=N), 1534 (C=C), 1481 (C–N). ¹H NMR (400 MHz) δ (ppm): 7.91 (d, $J = 7.6$ Hz, 1H, ArH), 7.82 (d, $J = 8.0$ Hz, 1H, ArH), 7.64 (d, $J = 6.8$ Hz, 1H, ArH), 7.24 (dd, $J_1 = 7.6$ Hz, $J_2 = 8.0$ Hz, 1H, ArH), 7.19 (m, 1H, ArH), 7.10 (d, $J = 8.0$ Hz, 1H, ArH), 6.80 (dd, $J_1 = 7.2$ Hz, $J_2 = 7.6$ Hz, ArH), 6.71 (s, 1H, ArH), 2.34 (m, 1H CH₂), 2.06 (m, 4H, CH₂), 1.86 (dt, $J_1 = 13.6$ Hz, $J_2 = 13.2$ Hz, 1H, CH), 1.71 (d, $J = 10.8$ Hz, 2H, CH), 1.12 (dt, $J_1 = 12$ Hz, $J_2 = 10.8$ Hz, 1H, CH), 0.93 (q, $J = 4.8$ Hz, 3H, CH₃). ¹³C NMR (100 MHz) δ (ppm): 148.3 (C), 144.9 (C), 142.8 (C), 132.8 (C), 131.8 (CH), 125.1 (CH), 122.4 (CH), 122.2 (C), 119.5 (CH), 118.6 (CH), 115.8 (CH), 113.2 (CH), 112.9 (C), 75.1 (C), 43.6 (CH₂), 34.6 (CH₂), 33.4 (CH₂), 27.6 (CH), 22.4 (CH₃), 21.2 (CH₃). Anal. calcd. for: C₂₀H₂₁N₃: C, 79.17; H, 6.98; N, 13.85. Found: C, 79.25; H, 6.89; N, 13.88. LRMS (m/z , M⁺): Found for C₁₇H₁₇N₃ 303.18, calcd. mass 303.40.

2.2. X-Ray Crystallography

X-Ray diffraction analysis of compound **I** was performed at 200 K using a Bruker Kappa Apex II diffractometer with monochromated Mo K α radiation ($\lambda = 0.71073$ Å). APEXII¹³ was used for data collection and SAINT¹² for cell refinement and data reduction. The structures were solved by direct methods using SHELXS-2013,¹³ and refined by least-squares procedures using SHELXL-2013,¹⁴ with SHELXLE,¹⁴ as a graphical interface. All non-hydrogen atoms were refined anisotropically. Carbon-bound H atoms were placed in calculated positions (C–H 0.95 Å for aromatic carbon atoms and C–H 0.99 Å for methylene groups) and were included in the refinement in the riding model approximation, with Uiso (H) set to 1.2Ueq (C). The H atoms of the methyl groups were allowed to rotate with a fixed angle around the C–C bond to best fit the experimen-

tal electron density (HFIX 137 in the SHELX program suite,¹³ with Uiso (H) set to 1.5Ueq (C). Nitrogen-bound H atoms were located on a difference Fourier map and refined freely. Data were corrected for absorption effects using the numerical method implemented in SADABS.¹³

2. 3. Computational Studies

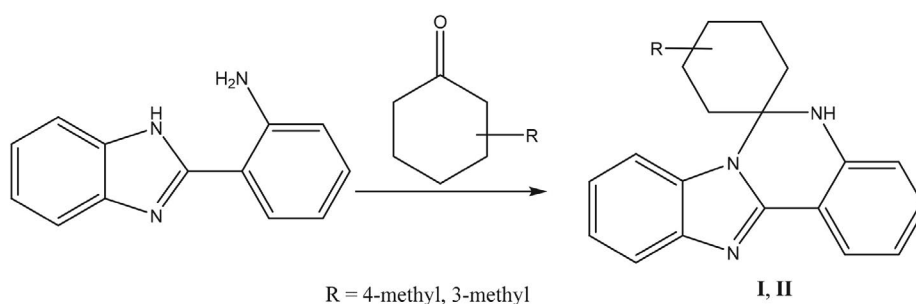
All calculations were performed using the GAUSSIAN program¹⁵ (version 03). The crystal structure was used as an initial molecular geometry for compound **I** but compound **II** was drawn using GAUSSIAN VIEW 03 software. The output files were visualized *via* GAUSSIAN VIEW 03 software.¹⁶ The molecular structures of both compounds in the ground state were optimized using DFT

with hybrid functionals B3LYP (Becke's three parameter hybrid functional using the LYP correlation functional),^{17–18} B3PW91 and wB97XD with 6-31G++ (d,p) basis set. None of the predicted vibrational spectra having any imaginary frequency prove that optimized geometry is located at the lowest point on the potential energy surface.

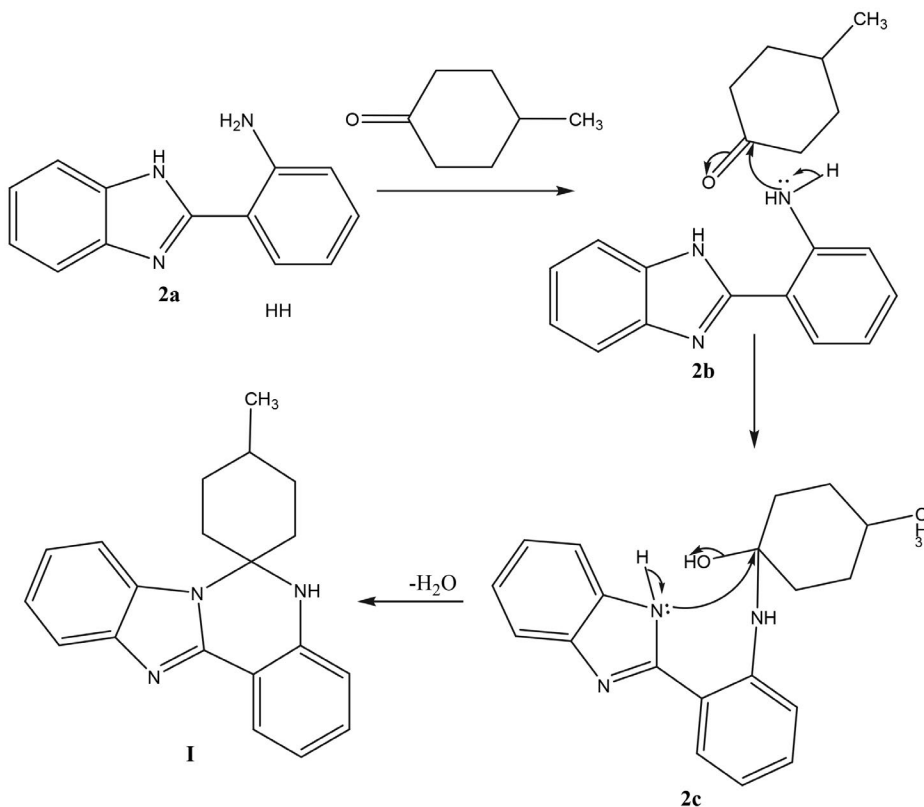
3. Results and Discussion

3. 1. General Studies

Aromatic protons in ¹H NMR were observed between 7.91 and 6.74 ppm for compound **I**, whilst the signals for compound **II** were observed between 7.91 and 6.71 ppm. The ¹H NMR spectrum of compound gave sig-



Scheme 1. Synthesis scheme for the formation of triazaspiro tetracycles **I** (R = 4-methyl) and **II** (R = 3-methyl).



Scheme 2. Proposed mechanism for the formation of compound **I**.

nals for aliphatic protons between 2.50 and 1.00 ppm for compound **I** and 2.34 and 0.93 ppm for compound **II**. The DEPT spectrum confirmed the presence of four methylene groups in both compounds.

The HMBC spectrum of compound **I** showed that the signal at 74.4 ppm is within three bonds of the signals at 6.74 and 6.80 ppm confirming the attachment of the carbonyl contributed by 4-methylcyclohexanone to the 2-aminophenyl moiety. In compound **II** the HMBC spectrum also showed that resonance at 75.1 ppm was with three bonds of the resonances at 115.8 and 113.2 ppm also confirming the attachment of the 3-methylcyclohexanone to the 2-aminophenyl moiety. Scheme 1 gives the synthesis overview for the formation of two triazaspiro tetracycles.

The proposed mechanism for the formation of triazaspiro tetracyclics is presented in Scheme 2. The reaction is thought to proceed by the attack of the carbonyl carbon of 3-methylcyclohexanone by the lone pair of electrons on the 2-aminophenyl group as shown in **2b**. The formation of the hydroxyl group in **2c** allows the lone pair of electrons on the nitrogen to attack the carbon of the hydroxyl group with the loss of water to form **I**.

3. 2. Reaction Mechanism Monitoring with ^1H NMR

Figure 1 gives the results of the ^1H NMR monitoring of the progress of the reaction of 4-methylcyclohexanone

with 2-(2'-aminophenyl)-1*H*-benzimidazole at 20 minutes intervals. Some of the aromatic signals merge into other signals due to the change in their environment after attachment of the ketone and consequently the aromatic ring.

3. 3. Characterization of Crystal Structures

Compound **I** was recrystallized as a white solid from ethanol:THF (1:1). The computed and experimental crystallographic data and selected bond angles for compound **I** are provided in Tables 1 and 2. The ORTEP diagram for compound **I** at 50% ellipsoid is presented in Figures 2. Two independent structures were obtained for compound **I** and both structures have been computed and discussed. **I** crystallized in the monoclinic space group P21/n.

The experimentally determined bond angle of N13–C121–C126 for compound **I** was $122.7(1)^\circ$ which deviates by between 1.0 to 1.2° for the computed bond angles of compounds **I** and **II** using the B3LYP, B3PW9 and wB97XD functionals at the 6-311+g(p,d) basis set. The computation of the bond angles of C122–C121–N13 for compounds **I** and **II** using the B3LYP, B3PW9 and wB97XD functionals and the 6-311+g(p,d) basis set gave deviations between 0 and 1.1° from the experimentally determined bond angle of $118.0(1)^\circ$ for compound **I**. The C122–C11–N11 bond angle for compound **I** was experimentally determined as $119.5(1)^\circ$. The computed bond angles for compounds **I** and **II** using the B3LYP, B3PW9 and

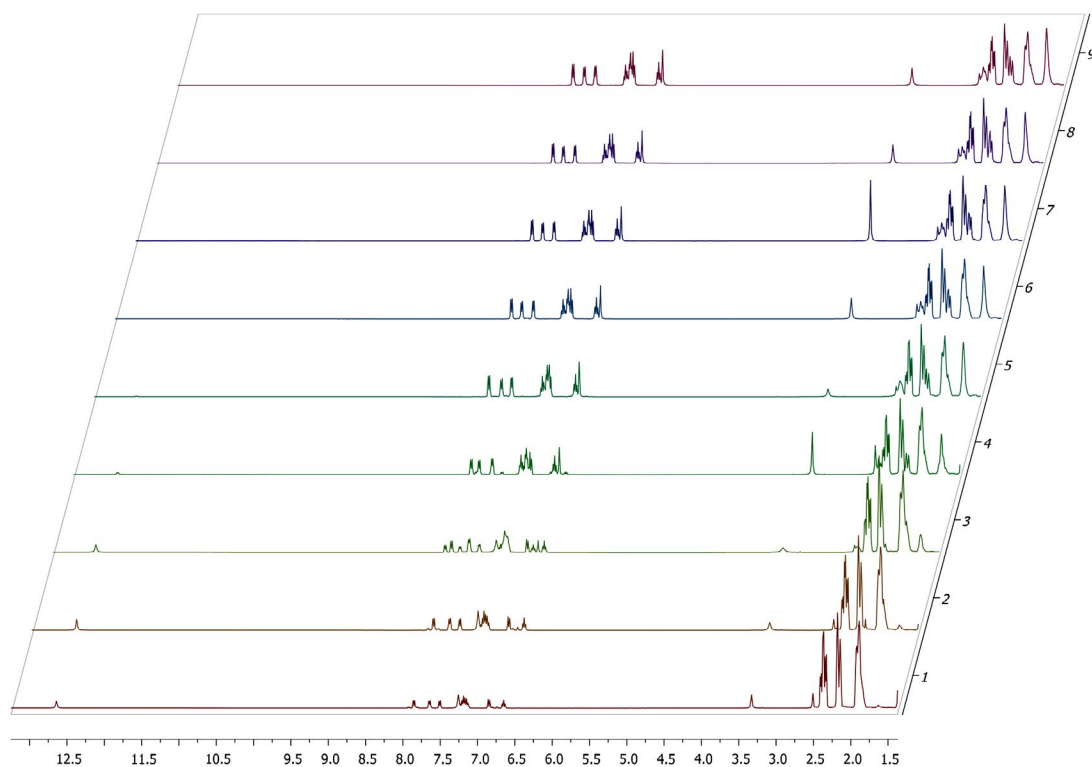


Figure 1. ^1H NMR monitoring of the reaction progress of 4-methylcyclohexanone and 2-(2'-aminophenyl)-1*H*-benzimidazole at 20 minute intervals.

Table 1. Crystallographic data and structure refinement summary for compound I

Property	Compound I
Formula	C ₂₀ H ₂₁ N ₃
CCDC number	1550687
Formula Weight	303.40
Crystal System	Monoclinic
Space group	P21/n
<i>a</i> [Å]	12.9495(4)
<i>b</i> [Å]	16.2186(4)
<i>c</i> [Å]	15.6429(3)
α [°]	90
β [°]	91.857(1)
γ [°]	90
<i>V</i> [Å ³]	3283.64(14)
<i>Z</i>	8
<i>d</i> (calc) [g/cm ³]	1.227
Mu(MoKa) [/mm]	0.074
F(000)	1296
Crystal Size [mm]	0.19 × 0.29 × 0.39
Temperature (K)	200
Radiation [Å]	MoKa 0.71073
Theta Min-Max [°]	2.4, 28.3
Dataset	−17: 17; −21: 21; −20: 20
Tot., Uniq. Data, R(int)	90703, 8160, 0.023
Observed Data [I > 2.0 sigma(I)]	6333
Nref,	8160
Npar	425
R	0.0404
wR2	0.1116
S	1.03
Max. and Av. Shift/Error	0.00, 0.00
Min. and Max. Resd. Dens. [e/Å ³]	−0.19
Min. and Max. Resd. Dens. [e/Å ³]	0.25

wB97XD functionals and the 6-311+g(p,d) basis set gave deviations of between 1.6 and 2.2°. The computed bond angles of C122–C11–N12 for compounds I and II using the B3LYP, B3PW9 and wB97XD yielded deviations of between 0.3 and 0.7° from the experimentally determined bond angle of compound I which was 126.7(1)°. The N11–C11–N12 bond angle for compound I obtained from experiment was 113.8(1)°. When computed using the B3LYP, B3PW9 and wB97XD functionals at the 6-311+g(p,d) basis set the results gave deviations between 1.1 and 1.8° from the experimental value. The C11–N11–C111 bond angle for compound I was experimentally determined as 106.2(1)°. Computation using the B3LYP, B3PW9 and wB97XD functional at the 6-311+g(p,d) basis set gave results which deviates from the experimental result by ±0.3°. The experimentally determined C11–N12–C112 bond angle for compound I was 104.3(1)°.

The computed results differed from the experimental values by between 1.1 to 1.4°. The experimentally determined N11–C111–C116 bond angle for compound I was 134.9(1)°. This differs from the computed values by between 0.8 and 1.4°. The N12–C112–C111 bond angle for compound I was experimentally determined as 111.0(1)°, which was approximately the same as the computed values with a difference of ± 0.1°. The experimentally determined N12–C112–C113 bond angle for compound I was 128.1(1)°. And this deviated from the computed values by between 0.2 and 0.4°. The experimentally determined bond angles of N11–C111–C112, C121–N13–C131 and N11–C131–N13 were 104.7(1), 118.8(1) and 104.6(1)° and differed by ±0.3, 3.0 to 11.1 and 2.8 to 3.1°, respectively. The N11–C131–C136 bond angle for compound I was ex-

Table 2. Summary of theoretical and experimental bond angles of 4-methylcyclohexanone derivative as well as the computed bond angles of 3-methylcyclohexanone

EXPERIMENTAL (I)	Bond Angles (°)					
	Compound I			Compound II		
	B3LYP/ 6-31++G (d,p)	B3PW91/ 6-31++G (d,p)	wB97XD/ 6-31++G (d,p)	B3LYP/ 6-31++G (d,p)	B3PW91/ 6-31++G (d,p)	wB97XD/ 6-31++G (d,p)
N13–C121–C126	122.7(1)	121.6	121.6	121.8	121.6	121.7
C122–C121–N13	118.0(1)	119.1	119.0	119.1	118.0	119.1
C122–C11–N11	119.5(1)	121.3	121.1	121.6	121.5	121.7
C122–C11–N12	126.7(1)	126.2	126.2	126.4	126.0	126.3
N11–C11–N12	113.8(1)	112.5	112.7	112.0	112.5	112.0
C11–N11–C111	106.2(1)	106.0	106.0	106.4	105.9	106.3
C11–N11–C131	120.7(1)	125.0	125.1	124.8	125.0	128.5
C11–N12–C112	104.3(1)	105.7	105.4	105.4	105.6	105.4
N11–C111–C112	104.7(1)	105.0	104.9	105.2	105.0	105.1
N11–C111–C116	134.9(1)	133.9	133.9	133.5	134.1	133.7
N12–C112–C111	111.0(1)	110.9	111.0	111.1	111.0	111.1
N12–C112–C113	128.1(1)	128.4	128.3	128.5	128.2	128.4
C121–N13–C131	118.8(1)	121.8	113.6	129.5	129.9	129.7
N11–C131–N13	104.6(1)	107.4	107.7	107.2	107.7	107.3
N11–C131–C136	109.3(1)	111.6	110.4	109.7	107.6	119.9
N11–C131–C132	111.8(1)	110.3	111.7	111.5	110.8	110.8
N13–C131–C132	108.9(1)	107.6	108.5	108.6	108.1	108.1

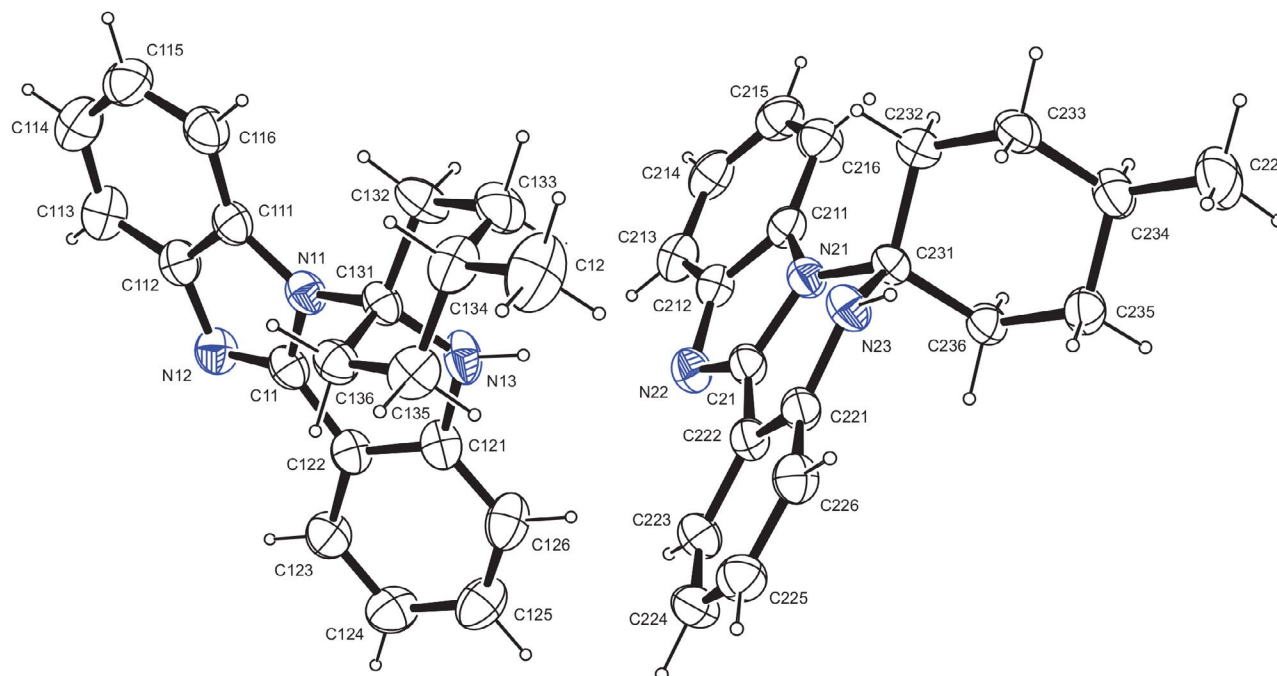


Figure 2. An ORTEP diagram of compound I at 50% ellipsoid

perimentally determined as $109.3(1)^\circ$. The computed values differed by between 0.4 and 10.6° . The experimentally determined bond angle of $N11-C131-C132$ for compound I was $111.8(1)^\circ$. It deviated from the computed values by between 0.1 and 1.5° . The $N13-C131-C132$ bond angle for compound I was experimentally determined as $108.9(1)^\circ$ this deviates by between 0.8 and 1.9° from the computed values.

3. 4. HOMO–LUMO Analysis

The HOMO and LUMO are the main orbitals that determine chemical stability of any species.¹⁹ The HOMO

represents the ability to donate an electron whilst the LUMO represents the ability to accept an electron. The energy of the HOMO is directly related to the ionization potential whilst the energy of the LUMO is related to the electron affinity. The energy difference between HOMO and LUMO orbitals, known as the energy gap, determines the stability or reactivity of molecules.²⁰ The energy gap is a critical parameter in determining molecular electrical transport properties because it is a measure of electron conductivity.²¹ The hardness of a molecule also corresponds to the gap between the HOMO and LUMO orbitals.²²

For the different functional and basis sets the HOMO and LUMO are mostly delocalized over the 2-aminophe-

Table 3. HOMO–LUMO orbitals of compounds I and II

	B3LYP/ 6-31++G (d,p)	B3PW91/ 6-31++G (d,p)	wB97XD/ 6-31++G (d,p)	B3LYP/ 6-31++G (d,p)	B3PW91/ 6-31++G (d,p)	wB97XD/ 6-31++G (d,p)
	Compound I (eV)			Compound II (eV)		
LUMO+4	-0.26632	-0.26676	-0.19315	-0.26627	-0.26677	-0.19278
LUMO+3	-0.26993	-0.27042	-0.19731	-0.26995	-0.27050	-0.19726
LUMO+2	-0.28531	-0.28641	-0.20932	-0.28549	-0.28662	-0.20952
LUMO+1	-0.34017	-0.34125	-0.27447	-0.34046	-0.34161	-0.27468
LUMO	-0.44433	-0.44683	-0.38954	-0.44436	-0.44691	-0.38944
HOMO	-0.50413	-0.50646	-0.57157	-0.50423	-0.50665	-0.57163
HOMO-1	-0.51472	-0.51723	-0.58780	-0.51501	-0.51760	-0.58781
HOMO-2	-0.53963	-0.54062	-0.61707	-0.54304	-0.54398	-0.62078
HOMO-3	-0.54610	-0.54062	-0.62392	-0.54862	-0.54964	-0.62663
HOMO-4	-0.55032	-0.54779	-0.62811	-0.55609	-0.55762	-0.63309
HOMO-LUMO GAP (eV)	0.0598	0.05963	0.18203	0.05987	0.05974	0.18219

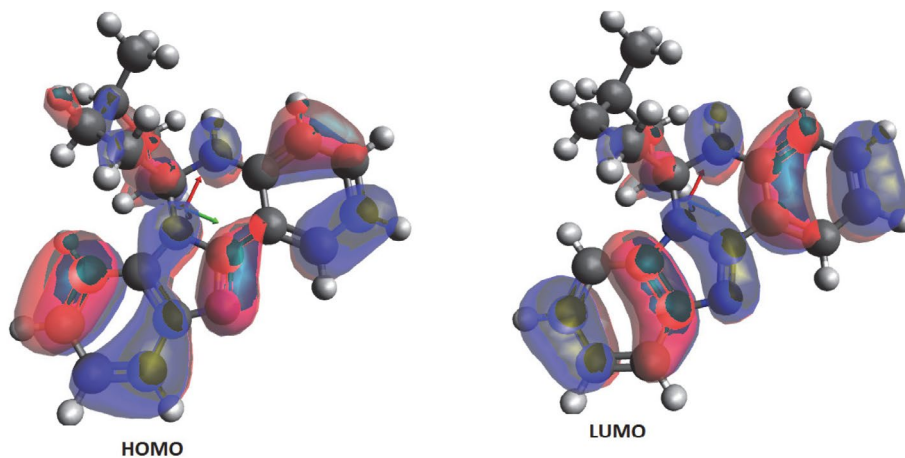


Figure 3. HOMO–LUMO of compound I computed using B3LYP/6-311++g(pd)

nyl-1*H*-benzimidazole delocalized indicating that during charge transfer in a reaction the molecule is stabilized by delocalization of electrons over the 2-aminophenylbenzimidazole, regardless of the level of theory and the basis set used. Table 3 gives the frontier orbitals for compounds I and II using the B3LYP, B3PW91 and wB97XD functional at the 6-31++ g(d,p) basis set.

4. Conclusion

In conclusion, 4-methyl-8¹,10¹,17¹-triazaspiro[cyclohexane-1,9¹-teracyclo[8.7.0^{2,7}.0^{11,16}]heptadecane]-1¹(17),2¹(7¹),3¹,5¹,11¹,13¹,15¹-heptaene and 3-methyl-8¹,10¹,17¹-triazaspiro[cyclohexane-1,9¹-teracyclo[8.7.0^{2,7}.0^{11,16}]heptadecane]-1¹(17),2¹(7¹),3¹,5¹,11¹,13¹,15¹-heptaene have been synthesized by a solvent-free method and characterized by IR, NMR, elemental analysis and GC-MS. The single crystal X-ray diffraction of compound I has been carried out and the results obtained were discussed. The bond lengths and bond angles of compound I have been compared with the computed bond lengths and bond angles. Whilst the bond lengths are mostly not in agreement with the computed results, the bond angles are very much in agreement with the computed results.

5. Acknowledgments

We thank MRC for the research funding (MRC-SIR). F. Odame thanks the National Research Foundation for awarding him a postdoctoral Fellowship.

6. Supplementary Material

Supplementary data associated with this article can be found, in the online version. CCDC number 1550687 contains the crystal structure associated with this article.

7. References

- G. D. Williams, R. A. Pike, C. E. Wade, M. Wills, *Org. Lett.* **2003**, 22, 4227–4230. DOI:10.1021/ol035746r
- M. K. Jegannath, K. Pitchumani, *ACS Sustainable Chem. Eng.* **2014**, 2, 1169–1176. DOI:10.1021/sc400560v
- F. Odame, P. Kleyi, E. Hosten, R. Betz, K. Lobb, Z. Tshentu, *Molecules* **2013**, 18, 14293–14305. DOI:10.3390/molecules181114293
- Y. Kurosaki, K. Shirokane, T. Toishi, T. Sato, N. Chida, *Org. Lett.* **2012**, 14, 2098–2101. DOI:10.1021/ol300622r
- B. K. Goering, Ph.D. Thesis, Cornell University, 1995.
- T. M. Das, C. P. Rao, E. Kolehmainen, *Carbohydr. Res.* **2001**, 334, 261–269. DOI:10.1021/ol300622r
- Y. S. Chhonker, B. Venu, S. R. Hasim, N. Kaushik, D. Kumar, P. Kumar, *Eur. J. Chem.* **2009**, 6(S1), S342–S346
- H. Pessoa-Mahana, C. D. Pessoa-Mahana, R. Salazar, J. A. Valderrama, E. Saez, R. Araya-Maturana, *Synthesis* **2004**, 3, 436–440. DOI:10.1055/s-2004-815924
- P. P. Joshi, S. G. Shirodkar, *World J. Pharm. Pharm. Sci.* **2014**, 3(9), 950–958.
- B. A. Insuasty, H. Torres, J. Quiroga, R. Abonia, R. Rodriguez, M. Nogeras, A. Sanchez, C. Saitz, S. L. Alvarez, S. A. Zacchino, *J. Chil. Chem. Soc.* **2006**, 51(2), 927–932. DOI:10.4067/S0717-97072006000200018
- P. Vachal, S. Miao, J. M. Pierce, D. Guiadeen, V. J. Colandrea, M. J. Wyvratt, S. P. Salowe, L. M. Sonatore, J. A. Milligan, R. Hajdu, A. Gollapudi, C. A. Keohane, R. B. Lingham, S. M. Mandala, J. A. DeMartino, X. Tong, M. Wolff, D. Steinhuebel, G. R. Kieczkowski, F. J. Fleitz, K. Chapman, J. Athanasopoulos, G. Adam, C. D. Akyuz, D. K. Jena, J. W. Lusen, J. Meng, B. D. Stein, L. Xia, E. C. Sherer, J. J. Hale, *J. Med. Chem.* **2012**, 55, 2945–295. DOI:10.1021/jm201542d
- APEX2, SADABS and SAINT. Bruker AXS Inc: Madison, WI, USA, 2010.
- G. M. Sheldrick, *Acta. Cryst. A* **2008**, 64, 112–122. DOI:10.1107/S0108767307043930
- C. B. Hübschle, G.M. Sheldrick, B. Dittrich, *J. Appl. Cryst.* **2011**, 44, 1281–1284. DOI:10.1107/S0021889811043202

15. M. J. Frisch, G. W. Trucks, H. B. Schlegel, G. E. Scuseria, M. A. Robb, J. R. Cheeseman, J. A. Montgomery Jr., T. Vreven, K. N. Kudin, J. C. Burant, J. M. Millam, S. S. Iyengar, J. Tomasi, V. Barone, B. Mennucci, M. Cossi, G. Scalmani, N. Rega, G. A. Petersson, H. Nakatsuji, M. Hada, M. Ehara, K. Toyota, R. Fukuda, J. Hasegawa, M. Ishida, T. Nakajima, Y. Honda, O. Kitao, H. Nakai, M. Klene, X. Li, J. E. Knox, H. P. Hratchian, J. B. Cross, V. Bakken, C. Adamo, J. Jaramillo, R. Gomperts, R. E. Stratmann, O. Yazyev, A. J. Austin, R. Cammi, C. Pomelli, J. W. Ochterski, P. Y. Ayala, K. Morokuma, G. A. Voth, P. Salvador, J. J. Dannenberg, V. G. Zakrzewski, S. Dapprich, A. D. Daniels, M. C. Strain, O. Farkas, D. K. Malick, A. D. Rabuck, K. Raghavachari, J. B. Foresman, J. V. Ortiz, Q. Cui, A. G. Baboul, S. Clifford, J. Ioslowski, B. B. Stefanov, G. Liu, A. Liashenko, P. Piskorz, I. Komaromi, R. L. Martin, D. J. Fox, T. Keith, M. A. AllLaham, C. Y. Peng, A. Nanayakkara, M. Challacombe, P. M. W. Gill, B. Johnson, W. Chen, M. W. Wong, C. Gonzalez, J. A. Pople, Gaussian 03, Revision E.01, Gaussian Inc, Wallingford, CT, 2004.
16. R. Dennington II., T. Keith, J. Millam, GaussView, Version 4.1.2, Semichem Inc, Shawnee Mission, KS, 2007.
17. A. D. Becke, *J. Chem. Phys.* **1993**, *98*, 5648–5652.
DOI:10.1063/1.464913
18. C. Lee, W. Yang, R. G. Parr, *Phys. Rev. B*, **1988**, *37*, 785–789.
DOI:10.1103/PhysRevB.37.785
19. D. F. V. Lewis, C. D. V. Ioannides, *Xenobiotica*, 1994, *24*, 401–408. DOI:10.3109/00498259409043243
20. L. Padmaja, R. C. Kunar, D. Sajan, I. H. Joe, V. S. Jayakumar, G. R. Pettit, O. F. Nielsen, *J. Raman Spectrosc.* 2009, *40*, 419–428. DOI:10.1002/jrs.2145
21. A. Poiyamozhi, N. Sundaraganesan, M. Karabacak, O. Tansiriverdi, M. Kurt, *J. Mol. Struct.* **2012**, *1024*, 1–12.
DOI:10.1016/j.molstruc.2012.05.008
22. P. Udhayakala, A. Jayanthi, T. V. Rajendiran, S. Gunasekaran, *Arch. Appl. Sci. Res.* **2011**, *3(4)*, 424–439.
DOI:10.1002/jrs.2145

Povzetek

Sintetizirali smo dva nova triazaspiro tetraciklična sistema, obe spojini karakterizirali s pomočjo spektroskopskih metod in elementne mikroanalize, v enem primeru pa izvedli tudi rentgensko difrakcijo na monokristalu. Rentgenska kristalna analiza spojine 4-metil-8¹,10¹,17¹-triazaspiro[cikloheksan-1,9¹-teraciklo[8.7.0^{2,7}.0^{11,16}]heptadekan]-1¹(17),2¹(7¹),3¹,5¹,11¹,13¹,15¹-heptaen (I) je služila za primerjavo eksperimentalnih veznih kotov z računskimi DFT rezultati, pridobljenimi za obe spojini. Ker so energije mejnih molekularskih orbital ključnega pomena za reaktivnost molekul, smo izračunali tudi njihove energije in jih primerjali med seboj.

Scientific paper

Determination of Biogenic Amines at Low $\mu\text{g L}^{-1}$ Levels as Acetylacetone Derivatives by RP-HPLC with UV-Visible Detection in Expired Apple Juice Samples

Bediha Akmeşe^{1,*} and Adem Asan²¹Department of Chemistry, Faculty of Science and Arts, Hitit University, Corum, Turkey²Department of Chemistry, Faculty of Science and Arts, Ondokuz Mayıs University, Samsun, Turkey

* Corresponding author: E-mail: bedihaakmese@hitit.edu.tr

Tel: +90 364 2277000 Fax: +90 364 2277005

Received: 18-12-2017

Abstract

An accurate and sensitive method for trace quantification of three biogenic amines in expired apple juice samples based on reversed-phase liquid chromatography (RP-HPLC) with UV-visible detection is described. Biogenic amines including cadaverine, histamine, and tyramine, were converted to their acetylacetone derivatives in water-methanol medium. The proposed method involves a pre-column derivatization of species followed by RP-HPLC separation with Thermo Hypersil Gold reversed-phase column and UV detection at 315 nm. A flow rate of 0.9 mL min^{-1} was used in the proposed method. An efficient separation of biogenic amines was successfully performed in 11 min with a good resolution using 35:65% (v/v) acetonitrile-water mixture as the mobile phase. Detection limits of 0.03, 0.23, and $0.08 \mu\text{g L}^{-1}$ were obtained for cadaverine, histamine and tyramine, respectively. The proposed method has been successfully applied for the analysis of two different commercially available expired apple juice samples. Recovery rates between 98.78 and 102.12% were obtained with an RSD of 0.16–1.65% for the analysis of 20 mL of expired apple juice samples indicating that the recoveries of biogenic amines were very satisfactory.

Keywords: Biogenic amines; acetylacetone; RP-HPLC; UV-visible spectrophotometry; expired apple juice

1. Introduction

Biogenic amines are aliphatic, alicyclic or heterocyclic organic bases of low molecular weight which arise as a consequence of metabolic processes in animals, plants, and microorganisms. These amines are found in a variety of foods and beverages. Their production occurs during a ripening or fermentation process. Biogenic amines can also occur naturally in foods and beverages.¹ Biogenic amines are also important for their role as indicators of quality and/or acceptability in some foods.² Furthermore, they have important metabolic roles in living cells; for instance, polyamines and putrescine are essential for cell growth, and other amines such as histamine, tyramine, and serotonin are involved in the central nervous system functioning for the regulation and control of the blood pressure.³

Biogenic amines generally do not cause any risk to human health unless they are ingested in large amounts or

the natural mechanism for their catabolism is genetically defective or inhibited.⁴ The consumption of food products containing $80\text{--}100 \text{ mg L}^{-1}$ biogenic amine level causes a variety of disorders. Thus, the formation of biogenic amines in food products should be controlled for the general public health. In addition, the storage time and temperature of food products may also bear a health risk for consumers. Therefore, the inhibition of effective microorganisms and decarboxylase enzyme activities are essential for the formation of biogenic amines.

The chemical structure of biogenic amines can be aliphatic (putrescine, cadaverine, spermine, spermidine), aromatic (tyramine, phenylethylamine), or heterocyclic (histamine, tryptamine).⁵ Histamine and cadaverine are classified as diamines containing two nitrogen groups in their structures. They are derived from decarboxylation of histidine and lysine, respectively. Tyramine is a monoamine compound containing one nitrogen in its structure and is derived from decarboxylation of tyrosine.

Histamine poisoning is a significant concern for the food safety. The ingestion of foods containing high levels of histamine affects human health, and the symptoms of histamine poisoning include difficulties in breathing, itching, rashes, vomiting, fever, and flushing.⁶ The European Food Safety Authority confirmed histamine and tyramine as the most toxic and particularly relevant for food safety and the products with high contents of biogenic amines may be harmful for susceptible individuals.⁷ Several methods for the determination of biogenic amines in foods have been developed and the most applied ones involve high performance liquid chromatography (HPLC) coupled with different detectors.^{8–23} However, HPLC generally suffers from the matrix effects. Therefore, extraction and purification steps must be undertaken prior to chromatographic analysis. These steps are the most critical aspects in terms of obtaining an adequate recovery for each amine. The aim of the extraction and purification steps is to remove interfering compounds from the matrix, but during these steps losses of biogenic amines must be kept as small as possible. The extraction of biogenic amines from a food matrix is generally carried out using hydrochloric acid, perchloric acid or trichloroacetic acid (TCA).


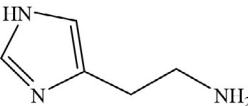
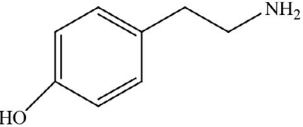
Biogenic amines have been detected in numerous kinds of foods and beverages, e.g. cheese, fish, vegetable, meat, wine, and beer.²⁴ In the literature there is no study of biogenic amine determination in expired apple juice samples. In the present study, biogenic amines were analyzed in expired apple juice samples. Various types of bacterial degradation in apple juice samples with the past expiration date can result in the formation of some amines and their derivatives. Biogenic amines produced by microbial contamination are mainly bacterial, e.g. cadaverine, histamine and tyramine.²⁵ Biogenic amines, especially histamine, tyramine, putrescine and cadaverine have been suggested as indicators of spoilage of some foods, such as fresh fish, meat and vegetables.²⁶ Biogenic amine concentrations are normally lower in non-fermented food (e.g., fruits, vegetables, meat, milk and fish), but higher in fermented foods (e.g., cheese, soybean products) and beverages as a result

of a contaminating microflora exhibiting amino acid decarboxylase activity.¹⁵ Therefore, three biogenic amines (cadaverine, histamine and tyramine), which have the most important role in foods and life, have been identified and included in the study.

The quantification of this group remains challenging due to the variation in the physico-chemical properties and potential matrix effects from other substances present within the sample. This problem has been addressed using a derivatization process, with pre- and post-column approaches in high-performance liquid chromatography most widely employed at present.²⁴ The pre-column derivatization technique is used more frequently than the post-column derivatization because of more sensitive detection. Derivatization may be a cause for the extended sample preparation time, but is often required to complement the analysis. The determination of biogenic amines is commonly achieved by chromatographic methods such as thin-layer chromatography (TLC), gas chromatography (GC), capillary electrophoresis (CE) and high performance liquid chromatography (HPLC). TLC does not have adequate sensitivity. CE requires complex operations. GC method is not so often applied for the determination of biogenic amines due to their low volatility. GC-MS and LC-MS/MS methods are generally non-derivative methods. But, MS detectors are very expensive and require a specially trained operator. On the other hand, there is difficulty in introduction of the small size sample into the high vacuum system. Therefore, it is highly expensive and requires technical skills and it is not widely preferred. Whereas, UV detectors are cheap devices and good enough for detection of biogenic amines. The most popular of all these methods is the HPLC for the determination of biogenic amines.

For HPLC analysis using spectrophotometric detectors the determination of biogenic amines needs a derivatization because most biogenic amines lack the chromophore. This derivatization, that occurs via amino groups with different tagging, or reagents helps to improve the selectivity and sensitivity of the methodology. In order to increase their absorption intensities, biogenic amines

Table 1. Biogenic amines studied

Name	Abbreviation	Structure	Molecular weight (g mol ⁻¹)	pKa ^{20, 40}
Cadaverine	CAD		102.2	pKa ₁ : 11.0 pKa ₂ : 9.9
Histamine	HIS		111.2	pKa ₁ : 9.8 pKa ₂ : 6.0
Tyramine	TYR		137.2	pKa ₁ : 9.6

should be converted to corresponding compounds using an organic chelator. The resulting compounds will allow the indirect determination of biogenic amines by UV-vis spectroscopy. *Ortho*-phthalaldehyde (OPA),^{18,27–32} dansyl chloride,^{13–15,33–37} and benzoyl chloride^{16–17} have been reported as the derivatizing agents for the determination of biogenic amines using HPLC. Acetylacetone has also been utilized by Nishikawa³⁸ and Asan and Isildak³⁹ in the derivatization of primary amines and aliphatic diamines.

In this study, we propose a procedure for the determination of biogenic amines which cannot be directly identified due to their low absorption intensities by UV-vis spectroscopy. Initially, biogenic amines reacted with acetylacetone to form derivatives and thus their absorption intensities were increased. Then, the chromatographic conditions and wavelength of detection were optimized in order to maximize the sensitivity of the procedure. Under the optimized conditions, the chromatographic separation of cadaverine, histamine and tyramine derivatives was carried out in a reverse-phase column. Finally, the proposed method was applied for the quantification of biogenic amines in expired apple juice samples. The biogenic amines analysed are shown in Table 1.

2. Materials and Methods

2.1. Chemical and Reagents

All chemicals and solvents used were of analytical and chromatographic grade, respectively. The biogenic amine compounds (cadaverine, histamine and tyramine) were provided by Fluka. HPLC-grade acetonitrile and HPLC-grade methanol were obtained from Sigma–Aldrich. Acetylacetone was supplied by Merck. Dipotassium hydrogenphosphate (K_2HPO_4) was purchased from Merck. Trichloroacetic acid was obtained from Kanto Chemical Co. Inc. Perchloric acid ($HClO_4$) was obtained from Sigma–Aldrich. Ultrapure water with conductivity $18.2 \mu S cm^{-1}$ was used for the preparation of all aqueous solutions.

2.2. Apparatus

The RP-HPLC analysis was performed on a Shimadzu HPLC system (Kyoto, Japan) equipped with an LC-20 AD pump, a SPD-M 20A DAD detector system, and a CTO 20 AC column oven. The instrument has a DGU 20A degassing system. The system operates at 315 nm for cadaverine, histamine and tyramine. Termo Hypersil Gold C18 (2.5 μm , 175 mm \times 5 mm) was used as stationary phase at 31 °C. The maximum operating pressure on the system was 400 bar. Mettler Toledo (Greifensee, Switzerland) MA 235 pH/ion analyser with Hanna HI 1332 Ag/AgCl combined glass electrode (USA) was used for pH measurements. Heidolph was used as the evaporator. Ultrapure water was obtained using a Zeneer Power I water system (Human Corp. Korea).

2.3. Preparation of Standard Solutions of Biogenic Amines

Stock solutions of cadaverine, histamine and tyramine were prepared by dissolving each biogenic amine in 10% (v/v) methanol-water. The final concentrations were 137, 102 and 111 $\mu g L^{-1}$ for cadaverine, histamine, and tyramine, respectively. Standard samples with lower concentrations were prepared by appropriate dilution in deionized water-methanol solution of the same ratio. All biogenic amine solutions were stored refrigerated at +4 °C and protected from light.

2.4. Derivatization Procedure

The acetylacetone derivatives of the biogenic amines were prepared following the procedure described by Asan and Isildak³⁹, after a major modification. Firstly, all parameters for the derivatization reaction between the biogenic amines and acetylacetone were optimized. An appropriate amount of each biogenic amine was added to a 100 mL solution containing 10 mL methanol, 1.0 g K_2HPO_4 , and 1.0 mL of acetylacetone were added under vigorous shaking for 10 min to complete the reaction at room temperature. Then, the reaction mixture was evaporated. The final concentration of each biogenic amine derivatives was 50 $\mu g L^{-1}$. The residue was redissolved in 1 mL of mobile phase and 20 μL of each sample was injected onto the RP-HPLC column. The biogenic amines were identified qualitatively from their retention times and they were determined quantitatively by their peak areas.

For sample analysis, firstly the expired apple juice samples were filtered through a membrane of 0.45 μm pore and 47 mm diameter. The homogenized sample was diluted to 50 mL with 5% trichloroacetic acid.³¹ And then, 20 mL of each sample was added to a mixture of 100 mL of 10% (v/v) methanol-water containing 1.0 g K_2HPO_4 , 10 mL methanol, and 1.0 mL of acetylacetone. The resulting mixture was shaken for 10 min to complete the reaction. The mixture was evaporated and the residue was redissolved in 1 mL of mobile phase and 20 μL of each sample was injected onto RP-HPLC system.

2.5. Chromatographic Procedure

To determine the biogenic amines in expired apple juice samples, an analytical method was established using reversed-phase high performance liquid chromatography coupled to diode-array detector. Firstly, chromatographic conditions (mobile phase, flow-rate, etc.) were optimized using standard biogenic amine solutions. The chromatographic separation of biogenic amines was carried out using a Termo Hypersil Gold C18 (2.5 μm , 175 mm \times 5 mm) reversed-phase column. The flow-rate in RP-HPLC system was 0.9 mL min^{-1} . The separation of acetylacetone derivatives of biogenic amines was suc-

cessfully performed with a good resolution in 11 min using acetonitrile-water mixture (35:65%, v/v) as the mobile phase and detected spectrophotometrically at a wavelength of 315 nm.

3. Results and Discussion

3.1. Analytical Characteristics of the Method

Optimal conditions for the separation of biogenic amines by HPLC were determined by using Thermo Hypersil Gold (reversed-phase column) as the stationary phase and 35:65% (v/v) acetonitrile-water mixture as the mobile phase at the column temperature of 31 °C and the flow-rate of 0.9 mL min⁻¹. Under these conditions, acetylacetone derivatives of biogenic amines were eluted for ca. 11 min. Fig. 1 shows the chromatogram of the standard biogenic amine solution where a good resolution for peaks relating to three biogenic amines examined was observed

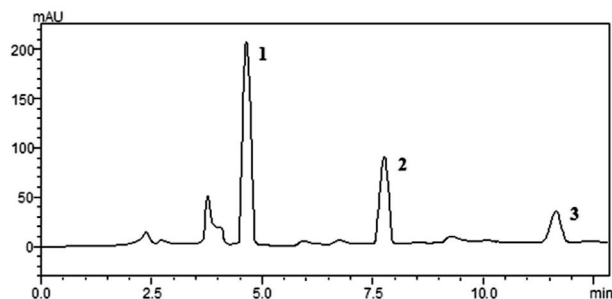


Figure 1. RP-HPLC chromatogram of the acetylacetone derivatives of biogenic amines. Amount of the biogenic amines: (1) histamine (15.78 µg L⁻¹); (2) tyramine (18.95 µg L⁻¹); (3) cadaverine (10.35 µg L⁻¹). Mobile phase: acetonitrile-water (35:65%, v/v); Flow-rate: 0.9 mL/min; Injection: 20 µL; Thermo Hypersil Gold C18 column (175 mm × 5 mm)

in a quite short analysis time. The analytical method was validated by determination the linear range, limit of detection (LOD) and limit of quantification (LOQ), precision and recovery. Results are summarized in Table 2 and Table 3. Linearity of the calibration curves was established by injecting five concentrations of the biogenic amines standard mixtures (1.02–21.95 µg L⁻¹). Good linearity (r^2 : 0.9925–0.9982) was obtained between peak area and analyte concentration.

The LOD was determined from the minimum concentration of the amine required to give a signal to noise ratio of 3 while the LOQ was determined with a signal to noise ratio of 10. The sensitivity of the method, as reflected by the LOD and LOQ values, is comparable to the previously reported data in the literature.^{41–42}

3.2. Recovery Studies

The repeatability and reproducibility of the RP-HPLC method were assessed by the injection of the each standard mixture for five times on the same day (intra-day) and over six days (inter-day), respectively. Good reproducibility of both the peak area (RSD ≤ 2.85%) and the retention times (RSD ≤ 0.89%) were found (Table 3). Intra-day repeatability (same analyst, apparatus and reagent) was assessed by injecting a mixture containing all the analytes five times during the same chromatographic run. Inter-day repeatability (the same analyst and apparatus but different reagents) was assessed by injecting individual samples of a standard mixture over seven days.

The proposed method of analysis was applied for recovery studies in order to examine the effect of sample matrices as the composition of apple juice samples is extremely complex. For this purpose, two concentrations (low and high) of cadaverine, histamine and tyramine

Table 2. Linearity and sensitivity data of the developed RP-HPLC method for the determination of the biogenic amines.

Biogenic amine	Retention time (min)	Regression equation ^a	Linear range (µg L ⁻¹)	R ²	LOD ^b (µg L ⁻¹)	LOQ ^c (µg L ⁻¹)
CAD	11.3	$y = 0.345x + 0.471$	1.02–16.35	0.9925	0.03	0.09
HIS	4.7	$y = 0.307x + 0.544$	1.11–17.78	0.9961	0.23	0.71
TYR	7.8	$y = 0.251x + 0.551$	1.37–21.95	0.9982	0.08	0.13

^a $y = bx + a$; y : area/area₁* (areas obtained for concentrations 1.02 µg L⁻¹ for cadaverine, 1.11 µg L⁻¹ for histamine and 1.37 µg L⁻¹ for tyramine)

^bS/N = 3; ^cS/N = 10

Table 3. Method accuracy and precision

	Intra-day (RSD%) (n = 5)		Inter-day (RSD%) (n = 5)		Recovery (%) ± RSD (%) (n = 5)	
	t_R	Area	t_R	Area	Low	High
CAD	0.89	0.41	0.49	1.72	98.78 ± 0.16	101.35 ± 1.65
HIS	0.74	0.32	0.35	2.23	101.07 ± 1.07	99.61 ± 0.68
TYR	0.47	0.58	0.64	2.85	100.33 ± 0.47	102.12 ± 0.22

Recovery (in%) found in the analysis of two different apple juice samples spiked at low (5 µg L⁻¹) and high (15 µg L⁻¹) levels; RSD, relative standard deviation; t_R , retention time

were added to the samples for the analysis using the proposed procedure. The expired juice sample was derivatized as previously described. The mixture was evaporated and the precipitates were redissolved in 1 mL of mobile phase and then 20 μL injected into the system. The recovery values were obtained from the regression equation.

The data obtained showed that cadaverine, histamine and tyramine produced peak heights as for their standard solutions at previously determined retention times on the chromatogram of the standard mixture. The accuracy of the method was evaluated from the calculation of recoveries after spiking expired apple juice at two different concentration ranges for each biogenic amine. Table 3 shows the corresponding results for cadaverine, histamine and tyramine with recoveries in the range from 98 to 102%. Consequently, these biogenic amines can be quantified using the proposed method with high accuracy.

The results showed that the accuracy, precision and reproducibility of the proposed procedure is excellent for the determination of biogenic amines in samples.

3. 3. Determination of Biogenic Amines in Expired Apple Juice Samples

The proposed procedure has been applied to expired apple juice samples for the determination of biogenic amines. The developed method was applied to expired apple juice samples since they contain biogenic amines due to the passing of the usage period. Two dif-

ferent brands of expired apple juice samples were purchased from local markets in Samsun (Turkey). After the optimization of chromatographic method, it was used to determine the biogenic amines in the expired apple juice samples. Fig. 2 shows typical chromatograms of biogenic amines in 20 mL of expired apple juice samples. The results are given in Table 4. The chromatogram of the expired apple juice sample indicates the sensitivity of the method. As may be seen from the chromatograms of the real samples, histamine and cadaverine were not detected in any of the two different brands of samples. The experimental results showed that tyramine at low concentration occurred in two expired apple juice samples. Thus, it was concluded that more tyramine was formed than the other biogenic amines resulting from degradation of apple juice. The peaks appearing for tyramine correspond to 5.16 and 2.21 $\mu\text{g L}^{-1}$ for sample 1 and sample 2, respectively. These results proved that low ppb levels of biogenic amines in real samples could successfully be determined.

3. 4. Comparison with the Reported Methods

The comparison of the proposed method with the previously reported methods (published over the period 2009–2017) is presented in Table 5. The proposed method enabled the LOD 1.02–21.95 $\mu\text{g L}^{-1}$ for biogenic amines without complex pre-treatment. The LOD obtained by the proposed procedure are well compared to the previously reported methods presented in Table 5.

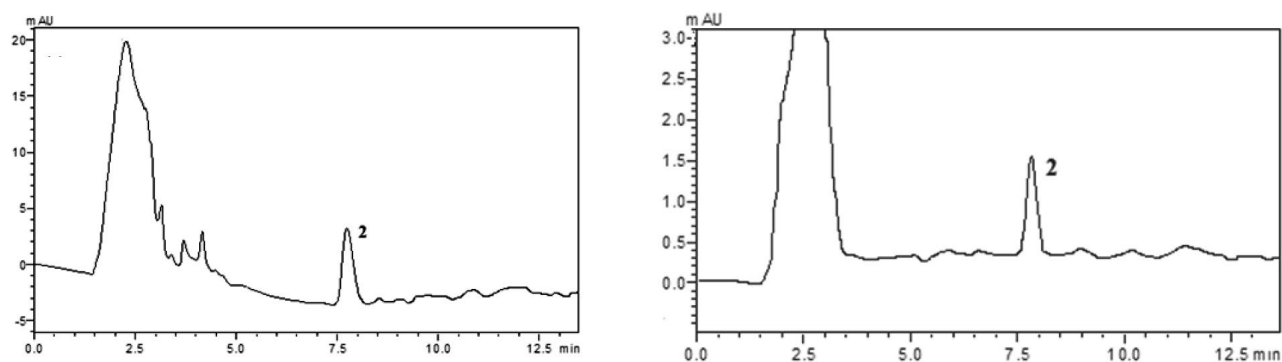


Figure 2. RP-HPLC chromatogram of biogenic amines obtained for the apple juice samples; (a): Sample 1, (b): Sample 2; (2) tyramine. Chromatographic conditions were the same as in given Fig. 1. (see Table 3 for analytical results)

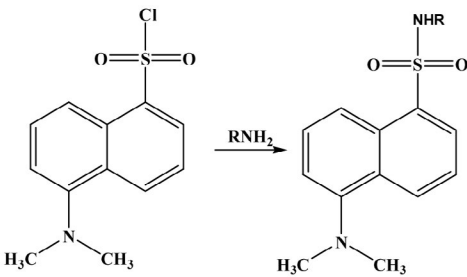
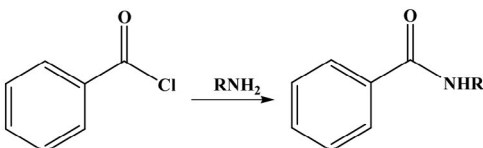
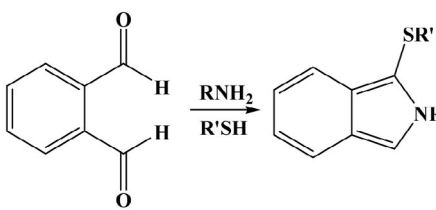
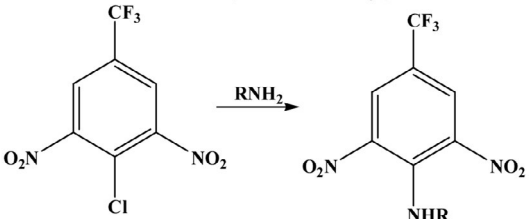
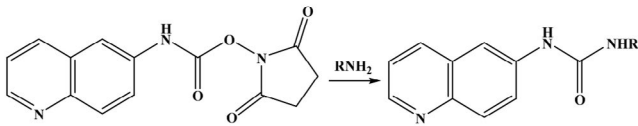
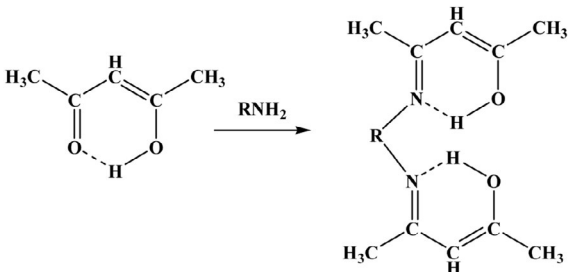
Table 4. Biogenic amine contents in two apple juice samples calculated as mean^a and RSD (%)^b.

Apple Juice Samples	CAD ($\mu\text{g L}^{-1}$)		HIS ($\mu\text{g L}^{-1}$)		TYR ($\mu\text{g L}^{-1}$)	
	Mean	RSD	Mean	RSD	Mean ^a	RSD ^b
Sample 1	BDL ^c	–	BDL	–	5.16	2.03
Sample 2	BDL	–	BDL	–	2.21	1.89

^a $\mu = \bar{x} \pm t_{\alpha} \frac{s}{\sqrt{n}}$ (The results were obtained with 95% confidence level for $n = 5$) ^bRelative standard deviation

^cBelow the detection limit

Table 5. Comparison of literature HPLC methods (published over the period 2009–2017) for biogenic amines involving the derivatization with principle reagents.

Derivatizing reagent/reaction scheme	Method	Sample	LOD	Reference
Dansyl chloride				
	HPLC-FD	Wine, fruit nectar	0.06–8 mg L ⁻¹	[13]
	HPLC-FD	Fruit juices	0.006–0.0077 mg L ⁻¹	[14]
	HPLC-UV	Tomato, ketchup, orange juice, soybeansauce, fish sauce	0.001–50 mg L ⁻¹	[15]
Benzoyl chloride				
	HPLC-UV	Wine	95.32–1433 mg L ⁻¹	[16]
	HPLC-UV	Wine, beer	0.05–8 µg mL ⁻¹	[17]
o-Phthaldialdehyde				
	HPLC-FD	Fish	1.5 mg kg ⁻¹	[18]
2-Chloro-1,3-dinitro-5-(trifluoromethyl)benzene				
	HPLC-UV	Wine	0.09–9 mg L ⁻¹	[19]
6-Aminoquinolyl-N-hydroxysuccinimidyl carbamate				
	HPLC-FD	Wine	0.027–0.070 mg L ⁻¹	[20]
Acetylacetone				
	HPLC-UV	Expired apple juice	1.02–21.95 µg L ⁻¹	This work

4. Conclusions

A reliable procedure was developed for the determination of biogenic amines in expired apple juice samples. Biogenic amines, cadaverine, histamine and tyramine, were converted to their acetylacetone derivatives in water-methanol medium. The proposed method involves a pre-column derivatization of species followed by HPLC separation with Thermo Hypersil Gold reversed-phase column and UV detection at 315 nm. The detection limits of 0.03, 0.23, and 0.08 $\mu\text{g L}^{-1}$ were obtained for cadaverine, histamine, and tyramine, respectively. The proposed procedure was applied to the analysis of two different brands of apple juice samples. The recovery rates obtained between 98.78 and 102.12% with RSD of 0.16–1.65% for biogenic amines from the analysis of 20 mL of expired juice samples were very satisfactory. The proposed chromatographic method presented here is simple, convenient and cost effective. The method is also accurate and precise for the determination of biogenic amines in real samples and it may have a potential for accurate determination of biogenic amines from other food and beverage samples.

5. Acknowledgement

We gratefully acknowledge the financial support of Ondokuz Mayıs University Research Foundation, Samsun, Turkey (BAP; Project number PYO. Fen.1904.12.009).

6. References

- J. Kirschbaum, K. Rebscher, H. Brückner, *J. Chromatogr. A* **2000**, *881*, 517–530. DOI:10.1016/S0021-9673(00)00257-0
- C. Ruiz-Capillas, F. Jiménez-Colmenero, *Crit. Rev. Food Sci. Nutr.* **2005**, *44*, 489–599. DOI:10.1080/10408690490489341
- A. Lonvaud-Funel, *FEMS Microbiol. Lett.* **2001**, *199*, 9–13. DOI:10.1111/j.1574-6968.2001.tb10643.x
- S. L. Rice, R. R. Eitenmiller, P. E. Kohler, *J. Milk Food Technol.* **1976**, *39*, 353–358. DOI:10.4315/0022-2747-39.5.353
- M. H. Silla Santos, *Int. J. Food Microbiol.* **1996**, *29*, 213–231. DOI:10.1016/0168-1605(95)00032-1
- A. Naila, S. Flint, G. Fletcher, P. Bremer, G. Meerdink, *J. Food Sci.* **2010**, *75*, 139–150. DOI:10.1111/j.1750-3841.2010.01774.x
- C. I. G. Tuberoso, F. Congiu, G. Serreli, S. Mameli, *Food Chem.* **2015**, *175*, 29–35. DOI:10.1016/j.foodchem.2014.11.120
- H. K. Mayer, G. Fiechter, E. Fischer, *J. Chromatogr. A* **2010**, *1217*, 3251–3257. DOI:10.1016/j.chroma.2009.09.027
- F. Gosetti, E. Mazzucco, M. C. Gennaro, E. Marengo, *Anal. Bioanal. Chem.* **2013**, *405*, 907–916. DOI:10.1007/s00216-012-6269-z
- G. Li, L. Dong, A. Wang, W. Wang, N. Hu, J. You, *LWT Food Sci. Technol.* **2014**, *55*, 355–361.
- J. Pradenas, O. Galarce-Bustos, K. Henríquez-Aedo, R. Mundaya-Urbe, M. Aranda, *Food Control* **2016**, *70*, 138–144. DOI:10.1016/j.foodcont.2016.05.043
- S. Lee, M. Yoo, D. Shin, *LWT-Food Sci. Technol.* **2015**, *62*, 350–356.
- R. Preti, M. L. Antonelli, R. Bernacchia, G. Vinci, *Food Chem.* **2015**, *187*, 555–562. DOI:10.1016/j.foodchem.2015.04.075
- R. Preti, R. Bernacchia, G. Vinci, *Eur. Food Res. Technol.* **2016**, *242*, 2031–2039. DOI:10.1007/s00217-016-2701-5
- A. A. Tameem, B. Saad, A. Makahleh, A. Salhin, M. I. Saleh, *Talanta* **2010**, *82*, 1385–1391. DOI:10.1016/j.talanta.2010.07.004
- O. Ozdestan, A. Uren, *Talanta* **2009**, *78*, 1321–1326. DOI:10.1016/j.talanta.2009.02.001
- S. Jia, Y. Ryu, S. W. Kwon, J. Lee, *J. Chromatogr. A* **2013**, *1282*, 1–10. DOI:10.1016/j.chroma.2013.01.041
- S. Tahmouzi, R. Khaksar, M. Ghasemlou, *Food Chem.* **2011**, *126*, 756–761. DOI:10.1016/j.foodchem.2010.11.060
- A. M. Piasta, A. Jastrzębska, M. P. Krzemiński, T. M. Muzioł, E. Szły, *Anal. Chim. Acta* **2014**, *834*, 58–66. DOI:10.1016/j.aca.2014.05.028
- J. L. Ordóñez, R.M. Callejón, A.M. Troncoso, M.C. García-Parrilla, J. *Food Compos. Anal.* **2017**, *63*, 139–147. DOI:10.1016/j.jfca.2017.07.042
- A. Jain, M. Gupta, K. K. Verma, *J. Chromatogr. A* **2015**, *1422*, 60–72. DOI:10.1016/j.chroma.2015.10.036
- G. Garai, M. T. Dueñas, A. Irastorza, P. J. Martín-Álvarez, M. V. Moreno-Arribas, *J. Food Protect.* **2006**, *69*, 3006–3012. DOI:10.4315/0362-028X-69.12.3006
- L. Romero, S. Keunchkarian, M. Reta, *Anal. Chim. Acta* **2006**, *565*, 136–144. DOI:10.1016/j.aca.2006.02.054
- A. Onal, S. E. K. Tekkeli, C. Onal, *Food Chem.* **2013**, *138*, 509–515. DOI:10.1016/j.foodchem.2012.10.056
- C. Almeida, J. O. Fernandes, S. C. Cunha, *Food Control* **2012**, *25*, 380–388. DOI:10.1016/j.foodcont.2011.10.052
- S. Riebroy, S. Benjakul, W. Visessanguan, K. Kijrongrojana, M. Tanaka, *Food Chem.* **2004**, *88*, 527–535. DOI:10.1016/j.foodchem.2004.01.067
- R. E. Anlı, N. Vural, S. Yılmaz, Y. H. Vural, *J. Food Compos. Anal.* **2004**, *17*, 53–62. DOI:10.1016/S0889-1575(03)00104-2
- O. Busto, M. Miracle, J. Guasch, F. Borrull, *J. Chromatogr. A* **1997**, *757*, 311–318. DOI:10.1016/S0021-9673(96)00693-0
- A. Marcobal, M. C. Polo, P. J. Martín-Alvarez, M. V. Moreno-Arribas, *Food Res. Int.* **2005**, *38*, 387–394. DOI:10.1016/j.foodres.2004.10.008
- E. J. Papavergou, *Procedia Food Sci.* **2011**, *1*, 1126–1131. DOI:10.1016/j.profoo.2011.09.168
- V. Simat, P. Dalgaard, *LWT Food Sci. Technol.* **2011**, *44*, 399–406.
- M. C. Vidal-Carou, F. Lahoz-Portoles, S. Bover-Cid, A. Marine-Font, *J. Chromatogr. A* **2003**, *998*, 235–241. DOI:10.1016/S0021-9673(03)00610-1

33. S. Casal, M. B. P. P. Oliveira, M. A. Ferreira, *J. Liq. Chromatogr. Relat. Technol.* **2002**, 25, 2535–2549.
DOI:10.1081/JLC-120014273
34. K. Henriquez-Aedo, K. M. Vega, S. Prieto-Rodriguez, M. Aranda, *Food Chem. Toxicol.* **2012**, 50, 2742–2750.
DOI:10.1016/j.fct.2012.05.034
35. J. Hernandez-Borges, G. D'orazio, Z. Aturki, S. Fanali, *J. Chromatogr. A* **2007**, 1147, 192–199.
DOI:10.1016/j.chroma.2007.02.072
36. Z. Loukou, A. Zotou, *J. Chromatogr. A* **2003**, 996, 103–113.
DOI:10.1016/S0021-9673(03)00558-2
37. R. Romero, M. Sanchez-Vinas, D. Gazquez, M. G. Bagur, *J. Agric. Food Chem.* **2002**, 50, 4713–4717.
DOI:10.1021/jf025514r
38. Y. Nishikawa, *J. Chromatogr. A* **1987**, 392, 349–353.
DOI:10.1016/S0021-9673(01)94278-5
39. A. Asan, I. Isildak, *Microchim. Acta* **1999**, 132, 13–16.
DOI:10.1007/s006040050036
40. F. Kvasnicka, M. Voldrich, *J. Chromatogr. A* **2006**, 1103, 145–149. DOI:10.1016/j.chroma.2005.11.005
41. S. R. Tambe, R. H. Shinde, L. R. Gupta, V. Pareek, S. B. Bhalerao, *J. Liq. Chromatogr. Relat. Technol.* **2010**, 33, 423–430.
DOI:10.1080/10826070903571358
42. P. Hernández-Orte, A. Peña-Gallego, M. J. Ibarz, J. Cacho, V. Ferreira, *J. Chromatogr. A* **2006**, 1129, 160–164.
DOI:10.1016/j.chroma.2006.06.111

Povzetek

Opisujemo točno in občutljivo metodo za kvantifikacijo sledov treh biogenih aminov v vzorcih jabolčnega soka s pretečenim rokom, ki je osnovana na reverznofazni tekočinski kromatografiji (RP-HPLC) z UV-vidno detekcijo. Biogene amine: kadaverin, histamin in tiramin smo pretvorili v njihove acetilacetonske derivate v vodno-metanolnem mediju. V predlagani metodi predkolonski derivatizaciji zvrsti sledi RP-HPLC separacija na Thermo Hypersil Gold reverznofazni koloni in UV detekcija pri 315 nm. V predlagani metodi smo uporabili pretok 0,9 mL min⁻¹. Učinkovito ločbo biogenih aminov smo z uporabo 35:65% (v/v) mešanice acetonitril-voda kot mobilne faze izvedli v 11 min z dobro ločljivostjo. Meje zaznave so bile 0,03 µg L⁻¹ za kadaverin, 0,23 µg L⁻¹ za histamin in 0,08 µg L⁻¹ za tiramin. Predlagano metodo smo uspešno uporabili za analizo dveh komercialno dosegljivih vzorcev jabolčnega soka s pretečenim rokom. Za analizo 20 mL vzorca smo dobili izkoristke med 98,78 in 102,12% z RSD 0,16–1,65%, kar kaže, da so bili izkoristki za biogene amine zelo zadovoljivi.

Scientific paper

Synthesis, Characterization and Cytotoxicity Evaluation of New Biimidazole Palladium(II) Complexes with Thioureas

Silmar José Spinardi Franchi,^{1,*} Rodrigo Alves de Souza,²
Antonio Eduardo Mauro,² Iracilda Zeppone Carlos,³ Livia Carolina
de Abreu Ribeiro,³ Fillipe Vieira Rocha⁴ and Adelino Viera de Godoy-Netto²

¹ UFSC – Universidade Federal de Santa Catarina, Departamento de Ciências Exatas e Educação, 89036-256, Blumenau, SC, Brazil.

² UNESP – Sao Paulo State Univ, Instituto de Química de Araraquara, C.P. 355, 14800-900, Araraquara, SP, Brazil.

³ UNESP – Sao Paulo State Univ, Faculdade de Ciências Farmacêuticas, 14801-902, Araraquara, SP, Brazil.

⁴ UFSCar – Universidade Federal de São Carlos, Departamento de Química, 13565-905, São Carlos, SP, Brazil.

* Corresponding author: E-mail: silmar.franchi@ufsc.br
Tel: + 55 48 37213339

Received: 19-12-2017

Abstract

The reactions between $[\text{PdCl}_2(\text{tmbiimH}_2)] \cdot \text{H}_2\text{O}$ (**1**) {tmbiimH₂ = 2,2'-bis(4,5-dimethylimidazole)} and thiourea (tu), N-methylthiourea (mtu), N-phenylthiourea (ptu), N,N'-dimethylthiourea (dmtu) or N,N'-diphenylthiourea (dptu) in the 1:2 molar ratio resulted in the compounds $[\text{PdL}_2(\text{tmbiimH}_2)]\text{Cl}_2 \cdot n\text{H}_2\text{O}$ {L = tu (**2**), mtu (**3**), ptu (**4**), dmtu (**5**) and dptu (**6**)}, which were characterized by elemental analyses, infrared (IR), and ¹H NMR spectroscopies and conductivity measurements. The IR spectra of **1–6** were consistent with the presence of chelating tmbimH₂ ligand. All compounds and cisplatin were tested *in vitro* by MTT assay for their cytotoxicity against three murine cancer cell lines: mammary adenocarcinoma (LM3), lung adenocarcinoma (LP07) and mouse fibroblast (L929) cells. Relating the series of compounds to their biological activities we found compound **6** as the most promising of them.

Keyword: Palladium(II); 2,2'-bis(4,5-dimethylimidazole); Thioureas; Cytotoxicity; Cancer

1. Introduction

Cisplatin is one of the most widely used and most effective chemotherapeutic agent for treatment of patients with epithelial malignancies such as lung, head, neck, ovarian, bladder and testicular cancer.¹ Despite its re-sounding success, cisplatin suffers from two major drawbacks which are severe side effects and intrinsic and acquired drug resistance.² Much current research work is aimed at the discovery of new complexes bearing platinum or other metals which may display a wide spectrum of activity and reduced toxicities, thus leading to improvements in the effectiveness of cancer chemotherapy regimens.^{3–4} In this context, numerous cisplatin analogues have been synthesized by modifying the nature of the leaving groups

and the carrier ligands.⁵ Nevertheless, such derivatives generally have shown similar DNA-binding modes which often result in a similar spectrum of activity. Therefore, one conceivable strategy to achieve a spectrum of activity distinct to that of cisplatin involves the development of agents capable of producing cytotoxicity through new types of DNA interaction.⁶

It is well-established that metal-based molecules are able to interact non-covalently with DNA by means of a non-specific (mainly electrostatic) binding along the DNA exterior, a specific groove binding and intercalation.⁷ Particularly, much effort has been directed towards the design of square-planar complexes of the type $[\text{M}(\text{N}-\text{N})\text{L}_2]^{2+}$ (M = Pd, Pt) incorporating chelating planar aromatic heterocycles with extended π -systems (N–N) such as 2,2'-bipyri-

dine, 1,10-phenanthroline, and kinetically less labile ligands (L), e.g. thiourea ligands.^{8–10} These compounds are relatively inert toward possible competitive covalent interactions and display the suitable shape for DNA intercalation.

Specifically, 2,2'-biimidazoles are *N,N*-donor ligands which can be used to obtain new metal complexes able to interact non-covalently to DNA as they can act as neutral bidentate ligands depending upon its protonation state.¹¹ Metal-based complexes containing neutral chelating 2,2'-biimidazole-type ligands have attracted considerable interest due to their externally-directed pair of N–H groups which are frequently involved in hydrogen bonding with solvent molecules and counterions¹². Indumathy and co-workers¹³ reported that the complexes [Co(N–N)₂(H₂biim)]³⁺ (N–N = 2,2'-bipyridine, 1,10-phenanthroline) interact with DNA through the groove *via* hydrogen bonding due to presence of –NH in the ancillary ligand 2,2'-biimidazole.

Inspired by the ability of 4,5-dialkylimidazoles in extracting metal complexes into hydrophobic or hydrophilic solvents,¹⁴ Stringfield and co-workers¹⁵ have employed 2,2'-bis(4,5-dimethylimidazole), tmbiimH₂, as a carrier ligand in order to facilitate transport of metal complexes across cell membranes. We assumed that the introduction of 2,2'-bis(4,5-dimethylimidazole) in the structure of Pd(II) complexes may improve the membrane penetration by increasing their lipid solubility and, consequently, resulting in an enhancement of the cytotoxicity.

Motivated by the aforementioned findings, and as a part of our continuing research program in the field of coordination and biological chemistry of Pd(II) complexes,^{16–21} we present herein the synthesis, characterization and cytotoxic evaluation of the compounds [PdL₂(tmbiimH₂)]Cl₂·nH₂O, where L is thiourea (**2**), *N*-methylthiourea (**3**), *N*-phenylthiourea (**4**), *N,N'*-dimethylthiourea (**5**), *N,N'*-diphenylthiourea (**6**); n = 3–5; tmbiimH₂ is 2,2'-bis(4,5-dimethylimidazole).

2. Experimental

2.1. Materials and Measurements

The syntheses were performed at room temperature. Commercial reagents and solvents were employed without further purification. The starting material Na₂[PdCl₄] was prepared as previously described.²²

Elemental analyses (C, N and H) were performed on an EA1110–CHNS–O microanalyzer from CE-Instruments. Infrared spectra were recorded on a Nicolet Impact 400 spectrophotometer in the spectral range 4000–400 cm⁻¹ (KBr pellets). Conductivities were measured with a Digimed-DM-31 conductimeter using 1 × 10⁻³ mol L⁻¹ solutions in methanol. ¹H NMR spectra were obtained as DMSO-*d*₆ solutions, on a Varian INOVA 500 spectrometer.

2.2. Preparation of the Coordination Compounds

Synthesis of [PdCl₂(tmbiimH₂)]·H₂O (**1**)

Briefly, the compound **1** was prepared similarly as described for [PdCl₂(biimH₂)] (Casas *et al.*, 2003).²³ To 20.0 mL of a deep orange solution of Na₂[PdCl₄] (200.0 mg, 0.68 mmol) was added a suspension of tmbiimH₂ (133.0 mg, 0.70 mmol) in methanol (20.0 mL), followed by the addition of 1.0 mL 37 % HCl solution. The reaction mixture was stirred for 2 h. The resulting red-brownish solution was concentrated and the obtained microcrystalline yellow solid was isolated and washed with cold water and ethanol, and dried under vacuum. The yield was 79%. Anal. Calc. for C₁₀N₄H₁₆Cl₂OPd (**1** · H₂O): C, 31.21; H, 4.11; N, 14.49. Found: C, 31.00; H, 4.47; N, 14.32. IR (KBr, cm⁻¹): 3488, 3230, 2926, 1650, 1594, 1379, 781.

Synthesis of [Pd(tu)₂(tmbiimH₂)]Cl₂ · 3H₂O (**2**)

To a yellow suspension of **1** (60.0 mg, 0.163 mmol) in 20.0 mL of MeOH, thiourea (24.8 mg, 0.33 mmol) in 10.0 mL of methanol was added slowly, affording a red brownish solution. The resulting solution was stirred for 2 h and then filtered to eliminate some impurities. The solution was evaporated to dryness and cooled diethyl ether (10.0 mL) added to the residue. The red brownish solid was filtered, washed with diethyl ether (5.0 mL) and dried under vacuum. The yield was 80%. Anal. Calc. for C₁₂N₈H₂₈Cl₂O₃S₂Pd (**2** · 2H₂O): C, 25.11; H, 4.87; N, 19.51. Found: C, 24.84; H, 4.43; N, 19.68. Λ_M : 205 Ω⁻¹ cm⁻² mol⁻¹. IR (KBr, cm⁻¹): 3379–2420, 1660, 1629, 1504, 709.

Synthesis of [Pd(mtu)₂(tmbiimH₂)]Cl₂ · 4H₂O (**3**)

Prepared similarly to **2** from the reaction between compound **1** (60.0 mg, 0.163 mmol) and *N*-methylthiourea (29.4 mg, 0.33 mmol). The yield was 80%. Anal. Calc. for C₁₄N₈H₃₄Cl₂O₄S₂Pd (**3** · 4H₂O): C, 27.11; H, 5.46; N, 18.13. Found: C, 26.72; H, 5.32; N, 17.84. Λ_M : 201 Ω⁻¹ cm⁻² mol⁻¹. IR (KBr, cm⁻¹): 3354, 2490, 1650, 1631, 1576, 1489, 767.

Synthesis of [Pd(ptu)₂(tmbiimH₂)]Cl₂ · 5H₂O (**4**)

Prepared similarly to **2** from the reaction between compound **1** (60.0 mg, 0.163 mmol) and *N*-phenylthiourea (49.6 mg, 0.33 mmol). The yield was 75%. Anal. Calc. for C₂₄N₈H₄₀Cl₂O₅S₂Pd (**4** · 5H₂O): C, 37.80; H, 5.33; N, 14.71. Found: C, 37.62; H, 5.51; N, 14.43. Λ_M : 194 Ω⁻¹ cm⁻² mol⁻¹. IR (KBr, cm⁻¹): 3499, 2487, 1648, 1620, 1463, 1402, 751.

Synthesis of [Pd(dmtu)₂(tmbiimH₂)]Cl₂ · 5H₂O (**5**)

Prepared similarly to **2** from the reaction between compound **1** (60.0 mg, 0.163 mmol) and *N,N'*-methylthiourea (34.0 mg, 0.33 mmol). The yield was 69%. Anal. Calc. for C₁₆N₈H₄₂Cl₂O₅S₂Pd (**5** · 5H₂O): C, 28.91; H, 6.08; N, 16.78. Found: C, 28.64; H, 5.79; N, 17.01. Λ_M : 199 Ω⁻¹ cm⁻² mol⁻¹. IR (KBr, cm⁻¹): 3471, 2600, 1620, 1593, 1517, 1377, 718.

Synthesis of $[\text{Pd}(\text{dptu})_2(\text{tmbiimH}_2)]\text{Cl}_2 \cdot 3\text{H}_2\text{O}$ (6)

Prepared similarly to **2** from the reaction between compound **1** (60.0 mg, 0.163 mmol) and *N,N'*-diphenylthiourea (74.4 mg, 0.33 mmol). The yield was 65%. Anal. Calc. for $\text{C}_{36}\text{N}_8\text{H}_{44}\text{Cl}_2\text{O}_3\text{S}_2\text{Pd}$ ($6 \cdot 3\text{H}_2\text{O}$): C, 53.44; H, 5.92; N, 10.11. Found: C, 53.10; H, 5.74; N, 9.78. ΔM : $192 \text{ } \Omega^{-1} \text{ cm}^{-2} \text{ mol}^{-1}$. IR (KBr, cm^{-1}): 3407, 2500, 1595, 1510, 1267, 1195, 729, 510.

2. 3 Cytotoxicity Activity

2. 3. 1. Cells

Mouse fibroblast cells (L929) were propagated in Eagle's Minimum Essential Medium, MEM, from Institute Adolfo Lutz, Sao Paulo, Brazil, supplemented with $80 \mu\text{g mL}^{-1}$ of gentamicin and 7.5% v/v fetal bovine serum (FBS). Murine mammary adenocarcinoma (LM3) and lung adenocarcinoma (LP07) cells were maintained in MEM, supplemented with 10% heat-inactivated FBS, 2 mmol L^{-1} of *L*-glutamine, and $80 \mu\text{g mL}^{-1}$ of gentamicin, defined as complete medium, in plastic flasks (Corning) at $37 \text{ }^\circ\text{C}$ in a humidified 5% CO_2 atmosphere. Passages were made by trypsinization of confluent monolayers (0.25% trypsin and 0.02% EDTA in Ca^{2+} - Mg^{2+} free phosphate-buffered saline). The cells number was counted by the Trypan blue dye exclusion method.

2. 3. 2. Compounds

Test solutions of the compounds ($1000 \mu\text{mol L}^{-1}$) were freshly prepared by dissolving the substances in $50 \mu\text{L}$ of DMSO and completing with $4950 \mu\text{L}$ of the culture medium. Afterwards, the tested compounds were diluted in a culture medium to reach the desired concentrations ranging from 10 to $300 \mu\text{mol L}^{-1}$. The DMSO solvent did not reveal any cytotoxic activity in the tested concentrations. Cisplatin (commercial compound from Sigma) was employed as the standard antitumor drug.

2. 3. 3. MTT Assay

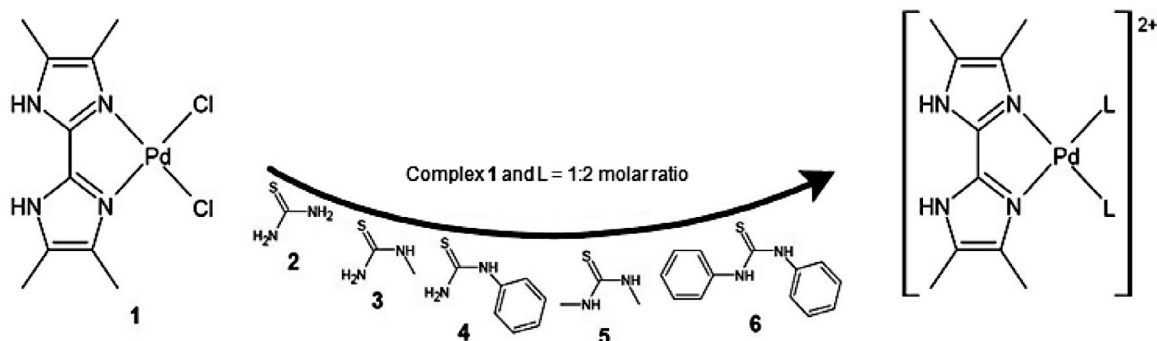
For the cytotoxicity evaluation, 200.0 ML samples of L929, LM3 and LP07 cells ($5 \times 10^4 \text{ cell mL}^{-1}$, adjusted in

MEM) were added to each well of a 96-well tissue culture plate and then preincubated in the absence of the compounds for 24 h to allow adaptation of the cells prior to the addition of the test agents. Afterwards, the supernatants were removed and 200.0 ML solutions of the compounds in concentrations ranging from 10 to $300 \mu\text{mol L}^{-1}$ or 200.0 ML of MEM-Complete as cell control of viability was added to each well. The effects of the compounds towards the cells were determined 24 h after the culture incubation. After that, the supernatants were removed and $100.0 \mu\text{L}$ solutions of [3-(4,5-dimethylthiazol-2-yl)-2,5-diphenyltetrazolium bromide], MTT, were added in each well containing the samples.²⁴ The MTT assay was performed and the plates were incubated for 3 h. Then, the absorbances were measured and the cytotoxic midpoint value, i.e. the concentration of the chemical agent needed to reduce the spectrophotometric absorbance to 50%, was determined by linear regression analysis with 95% of confidence limits. The IC_{50} was defined as the medium of three independent experiments through the equation of graphic line obtained (Microcal Origin 8.0TM). Triplicates tests were performed for each concentration of each compound.

3. Results and Discussion

The precursor $\text{Na}_2[\text{PdCl}_4]$ reacts with 2,2'-bis(4,5-dimethylimidazole) in acidified methanol, to afford $[\text{PdCl}_2(\text{tmbiimH}_2)] \cdot \text{H}_2\text{O}$ (**1**). Compounds $[\text{Pd}(\text{tu})_2(\text{tmbiimH}_2)]\text{Cl}_2 \cdot 3\text{H}_2\text{O}$ (**2**), $[\text{Pd}(\text{mtu})_2(\text{tmbiimH}_2)]\text{Cl}_2 \cdot 4\text{H}_2\text{O}$ (**3**), $[\text{Pd}(\text{ptu})_2(\text{tmbiimH}_2)]\text{Cl}_2 \cdot 5\text{H}_2\text{O}$ (**4**), $[\text{Pd}(\text{dmtu})_2(\text{tmbiimH}_2)]\text{Cl}_2 \cdot 5\text{H}_2\text{O}$ (**5**), and $[\text{Pd}(\text{dptu})_2(\text{tmbiimH}_2)]\text{Cl}_2 \cdot 3\text{H}_2\text{O}$ (**6**) are readily obtained by reacting **1** with thiourea, and *N*-methylthiourea, *N*-phenylthiourea, *N,N*-dimethylthiourea and *N,N'*-diphenylthiourea, respectively. The six compounds presented here are in square planar molecular geometry surrounding of Pd(II) center, according to spectroscopic results and in analogy with literature.^{8,10} A representation of the strategy employed for to obtain the complexes is pointed in Scheme 1.

The syntheses were carried out at room temperature under constant magnetic stirring. The complexes are



Scheme 1: General representation for the synthesis of the complexes (water of hydration is omitted).

Table 1. Analytical and physicochemical data for the compounds 1–6.

Complex	Λ_M ($\Omega^{-1} \text{ cm}^{-2} \text{ mol}^{-1}$)	M. p. ($^{\circ}\text{C}$)	Carbon (%)		Nitrogen (%)		Hydrogen (%)	
			Found	Calc.	Found	Calc.	Found	Calc.
$\text{C}_{10}\text{N}_4\text{H}_{16}\text{Cl}_2\text{OPd}$ (1 · H_2O)	–	178	31.00	31.21	14.32	14.49	4.47	4.11
$\text{C}_{12}\text{N}_8\text{H}_{28}\text{Cl}_2\text{O}_3\text{S}_2\text{Pd}$ (2 · $3\text{H}_2\text{O}$)	205	155	24.84	25.11	19.68	19.51	4.43	4.87
$\text{C}_{14}\text{N}_8\text{H}_{34}\text{Cl}_2\text{O}_4\text{S}_2\text{Pd}$ (3 · $4\text{H}_2\text{O}$)	201	143	26.72	27.11	17.84	18.13	5.32	5.46
$\text{C}_{24}\text{N}_8\text{H}_{40}\text{Cl}_2\text{O}_5\text{S}_2\text{Pd}$ (4 · $5\text{H}_2\text{O}$)	194	146	37.62	37.80	14.43	14.71	5.51	5.33
$\text{C}_{16}\text{N}_8\text{H}_{42}\text{Cl}_2\text{O}_5\text{S}_2\text{Pd}$ (5 · $5\text{H}_2\text{O}$)	199	138	28.64	28.91	17.01	16.78	5.79	6.08
$\text{C}_{36}\text{N}_8\text{H}_{44}\text{Cl}_2\text{O}_3\text{S}_2\text{Pd}$ (6 · $3\text{H}_2\text{O}$)	192	117	53.10	53.44	9.78	10.11	5.74	5.92

air-stable powders and exhibit a red brownish color. The molar conductivities of complexes **2–6** in methanol are between 185–214 $\Omega^{-1} \text{ cm}^2 \text{ mol}^{-1}$ and is in agreement with their 1:2 electrolytic character.²⁵ The low solubility of **1** in methanol (and other non-coordinating solvents) has precluded measurements of its molar conductivity. Analytical results are in agreement with their proposed formulae (Table 1).

3. 1. IR and NMR Studies

The neutral bidentate chelating coordination mode of tmbiimH_2 was clearly evidenced in the IR spectrum of **1**. Firstly, the presence of an intense $\nu\text{N–H}$ absorption at 3227 cm^{-1} is indicative of the neutral character of the imidazolyl ligand. According to the literature, the shift of $\nu\text{N–H}$ absorption to higher energies in the IR spectrum of **1** compared to the position found in that of the free tmbimH_2 ($\sim 3000 \text{ cm}^{-1}$) is typical of neutral bidentate chelating coordination mode.²⁶ Second, the decrease in intensity and shift to lower frequency of the band attributed to the $\nu\text{C=N}$ and in-plane N–H bending mode ($\delta\text{N–H}$) in **1** (1594 cm^{-1}), compared with that of the ligand (1604 cm^{-1}), is also an evidence of the chelating coordination mode of tmbiimH_2 . The presence of water of hydration was detected by the appearance of its characteristic absorptions at 3485 cm^{-1} ($\nu\text{O–H}$) and 1660 cm^{-1} (δHOH).

IR spectra of compounds **2–6** exhibited a very broad continuum band over the spectral range of 3560–2500 cm^{-1} assigned to the vibrations of water molecules, counterions and coordinated ligands involved in hydrogen bonding interactions. It is important to point out that the expected $\nu\text{C=N}$ band of the neutral bidentate chelating tmbiimH_2 ligand was observed in IR spectra of compounds **2** to **6**.

Among the physical techniques employed to evidence the coordination mode of thiourea-type ligands, IR spectroscopy is one of the most widely used method.^{27–30} The shift of νCN and νCS absorptions is frequently used as diagnosis for *S*-coordination. Firstly, the intense νCN absorption at 1475 cm^{-1} (*tu*), 1556 cm^{-1} (*mtu*), 1463 cm^{-1} (*ptu*), 1560 cm^{-1} (*dmtu*) and 1326 cm^{-1} (*dptu*) observable in the IR spectra of the ligands,^{30–35} decreased in intensity and shifted to 1504 cm^{-1} (**2**), 1576 cm^{-1} (**3**), 1448 cm^{-1} (**4**),

1593 cm^{-1} (**5**) after coordination. In **6**, the νCN shift has small displacement. Secondly, it was noticed a shift of the νCS band to lower frequency [**2** (709 cm^{-1}), **3** (767 cm^{-1}), **4** (751 cm^{-1}), **5** (718 cm^{-1}) and **6** (906 cm^{-1})] when compared with that of the free ligands [*tu* (730 cm^{-1}), *mtu* (776 cm^{-1}), *ptu* (811 cm^{-1}), *dmtu* (725 cm^{-1}) and *dptu* (933 cm^{-1})].^{30–35} These spectroscopic modifications clearly indicated an increase of the double bond character of the CN bond and a weakening of the C=S bond, being consistent with *S*-bonding of thiourea-type ligands in **2–6**.³⁶

According to the literature,¹⁵ one singlet at 2.19 ppm is observed in the ^1H NMR spectrum of the free tmbiimH_2 . The appearance of this single signal indicates that $\text{Me}^{4,4'}$ and $\text{Me}^{5,5'}$ must be magnetically equivalent, possibly due to the rapid migration of the nitrogen atom's protons.³⁷ ^1H NMR spectra of freshly prepared samples of **1**, **2** and **3** showed the presence of one single peak at *ca.* 2.20 ppm (Table 2), which may indicate that the tmbiimH_2 is totally dissociated in $\text{DMSO-}d_6$. This behavior has also been observed in other 2,2'-bisimidazolyl-based metal complexes in DMSO solutions.³⁷

On the other hand, in the ^1H NMR spectrum of **4**, two singlet resonances of equal integrated area were observed at 2.23 and 1.19 ppm and assigned to chemically inequivalent tmbiimH_2 ring methyl groups ($\text{Me}^{4,4'}$, $\text{Me}^{5,5'}$), in agreement with the bidentate chelating coordination mode of tmbiimH_2 ligand. Over a period of time, these signals attributed to the mononuclear compound in solution decrease in intensity with the appearance and increase in intensity of one single peak at 2.19 ppm, suggesting that the dissociation rate of the tmbiimH_2 ligand in **4**, in $\text{DMSO-}d_6$, is relatively slower than observed for **1–3**. This finding could be probably related to the expected decrease of the rate of substitution reactions in square planar complexes due to the presence of more sterically demanding *N*-phenylthiourea ligands, increasing the difficulty encountered by the entering ligand in binding to the metal center during an associative substitution process.³⁸

In **5**, two signals groups were observed. The first group show one signal in 2.23 ppm, assigned to chemically equivalent tmbiimH_2 ring methyl groups ($\text{Me}^{4,4'}$, $\text{Me}^{5,5'}$) for free ligand in solution and two singlet resonances of equal integrated area in 2.11 and 1.20 ppm, assigned to chemically inequivalent tmbiimH_2 ring methyl groups

(Me^{4,4'}, Me^{5,5'}) for coordinated ligand. The same manner as **4**, over a period of time, the signals attributed to the mononuclear compound in solution (2.11 and 1.20 ppm) decrease in intensity with the appearance and increase in intensity of one single peak at 2.23 ppm. The second group shows one signal in 3.43 ppm and two signals in 3.67 and 3.65 ppm, assigned for methyl groups for coordinated *N,N'*-dimethylthiourea ligand.³⁹

The ¹H NMR spectrum of **6** were obtained in DMSO-*d*₆ solution and only one signal in 2.20 ppm assigned to chemically equivalent tmbiimH₂ ring methyl groups (Me^{4,4'}, Me^{5,5'}) for free ligand in solution.

In short, when solubilized, all compounds showed a possible dynamic equilibrium between the partial exit of the coordinated ligands and the coordination of solvent molecules (such as H₂O, present in the composition of the compounds themselves, or the deuterated solvent itself). Even when spectra were obtained immediately after solubilization and with times oscillating between 1 h and 48 h, these same behaviors were noticed, even when other deuterated solvents were used. However, due to the low resolution of the spectra obtained in other solvents, we chose to maintain the data presented in DMSO-*d*₆, since the compounds were appreciably more soluble in this solvent, compared to the other deuterated solvents used.

Electronic delocalisation in a copper-(1-phenylthiourea) complex,⁴⁰ which has a thiourea-derived ligand,

as well as our compounds, also seems to corroborate us for a dynamics of exchange processes.

3. 2. Cytotoxic Activities Against Murine Tumor Cell Lines

The cytotoxic activities of the palladium(II) complexes **1–6** were tested against murine mammary adenocarcinoma (LM3), lung adenocarcinoma (LP07) and mouse fibrosarcoma (L929) cell lines. Cells were exposed to a range of drug concentrations (300–10 μmol L⁻¹) for 24 h and cell viability was analyzed by MTT assay. IC₅₀ values (the concentration that inhibited in 50% the cellular proliferation) are presented in Table 3. The cytotoxicity data of cisplatin against the selected tumor cell lines were used for comparison purposes.^{16,41}

Compounds **1–6** showed no drug response at drug concentrations < 300 μmol L⁻¹ against LP07 cells, and thus they were considered inactive. After treatment of LM3 cells with compounds **1–6**, it was observed that the replacement of two chlorido by two thiourea (**1** → **2**), two *N*-methylthiourea ligands (**1** → **3**) or two *N,N'*-methylthiourea ligands (**1** → **5**) did not result in any increase in the cytotoxic activity towards LM3 cell line. On the other hand, **4**, containing the sterically demanding *N*-phenylthiourea ligand, was *ca.* 2 fold more active than compounds **1–3** and **5**, and approximately 4 times less active than cis-

Table 2. ¹H-NMR chemical shift (ppm) for the compounds at 298 K.

Compound	Me ^{4,4'} / Me ^{5,5'}	¹ H NMR data		Numbering scheme
		<i>N</i> -derivative thiourea group (R)		
1	2.20 (<i>s</i> , 12H)	–		
2	2.23 (<i>s</i> , 12H)	–		
3	2.19 (<i>s</i> , 12H)	2.78 (<i>s</i> , 6H)		
4	2.23 (<i>s</i> , 6H) 1.19 (<i>s</i> , 6H)	7.80–7.20 (<i>br</i> , 10H)		
5	2.11 (<i>s</i> , 6H) 1.20 (<i>s</i> , 6H)	3.67 (<i>s</i> , 6H) 3.65 (<i>s</i> , 6H)		
6	2.20 (<i>s</i> , 12H)	7.60–6.90 (<i>br</i> , 20H)		

Abbreviations: *s* = singlet; *br* = broadened; R = H (**2**), Me (**3**), and Ph (**4**); R = R' = Me (**5**), and Ph (**6**). Deuterated solvent employed: DMSO-*d*₆ (for **1–6**). NH signals could not be observed.

Table 3. Cytotoxicity (IC₅₀) of the coordination compounds **1–6** and cisplatin against murine LM3, L929 and LP07 cell lines.

Compound	IC ₅₀ (μmol L ⁻¹)			Reference
	LM3	L929	LP07	
1	289.6 ± 1.9	Inactive	Inactive	This work
2	278.2 ± 1.3	241.9 ± 1.1	Inactive	This work
3	260.9 ± 1.1	88.1 ± 0.4	Inactive	This work
4	109.5 ± 0.9	30.7 ± 0.2	Inactive	This work
5	255.4 ± 1.7	40.9 ± 0.2	Inactive	This work
6	8.9 ± 0.3	7.3 ± 0.1	Inactive	This work
Cisplatin	30.6 ± 3.7	65.3 ± 1.9	4.34 ± 0.4	16,41

platin. The compound **6** showed drug response at drug concentrations $8.9 \mu\text{mol L}^{-1}$, approximately 3 times more active than cisplatin. In this case, the presence to more sterically ligand (*N,N'*-diphenylthiourea) increases cytotoxic activity against this cell line.

With respect to the cytotoxic effects on L929 cells, a progressive increase on the cytotoxic activity of Pd(II) complexes was noticed according to the ancillary ligand bulkiness of substituents on thiourea moiety, following the order $\text{tu} < \text{mtu} < \text{dmu} < \text{ptu} < \text{dptu}$. Probably, a lipophilic effect is prevalent for this series of compounds when H atoms are substituted by methyl and phenyl groups. Compound **6** not only showed the highest cytotoxic activity against L929 cell line (IC_{50} value of $7.3 \mu\text{mol L}^{-1}$) among all tested compounds, but also it was more active than cisplatin ($65.3 \mu\text{mol L}^{-1}$).⁴¹

Our findings agree well with those described by Marverti and co-workers,⁸ in which it was verified that the cytotoxicity of the metallointercalators $[\text{Pt}(\text{bpy})\text{L}_2]\text{Cl}_2$ ($\text{bpy} = 2,2'$ -bipyridine; $\text{L} =$ thioureas) was dependent on the structure of thiourea substituents.

4. Conclusions

The synthesis, structural and spectroscopic characterization, as well as the biological activity of palladium(II) compounds containing 2,2'-bis(4,5-dimethylimidazole) and thiourea-type ligands were described in this work. Conductivity data in methanol were in agreement with a 1:2 electrolyte nature for compounds **2–6**. The IR data of **1–6** were consistent with the presence of chelating tmbiimH_2 ligand and S-coordination of thioureas. NMR studies on compounds **1–3** and **6** in $\text{DMSO}-d_6$ indicated that tmbiimH_2 ligand is completely dissociated. On contrary, the dissociation rate of the tmbiimH_2 in **4** and **5** is slower than that observed for **1–3**. The distinct behavior of **4** in solution may be responsible for the maintenance of its structural integrity long enough to reach the pharmacological targets as well as for its highest cytotoxicity against LM3 and L929 cell lines, when compared to compounds **1–3**. The substituent groups in thiourea-type ligands are directly related to the increase in cytotoxicity.

The good cytotoxicity presented by compound **6** deserves considerable attention, which presents us the challenge of finding better conditions of stability for it in solution, either by drug delivery systems or structural modifications to fulfill with greater success its action in the pharmacological targets.

5. Acknowledgements

This research was supported by FAPESP, CNPq and Capes (Brazilian agencies of research).

6. References

- L. Kelland, *Nat. Rev. Cancer* **2007**, *7*, 573–584. DOI:10.1038/nrc2167
- D. Wang, S. J. Lippard, *Nat. Rev. Drug Discov.* **2005**, *4*, 307–320. <https://www.nature.com/articles/nrd1691>
- F. Arnesano, G. Natile, *Coord. Chem. Rev.* **2009**, *253*, 2070–2081. DOI:10.1016/j.ccr.2009.01.028
- S. H. van Rijt, P. J. Sadler, *Drug Discov. Today* **2009**, *14*, 1089–1097. DOI:10.1016/j.drudis.2009.09.003
- B. Lippert, *Coord. Chem. Rev.* **1999**, *182*, 263–295. DOI:10.1016/S0010-8545(98)00192-1
- G. Momekov, A. Bakalova, M. Karaivanova, *Curr. Med. Chem.* **2005**, *12*, 2177–2191. DOI:10.2174/0929867054864877
- M. J. Hannon, *Chem. Soc. Rev.* **2007**, *36*, 280–295. DOI:10.1039/b606046n
- A. Mushtaq, S. Ali, M. N. Tahir, H. Ismail, B. Mirza, M. Saadiq, M. A. Haleem, M. Iqbal, *Acta Chim. Slov.* **2017**, *64*, 397–408. DOI:10.17344/acsi.2017.3250
- S. Tsiliou, L.-A. Kefala, A. G. Hatzidimitriou, D. P. Kessissoglou, F. Perdih, A. N. Papadopoulos, I. Turel, G. Psomas, *J. Inorg. Chem.* **2016**, *160*, 125–139. DOI:10.1016/j.jinorgbio.2015.12.015
- E. P. Irgi, G. D. Geromichalos, S. Balala, J. Kljun, S. Kalogiannis, A. Papadopoulos, I. Turel, G. Psomas, *RSC Adv.* **2015**, *5*, 36353–36367. DOI:10.1039/C5RA05308K
- G. Marverti, M. Cusumano, A. Ligabue, M. L. Pietro, P. A. Vainiglia, A. Ferrari, M. Bergomi, M. S. Moruzzi, C. Frassinetti, *J. Inorg. Biochem.* **2008**, *102*, 699–712. DOI:10.1016/j.jinorgbio.2007.10.015
- M. Cusumano, M. L. Di Pietro, A. Giannetto, P. A. Vainiglia, *J. Inorg. Biochem.* **2005**, *99*, 560–565. DOI:10.1016/j.jinorgbio.2004.11.002
- A. Rotondo, S. Barresi, M. Cusumano, E. Rotondo, *Polyhedron* **2012**, *45*, 23–29. DOI:10.1016/j.poly.2012.07.064
- M. A. M. Lorente, F. Dahan, Y. Sanakis, V. Petrouleas, A. Bousseksou, J. P. Tuchagues, *Inorg. Chem.* **1995**, *34*, 5346–5357. DOI:10.1021/ic00125a039
- I. G. Dance, A. S. Abushamleh, H. A. Goodwin, *Inorg. Chim. Acta* **1980**, *43*, 217–221. DOI:10.1016/S0020-1693(00)90532-2
- R. Indumathy, T. Weyhermuller, B. U. Nair, *Dalton Trans.* **2010**, *39*, 2087–2097. DOI:10.1039/b913464f
- K. Kurdzeil, *Solvent Extr. Ion Exc.* **1994**, *12*, 687–699. DOI:10.1080/07366299408918232
- T. W. Stringfield, K. V. Somayajula, D. C. Muddiman, J. W. Flora, R. E. Shepherd, *Inorg. Chim. Acta* **2003**, *343*, 317–328. DOI:10.1016/S0020-1693(02)01243-4
- R. A. de Souza, A. Stevanato, O. Treu-Filho, A. V. G. Netto, A. E. Mauro, E. E. Castellano, I. Z. Carlos, F. R. Pavan, C. Q. F. Leite, *Eur. J. Med. Chem.* **2010**, *45*, 4863–4868. DOI:10.1016/j.ejmech.2010.07.057
- F. V. Rocha, C. V. Barra, A. V. G. Netto, A. E. Mauro, I. Z. Carlos, R. C. G. Frem, S. R. Ananias, M. B. Quilles, A. Stevanato, M. C. da Rocha, *Eur. J. Med. Chem.* **2011**, *45*, 1698–1702. DOI:10.1016/j.ejmech.2009.12.073

18. R. A. de Souza, A. E. Mauro, A. V. G. Netto, G. A. Cunha, E. T. de Almeida, *J. Therm. Anal. Calorim.* **2011**, *106*, 375–378. DOI:10.1007/s10973-010-1216-8
19. A. C. Moro, G. A. da Silva, R. F. F. de Souza, A. E. Mauro, A. V. G. Netto, I. Z. Carlos, F. A. Resende, E. A. Varanda, F. R. Pavan, C. Q. F. Leite, *Med. Chem. Res.* **2015**, *24*, 2879–2888. DOI:10.1007/s00044-015-1339-3
20. A. M. A. Velásquez, R. A. de Souza, T. G. Passalacqua, A. R. Ribeiro, M. Scontri, C. M. Chin, L. Almeida, M. L. Del Cistia, J. A. da Rosa, A. E. Mauro, M. A. S. Graminha, *J. Braz. Chem. Soc.* **2016**, *27*, 1032–1039. DOI:10.5935/0103-5053.20150360
21. A. M. A. Velásquez, W. C. Ribeiro, V. Venn, S. Castelli, M. S. Camargo, R. P. de Assis, R. A. de Souza, A. R. Ribeiro, T. G. Passalacqua, J. A. da Rosa, A. M. Baviera, A. E. Mauro, A. Desideri, E. E. Almeida-Amaral, M. A. S. Graminha, *Antimicrob. Agents Chemother.* **2017**, *61*, e00688-17. DOI:10.1128/AAC.00688-17
22. P. Chattopadhyay, M. K. Nayak, S. P. Bhattacharya, C. Sinha, *Polyhedron* **1997**, *16*, 1291–1295. DOI:10.1016/S0277-5387(96)00422-6
23. J. S. Casas, A. Castineiras, Y. Parajó, M. L. Pérez-Parallé, A. Sánchez, A. Sánchez-González, J. Sordo, *Polyhedron*, **2003**, *22*, 1113–1121. DOI:10.1016/S0277-5387(03)00097-4
24. T. Mosmann, *J. Immunol. Methods* **1983**, *65*, 55–63. DOI:10.1016/0022-1759(83)90303-4
25. W. J. Geary, *Coord. Chem. Rev.* **1971**, *7*, 81–122. DOI:10.1016/S0010-8545(00)80009-0
26. C. Kirchner, B. Krebs, *Inorg Chem*, **1987**, *26*, 3569–3576. DOI:10.1021/ic00268a030
27. D. Gambino, L. Otero, E. Kremer, O. E. Piro, E. E. Castellano, *Polyhedron*, **1997**, *16*, 2263–2270. DOI:10.1016/S0277-5387(96)00534-7
28. G. M. S. El-Bahy, B. A. El-Sayed, A. A. Shabana, *Vib. Spectrosc.* **2003**, *31*, 101–107. DOI:10.1016/S0924-2031(02)00099-1
29. S. Ahmad, A. A. Isab, S. Ahmad, *J. Coord. Chem.* **2003**, *56*, 1587–1595. DOI:10.1080/00958970310001641688
30. S. Nadeem, M. K. Rauf, M. Bolte, S. Ahmad, S. A. Tirmizi, M. Asma, A. Hameed, *Transition Met. Chem.* **2010**, *35*, 555–561. DOI:10.1007/s11243-010-9363-0
31. L. Bencivenni, S. N. Cesaro, A. Pieretti, *Vib. Spectrosc.* **1998**, *18*, 91–102. DOI:10.1016/S0924-2031(98)00039-3
32. Y. Mido, I. Kitagawa, M. Hashimoto, H. Matsuura, *Spectrochim. Acta A* **1999**, *55*, 2623–2633. DOI:10.1016/S1386-1425(99)00062-1
33. H. M. Badawi, *Spectrochim Acta A* **2009**, *72*, 523–527. DOI:10.1016/j.saa.2008.10.042
34. K. R. G. Devi, D. N. Sathyanarayana, *Bull. Chem. Soc. Jpn.* **1980**, *53*, 2990–2994. DOI:10.1246/bcsj.53.2990
35. C. Y. Panicker, H. T. Varghese, A. George, P. K. V. Thomas, *Eur. J. Chem.* **2010**, *1*, 173–178. DOI:10.5155/eurjchem.1.3.173-178.42
36. L. Fuks, N. Sadlej-Sosnowska, K. Samochocka, W. Starosta, *J. Mol. Struct.* **2005**, *740*, 229–235. DOI:10.1016/j.molstruc.2005.01.008
37. A. S. González, J. S. Casas, J. Sordo, U. Russo, M. I. Lareo, B. J. Regueiro, *J. Inorg. Biochem.* **1990**, *39*, 227–235. DOI:10.1016/0162-0134(90)84006-B
38. J. Berger, M. Kotowski, R. van Eldik, U. Frey, L. Helm, A. E. Merbach, *Inorg. Chem.* **1989**, *28*, 3759–3765. DOI:10.1021/ic00318a028
39. Y. Mido, H. Mizuno, T. Suzuki, T. Okuno, *Spectrochim. Acta A* **1986**, *42*, 807–809. DOI:10.1016/0584-8539(86)80108-8
40. Y. Liu, D. -J. Xu, *Acta. Cryst.* **2004**, *E60*, m1057–m1059. DOI:10.1107/S160053680401582X
41. V. M. Leovac, G. A. Bogdanović, L. S. Jovanović, L. Joksović, V. Marković, M. D. Joksović, S. M. Denčić, A. Isaković, I. Marković, F. W. Heinemann, S. Trifunović, I. Đalović, *J. Inorg. Biochem.* **2011**, *105*, 1413–1421. DOI:10.1016/j.jinorgbio.2011.07.021

Povzetek

Z reakcijami med $[\text{PdCl}_2(\text{tmbiimH}_2)] \cdot \text{H}_2\text{O}$ (**1**) { $\text{tmbiimH}_2 = 2,2'$ -bis(4,5-dimetilimidazol)} in tioureo (tu), *N*-metiltioureo (mtu), *N*-feniltioureo (ptu), *N,N'*-dimetiltioureo (dmu) oziroma *N,N'*-difeniltioureo (dptu) v 1:2 molskem razmerju smo izolirali spojine $[\text{PdL}_2(\text{tmbiimH}_2)]\text{Cl}_2 \cdot n\text{H}_2\text{O}$ { $L = \text{tu}$ (**2**), mtu (**3**), ptu (**4**), dmu (**5**) and dptu (**6**)}, ki smo jih okarakterizirali z elementno analizo, infrardečo (IR) in ^1H NMR spektroskopijo in merjenjem prevodnosti. IR spektri spojin **1–6** kažejo, da je v kompleksih prisoten kelatni tmbimH₂ ligand. Vse pripravljene spojine in cisplatin smo testirali *in vitro* z MTT testom njihove citotoksičnosti na treh mišjih rakavih celičnih linijah: mišji adenokarcinom dojke (LM3), mišji pljučni adenokarcinom (LP07) in mišji fibroblasti (L929). Na podlagi primerjave biološke aktivnosti spojin, se izkazuje spojine **6** kot najobetavnejša.

Scientific paper

Uses of Anthranilic Acid for the Synthesis of Dihydroquinazolin Derivatives with Antitumor, Antiproliferative and Pim-1 kinase Activities

Rafat M. Mohareb^{1,*} and Peter A. Halim²¹ Department of Chemistry, Faculty of Science, Cairo University, Giza, A. R. Egypt² Pharmaceutical Organic Chemistry Department, Faculty of Pharmacy, Cairo University, Cairo 11562, Egypt

* Corresponding author: E-mail: raafat_mohareb@yahoo.com

Received: 26-12-2017

Abstract

The reaction of anthranilic acid with ethoxycarbonylisothiocyanate gave the ethyl 4-oxo-2-thioxo-1,2-dihydroquinazoline-3(4*H*)-carboxylate (**4**). The reaction of compound **4** with hydrazine hydrate and α -halocarbonyl derivatives was found to give either hydrazono or *S*-alkylated products. Heterocyclization reactions of some of the *S*-alkylated derivatives **8** and **12** were carried out to afford thiazole, pyran and pyridine derivatives. The cytotoxicity of the newly synthesized compounds towards the six cancer cell lines NUGC, DLD-1, HA22T, HEPG-2, HONE-1 and MCF-7 showed that compounds **6**, **8**, **13**, **19c–f**, **21b–f**, **24a** and **24c** with the highest cytotoxicity. The *c*-Met kinase inhibition for some of the selected compounds showed that compounds **8**, **13**, **19d**, **21e**, **21f** and **24a** were the most active compounds. Screening toward tyrosine kinases revealed that compounds **13**, **21e** and **24a** exhibit the highest inhibitions and therefore their molecular modeling was described. In addition, compounds **13** and **24a** showed the highest activities towards Pim-1 kinase.

Keywords: Dihydroquinazolin; thiophene; thiazole; pyran; pyridine; cytotoxicity

1. Introduction

2-Thioxoquinazolin-4(1*H*)-ones are important heterocyclic compounds that are widely present in natural products as well as medicinal, and pharmacological compounds.¹ In addition, several thioxoquinazolin analogues have been developed as antitumor, antibiotic, antifibrilator and antipyretic agents (Fig. 1). Furthermore, they display a broad range of applications against diabetes,² cancer,³ and as selective plant grow regulators.^{4,5} Given the importance of these nitrogen heterocyclic compounds, the development of mild, high-yielding and clean synthesis of these important compounds is a daunting challenge and has been extensively investigated and described in the literature.^{6–12} The classical methods for the synthesis of quinazolinone ring system are the reaction of anthranilic acid and its derivatives with isothiocyanates or their equivalents.^{13–27} Recently, our research group was involved in the synthesis and determination of the anti-proliferative and anti-inflammatory activity of a large number of heterocyclic compounds.^{28,29} In the continuation of this pro-

gram, in this context, we aimed to develop an efficient and facile approach to synthesize and measure the cytotoxicity of a series of thioxoquinazolin-4(1*H*)-ones from anthranilic acid and ethoxycarbonylisothiocyanate.

2. Results and Discussion

Quinazoline derivatives showed a wide range spectrum of biological applications, especially in the field of anti-cancer therapy³⁰ which encouraged us to direct our work towards their synthesis. Thus, in the present work we aimed to synthesis a series of heterocyclic compounds derived from dihydroquinazoline derivative. The reaction of anthranilic acid (**1**) with ethoxycarbonylisothiocyanate (**2**) in 1,4-dioxane gave the ethyl 4-oxo-2-thioxo-1,2-dihydroquinazoline-3(4*H*)-carboxylate (**4**). The formation of the latter product took place through intermediate formation of the thiourea derivative followed by cyclization. Compound **4** was used for the synthesis of different heterocyclic compounds through its reaction with various chemi-

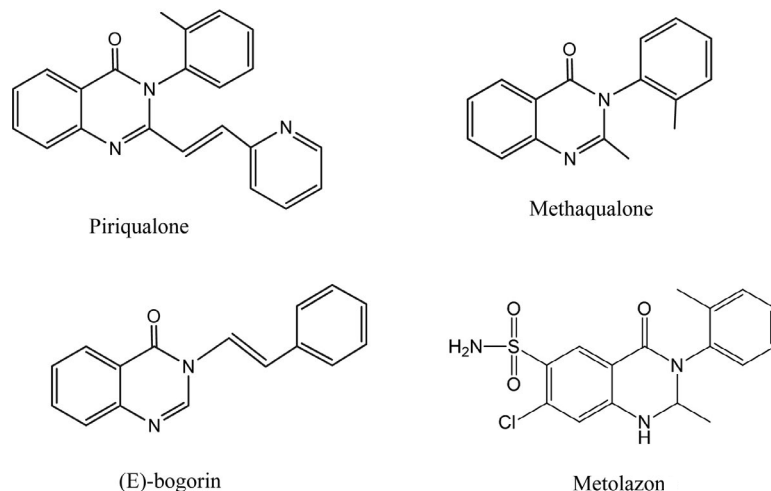
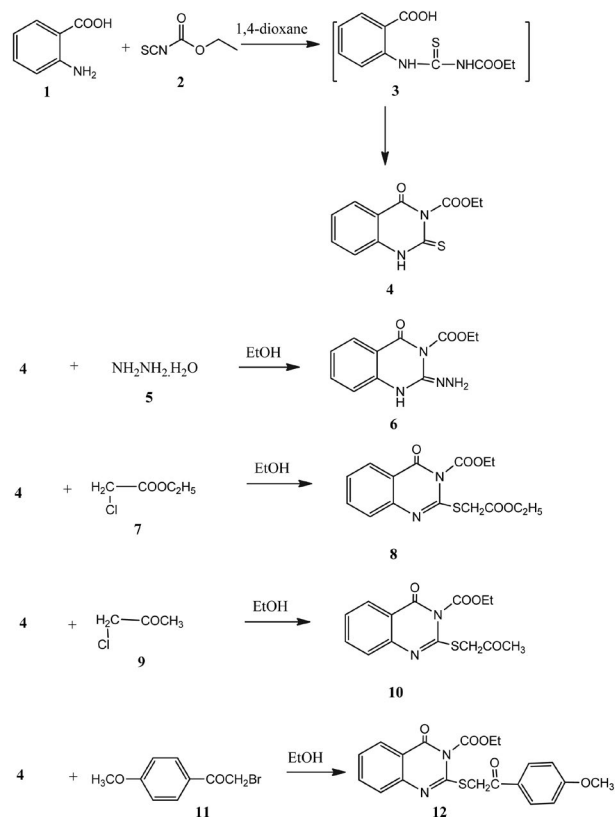


Fig. 1. Selected examples of quinazolin analogues with pharmacological activities

cal reagents. Thus, the reaction of compound **4** with hydrazine hydrate (**5**) gave the hydrazone derivative **6**. Compound **4** was capable to form thioether derivatives through its reaction with α -halocarbonyl compounds. Thus, the reaction of compound **4** with any of the following: ethyl chloroacetate (**7**), chloroacetone (**9**) or 2-bromo-1-(4-methoxyphenyl)ethanone (**11**), gave the thioether derivatives **8**, **10** and **12**, respectively (Scheme 1). The structures of compounds **8**, **10** and **12** were established on the basis of their analytical and spectral data. Thus, the ^1H NMR spectrum of compound **12** (as an example) showed the presence of a triplet at δ 1.13 and a quartet at δ 4.22 ppm showing the presence of an ester CH_3 and CH_2 , respectively, a singlet at δ 3.73 ppm showing the OCH_3 group, a singlet at δ 5.49 ppm for the CH_2 group and a multiplet at δ 7.23–7.42 ppm for the two C_6H_4 groups. In addition, the ^{13}C NMR spectrum showed signals at δ 16.4 (ester CH_3), 37.5 (CH_2), 53.4 (ester CH_2), 55.2 (OCH_3), 119.2, 120.8, 122.3, 124.4, 124.9, 126.2, 126.8, 127.8, 128.4, 129.1 indicating the presence of two C_6H_4 groups and three signals at δ 163.2, 164.4, 165.8 confirming the three CO groups.

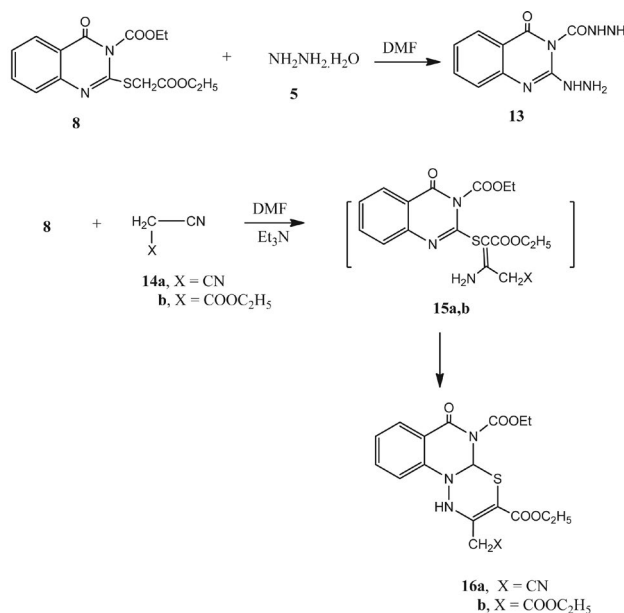
The reaction of compound **8** with hydrazine hydrate (**5**) gave the hydrazino derivative **13**. On the other hand, the reaction of compound **8** with either of malononitrile (**14a**) or ethyl cyanoacetate (**14b**) gave the dihydro[1,3,4]thiadiazino[3,2-*a*]quinazolin-6(1*H*)-one derivatives **16a** and **16b**, respectively (Scheme 2). Formation of compounds **16a** and **16b** took place through the intermediate formation of **15a,b** followed by cyclization. The structures of compounds **16a** and **16b** were confirmed on the basis of analytical and spectral data. Thus, the ^1H NMR spectrum of **16a** showed, besides the expected signals, two triplets at δ 1.12, 1.15 and two signals at δ 4.16, 4.20 ppm indicating the presence of two ester CH_3 and CH_2 groups, respectively, a singlet at δ 6.01 ppm belonging to the pyrimidine H-2 and a singlet at δ 8.28 ppm for the NH group. In addition its ^{13}C NMR spectrum showed two signals at δ 16.3, 16.5



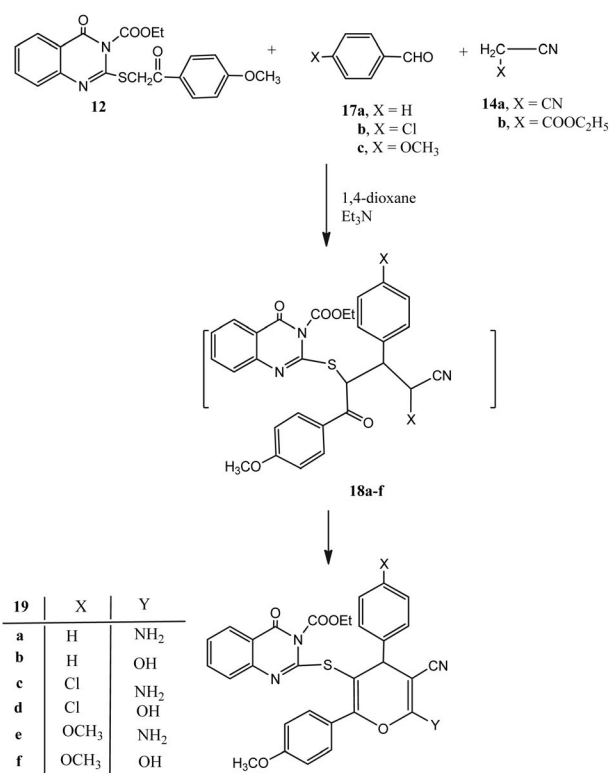
Scheme 1: Synthesis of compounds **4**, **6**, **8**, **10** and **12**.

for the two ester CH_3 groups and two quartets at δ 52.1, 53.8 for the two ester CH_2 groups as well as three signals at δ 163.8, 164.4, 165.2 belonging to the three CO groups.

In continuation of our recent interest to conduct multi-component reactions using aromatic aldehydes and cyanomethylene reagents^{31–33} we studied the multi-component reactions of compound **12**. Thus, the multi-component reaction of compound **12** with any of the aromatic



Scheme 2: Synthesis of compounds 13 and 16a,b.



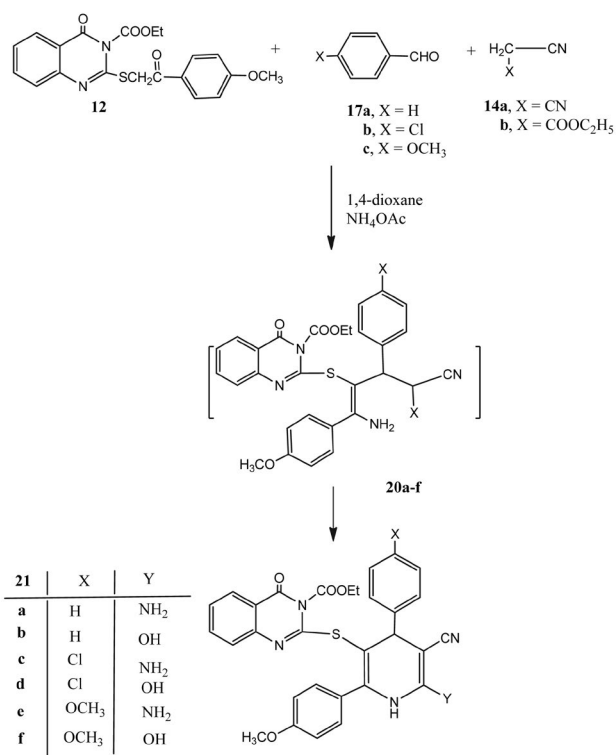
Scheme 3: Synthesis of compounds 19a-f.

aldehydes namely, benzaldehyde (17a), 4-chlorobenzaldehyde (17b) or 4-methoxybenzaldehyde (17c) and either of malononitrile (14a) or ethyl cyanoacetate (14b) in 1,4-dioxane containing triethylamine gave the pyridine derivatives 19a–f, respectively through the intermediate formation of 18a–f. The characterization of the compounds 19a–f

(Scheme 3) is based on their respective analytical and spectral data (see Experimental section).

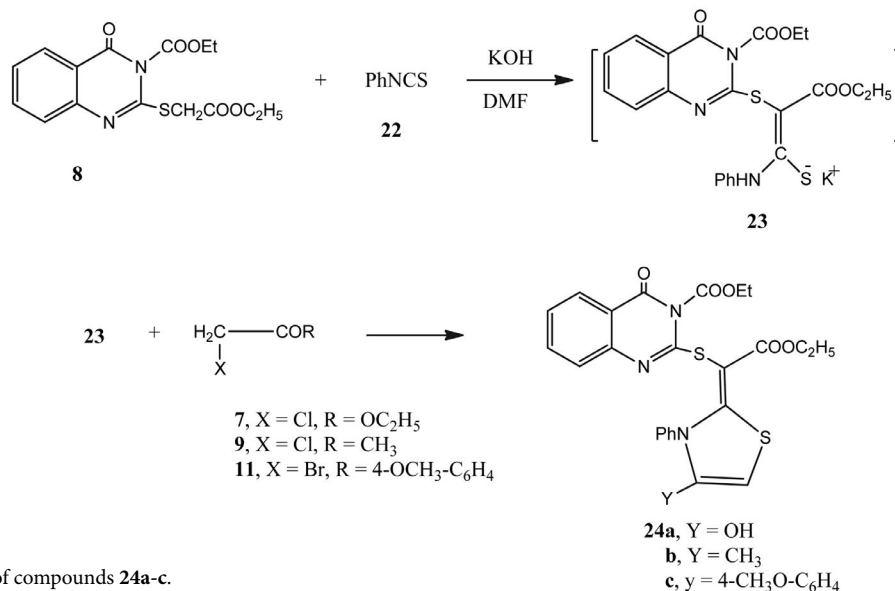
On the other hand, the multi-component reaction of compound 12 with any of benzaldehyde (17a), 4-chlorobenzaldehyde (17b) or 4-methoxybenzaldehyde (17c) and either of malononitrile (14a) or ethyl cyanoacetate (14b) in 1,4-dioxane containing ammonium acetate gave the pyridine derivatives 21a–f, respectively (Scheme 4). Formation of the latter products took place through the intermediate formation of 20a–f.

Recently, our research group was involved in a comprehensive program involving the reactions of active methylene reagents with phenylisothiocyanate in basic dimethylformamide solutions, followed by heterocyclization with α -halocarbonyl compounds.^{34–36} Products of the re-



Scheme 4: Synthesis of compounds 21a-f.

actions were either thiophene or thiazole derivatives or a mixture of both depending on the reaction conditions and the nature of the α -halocarbonyl compound. In continuation of this program we carried out the reaction of compound 8 with phenylisothiocyanate (22) in dimethylformamide containing potassium hydroxide to give the intermediate potassium salt 23. The reaction of the intermediate 23 with any of ethyl chloroacetate (7), chloroacetone (9) or 2-bromo-1-(4-methoxyphenyl)ethanone (11) afforded the thiazole derivatives 24a–c, respectively (Scheme 5). All synthesized compounds were obtained in good yields and their cytotoxicity against cancer cell lines was measured.



Scheme 5: Synthesis of compounds 24a-c.

2. 1. Biological Evaluation

2. 1. 1. *In vitro* Cytotoxic Assay

Chemicals

Fetal bovine serum (FBS) and L-glutamine were purchased from Gibco Invitrogen Co. (Scotland, UK). RPMI-1640 medium was purchased from Cambrex (New Jersey, USA). Dimethyl sulfoxide (DMSO), foretinib, penicillin, streptomycin and sulforhodamine B (SRB) were purchased from Sigma Chemical Co. (Saint Louis, USA).

Cell Cultures

Were obtained from the European Collection of Cell Cultures (ECACC, Salisbury, UK) and human gastric cancer (NUGC), human colon cancer (DLD1), human liver cancer (HA22T and HEPG2), human breast cancer (MCF-7), nasopharyngeal carcinoma (HONE1) and normal fibroblast cells (WI38) were kindly provided by the National Cancer Institute (NCI, Cairo, Egypt). They grow as a monolayer and were routinely maintained in RPMI-1640 medium supplemented with 5% heat inactivated FBS, 2 μM glutamine and antibiotics (penicillin 100 U/mL, streptomycin 100 $\mu\text{g}/\text{mL}$), at 37 °C in a humidified atmosphere containing 5% CO₂. Exponentially growing cells were obtained by plating 1.5 $\times 10^5$ cells/mL for the six human cancer cell lines including cells derived from 0.75 $\times 10^4$ cells/mL followed by 24 h of incubation. The effect of the vehicle solvent (DMSO) on the growth of these cell lines was evaluated in all the experiments by exposing untreated control cells to the maximum concentration (0.5%) of DMSO used in each assay.

The heterocyclic compounds, prepared in this study, were evaluated according to standard protocols for their *in vitro* cytotoxicity against six human cancer cell lines, including cells derived from human gastric cancer (NUGC), human colon cancer (DLD1), human liver cancer (HA22T and HEPG2), human breast cancer (MCF), nasopharynge-

al carcinoma (HONE1) and a normal fibroblast cells (WI38). All of IC₅₀ values are listed in Table 1. Some heterocyclic compounds were observed to display significant cytotoxicity against most of the cancer cell lines tested (IC₅₀ = 10–1000 nM). Normal fibroblasts cells (WI38) were affected to a much lesser extent (IC₅₀ >10,000 nM). The reference compound used was the foretinib anti-tumor agent.

2. 1. 2. Structure Activity Relationship

It is clear from Table 1 that most of the tested compounds showed cytotoxicity against the selected cancer cell lines. Compound 4 showed high cytotoxicity against HEPG-2 and MCF-7 cell lines with IC₅₀ values of 683 and 460 nM, respectively. The reaction of compound 4 with hydrazine hydrate gave the hydrazone derivative 6 which showed high potency against the six cancer cell lines, this was attributed to the high nitrogen content in this compound. It is worthy to note that compound 6 showed higher cytotoxicity than foretinib against DLD-1 and HEPG-2 cell lines with IC₅₀ values of 69 and 125 nM, respectively. On the other hand, the reaction of compound 4 with ethyl α -chloroacetate gave the thioether derivative 8 with high cytotoxicity against the six cancer cell lines but its potency is a little bit less than that of compound 6. It is obvious that compound 8 showed higher cytotoxicity than foretinib against DLD-1 and HEPG-2 cell lines with IC₅₀ values of 230 and 64 nM, respectively. On the other hand, the thioether 10 showed high potency against HONE-1 and MCF-7 cell lines but compound 12 showed low potency against the six cancer cell lines. The reaction of compound 8 with hydrazine hydrate gave the hydrazino derivative 13 with a high nitrogen content, showing relatively high potency against the six cancer cell lines. On the other hand, the dihydro-[1,3,4]thiadiazino[3,2-*a*]quinazoline deriva-

Table 1: Cytotoxicity of the newly synthesized products against a variety of cancer cell lines [IC₅₀^a (nM)]

Compound No.	Cytotoxicity (IC ₅₀ in nM)						
	NUGC ^b	DLD-1 ^b	HA22T ^b	HEPG-2 ^b	HONE-1 ^b	MCF-7 ^b	WI-38 ^b
4	1250	1280	1088	683	1159	460	NA
6	75	69	59	125	312	189	NA
8	137	230	219	64	312	109	NA
10	1089	1694	1741	2493	253	290	NA
12	1224	1476	2251	1122	1373	1229	NA
13	430	784	352	280	1879	128	NA
16a	1466	2369	1763	2461	2749	1863	NA
16b	2557	2590	2430	1461	2893	1279	NA
19a	2539	3167	2577	2690	1993	3289	NA
19b	1368	1273	1549	1366	2165	2540	NA
19c	65	530	250	149	259	426	NA
19d	159	250	59	114	189	550	NA
19e	30	62	74	39	1330	88	NA
19f	1089	1146	89	122	320	422	320
21a	2166	2253	1259	2769	2429	2760	NA
21b	88	79	194	520	287	1221	NA
21c	1243	138	229	1821	128	220	NA
21d	480	679	1293	580	744	124	NA
21e	129	226	183	480	136	229	NA
21f	55	79	134	109	85	93	NA
24a	380	219	179	229	312	59	NA
24b	2848	2218	2214	2373	1072	1238	NA
24c	93	68	169	421	629	229	NA
Foretinib	23	258	48	240	35	35	NA

^a Drug concentration required to inhibit tumor cell proliferation by 50% after continuous exposure of 48 h. ^b NUGC, gastric cancer; DLD-1, colon cancer; HA22T, liver cancer; HEPG-2, liver cancer; HONE-1, nasopharyngeal carcinoma; MCF-7, breast cancer; WI-38, normal fibroblast cells. NA: Not Active.

tives **16a,b** showed low potency. The multi-component reactions of compound **12** with any of the aromatic aldehydes **17a–c** and either of malononitrile or ethyl cyanoacetate gave the pyran derivatives **19a–f**. Compounds **19c** (X = Cl, Y = NH₂), **19d** (X = Cl, Y = OH) and **19e** (X = OCH₃, Y = NH₂) showed the highest cytotoxicity among this series of compounds. On the other hand, the pyridine derivatives **21a–f** where the four compounds **21b** (X = H, Y = OH), **21d** (X = Cl, Y = OH), **21e** (X = OCH₃, Y = NH₂) and **21f** (X = OCH₃, Y = OH) showed the highest potency. Compound **21f** showed cytotoxicity higher than foretinib against the DLD-1 cell line with IC₅₀ 79 nM. Considering the thiazole derivatives **24a–c**, it is obvious that compounds **24a** (Y = OH) and **24c** (Y = 4-OCH₃-phenyl) showed higher potency than **24b** (Y = CH₃). It is clear that throughout the synthesized compounds the presence of the electronegative groups, like the Cl and OH groups, or the electron-rich NH₂ groups enhance the potency of the compound.

2. 1. 3. Cell Proliferation Assay

The anti-proliferative activity of compounds **6**, **8**, **13**, **19c**, **19d**, **19e**, **21b**, **21d**, **21e**, **21f**, **24a** and **24c** was evaluated (Table 2) against the five c-Met-dependent cancer cell lines (A549, HT-29, MKN-45, U87MG, and SMMC-7721)

and one c-Met-independent cancer cell line (H460) using the standard MTT assay *in vitro*, with foretinib as the positive control.^{37,38} The cancer cell lines were cultured in the minimum essential medium (MEM) supplemented with 10% fetal bovine serum (FBS). Approximate 4 × 10³ cells, suspended in MEM medium, were plated onto each well of a 96-well plate and incubated in 5% CO₂ at 37 °C for 24 h. The compounds tested at the indicated final concentrations were added to the culture medium and the cell cultures were continued for 72 h. Fresh MTT was added to each well at a terminal concentration of 5 mg/mL, and incubated with cells at 37 °C for 4 h. The formazan crystals were dissolved in 100 μL of DMSO for each well, and the absorbance at 492 nM (for absorbance of MTT formazan) and 630 nM (for the reference wavelength) was measured with an ELISA reader. All of the compounds were tested three times in each cell line. The results expressed as IC₅₀ (inhibitory concentration 50%) are the averages of three determinations and were calculated by using the Bacus Laboratories Incorporated Slide Scanner (Bliss) software.

2. 1. 4. *In vitro* Cell Assays

The antitumor evaluations³⁹ of the synthesized compounds were measured against A549 (non-small cell lung

Table 2. In vitro growth inhibitory effects $IC_{50} \pm SEM$ (μM) of the most potent compounds

Compound No	$IC_{50} \pm SEM$ (μM)					
	A549	H460	HT29	MKN-45	U87MG	SMMC-7721
6	1.28 ± 0.67	1.58 ± 0.65	0.65 ± 0.32	1.58 ± 0.49	0.39 ± 0.18	0.29 ± 0.19
8	1.02 ± 0.80	1.27 ± 0.69	1.28 ± 0.79	1.04 ± 0.48	1.49 ± 0.72	1.26 ± 0.73
13	0.09 ± 0.06	0.06 ± 0.01	0.04 ± 0.06	0.83 ± 0.26	0.69 ± 0.32	0.73 ± 0.25
19c	0.77 ± 0.34	0.28 ± 0.06	0.93 ± 0.24	0.72 ± 0.14	0.48 ± 0.13	0.93 ± 0.18
19d	1.02 ± 0.36	1.18 ± 0.42	0.93 ± 0.26	0.63 ± 0.14	1.63 ± 0.87	0.32 ± 0.16
19e	0.63 ± 0.28	0.36 ± 0.25	0.03 ± 0.53	0.28 ± 0.11	0.26 ± 0.07	0.80 ± 0.24
21b	3.26 ± 1.72	3.59 ± 1.30	1.42 ± 0.80	2.83 ± 0.46	1.74 ± 0.79	1.40 ± 0.73
21d	0.87 ± 0.22	0.69 ± 0.21	0.59 ± 0.11	0.69 ± 0.21	0.70 ± 0.12	0.83 ± 0.24
21e	0.18 ± 0.02	0.25 ± 0.09	0.36 ± 0.09	0.16 ± 0.07	0.42 ± 0.16	0.55 ± 0.19
21f	2.31 ± 0.69	2.49 ± 0.80	1.43 ± 0.79	1.08 ± 0.75	2.39 ± 0.93	1.38 ± 0.91
24a	1.02 ± 0.53	1.08 ± 0.55	2.39 ± 0.88	1.48 ± 0.93	0.95 ± 0.29	1.63 ± 0.82
24c	0.19 ± 0.01	0.28 ± 0.07	0.80 ± 0.09	0.57 ± 0.08	0.93 ± 0.27	0.75 ± 0.16
Foretinib	0.08 ± 0.01	0.18 ± 0.03	0.15 ± 0.023	0.03 ± 0.0055	0.90 ± 0.13	0.44 ± 0.062

cancer), H460 (human lung cancer), HT-29 (human colon cancer) and MKN-45 (human gastric cancer), U87MG (human glioblastoma) and SMMC-7721 (human liver cancer) cancer cell lines. Foretinib was used as the positive control by a MTT assay. The results are expressed as IC_{50} after three different experiments were summarized and are shown in Table 2. The data listed in Table 2 reveal that the compounds possess moderate to strong cytotoxicity against the six tested cell lines in the single-digit μM range, and high selectivity for inhibition of A549, H460 and MKN-45 cells. The promising compounds were **13**, **19c**, **19e**, **21d**, **21e** and **24c**, these were the most active with IC_{50} values of 0.09 and 0.93 μM , respectively. Moreover, compound **13** showed potency higher than foretinib towards H460 with IC_{50} 0.06 μM . Compounds **6**, **13**, **19e**, **21d**, **21e** showed activities toward U87MG cell line higher than foretinib with IC_{50} values of 0.39, 0.69, 0.26, 0.70 and 0.42 μM , respectively. It is of great value to note that compound **6** showed higher potency than foretinib with IC_{50} 0.29 μM against SMMC-7721.

2. 1. 5. HTRF Kinase Assay

The c-Met kinase activities (Table 3) of the most potent compounds **6**, **8**, **13**, **19c**, **19d**, **19e**, **21b**, **21d**, **21e**, **21f**, **24a** and **24c** were measured using homogeneous time-resolved fluorescence (HTRF) assay as previously reported.^{40,41} In addition, the most potent compounds toward c-Met kinase were further evaluated against other five tyrosine kinases (c-Kit, Flt-3, VEGFR-2, EGFR, and PDGFR) using the same method (Table 4). Briefly, 20 mg/mL poly (Glu, Tyr) 4:1 (Sigma) was used as a substrate in 384-well plates. Then, 50 μL of 10 mM ATP (Invitrogen) solution diluted in kinase reaction buffer (50 mM HEPES, Ph 7.0, 1 M DTT, 1 M $MgCl_2$, 1 M $MnCl_2$, and 0.1% NaN_3) was added to each well. Various concentrations of the tested compounds diluted in 10 μL of 1% DMSO (v/v) were used as the negative control. The kinase reaction was start-

ed by the addition of the purified tyrosine kinase proteins diluted in 39 μL of kinase reaction buffer solution. The incubation times for the reactions were 30 min at 25 °C and were ceased by the addition of 5 μL of Streptavidin-XL665 and 5 μL Tk Antibody Cryptate working solution added to all of wells. The plates were read using Envision (Perkin-Elmer) at 320 and 615 nm. The inhibition rate (%) was calculated using the mathematical equation: % inhibition = $100 - [(Activity\ of\ enzyme\ with\ tested\ compounds - Min)/(Max - Min)] \times 100$ (Max: the observed enzyme activity measured in the presence of enzyme, substrates, and cofactors; Min: the observed enzyme activity in the presence of substrates, cofactors and in the absence of enzyme). IC_{50} values were calculated using the inhibition curves.

According to Table 3 it is clear that compounds **8**, **13**, **19d**, **21e**, **21f** and **24a** were the most active compounds towards c-Met kinase. Moreover, compounds **13**, **19d** and **24a** showed activity towards c-Met enzymatic activity higher than that of foretinib.

Table 3. c-Met enzymatic activity and line of the most potent compounds

Compound No	X	Y	IC_{50} (nM) c-Met
6	-	-	10.22 ± 2.38
8	-	-	1.34 ± 0.81
13	-	-	0.06 ± 0.001
19c	Cl	NH ₂	2.26 ± 0.80
19d	Cl	OH	0.83 ± 0.19
21b	H	OH	4.30 ± 1.89
21d	Cl	OH	12.28 ± 2.69
21e	OCH ₃	NH ₂	1.27 ± 0.98
21f	OCH ₃	OH	1.40 ± 0.51
24a	-	OH	0.79 ± 0.09
24c	-	4-OCH ₃ -C ₆ H ₄	8.50 ± 2.19
Foretinib	-	-	1.16 ± 0.17

2. 1. 6. Inhibitory Effects of the Most Active Compounds Towards Tyrosine Kinases

The most potent compounds **8**, **13**, **19d**, **21e**, **21f** and **24a** towards c-Met enzymatic activity of the five tyrosine kinases (c-Kit, Flt-3, VEGFR-2, EGFR, and PDGFR) were determined using the same method described for c-Meth enzymatic activity and the data are shown in Table 4. Here foretinib was also used as the reference drug. It is clear from Table 4 that compounds **13**, **21e** and **24a** showed the highest inhibitory effect towards the five tyrosine kinases.

Table 4. inhibitory effect of compounds **8**, **13**, **19d**, **21e**, **21f** and **24a** towards tyrosine kinases [Enzyme IC₅₀ (nM)]

Compound	c-Kit	Flt-3	VEGFR-2	EGFR	PDGFR
8	9.26	8.18	7.66	4.50	6.85
13	1.32	2.59	1.08	1.26	0.99
19d	10.39	8.68	9.09	6.49	7.30
21e	0.42	0.76	0.69	0.74	0.25
21f	8.57	8.55	10.39	8.48	10.99
24a	0.82	2.80	0.79	1.59	1.33
Foretinib	0.19	0.17	0.20	0.13	0.26

2. 1. 7. Pim-1 Kinase Inhibition of Compounds **13**, **21e** and **24a**

Compounds **13**, **21e** and **24a** were selected to examine their Pim-1 kinase inhibition activity⁴² at a range of 10 concentrations and the IC₅₀ values were calculated. Our selection for **13**, **21e** and **24a** was based on their relative activity towards c-Met kinase, together with their inhibition towards tyrosine kinases; the more potent to inhibit Pim-1 activity were **13** and **24a** with IC₅₀ value of 0.36 and 0.28

Table 6. Docking study data showing amino acid interactions and the hydrogen bond lengths of target compounds and foretinib on c-Met kinase enzyme.

Compound number	Number of H-bonds	Number of π - π interactions with Phe ¹²²³	Atoms of compound forming H-bond	Amino acid residues forming H-bonds (H-bond length in Å)	Binding energy score (kcal/mol)
Ligand (Foretinib)	2	1	Quinazoline N (H-acceptor) CO (H-acceptor)	Met ¹¹⁶⁰ (3.05) Lys ¹¹¹⁰ (2.89)	-16.37
13	3	-	Quinazoline N (H-acceptor) NHNH ₂ (H-acceptor) CONHNH ₂ (H-acceptor)	Asp ¹²²² (3.03) Asp ¹²²² (2.98) Lys ¹¹¹⁰ (2.75)	-11.45
21e	3	-	NH ₂ (H-donor) OCH ₃ (H-acceptor) OCH ₃ (H-acceptor)	Asp ¹¹⁶⁴ (1.46) Asn ¹¹⁷¹ (2.94) His ¹⁰⁹⁴ (2.86)	-7.83
24a	2	-	OH (H-donor) OH (H-acceptor)	Asp ¹¹⁶⁴ (1.23) Asn ¹¹⁷¹ (2.66)	-11.58

μM , while **21e** was less effective (IC₅₀ > 10 μM). SGI-1776 was used as the positive control with IC₅₀ 0.048 μM in the assay. These profiles in combination with cell growth inhibition data of compounds **13**, **21e** and **24a** are listed in Table 5 and indicate that Pim-1 is a potential target of these compounds.

Table 5. The inhibitor activity of compounds **13**, **21e** and **24a** on Pim-1 Kinase.

Compound	Inhibition ratio At 10 μM	IC ₅₀ (μM)
13	86	0.36
21e	34	> 10
24a	95	0.28
SGI-1776	-	0.048

Experimental Protocol of Docking Study

All the molecular modeling studies were carried out on an Intel Pentium 2.3 GHz processor, 8 GB memory with Windows 7 operating system using Molecular Operating Environment (MOE, 10.2008; Chemical Computing Group, Canada) software. The X-ray crystallographic structure of c-Met kinase enzyme with its co-crystallized ligand XL880 (Foretinib) in the file (PDB ID: 3LQ8) was obtained from RCSB Protein Data Bank with a 2.02 Å resolution. All water of crystallization was deleted from the active site except the one involved in interactions with the ligand. Hydrogens and partial charges were added to the system using protonate 3D application. Isolation of the active site, recognition of the amino acids and the backbone was hidden. The docking algorithm was validated via docking of the native ligand (Foretinib) into its c-Met kinase active site where the docking procedure was able to

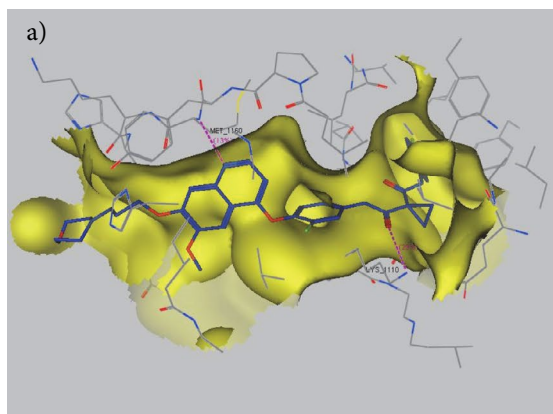


Figure 2. Interactions of XL880 (foretinib) with the amino acid residues of the active site of c-Met 3D(a) and 2D(b)

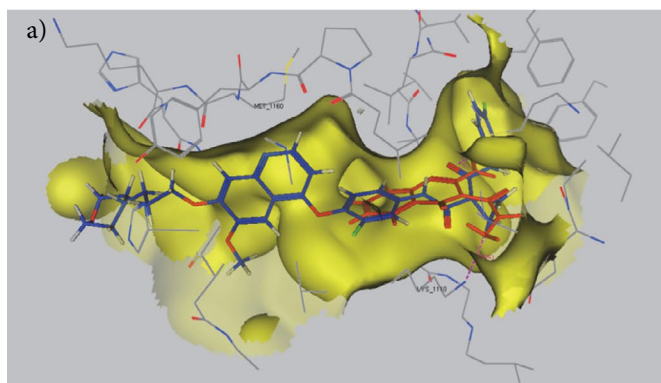
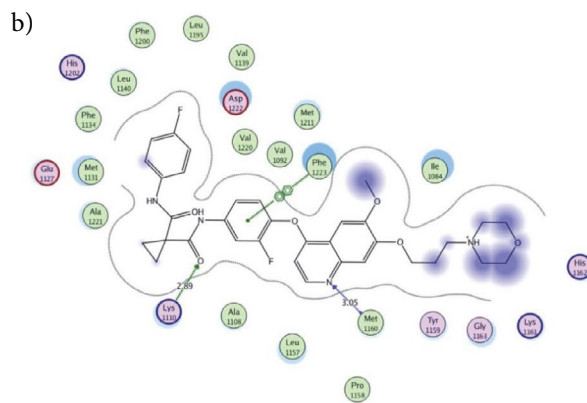


Figure 3. (a) The superposition of foretinib (blue) and compound **13** (red) docked in the binding site of c-Met, the dotted lines represent H-bonding interactions; (b) 2D ligand interaction of **13** in binding site of c-Met.

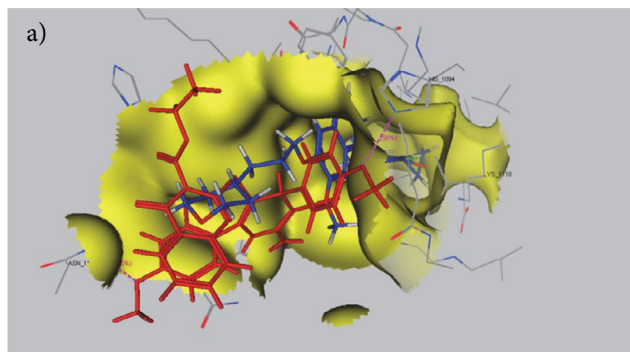
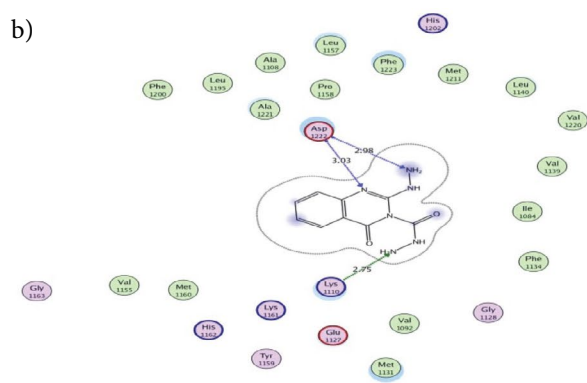


Figure 4. (a) The superposition of foretinib (blue) and compound **21e** (red) docked in the binding site of c-Met, the dotted lines represent H-bonding interactions; (b) 2D ligand interaction of **21e** in binding site of c-Met.

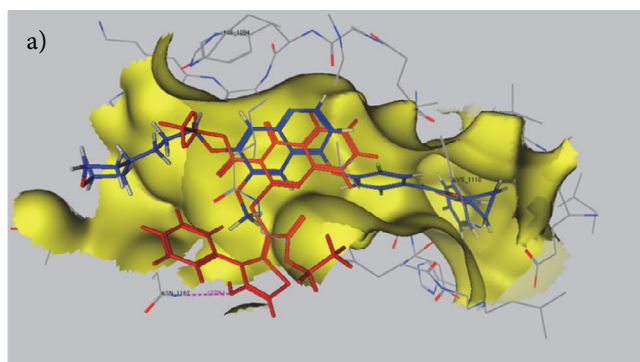
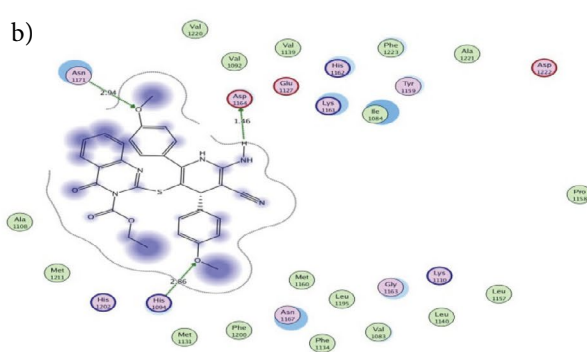
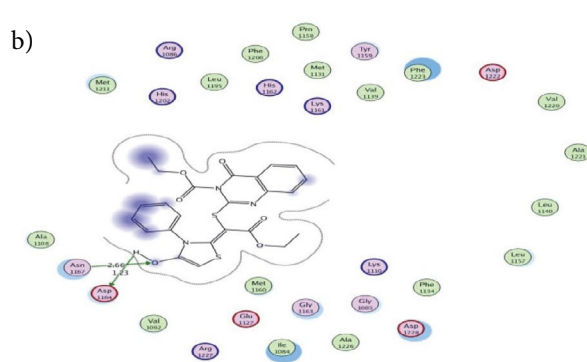


Figure 5. (a) The superposition of foretinib (blue) and compound **24a** (red) docked in the binding site of c-Met, the dotted lines represent H-bonding interactions; (b) 2D ligand interaction of **24a** in binding site of c-Met.



retrieve the co-crystallized pose with RMSD value of 0.55 Å. The three-dimensional structures of the most active compounds **13**, **21e** & **24a** were built using MOE molecular builder, then their energy was minimized by Merck Molecular Force Field (MMFF94x). Hydrogens and partial charges were added to the system using protonate 3D application.

Docking Results

For each docked compound, only one pose was selected based on number of binding interactions, superposition with the original ligand, docking score and the formed H-bonds were measured. The docking results obtained from the docking study are summarized in Table 6.

Discussion of Molecular Modeling

The X-ray crystallographic structure of XL880 (foretinib) in complex with c-Met kinase shows that the inhibitor forms two hydrogen bonds between quinoline N and Met¹¹⁶⁰, CO of malonamide moiety and Lys¹¹¹⁰. Phe¹²²³ of the activation loop has relocated from the position in the active conformation to stack underneath the fluorophenyl ring (π - π interaction), placing the kinase in a pseudo-unactivated conformation⁴³ (Fig. 2). Compounds **13**, **21e** and **24a** showed good fitting to the active binding site of c-Met kinase by interaction with Asp¹²²², Lys¹¹¹⁰, Asp¹¹⁶⁴, Asn¹¹⁷¹ and His¹⁰⁹⁴ amino acid residues (Fig. 3–5).

3. Experimental

3.1. General

All melting points were determined on an electrothermal apparatus (Büchi 535, Switzerland) in an open capillary tube and are uncorrected. ¹³C NMR and ¹H NMR spectra were recorded on Bruker DPX200 instrument in DMSO with TMS as internal standard for proton spectra and solvent signals as internal standard for carbon spectra. Chemical shift values are given in δ (ppm). Mass spectra were recorded on EIMS (Shimadzu) and ESI-esquire 3000 Bruker Daltonics instrument. Elemental analyses were carried out by the Microanalytical Data Unit at Cairo University. The progress of all reactions was monitored by TLC on 2 × 5 cm pre-coated silica gel 60 F254 plates of thickness of 0.25 mm (Merck).

3.1.1. Ethyl 4-oxo-2-thioxo-1,2-dihydroquinazoline-3(4H)-carboxylate (4)

To a solution of anthranilic acid (1.37 g, 0.01 mol) in 1,4-dioxane (40 mL) a solution of ethyl carbonisothiocyanatide (1.31 g, 0.01 mol) in 1,4-dioxane [prepared by the addition of ammonium thiocyanate (0.76 g, 0.01 mol) to ethyl chloroformate (1.08 g, 0.01 mol) in 1,4-dioxane (20 mL) and heating under reflux for 10 min] was added. The reaction mixture was heated under reflux for 1 h, then

poured onto ice/water and the formed solid product was collected by filtration.

Yellow crystals from ethanol; m.p. 210–212 °C; IR (KBr) ν_{max} 3480–3345 (NH), 3054 (CH aromatic), 2987, 2880 (CH₃, CH₂), 1688, 1682 (2CO), 1631 (C=C), 1205 (C=S) cm^{-1} ; ¹H NMR (200 MHz, DMSO-*d*₆) δ 1.13 (t, 3H, *J* = 5.82 Hz, CH₃), 4.19 (q, 2H, *J* = 5.85, CH₂), 7.29–7.38 (m, 4H, C₆H₄), 8.34 (s, 1H, D₂O exchangeable, NH); ¹³C NMR (75 MHz, DMSO-*d*₆) δ 16.2 (OCH₂CH₃), 53.8 (OCH₂CH₃), 119.4, 122.3, 125.4, 126.3, 128.4, 130.3 (C₆H₄), 164.2, 164.8 (2CO), 179.4 (C=S); Anal. Calcd. for C₁₁H₁₀N₂O₃S (250.27): C, 52.79; H, 4.03; N, 11.19; S, 12.81. Found: C, 52.83; H, 3.86; N, 11.37; S, 13.05; EI-MS (*m/z*, %): 250 [M⁺, 42].

3.1.2. Ethyl 2-hydrazono-4-oxo-1,2-dihydroquinazoline-3(4H)-carboxylate (6)

To a solution of compound **4** (2.50 g, 0.01 mol) in ethanol (50 mL) hydrazine hydrate (0.50 g, 0.01 mol) was added. The reaction mixture was heated under reflux for 4 h then poured onto ice/water containing a few drops of hydrochloric acid and the formed solid product was collected by filtration.

Yellow crystals from ethanol; m.p. 266–268 °C; IR (KBr) ν_{max} 3469–3339 (NH₂, NH), 3056 (CH aromatic), 2989, 2883 (CH₃, CH₂), 1689, 1684 (2CO), 1655 (C=N), 1630 (C=C) cm^{-1} ; ¹H NMR (200 MHz, DMSO-*d*₆) δ 1.14 (t, 3H, *J* = 7.04 Hz, CH₃), 4.19 (q, 2H, *J* = 7.04 Hz, CH₂), 4.76 (s, 2H, D₂O exchangeable, NH₂), 7.26–7.37 (m, 4H, C₆H₄), 8.31 (s, 1H, D₂O exchangeable, NH); ¹³C NMR (75 MHz, DMSO-*d*₆) δ 16.1 (OCH₂CH₃), 53.6 (OCH₂CH₃), 120.5, 121.8, 124.8, 125.1, 127.8, 129.1 (C₆H₄), 164.3, 164.7 (2CO), 174.6 (C=N); Anal. Calcd. for C₁₁H₁₂N₄O₃ (248.24): C, 53.22; H, 4.87; N, 22.57. Found: C, 53.41; H, 4.69; N, 22.69; EI-MS (*m/z*, %): 248 [M⁺, 26].

3.1.3. Synthesis of the thioether derivatives **8**, **10**

To a solution of compound **4** in ethanol (40 mL) any of compounds **7** (1.22 g, 0.01 mol), **9** (0.92 g, 0.01 mol) or **11** (2.29 g, 0.01 mol) was added. The reaction mixture, in each case, was heated under reflux for 3 h then poured into ice/water mixture containing a few drops of sodium hydroxide solution and the formed solid product was collected by filtration.

Ethyl 2-((2-ethoxy-2-oxoethyl)thio)-4-oxoquinazoline-3(4H)-carboxylate (8)

Yellow crystals from ethanol; m.p. 168–171 °C; IR (KBr) ν_{max} 3055 (CH aromatic), 2989, 2883 (CH₃, CH₂), 1691, 1686, 1684 (3CO), 1654 (C=N), 1630 (C=C) cm^{-1} ; ¹H NMR (200 MHz, DMSO-*d*₆) δ 1.12, 1.14 (2t, 6H, *J* = 5.93, 6.73 Hz, 2CH₃), 4.16, 4.20 (2q, 4H, *J* = 5.93, 6.73 Hz, 2CH₂), 5.21 (s, 2H, CH₂), 7.28–7.38 (m, 4H, C₆H₄); ¹³C NMR (75 MHz, DMSO-*d*₆) δ 16.2, 16.4 (two OCH₂CH₃), 37.5 (CH₂),

53.3, 53.5 (two OCH_2CH_3), 120.8, 122.5, 125.3, 127.5, 127.8, 130.2 (C_6H_4), 164.3, 164.5, 165.0 (3CO), 174.6 (C=N); Anal. Calcd. for $\text{C}_{15}\text{H}_{16}\text{N}_2\text{O}_5\text{S}$ (336.36): C, 53.56; H, 4.79; N, 8.33; S, 9.53. Found: C, 53.63; H, 4.49; N, 8.40; S, 9.70; EI-MS (m/z , %): 336 [M^+ , 36].

Ethyl 4-oxo-2-((2-oxopropyl)thio)quinazoline-3(4H)-carboxylate (10)

Orange crystals from ethanol; m.p. 210–213 °C; IR (KBr) ν_{max} 3055 (CH aromatic), 2986, 2887 (CH_3 , CH_2), 1694, 1686, 1682 (3CO), 1655 (C=N), 1631 (C=C) cm^{-1} ; ^1H NMR (200 MHz, $\text{DMSO}-d_6$) δ 1.13 (t, 3H, $J = 7.04$ Hz, CH_3), 2.68 (s, 3H, CH_3), 4.23 (q, 2H, $J = 7.04$ Hz, CH_2), 5.38 (s, 2H, CH_2), 7.25–7.35 (m, 4H, C_6H_4); ^{13}C NMR (75 MHz, $\text{DMSO}-d_6$) δ 16.3 (OCH_2CH_3), 24.8 (CH_3), 37.8 (CH_2), 53.2 (OCH_2CH_3), 120.4, 121.6, 123.4, 125.0, 127.8, 129.1 (C_6H_4), 163.8, 164.2, 165.2 (3CO), 174.8 (C=N); Anal. Calcd. for $\text{C}_{14}\text{H}_{14}\text{N}_2\text{O}_4\text{S}$ (306.34): C, 54.89; H, 4.61; N, 9.14; S, 10.47. Found: C, 55.17; H, 4.53; N, 9.05; S, 10.66; EI-MS (m/z , %): 306 [M^+ , 28].

Ethyl 2-((2-(4-methoxyphenyl)-2-oxoethyl)thio)-4-oxoquinazoline-3(4H)-carboxylate (12)

Orange crystals from ethanol; m.p. 148–151 °C; IR (KBr) ν_{max} 3056 (CH aromatic), 2983, 2889 (CH_3 , CH_2), 1690, 1689, 1682 (3CO), 1653 (C=N), 1630 (C=C) cm^{-1} ; ^1H NMR (200 MHz, $\text{DMSO}-d_6$) δ 1.13 (t, 3H, $J = 6.99$ Hz, CH_3), 3.73 (s, 3H, OCH_3), 4.22 (q, 2H, $J = 6.99$ Hz, CH_2), 5.49 (s, 2H, CH_2), 7.23–7.42 (m, 8H, $2\text{C}_6\text{H}_4$); ^{13}C NMR (75 MHz, $\text{DMSO}-d_6$) δ 16.4 (OCH_2CH_3), 37.5 (CH_2), 53.4 (OCH_2CH_3), 55.2 (OCH_3), 119.2, 120.8, 122.3, 124.4, 124.9, 126.2, 126.8, 127.8, 128.4, 129.1 ($2\text{C}_6\text{H}_4$), 163.2, 164.4, 165.8 (3CO), 174.6 (C=N); Anal. Calcd. for $\text{C}_{20}\text{H}_{18}\text{N}_2\text{O}_5\text{S}$ (398.43): C, 60.29; H, 4.55; N, 7.03; S, 8.05. Found: C, 60.46; H, 4.69; N, 7.27; S, 7.86; EI-MS (m/z , %): 398 [M^+ , 24].

3. 1. 4. 2-Hydrazinyl-4-oxoquinazoline-3(4H)-carbohydrazide (13)

To a solution of compound **8** (3.36 g, 0.01 mol) in dimethylformamide (30 mL) hydrazine hydrate (1.0 mL, 0.02 mol) was added. The reaction mixture was heated under reflux for 1 h then poured onto ice/water mixture containing a few drops of hydrochloric acid and the formed solid product was collected by filtration.

White crystals from ethanol; m.p. 233–236 °C; IR (KBr) ν_{max} 3480–3320 (2NH_2 , 2NH), 3053 (CH aromatic), 1687, 1683 (2CO), 1656 (C=N), 1632 (C=C) cm^{-1} ; ^1H NMR (200 MHz, $\text{DMSO}-d_6$) δ 4.83, 4.91 (2s, 4H, D_2O exchangeable, 2NH_2), 7.26–7.36 (m, 4H, C_6H_4), 8.21, 8.27 (2s, 2H, D_2O exchangeable, 2NH); ^{13}C NMR (75 MHz, $\text{DMSO}-d_6$) δ 120.3, 124.4, 127.5, 127.8, 128.0, 129.1 (C_6H_4), 163.0, 164.2 (2CO), 174.4 (C=N); Anal. Calcd. for $\text{C}_9\text{H}_{10}\text{N}_6\text{O}_2$ (234.21): C, 46.15; H, 4.30; N, 35.88. Found: C, 46.28; H, 4.46; N, 35.93; EI-MS (m/z , %): 234 [M^+ , 36].

3. 1. 5. Synthesis of the 4a,5-dihydro-[1,3,4]thiadiazino[3,2-a]quinazolin-6(1H)-one derivatives 16a,b

To a solution of compound **8** (3.36 g, 0.01 mol) in dimethylformamide (30 mL) containing triethylamine (1.0 mL) either of malononitrile (0.66 g, 0.01 mol) or ethyl cyanoacetate (1.13 g, 0.01 mol) was added. The reaction mixture was heated under reflux for 2 h then poured onto ice/water mixture containing a few drops of hydrochloric acid and the formed solid product was collected by filtration.

Diethyl 2-(ccyanomethyl)-6-oxo-4a,6-dihydro-[1,3,4]thiadiazino[3,2-a]quinazoline-3,5(1H)-dicarboxylate (16a)

Pale yellow crystals from 1,4-dioxane; m.p. 184–186 °C; IR (KBr) ν_{max} 3468–3341 (NH), 3056 (CH aromatic), 1689, 1685–1683 (3CO), 2220 (CN), 1653 (C=N), 1630 (C=C) cm^{-1} ; ^1H NMR (200 MHz, $\text{DMSO}-d_6$) δ 1.12, 1.15 (2t, 6H, $J = 6.16$, 6.90 Hz, $2\text{OCH}_2\text{CH}_3$), 4.16, 4.20 (2q, 4H, $J = 6.16$, 6.90 Hz, $2\text{OCH}_2\text{CH}_3$), 5.29 (s, 2H, CH_2), 6.01 (s, 1H, pyrimidine H-2), 7.27–7.38 (m, 4H, C_6H_4), 8.28 (s, 1H, D_2O exchangeable, NH); ^{13}C NMR (75 MHz, $\text{DMSO}-d_6$) δ 16.3, 16.5 ($2\text{OCH}_2\text{CH}_3$), 28.1 (CH_2), 52.1, 53.8 ($2\text{OCH}_2\text{CH}_3$), 92.6 (pyrimidine C-2), 117.8 (CN), 122.4, 124.8, 125.6, 126.3, 128.6, 143.8, (C_6H_4 , thiadiazine C-5, C-6), 163.8, 164.4, 165.2 (3CO); Anal. Calcd. for $\text{C}_{18}\text{H}_{18}\text{N}_4\text{O}_5\text{S}$ (402.42): C, 53.72; H, 4.51; N, 13.92; S, 7.97. Found: C, 53.92; H, 4.61; N, 14.05; S, 8.29; EI-MS (m/z , %): 402 [M^+ , 18].

Diethyl 2-(2-ethoxy-2-oxoethyl)-6-oxo-4a,6-dihydro-[1,3,4]thiadiazino[3,2-a]quinazoline-3,5(1H)-dicarboxylate (16b)

Pale yellow crystals from 1,4-dioxane; m.p. 132–135 °C; IR (KBr) ν_{max} 3468–3341 (NH), 3056 (CH aromatic), 1689–1683 (4CO), 1630 (C=C) cm^{-1} ; ^1H NMR (200 MHz, $\text{DMSO}-d_6$) δ 1.12–1.15 (3t, 9H, $3\text{OCH}_2\text{CH}_3$), 4.16–4.20 (3q, 6H, $3\text{OCH}_2\text{CH}_3$), 5.29 (s, 2H, CH_2), 6.01 (s, 1H, pyrimidine H-2), 7.27–7.38 (m, 4H, C_6H_4), 8.28 (s, 1H, D_2O exchangeable, NH); ^{13}C NMR (75 MHz, $\text{DMSO}-d_6$) δ 16.3, 16.4, 16.9 (three OCH_2CH_3), 28.1 (CH_2), 52.6, 52.9, 53.8 (three OCH_2CH_3), 92.6 (pyrimidine C-2), 120.8, 122.4, 123.9, 125.3, 125.8, 129.3, 141.3, 144.2 (C_6H_4 , thiadiazine C-5, C-6), 163.3, 163.8, 164.4, 165.8 (4CO); Anal. Calcd. for $\text{C}_{20}\text{H}_{23}\text{N}_3\text{O}_7\text{S}$ (449.48): C, 53.44; H, 5.16; N, 9.35; S, 7.13. Found: C, 53.28; H, 5.28; N, 9.53; S, 7.32; EI-MS (m/z , %): 449 [M^+ , 48].

3. 1. 6. General procedure for the synthesis of the pyran derivatives 19a–4

To a solution of compound **12** (3.06 g, 0.01 mol) in 1,4-dioxane (40 mL) containing triethylamine (0.50 mL) any of benzaldehyde (1.06 g, 0.01 mol), 4-chlorobenzaldehyde (1.40 g, 0.01 mol) or 4-methoxybenzaldehyde (1.36 g, 0.01 mol) and either of malononitrile (0.66 g, 0.01 mol) or

ethyl cyanoacetate (1.13 g, 0.01 mol) were added. The whole reaction mixture was heated under reflux for 3 h then left to cool and the formed solid product, in each case, was collected by filtration.

Ethyl 2-((6-amino-5-cyano-2-(4-methoxyphenyl)-4-phenyl-4H-pyran-3-yl)thio)-4-oxoquinazoline-3(4H)-carboxylate (19a)

Yellow crystals from ethanol; m.p.: 188–190 °C; IR (KBr) ν_{max} 3469–3316 (NH₂), 2223 (CN), 3056 (CH aromatic), 2984, 2870 (CH₃, CH₂), 1688, 1686 (2CO), 1652 (C=N), 1630 (C=C) cm⁻¹; ¹H NMR (200 MHz, DMSO-*d*₆) δ 1.14 (t, 3H, *J* = 7.18 Hz, OCH₂CH₃), 3.65 (s, 3H, OCH₃), 4.22 (q, 2H, *J* = 7.18 Hz, OCH₂CH₃), 4.58 (s, 2H, D₂O exchangeable, NH₂), 6.92 (s, 1H, pyran H-4), 7.27–7.36 (m, 13H, C₆H₅, 2C₆H₄); ¹³C NMR (75 MHz, DMSO-*d*₆) δ 16.2 (OCH₂CH₃), 52.8 (OCH₃), 55.3 (OCH₂CH₃), 59.6 (pyran C-4), 116.6 (CN), 119.6, 120.8, 122.5, 125.5, 127.4, 127.8, 130.9, 134.4, 136.8, 137.9, 138.8, 139.2, 140.6, 141.3, 142.6, 144.6 (C₆H₅, 2C₆H₄, pyran C), 164.3, 164.8 (2CO), 174.8 (C=N); Anal. Calcd. for C₃₀H₂₄N₄O₅S (552.60): C, 65.20; H, 4.38; N, 10.14; S, 5.80. Found: C, 65.42; H, 4.63; N, 9.87; S, 5.83; EI-MS (*m/z*, %): 552 [M⁺, 25].

Ethyl 2-((5-cyano-6-hydroxy-2-(4-methoxyphenyl)-4-phenyl-4H-pyran-3-yl)thio)-4-oxoquinazoline-3(4H)-carboxylate (19b)

Yellow crystals from 1,4-dioxane; m.p.: 203–205 °C; IR (KBr) ν_{max} 3583–3327 (OH), 2222 (CN), 3058 (CH aromatic), 2986 (CH₃), 1687, 1665 (2CO), 1650 (C=N), 1632 (C=C) cm⁻¹; ¹H NMR (200 MHz, DMSO-*d*₆) δ 1.14 (t, 3H, *J* = 6.80 Hz, OCH₂CH₃), 3.67 (s, 3H, OCH₃), 4.26 (q, 2H, *J* = 6.80 Hz, OCH₂CH₃), 6.94 (s, 1H, pyran H-4), 7.24–7.43 (m, 13H, C₆H₅, 2C₆H₄), 10.33 (s, 1H, D₂O exchangeable, OH); ¹³C NMR (75 MHz, DMSO-*d*₆) δ 16.1 (OCH₂CH₃), 52.6 (CH₃), 55.1 (OCH₂CH₃), 59.2 (pyran C-4), 116.7 (CN), 120.2, 120.6, 121.9, 124.9, 126.2, 127.1, 129.1, 131.4, 132.3, 133.9, 134.2, 136.3, 138.5, 139.0, 141.2, 141.8, 142.9, 143.7 (C₆H₅, 2C₆H₄, pyran C), 164.5, 164.7 (2CO), 174.3 (C=N); Anal. Calcd. for C₃₀H₂₃N₃O₆S (553.59): C, 65.09; H, 4.19; N, 7.59; S, 5.79. Found: C, 65.28; H, 4.38; N, 7.62; S, 5.68; EI-MS (*m/z*, %): 553 [M⁺, 32].

Ethyl 2-((6-amino-4-(4-chlorophenyl)-5-cyano-2-(4-methoxyphenyl)-4H-pyran-3-yl)thio)-4-oxoquinazoline-3(4H)-carboxylate (19c)

Yellow crystals from ethanol; m.p.: 166–169 °C; IR (KBr) ν_{max} 3472, 3329 (NH₂), 2220 (CN), 3052 (CH aromatic), 2986 (CH₃), 1688, 1686 (2CO), 1653 (C=N), 1633 (C=C) cm⁻¹; ¹H NMR (200 MHz, DMSO-*d*₆) δ 1.13 (t, 3H, *J* = 6.29 Hz, OCH₂CH₃), 3.69 (s, 3H, OCH₃), 4.19 (q, 2H, *J* = 6.29 Hz, OCH₂CH₃), 4.28 (s, 2H, D₂O exchangeable, NH₂), 6.91 (s, 1H, pyran H-4), 7.25–7.48 (m, 12H, 3C₆H₄); ¹³C NMR (75 MHz, DMSO-*d*₆) δ 16.1 (OCH₂CH₃), 52.6 (CH₃), 54.3 (OCH₂CH₃), 59.3 (pyran C-4), 116.4 (CN),

120.3, 121.3, 122.4, 123.5, 126.8, 127.8, 129.1, 130.2, 132.3, 132.7, 134.0, 135.2, 138.9, 139.3, 140.0, 141.4, 142.5, 143.9 (3C₆H₄, pyran C), 164.3, 165.0 (2CO), 174.6 (C=N); Anal. Calcd. for C₃₀H₂₃ClN₄O₅S (587.05): C, 61.38; H, 3.95; N, 9.54; S, 5.46. Found: C, 61.27; H, 4.04; N, 9.59; S, 5.53; EI-MS (*m/z*, %): 587 [M⁺, 28].

Ethyl 2-((4-(4-chlorophenyl)-5-cyano-6-hydroxy-2-(4-methoxyphenyl)-4H-pyran-3-yl)thio)-4-oxoquinazoline-3(4H)-carboxylate (19d)

Pale yellow crystals from 1,4-dioxane; m.p.: 193–195 °C; IR (KBr) ν_{max} 3563–3336 (OH), 2221 (CN), 3054 (CH aromatic), 2987 (CH₃), 1689, 1687 (2CO), 1650 (C=N), 1632 (C=C) cm⁻¹; ¹H NMR (200 MHz, DMSO-*d*₆) δ 1.15 (t, 3H, *J* = 7.37 Hz, OCH₂CH₃), 3.69 (s, 3H, CH₃), 4.19 (q, 2H, *J* = 7.37 Hz, OCH₂CH₃), 6.91 (s, 1H, pyran H-4), 7.25–7.46 (m, 12H, 3C₆H₄), 10.31 (s, 1H, D₂O exchangeable, OH); ¹³C NMR (75 MHz, DMSO-*d*₆) δ 16.4 (OCH₂CH₃), 52.4 (CH₃), 54.8 (OCH₂CH₃), 59.4 (pyran C-4), 116.4 (CN), 120.3, 121.4, 123.6, 126.0, 127.3, 129.6, 130.9, 131.6, 132.8, 133.4, 134.5, 135.1, 136.8, 138.3, 141.1, 142.3, 142.9, 143.4 (3C₆H₄, pyran C), 164.2, 164.5 (2CO), 174.6 (C=N); Anal. Calcd. for C₃₀H₂₂ClN₃O₆S (588.03): C, 61.28; H, 3.77; N, 7.15; S, 5.45. Found: C, 61.18; H, 3.80; N, 7.29; S, 5.64; EI-MS (*m/z*, %): 588 [M⁺, 25].

Ethyl 2-((6-amino-5-cyano-2,4-bis(4-methoxyphenyl)-4H-pyran-3-yl)thio)-4-oxoquinazoline-3(4H)-carboxylate (19e)

Yellow crystals from ethanol; m.p.: 148–150 °C; IR (KBr) ν_{max} 3468–3315 (NH₂), 3056 (CH aromatic), 2987 (CH₃), 2220 (CN), 1689, 1687 (2CO), 1633 (C=C) cm⁻¹; ¹H NMR (200 MHz, DMSO-*d*₆) δ 1.13 (t, 3H, *J* = 7.26 Hz, OCH₂CH₃), 3.67, 3.72 (2s, 6H, 2 OCH₃), 4.19 (q, 2H, *J* = 7.26 Hz, OCH₂CH₃), 4.28 (s, 2H, D₂O exchangeable, NH₂), 6.93 (s, 1H, pyran H-4), 7.24–7.49 (m, 12H, 3C₆H₄); ¹³C NMR (75 MHz, DMSO-*d*₆) δ 16.0 (OCH₂CH₃), 52.6, 53.2 (2 OCH₃), 54.3 (OCH₂CH₃), 59.1 (pyran C-4), 116.4 (CN), 120.6, 121.8, 123.9, 125.8, 127.9, 128.8, 131.6, 132.6, 133.8, 134.8, 135.3, 135.6, 136.3, 137.1, 140.9, 142.1, 143.0, 143.5 (3C₆H₄, pyran C), 164.3, 164.8 (2CO), 174.4 (C=N); Anal. Calcd. for C₃₁H₂₆N₄O₆S (582.63): C, 63.91; H, 4.50; N, 9.62; S, 5.50. Found: C, 63.73; H, 4.53; N, 9.63; S, 5.72; EI-MS (*m/z*, %): 582 [M⁺, 18].

Ethyl 2-((5-cyano-6-hydroxy-2,4-bis(4-methoxyphenyl)-4H-pyran-3-yl)thio)-4-oxoquinazoline-3(4H)-carboxylate (19f)

Yellow crystals from ethanol; m.p.: 242–246 °C; IR (KBr) ν_{max} 3530–3336 (OH), 3056 (CH aromatic), 2986 (CH₃), 2221 (CN), 1689, 1687 (2CO), 1634 (C=C) cm⁻¹; ¹H NMR (200 MHz, DMSO-*d*₆) δ 1.14 (t, 3H, *J* = 6.52 Hz, OCH₂CH₃), 3.66, 3.73 (2s, 6H, 2 OCH₃), 4.20 (q, 2H, *J* = 6.52 Hz, OCH₂CH₃), 6.90 (s, 1H, pyran H-4), 7.23–7.48 (m, 12H, 3C₆H₄), 10.37 (s, 1H, D₂O exchangeable, OH); ¹³C NMR (75 MHz, DMSO-*d*₆) δ 16.4 (OCH₂CH₃), 52.8,

53.4 (2 OCH₃), 54.6 (OCH₂CH₃), 59.0 (pyran C-4), 116.7 (CN), 120.2, 123.1, 124.2, 126.8, 127.9, 129.4, 131.8, 133.3, 133.8, 134.3, 135.3, 135.6, 136.3, 137.1, 141.3, 142.6, 142.50, 143.9 (3C₆H₄, pyran C), 164.3, 164.6 (2CO), 174.8 (C=N); Anal. Calcd. for C₃₄H₂₅N₃O₇S (583.61): C, 63.80; H, 4.32; N, 7.20; S, 5.49. Found: C, 63.69; H, 4.48; N, 7.29; S, 5.53; EI-MS (*m/z*, %): 583 [M⁺, 18].

3. 1. 7. General procedure for the synthesis of the pyridine derivatives 21a–f

To a solution of compound **12** (3.06 g, 0.01 mol) in 1,4-dioxane (40 mL) containing ammonium acetate (0.50 g) any of benzaldehyde (1.06 g, 0.01 mol), 4-chlorobenzaldehyde (1.40 g, 0.01 mol) or 4-methoxybenzaldehyde (1.36 g, 0.01 mol) and either of malononitrile (0.66 g, 0.01 mol) or ethyl cyanoacetate (1.13 g, 0.01 mol) were added. The whole reaction mixture was heated under reflux for 3 h then left to cool and the formed solid product, in each case, was collected by filtration.

Ethyl 2-((6-amino-5-cyano-2-(4-methoxyphenyl)-4-phenyl-1,4-dihydropyridin-3-yl)thio)-4-oxoquinazoline-3(4H)-carboxylate (21a)

Yellow crystals from ethanol; m.p.: 231–235 °C; IR (KBr) ν_{max} 3483–3342 (NH, NH₂), 2220 (CN), 3054 (CH aromatic), 2989 (CH₃), 1689, 1687 (2CO), 1656 (C=N), 1630 (C=C) cm⁻¹; ¹H NMR (200 MHz, DMSO-*d*₆) δ 1.15 (t, 3H, *J* = 7.28 Hz, OCH₂CH₃), 3.66 (s, 3H, CH₃), 4.23 (q, 2H, *J* = 7.28 Hz, OCH₂CH₃), 4.59 (s, 2H, D₂O exchangeable, NH₂), 6.89 (s, 1H, pyridine H-4), 7.27–7.38 (m, 13H, C₆H₅, 2C₆H₄), 8.29 (s, 1H, D₂O exchangeable NH); ¹³C NMR (75 MHz, DMSO-*d*₆) δ 16.1 (OCH₂CH₃), 52.5 (CH₃), 54.1 (OCH₂CH₃), 59.5 (pyridine C-4), 116.5 (CN), 120.8, 121.6, 123.1, 125.8, 126.9, 128.3, 128.9, 129.6, 132.3, 131.6, 135.2, 136.5, 138.3, 139.7, 140.3, 142.6, 143.3, 144.3 (C₆H₅, C₆H₄, pyridine C), 164.2, 164.7 (2CO), 174.3 (C=N); Anal. Calcd. for C₃₀H₂₅N₅O₄S (551.62): C, 65.32; H, 4.57; N, 12.70; S, 5.81. Found: C, 65.48; H, 4.61; N, 12.87; S, 5.92; EI-MS (*m/z*, %): 551 [M⁺, 25].

Ethyl 2-((5-cyano-6-hydroxy-2-(4-methoxyphenyl)-4-phenyl-1,4-dihydropyridin-3-yl)thio)-4-oxoquinazoline-3(4H)-carboxylate (21b)

Yellow crystals from 1,4-dioxane; m.p.: 230–233 °C; IR (KBr) ν_{max} 3571–3320 (OH, NH), 3055 (CH aromatic), 2989 (CH₃), 2220 (CN), 1689, 1684 (2CO), 1653 (C=N), 1630 (C=C) cm⁻¹; ¹H NMR (200 MHz, DMSO-*d*₆) δ 1.14 (t, 3H, *J* = 6.89 Hz, OCH₂CH₃), 3.68 (s, 3H, CH₃), 4.22 (q, 2H, *J* = 6.89 Hz, OCH₂CH₃), 6.93 (s, 1H, pyridine H-4), 7.26–7.46 (m, 13H, C₆H₅, 2C₆H₄), 8.23 (s, 1H, D₂O exchangeable, NH), 10.33 (s, 1H, D₂O exchangeable, OH); ¹³C NMR (75 MHz, DMSO-*d*₆) δ 16.4 (OCH₂CH₃), 52.8 (CH₃), 54.6 (OCH₂CH₃), 59.9 (pyridine C-4), 116.7 (CN), 120.4, 121.2, 121.9, 122.6, 125.9, 126.2, 128.2, 129.2, 131.7, 132.3, 134.2, 136.3, 138.5, 139.0, 139.6, 141.8, 142.9, 143.8

(C₆H₅, 2C₆H₄, pyridine C), 164.2, 164.8 (2CO), 174.6 (C=N); Anal. Calcd. for C₃₀H₂₄N₄O₅S (552.60): C, 65.20; H, 4.38; N, 10.14; S, 5.80. Found: C, 65.14; H, 4.42; N, 10.08; S, 5.72; EI-MS (*m/z*, %): 552 [M⁺, 32].

Ethyl 2-((5-cyano-6-hydroxy-2-(4-methoxyphenyl)-4-phenyl-1,4-dihydropyridin-3-yl)thio)-4-oxoquinazoline-3(4H)-carboxylate (21c)

Yellow crystals from ethanol; m.p.: 184–187 °C; IR (KBr) ν_{max} 3480, 3323 (NH₂, NH), 3054 (CH aromatic), 2988 (CH₃), 2220 (CN), 1687, 1683 (2CO), 1656 (C=N), 1633 (C=C) cm⁻¹; ¹H NMR (200 MHz, DMSO-*d*₆) δ 1.13 (t, 3H, *J* = 7.01 Hz, OCH₂CH₃), 3.66 (s, 3H, OCH₃), 4.19 (q, 2H, *J* = 7.01 Hz, OCH₂CH₃), 4.68 (s, 2H, D₂O exchangeable, NH₂), 6.93 (s, 1H, pyridine H-4), 7.22–7.45 (m, 12H, 3C₆H₄), 8.28 (s, 1H, D₂O exchangeable, NH); ¹³C NMR (75 MHz, DMSO-*d*₆) δ 16.3 (OCH₂CH₃), 52.8 (OCH₃), 54.3 (OCH₂CH₃), 59.6 (pyridine C-4), 116.7 (CN), 120.3, 122.0, 123.5, 124.6, 126.8, 127.4, 129.0, 130.2, 132.3, 132.7, 134.0, 135.2, 138.9, 139.3, 140.0, 141.4, 142.5, 143.9 (3C₆H₄, pyridine C), 164.2, 164.6 (2CO), 174.8 (C=N); Anal. Calcd. for C₃₀H₂₄ClN₅O₄S (586.06): C, 61.48; H, 4.13; N, 11.95; S, 5.47. Found: C, 61.53; H, 4.24; N, 12.28; S, 5.60; EI-MS (*m/z*, %): 586 [M⁺, 36].

Ethyl 2-((4-(4-chlorophenyl)-5-cyano-6-hydroxy-2-(4-methoxyphenyl)-1,4-dihydropyridin-3-yl)thio)-4-oxoquinazoline-3(4H)-carboxylate (21d)

Yellow crystals from 1,4-dioxane; m.p.: 166–168 °C; IR (KBr) ν_{max} 3572–3333 (OH, NH), 2221 (CN), 3054 (CH aromatic), 2987 (CH₃), 1689, 1684 (2CO), 1650 (C=N), 1632 (C=C) cm⁻¹; ¹H NMR (200 MHz, DMSO-*d*₆) δ 1.13 (t, 3H, *J* = 6.47 Hz, OCH₂CH₃), 3.69 (s, 3H, OCH₃), 4.18 (q, 2H, *J* = 6.47 Hz, OCH₂CH₃), 6.90 (s, 1H, pyridine H-4), 7.22–7.46 (m, 12H, 3C₆H₄), 8.28 (s, 1H, D₂O exchangeable, NH), 10.31 (s, 1H, D₂O exchangeable, OH); ¹³C NMR (75 MHz, DMSO-*d*₆) δ 16.6 (OCH₂CH₃), 52.6 (OCH₃), 54.6 (OCH₂CH₃), 59.4 (pyridine C-4), 116.6 (CN), 120.6, 122.8, 123.4, 125.2, 126.8, 127.3, 130.9, 131.3, 132.5, 133.4, 134.5, 135.5, 136.8, 138.3, 141.0, 142.3, 142.9, 143.6 (3C₆H₄ pyran C), 164.2, 164.8 (2CO), 174.6 (C=N); Anal. Calcd. for C₃₀H₂₃ClN₄O₅S (587.05): C, 61.38; H, 3.95; N, 9.54; S, 5.46. Found: C, 61.42; H, 3.69; N, 9.70; S, 5.59; EI-MS (*m/z*, %): 587 [M⁺, 48].

Ethyl 2-((6-amino-5-cyano-2,4-bis(4-methoxyphenyl)-1,4-dihydropyridin-3-yl)thio)-4-oxoquinazoline-3(4H)-carboxylate (21e)

Yellow crystals from ethanol; m.p.: 148–152 °C; IR (KBr) ν_{max} 3468–3315 (NH₂, NH), 3056 (CH aromatic), 2987 (CH₃), 2220 (CN), 1689, 1682 (2CO), 1633 (C=C) cm⁻¹; ¹H NMR (200 MHz, DMSO-*d*₆) δ 1.14 (t, 3H, *J* = 7.19 Hz, OCH₂CH₃), 3.65, 3.74 (2s, 6H, 2 OCH₃), 4.20 (q, 2H, *J* = 7.19 Hz, OCH₂CH₃), 4.67 (s, 2H, D₂O exchangeable, NH₂), 6.91 (s, 1H, pyridine H-4), 7.25–7.47 (m, 12H, 3C₆H₄), 8.30 (s, 1H, D₂O exchangeable, NH); ¹³C NMR

(75 MHz, DMSO- d_6) δ 16.3 (OCH₂CH₃), 52.5, 53.8 (2CH₃), 54.6 (OCH₂CH₃), 59.5 (pyridine C-4), 116.8 (CN), 119.3, 123.4, 124.1, 124.5, 128.3, 129.6, 130.3, 132.8, 134.3, 134.8, 135.6, 136.3, 137.1, 140.9, 142.7, 143.5, 143.5 (3C₆H₄, pyridine C), 163.9, 164.5 (2CO), 174.6 (C=N); Anal. Calcd. for C₃₁H₂₇N₅O₅S (581.64): C, 64.01; H, 4.68; N, 12.04; S, 5.51. Found: C, 63.93; H, 4.56; N, 11.84; S, 5.69; EI-MS (m/z , %): 581 [M⁺, 22].

Ethyl 2-((5-cyano-6-hydroxy-2,4-bis(4-methoxyphenyl)-1,4-dihydropyridin-3-yl)thio)-4-oxoquinazoline-3(4H)-carboxylate (21f)

Yellow crystals from ethanol; m.p.: 263–265 °C; IR (KBr) ν_{\max} 3548–3322 (OH NH), 3054 (CH aromatic), 2987 (CH₃), 2221 (CN), 1688, 1684 (2CO), 1635 (C=C) cm⁻¹; ¹H NMR (200 MHz, DMSO- d_6) δ 1.13 (t, 3H, J = 7.08 Hz, OCH₂CH₃), 3.62, 3.73 (2s, 6H, 2 OCH₃), 4.21 (q, 2H, J = 7.08 Hz, OCH₂CH₃), 6.91 (s, 1H, pyridine H-4), 7.25–7.48 (m, 12H, 3C₆H₄), 8.26 (s, 1H, D₂O exchangeable, NH), 10.31 (s, 1H, D₂O exchangeable, OH); ¹³C NMR (75 MHz, DMSO- d_6) δ 16.1 (OCH₂CH₃), 52.4, 53.8 (2CH₃), 54.4 (OCH₂CH₃), 59.6 (pyridine C-4), 116.6 (CN), 119.6, 121.8, 128.3, 130.3, 133.6, 133.8, 135.8, 136.1, 136.3, 137.1, 140.2, 142.3, 143.5, 143.8 (3C₆H₄, pyridine C), 164.1, 164.3 (2CO), 174.3 (C=N); Anal. Calcd. for C₃₁H₂₆N₄O₆S (582.63): C, 63.91; H, 4.50; N, 9.62; S, 5.50. Found: C, 63.88; H, 4.53; N, 9.71; S, 5.73; EI-MS (m/z , %): 582 [M⁺, 31].

Synthesis of the thiazole synthesis of the thiazole derivatives 24a–c

To a solution of compound **8** (3.36 g, 0.01 mol) in dimethylformamide (40 mL) containing potassium hydroxide (0.40 g, 0.01 mol), phenylisothiocyanate (1.30 g, 0.01 mol) was added. The reaction mixture was stirred at room temperature for 24 h. On the second day any of ethyl chloroacetate (1.22 g, 0.01 mol), α -chloroacetone (0.92 g, 0.01 mol) or 2-bromo-1-(4-bromophenyl)ethanone (2.75 g, 0.01 mol) was added. The whole reaction mixture was stirred at room temperature for an additional 24 h then poured onto ice/water containing a few drops of hydrochloric acid and the formed solid product was collected by filtration.

Ethyl 2-((2-ethoxy-1-(4-hydroxy-3-phenylthiazol-2(3H)-ylidene)-2-oxoethyl)thio)-4-oxo-quinazoline-3(4H)-carboxylate (24a)

Orange crystals from ethanol; m.p.: 193–196 °C; IR (KBr) ν_{\max} 3562–3345 (OH), 3055 (CH aromatic), 2985, 2889 (CH₃, CH₂), 1689, 1685, 1682 (3CO), 1632 (C=C) cm⁻¹; ¹H NMR (200 MHz, DMSO- d_6) δ 1.13, 1.15 (2t, 6H, J = 6.59, 6.18 Hz, 2 OCH₂CH₃), 4.18, 4.26 (2q, 4H, J = 6.59, 6.18 Hz, 2 OCH₂CH₃), 6.06 (s, 1H, thiazole H-5), 7.28–7.41 (m, 9H, C₆H₅, C₆H₄), 9.42 (s, 1H, D₂O exchangeable, OH); ¹³C NMR (75 MHz, DMSO- d_6) δ 16.1, 16.8 (2 OCH₂CH₃), 54.2, 54.6 (2 OCH₂CH₃), 84.5, 148.2 (C=C),

119.3, 124.1, 124.5, 128.3, 130.3, 132.8, 134.3, 135.6, 135.6, 137.1, 142.7, 143.5 (C₆H₅, C₆H₄, thiazole C-4, C-5), 163.4, 164.3, 164.6 (3CO), 174.4 (C=N); Anal. Calcd. for C₂₄H₂₁N₃O₆S₂ (511.57): C, 56.35; H, 4.14; N, 8.21; S, 12.54. Found: C, 56.48; H, 4.32; N, 8.40; S, 12.70; EI-MS (m/z , %): 511 [M⁺, 38].

Ethyl 2-((2-ethoxy-1-(4-methyl-3-phenylthiazol-2(3H)-ylidene)-2-oxoethyl)thio)-4-oxoquinazoline-3(4H)-carboxylate (24b)

Orange crystals from acetic acid; m.p.: 205–208 °C; IR (KBr) ν_{\max} 3053 (CH aromatic), 2989, 2884 (CH₃, CH₂), 1688, 1686, 1680 (3CO), 1634 (C=C) cm⁻¹; ¹H NMR (200 MHz, DMSO- d_6) δ 1.14, 1.15 (2t, 6H, J = 7.26, 6.37 Hz, 2 OCH₂CH₃), 2.80 (s, 3H, CH₃), 4.18, 4.23 (2q, 4H, J = 7.26, 6.37 Hz, 2 OCH₂CH₃), 6.07 (s, 1H, thiazole H-5), 7.26–7.44 (m, 9H, C₆H₅, C₆H₄); ¹³C NMR (75 MHz, DMSO- d_6) δ 16.6, 16.9 (two OCH₂CH₃), 54.6, 54.8 (two OCH₂CH₃), 69.1 (thiazole C-5), 88.6, 148.0 (C=C), 119.8, 124.3, 124.8, 129.1, 130.6, 133.2, 134.6, 135.4, 136.3, 137.5, 140.8, 143.7 (C₆H₅, C₆H₄, thiazole C-4, C-5), 163.8, 164.8, 164.9 (3CO), 174.2 (C=N); Anal. Calcd. for C₂₅H₂₃N₃O₆S₂ (509.60): C, 58.92; H, 4.55; N, 8.25; S, 12.58. Found: C, 58.79; H, 4.70; N, 8.39; S, 12.39; EI-MS (m/z , %): 509 [M⁺, 19].

Ethyl 2-((2-ethoxy-1-(4-(4-methoxyphenyl)-3-phenylthiazol-2(3H)-ylidene)-2-oxoethyl)thio)-4-oxoquinazoline-3(4H)-carboxylate (24c)

Orange crystals from acetic acid; m.p.: 177–179 °C; IR (KBr) ν_{\max} 3055 (CH aromatic), 2987, 2888 (CH₃, CH₂), 1689, 1686, 1683 (3CO), 1632 (C=C) cm⁻¹; ¹H NMR (200 MHz, DMSO- d_6) δ 1.16, 1.18 (2t, 6H, J = 7.42, 7.07 Hz, 2 OCH₂CH₃), 3.69 (s, 3H, OCH₃), 4.18, 4.23 (2q, 4H, J = 7.42, 7.07 Hz, 2 OCH₂CH₃), 6.06 (s, 1H, thiazole H-5), 7.22–7.48 (m, 13H, C₆H₅, 2C₆H₄); ¹³C NMR (75 MHz, DMSO- d_6) δ 16.6, 16.8 (two OCH₂CH₃), 52.6 (OCH₃), 54.3, 54.6 (two OCH₂CH₃), 69.3 (thiazole C-5), 88.7, 148.0 (C=C), 120.3, 122.4, 123.8, 124.1, 124.8, 125.6, 126.9, 129.2, 130.8, 133.2, 134.6, 135.4, 136.3, 137.6, 142.4, 143.5 (C₆H₅, C₆H₄, thiazole C-4, C-5), 163.3, 164.6, 164.5 (3CO), 174.5 (C=N); Anal. Calcd. for C₃₁H₂₇N₃O₆S₂ (601.69): C, 61.88; H, 4.52; N, 6.98; S, 10.66. Found: C, 61.79; H, 4.66; N, 7.05; S, 10.81; EI-MS (m/z , %): 601 [M⁺, 22].

4. Conclusions

The work deals with the synthesis of a series of 1,2-dihydroquinazoline derivatives. The cytotoxicity of the newly synthesized compounds towards the six cancer cell lines NUGC, DLD-1, HA22T, HEPG-2, HONE-1 and MCF-7 showed that compounds **6**, **8**, **13**, **19c–f**, **21b–f**, **24a** and **24c** displayed the highest cytotoxicity. The c-Met kinase inhibition for some selected compounds showed that compounds **8**, **13**, **19d**, **21e**, **21f** and **24a** possess the high-

est inhibitory effect. Activities towards tyrosine kinases revealed that compounds **13**, **21e** and **24a** have the highest potency. Compounds **13** and **24a** showed the highest activities towards Pim-1 kinase.

5. Acknowledgments

R. M. Mohareb would like to thank the Alexander von Humboldt for affording him regular fellowships in Germany for doing research and completing this work.

6. References

- M. A. H. Ismail, S. Barker, D. A. A. El Ella, K. A. M. Abouzeid, R. A. Toubar, M. H. Todd, *J. Med. Chem.* **2006**, *49*, 1526–1535. DOI:10.1021/jm050232e
- S. B. Mhaske, N. P. Argade, *Tetrahedron* **2006**, *62*, 9787–9826. DOI:10.1016/j.tet.2006.07.098
- J. B. Koepfli, J. A. Brockman, J. Moffat, *J. Am. Chem. Soc.* **1950**, *72*, 3323–3323. DOI:10.1021/ja01163a555
- H. Y. P. Choo, M. Kim, S. K. Lee, S. W. Kim, I. K. Chung, *Bioorg. Med. Chem.* **2002**, *10*, 517–523. DOI:10.1016/S0968-0896(01)00299-1
- J. Panchompoo, L. Aldous, M. Kabeshov, Ben S. Pilgrim, T. J. Donohoe, R. G. Compton, *New J. Chem.* **2012**, *36*, 1265–1272. DOI:10.1039/C2NJ21007J
- L. He, H. Li, J. Chen, X. F. Wu, *RSC Adv.* **2014**, *4*, 12065–12079. DOI:10.1039/c4ra00351a
- W. Y. Li, Y. X. Zong, J. K. Wang, Y. Y. Niu, *Chin. Chem. Lett.* **2014**, *25*, 575–578. DOI:10.1016/j.ccllet.2013.11.022
- F. R. Alexandre, A. Berecibar, T. Besson, *Tetrahedron Lett.* **2002**, *43*, 3911–3913. DOI:10.1016/S0040-4039(02)00619-6
- S. Oschatz, T. Brunzel, X. F. Wu, P. Langer, *Org. Biomol. Chem.* **2015**, *13*, 1150–1158. DOI:10.1039/C4OB02207F
- J. Chen, K. Natta, H. Neumann, X. F. Wu, *RSC Adv.* **2014**, *4*, 56502–56505. DOI:10.1039/C4RA11303A
- L. He, M. Sharif, H. Neumann, M. Beller, X. F. Wu, *Green Chem.* **2014**, *16*, 3763–3767. DOI:10.1039/c4gc00801d
- Z. Zhang, M. Wang, C. Zhang, Z. Zhang, J. Lua, F. Wang, *Chem. Commun.* **2015**, *51*, 9205–9207. DOI:10.1039/C5CC02785C
- D. Kumar, P. S. Jadhavar, M. Nautiyal, H. Sharma, P. K. Meena, L. Adane, S. Pancholia, A. K. Chakrabort, *RSC Adv.* **2015**, *5*, 30819–30825. DOI:10.1039/c5ra03888j
- B. Tanwar, P. Purohit, B. N. Raju, D. Kumar, D. N. Kommi, A. K. Chakraborti, *RSC Adv.* **2015**, *5*, 11873–11883. DOI:10.1039/C4RA16568C
- M. Rahman, I. Ling, N. Abdullah, R. Hashim, A. Hajra, *RSC Adv.* **2015**, *5*, 7755–7760. DOI:10.1039/c4ra16374e
- X. S. Wang, K. Yang, J. Zhou, S. J. Tu, *J. Comb. Chem.* **2010**, *12*, 417–421. DOI:10.1021/cc900174p
- Y. H. Shang, L. Y. Fan, X. X. Li, M. X. Liu, *Chin. Chem. Lett.* **2015**, *26*, 1355–1358. DOI:10.1016/j.ccllet.2015.07.026
- V. Alagarsamy, V. R. Solomon, M. Murugan, *Bioorg. Med. Chem.* **2007**, *15*, 4009–4015. DOI:10.1016/j.bmc.2007.04.001
- G. Gomathi, S. H. Dar, S. Thirumaran, S. Ciattini, S. Selvanayagam, *Compt. R. Chim.* **2015**, *18*, 499–510. DOI:10.1016/j.crci.2014.10.003
- S. P. Bahekar, N. D. Dahake, P. B. Sarode, H. S. Chandak, *Synlett* **2015**, 2575–2577. DOI:10.1055/s-0035-1560483
- F. Hatamjafari, *Organic Chem. Inter.* **2014**, 1–5. DOI:10.1155/2014/761209
- N. Azizi, M. R. Saidi, *J. Mol. Catal. A: Chem.* **2005**, *238*, 138–141. DOI:10.1016/j.molcata.2005.05.022
- M. R. Mahmoud, W. S. I. Abou-Elmagd, S. S. Abdelwahab, E. S. A. Soliman, *Synth. Commun.* **2013**, *43*, 1484–1490. DOI:10.1080/00397911.2011.642924
- I. Ghiviriga, B. El-Dien, M. El-Gendy, P. J. Steel, A. R. Katritzky, *Org. Biomol. Chem.* **2009**, *7*, 4110–4119. DOI:10.1039/b907577a
- A. V. D. Rao, B. P. Vykundeswararao, T. Bhaskarkumar, N. R. Jogdand, D. Kalita, J. K. D. Lilakar, V. Siddaiah, P. D. Sanasi, A. Raghunadh, *Tetrahedron Lett.* **2015**, 56 4714–4717. DOI:10.1016/j.tetlet.2015.06.004
- A. M. S. El-Sharief, Y. A. Ammar, Y. A. Mohamed, M. S. A. El-Gaby, *Heteroat. Chem.* **2002**, *13*, 291–298. DOI:10.1002/hc.10031
- B. Pawlewski, *Chem. Ber.* **1906**, *39*, 1732–1736. DOI:10.1002/cber.190603902109
- R. M. Mohareb, N. Y. M. Abdo, F. Al-farouk, *Acta Chim. Slov.* **2017**, *64*, 117–128. DOI:10.17344/acsi.2016.2920
- R. M. Mohareb, F. Al-Omran, M. A. Abdelaziz, R. A. Ibrahim, *Acta Chim. Slov.* **2017**, *64*, 349–364. DOI:10.17344/acsi.2017.3200
- O. Antypenko, S. Kovalenko, B. Rasulev, J. Leszczynski, *Acta Chim. Slov.* **2016**, *63*, 638–645. DOI:10.17344/acsi.2016.2464
- N. N. Elsayed, M. A. Abdelaziz, W. W. Wardakhan, R. M. Mohareb, *Steroids* **2016**, *107*, 98–111. DOI:10.1016/j.steroids.2015.12.023
- M. Mohareb, A. A. Mohamed, A. E. M. Abdallah, *Acta Chim. Slov.* **2016**, *63*, 227–240. DOI:10.17344/acsi.2015.1668
- R. M. Mohareb, N. Y. M. Abdo, A. A. Mohamed, *Anti-Cancer Agents in Medicinal Chemistry*, **2016**, *16*, 1043–1054. DOI:10.2174/1871520616666160310142204
- R. M. Mohareb, F. Al-Omran, *Steroids*, **2012**, *77*, 1551–1559. DOI:10.1016/j.steroids.2012.09.007
- R. M. Mohareb, S. M. Sherif, A. M. Sami, *Phosphorous Sulfur Silicon Relat. Elem.*, **1995**, *101*, 57–65. DOI:10.1080/10426509508042499
- R. M. Mohareb, N. A. Abbas, R. A. Ibrahim, *Acta Chim. Slov.*, **2013**, *60*, 583–594. DOI: chem-soc.si/60/60-3-583
- L. Liu, A. Siegmund, N. Xi, P. Kaplan-Lefko, K. Rex, A. Chen, J. Lin, J. Moriguchi, L. Berry, L. Y. Huang, Y. Teffera, Y. J. Yang, Y. H. Zhang, S. F. Bellon, M. Lee, R. Shimanovich, A. Bak, C. Dominguez, M. H. Norman, J. C. Harmange, I. Dussault, T. S. Kim, *J. Med. Chem.*, **2008**, *51*, 3688–3691. DOI: 10.1021/jm800401t
- M. L. Peach, N. Tan, N. Tan, S. J. Choyke, A. Giubellino, G. Athauda, T. R. Burke, M. C. Nicklaus, D. P. Bottaro, *J. Med. Chem.*, **2009**, *52*, 943–951. DOI: 10.1021/jm800791f

39. S. Li, Q. Huang, Y. Liu, X. Zhang, S. Liu, C. He, P. Gong, *Eur. J. Med. Chem.*, **2013**, *64*, 62–73.
DOI: 10.1016/j.ejmech.2013.04.001
40. L. Liu, A. Siegmund, N. Xi, P. Kaplan-Lefko, K. Rex, A. Chen, J. Lin, J. Moriguchi, L. Berry, L. Y. Huang, Y. Teffera, Y. J. Yang, Y. H. Zhang, S. F. Bellon, M. Lee, R. Shimanovich, A. Bak, C. Dominguez, M. H. Norman, J. C. Harmange, I. Dussault, T. S. Kim, *J. Med. Chem.*, **2008**, *51*, 3688–3691.
DOI: 10.1021/jm800401t
41. M. L. Peach, N. Tan, S. J. Choyke, A. Giubellino, G. Athauda, T. R. Burke Jr., M. C. Nicklaus, D. P. Bottaro, *J. Med. Chem.*, **2009**, *52*, 943–951. DOI: 10.1021/jm800791f
42. K. Li, Y. Li, D. Zhou, Y. Fan, H. Guo, T. Ma, J. Wen, D. Liu, L. Zhao, *Bioorg. Med. Chem.*, **2016**, *24*, 889–1897.
DOI:10.1016/j.bmc.2016.03.016
43. F. Qian, S. Engst, K. Yamaguchi, P. Yu, K. A. Won, L. Mock, T. Lou, J. Tan, C. Li, D. Tam, J. Loughheed, F. M. Yakes, F. Bentzien, W. Xu, T. Zaks, R. Wooster, J. Greshock, A. H. Joly, *Cancer Research*, **2009**, *69* 8009–8016.
DOI:10.1158/0008-5472.CAN-08-4889

Povzetek

Pri reakciji antranilne kisline z etoksikarbonilizotiocianatom nastane etil 4-okso-2-tioakso-1,2-dihidrokinazolin-3(4*H*)-karboksilat (**4**). Ugotovili smo, da reakcija spojine **4** s hidrazin hidratom in α -halokarbonilnimi derivati daje ali hidrazono ali *S*-alkilirane produkte. Izvedli smo tudi heterociklizacijske reakcije nekaterih *S*-alkiliranih derivatov **8** in **12** in na ta način pripravili tiofenske, tiazolne, piranske in piridinske derivate. Raziskali smo citotoksičnost novih sintetiziranih spojin na šest rakavih celičnih linij: NUGC, DLD-1, HA22T, HEPG-2, HONE-1 in MCF-7. Ugotovili smo, da spojine **8**, **10**, **16a**, **19d–f**, **21c**, **21e**, **21f**, **24a** in **24b** izkazujejo največjo citotoksičnost. Test inhibicije *c*-Met kinaze za nekatere izbrane spojine je pokazal, da derivati **8**, **13**, **19d**, **21e**, **21f** in **24a** predstavljajo najbolj aktivne spojine. Test s tirozin kinazo pa je razkril, da spojine **13**, **21e** in **24a** kažejo največjo inhibitorno aktivnost in zato smo zanje izvedli študijo molekulskega modeliranja. Dodatno se je pokazalo, da spojini **13** in **24a** izkazujeta največjo aktivnost na Pim-1 kinazo.

Scientific paper

Improving Polyaspartic Anti-Corrosion Coating Protective Properties with the use of Nano-silica

Arezoo Assarian^{1,*} and Sanja Martinez¹

¹ University of Zagreb, Faculty of Chemical Engineering and Technology, Department of Electrochemistry, Savska cesta 16/I, 10000 Zagreb, Croatia

* Corresponding author: E-mail: assarian@fkit.hr
Phone: +385991953086; Fax: +385 1 4597 260

Received: 12-01-2018

Abstract

The purpose of this study was to investigate and develop a polyaspartic coating, using nano-silica modified with an amino group (NH₂-) in order to enhance adhesion on metallic surfaces and increase the effectiveness of the coating protective action against corrosion. Seven samples of polyaspartic coating with different amounts of nano-silica were prepared and applied to low carbon steel plates. The results showed that only 2% of the nano-silica per total weight formulation gave excellent protective as well as physical properties to the coating. The unique result was non-agglomeration and compatibility of nano-particles with the other compounds in the formulation structure. Time dependant behaviour of the coatings was followed by the EIS, SEM and FTIR methods and by exposure in a salt spray chamber. The main advantage was superior mechanical and chemical resistance and durability of a single coat, the properties that reduce emission of VOC and overall cost of the coating application process.

Keywords: Polyaspartic coating; Nano-silica; Adhesion; Corrosion; Protective coating

1. Introduction

Nowadays, protective coating development is undergoing significant advances due to the new characteristics attained through the application of nano- and micro-fillers.¹⁻³ The coating producer's interest in scientific research is driven by the desire to differentiate their products from those of competitors, in the otherwise commodity based industry, by producing coatings of unique characteristics, while at the same time, meeting continually higher and more numerous demands imposed upon the coatings performance.⁴ A range of compulsory requirements is often prescribed for a coating product, in order to make it acceptable from economical and ecological aspects as well as rendering it durable under highly corrosive environments. A serious concern in the field of paint and coatings is that the product life exceeds the coating life, and all manufacturers of coatings are trying to extend the lifetime of coatings.⁵

From preparation to application of coatings on surfaces, there are many factors that are very important and intended to improve the lifetime of coatings. Some of the challenges that play a major role in decreasing the lifetime of coatings are listed below:⁶

- Lack of sufficient adhesion between the surface and coating film
- Low resistance of film coatings to sunlight exposure
- Meager stability of film coatings when exposed to humidity, or corrosive and abrasive environments
- Difficulty in securing stable film coatings due to difficulties in the application of two component coatings, multiple layers of coatings, the accuracy of measurement and application, and the achievement of uniform and homogenous film coatings
- Difficulty to produce an eco-friendly coatings with high performance properties because many of the coating properties are reinforced with organic and inorganic materials, which are hazardous and pollutants⁷
- Excessive energy, manpower, and financial expense
- Need to maintain and re-apply coatings on coated surfaces due to polymer ageing
- Lack of customer satisfaction due to quality, stability, performance, and overall cost of coating

The main purpose of this research is to formulate a new type of coating for metallic surfaces with the aim of alleviating the aforementioned problems. The general target was

to increase the productivity of a coating and decrease the volume of volatile organic compound emission. In particular, the study presents an investigation into polyaspartic coating polymer base improvement by using nano-silica filler.

2. Experimental Details

The manufacturer of the polyaspartic resin and its hardener used in this research is Covestro (Leverkusen, Germany, formerly Bayer Material Science).

The binder that was used was polyisocyanates with an aminofunctional co-reactant, because it has the ability to form as a high solid, solvent-free, and a topcoat polyurethane coating, whereas the hardener was a solvent-free aliphatic polyisocyanate. The weight ratio of polyisocyanate resin to hardener was 2:1. The diameter of SiO₂ nanoparticles was 10–20 nm, with a specific surface area of 90–130 m²/g obtained from IoLiTec Ionic Liquids Technologies GmbH (Heilbronn, Germany).

For the first step, the start formulation of the coating was considered. Choosing a suitable raw material with regard to the expected coating properties was the most important factor for the start formulation (Table 1).

Table 1. Initial composition of the formula

Binder	51%
Solvent	3%
Additives*	2.5%
Pigments/Extenders	43.5%
	100%

* Defoamer, rheology modifier, leveling agent, adhesion promoter, UV stabilizer, dispersing agent, anti-sedimentation agents.

The types of additives used in the coating formulation were carefully selected in order to improve the quality of the coating. One of the most important aims of the coating was to increase adhesion to the metal/coating interface. For this reason, the adhesion promoter Byk-4510 (a solution of a hydroxy-functional copolymer with acidic groups) produced by the company was used and the concentration of Byk-4510 was 1.1% based on the total formulation.

In addition, some other different additives were used in order to improve the impact, warp, and scratch resistance and to increase flexibility.

According to recommendations by the nano-silicon oxide manufacturer, the range of use was between 0.1–2.0% of the weight of the total coating formulation (Table 2).

The samples were produced by increasing the nano-silica percentage. Then their qualities and properties were evaluated respectively in a mechanical laboratory test.⁹

The metal panels were prepared by surface preparation method Sa 2.5 from mild steel 2 mm thick) with dimensions of 15 × 10 cm. Using airless spray, the panels were coated with PA7, then after 48 hours they were ready

Table 2. Produced samples using a different amount of the nano-silica

No.	Name of the sample	Amount of nano-silicon oxide (per weight of total formulation)
1	PA1	0.1%
2	PA2	0.5%
3	PA3	0.9%
4	PA4	1.2%
5	PA5	1.6%
6	PA6	1.9%
7	PA7	2.0%

to set in a salt spray cabinet SF/100 CW (5% NaCl 99.8% and 38 °C).

Three coated samples with PA7 were considered: 1) PA7-N without any cuts on the surface, 2) PA7-1 with a 7 cm cut in the center of the panels, 3) PA7-2 with x-cut (7 cm per cut) in the center of the panel. The degradation of sample PA7 was examined by Fourier transform infrared spectroscopy (FTIR) (PerkinElmer spectrometer Spectrum One, USA) during the exposure in salt chamber. The recorded spectra were in the range of 650 to 4000 cm⁻¹ and under the standard ASTM E1252-98(2007).

The electrochemical impedance spectroscopy (EIS) of the sample PA7 exposed to 3% NaCl was measured by PalmSens3 potentiostat during 446 days. The procedure was done according to ISO 16773-1 to 4.

Finally, the polyaspartic coating (sample PA7) was applied to the panel with dimensions of 2 × 2 cm of low carbon steel and analyzed by SEM and EDX (Tescan Vega III, SBU EasyProbe scanning electron microscope) in order to examine the existing agglomeration of nano-particles in the coating structure. Scanning electron microscopy was conducted with the use of the Tescan Vega III, SBU Easyprobe devices, with a tungsten filament, at a charge of 10 kV (to obtain the picture) and 20 kV (to obtain the X-ray spectrum). Before testing, the sample was steamed with a conductive layer of gold and palladium.¹⁰

3. Results and Discussion

After the coating film on the metal surface dries, it plays a protective role against mechanical and chemical damage. The hardness of the dried coating film is as important as its flexibility. Both of these properties are indirectly related to coating adhesion. If the dried coating film is very hard after the first reverse impact test on the coated metal surface, it creates many micro cracks, which lead to the penetration of humidity, dust, grease, and contaminants under the coating/metal interface layer, and a consequence of this penetration is the loss of adhesion in this area and separation of the dried coating film from the substrate.

The main structure of the investigated resin is created by the reaction between an aliphatic isocyanate and an aspartic acid ester to create a polyaspartic resin with a urea structure (Fig.1).

This resin has excellent properties such as: fast curing even at ambient temperature, durability, and chemical

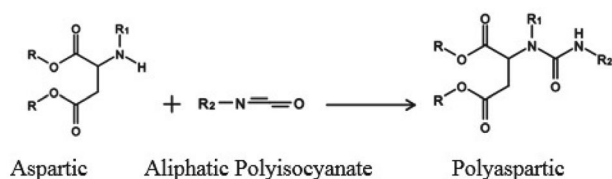


Figure 1. Chemical structure of a polyaspartic coating

resistance. Its two components, high film build and possibility of ultra-high solid content, offer potentially excellent resistance against mechanical damages.¹¹

The nano-silica particles were used (silicon oxide, SiO₂) as an additive in this coating in order to increase and improve adhesion and protective properties. But it was important to create compatibility between extenders, pigments and binder. A combination of anticorrosive pigments was used in the coating, which was improved by nano-silica and sufficient additives. The surface of the nano-silica was modified with an amino group. The reason for selecting this amino group nano-silica was that the alpha amino acid group was used in the coating structure. Besides, it seemed that use of nano-silica was required to increase the adhesion on the coating/metal interface.¹²

The first step was to make a coating sample based on the initial formula. For this purpose, a sufficient amount of polyaspartic acid ester resin was weighed and different additives were respectively added to the resin. It was important to add these additives in this formulation method sequentially. The second essential thing was to select the proper additives based on the chemical structure, because the chemical structures and compatibility of the selected additives were significant issues.¹³ These factors had a major influence on the characteristics of the coating in order to reach the main target, which was to enhance adhesion in the coating/metal interface.¹⁴ The next major property was surface wettability. Enhancing the degree of wetting is directly related to a suitable and comprehensive distribution of the pigment and extender particles. Therefore, it was necessary, at this stage, to improve the dispersal and wetting of the solid particles in the resin.^{12–15}

Samples PA1 and PA2 were rejected because there was flocculation and unstabilized pigment, blushing, and pinholes, which after 24 hours began creating sedimentation and created a sticky layer on the bottom of the coating cans (Figs. 2 and 3).^{16–18}

These problems did not appear immediately in samples PA3 and PA4. There was no visual defect in the

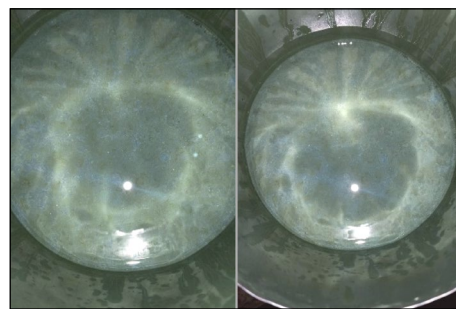


Figure 2. Samples PA1 and PA2 in the can with visible flocculation, unstabilized pigment in vehicle and blushing.

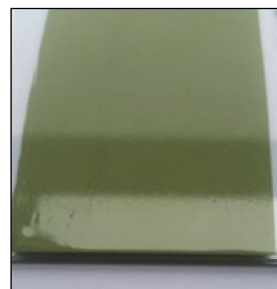


Figure 3. Excessive pinholes on the dried film coating of PA1 and PA2.

liquid coatings but their particle size was not acceptable, so the result of adhesion test was 2B.¹⁸

Sample PA5, with 1.6% the nano-particles, was rejected because the results of impact and bending (coating flexibility) tests were not acceptable (the results according to ASTM D2794 were 35 cm direct impact and indirect impact, and coating flexibility according to ASTM D1737 resulted in 18 mm/180°, where an acceptable result is 4 mm/180°).¹⁹

In sample PA6, the amount of dispersing and surface agents were increased from 0.3% of total weight formulation to 0.8% thereof in order to achieve a better particle size result, but the coating was incompatible with the enhancing quantity of the dispersing agent, as well as nano-silica (Fig. 4).²⁰

So after careful consideration, it was concluded that chromium oxide (Cr₂O₃) was the cause of problems in

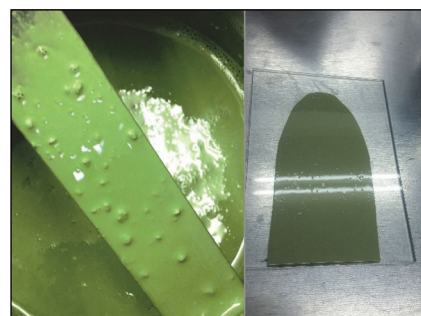


Figure 4. Incompatibility in sample PA6.

compatibility when the amount of the nano-silica was increased (Fig. 4).

Then sample PA7, with 2.0% nano-silica was formulated and consequently the quantity of additives was changed proportionally and the main coating formulation in this phase was modified, which eliminated the chromium oxide (Cr_2O_3). So after that the zinc aluminum orthophosphate hydrate ZPA (manufactured by Heubach GmbH) was used instead of chromium oxide (Cr_2O_3).²¹

The improved impenetrability property of the coating was achieved with a micronized rutile titanium dioxide pigment treated with alumina and zirconia compounds and a fumed silica that was surface-treated with polydimethylsiloxane (PDMS). These pigments were responsible for providing a well-balanced combination of high durability and very good optical properties and stable rheological performance over time.²²

The result was excellent, with remarkable improvement in adhesion in the coating/metal interface.

3. 1. Mechanical Results

The significant test results for PA6 are shown in Table 3. According to the mechanical test, film flexibility intensified due to a lack of sufficient adhesion in the interface PA6 /metal.

Adhesion should be improved as much as expected and appropriate to extend elongation of the coating and remedy related imperfections.^{1, 21}

Hence, some pigments in the main coating formulation were altered to enhance wetting, consequently reducing the surface tension that was responsible for the sufficient and spontaneous spread of the coating over metal surfaces.

As indicated by the data in Table 4, sample PA7 was a desirable and sought-after coating, as expected.

The final formulation was based on 2% nano-silica (99.8%, with amino group), but the main concern was the structure of nano-particles in the coating, because they have a tendency to be an elastomer. In this case, the coating wettability was expected to decrease, and to solve this problem two different vital additives were used to enhance the wetting and dispersing agent.^{23–25}

The molecule size of additives was quite important, so there is a possibility that large molecules in instant dispersant additives retain the nanoparticles inside their massive volume and trap them. This was considered in the selection of a nano-dispersing agent to disperse the nano-silica.²⁵

The wetting and dispersing additive structures are amphiphilic, which means both of them possess hydrophilic and lipophilic properties and the difference between them is that the wetting agent has a very low molecular weight and dispersing additives have a high molecular weight.²⁶

Generally, nano-silica may provide a high level of scratch and wear resistance that indirectly affect adhesion. It is clear that the adhesion strength of coating depends on many factors such as suitable wetting and spread of the liquid phase (coating), time, pressure, and temperature, the chemical compatibility of the material, surface roughness, etc.^{26–28}

Sample PA7 in the first step indicated a lack of adhesion after 1000h in the salt spray test, which was demonstrated by considerable blistering around the entire panel, as shown in Fig. 5.

This result showed that the amount of adhesion promoter and surface agent additive should be increased to enhance adhesion of sample PA7 under arduous situations and in case of mechanical damage.^{29,30}

The adhesion promoter (Byk-4510) that was used is a hydroxy-functional copolymer with acidic groups. Obviously the silicon-free adhesion promoter with acidic groups caused an intense chemical affinity, especially to metallic surfaces. BYK-4510 reacts with polyisocyanates and is consequently

Table 3. Mechanical result of sample PA6

No.	Name of test	Result	Acceptable result	Standard method
1	Fineness	15 micron	OK	ASTM D1210
2	Adhesion	4B	5B	ASTM D3359
3	Film Flexibility	10 mm/180°	4mm/180°	ASTM D522
4	Impact	Direct 55 cm Reverse 70 cm	Direct 80 cm Reverse 90 cm	ASTM D2794
5	Surface drying time 20 °C	48 min	30 min	ASTM D1640
6	Drying time 20 °C	1h and 53 min	1 h	ASTM D1640
7	Dry to handle 20 °C	11 h	5 h	ASTM D1640
8	Hardness by Konig after 7 days	181 s	250 s	ASTM D4366
9	Pot life	1 h and 17 min	2 h	ASTM D2196 – 15



Figure 5. PA7 after 1000h under the salt spray test before adding more adhesion promoter and surface agent.

merges in the polymer matrix. The adhesion promoter, without reduction of hardness, may improve the flexibility of the coating but it is dependent on the coating system.

Table 4. Mechanical results of sample PA7 as a final formulation

No.	Name of test	Result	Acceptable result	Standard method	Remark
1	Fineness	15 micron	OK	ASTM D 1210	
2	Adhesion	5B	5B	ASTM D3359	
3	Film Flexibility	2 mm/180°	4mm/180°	ASTM D522	
4	Impact	Direct 100 cm Reverse 100 cm	Direct 80 cm Reverse 90 cm	ASTM D2794	
5	Surface drying time	20 min	30 min	ASTM D1640	20 °C
6	Drying time	45 min	1h	ASTM D1640	20 °C
7	Dry to handle	5 h	5 h	ASTM D1640	20 °C
8	Hardness	261 s	250 s	ASTM D4366	By Konig after 7 days, Test method A
9	Pot life at 25 °C	3h	2h	ASTM D2196 – 15	
10	Volume solid	86%	87%	ASTM D5201 – 05a	may vary by color
11	Density	1.47 g/l	1.5 g/l	ASTM D 1475	
12	VOC	114 g/l	120 g/l	ASTM D2369 – 10	
13	Theoretical coverage	16 Sq m/L	12 Sq m/L		
14	Settling	10	10	ASTM D869	10 → perfect suspension and 0 → fail
15	Dry film thickness	85 micron	N/A	ISO 2808	
16	Sag resistance	No sagging	N/A	ASTM D4400	(75–300 μm)
17	Wet film thickness	100 micron	N/A	ASTM D1212	
18	Weathering resistance, UVA 340 nm	<2100 h No chalking	N/A	ASTM D4587	Cycle: 8h UV/4h condensation, 60 ± 5 °C
19	Corrosion resistance (salt spray)	2500 h, no rust and blisters on the panel with	N/A	ASTM B117	Dry film thickness of the horizontal cut tested panel was 200 μ.
20	Gloss	60°–98 (before UV test) 60°–86 (after 2000 h of UV test)	N/A	ASTM D523	After 2000h in UVA cabinet the reduction was approximately 12%

The adhesion test results are presented in Table 4, which shows that the complete wetting and low surface tension of sample are the two main factors in improving adhesion, and the result according to the cross-cut test was excellent (5B). Also, Fig. 6 shows that the horizontal and X-cut damage to the surface of the coated by PA7 are protective and as strong as the sample PA7-N (without any damage).

3. 2. Scanning Electron Microscopy (SEM):

The polyaspartic coating (sample PA7) was applied to the panel of low carbon steel with dimensions of 2 × 2 cm and analyzed by SEM and EDX (Tescan Vega III, SBU EasyProbe scanning electron microscope) in order to examine the existence of agglomeration of nano-particles in the coating structure. The evaluation was done under acce-

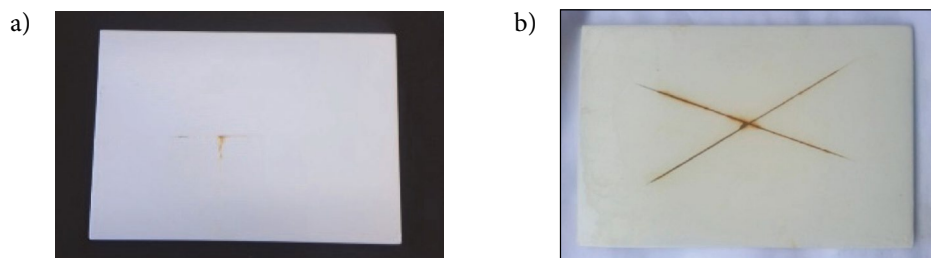


Figure 6. (a) Coated panel with PA7-N coating with horizontal cutting after 2500 hours in a salt spray cabin and (b) panel with PA7-N coating and X-cut after 2500 hours in a salt spray cabin.

lating voltage of electron beam (10 kV) and at different magnifications.¹⁰

An analysis of the protective coating on the metal substrate via scanning electron microscopy (SEM) with energy dispersive X-ray spectrometry (EDX) was performed. The analysis should determine the possibility of presence of any agglomerates of the SiO₂ nano-particles in the dried coating film structure. SEM micrograph of the PA7 coating is shown in Fig. 7.

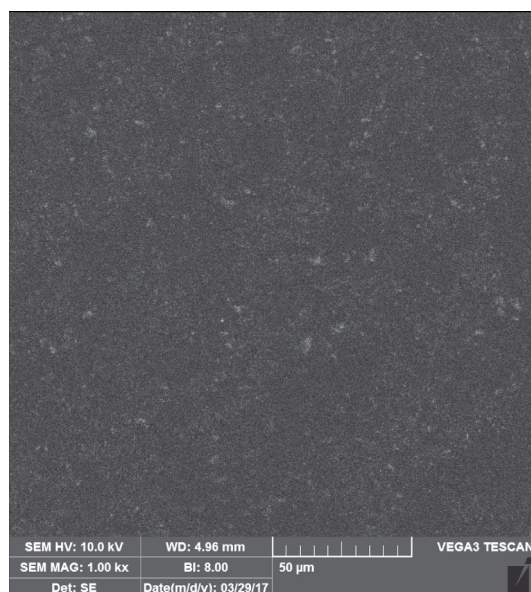


Figure 7. SEM micrograph of the PA7 coating.

Larger particles were observed in the dried film of sample PA7, but the EDX analysis (not shown) confirmed that in all cases those were pigment or filler particles. No signs of agglomerates of SiO₂ nano-fillers were detected.³¹

3. 3. Electrochemical Impedance Spectroscopy (EIS)

In impedance spectroscopy, a small sinusoidal voltage was applied to the sample over a wide frequency range, from 10⁴ to 10⁻² Hz. The controlling computer system

recorded the extent of current induced by the potential and also the phase angle between the potential and current maxima.³² High-performance sample PA7 was exposed to 5% NaCl at 38 °C for 446 days and the impedance was measured continually. Fig. 8 shows Nyquist plots for different exposure times. Sample PA7 initially had very high impedance but its impedance slowly declined over time and then rose again.

The impedance of protective coatings at 0.1 Hz may be taken as an indicator of the protective capacity of the coating. High quality coatings are excellent electrical insulators and typically have electrical resistivity greater than 10⁹ ohm cm². Coatings of good quality have resistivity between 10⁸ and 10⁹ ohm cm², fair-quality coatings have resistivity between 10^{6.5} and 10⁸ ohm cm², and poor coatings have resistivity lower than 10^{6.5} ohm cm².³⁰ Fig. 8 shows variation at 0.1 Hz over time. As may be seen, after 446 days the result demonstrated impedance that was higher than 10, meaning excellent protection from corrosion. The average impedance logarithm equals 9.50 ± 0.44.

From the impedance recorded at 100 Hz, the capacitance, dielectric constant and water uptake of the coating (shown in Fig. 9) may be calculated by the following formulas:³³

$$C = \frac{1}{2\pi f |Z|_{@100\text{Hz}}} \quad (3a)$$

$$\varepsilon_r = \frac{Cd}{\varepsilon_0 A} \quad (3b)$$

$$\varphi = \frac{\log_{10} \left(\frac{C_t}{C_0} \right)}{d \log_{10} \varepsilon_w} \quad (3c)$$

Where,

C = coating capacitance

*C*₀ = initial coating capacitance

*C*_{*t*} = coating capacitance over time *t*

ε_0 = vacuum electrical permittivity

ε_r = relative electrical permittivity (dielectric)

ε_w = water electrical permittivity

φ = water uptake

A = surface area of a panel and, d = coating thickness

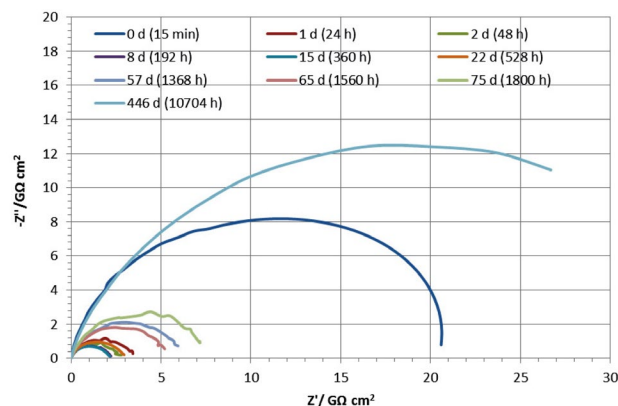


Figure 8. EIS spectra of the test panel as a function of immersion time (Nyquist plot – $\log IZ_{Rc}I$ vs. $\log IZ_{Im}I$) during 466 d.

The average value of capacitance equals 1.30 ± 0.13 nF cm⁻², of the dielectric constant 4.43 ± 0.45 and of the water uptake $7.12 \pm 1.41\%$. These values indicate that the coating has retained its protective properties throughout the exposure period.^{34,35}

3. 4. Fourier Transform- Infrared Spectroscopy (FTIR)

The degradation of sample PA7 was studied by Fourier transform infrared (FTIR) spectroscopy, as this is the standard method for predicting the long-term degradation and performance of the film coating. So the characterizations of sample PA7-N were evaluated by FTIR before starting the corrosion resistance test. The recorded spectra were within a range of 650 to 4000 cm⁻¹ and under the standard ASTM E1252-98(2007).³⁴ FTIR is a practical

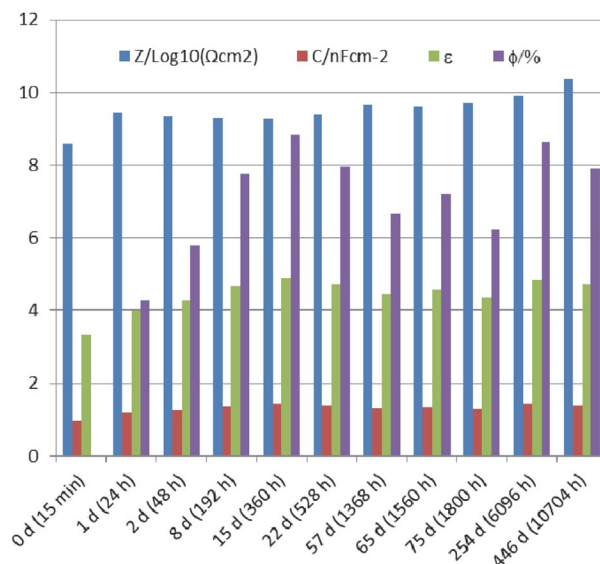


Figure 9. PA7 coating parameters calculated from EIS measurements for different times of exposure to 3.5% NaCl.

technique for evaluating and diagnosing the reason for decreasing adhesion in organic coatings.

The main absorption bands were demonstrated at ≈ 3356 cm⁻¹; ≈ 2927 cm⁻¹; ≈ 2856 cm⁻¹; ≈ 1713 cm⁻¹; ≈ 1519 cm⁻¹; ≈ 1453 cm⁻¹; ≈ 1361 cm⁻¹, ≈ 1218 cm⁻¹, and ≈ 1016 cm⁻¹, which may be appropriate for the vibration of groups N-H, C-H, C = O (ester), C = O (amide), CH₂, and CH₃. Therefore, these graphs indicate the presence of the ester and amine groups. The band at 3356 cm⁻¹ is attributed to the N-H cause of polyurethane. However, the absorption bands there are at ≈ 1218 cm⁻¹; ≈ 1016 cm⁻¹ with emphasis on the vibration of the Si-O groups. The absorbance intensity value of the bands remained unchanged during research.³⁵ Consequently, during the first day up to 2500 h exposure in the salt spray cabinet there was no degradation (as shown in

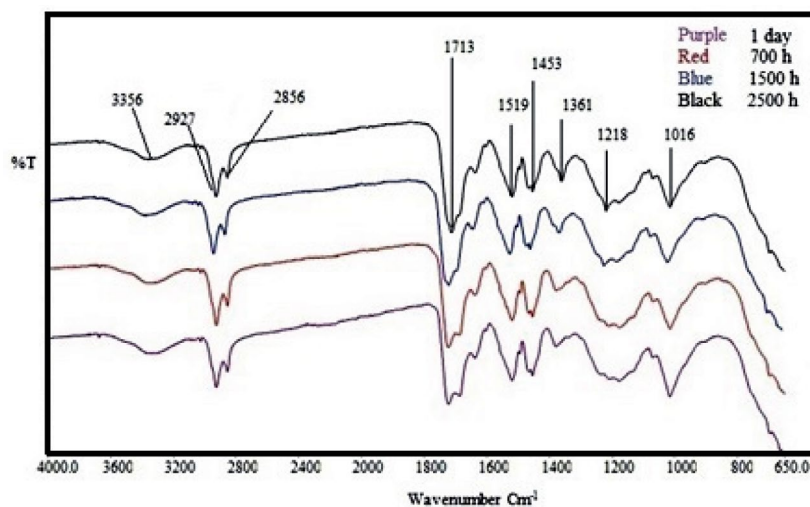


Figure 10. FTIR spectrum of the polyaspartic coating of sample PA7.

Table 5. Comparison of some properties of the improved polyaspartic coating and conventional anti-corrosive coating systems.

No.	Property in corrosivity category C5-M Very high (Marine)	Sample A	Sample B	Sample C	Sample D
1	VOC	114 g/L	250 g/L	442 g/L	276 g/L
2	Coverage	16 Sq m/L	8 Sq m/L	7–9 Sq m/L	10 Sq m/L
3	Dry to handle time at 25 °C	8 h	12 h	24 h	24 h

Sample A = improved polyaspartic coating (DTM) Sample B = polyaspartic coating (Conventional, DTM) Sample C = Zn Rich Epoxy/Epoxy/PU
Sample D = Epoxy/Epoxy/PU Sample D = Epoxy/Epoxy/PU

Fig. 10), which means it has high adhesion in the boundary layer and it is expected to have a long-term service life. The results also indicated that the degradation on the film coating of the sample could be considered negligible.

3. 4. Comparison of Results

Table 5 demonstrates the comparative results of the improved polyaspartic coating and the conventional commercially available protective coating system for a highly corrosive environment such as splash zones.

As seen in Table 5, there is an immense difference in results. The VOC has been significantly decreased. In addition, the coverage of the coating has been increased practically in comparison to other coating samples. Drying time has been decreased.

4. Conclusion

The polyaspartic coating polymer base was improved by adding nano-silica. The coating applied directly to the carbon steel surface in a thin layer of 85 micron DFT showed excellent protection against chemical and mechanical damage. According to the test results, this coating reduces the number of layers to be applied compared to the conventional coating systems, has high resistance, ultra-low volatile organic compound (VOC) content (114 g/L), and consequently reduces maintenance costs and environmental impact.

Various coating characteristics indicate that it has retained its protective properties throughout the period of exposure of 2500 h in the salt spray cabinet, showing no signs of degradation, as confirmed by FTIR measurements. Additionally, SEM and EDX analysis results show no signs of agglomeration of nano-silica filler. High coating impedance ($>10^9$ Wcm²) was retained throughout the period of 10704 h of exposure to 3% NaCl solution, while the coating capacitance remained practically constant, and water uptake remained <9%, so the results indicate that using nano-silica with other suitable pigments and additives in the coating formulation provides resilient coating with good prospects of attaining long service lifetime. According to these results, the investigated nano-silica polyaspartic coating shows outstanding properties and presents a

significant progress in formulating nanocomposite protective coating systems.

5. Acknowledgments

I would like to thank Prof. Marko Rogošič, Ph.D., for his assistance and support.

6. References

1. T. B. T. Nguyen, N. T. Nguyen, T. H. Ha, B.T.T Nguyen, *Viet. J. Sci. Tech.* **2017**, 55, 153–163.
2. Z. S. Poura, M. Ghaemya, S. Bordbarb, H. Karimi-Malehc, *Prog. Org. Coat.* **2018**, 119, 99–108.
DOI:10.1016/j.porgcoat.2018.02.019
3. S. B. Ulaetoa, R. Rajana, J. K. Pancrecioua, T.P.D. Rajana, B.C. Paia, *Prog. Org. Coat.* **2017**, 111, 294–314.
DOI:10.1016/j.porgcoat.2017.06.013
4. J. Viertel, L. Neuer, B. Mauch, T. Czyborra, *Mater. Corros.* **2017**, 68, 1321–1325. DOI:10.1002/maco.201709464
5. J. W. Martin, *Methodologies for Predicting the Service Lives of Coating Systems*, DIANE Publishing, USA, **1994**, pp. 1–34.
DOI:10.6028/NIST.BSS.172
6. W. M. Bos, T. Bos, *Prediction of Coating Durability – Early Detection Using Electrochemical Methods*, Gildeprint Drukkerijen B.V., Enschede, The Netherlands, **2008**, pp. 1–139.
7. J. R. Davis, *Corrosion: Understanding the Basics*, ASM International, USA, **2000**, pp. 1–49.
8. T. Bäker, M. Casimir, M. Homann, *Paint Coat. Ind.* **2007**, 23, 40–42.
9. G. Gündüz, *Chemistry, Materials, and Properties of Surface Coatings: Traditional and Evolving Technologies*, DEStech Publications, Inc, USA, **2015**, pp. 641–701.
10. X. J. Raj, T. Nishimura, *International Journal of Petrochemical Science & Engineering* **2017**, 2, 00028.
DOI:10.15406/ipcse.2017.02.00028
11. K. H. Wuehrer, *Bringing Polyaspartic Technology to the Next Level: Low Viscous Solvent-free Floor Coatings*, ENVVT **2014 / 2014-11-25**.
12. A. Goldschmidt, H. J. Streitberger, *BASF Handbook on Basics of Coating Technology*, Vincentz, Germany, **2003**, pp. 27–253.
13. John J. Florio, Daniel J. Miller, *Handbook of Coating Additives*, CRC Press, USA, **2004**, pp. 145–159.

14. A. Forsgren, Corrosion Control Through Organic Coatings, CRC Press Taylor & Francis Group, USA, **2006**, pp. 11–51. DOI:10.1201/9781420007022.ch2
15. A. A. Tracton, Coating Technology Fundamentals, Testing and Processing Technology, CRC Press Taylor & Francis Group, New York, **2007**, pp. 1–18.
16. R. Lambourne, T. A. Strivens, Paint and Surface Coatings; Theory and Practice, Vol. 2, William Andrew Publishing, USA, **1999**, pp. 185–283.
17. J. Bieleman, Additives for Coatings, Wiley-Vch Press, Germany, **2000**, pp. 65–224. DOI:10.1002/9783527613304.ch4
18. P. A. Sørensen, S. Kiil, K. Dam-Johansen, C. E. Weinell, *J. Coat. Technol. Res.* **2009**, *6*, 135–176. DOI:10.1007/s11998-008-9144-2
19. A. S. Khanna, High-Performance Organic Coatings, CRC Press, USA, **2008**, pp. 56–120.
20. G. T. Bayer, M. Zamanzadeh, Failure Analysis of Paints and Coatings, Matco Associates, PA, **2004**.
21. Z. W. Wicks Jr, F. N. Jones, S. P. Pappas, Organic Coatings: Science and Technology, 2nd ed., Wiley-Interscience, New York, **1999**, pp. 675–680.
22. G. Gündüz, Chemistry, Materials, and Properties of Surface Coatings: Traditional and Evolving Technologies, DEStech Publications, Inc, USA, **2015**, pp. 343–515.
23. M. M. Mirza, E. Rasu, A. Desilva, *Int. J. Chem. Eng. Appl.* **2016**, *7*, 221–225.
24. P. A. Schweitzer, Paint and Coatings; Applications and Corrosion Resistance, CRC Press Taylor & Francis Group, USA, **2006**, pp. 19–245.
25. S. Pilotek, F. Tabellion, *Eur. Coat. J.* **2005**, *170*, 04.
26. E. M. Petrie, Handbook of Adhesives and Sealants, MacGraw-Hill, USA, **2000**, pp. 49–89, 253–273.
27. M. A. Butt, A. Chughtai, J. Ahmad, R. Ahmad, U. Majeed, I. H. Khan, *Journal Faculty of Engineering & Technology* **2008**, *15*, 21–45.
28. A. Jarray, V. Gerbaud, M. Hémati, *Powder Technol.* **2015**, *271*, 61–75. DOI:10.1016/j.powtec.2014.11.004
29. American National Standards Institute, Test Procedure and Acceptance Criteria for Factory Applied Finish Coatings for Steel Doors and Frames, Steel Door Institute, USA, **2012**.
30. H. L. Lee, Fundamental of Adhesion, Springer Science & Business Media, New York, **2013**, p. 14.
31. X. Shi, T. A. Nguyen, Z. Suo, Y. Liu, R. Avci, *Surf. Coat. Technol.* **2009**, *204*, 237–245. DOI:10.1016/j.surfcoat.2009.06.048
32. E. Barsoukov, J. R. Macdonald, Impedance Spectroscopy: Theory, Experiment, and Applications Wiley-Interscience, USA, **2005**, pp. 129–205. DOI:10.1002/0471716243
33. C. Moreno, S. Hernandez, J. J. Santana, J. Gonzalez-Guzman, R. M. Souto, S. Gonzalez, *Int. J. Electrochem. Sci.* **2012**, *7*, 8444–8445.
34. B. Stuart, Infrared Spectroscopy: Fundamentals and Applications, Wiley, England, **2004**, pp. 15–135. DOI:10.1002/0470011149
35. X. F. Yang, C. Vang, D. E. Tallman, G. P. Bierwagen, S. G. Croll, S. Rohlik, *Polym. Degrad. Stab.* **2001**, *74*, 341–351. DOI:10.1016/S0141-3910(01)00166-5

Povzetek

V pričujočem prispevku smo želeli raziskati in razviti poliaspartatne prevleke z uporabo nano SiO₂ modificiranega z amino skupino (NH₂-) z namenom povečanja adhezije na kovinskih površinah in učinkovitejše zaščite proti koroziji. Pripravili smo sedem vzorcev poliaspartatne prevleke z različnimi količinami nano SiO₂ in jih nanесли na pločevine z nizko vsebnostjo ogljika. Rezultati so pokazali, da je le 2% nano-silicijevega dioksida na celotno masno sestavo zagotovilo odlične zaščitne in fizikalne lastnosti prevleke. Pomemben rezultat je tudi združljivost nanodelcev z drugimi spojinami v sestavi premaza. Časovno odvisno obnašanje prevlek smo sledili z metodami EIS, SEM in FTIR ter izpostavili v korni za razprševanje soli. Glavna prednost tako pripravljenih prevlek je bila odlična mehanska in kemična odpornost ter obstojnost enoslojnega premaza in hkrati zmanjšana emisija hlapnih organskih spojin ter nižji skupni stroški postopka nanosa premaza.

Scientific paper

Synthesis and Characterization of Zinc Oxide Nanoparticles with Small Particle Size Distribution

Nuraqeelah Mohammad Shamhari,¹ Boon Siong Wee,^{1,*}
Suk Fun Chin¹ and Kuan Ying Kok²

¹ Faculty of Resource Science and Technology, Universiti Malaysia Sarawak, Kota Samarahan, 94300 Sarawak, Malaysia.

² Malaysian Nuclear Agency, Bangi, Kajang, 43000 Selangor, Malaysia.

* Corresponding author: E-mail: swboon@unimas.my

Tel: +60 82582965

Received: 24-01-2018

Abstract

Solvothermal synthesis has shown to have a great potential to synthesize Zinc Oxide nanoparticles (ZnO NPs) with less than 10 nm size. In this study, we present a rapid synthesis of ZnO NPs in which ZnO NPs with more uniform shape and highly dispersed were synthesized using zinc acetate dihydrate ($\text{Zn}(\text{CH}_3\text{COO})_2 \cdot 2\text{H}_2\text{O}$) and potassium hydroxide (KOH) as a precursor and absolute ethanol as solvent via solvothermal method. Few techniques were exploited to characterize synthesized ZnO NPs including X-ray diffraction (XRD), transmission electron microscope (TEM), Brunauer-Emmett-Teller (BET), energy-dispersive X-ray spectroscopy (EDX), fourier transform infrared (FT-IR) spectroscopy, and ultraviolet visible (UV-Vis) spectroscopy. Synthesized ZnO NPs that were prepared via solvothermal synthesis method at 60 °C for 3 hours exhibited a wurtzite structure with a crystalline size of 10.08 nm and particle size of 7.4 ± 1.2 nm. The UV-vis absorption spectrum has shown peak at 357 nm indicate the presence of ZnO NPs. Hence, better quality with uniform size ZnO NPs can be easily synthesized with reduced amount of time via solvothermal synthesis method rather than using other complicated and lengthy synthesis methods.

Keywords: Zinc Oxide nanoparticles; Solvothermal method; Small particle size; Spectroscopy

1. Introduction

High demands of nanomaterials have produced enormous applications in global industries. Due to high demand as NPs based products, various types of engineered nanoparticles (ENPs) are synthesized for myriad of applications.¹ These days, ZnO NPs have become a promising candidates and gained more attention especially in nanomedicine and nano-semiconductors.^{2–4} ZnO NPs exhibit wurtzite crystal structure that has been widely used in industries due to its unique optoelectric properties.⁵ ZnO NPs are among of various semiconductivity materials with a distinctive electronic and photonic wurtzite semiconductor with a wide direct band gap (3.37eV) and high exciton binding energy (60 meV) at room temperature.⁶ This makes ZnO NPs particularly popular for use in commercially available especially in sunscreens and cosmetics which able to block UV radiation when they are less than 50 nm.^{7–9} Heiligtag *et al.*¹⁰ stated that smaller size of NPs provide a better protection of skin against UV damage.

Besides, high optical absorption UVA and UVB in ZnO NPs are also beneficial in antimicrobial products in nanomedicine as nowadays various nanomaterials development have been applied to improve drugs and other medicine.¹¹ Among other MO NPs, Salem *et al.*¹² stated that ZnO NPs are the most recommended for antibacterial agent. Hence, the increase productions of consumer products eventually increase the productions of ZnO NPs. Heiligtag *et al.*¹⁰ has also stated that the potential applications of ZnO NPs make them one of a primary focus in NPs research. Naveed Ul Haq *et al.*¹³ also described that ZnO NPs is one of the cheap materials that this causes the extensive productions in industries. Morphologically, ZnO NPs is an attractive compound that possess thermal and chemical stability.¹⁴ ZnO NPs are made into various shapes and sizes depending on the use of NPs in industries including textile, energy, food, cosmetics, and medicines and other characteristics that make them attractive for broad range of application.¹⁵

Various synthesis methods of ZnO NPs were developed into different size and forms in order to be used in commercial products. This includes sol-gel method, precipitation, microwave assisted, and thermal oxidation.⁴ However, these methods are considered complicated as they involve multiple steps procedures, lengthy reaction period, and toxic solvent and reactants might be used for synthesis.^{16,17} Prominent methods usually have undergone approximately 24 hours of reaction time to yield NPs products. For instance, Zarei *et al.*¹⁸ has synthesized ZnO NPs via sol-gel method in which more than 12 hours and high calcined temperature were required to produce ZnO NPs. Other than that, ZnO NPs synthesis via room-temperature method was also lengthy, as at least 4 days of synthesis was needed to prepare ZnO NPs.¹⁹ Due to high cost and maintenance as well as lengthy preparation time to set up expensive equipment for synthesis, solvothermal synthesis was developed to synthesize NPs. Previous studies have carried out NPs synthesis via solvothermal method thus this study was carried out in order to support the method with some modifications mainly the use of absolute ethanol as a solvent.

According to Li *et al.*,²⁰ solvothermal process is defined as performing chemical reactions in solvents under specific temperature. Matei *et al.*²¹ also stated that solvothermal synthesis can be easily performed under controlled condition as ZnO NPs can be synthesized into different morphologies depending on the reaction conditions. Bai *et al.*²² has stated that solvothermal method has the ability in enhancing the dispersity of ZnO NPs. Besides, this process has been widely used specially to synthesize metal oxides NPs since it is more reliable, affordable, and undergo simpler process of synthesis.²³ Wu *et al.*¹⁷ also described that solvothermal synthesis method is free from using surfactant in which this offers a better potential for environmental friendly synthesis that can be produce in large quantities. Besides, solvothermal synthesis is considered one of the most promising approach to synthesize NPs.²⁰ In solvothermal synthesis, organic solvent mainly alcohol such as ethanol as being used by previous researchers to synthesize ZnO NPs.^{4,23,24}

Furthermore, NPs characterization using XRD, TEM, BET, EDX, FT-IR spectroscopy, and UV-Vis spectroscopy are fundamental steps especially for examining NPs surface properties and functionality. It is important to characterize NPs in order to determine the behaviour of NPs for further study such as toxicological studies.¹⁷ Due to extensive usage of ZnO NPs, ZnO NPs were prepared via solvothermal synthesis by using zinc acetate dihydrate ($\text{Zn}(\text{CH}_3\text{COO})_2 \cdot 2\text{H}_2\text{O}$) as a zinc source and potassium hydroxide (KOH) as a precursor which dissolved in organic solvent mainly ethanol as only short reaction period is required for the synthesis.

Ethanol was used for ZnO NPs synthesis as it has hydroxyl group that interact better with NPs as well as increase solubility to allow more interaction between parti-

cles and capping molecules.²⁵ This method has utilized the organic solvent mainly ethanol which generally has low boiling point and generate high pressure that are conducive to obtain a better product crystallization.²⁶ The utilization of absolute ethanol as a solvent has proven to be monodisperse size and shape of ZnO NPs via solvothermal methods. Wang *et al.*²⁶ has also explained that the presence of smaller surface tension of ethanol as compared to other alcohol has effectively contribute to inhibit the oxidation of powders thus uniform spherical ZnO NPs were formed. The aim of this research are to synthesize spherical ZnO NPs with less than 10 nm size by using zinc acetate dihydrate and potassium hydroxide with a absolute ethanol as solvent via solvothermal method and to characterize synthesized ZnO NPs using few techniques including XRD, TEM, BET, EDX, FT-IR, and UV-Vis spectroscopy.

2. Experimental

2. 1. Synthesis of Zinc Oxide Nanoparticles

Zinc oxide nanoparticles was synthesized using solvothermal synthesis process from modified published procedures.²⁴ Briefly, 1.48 g of $\text{Zn}(\text{CH}_3\text{COO})_2 \cdot 2\text{H}_2\text{O}$ (Sigma-Aldrich, India) was dissolved in 63 ml of absolute ethanol (HmBG Chemicals) in a 250 ml Schott bottle and was heated under 60 °C with constant stirring. 0.74 g of KOH (VWR Amresco, US) was also dissolved separately in 33 ml of absolute ethanol in 100 ml Schott bottle under same condition of $\text{Zn}(\text{CH}_3\text{COO})_2 \cdot 2\text{H}_2\text{O}$. After both solutions have dissolved completely, dropwise, KOH was added into $\text{Zn}(\text{CH}_3\text{COO})_2 \cdot 2\text{H}_2\text{O}$ slowly under 60 °C with vigorous stirring. The mixture solution was left for 3 hours until the reaction was completed. A white precipitate (ZnO) was formed and collected by centrifugation at 4000 rpm for 10 minutes, washed with acetone twice and ultra-pure water once to remove all the impurities. The obtained product was then dried at room temperature and ground to form powder.

2. 2. Characterization of ZnO Nanoparticles

Different techniques were used to characterize the synthesized ZnO NPs. Crystal structure and primary crystal size was characterized using XRD (Xpert Pro Diffractometer, Netherlands). The XRD pattern was obtained using X-ray diffractometer with Cu-K α radiation of 40 kV and 30 mA with step size of 0.017°.

Other than that, the morphological features especially the size and the shape of ZnO NPs were determined using TEM (JOEL 1230, Japan). Basically, copper grid was prepared by applying fomvar coating on the copper grid. ZnO NPs were diluted with ethanol and sonicated with ultrasonic cleaner (Elma, Germany) for 30 minutes. Then, 4 μl of ZnO NPs sample was loaded onto the coated copper grid before being observed under TEM.

Besides, Brunauer-Emmett-Teller (BET) (Quantachrome, US) was used to analyse the surface area of the synthesized ZnO NPs. About 0.3 g of ZnO NPs powder were placed in the tube and was allowed to degas at 175 °C for 2 hours as referred to Zhou *et al.*²⁷ in flowing nitrogen. The N₂ absorption-desorption isotherms of samples were then be measured. Energy-dispersive X-ray spectroscopy (EDX) was also being used for ZnO NPs characterization. EDX (JOEL 6390LA, Japan) was used in order to determine the purity of synthesized ZnO NPs. Meanwhile, Fourier transform infrared spectroscopy (FT-IR) was used in order to obtain the surface functional group that was present in ZnO NPs. ZnO NPs powder was mixed with potassium bromide (KBr) with ratio of 1: 19.²⁸ The sample was then placed in the metal hole, pressed until the sample compressed inside the hole, and analysed using FT-IR (Thermo scientific Nicolet iS10, US). Ultraviolet visible spectroscopy (UV-vis) (Perkin Elmer Lamda 25) was also used in order to determine the optical absorption spectra of ZnO NPs that was dispersed in water.

3. Result and Discussion

3.1. X-Ray Diffraction (XRD)

XRD pattern of synthesized ZnO NPs is shown in Figure 1. Based on the XRD pattern, synthesized ZnO NPs has high purity of wurtzite crystalline structure as the diffraction peak is seen to be intense and narrower. This result was also being compared with the given standard XRD pattern of ZnO (JCPDS 36-1451) for confirmation purpose. The peak shown is broad which indicates that the particles is smaller which were also described in previous literature.^{22,26} Apart from that, as mentioned by Tagreed *et al.*²⁹ the average crystalline structure (D) was calculated according to Debye-Scherrer's formula:

Scherrer's Equation:

$$\text{Particle size } (D_p) = \frac{0.89 \lambda}{d \cos \theta}$$

Where 0.89 refers to Scherrer's constant, is λ a wavelength of X-rays, θ refers to Bragg diffraction angle, and d is full width at half maximum (FWHM) of diffraction peak. The most intense diffraction was chosen which is <010> and the crystalline size of synthesized ZnO NPs was determined to be 10.08 nm. Besides, the percentage of zinc content from the synthesized ZnO NPs via the XRD analysis, which revealed that there is 99% of zinc without any

Table 1. Pattern list of ZnO NPs obtained from XRD.

Chemical formula	Reference code	Compound name	Score (%)
Zn	98-000-9346	Zincite	99

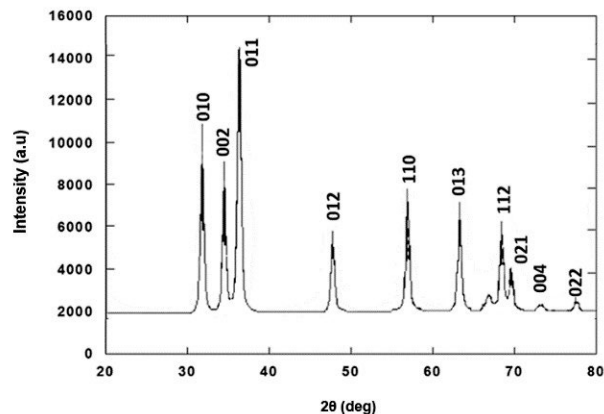


Figure 1. XRD pattern of synthesized ZnO nanoparticles.

other elements being detected as shown in Table 1. From this obtained data, it shows that synthesized ZnO NPs were determined to be of high purity.

3.2. Transmission Electron Microscope (TEM)

Physical characterization of NPs is commonly characterized using transmission electron microscope (TEM). Phoohinkong *et al.*³⁰ stated that TEM was carried out in order to obtain high accuracy of the actual particle size and shape pattern. This shows that TEM is one of the reliable tools for NPs characterization. The morphological feature of synthesized ZnO NPs was determined using TEM as shown in Figure 2. Size of less than 10 nm was obtained by using solvothermal synthesis method. About 200 particles were chosen randomly and measured. The calculated mean size of synthesized ZnO NPs was determined to be 7.4 ± 1.2 nm. TEM particle distribution result in Figure 2 also confirmed that a narrow size distribution of ZnO NPs can be obtained via solvothermal synthesis

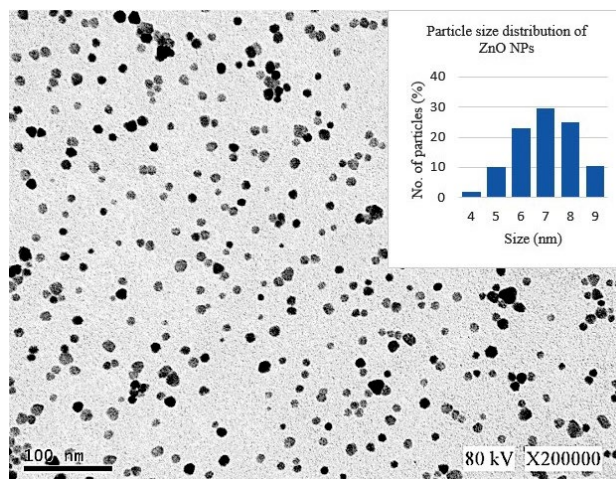


Figure 2. ZnO NPs image under transmission electron microscope (TEM) and particle size distribution of ZnO NPs.

method. Based on the particle size distribution in the figure, most of the NPs measured were determined to be 6, 7, and 8 nm which attribute to 23%, 29.5% and 25%, respectively. The biggest size of ZnO NPs measured is about 9 nm which only attribute to 10.5%. Besides, synthesized ZnO NPs that was observed under TEM showed a homogenous shape that seem to be near hexagonal or nanosphere that was also described from previous study in which solvothermal synthesis was being conducted by Zak *et al.*²³ which obtained 50 nm ZnO NPs. The synthesized ZnO NPs observed under TEM also correlates with the XRD patterns that reveal high purity of wurtzite crystalline structure of ZnO NPs. Therefore, this shows that solvothermal synthesis can be used to obtain a better image that proves the presence of less than 10 nm of synthesized ZnO NPs with high dispersity.

3. 3. Brunauer-Emmett-Teller (BET)

BET was carried out in order to determine the specific surface area for three different sized of ZnO NPs by N₂ adsorption temperature of 77 K. Figure 3 shows nitrogen (N₂) adsorption-desorption isotherms of ZnO NPs obtained from BET analysis (Quantachrome, US). Figure 3 also shows a typical type IV adsorption obtained from synthesized ZnO NPs. The isotherm relative was observed to be relative flat and similar result was also obtained by Zhou *et al.*²⁷. Zhou *et al.*²⁷ has described that the adsorption iso-

therm was completely under superposition which usually occurs in micropores.

The specific surface area was also determined to be 101.32 m²/g. Similar finding was also found from previous literature by Bian *et al.*²⁴ which obtained 105 m²/g for 4 nm ZnO NPs as measured by TEM. This shows that smaller NPs attribute to high surface area. Furthermore, the average particle can also be calculated from BET data. Since the shape of ZnO NPs was determined to be in spherical shape, average particle size can be calculated based on the equation $D_{\text{BET}} = 6000 / \rho \cdot S_w$ in which D_{BET} is the average particle size, ρ is the theoretical density of the sample which was 6.11 g cm⁻³, and S_w is the obtained surface area as referred to Zhou *et al.*²⁷ and Ghasemzadeh *et al.*³¹. Table 2 summarised the BET results of ZnO NPs. The mean particle size of ZnO NPs obtained from BET (9.7 nm) is in agreement with the particle size obtained from TEM (7.4 nm) and XRD (10.8 nm). Thus, this confirms that the particle size of synthesized ZnO NPs was in nanoscale which is approximately 10 nm.

3. 4. Energy-dispersive X-ray Spectroscopy (EDX)

The purity of ZnO NPs was determined via the EDX analysis. Figure 4 shows the EDX spectrum of ZnO NPs. EDX was used in order to determine the element composition that present in the samples. Result revealed that the

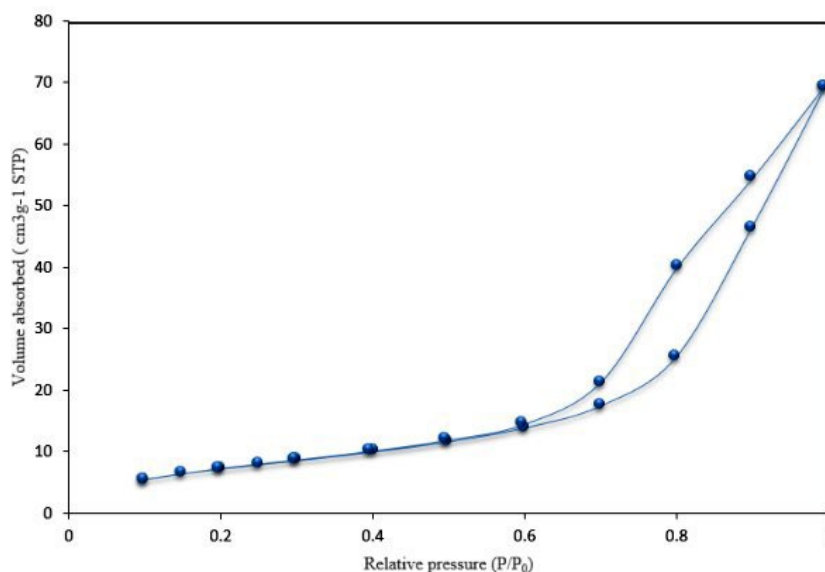


Figure 3. N₂ adsorption- desorption isotherms of ZnO NPs

Table 2. BET results of synthesized ZnO NPs in comparison with other analytical techniques.

Constant/ C	BET surface area	Average particle size D_{BET}	Average size via TEM	Crystal size via XRD
28.904	101.32 m ² /g	9.7 nm	7.4 nm	10.8 nm

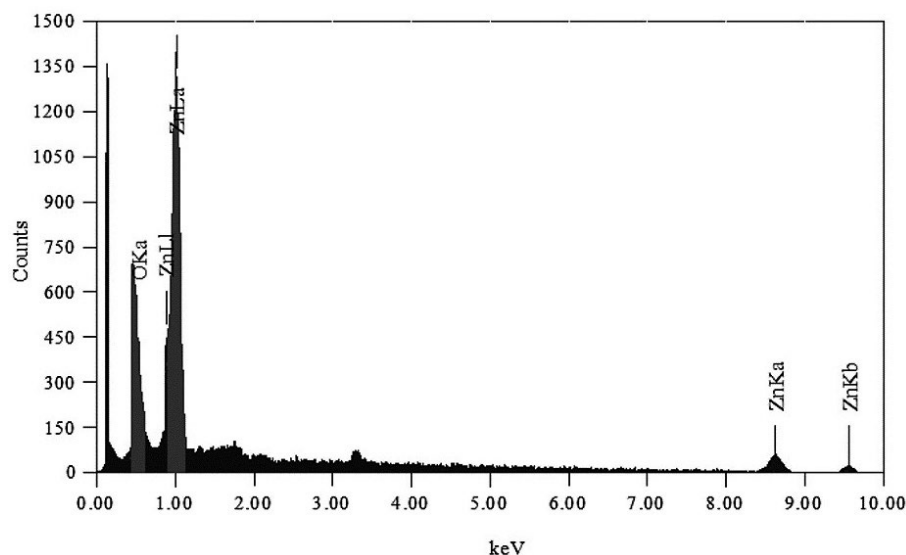


Figure 4. EDX pattern of ZnO NPs

EDX data was composed of two elements which are Zn (76.3%) and O (23.7%). This result has confirmed that the ZnO NPs has high purity. Similar finding was also found in previous studies by Brintha and Ajitha³² that obtained the mass percentage of Zn and O were 73.9% and 26.1 %, respectively. Hasnidawi *et al.*³³ has stated that the theoretical expected mass percent of Zn and O were 80.3% and 19.7%. Thus, the EDX result revealed that the synthesized ZnO NPs were of high purity, which contain high Zn and O element composition.

3. 5. Fourier Transform Infrared Spectroscopy (FT-IR)

FT-IR was performed in order to study and determine the functional groups of synthesized ZnO NPs. Fig-

ure 5 showed the FT-IR spectrum of synthesized ZnO NPs that were obtained from solvothermal synthesis procedure. FT-IR spectrum analysis was done by referring to Yang *et al.*²⁸ where a broad absorption band was observed at 414 cm^{-1} that attribute to Zn-O stretching vibration. In previous studies regarding ZnO NPs they were also able to observe FT-IR spectrum with the band around 400 cm^{-1} .^{23,28,34}

All the observed peaks were referred from previous literatures in order to confirm the findings. Similar findings were also found from previous studies related to ZnO NPs synthesis and characterization. The peaks at 1339 and 1556 cm^{-1} were symmetric and asymmetric O-C-O stretching vibration of adsorbed carbonate anion respectively. Meanwhile, the peaks at 1047 cm^{-1} that indicate the lattice vibration of carbonate generated absorption peaks.

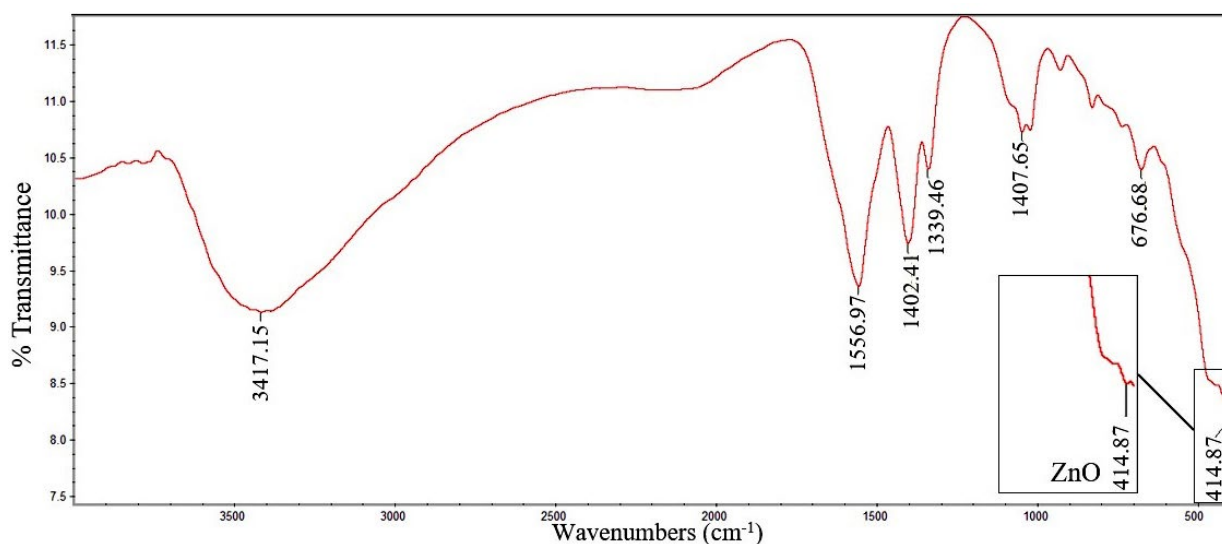


Figure 5. FT-IR spectrum of synthesized ZnO NPs.

Besides, hydroxyl group stretching can be seen at the absorption peak of 3417 cm^{-1} .

Apart from that, peaks of 1402 cm^{-1} and 1339 cm^{-1} indicate the presence of $\text{Zn}(\text{CH}_3\text{COO})_2 \cdot 2\text{H}_2\text{O}$ that associate with CH_3 bending modes similar with result obtained by previous literature.¹⁷ Many ZnO NPs has been made using different types of synthesis method, however the obtained FT-IR spectrum regarding ZnO NPs synthesis have shown similarities.^{35,36} Therefore, FT-IR result has shown to be high purity of synthesized ZnO NPs. Wu *et al.*¹⁷ has stated that this technique provides information about surface functional group that are present on surface that give a useful description of surface speciation.

3. 6. UV-Vis Absorption Spectrum

UV-Vis spectroscopy was also performed to further confirm the formation of ZnO NPs. The absorption spectrum of synthesized ZnO NPs was shown in Figure 6. The UV-Vis measurement was performed after the ZnO NPs was dispersed in ultrapure water. The absorption peak was observed at 357 nm, which attribute to the intrinsic band-gap of Zn-O absorption. Similar result of absorption band that represent ZnO NPs was also obtained from previous research in which the range of ab-

sorption band were from 355 to 380 nm as summarised in Table 3.^{4,23,24,34,37} These supporting data confirm the presence of ZnO NPs as the absorption band obtained are similar. Wang *et al.*²⁶ also obtained similar findings which deduced that the obtained peak showed a better UV absorption for ZnO NPs.

Furthermore, the absorption peak of ZnO NPs also confirmed the properties of ZnO NPs, which is known for UV protections in sunscreens products.³⁸

3. 5. Absolute Ethanol as a Solvent

From the obtained TEM result as shown in Figure 2, it shows that solvent also plays an important role for ZnO NPs synthesis. This includes the physico-chemical properties of ZnO NPs in terms of size and shape. The utilization of absolute ethanol as a solvent has formed a highly dispersed small ZnO NPs with uniform shape and size that was determined to be less than 10 nm as expected. Similar finding also described the formation of spherical shape of ZnO when ethanol was being used as a solvent.¹⁴ This study has shown that the absolute ethanol is one of the suitable solvent to be used to synthesize ZnO NPs via solvothermal synthesis method. Wang *et al.*²⁶ has found that different alcohol gives significant effect on ZnO NPs in terms of their morphology. Previous studies have also used other alcohol for ZnO NPs synthesis however, different forms of ZnO NPs were produced such as rod, flower-shaped, tubes, and etc.²² Therefore, eminent production of ZnO NPs with uniform spherical shape with high dispersity can be easily obtained by utilizing ethanol as a solvent for solvothermal synthesis method. Other benefit of using absolute ethanol would be the short period of synthesis process needed to produce less than 10 nm of ZnO NPs with uniform size.

Table 3. UV vis absorption peak of ZnO from previous literatures.

Author	UV absorption peak (nm)
Talam <i>et al.</i> ⁴	355
Zak <i>et al.</i> ²³	370
Bian <i>et al.</i> ²⁴	371
Lavand <i>et al.</i> ³⁴	375
Akhil <i>et al.</i> ³⁷	370

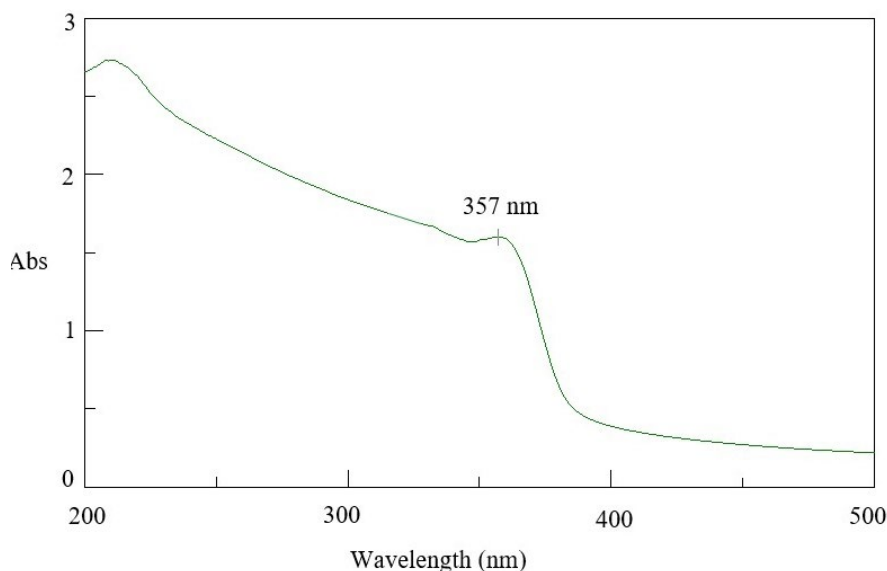


Figure 6. UV-Vis absorption spectra of synthesized ZnO NPs.

4. Conclusion

ZnO NPs with less than 10 nm (7.4 nm) was successfully prepared by using zinc acetate dihydrate and potassium hydroxide via the solvothermal synthesis process. The utilization of absolute ethanol as a solvent was able to produce uniform shape and better dispersity of ZnO NPs. Synthesized ZnO NPs were also able to be confirmed by various characterization techniques including XRD, TEM, FT-IR, and UV-vis spectroscopy. XRD has revealed a wurtzite crystalline structure of ZnO NPs where by physical characterization of ZnO NPs was determined by using TEM and size less than 10 nm of ZnO NPs was obtained. BET revealed that the synthesized ZnO NPs has high surface area that correlate with the particle size obtained from TEM. EDX has proven the purity of synthesized ZnO NPs which contain high Zn and O element composition. FT-IR and UV-vis spectroscopy also showed the absorbance spectrum that indicates the presence of ZnO NPs. Therefore, solvothermal synthesis method is one of the most suitable methods to obtain a better quality of ZnO NPs. This study also presents a potential effective method to prepare ZnO NPs within shorter time with smaller particle size distribution.

5. Acknowledgement

Authors sincerely thank MOHE grant FRGS/ST01(01)/1208/2014(09) for the funding, Faculty of Resource Science and Technology (FRST) for providing the necessary facilities to carry out this research. Authors also want to thank Mdm Ting Woei for the TEM image results.

6. References

1. M. A. Maurer-Jones, I. L. Gunsolus, C. J. Murphy, C. L. Haynes, *Anal. Chem.*, **2013**, 85, 3036–3049. DOI: 10.1021/ac303636s
2. B. Liu & H. C. Zeng, *J. Am. Chem. Soc.*, **2003** 125, 4430–4431. DOI: 10.1021/ja0299452
3. V. Sharma, R. K. Shukla, N. Saxena, *Toxicol. Lett.*, **2009**, 185, 211–218. DOI 10.1016/j.toxlet.2009.01.008
4. S. Talam, S. R. Karumuri, & N. Gunnam, *ISRN Nano*, **2012**, 1–6. DOI: 10.5402/2012/372505
5. H. Ma, P. L. Williams, S. A. Diamond. *Environ. Pollut.*, **2013**, 172, 76–85. DOI: 10.1016/j.envpol.2012.08.011.
6. A. Kołodziejczak-Radzimska, T. Jesionowski, *Mater*, **2014**, 7, 2833–2881. DOI:10.3390/ma7042833
7. L. K. Adams, D. Y. Lyon, P. J. Alvarez, *Water Res.*, **2006**, 40, 3527–3532. DOI: 10.1016/j.watres.2006.08.004
8. I. Blinova, A. Ivask, M. Heinlaan, M. Mortimer, A. Kahru, *Environ. Pollut.*, **2010**, 158, 41–47. DOI: 10.1016/j.envpol.2009.08.017
9. L. C. Wehmas, C. Anders, J. Chess, A. Punnoose, C. B. Pereira, J. A. Greenwood, R. L. Tanguay, *Toxicol Rep*, **2015**, 2, 702–715. DOI:10.1016/j.toxrep.2015.03.015
10. F. J. Heiligtag & M. Niederberger, *Mater. Today*, **2013**, 16, 262–271. DOI: 10.1016/j.mattod.2013.07.004
11. S. Gunalan, R. Sivaraj, V. Rajendran, *Mater Int.*, **2012**, 22, 693–700. DOI: 10.1016/j.pnsc.2012.11.015
12. W. Salem, D. R. Leitner, F. G. Zingl, G. Schratte, R. Prassl, W. Goessler, S. Schild, *Int J Med Microbiol*, **2015**, 305, 85–95. DOI: 10.1016/j.ijmm.2014.11.005
13. A. Naveed Ul Haq, A. Nadhman, I. Ullah, G. Mustafa, M. Yasinza, & I. Khan. *J. Nanomater.*, **2017**. DOI: 10.1155/2017/8510342
14. A. Šarić, G. Štefanić, G. Dražić, & M. Gotić, *J. Alloys Compd*, **2015**, 652, 91–99. DOI: 10.1016/j.jallcom.2015.08.200
15. E. Hughes, Big problems with little particles? Chemistry World, <http://www.rsc.org/chemistryworld/2015/04/nanoparticle-toxicology> (assessed: September 16, 2017)
16. K. D. Bhatte, D. N. Sawant, R. A. Watile, B. M. Bhanage, *Mater. Lett.*, **2012**, 69, 66–68. DOI: 10.1016/j.matlet.2011.10.112
17. C. M. Wu, J. Baltrusaitis, E. G. Gillan, V. H. Grassian, *J. Phys. Chem. C*, **2011**, 115, 10164–10172. DOI: 10.1021/jp201986j
18. N. Zarei, & M. A. Behnajady, *J. Ind. Eng. Chem. Res.*, **2016**, 57(36), 16855–16861. DOI: 10.1080/19443994.2015.1083479
19. A. Bagabas, A. Alshammari, M. F. Aboud, & H. Kosslick, *Nanoscale Res Lett.*, **2013**, 8(1), 516. DOI: 10.1186/1556-276X-8-516
20. J. Li, Q. Wu, J. Wu, *Handb. Nano.*, **2016**, 295–328. DOI: 10.1007/978-3-319-15338-4_17
21. A. Matei, V. Tucureanu, L. Dumitrescu, *Bull. Transilv. Univ. Brasov Ser. I*, **2014**, 7, 45.
22. X. Bai, L. Li, H. Liu, L. Tan, T. Liu, & X. Meng, *ACS Appl. Mater. Interface*, **2015**, 7, 1308–1317. DOI: 10.1021/am507532p
23. A. K. Zak, R. Razali, W. H. Majid, M. Darroudi, *Int. J. Nanomedicine.*, **2011**, 6, 1399–1403. DOI: 10.2147/IJN.S19693.
24. S. W. Bian, I. A. Mudunkotuwa, T. Rupasinghe, V. H. Grassian, *Langmuir*, **2011**, 27, 6059–6068. DOI: 10.1021/la200570n
25. P. B. Khoza, M. J. Moloto, L. M. Sikhwivhilu. *J. Nanotechnol.*, **2012**, 1–7. DOI: 10.1155/2012/195106
26. Y. X. Wang, J. Sun, & X. Yu, In *Mater. Sci. Forum*, **2011**, 663, 1103–1106. DOI:10.4028/www.scientific.net/MSF.663-665.1103
27. M. Zhou, Z. Wei, Qiao, H., L. Zhu, H. Yang, & T. Xia. Particle size and pore structure characterization of silver nanoparticles prepared by confined arc plasma. *J. Nanomater*, **2009**, 3.
28. K. Yang, D. Lin, B. Xing, *Langmuir*, **2009**, 25, 3571–3576. DOI: 10.1021/la803701b.
29. M. A. Tagreed, A. B. Nabeel, A. H. Noor, *Int. J. Eng. Tech. Res.*, **2014**, 2, 191–195.
30. W. Phoohinkong, T. Foophow, & W. Pecharapa, *Adv. Nat. Sci.*, **2017**, 8, 035003.
31. M. A. Ghasemzadeh, & J. Safaei-Ghomi, *Cogent Chem.*, **2015** 1(1), 1095060. DOI: 10.1080/23312009.2015.1095060
32. S. R. Brintha, & M. Ajitha, Synthesis and characterization of ZnO nanoparticles via aqueous solution, sol-gel and hydrothermal methods. *IOSR J. Appl. Chem*, **2015** 8(11), 66–72.

33. J. N. Hasnidawani, H. N. Azlina, H. Norita, N. N. Bonnia, S. Ratim, & E. S. Ali, Synthesis of ZnO nanostructures using sol-gel method. *Pro Chem*, **2016**, 19, 211–216.
34. A. B. Lavand, Y. S. Malghe. *Int. J. Photochem.*, **2015**, 305–310. DOI: 10.1016/j.jksus.2016.08.009
35. M. A. Mustafa, D. A. M. Osman. *J. Nanosci. Nanoeng.*, **2016**, 1, 248–251.
36. C. Jayaseelan, A. A. Rahuman, A. V. Kirthi, S. Marimuthu, T. Santhoshkumar, A. Bagavan, K. B. Rao. *Spectrochim Acta A*, **2012**, 90, 78–84. DOI: 10.1016/j.saa.2012.01.006.
37. K. Akhil, S. S. Khan, *J. Photochem. Photobio. B*, **2017**, 167, 136–149. DOI: 10.1016/j.jphotobiol.2016.12.010.
38. M. M. N. Yung, C. Mouneyrac, K. M. Y. Leung. *Encyclop. Nano.*, **2014**, 1–17. DOI: 10.1007/978-94-007-6178-0_100970-1

Povzetek

Solvotermalna sinteza ima velik potencial za pripravo nanodelcev cinkovega oksida (ZnO) manjših od 10 nm. V tej študiji predstavljamo razmeroma hitro in enostavno sintezo nanodelcev ZnO pri kateri imajo sintetizirani nanodelci ZnO bolj enakomerno obliko in so visoko dispergirani. Za sintezo smo uporabili cinkov acetat dihidrat ($\text{Zn}(\text{CH}_3\text{COO})_2 \cdot 2\text{H}_2\text{O}$) in kalijev hidroksid (KOH) ter absolutni etanol kot topilo. Tako sintetizirane nanodelce ZnO smo karakterizirali z naslednjimi metodami: rentgensko praškovo difrakcijo (XRD), presevno elektronsko mikroskopijo (TEM), Brunauer-Emmett-Tellerjem metodo merjenja specifične površine (BET), energijsko disperzivno rentgensko spektroskopijo (EDX), infrardečo spektroskopijo (FT-IR) in UV-Vis spektroskopijo. Nanodelce ZnO s strukturo wurtzita, kristalinično velikostjo 10,08 nm in velikostjo delcev $7,4 \pm 1,2$ nm smo pripravili s solvotermalne sintezno metodo pri 60 °C v treh urah. UV-Vis absorpcijski spekter je pokazal vrh pri 357 nm, kar kaže na prisotnost nanodelcev ZnO. S predlagano solvotermalno metodo lahko pripravimo nanodelce ZnO, ki so enake velikosti in hkrati skrajšamo čas priprave.

Scientific paper

Role of Modification of Natural Zeolite in Removal of Arsenic from Aqueous Solutions

Ayten Ates,* İnci Özkan and Gamze Topal Canbaz

Department of Chemical Engineering, Engineering Faculty, Cumhuriyet University, 58140 Sivas, Turkey

* Corresponding author: E-mail: ates@cumhuriyet.edu.tr;

Tel: +90 2191010/2248; Fax: +903462191165

Received: 25-01-2018

Abstract

The adsorption of arsenic from aqueous solution onto natural and modified zeolites was investigated. The natural zeolites were modified by ion-exchange (NH_4NO_3) and addition of aluminum ($\text{Al}_2(\text{SO}_4)_3$). The natural and modified zeolites were characterized by XRF, XRD, N_2 sorption, FTIR, NH_3 -TPD, zeta potential and SEM. Ion-exchange with NH_4^+ of NZ results in the significant exchange of most cations and an increase in surface area and pore volume of samples as well as surface acidity. While the introduction of aluminum into the zeolite increased its As (V) removal amount, it decreased its As (III) removal. Ion-exchange with NH_4^+ of the natural zeolite increased significantly its As(III) and As(V) adsorption capacity. The adsorption of both As(III) and As(V) with natural and modified zeolites obeys pseudo second order kinetics. The Langmuir isotherm model for all adsorbents was best fitted to the isotherm data obtained. The highest adsorption capacity for As(III) and As(V) was obtained onto the zeolite modified with ammonia and their calculated q_m values are 28.7 mg/g and 36.6 mg/g, respectively. The calculated thermodynamic parameters indicated that the adsorption process was spontaneous and favorable.

Keywords: Natural zeolite; Arsenic; Decationisation; Ion exchange; Adsorption

1. Introduction

Arsenic is one of the most toxic elements occurring naturally in environment and its presence in the drinking water can lead to deadly effects on the human health. Due to the toxicological impacts of arsenic, the maximum contaminant level (MCL) for arsenic of 10 $\mu\text{g}/\text{L}$ was set by the World Health Organization (WHO).¹ Furthermore, the arsenic contamination has been reported in numerous regions such as Bangladesh and West Bengal (India) as well as the USA, Argentina, China, Hungary, and Poland.^{2,3}

Arsenic species in the environment come from the natural weathering of arsenic-containing rocks, industrial waste discharges and application of arsenical herbicides and pesticides. Drinking water mainly contains inorganic arsenic species, arsenite (AsO_3^{3-}) and arsenate (AsO_4^{3-}). Generally, arsenate [As (V)] in natural surface water and arsenite [As(III)] in the groundwater mainly exist.³ As (III) is usually more toxic than As (V) and its removal from water is difficult due to its difficult dissociation. Therefore, As (III) has been oxidized to As (V) and then removed from water by various technologies such as oxi-

dation, reverse osmosis, chemical coagulation followed by filtration and adsorption.³⁻⁵

Among removal technologies, adsorption is the most promising technology due to the advantages of treatment stability, easy operation, lower environmental impacts, and low cost if suitable adsorbent can be either chosen or designed. Recently many materials have been used and studied as adsorbent for removal of As (III) and As (V) from water. In addition to commercial activated carbons,⁶ several types of activated carbons were synthesized and used for the removal of arsenic from water/wastewater.⁷⁻¹⁰ Besides, the reported adsorbents are given as follows: Agricultural products and by-products, industrial by-products/wastes such as chars and coals,^{10,11} red muds,¹² blast furnace slag,^{13,14} Fe(III)/Cr(III) hydroxide waste,¹⁵ fly ash,¹⁶ soil¹⁷ sand,¹⁸⁻²⁰ clay minerals,²¹⁻²³ zeolites,²⁴ single or mixed oxides or hydroxides,²⁵⁻³¹ hydrotalcites,³² phosphates,³³ metal-based materials,³⁴ and biosorbents.³⁵⁻³⁸ However, many of these materials cannot be used in developing countries due to their financially infeasible. When natural material as an adsorbent is used, sustainable and cost-effective solutions for the removal of As pollution can be obtained in the low-income regions. Several studies

have explored a variety of adsorbents for As removal, and it is reported that naturally formed materials provide the benefits due to their abundance and local availability. Among them, natural zeolites have been widely used as an effective adsorbents in treatment of water due to their mechanical and thermal properties.^{39,40}

Elizalde-González *et al.*⁴¹ reported that adsorption capacity of H_2AsO_4^- with natural Mexican zeolites, ZMA (Sonora), ZME (Oaxaca), ZMS (San Luis Potosí) and ZMT (Puebla) is more than H_3AsO_3 and their iron modified forms insignificantly improve the level of removal efficiency. Arsenic sorption results from aqueous solutions onto clinoptilolite-rich tuffs modified with lanthanum, hexadecyltrimethylammonium or iron of MacE-do-Miranda and Olguín⁴² showed that arsenic removal depends on the origin of the zeolitic material, the nature of the arsenic chemical species, the pH and characteristics of the modified natural zeolites. As(V) adsorption from aqueous solutions onto clinoptilolite–heulandite-rich tuffs modified with iron, manganese, or a mixture of both iron and manganese was studied by Jiménez-Cedillo *et al.*⁴⁰ They reported that adsorption of As(V) on the modified clinoptilolite-rich tuffs depends on the metallic species introduced into zeolites, the chemical nature of the metal introduced, and the interaction between the different metallic chemical species on the zeolite surface. Consequently, the studies on natural and modified zeolites showed that the type and charge of the zeolite framework mostly affect their adsorption mechanisms and capacities. Furthermore, the other important parameter effecting adsorption mechanisms and capacities can be sorted such as the amount of aluminium present in the zeolite, the size and shape of the pores, the phase composition of the zeolitic material, the nature and concentration of the extra-framework cationic species and the pH of the solution along with the size and distribution of zeolite particles, the temperature of adsorption, *etc.*⁴³

After ammonia treatment of the zeolites, Na^+ and Ca^{2+} with NH_4^+ are mostly exchangeable in contrast to partly exchangeable of Fe^{3+} and Mg^{2+} in zeolites.⁴⁴ The introduction of aluminium into zeolites was studied by Kamali *et al.*⁴⁵ and then the Ates⁴⁶ applied it into natural zeolite obtained from Sivas-Yavu of Turkey for removal of manganese from drinking water and its adsorption capacity increased two times with enhanced aluminum content.

Based on aforementioned results, in this study the natural zeolite originated from Sivas-Yavu of Turkey was modified via ion exchange with NH_4^+ and introduction of aluminum for removal of arsenic from aqueous solution. The natural and modified zeolites were characterized by XRF, XRD, N_2 sorption, FTIR, NH_3 -TPD, particle size distribution, zeta potential and SEM. The influence of specific adsorption parameters on removal of arsenic from aqueous solution was studied and the data obtained were applied to isotherm models.

2. Experimental Method

2. 1. Material

Arsenic stock solutions were prepared using 1000 mg/L of As (III&V) prepared with As_2O_3 (Fluka, 39436) in 2% HNO_3 for As(V) and H_3AsO_4 (Merck, 1.19773.0500) in 0.5 mol/L of HNO_3 for As(III). Arsenic solutions used in the batch experiments were obtained by diluting the arsenic stock solution to the desired concentrations with deionized water. HCl and NaOH solutions were used to adjust pH of arsenite and arsenate solutions.

The natural zeolite was obtained from Sivas–Yavu (NZ-Y) region of Turkey and first ball milled to particle size in range of 0.25–0.5 mm. The NZ-Y was washed and dried in an oven at 120 °C overnight. The zeolite was transformed to the NH_4 -form by a twofold exchange with a 0.5 M NH_4NO_3 solution at 80 °C. After washing and drying, the sample was calcined at 500 °C for 2 h and denoted as NH_4 -NZ-Y.

After washing and drying, 1 g of the NZ-Y was mixed with sodium hydroxide and water with 5:50 mass ratios for 1 h at 90 °C and then the mixture was filtered and the filtrate was denoted as Na-NZ-Y.

Preparation of aluminum introduced zeolite is based on the study of Kamali *et al.*⁴⁵ For preparation of aluminum solutions, sodium chloride, aluminum sulphate ($\text{Al}_2(\text{SO}_4)_3$) and water with 1:5.4:10 mass ratios were mixed to make a clear solution (solution A). Aluminum sulphate, sodium hydroxide and water with 1:1.5:7.8 mass ratios were mixed and heated to make a clear solution (solution B). The A, Na-NZ and B with 1:7.1: 1 mass ratios were mixed at 90 °C for 2 h with a mixing rate of 500 rpm. The product was filtered, washed and dried at 80 °C. The product was denoted as Al-NZ-Y.

2. 2. Characterization of Samples

An X-ray fluorescence (XRF, PANanalytical) analyzer was used for the chemical composition of the samples.

The specific surface area and micropore volume of the samples were measured using N_2 adsorption–desorption (AUTOSORB 1C) at –196 °C. The surface area, pore volume and micropore volume were determined by multi-point BET, DFT (Density Functional Theory) and DR (Dubinin–Radushkevich), respectively.

XRD, SEM-EDS and NH_3 -TPD results of natural and modified samples were reported in the previous study.⁴⁶

The effect of adsorbent on solution pH was measured with time (0–7 h) for 2 g/L adsorbent in distilled water.

Zeta potential measurements were conducted using a zetameter (Malvern Zetasizer- Nano-Z). 0.005 g of samples was suspended in 100 ml of water and the particles were homogenized at 2 h using an ultrasonic bath. After ultrasonication, the aqueous suspension was equilibrated at different pH values for 30 min. The equilibrated slurry

was injected into the micro electrophoresis cell using disposable syringes. Prior to each measurement, the electrophoresis cell was washed repeatedly before reuse.

2. 3. Adsorption Experiments

Batch adsorption experiments were carried out in a glass flasks (20 mL) using a magnetic shaker (IKA Magnetic stirrer RO10) at 25 °C at a constant agitation of 200 rpm. In the kinetic studies suspensions containing the range of 25–200 mg L⁻¹ of As(III & V) were stirred for different periods of time at optimum pH. After the reaction, suspensions were centrifuged at 5000 rpm for 3 min in order to separate the solution and solid. The initial and non-adsorbed concentrations of As(III & V) in supernatants were determined by hydride generation atomic absorption spectroscopy (HG-AAS)- and ICP-MS (Thermo Scientific iCAP Q Series ICP-MS).

During adsorption of As(III & V), dissolution of cations with varying pH was studied for 20 cm³ solution containing 50 mg L⁻¹ of As (V) and 0.02 g of adsorbent for 3h. After adsorption, cations in supernatants were measured by ICP-MS. Adsorption studies of As(III & V) onto NZ-Y, NH₄-NZ-Y and Al- NZ-Y were conducted using the same procedure in sufficient time for varying feed solution concentrations (25–200 mg L⁻¹) at different temperatures (298–313 K). All results were averaged values of duplicate tests.

The adsorption capacity (q_e , mg g⁻¹) and removal percent (%) of As(III & V) were determined using following equations:

$$q_e = \frac{(C_0 - C_e)V}{m} \quad (1)$$

$$\text{Removal percent } (R, \%) = \frac{C_0 - C_e}{C_0} \times 100 \quad (2)$$

where C_0 and C_e are the initial and final concentrations of As(III & V) (mg L⁻¹), respectively, V is the volume of solution (L) and m is the amount of adsorbent (g).

In order to investigate the nature and mechanism of arsenic adsorption with natural and modified zeolite, several models such as pseudo-first-order, pseudo-second-order and intra-particle diffusion were applied.⁴⁴ For this aim, the adsorbents were loaded in the stirrer cell to be spun at 1500 rpm to cause a vigorous flow of solution. The diffusional resistances in the liquid film were neglected because of the high rotational speed. 3 mL of samples was periodically withdrawn from the solution and analyzed using HG-AAS.

The pseudo-first order kinetic model of Lagergren is given as:

$$\log(q_e - q_t) = \log q_e - \frac{k_1}{2.303} t \quad (3)$$

where q_t (mg/g) is the amount of As adsorbed on the adsorbent at time and k_1 (min⁻¹) is the rate constant of pseudo first order kinetic model.⁴⁷

The equation for the pseudo-second order kinetic model⁴⁷ is as follows:

$$\frac{dq_t}{dt} = K(q_e - q_t)^2 \quad (4)$$

where q_e and q_t are the amount of As adsorbed per unit of mass of the adsorbent at equilibrium and time t , respectively.

Linearized form of pseudo-second order rate kinetics is expressed as follows:

$$\frac{t}{q_t} = \frac{1}{kq_e^2} + \frac{1}{q_e} t \quad (5)$$

In addition, initial rate of adsorption is h :

$$h = kq_e^2 \quad (6)$$

The intraparticle diffusion model can be described as follows:

$$q_t = k_d t^{1/2} + C \quad (7)$$

where k_p is the intra-particle diffusion rate constant (mg g⁻¹ min^{-0.5}) obtained from the slope and C is the adsorption constant obtained from the intercept.

The Langmuir model essentially describes the monolayer type of adsorption.⁴⁸ It is expressed as follows:

$$q_e = \frac{q_m b C_e}{1 + b C_e} \quad (8)$$

where q_m (mg/g) is the maximum adsorption capacity and b (L mg⁻¹) is the Langmuir constant.

The Freundlich isotherm is derived from a multilayer heterogeneous adsorption model. The Freundlich isotherm is as follows:

$$q_e = k_F C_e^{1/n} \quad (9)$$

where k_F (((mg g⁻¹) (mg L⁻¹)⁻ⁿ) is the Freundlich adsorption constant related to adsorption capacity and n is the adsorption intensity. The $1/n$ value was between 0 and 1, indicating that the adsorption was favorable at the studied conditions.

In order to express the adsorption mechanism with Gaussian energy distribution onto a heterogeneous surface, equilibrium data was applied to Dubinin-Radushkevich (DR) model shown as following:

$$q_e = q_s \exp(-k\epsilon^2) \quad (10)$$

$$\ln q_e = \ln q_s - k\epsilon^2 \quad (11)$$

$$E = 1/(2k)^{0.5} \quad (12)$$

where ϵ (Polanyi Potential, J/mol) is $[RT \ln(1+(1/C_e))]$, q_e refers to the amount of As adsorbed per unit weight of adsorbent (mg g^{-1}), q_s refers to theoretical isotherm saturation capacity (mg g^{-1}), C_e is the equilibrium concentration of As in aqueous solution, k is a constant related to adsorption energy, R is the ideal gas constant and T the temperature (K).^{49–51}

2. 3. 1. Adsorption Thermodynamics

Gibbs free energy change (ΔG°), enthalpy change (ΔH°) and entropy change (ΔS°) of the adsorption of As (III&V) were evaluated. The value of ΔG° is a crucial due to an indication of spontaneity of a chemical reaction, which can be calculated as follows:

$$\Delta G = RT \ln K_c \quad (13)$$

where K_c ((the amount of As in adsorbent)/(the amount of As in solution)) is the distribution coefficient.

The enthalpy change (ΔH) and entropy change (ΔS) were estimated from the following equation:

$$\ln K_c = \frac{\Delta S}{R} - \frac{\Delta H}{RT} \quad (14)$$

3. Results and Discussion

3. 1. Characterization of Samples

XRD results in previous studies^{52,53} showed that NZ-Y contains mainly clinoptilolite ($(\text{Na}, \text{K}, \text{Ca})_{2-3}\text{Al}_3(\text{Al}, \text{Si})_2\text{Si}_{13}\text{O}_{36} \cdot 12(\text{H}_2\text{O})$) and mordenite ($(\text{Ca}, \text{Na}_2, \text{K}_2)\text{Al}_2\text{Si}_{10}\text{O}_{24} \cdot 7\text{H}_2\text{O}$) as well as quartz (SiO_2) and feldspar ($\text{KAlSi}_3\text{O}_8 - \text{NaAlSi}_3\text{O}_8 - \text{CaAl}_2\text{Si}_2\text{O}_8$). Based on XRD and SEM results,⁵³ after treatment with NH_4NO_3 of NZ-Y, the peak intensities are hardly changed and the particle size of NZ-Y decreased. Composition results listed in Table 1 show that the ion exchange with NH_4^+ of the zeolite leads to the efficient removal of Sr^{2+} and Ca^{2+} and the partial removal of Mg^{2+} , K^+ , Ba^{2+} and Ti^{4+} because cations such as Fe^{3+} , Mg^{2+} and K^+ are strongly bound in clinoptilolite. In contrast, after the treatment with NaOH and the introduction of aluminum, mordenite and feldspar phases disappeared and the phase intensity of clinoptilolite and quartz decreased significantly. In addition, the treatment with NaOH led to the formation of hydroxysodalite at 35° of 2θ ⁵⁴ and significant removal of Sr^{2+} along with significant dealumination and desilication in NZ-Y. It was reported that the Si–O–Al bond is relatively stronger than the Si–O–Si bond because of the negative charge of AlO_4^- tetrahedron.⁵⁵ The desilication process strongly relates with the concentration of NaOH solution in order to the extraction of Si from the zeolites. The aluminum introduction into Na-NZ-Y led to an increase in the aluminum content

and the percentage of various cations such as Mg^{2+} , Ca^{2+} and Fe^{3+} in the zeolite.

The N_2 -physorption^{52,53} showed that the shape of NZ-Y is consistent with Type I, which is characteristic of microporous materials with a plateau at high relative pressures. After ion exchange with NH_4^+ , a considerable increase in the specific surface area, micropore volume and total volume of zeolites was observed in Table 1. These results are in accordance with those reported previously.^{53,56,57} In addition, the replacement of the metal cations by H^+ and/or removal of some impurities may lead to an increase of the surface characteristics. The surface area and micropore volume of samples treated with NaOH significantly decreased due to loss of crystalline, sintering of phases and the formation of amorphous material. The aluminum introduction into Na-NZ-Y slightly increased its surface area and micropore volume due to reorganization of crystal structure in the presence of aluminum.

NH_3 -TPD results⁵³ showed that the NH_4^+ exchange of NZ-Y leads to a significant increase in the total acidity of the zeolite. This is related with the exchange of the K^+ , Fe^{3+} and Ca^{2+} ions with NH_4^+ and H^+ since the strong acid sites ($>300^\circ\text{C}$) generally result of structural hydroxyl groups. The generation of these framework OH groups and the re-appearance of structural hydroxyls blocked by cations can be obtained by means of decationisation and dealumination, which is consistent with FTIR results reported in reference.⁵³ In addition, the increase in the intensity of peak at higher than 600°C is a result of hydroxylation of samples. Aluminum introduction into Na-NZ-Y leads to an increase in a number of weak acid sites and a decrease in a number of strong acid sites, which is related with increasing extra-framework aluminum content and OH groups as seen in XRF and FTIR results reported in reference.⁵³

The pH variation of solution in the presence of adsorbents is illustrated in Fig. 1. For 30 min- contact time,

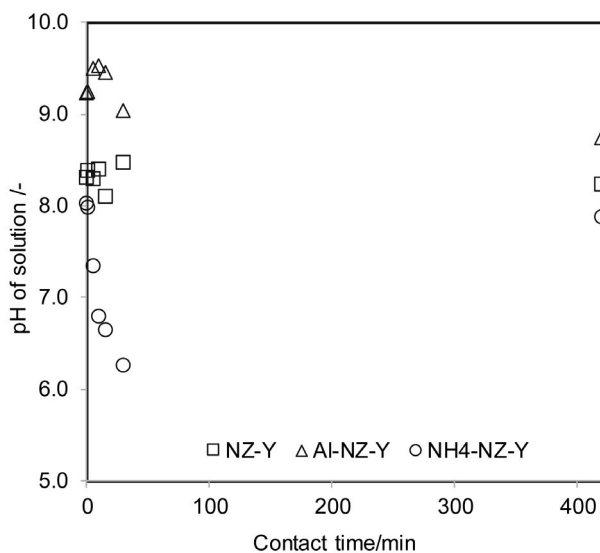


Figure 1. pH variation of solution with adsorbent

Table 1. The composition, surface area and pore characteristics of natural and modified zeolites.

Element	NZ-Y wt.%	NH ₄ -NZ-Y wt.%	Na-NZ-Y wt.%	Al-NZ-Y wt.%
Al	15.4	17.0	11.6	19.5
Si	79.6	80.2	77.0	70.6
Mg	1.25	0.74	2.2	2.4
Ca	2.1	0.3	5.2	4.3
K	0.4	0.3	0.7	0.6
Fe	0.7	0.9	1.8	1.4
Sr	3.9	0.04	0.6	0.5
Ti	0.2	0.2	0.4	0.3
Ba	0.05	0.04	0.18	0.14
Zr	0.01	0.01	0.04	0.04
Surface area and pore characteristics				
SA ^a (m ² g ⁻¹)	62.4	83.2	12.9	37.4
V _T (cm ³ g ⁻¹)	0.140	0.223	0.037	0.220
V _{MP} ^b (cm ³ g ⁻¹)	2.7 × 10 ⁻²	2.8 × 10 ⁻²	5.1 × 10 ⁻³	1.42 × 10 ⁻²
D ^c (Å)	94	107	116	241

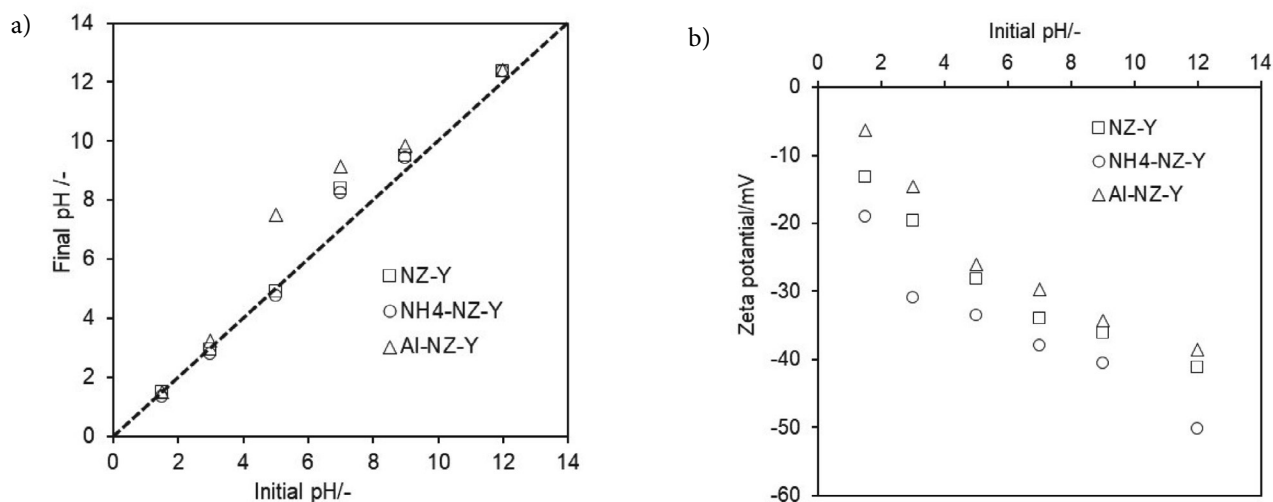
^a Surface area calculated using Multipoint BET; ^b Micro pore volume calculated using DR method; ^c Average pore diameter determined by DFT

whereas NZ-Y and Al-NZ-Y change insignificantly pH of solution, NH₄-NZ-Y decreases significantly the pH of solution due to dissolution of cations. However, after 7 h-contact time, scenario of pH variation changed and all adsorbents decreased slightly pH of solution. After 7 h-contact time, the variation of pH can be listed as 0.07 for NZ-Y, 0.49 for Al-NZ-Y and 0.15 for NH₄-NZ-Y as seen in Fig. 1. The pH variation with increasing contact time may be due to dissolution of cations in distilled water.

Fig. 2a illustrates final pH value with varying solution pH. The final pH value of solution for all samples is almost proportional with the initial pH until pH 5. However, above pH 5, it shifts slightly higher values when the

initial pH is increased, particularly for ranges from pH 5 to 9. This might be due to partial solubility of silica and cations under basic conditions.

Fig. 2b shows the results of zeta potential measurements of the natural and modified zeolites. In addition to zeta potential, the point of zero charge (pH_{PZC}) of samples was estimated where the net surface charge on metal oxides is zero, which was determined using ΔpH from Fig. 2a. The PZC of natural zeolite is pH 5.2, confirmed the results reported by various researchers.^{58,59} The PZCs of NH₄-NZ-Y and Al-NZ-Y are pH = 5.4 and pH = 1.5, respectively. Introduction of aluminum into natural zeolite decreases its PZC, which may be due to increasing aluminum content.

**Figure 2.** pH variation (a) and zeta potential (b) of natural and modified zeolites.

3. 2. Adsorption of Arsenic by the Natural and Modified Zeolites

3. 2. 1. Influence of pH

The pH of solution during adsorption process affects the surface characteristics and speciation of adsorbate. Therefore, pH of solution is crucial parameter on the removal of arsenic. The influence of initial solution pH on the arsenic adsorption with natural and modified zeolites was examined at the pH values ranging from 1.5 to 9.0 and the obtained results are illustrated in Table 2. The maximum removal amount of As(V) was found at pH 5.0 for NZ-Y, pH 3.0 for NH₄-NZ-Y and pH 1.5 for Al-NZ-Y, indicating that the modification of the zeolites affects significantly optimum As (V) removal pH. However, maximum removal amount of As(III) was observed at pH 7.0 on both NZ-Y and NH₄-NZ-Y. In this study, As (III) adsorption data on Al-NZ-Y cannot be showed due to its lower As(III) adsorption capacity. These results show that the adsorption behavior depends on not only the charge properties of the adsorbent surface but also the specific interactions between functional groups on the adsorbent surface and the adsorbed species.⁴⁹ Deliyanni and coworkers⁶⁰ reported that stable pH values of As (V) are H₃AsO₄ (pH < 2.25), H₂AsO₄⁻ (pH 2.25–6.77), HAsO₄²⁻ (pH 6.77–11.53), and AsO₄³⁻ (pH > 11.53). In addition, it is related with the determined p*H*_{pzc} values of adsorbents that the optimum As(V) removal pH and p*H*_{pzc} of NZ-Y and Al-NZ-Y are almost same and they are almost 5.0 for NZ-Y and are 1.5 for Al-NZ-Y. A shift between optimum As(V) removal pH and p*H*_{pzc} of NH₄-NZ-Y is observed that it may be related with ammonia dissolved during adsorption. Based on pre-

Table 2. The removal percentage of arsenic (III, V) with natural and modified zeolites as a function of pH (*C*_{As0} = 100 mg/L).

pH	As(V)			As(III)	
	NZ-Y	NH ₄ -NZ-Y	Al-NZ-Y	NZ-Y	NH ₄ -NZ-Y
1.5	12.5	4.0	32.0	0.8	12.0
3.0	18.8	12.4	14.8	4.0	25.4
5.0	19.0	6.8	24.8	3.6	16.3
6.0	–	–	7.6	–	–
7.0	15.4	1.6	9.0	4.1	25.0
9.0	6.70	–	16.9	5.0	–

viously reported results,⁶¹ as pH is lower than 6.8, the amount of multivalent species were dominated by H₃AsO₄ and H₂AsO₄⁻ in which the surfaces of adsorbent are positively charged and could bind negatively charged H₂AsO₄⁻ anions, which was responsible for the adsorption via electrostatic attraction and/or ligand change mechanism.⁶²

For influence of pH value in the solution, in the pH range of 1.5–5.0⁶³ electrostatic attraction occurs since As(V) generally exists in the forms of H₂AsO₄⁻ and HAsO₄²⁻ and the adsorbents possess negative charge, facilitating arsenic removal. However, an increase in solution pH leads to the gradual deprotonation of surface hydroxyl groups, made the adsorbents negatively charged, and the adsorption capacity is consequently decreased because of electrostatic repulsion effect. For As (III), the opposite behavior is observed due to its non-ionic (H₃AsO₃) species. The maximum As(III) removal is found at pH 7 because the adsorbents possess negative charge and the As(III) possesses approximately equimolar mixture of H₃AsO₃ and H₂AsO₃⁻ in the solution. For this result, Dutta *et al.*⁶⁴ suggested that the formation of surface complex might depend on solution pH.

Table 3 shows concentration (mg L⁻¹) of metals dissolved from adsorbents into solution with varying pH after 3 h- contact time. The amount of dissolved cations at pH 1.5 is high for both NZ-Y and Al-NZ-Y. Increasing pH leads to a decrease in dissolution, however the dissolution of Si is insignificantly changed that it should be related with insensitivity of silicon analysis with ICP-MS. Dissolved amount of aluminum from Al-NZ-Y at pH 1.5 is almost three times higher than that of NZ-Y, which is due to dissolution of introduced aluminum into NZ-Y. In order to reduction of aluminum dissolution, further adsorption studies for Al-NZ-Y were done at pH = 5.0. Although the amount of Fe and Mg with increasing pH is almost stable, the amount of Ca is similar to silicon results.

3. 2. 2. Contact Time and Adsorption Kinetic Studies

Adsorption capacity of adsorbents with contact time for As(V) is shown in Fig 3. Although the equilibrium time of As(V) on NZ-Y and Al-NZ-Y is determined as 120 min, the equilibrium time on the NH₄-NZ-Y is 480 min. Slow adsorption rate of As(V) on NH₄-NZ-Y may be due to in-

Table 3. Concentration(mg L⁻¹) of metals dissolved from adsorbent into solution with varying pH after 3h- contact time

pH	NZ-Y					Al-NZ-Y				
	1.5	3	5	7	9	1.5	3	5	7	9
Al	12.77	0.59	4.94	5.73	4.58	38.5	1.19	1.27	0.91	2.32
Si	18.01	19.31	31.34	30.86	31.54	63.0	21.0	20.80	17.12	20.10
Ca	14.70	13.59	13.38	12.66	12.33	28.4	15.4	16.06	12.90	13.49
Fe	2.33	1.94	3.13	3.43	2.92	13.03	1.96	2.05	1.55	2.35
Mg	1.47	0.82	1.13	1.09	1.01	10.24	1.87	1.81	1.20	1.47

creasing ion exchange capacity with cation exchange and increasing acidity based on XRF and NH_3 -TPD results reported in reference.⁵³ Equilibrium time of As (III) on ad-

sorbents is shown in Fig. 4 and almost opposite trend of As(V) is observed. Namely, the equilibrium time of As(III) on NZ-Y and NH_4 -NZ-Y is determined as 480 min.

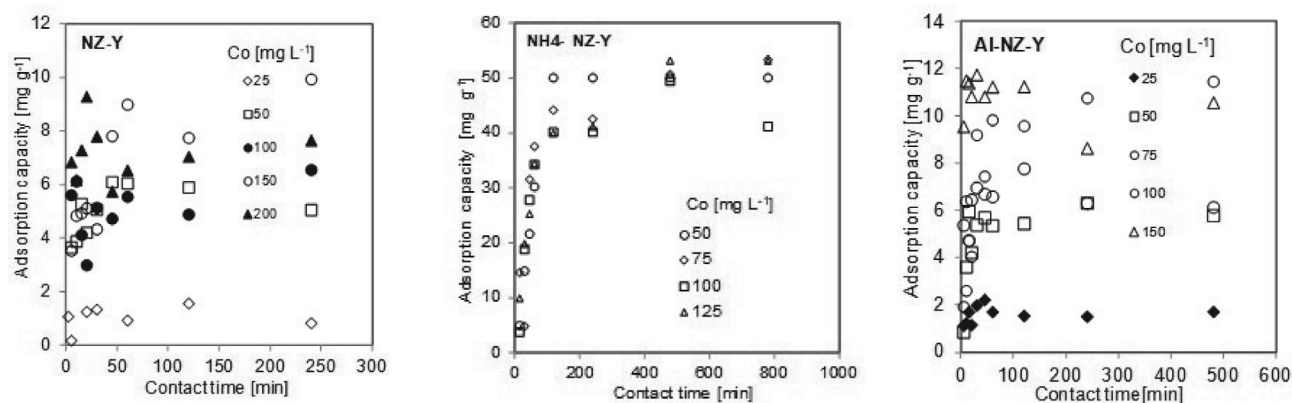


Figure 3. Adsorption capacity of NZ-Y, NH_4 -NZ-Y and Al-NZ-Y for removal of As(V) as a function of contact time.

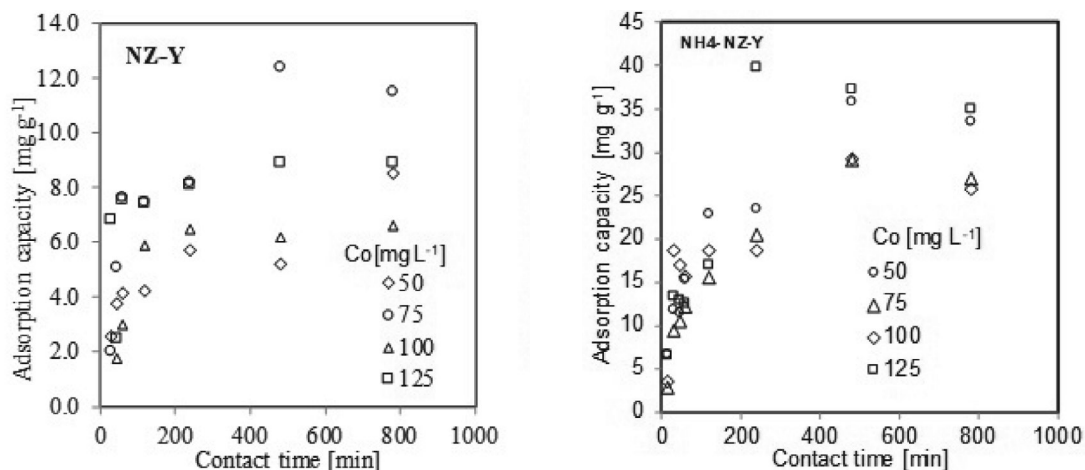


Figure 4. Adsorption capacity of NZ-Y and NH_4 -NZ-Y for removal of As(III) as a function of contact time.

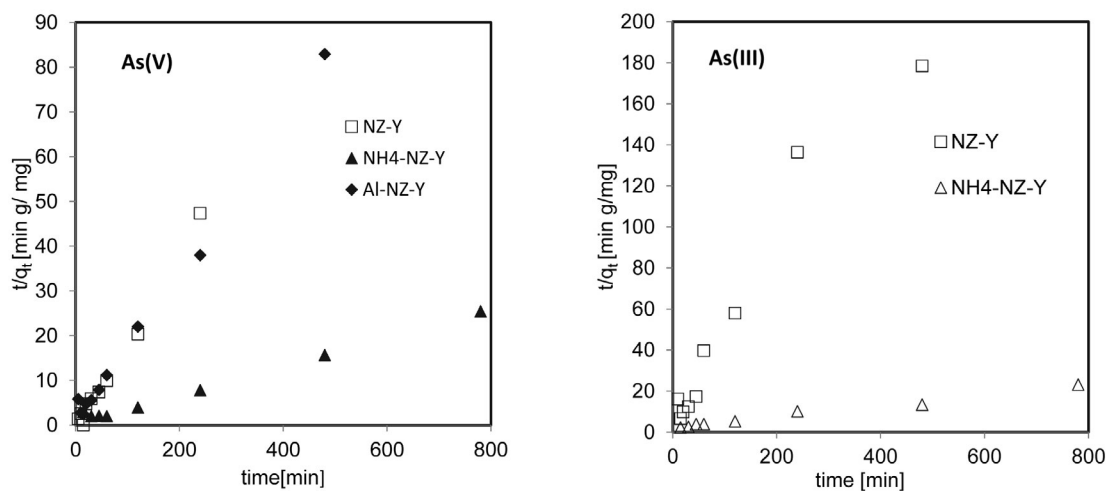


Figure 5. The linear second-order kinetic adsorption data for arsenic by natural and modified zeolites

To describe the adsorption behavior of an adsorbent, the adsorption results of As (III) and As(V) by NZ-Y, NH₄-NZ-Y and Al-NZ-Y shown in Figs 3 and 4 were fitted with pseudo-first-order, pseudo-second-order and intraparticle diffusion kinetic rate equations. Table 4 shows the relevant parameters and correlation coefficients (R²) obtained from the kinetic models. Based on correlation coefficients (R²), the pseudo-second-order model has higher R² values for As (III,&V) than pseudo-first-order and intraparticle diffusion models. In addition, the linear second-order kinetic adsorption data for arsenic by natural and modified zeolites are shown in Fig. 5. The finding implies that the adsorption of arsenic occurs in the pores of the adsorbents.

3. 2. 3. Adsorption Isotherms

Based on the results in Figs. 3 and 4, Langmuir and Freundlich, D-R isotherm models were fitted to adsorption isotherms and the adsorption constants obtained from the isotherms are presented in Table 4. Higher regression coefficient in Table 5 suggests that the Langmuir model is more suitable for arsenic removal than the Freundlich model. This indicates that arsenic adsorption occurs on a homogenous surface irrespective of modification.

q_m calculated from the Langmuir parameters represents the monolayer saturation at equilibrium and b indi-

cates the binding affinity for arsenic. The high b value indicates a high affinity that the affinity of NH₄-NZ-Y for As(III&V) ions is higher than those of NZ-Y and Al-NZ.

The value of k_F constant calculated from Freundlich isotherms is changed depending on the type of adsorbent. 1/n values of samples are in the range of 0 and 1, showing strong adsorption capacity as reported previously.⁶⁵ 1/n values calculated from all adsorbents are in the range of 0 and 1.

Based on results calculated from Langmuir model, the maximum As(III) and As(V) removal amounts with NH₄-NZ-Y are found as 28.7 mg g⁻¹ and 36.6 mg g⁻¹, respectively. The high adsorption capacity of NH₄-NZ-Y is a result of increasing adsorption sites with increasing surface area via decahedralisation as well as increasing surface acidity.

D-R isotherm model gives information on physical or chemical adsorption of adsorption process. Activation energy variations (E) are E < 8 kJ/mol for physical adsorption and 8 < E < 16.8 kJ/mol for chemical adsorption in which energy is needed for removing a molecule from its location into the surface of adsorbent.⁶⁶

From the linear fitting of D-R model, the obtained R² values for As(V) are higher than those of As(III) and E values for all samples in Table 4 are lower than 8 kJ/mol, indicating that the mechanism of adsorption is physical process.

Influence of temperature on adsorption of arsenic was studied and is shown in Figs. 6 and 7. The adsorption

Table 4. Kinetic parameters for adsorption of As (III&V) by NZ-Y, NH₄-NZ-Y and Al-NZ-7 in water.

Adsorbent	Pseudo first order				Pseudo second order			Intraparticle diffusion		
	q _e (mg/g)	k ₁	q _e (mg/g)	R ²	k	q _e (mg/g)	R ²	k _d	C (mg/g)	R ²
As(III)										
NZ-Y	2.69	0.002	1.37	0.24	0.017	2.57	0.94	0.067	1.24	0.23
NH ₄ -NZ-Y	26.99	0.004	4.03	0.81	0.0003	38.02	0.98	1.175	5.45	0.89
As(V)										
NZ-Y	5.06	0.033	1.24	0.99	0.052	5.13	0.98	0.217	2.99	0.23
NH ₄ -NZ-Y	30.23	0.043	4.81	0.74	0.001	32.25	0.99	0.749	14.89	0.44
Al-NZ-Y	5.79	0.055	1.79	0.66	0.022	5.99	0.99	0.141	3.70	0.29

Table 5. Adsorption constants for removal of arsenic (III, V) from aqueous solution with natural and modified zeolites

Adsorbent	Freundlich isotherm			Langmuir isotherm			D-R isotherm			
	k _F (mg g ⁻¹)(mg L ⁻¹) ⁻ⁿ	1/n	R ²	q _m (mg/g)	b (L/mg)	R ²	q _s (mol/g)	k (mol ² /J ²)	E (kJ/mol)	R ²
As(III)										
NZ-Y	6.40	0.22	0.86	2.2	0.11	0.99	4.29	2.472	0.446	0.01
NH ₄ -NZ-Y	474.71	0.10	0.99	28.7	0.46	0.98	28.85	2.976	0.409	0.21
As(V)										
NZ-Y	1.74	0.34	0.92	12.3	0.024	0.96	73.27	139.58	0.059	0.88
NH ₄ -NZ-Y	64.97	0.12	0.97	36.6	0.22	0.99	9.81	141.63	0.059	0.90
Al-NZ-Y	0.66	0.58	1.00	18.8	0.01	0.99	18.61	136.3	0.060	0.89

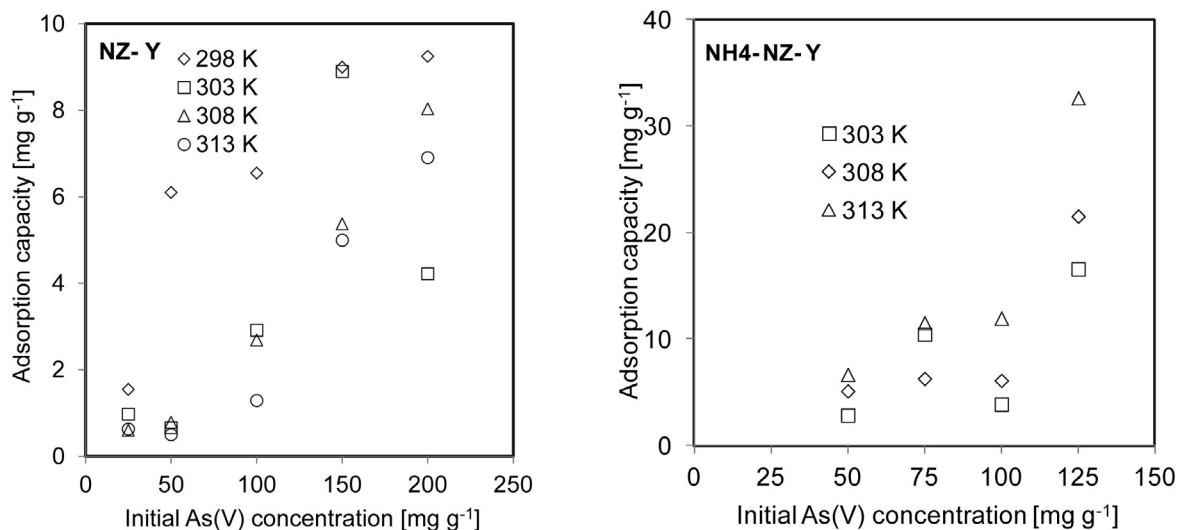


Figure 6. Adsorption capacity of NZ-Y and NH₄-NZ-Y for removal of As(V) at different temperatures as a function of initial As(V) concentration.

Table 6. Thermodynamic data for As (III&V) on NH₄-NZ-Y

Adsorbent	As (III) concentration	T (K)	ΔG (kJ/mol)	ΔH (kJ/mol)	ΔS (J/mol K)	R ²	
NH ₄ -NZ-Y	50 mg/L	298	-19.95	-99.0	-264.9	0.99	
		303	-18.90				
		308	-				
		313	16.02				
	75mg/L	298	-16.19	-14.51	5.61	0.99	
		303	-16.21				
		313	-16.28				
	100 mg/L	298	-14.37	39.40	180.51	0.99	
		303	-15.32				
		308	-16.17				
	125 mg/L	298	298	-	22.85	122.57	0.98
			303	-14.31			
308			-14.84				
313			-15.54				
NH ₄ -NZ-Y	As (V) concentration 50 mg/L	303	-9.1	71.4	266.2	0.96	
		308	-10.8				
		313	-11.8				
		303	-13.1				-14.9
	308	-13.1					
	313	-13.0					
	75mg/L	303	-9.1	95.0	343.4	0.98	
		308	-10.5				
		313	-12.6				
	100 mg/L	303	-12.4	64.9	255.1	0.97	
		308	-13.4				
		313	-15.0				

capacity of NZ-Y and NH₄-NZ-Y for As (V) and of NH₄-NZ-Y for As(III) increases with increasing temperature, indicating endothermic nature of arsenic adsorption.

However, the removal amount of As (III) on NZ-Y decreased with increasing temperature due to its exothermic nature.

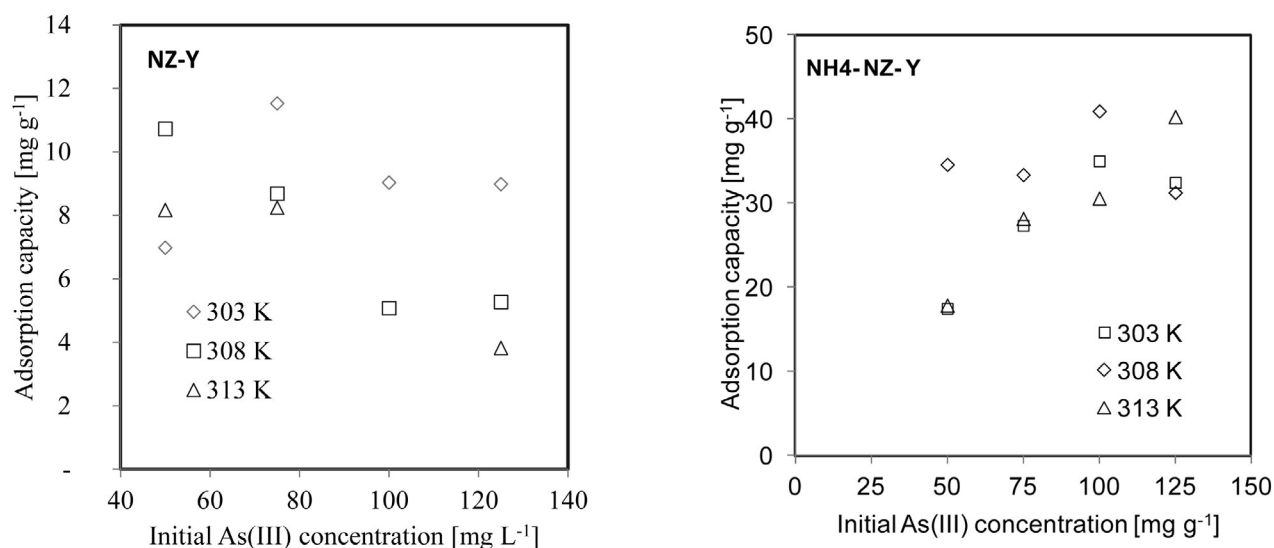


Figure 7. Adsorption capacity of NZ-Y and NH₄-NZ-Y for removal of As(III) at different temperatures as a function of initial As(III) concentration

Thermodynamic parameters for adsorption of As (III&V) on NH₄-NZ-Y with high arsenic adsorption capacity were calculated using experimental results in Fig. 6 and 7 via equations (13 and 14) in section 2.3 and the results are listed in Table 6. The Gibbs free energies were found as negative for NH₄-NZ-Y, indicating that the adsorption of arsenic on NH₄-NZ-Y is feasible and spontaneous (Table 6). The positive values of ΔH° for NH₄-NZ-Y supported the endothermic nature of adsorption process. The positive values of ΔS° for NH₄-NZ-Y increase with increasing initial concentration of As(III&V), supporting randomness on the solid-liquid interface.

3. 2. 4. Comparison of Results With Literature

The comparison of results with literature shows that the adsorption capacity of NZ-Y varies with source, composition and modification of NZ as seen in Table 7. The results of NZ-Y for As(V) are consistent with Slovakia clinoptilolite reported by Dousova *et al.*⁶⁷ Adsorption results of the modified zeolites with NH₄⁺ is similar to synthetic zeolites reported by Chutia *et al.*⁵⁹ However, the effect of Al modification on arsenic adsorption capacity of zeolite varies with source and composition of zeolite. Although the influence of Al on Gordes-clinoptilolite⁶⁸ for As(V) adsorption is low, its effect on montmorillonite⁶⁹ is significant. In this study, the findings on Sivas-Yavu zeolitic tuff for As(V) are in accordance with montmorillonite, which may be associated with significant mordenite content and high surface area of NZ-Y.

4. Conclusion

Natural zeolite obtained from Sivas-Yavu region of Turkey was modified with ion-exchange using NH₄NO₃

and introduction of aluminum using Al₂(SO₄)₃. Chemical and physical properties of natural and modified zeolites were characterized by various techniques such as XRF, XRD, N₂ sorption, FTIR, NH₃-TPD, zeta potential and SEM. The influence of specific adsorption parameters on removal of arsenic from aqueous solution was studied and the data obtained were applied to isotherm models. From the experimental results it can be concluded that adsorption of arsenic depends on the textural properties such as composition, the size and distribution of pores and crystal structure of the adsorbate. Ion exchange and aluminum introduction increased the arsenic adsorption capacity of natural zeolite. The Langmuir isotherm model was best fitted to the isotherm data obtained. In addition, D-R isotherms showed physical adsorption of arsenic on the natural and modified zeolites. Based on thermodynamic investigation, whereas adsorption of As(III) with natural zeolite has exothermic nature, the adsorption of As (III &V) with NH₄⁺ exchanged zeolite is endothermic.

5. Acknowledgements

I gratefully acknowledge the financial support of this work by Research fond of Cumhuriyet University (M-492) and The Scientific & Technology Research Council of Turkey (TUBİTAK) (113M813).

6. References

1. WHO, *Guidelines for drinking-water quality (4 ed)* World Health Organization, Geneva, Switzerland, 1993.
2. T. Tuutijärvi, J. Lu, M. Sillanpää, G. Chen, *J. Hazard. Mater.* 2009, 166, 1415–1420. DOI:10.1016/j.jhazmat.2008.12.069

Table 7. Comparison of adsorption capacities of different types of zeolites

Adsorbent	Treatment	Metal oxide	As(III) (mg/g)	As (V) (mg/g)	Reference
Zeolitic tuff(ZMA)	–	–	–	0.004	Elizalde-González <i>et al.</i> ⁷⁰
	–	–	–	0.0018	
Zeolite	HDTMA			0.539	Li <i>et al.</i> ⁷¹
Clinoptilolite	NaCl			0.428	Chutia <i>et al.</i> ⁵⁹
Winston clinoptilolite	–	FeCl ₃ , FeSO ₄	–	0.05	Li <i>et al.</i> ⁷²
Tehuacan natural zeolite	NaCl	FeCl ₃	0.06	0.186	Jiménez-Cedillo ⁴⁰
		MnCl ₂	0.06	0.170	
Mexica clinoptilolite	NaCl	FeCl ₃	0.01	0.022–0.053	MacEdo-Miranda <i>et al.</i> ⁴²
Clinoptilolite	–	FeCl ₃	–	0.68	Jeon <i>et al.</i> ⁷³
Mexica clinoptilolite	NaCl	FeCl ₃	0.012	0.006	Davilla-Jimenez <i>et al.</i> ⁷⁴
Gordes clinoptilolite	NaCl	FeCl ₃	–	0.0084–0.0092	Baskan and Pala ⁷⁵
Slovakia clinoptilolite	–	FeSO ₄	–	18.0	Dousova <i>et al.</i> ⁷⁶
Montmorillonite	–	AlCl ₃ and FeCl ₃	19.11	21.23	Ramesh <i>et al.</i> ⁷⁷
Gordes clinoptilolite	NaCl	FeCl ₂	–	3.02	Simsek <i>et al.</i> ⁷⁸
		FeCl ₂ and AlCl ₃	–	3.86	
		AlCl ₃	–	1.60	
Synthetic zeolite	–	–	–	35.89	Chutia <i>et al.</i> ³⁹
Sivas- Yavu- clinoptilolite	–	–	1.1	12.33	This study
		NH ₄ NO ₃	28.7	36.6	
		Al ₂ (SO ₄) ₃	–	18.83	

- W. Song, M. Zhang, J. Liang, G. Han, *J. Mol. Liq.* **2015**, *206*, 262–267. DOI:10.1016/j.molliq.2015.03.007
- A. Nilchi, S. R. Garmarodi, S. J. Darzi, *J. Appl. Polym. Sci.* **2011**, *119*, 3495–3503. DOI:10.1002/app.33003
- Z. Li, J.-S. Jean, W.-T. Jiang, P.-H. Chang, C.-J. Chen, L. Liao, *J. Hazard. Mater.* **2011**, *187*, 318–23. DOI:10.1016/j.jhazmat.2011.01.030
- P. Navarro, F. J. Alguacil, *Hydrometallurgy.* **2002**, *66*, 101–105. DOI:10.1016/S0304-386X(02)00108-1
- C. L. Chuang, M. Fan, M. Xu, R. C. Brown, S. Sung, B. Saha, C. P. Huang, *Chemosphere.* **2005**, *61*, 478–483. DOI:10.1016/j.chemosphere.2005.03.012
- B. Daus, R. Wennrich, H. Weiss, *Water Res.* **2004**, *38*, 2948–2954. DOI:10.1016/j.watres.2004.04.003
- Z. M. Gu, J. Fang, B. L. Deng, *Environ. Sci. Technol.* **2005**, *39*, 3833–3843. DOI:10.1021/es048179r
- D. Mohan, S. Chander, *J. Hazard. Mater.* **2006**, *137*, 1545–1553. DOI:10.1016/j.jhazmat.2006.04.053
- M. Fan, W. Marshall, D. Daugaard, R. C. Brown, *Bioresour. Technol.* **2004**, *93*, 103–107. DOI:10.1016/j.biortech.2003.08.016
- H. S. Altundoan, S. Altundoan, F. Tümen, M. Bildik, *Waste Manag.* **2002**, *22*, 357–363. DOI:10.1016/S0956-053X(01)00041-1
- F. S. Zhang, H. Itoh, *Chemosphere.* **2005**, *60*, 319–325. DOI:10.1016/j.chemosphere.2004.12.019
- J. S. Ahn, C. M. Chon, H. S. Moon, K. W. Kim, *Water Res.* **2003**, *37*, 2478–2488. DOI:10.1016/S0043-1354(02)00637-1
- K. S. Low, C. K. Lee, *Environ. Technol.* **1995**, *16*, 65–71. DOI:10.1080/09593331608616246
- A. Mittal, L. Kurup, V. K. Gupta, *J. Hazard. Mater.* **2005**, *117*, 171–178. DOI:10.1016/j.jhazmat.2004.09.016
- H. Zhang, H. M. Selim, *Environ. Sci. Technol.* **2005**, *39*, 6101–6108. DOI:10.1021/es050334u
- B. Petrusevski, S. K. Sharma, F. Kruijs, P. Omeruglu, J. C. Schippers, in *Water Science and Technology: Water Supply.* **2002**, *2*, 127–133. DOI:10.2166/ws.2002.0160
- C. Y. Jing, S. Q. Liu, M. Patel, X. G. Meng, *Environ. Sci. Technol.* **2005**, *39*, 5481–5487. DOI:10.1021/es050290p
- M. Vithanage, W. Senevirathna, R. Chandrajith, R. Weerasooriya, *Sci. Total Environ.* **2007**, *379*, 244–248. DOI:10.1016/j.scitotenv.2006.03.045
- Y. Arai, D. L. Sparks, J. A. Davis, *Environ. Sci. Technol.* **2005**, *39*, 2537–2544. DOI:10.1021/es0486770
- P. Lakshmipathiraj, B. R. Narasimhan, S. Prabhakar, G. B. Raju, *J. Hazard. Mater.* **2006**, *136*, 281–287. DOI:10.1016/j.jhazmat.2005.12.015

23. G. P. Gillman, *Sci. Total Environ.* **2006**, 366, 926–931.
DOI:10.1016/j.scitotenv.2006.01.036
24. K. B. Payne, T. M. Abel-Fattah, *J. Environ. Sci. Heal. Part a-Toxic/Hazardous Subst. Environ. Eng.* **2005**, 40, 723–749.
25. M. Badruzzaman, P. Westerhoff, D. R. U. Knappe, *Water Res.* **2004**, 38, 4002–4012. DOI:10.1016/j.watres.2004.07.007
26. S. Bang, M. Patel, L. Lippincott, X. Meng, *Chemosphere.* **2005**, 60, 389–397. DOI:10.1016/j.chemosphere.2004.12.008
27. T. F. Lin, J. K. Wu, *Water Res.* **2001**, 35, 2049–2057.
DOI:10.1016/S0043-1354(00)00467-X
28. T. Nakajima, Y. H. Xu, Y. Mori, M. Kishita, H. Takanashi, S. Maeda, A. Ohki, *J. Hazard. Mater.* **2005**, 120, 75–80.
DOI:10.1016/j.jhazmat.2004.11.030
29. M. Pena, X. G. Meng, G. P. Korfiatis, C. Y. Jing, *Environ. Sci. Technol.* **2006**, 40, 1257–1262. DOI:10.1021/es052040e
30. A. C. Q. Ladeira, V. S. T. Ciminelli, *Water Res.* **2004**, 38, 2087–2094. DOI:10.1016/j.watres.2004.02.002
31. C. M. Su, R. W. Puls, *Environ. Sci. Technol.* **2003**, 37, 2582–2587. DOI:10.1021/es026351q
32. Y. Kiso, Y. J. Jung, T. Yamada, M. Nagai, K. S. Min, *Leading-Edge Technol. 2005 – Water Treat.* **2005**, 5, 75–81.
33. W. Lenoble, C. Laclautre, W. Deluchat, B. Serpaud, J. C. Bollinger, *J. Hazard. Mater.* **2005**, 123, 262–268.
DOI:10.1016/j.jhazmat.2005.04.005
34. D. F. Martin, L. O'Donnell, B. B. Martin, R. Alldredge, *J. Environ. Sci. Heal. Part a-Toxic/Hazardous Subst. Environ. Eng.* **2007**, 42, 97–102.
35. C. C. Chen, Y. C. Chung, *J. Environ. Sci. Heal. Part a-Toxic/Hazardous Subst. Environ. Eng.* **2006**, 41, 645–658.
36. D. Pokhrel, T. Viraraghavan, *Water Res.* **2006**, 40, 549–552.
DOI:10.1016/j.watres.2005.11.040
37. M. N. Haque, G. M. Morrison, G. Perrusquia, M. Gutierrez, A. R. Aguilera, I. Cano-Aguilera, J. L. Gardea-Torresdey, *J. Hazard. Mater.* **2007**, 145, 30–35.
DOI:10.1016/j.jhazmat.2006.10.080
38. M. Srivastava, L. Q. Ma, J. A. G. Santos, *Sci. Total Environ.* **2006**, 364, 24–31. DOI:10.1016/j.scitotenv.2005.11.002
39. P. Chutia, S. Kato, T. Kojima, S. Satokawa, *J. Hazard. Mater.* **2009**, 162, 440–447. DOI:10.1016/j.jhazmat.2008.05.061
40. M. J. Jiménez-Cedillo, M. T. Olguín, C. Fall, A. Colín, *Appl. Clay Sci.* **2011**, 54, 206–216. DOI:10.1016/j.clay.2011.09.004
41. M. P. Elizalde-González, J. Mattusch, W.-D. Einicke, R. Wenrich, *Chem. Eng. J.* **2001**, 81, 187–195.
DOI:10.1016/S1385-8947(00)00201-1
42. M. G. MacEdo-Miranda, M. T. Olgun, *J. Incl. Phenom. Macrocycl. Chem.* **2007**, 59, 131–142.
DOI:10.1007/s10847-007-9306-3
43. K. Margeta, Š. C. Stefanović, V. Kaučič, N. Z. Logar, *Appl. Clay Sci.* **2015**, 116–117, 111–119.
DOI:10.1016/j.clay.2015.08.021
44. X. Jiang Hu, J. Song Wang, Y. Guo Liu, X. Li, G. Ming Zeng, Z. Lei Bao, X. Xia Zeng, A. Wei Chen, F. Long, *J. Hazard. Mater.* **2011**, 185, 306–314.
45. M. Kamali, S. Vaezifar, H. Kolahduzan, A. Malekpour, M. R. Abdi, *Powder Technol.* **2009**, 189, 52–56.
DOI:10.1016/j.powtec.2008.05.015
46. A. Ates, *Powder Technol.* **2014**, 264, 86–95.
DOI:10.1016/j.powtec.2014.05.023
47. Y. S. Ho, G. McKay, *Water Res.* **2000**, 34, 735–742.
DOI:10.1016/S0043-1354(99)00232-8
48. Y. C. Wong, Y. S. Szeto, W. H. Cheung, G. McKay, *Process Biochem.* **2004**, 39, 693–702.
DOI:10.1016/S0032-9592(03)00152-3
49. H. Javadian, M. Ahmadi, M. Ghiasvand, S. Kahrizi, R. Katal, *J. Taiwan Inst. Chem. Eng.* **2013**, 44, 977–989.
50. A. Günay, E. Arslankaya, I. Tosun, *J. Hazard. Mater.* **2007**, 146, 362–371. DOI:10.1016/j.jhazmat.2006.12.034
51. H. Javadian, M. Taghavi, *Appl. Surf. Sci.* **2014**, 289, 487–494.
DOI:10.1016/j.apsusc.2013.11.020
52. A. Ates, C. Hardacre, *J. Colloid Interface Sci.* **2012**, 372, 130–140. DOI:10.1016/j.jcis.2012.01.017
53. A. Ates, *Powder Technol.* **2014**, 264, 86–95.
DOI:10.1016/j.powtec.2014.05.023
54. S. J. Kang, K. Egashira, A. Yoshida, *Appl. Clay Sci.* **1998**, 13, 117–135. DOI:10.1016/S0169-1317(98)00019-2
55. S. R. Taffarel, J. Rubio, *Miner. Eng.*, 2010, **23**, 1131–1138.
DOI:10.1016/j.mineng.2010.07.007
56. M. Kamali, S. Vaezifar, H. Kolahduzan, A. Malekpour, M. R. Abdi, *Powder Technol.* **2009**, 189, 52–56.
DOI:10.1016/j.powtec.2008.05.015
57. K. Zhang, V. Dwivedi, C. Chi, J. Wu, *J. Hazard. Mater.* **2010**, 182, 162–168. DOI:10.1016/j.jhazmat.2010.06.010
58. A. Teutli-Sequeira, M. Solache-Rios, V. Martínez-Miranda, I. Linares-Hernández, *J. Colloid Interface Sci.* **2014**, 418, 254–260. DOI:10.1016/j.jcis.2013.12.020
59. P. Chutia, S. Kato, T. Kojima, S. Satokawa, *J. Hazard. Mater.* **2009**, 162, 204–211. DOI:10.1016/j.jhazmat.2008.05.024
60. E. A. Deliyanni, D. N. Bakoyannakis, A. I. Zouboulis, K. A. Matis, *Chemosphere.* **2003**, 50, 155–163.
DOI:10.1016/S0045-6535(02)00351-X
61. D. Fu, Z. He, S. Su, B. Xu, Y. Liu, Y. Zhao, *J. Colloid Interface Sci.* **2017**, 505, 105–114. DOI:10.1016/j.jcis.2017.05.091
62. G. A. Waychunas, J. A. Davis, C. C. Fuller, *Geochim. Cosmochim. Acta.* **1995**, 59, 3655–3661.
DOI:10.1016/0016-7037(95)00276-6
63. G. Zhang, J. Qu, H. Liu, R. Liu, R. Wu, *Water Res.* **2007**, 41, 1921–1928. DOI:10.1016/j.watres.2007.02.009
64. P. K. Dutta, A. K. Ray, V. K. Sharma, F. J. Millero, *J. Colloid Interface Sci.* **2004**, 278, 270–275.
DOI:10.1016/j.jcis.2004.06.015
65. N. D. Hutson, R. T. Yang, *Adsorption.* **1997**, 3, 189–195.
DOI:10.1007/BF01650130
66. K. Y. Foo, B. H. Hameed, *Chem. Eng. J.* **2010**, 156, 2–10.
DOI:10.1016/j.cej.2009.09.013
67. B. Dousova, T. Grygar, A. Martaus, L. Fuitová, D. Kolousek, V. Machovic, *J. Colloid Interface Sci.* **2006**, 302, 424–431.
DOI:10.1016/j.jcis.2006.06.054
68. E. B. Simsek, E. Özdemir, U. Beker, *Chem. Eng. J.* **2013**, 220, 402–411. DOI:10.1016/j.cej.2013.01.070
69. A. Ramesh, H. Hasegawa, T. Maki, K. Ueda, *Sep. Purif. Technol.* **2007**, 56, 90–100.
70. M. P. Elizalde-González, J. Mattusch, W. D. Einicke, R. Wen-

- nrich, *Chem. Eng. J.* **2001**, *81*, 187–195.
71. Z. Li, R. Beachner, Z. McManama, H. Hanlie, *Microporous Mesoporous Mater.* **2007**, *105*, 291–297. DOI:10.1016/j.micromeso.2007.03.038
72. Z. Li, J.-S. Jean, W.-T. Jiang, P.-H. Chang, C.-J. Chen, L. Liao, *J. Hazard. Mater.* **2011**, *187*, 318–323. DOI:10.1016/j.jhazmat.2011.01.030
73. C.-S. Jeon, K. Baek, J.-K. Park, Y.-K. Oh, S.-D. Lee, *J. Hazard. Mater.* **2009**, *163*, 804–808. DOI:10.1016/j.jhazmat.2008.07.052
74. M. M. Dávila-Jiménez, M. P. Elizalde-González, J. Mattusch, P. Morgenstern, M. A. Pérez-Cruz, Y. Reyes-Ortega, R. Wen-
nrich, H. Yee-Madeira, *J. Colloid Interface Sci.* **2008**, *322*, 527–536. DOI:10.1016/j.jcis.2008.03.042
75. M. Bilici Baskan, A. Pala, *Desalination.* **2011**, *281*, 396–403. DOI:10.1016/j.desal.2011.08.015
76. B. Doušová, T. Grygar, A. Martaus, L. Fuitová, D. Koloušek, V. Machovič, *J. Colloid Interface Sci.* **2006**, *302*, 424–431. DOI:10.1016/j.jcis.2006.06.054
77. A. Ramesh, H. Hasegawa, T. Maki, K. Ueda, *Sep. Purif. Technol.* **2007**, *56*, 90–100. DOI:10.1016/j.seppur.2007.01.025
78. E. B. Simsek, E. Özdemir, U. Beker, *Chem. Eng. J.* **2013**, *220*, 402–411. DOI:10.1016/j.cej.2013.01.070

Povzetek

Preučevali smo adsorpcijo arzena iz vodnih raztopin na naravni zeolit (NZ), zeolit predhodno izpostavljen raztopini NH_4NO_3 in zeolit izpostavljen raztopni $\text{Al}_2(\text{SO}_4)_3$. Zeoliti so bili okarakterizirani z XRF, XRD, N_2 adsorpcijo, FTIR, NH_3 -TPD, zeta potencialom in SEM. Zeolit predhodno obdelan z NH_4^+ kaže znatno ionsko izmenjavo z večino kationov ter povečanje specifične površine, poroznosti in površinske kislosti. Prisotnost aluminija v zeolitu je povečala adsorpcijo As(V) in znižala adsorpcijo As(III) medtem ko izpostavljenost naravnega zeolita NH_4^+ ionom povzroči povečanje adsorpcijske kapacitete obeh zvrsti. Hitrost adsorpcije obeh zvrsti arzena na naravni in modificirana zeolita lahko opišemo s kinetiko pseudo-drugerega reda, adsorpcijsko ravnotežje pa z Langmuirjevo izotermo. Najvišjo adsorpcijsko kapaciteto kaže zeolit izpostavljen vodni raztopini amonijaka in znaša 28.7 mg/g za As(III) in 36.6 mg/g za As(V). Izračunani termodinamski parametri kažejo, da je adsorpcijski proces spontan in ravnotežje ugodno.

Scientific paper

Adsorptive Removal of Selected Anionic and Cationic Dyes by Using Graphitic Carbon Material Prepared from Edible Sugar: A Study of Kinetics and Isotherms

Lakshmi Prasanna Lingamdinne,¹ Jong-Soo Choi,¹ Jae-Kyu Yang,² Yoon-Young Chang,¹ Janardhan Reddy Koduru^{1,*} and Jiwan Singh^{3,*}

¹ Department of Environmental Engineering, Kwangwoon University, Seoul 01897, Republic of Korea.

² Ingenium College of Liberal Arts, Kwangwoon University, Seoul 01897, Republic of Korea.

³ Department of Environmental Science, Babasaheb Bhimrao Ambedkar University, Lucknow-226025, India.

* Corresponding author: E-mail: reddyjchem@gmail.com; jiwansingh95@gmail.com
Phone: +82-2-940-5496; Fax: +82-2-9185774

Received: 07-02-2018

Abstract

Graphitic carbon-like material (GCM) derived from edible sugar under a nitrogen environment was applied as an adsorbent for the removal of anionic and cationic dyes (methyl orange, MO) and methylene blue (MB) from wastewater. The physico-chemical characterization of GCM was analyzed by scanning electron microscopy (SEM), X-ray diffraction (XRD), Fourier transform infrared (FT-IR) spectroscopy, and X-ray photoelectron spectroscopy (XPS). The plate-like morphology with an average size of 50–100 nm was measured from the SEM images. The measured BET surface area and pore volume were 574 m²/g and 0.248 cm³/g, respectively with pore diameter (*d*), 1.847 (< 2 nm) indicates that the GCM classified as a microporous. The effects of dosage, pH, contact time and concentration on the adsorption of MB and MO onto GCM were studied to unveil the adsorption process. The experimental isotherm data concurred with the Langmuir isotherm model ($R^2 = 0.990$) for MB, while the MO isotherm data concurred with Freundlich model ($R^2 = 0.995$). The maximum adsorption capacity achieved from the Langmuir isotherm equation at 25 °C was 38.75 and 43.48 mg/g for MB and MO, respectively, which indicates that GCM is a suitable adsorbent for the adsorption of both anionic and cationic dyes. The kinetic study demonstrated that the adsorption of both dyes onto GCM was the pseudo-second-order diffusion kinetics. The thermodynamic parameters reveal the adsorption of both dyes was endothermic spontaneous through chemical interactions. The GCM was found to be a potential adsorbent for the removal of MB and MO from an aqueous solution.

Keywords: Graphitic carbon material; Anionic dye; Cationic dye; Adsorption efficiency; Kinetics isotherms; Thermodynamics

1. Introduction

The releasing of dye-containing wastewaters in to the environment is a significant cause of poor water quality, and leads to eutrophication and distressing aquatic life. Dye-containing wastewater can increase the toxicity, biochemical oxygen demand, and chemical oxygen demand of the affected water.¹ Therefore, developing a cost-effective process for the removal of dyes from the effluents of industries has been one of the most challenging tasks around the world. Many treatment methods including physical, chemical, and biological methods have been re-

ported to remove dyes from wastewater.² However, these methods have a number of disadvantages, such as the production of large amounts of toxic and carcinogenic by-products, and are not cost-effective.³ Adsorption is an economic, effective, and easily operated process in dye removal.⁴ Hence, continued attempts have been made by investigators to discover a new adsorbent material which can give results that are more efficient. Methylene blue (MB) is a cationic dye and is most commonly used for dyeing materials such as wood, silk, and cotton.⁵ Methyl orange (MO) is an acidic/anionic dye, and has been widely used in the textile, printing, paper, food, and pharmaceuti-

cal industries.⁶ Because of their toxic nature, the removal of MO and MB from wastewater is essential.^{5,7}

Graphene is an attractive new material composed of carbon ingredients with a honeycomb-like structure. It has motivated massive interest over the last few years because of its excellent properties such as stability,⁸ high thermal conductivity,⁹ and fast mobility of charge carriers.¹⁰ Various studies have shown that graphene/graphene oxide is a perfect material for the removal of dyes due to its good mechanical strength, large surface area, 2D structure, abundant surface functional groups, and its electrostatic interaction with cationic dyes.^{11–13} However, the preparation of graphene from graphite is expensive and using toxic chemicals. A biologically derived graphene is possibly the most reasonable and chemically most adaptable graphene. Graphene or carbon-like materials derived from plant sources are typically eco-friendlier than those from fossil sources such as petroleum. There are many reports prepared carbon materials from biomaterials or plant continents and were utilized for adsorption.¹⁴ Edible sugar is one of the simplest natural sources of carbon, and converts completely into elemental carbon upon dehydration.¹⁵

In this work, we report the results of the adsorption of an anionic dye (MO) and a cationic dye (MB) on a sugar-based graphitic carbon-like material (GCM). We developed GCM from a low-cost crystal sugar in the presence of nitrogen gas. Crystal sugar is a type of edible sugar, an inexpensive and sustainable raw material that can be easily produced from agricultural products such as sugar cane and beet. Synthesized low-cost GCM was examined as an adsorbent for the removal of MB and MO from aqueous solutions. Studies were conducted with a parameter (equilibrium time, pH, temperature, and initial dye concentra-

tion) that affect the adsorption process. Kinetic models and isotherm models were also studied. This study clearly confirmed that GCM signified a high adsorption performance for the removal of the both dyes (MB and MO) from aqueous solutions. Moreover, the adsorption capacity of GCM for MB and MO was comparable or near with previous reported similar activated carbons or graphene type materials.^{5,13,16,17} Hence, as prepared GCM has potential adsorption capacity for the removal organic dye pollutants and thereby significant reducing human health and environmental risks.

2. Experimental

2.1. Materials

Methylene Blue (molecular formula $C_{16}H_{18}ClN_3S \cdot 3H_2O$) and methyl orange ($C_{14}H_{14}N_3NaO_3S$) were purchased from Samchun pure chemical Co., Ltd. Korea. Edible sugar was purchased from the local market. Figure 1 represents the molecular structure of MB and MO.

2.2. Preparation of the GCM

Scheme 1 represents the synthesis of graphitic carbon-like material (GCM) from the edible sugar. At first, the sugar was dissolved in water thoroughly, then the mixture was heated at $\sim 120^\circ C$ with continuous stirring for getting caramel. The sugar solution (caramel) was then transferred to a silica crucible and heated in a furnace at N_2 atmosphere.

The furnace temperature was programmed as follows: (a) from room temperature to $100^\circ C$ in 30 min, (b)

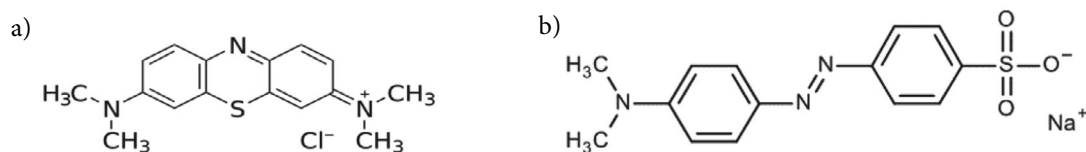
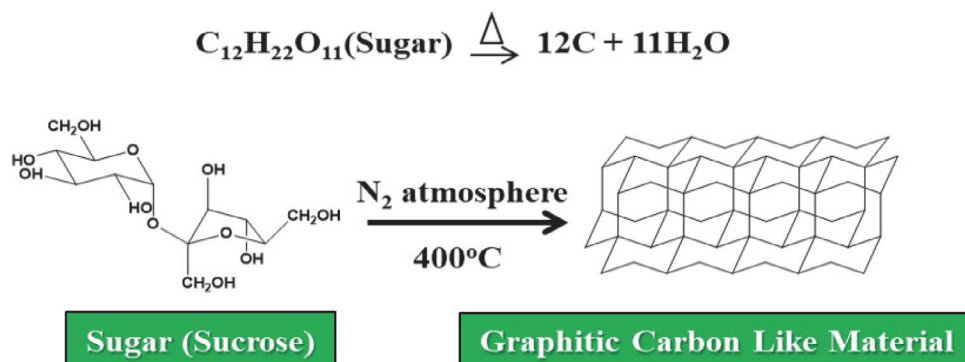


Figure 1. The molecular structure of MB (a) and MO (b).



Scheme 1. The schematic representation of the green synthesis of graphitic carbon material (GCM) from edible sugar.

100–200 °C in 30 min (c), held at 200 °C for 1 h (sugar melting point of sucrose is around 186 °C), (d) ramped to 400 °C in 1 h, and (e) held for 3 h at 400 °C (to ensure complete graphitization of sugar). The furnace was then switched off and the material was cooled down to room temperature. The temperature of 400 ± 5 °C was chosen as the final temperature after several experiments showed this to provide optimized results. No special care was taken in controlling the cooling rate. The black material obtained was named as the graphitic carbon-like material (GCM).

2. 3. Adsorption Experiments

A batch study was carried out for the evaluation of adsorption equilibrium and kinetic studies of MB and MO. The effects of different operating parameters (solution pH, adsorbent dosage, initial MB concentration, contact time, and temperature) were studied about MB and MO removal using the GCM. Enough adsorbent dose was added to separate solutions of 50 mL of MB and 50 mL of MO at the desired concentrations. These solutions were placed into 100 mL glass flasks and the samples were then shaken at 25 ± 0.5 °C. The effect of the pH on the adsorption of MB and MO was studied while varying the pH values in the range of 2 to 10. Various adsorbent dosages (0.5, 1.0, 2.0, and 4.0 g/L) were mixed in a dye solution (50 mL) in a concentration range of 5 to 50 mg/L. These solutions were then continuously stirred at 60 rpm in a water bath shaker. Samples were collected at different times. After reach adsorption equilibrium, the residue dye concentration in the solutions was measured using a UV–Vis spectrophotometer (UV 1601, Shimadzu) with maximum wavelength (λ_{\max}) of 665 nm and 465 nm for MB and MO, respectively. Experiments were performed in triplicate to check the reproducibility of the data.

The adsorption amount and adsorption efficiency of MB and MO were calculated according to Eqs. 1 and 2 as follows:

$$qe = (C_0 - C_e)V/W \quad (1)$$

$$qe = (C_0 - C_t)V/W \quad (2)$$

$$\text{Removal efficiency (\%)} = ((C_0 - C_e) / C_0) \times 100 \quad (3)$$

where C_0 (mg/L) is the initial MB or MO concentration, C_e (mg/L) is the MB or MO equilibrium concentration at equilibrium time t (min), V (L) is volume of solution, W (g) is the weight of adsorbent, and q_e (mg/g) is the amount of MB or MO adsorbed by GCM.

2. 4. Instrumental Analysis

Scanning electron microscopy (SEM) and energy-dispersive X-ray spectroscopy (EDS) (S-4300 & EDX-

350, Hitachi, Japan) were used to measure the surface morphology GCM. To identify the functional groups in the GCM, a Fourier transform infrared (FT-IR) spectrometer (Perkin-Elmer, USA) was used. X-ray diffraction (XRD) analysis of the GCM nanoparticles was conducted using a D/Max-2500 diffractometer (Rigaku, Japan). Elemental composition analysis of GCM was performed by using ESCALAB-210 (Spain) X-ray photoelectron spectroscopy (XPS). Quantachrome Instruments (Boynton Beach, FL, USA) was used to Brunauer-Emmett-Teller (BET) surface analysis of GCM.

3. Results and Discussion

3. 1. Characterizations of GCM

Figure 2a and 2b present the SEM images of the GCM at low and high resolution respectively, showing the rough surface morphology of GCM, indicating the considerable adsorption potential of MB and MO. The structure and morphology of the GCM were investigated from the SEM images. A plate-like morphology with an average size of 50–100 nm was detected from the magnification images. The XRD pattern (Fig. 2c) of the GCM shows a broad peak at $2\theta = 23.4^\circ$, corresponding to the phase of graphitic hexagonal carbon (JCPDF No: 75-1621 of graphene XRD pattern); however, the small peaks located at 43.5° could be attributed to the characteristic peaks of the oxidized form of GCM.¹⁸ The crystalline nature of GCM is also concluded from that the XRD pattern. The surface physical characteristics of GCM was measured by using Brunauer-Emmett-Teller (BET) surface analysis with nitrogen (N_2) adsorption-desorption isotherms. It was found that the surface area and pore volume was 574 m²/g and 0.248 cm³/g, respectively. And the measured pore diameter (d), 1.847 (< 2 nm) indicates that the GCM classified as a microporous crystalline material.

To better understand the functional groups of the GCM, we applied Fourier transform infrared (FT-IR) spectroscopy, as shown in Figure 3a. The FT-IR spectra of the GCM shows the availability of numerous functional groups before and after adsorption. The peaks occur at 1200 cm⁻¹ on GCM, which might have designated -C-O-C- stretching vibrations. However, after adsorption, this peak was broadened and shifted at 1170.3 cm⁻¹ and 1178.4 cm⁻¹, confirming the adsorption of MB and MO, respectively, onto the GCM. While a peak at 1598.7 cm⁻¹ was observed on GCM, after adsorption of MB and MO, this peak shifted to 1590.4 cm⁻¹ and the peak intensity increased, representing the -C=C- stretching vibrations.¹⁹ A peak at 1717 cm⁻¹ on GCM was also observed before and after adsorption, and the peak intensity increased after adsorption of both dyes, representing the -C=O stretching vibrations.¹⁹

The GCM sample is analyzed by XPS in the range of binding energies, 0.0–1400 eV. The XPS survey (Fig. 3b)

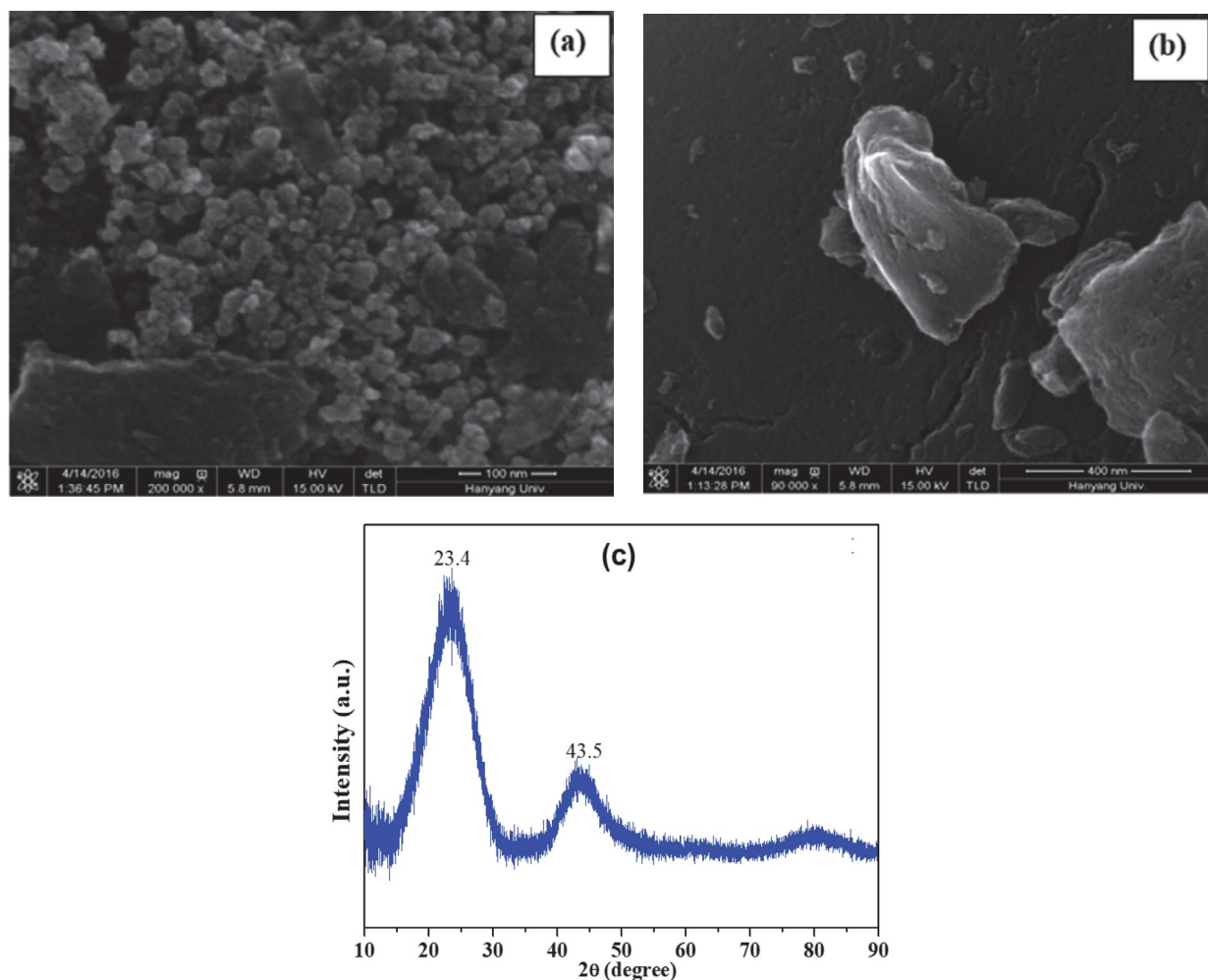


Figure 2. SEM images of GCM (a & b) and XRD spectra (c) of GCM.

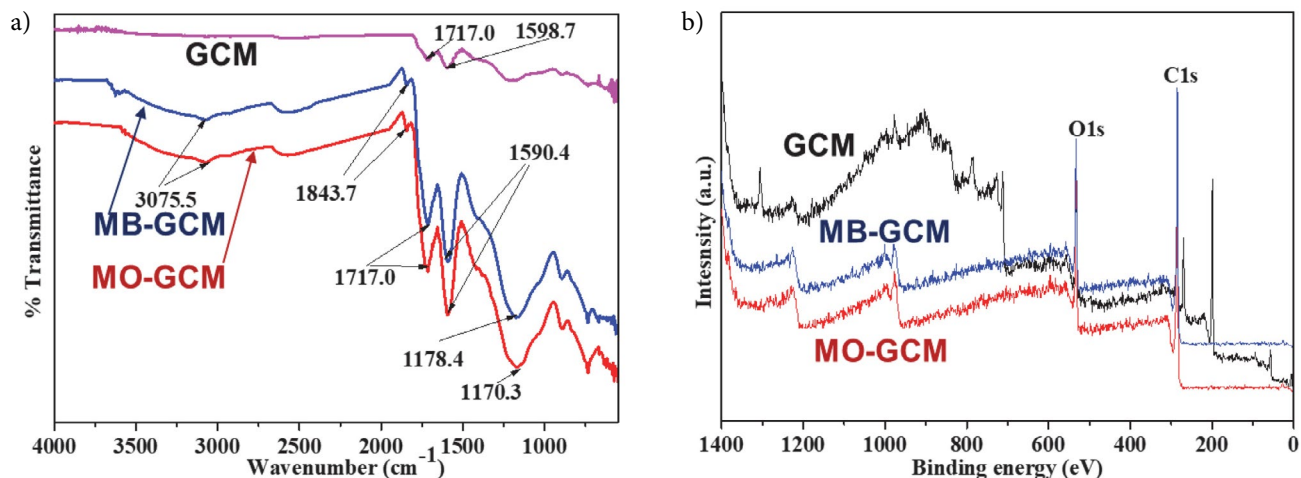


Figure 3. FT-IR spectra (a) and XPS spectra (b) of GCM and dyes loaded GCM.

of the GCM shows the presence of O and C elements. The presence of a high percentage of non-oxygenated C 1s (peak centered at 285.8 eV) indicates the presence of a carbon backbone. The O1s spectrum shows a peak at

532.2 eV, which might represent $-C=O$ from carbonyl, epoxy or carboxylic groups.¹⁸ The intensities of the peaks of C1s and O1s were increased after the adsorption of MB and MO.

3. 2. Effect of Operational Parameters on Adsorption Process of MB and MO onto GCM

The effect of adsorbent mass on the removal of pollutants was studied to select the suitable amount of adsorbent for industrial applications. The effect of adsorbent dose on the MB and MO removal was studied by changing the dosages of GCM from 0.5 to 4.0 g/L (experimental conditions: MB or MO initial concentration of 10 mg/L, pH 8, temperature of 25 °C, shaking speed of 60 rpm, and shaking time of 420 min) (Figs. 4a and 4b).

The removal efficiencies of MB and MO increased to around 99.9% and 92.6%, respectively, with the increase of adsorbent dosages; this occurred because more

adsorption sites were available at higher adsorbent dosages.²⁰ However, the adsorption capacity decreased from 19.5 to 2.6 mg/g for MB and from 19.7 to 2.7 mg/g from MO by increasing the adsorbent dose from 0.5 to 4.0 g/L. This decrease of adsorption capacity may have occurred in two ways, the first reason is due to the decrease of a number of available adsorption site per unit area by the increase of adsorbent molecules interactions or aggregation of adsorbent molecules as an increase of adsorbent dosage.²¹ The second reason is may be due to the collision between the particles of adsorbent sites and the dye molecules.²² Considering the removal efficiency and practicality, the optimal adsorbent dosage was maintained at 2.0 g/L for the both MB and MO in all subsequent experiments.

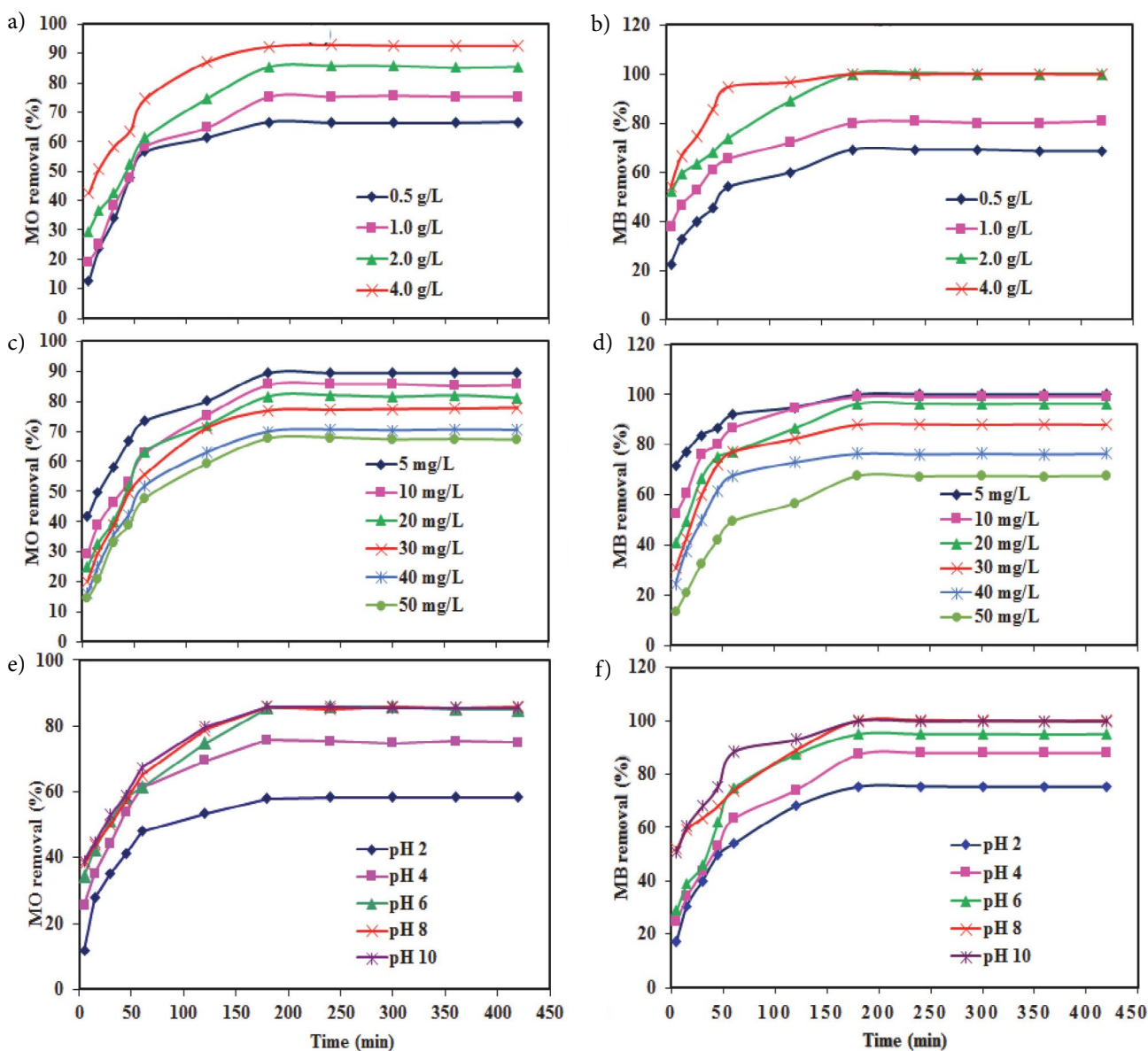


Figure 4. Effects of the different parameters on adsorption of MB and MO: dosages of GCM (a), initial concentrations of dyes (b), and different pH values of aqueous solutions (c).

The effect of the initial dye concentrations (5, 10, 20, 30, 40, and 50 mg/L) on the percentage removal and the uptake (q_e) of MB and MO was studied (experimental conditions: GCM dose of 2.0 g/L, pH 8 for MB, pH 6 for MO, temperature of 25 °C, shaking speed of 60 rpm, and shaking time of 420 min) (Figs. 4c and 4d). The adsorption capacities of MO and MB on GCM were increased from 2.6 to 24.3 mg/g and from 2.5 to 24.0 mg/g, respectively with an increasing concentration of both dyes from 5.0 to 50 mg/L. However, the percentage removal of both dyes was decreased from 89.4% to 67.5% and from 99.9% to 67.3% for MO and MB, respectively, with increasing concentration.

Decreased the adsorption removal percentages of MO and MB on to GCM with increasing dyes initial concentrations, it might be due to the driving force created by the dye molecules, which could resist the mass transfer of the dyes.²³ The time profile shows that equilibrium of dye uptake was reached after a contact time of 180 min for both dyes. It was observed that the adsorption capacity of MO and MB onto the GCM increased with the initial concentration of both dyes during the initial stage, and this increasing tendency continued until equilibrium was reached after 180 min. This can be attributed to the fact that most vacant surface sites of GCM are occupied for the adsorption of dyes during the initial stage, and adsorption of pollutants is difficult in the remaining unoccupied surface sites due to the repulsive forces between the adsorbed dye molecules on the GCM and the bulk phase.²⁴

The effect of different solution pH values (pH 2.0, 4.0, 6.0, 8.0, and 10) was studied on the percentage removal and the uptake (q_e) of MO and MB (experimental conditions: initial MO or MB concentration of 10 mg/L, GCM dose of 2.0 g/L, temperature of 25 °C, shaking speed of 60 rpm, and shaking time of 7 hr). The solution pH values were adjusted by adding 0.1 N HCl and 0.1 N NaOH. As shown in Figure 4e and 4f, the percentage removal of MO increased up to the pH 6 solution; however, the percentage removal of MB was increased up to the pH 8 solution and the further increase in the values of pH removal percentage was found to be almost constant for both dyes. A very low removal of MB was observed at an acidic pH (pH 2.0), this can be attributed to the repulsive force between the cationic dye (MB) and the surface of GCM. An addition of H^+ ions might compete with the cation of the MB molecule for vacant adsorption sites of GCM.

The removal percentage of MB on the GCM was increased from 75.0% to 99.9% with increasing pH values from 2.0 to 8.0. This is due to the increased number of negatively charged sites with maintaining basic pH, which could be favoring the adsorption of MB onto GCM due to the electrostatic force of attraction.²⁴ At pH above 8 for MB and pH 6 for MO, the removal percentage was found to be constant. The optimum pH values for the removal of MO and MB were found to be 6 and 8, respectively. In alkaline condition, the adsorption of MO onto the GCM was lower

and was possibly due to the existence of OH^- ions on the adsorbent surface, which competes with the anionic dye.²⁵ However, the best results were obtained at neutral pH for both dyes.

3. 3. Equilibrium Adsorption Isotherm

The Langmuir isotherm as shown in Eq. 4 is widely used in the scientific assessment of the adsorption process. This model assumes that the adsorbent surface can only occur at the surface monolayer and adsorption follows homogeneously.¹²

$$C_e/q_e = (1/Q_0b) + (1/Q_0) C_e \quad (4)$$

In equation (4), C_e is the equilibrium concentration of MB or MO in solution (mg/L), q_e is the amount of MB (mg/g) or MO (mg/g) adsorbed on GCM at equilibrium, Q_0 is the maximum adsorption capacity (mg/g), and b is the Langmuir constant. The slope $1/Q_0$ and intercept $(1/bQ_0)$ can be calculated by straight line equation obtained through a plot of C_e/q_e and C_e (Figs. 5a and 5b). The linear correlation coefficients R^2 are 0.990 for MB and 0.976 for MO, indicating that the adsorption of MB followed the Langmuir adsorption model. The calculated values of Q_0 are 38.75 and 43.48 mg/g for MB and MO, respectively, at 25 °C. The Langmuir parameters for both the MB and MO dyes are presented in Table 1.

Table 1. Isotherm parameters of MB and MO onto GCM at 25 °C ($n = 3$, the reported values are mean of three measurements).

Dyes	Langmuir			Freundlich		
	Q_0 (mg/g)	b (L. m/g)	R^2	K_F (mg/g)	n	R^2
MB	38.75	0.54	0.990	12.07	1.30	0.986
MO	43.48	0.52	0.976	13.87	1.27	0.995

The linear form of the Freundlich isotherm is given in Figure 5c and d for MB and MO respectively, and its linear equation is shown here.²⁶

$$\log q_e = \ln K_F + (1/n) \ln C_e \quad (5)$$

In equation (5), q_e is the amount of MB or MO adsorbed at equilibrium (mg/g) and C_e is the equilibrium concentration (mg/L) of the MB or MO. K_F and $1/n$ are the Freundlich binding constant and constant related to the surface heterogeneity, respectively. A straight line was obtained when plotted $\ln q_e$ against $\ln C_e$ (Fig. 5c and d) and n and K_F were obtained from the slopes and intercepts, respectively. The Freundlich constant n was found to be 1.30 and 1.27 for MB and MO, respectively, when the value of n is greater than 1. This result demonstrates that the materials are heterogeneous in nature and could thus adsorb MB or MO successfully. The adsorption data of MB was better fitted by the

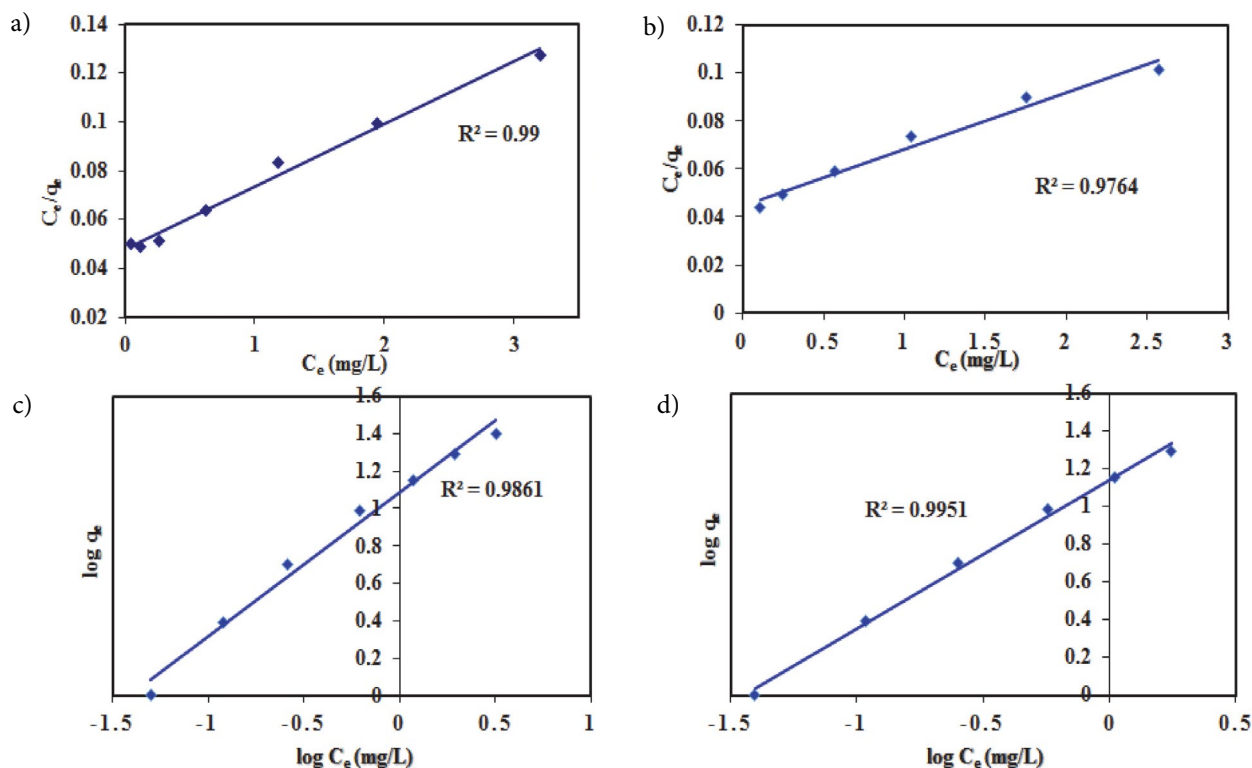


Figure 5. Langmuir adsorption isotherm of MB (a) and MO (b) and Freundlich isotherms of MB (c) and MO (d) (experimental condition: MB/MO concentrations = 5, 10, 20, 30, 40, and 50 mg/L, adsorbent dose = 2 g/L, pH = 8 for MB and pH 6 for MO, temperature = 25 °C).

Langmuir isotherm ($R^2 = 0.99$) compared to the Freundlich isotherm; however, adsorption data of MO fitted well with the Freundlich isotherm ($R^2 = 0.995$) in comparison to the Langmuir isotherm (Table 1). Hence, the overall isotherm results demonstrated that the adsorption process of MB and MO onto GCM is complexed. The obtained adsorption capacity of GCM for MB and MO was comparable or near with the reported the similar type of materials such as activated carbons and graphene or its composites (Table 2) indicates that the GCM was potentially applicable for adsorption removal of dyes as it is reported methods.

3. 4. Kinetic Study of Removal of MB or MO

A kinetics study for the adsorption of MB or MO onto the GCM was carried out under the following experimental

condition: pH 8 for MB, pH 6 for MO, a dose of 4.0 g/L, and temperature of 25 °C. A kinetic study was conducted with six different initial concentrations (5, 10, 20, 30, 40, and 50 mg/L) to recognize the adsorption kinetics (Fig. 6). It was observed that the kinetic equilibrium for adsorption of the MB and MO on the GCM was reached at 180 min, and the adsorption capacity of these dyes onto GCM increases with increasing initial concentration. The adsorption of the dyes (MB and MO) molecule increases with the increasing initial concentration, which might be due to the initial concentrations of dye, offering a driving force to restrain the mass transfer conflict of the dye molecules between the liquid phases and the solid phases.²⁷ The kinetic parameters of the adsorption of the MB and MO on GCM–water interface was studied by applying the pseudo-first-order and pseudo-second-order kinetic models for the data, with initial dye con-

Table 2. Comparison of GCM adsorption capacity with previous reported activated carbons and graphene materials.

Adsorbents	Adsorption capacity (mg/g)		References
	MB	MO	
GCM	38.75	43.48	(This work)
Charcoal	62.70	–	(Rafatullah <i>et al.</i> , 2010) ⁵
Activated carbon	9.81	–	(Rafatullah <i>et al.</i> , 2010) ⁵
Zeolite-rGO	53.30	–	(Zhu <i>et al.</i> , 2014) ¹³
Ferric oxide-biochar (Fe ₂ O ₃ -BC)	–	20.53	(Chaukura <i>et al.</i> , 2017) ¹⁶
Multiwalled carbon nanotubes (MWCNT)	–	50.25	(Yao <i>et al.</i> , 2011) ¹⁷

concentrations of 5, 10, 20, 30, 40, and 50 mg/L. In this study, the Lagergren's pseudo-first-order kinetic model²⁸ was applied to assess the adsorption rate, as expressed in Eq. 6.

$$\text{Log}(q_e - q_t) = \text{Log} q_e - (k_1/2.303) t \quad (6)$$

where k_1 is the rate constant of the pseudo-first-order kinetic equation, and q_t and q_e are the adsorption masses of MB or MO onto GCM at time t and at equilibrium, respectively. The q_e values were calculated from Figure 6a and 6b and the results reported in Table 3. The R^2 value of the plot was found to be in the range from 0.694 to 0.882 for MB; however, the R^2 value for MO was found to be in the range of from 0.533 to 0.996. The calculated value of q_e (15.6 mg/g) for MB was observed to be lower than that of the theoretical values (23.96 mg/g) for the highest initial concentration (50 mg/L). The calculated value of q_e for MO (2.1 mg/g) was found to be lower than that of the theoretical values (34.5 mg/g) for the highest initial concentration (50 mg/L).

The linear form of pseudo-second-order kinetics is indicated by Eq. 7²⁹ as

$$t/q_t = 1/(k_2 q_e^2) + (1/q_e) t \quad (7)$$

where k_2 is the pseudo-second-order adsorption rate constant. The values of k_2 and q_e for MB and MO were calcu-

lated from the slope and intercept of plots of t/q_t versus t as presented in Figure 6c and 6d. The R^2 values for both dyes were found to be greater than 0.99, representing the better fit of the pseudo-second-order model than the pseudo-first-order kinetic model (Table 3).

The empirical model described by Weber and Morris (1963) was applied for the evaluation of the intra-particle diffusion mechanism. This process is generally the rate-controlling phase in most of the adsorption processes. In this process, the adsorbate is possibly transferred from the bulk phase of the solution to the solid phase.³⁰

The intra-particle diffusion model can be represented as follows (Eq. 8):

$$q_t = k_i t^{1/2} + C, \quad (8)$$

where k_i is the intraparticle diffusion rate constant and C is represented as a constant.

The k_i values can be calculated from the linear plots of the adsorbate uptake (q_t) versus the square root of time ($t^{1/2}$) (Fig. 7). In the present study, the linear plots are not passed through the origin, it confirms that the intra-particle diffusion was not the only rate-controlling step occurring in the adsorption process. However, the intra-particle diffusion curves do not fully concur with the linear fitting. This suggests that intra-particle diffusion along with out-

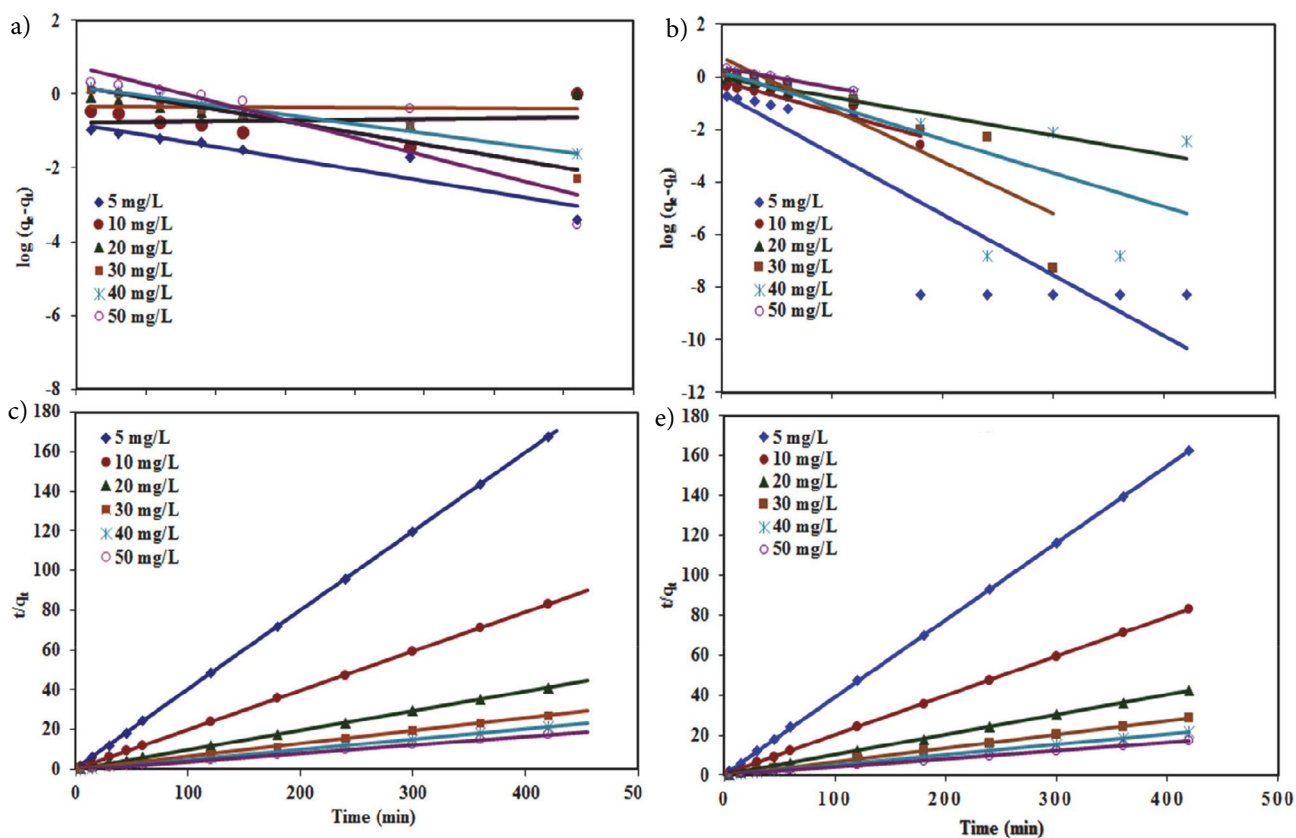


Figure 6. Pseudo-first-order kinetic model for MB (a) and MO (b), and pseudo-second-order kinetics model for MB (c) and MO (d) (experimental conditions: MB/MO concentrations = 5, 10, 20, 30, 40, and 50 mg/L, adsorbent dose = 2 g/L, pH 8 for MB and pH 6 for MO, temperature = 25 °C).

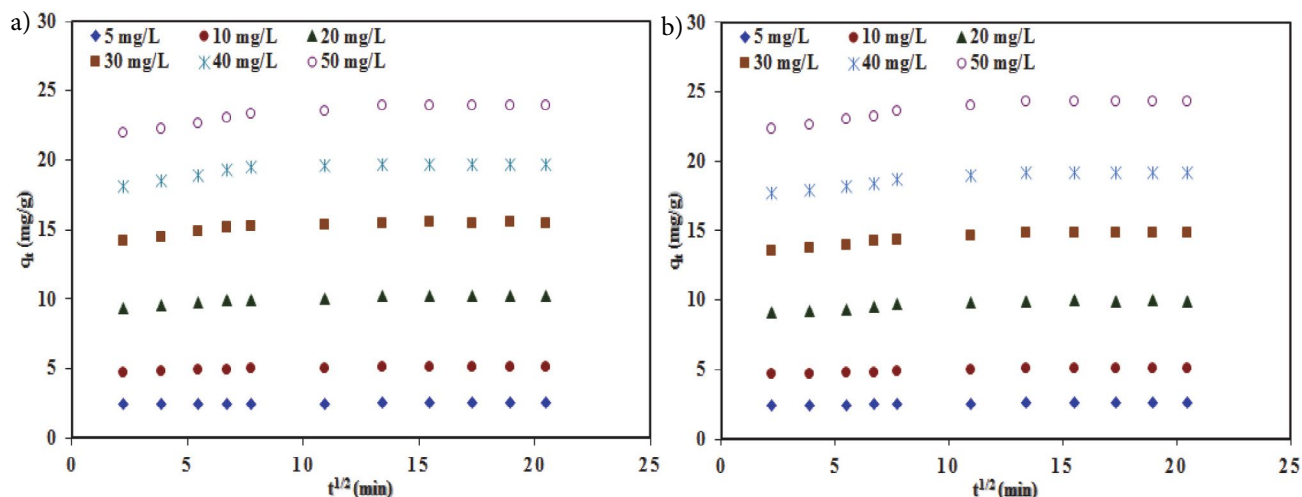


Figure 7. Intra-particle diffusion plots for the removal of MB (a) and MO (b) by GCM (MB/MO concentration = 5, 10, 20, 30, 40, and 50 mg/L, adsorbent dose = 2 g/L, pH 8 for MB and pH 6 for MO for, temperature = 25 °C).

Table 3. Kinetic parameters of MB and MO sorption onto GCM at 25 °C (n = 3, the reported values are mean of three measurements).

Dyes	The initial concentration of dyes (mg/L)	$q_{e,Th}$ (mg/g)	Pseudo-First-Order			Pseudo-second-order			Weber and Morris		
			$q_{e,Cal}$ (mg/g)	K_1	R^2	$q_{e,Cal}$ (mg/g)	K_2	R^2	K_i	C	R^2
MB	5	2.50	1.97	0.065	0.882	2.51	0.580	1	0.006	2.413	0.837
	10	5.06	1.87	0.004	0.782	5.07	0.980	1	0.018	4.764	0.796
	20	10.22	4.62	0.009	0.801	10.27	0.070	0.999	0.043	9.499	0.826
	30	15.51	9.34	0.014	0.697	15.56	0.061	0.999	0.063	14.456	0.738
	40	19.74	13.8	0.017	0.700	19.76	0.056	1	0.0731	18.509	0.728
	50	23.96	15.6	0.044	0.797	24.06	0.027	1	0.109	22.114	0.853
MO	5	4.71	0.23	0.053	0.813	2.59	0.312	1	0.01	2.417	0.855
	10	8.90	0.69	0.027	0.898	5.09	0.122	0.999	0.024	4.665	0.878
	20	16.77	0.89	0.017	0.971	10.0	0.066	0.998	0.047	9.166	0.850
	30	23.69	5.62	0.046	0.796	14.90	0.044	1	0.069	13.658	0.854
	40	28.36	1.56	0.030	0.533	19.31	0.036	0.999	0.085	17.776	0.853
	50	34.50	2.10	0.017	0.996	24.39	0.029	1	0.108	22.482	0.858

er-sphere diffusion was involved in the rate-controlling step for the adsorption process.

3. 5. Thermodynamic Studies

The thermodynamic parameter such as Gibbs free energy change (ΔG^0), the enthalpy change (ΔH^0) and the entropy change (ΔS^0) of the present system are illustrated from Figure 8 and reported in Table 4, which can provide an important information regarding adsorption process. The thermodynamic parameters can be illustrating from the following Van't Hoff equation:

$$-RT \log K_c = \Delta H^0 - T \Delta S^0 \quad (9)$$

As we know, $\Delta G^0 = -RT \log K_c$, where R (0.008314 kJ/mol. K) is universal gas constant, T (K) is the temperature and $K_c = q_e / C_e$ at equilibrium. From the Table 4, it was clearly observed

that the resultant ΔG^0 is negatively increased with initial concentration with positive ΔH^0 and ΔS^0 . The resultant thermodynamic parameters revealed the favor of adsorption process, was the spontaneous endothermic process. However, Table 4 reveals, the increased K_c with increasing temperature, which indicate chemical interactions between the adsorbate and adsorbent.^{31,32} In addition, the resultant ΔH^0 and ΔS^0 values are supports the present system percentage of adsorption data, where a higher rate of adsorption is found for low initial dye concentration with high ΔH^0 and ΔS^0 , and a low rate of adsorption is observed for a high initial concentration with low ΔH^0 and ΔS^0 .

3. 6. Possible Adsorption Mechanism of MB and MO onto GCM

From FT-IR and XPS studies (Fig. 3) of dyes loaded GCM, it was concluded that the adsorption process of MB

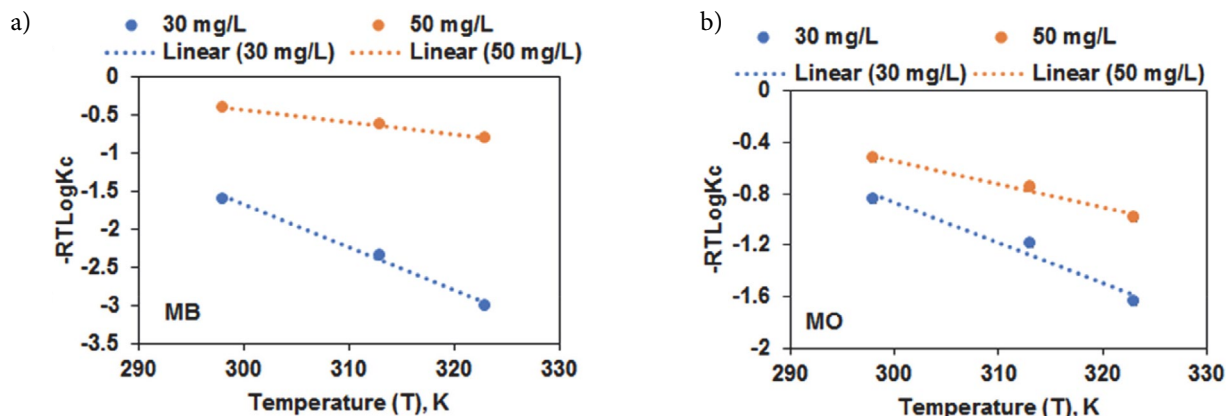


Figure 8. Thermodynamic illustrations ($\Delta G^0 = -RT \text{Log}K_c$ vs. T) of MB and MO adsorption onto GCM at pH 8.0 for MB and pH 6.0 for MO with 2.0 g/L adsorbent dosage for 180 min equilibrium for calculating to thermodynamic parameters ΔH^0 and ΔS^0 .

and MO onto GCM can be caused by the interaction of dyes with organic functions such as carbonyl, epoxy or carboxylic groups on the surface of as prepared GCM. From Figure 3, it was clearly observed that the organic functional groups at GCM altering their positions by adsorption of MB and MO dyes. It may be the chemical interaction between dyes (MB/MO) and surface functional groups of GCM. Further, it was proved from thermodynamic, kinetic isotherms and pH studies, the adsorption of MB or MO was endothermic chemical interaction through diffusion.

4. Conclusions

A graphitic carbon-like material (GCM) was prepared from edible sugar used as an adsorbent, which was highly effective for the removal of methylene blue (MB) and methyl orange (MO) from its aqueous solution. In this study, it was confirmed that the adsorption was affected by pH, dosage amount, and the initial concentration of both dyes. The removal efficiencies of MB and MO onto the GCM increased with an increase in the dosages of adsorbent up to a certain limit and then became constant. The initial solutions of pH 6 and pH 8 were found to be optimum for the removal of MO and MB, respectively. However, the removal efficiency decreased for both dyes when the initial concentrations were increased from 5 to 50 mg/L.

While the equilibrium data were well fitted to the Langmuir isotherm model for MB, for MO, they were well fitted to the Freundlich model. The experimental data of both dyes fitted better with the pseudo-second-order model than compared with the pseudo-first-order model. The resultant thermodynamic parameters concluded that the adsorption process was endothermic with spontaneous at interfaces of equilibrium. From thermodynamic, kinetic and pH studies, it was also concluded that the adsorption process was through the chemical interaction between adsorbent and adsorbate. In this study, the GCM synthesized from the edible sugar can be used as a potential adsorbent in the treatment of wastewater containing dye for effective removal performance and thereby significantly reducing human health and environmental risks. Moreover, the obtained adsorption capacity of GCM for MB and MO was comparable or near with the reported similar type of materials such as activated carbons and graphene or its composites. Hence, as prepared GCM has potential adsorption capacity for the removal organic dye pollutants and thereby significantly reducing human health and environmental risks.

5. Acknowledgments

This research was supported by Startup Research Program through the National Research Foundation of

Table 4. Thermodynamic parameters of MB and MO onto GCM at pH 8.0 for MB and pH 6.0 for MO, 2.0 g/L dosage and 180 min equilibrium time in the range of temperature, 298–323 ± 0.5 K ($n = 3$, the reported values are mean of three measurements).

Name of dye	Dye initial concentration, mg/L	$K_c = q_e/C_e$ L/g			$\Delta G^0 = -RT \text{Log}K_c$ kJ/mol			ΔH^0 , kJ/mol	ΔS^0 , kJ/mol K	R^2
		298 K	313 K	323 K	298K	313 K	323 K			
MB	30.00	4.40	7.92	13.09	-1.59	-2.34	-2.99	15.02	0.056	0.994
	50.00	1.44	1.74	1.99	-0.39	-0.63	-0.80	4.45	0.016	0.999
MO	30.00	2.19	2.84	4.07	-0.84	-1.18	-1.64	8.43	0.310	0.959
	50.00	1.63	1.94	2.32	-0.52	-0.75	-0.98	4.90	0.018	0.985

Korea (NRF) funded by Ministry of Science, ICT & Future Planning (MSIP) (2017R1C1B5016656) and partially supported by Kwangwoon University Research Grant-2018.

6. Author Disclosure Statement

No competing financial interests exist.

7. References

- X. Rong, F. Qiu, C. Zhang, L. Fu, Y. Wang and D. Yang, *J. Powder Technol.* **2015**, 275, 322–328. DOI:10.1016/j.powtec.2015.01.079
- T. Madrakian, A. Afkhami, M. Ahmadi and H. Bagheri, *J. Hazard. Mater.* **2011**, 196, 109–114. DOI:10.1016/j.jhazmat.2011.08.078
- M. S. Sajab, C. H. Chia, S. Zakaria and P. S. Khiew, *Bioresource Technol.* **2013**, 128, 571–577. DOI:10.1016/j.biortech.2012.11.010
- P. Sivakumar and P. Palanisamy, *Int. J. Chem. Tech. Res.* **2009**, 1, 502–510.
- M. Rafatullah, O. Sulaiman, R. Hashim and A. Ahmad, *J. Hazard. Mater.* **2010**, 177, 70–80. DOI:10.1016/j.jhazmat.2009.12.047
- A. Mittal, A. Malviya, D. Kaur, J. Mittal and L. Kurup, *J. Hazard. Mater.* **2007**, 148, 229–240. DOI:10.1016/j.jhazmat.2007.02.028
- E. Haque, J. W. Jun and S. H. Jhung, *J. Hazard. Mater.* **2011**, 185, 507–511. DOI:10.1016/j.jhazmat.2010.09.035
- D. Eom, D. Prezzi, K. T. Rim, H. Zhou, M. Lefenfeld, S. Xiao, C. Nuckolls, M. S. Hybertsen, T. F. Heinz and G. W. Flynn, *Nano Lett.* **2009**, 9, 2844–2848. DOI: 10.1021/nl900927f
- A. A. Balandin, S. Ghosh, W. Bao, I. Calizo, D. Teweldebrhan, F. Miao and C. N. Lau, *Nano Lett.* **2008**, 8, 902–907. DOI: 10.1021/nl0731872
- S. Latil and L. Henrard, *Phys. Rev. Lett.* **2006**, 97, 036803. DOI: 10.1103/PhysRevLett.97.036803
- R. Li, C. Chang, J. Zhou, L. Zhang, W. Gu, C. Li, S. Liu and S. Kuga, *Ind. Eng. Chem. Res.* **2010**, 49, 11380–11384. DOI: 10.1021/ie101144h
- H. Shi, W. Li, L. Zhong and C. Xu, *Ind. Eng. Chem. Res.* **2014**, 53, 1108–1118. DOI: 10.1021/ie4027154
- J. Zhu, Y. Wang, J. Liu and Y. Zhang, *Ind. Eng. Chem. Res.* **2014**, 53, 13711–13717. DOI: 10.1021/ie502030w
- J. S. Cha, S. H. Park, S.-C. Jung, C. Ryu, J.-K. Jeon, M.-C. Shin and Y.-K. Park, *J. Ind. Eng. Chem.* **2016**, 40, 1–15. DOI: 10.1016/j.jiec.2016.06.002
- S. S. Gupta, T. S. Sreeprasad, S. M. Maliyekkal, S. K. Das and T. Pradeep, *ACS Appl. Mater. Interf.* **2012**, 4, 4156–4163. DOI: 10.1021/am300889u
- N. Chaukura, E. C. Murimba and W. Gwenzi, *Appl. Water Sci.* **2017**, 7, 2175–2186. DOI: 10.1007/s13201-016-0392-5
- Y. Yao, H. Bing, X. Feifei and C. Xiaofeng, *Chem. Eng. J.* **2011**, 170, 82–89. DOI: 10.1016/j.cej.2011.03.031
- X.-L. Wu, Y. Shi, S. Zhong, H. Lin and J.-R. Chen, *Appl. Surf. Sci.* **2016**, 378, 80–86. DOI: 10.1016/j.apsusc.2016.03.226
- Y. Gokce and Z. Aktas, *Appl. Surf. Sci.* **2014**, 313, 352–359. DOI: 10.1016/j.apsusc.2014.05.214
- J. Singh, K. J. Reddy, Y.-Y. Chang, S.-H. Kang and J.-K. Yang, *Proc. Saf. Environ. Prot.* **2016**, 99, 88–97. DOI:10.1016/j.psep.2015.10.011
- L. P. Lingamdinne, H. Roh, Y.-L. Choi, J. R. Koduru, J.-K. Yang and Y.-Y. Chang, *J. Ind. Eng. Chem.* **2015**, 32, 178–186. DOI:10.1016/j.jiec.2015.08.012
- R. Gong, Y. Ding, M. Li, C. Yang, H. Liu and Y. Sun, *Dyes and Pigments* **2005**, 64, 187–192. DOI:10.1016/j.dyepig.2004.05.005
- J. Fu, Z. Chen, M. Wang, S. Liu, J. Zhang, J. Zhang, R. Han and Q. Xu, *Chem. Eng. J.* **2015**, 259, 53–61. DOI:10.1016/j.cej.2014.07.101
- L. Borah, M. Goswami and P. Phukan, *J. Environ. Chem. Eng.* **2015**, 3, 1018–1028. DOI:10.1016/j.jece.2015.02.013
- E. N. El Qada, S. J. Allen and G. M. Walker, *Chem. Eng. J.* **2008**, 135, 174–184. DOI:10.1016/j.cej.2007.02.023
- B. Hameed and A. Ahmad, *J. Hazard. Mater.* **2009**, 164, 870–875. DOI:10.1016/j.jhazmat.2008.08.084
- P. Sharma, H. Kaur, M. Sharma and V. Sahore, *Environ. Monit. Assess.* **2011**, 183, 151–195. DOI:10.1007/s10661-011-1914-0
- K. Periasamy and C. Namasivayam, *Ind. Eng. Chem. Res.* **1994**, 33, 317–320. DOI: 10.1021/ie00026a022
- Y. Li, Q. Du, T. Liu, J. Sun, Y. Wang, S. Wu, Z. Wang, Y. Xia and L. Xia, *Carbohydr. Polymers* **2013**, 95, 501–507. DOI: 10.1016/j.carbpol.2013.01.094
- M. Doğan, H. Abak and M. Alkan, *J. Hazard. Mater.* **2009**, 164, 172–181. DOI:10.1016/j.jhazmat.2008.07.155
- L. P. Lingamdinne, Y.-Y. Chang, J.-K. Yang, J. Singh, E.-H. Choi, M. Shiratani, J. R. Koduru and P. Attri, *Chem. Eng. J.* **2017**, 307, 74–84. DOI: 10.1016/j.cej.2016.08.067
- C. N. R. Rao, A. K. Sood, K. S. Subrahmanyam and A. Govindaraj, *Ange. Chem. Int. Ed.* **2009**, 48, 7752–7777. DOI:10.1002/anie.200901678

Povzetek

Grafitu podobni material (ang. graphitic carbon-like material-GCM), proizveden iz jedilnega sladkorja pod atmosfero dušika, smo uporabili kot adsorbent za odstranjevanje anionskih in kationskih barvil (metil oranžno-MO ter metilensko modro-MB) iz odpadnih vod. Za fizikalno-kemijsko karakterizacijo GCM smo uporabili vrstično elektronsko mikroskopijo (SEM), rentgensko difrakcijo (XDS), infrardečo spektroskopijo s Fourierjevo transformacijo (FTIR) in rentgensko fotoelektronsko spektroskopijo (XPS). Iz SEM-a je bila razvidna ploščičasta morfologija povprečne velikosti 50–100 nm. S pomočjo BET smo določili specifično površino 574 m²/g in volumen por 0.248 cm³/g s povprečno velikostjo por 1.847 (< 2 nm) kar uvršča GCM med mikroporozne materiale. Preučili smo vpliv količine, pH vrednosti, kontaktnega časa in koncentracije na adsorpcijo MB in MO. Eksperimentalno določene izoterme MB smo lahko opisali z Langmuirjevo izotermo ($R^2 = 0.990$) medtem ko smo adsorpcijo MO bolje opisali s Freundlichovo izotermo ($R^2 = 0.995$). Maksimalna adsorpcijska kapaciteta določena na osnovi opisa podatkov z Langmuirjevo izotermo je bila pri 25 °C enaka 38.75 mg/g za MB in 43.48 mg/g za MO, kar dokazuje, da je GCM primeren za adsorpcijo tako anionskih kot kationskih barvil. Hitrost adsorpcije obeh barvil na GCM smo lahko opisali s kinetiko pseudo-drugega reda. Termodinamski parametri so pokazali, da je adsorpcija obeh barvil endotermna. Na osnovi dobljenih rezultatov lahko zaključimo, da je GCM potencialni adsorbent za odstranjevanje MB in MO iz vodnih raztopin.

Scientific paper

Selective Protection/Deprotection in 1-Deoxynojirimycin Scaffold: Regioselective Mono-Benzoylation and Alkylation using TBAB-NaOH Catalytic System

Mehwish Iftikhar and Zhijie Fang*

School of Chemical Engineering, Nanjing University of Science & Technology, Nanjing 210094, Jiangsu, P. R. China

* Corresponding author: E-mail: zjfang@njust.edu.cn

Tel: +86-25-84303232; fax: +86-25-84315520

Received: 07-02-2018

Abstract

Protecting groups play an important role in the carbohydrate chemistry and considerably influence the reactivity of substrate. A study of the substitution of various protecting groups in 1-deoxynojirimycin was carried out. Substrate *N*-benzyloxycarbonyl-1,5-dideoxy-1,5-imino-4,6-*O*-isopropylidene-*D*-glucitol was subjected to alkylation at positions 2- and 3- to obtain di-substituted products and *N*-Cbz group was selectively removed by using NaOH in EtOH/H₂O. Regioselective benzoylation and alkylation of *N*-benzyloxycarbonyl-1,5-dideoxy-1,5-imino-4,6-*O*-isopropylidene-*D*-glucitol were conducted under the action of TBAB-NaOH catalytic system. It was found that all protected and mono-protected analogs form simultaneously and their structures were confirmed by spectroscopic means. The results showed that electrophiles play an important role in determining the product distribution.

Keywords: 1-Deoxynojirimycin; protecting groups; regioselectivity; TBAB-NaOH catalytic system

1. Introduction

1-Deoxynojirimycin (1-DNJ) **1** is a naturally occurring polyhydroxylated alkaloid containing an endocyclic nitrogen atom (Figure 1).¹ It is a true structural analogue of pyranosides which is therefore well recognized by glycosidases (enzymes that catalyze the cleavage of glycosidic bonds in oligosaccharides and glycoconjugates).^{2–4} This sugar-shaped alkaloid has been found to be a potent inhibitor of a number of sugar processing enzymes, *e.g.* glycosi-

dases and glycosyltransferases.^{5,6} There has been a considerable interest in the synthesis of 1-DNJ analogs because they have demonstrated anti HIV, antiviral, antidiabetic, immunorepressive and anti-cancer properties.^{7–14} Besides this, 1-DNJ derivatives which have pharmacophoric groups attached, are potentially bioactive compounds.¹⁵

Protecting groups play a crucial role in carbohydrate chemistry and glycosylation chemistry due to the presence of multiple functional groups.¹⁶ They not only give protection but also influence the reactivity of substrates (imino-

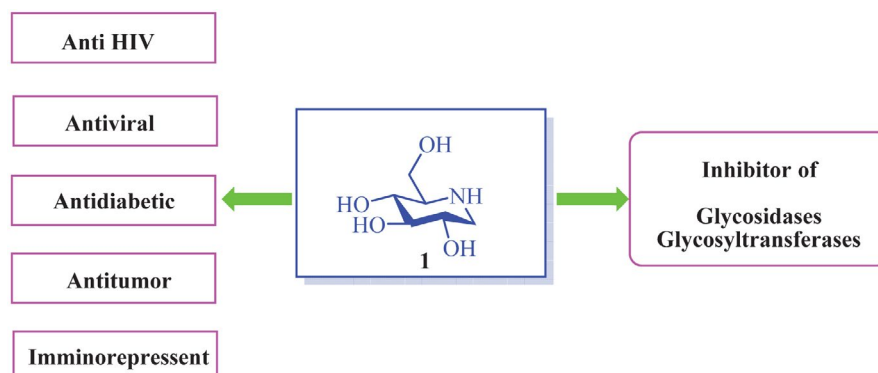


Figure 1. Structure of 1-deoxynojirimycin **1** and a short summary of its properties.

sugar) and their selectivity in glycosylations. It has been observed that benzylidene and isopropylidene groups grafted onto the DNJ scaffold have potential bioactivities towards different sugar-processing enzymes. With the increasing need for biologically active oligosaccharides and glycoconjugates, glycosylation chemistry has been extensively studied.¹⁷ However, few synthetic methods exist for the replacement of hydroxy groups by other groups.¹⁸ Therefore, advanced methods are required for selective protection and deprotection to improve synthetic efficacy.¹⁹

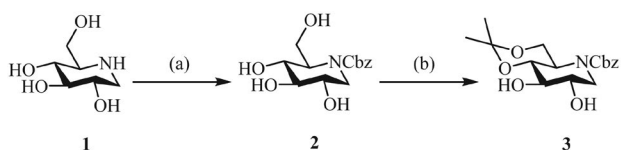
The control of regioselectivity is one of the major tasks and is conventionally accomplished by protecting group chemistry.²⁰ Therefore, the preparation of selectively protected iminosugars bearing a single free hydroxy group symbolizes a breakthrough in carbohydrate chemistry. Bu_2SnO , an organotin catalyst has previously been used for regioselective mono-alkylation of *N*-benzyloxycarbonyl-1,5-dideoxy-1,5-imino-4,6-*O*-benzylidene-*D*-glucitol at elevated temperature.^{18,21} We have used TBAB- NaOH catalytic system for regioselective mono-alkylation and mono-benzoylation of *N*-benzyloxycarbonyl-1,5-dideoxy-1,5-imino-4,6-*O*-isopropylidene-*D*-glucitol at room temperature. The choice of this new catalytic system is due to its easy availability and its activity under mild reaction conditions.

Herein, we describe the synthesis of 1-DNJ derivatives, selectively protected at positions 2- or 3- by varying reaction parameters. Partially protected derivatives were subjected to selective removal of the *N*-protecting group (Cbz) by using NaOH as the base. Regioselective benzoylation and alkylation of *N*-benzyloxycarbonyl-1,5-dideoxy-1,5-imino-4,6-*O*-isopropylidene-*D*-glucitol was carried out using a TBAB- NaOH catalyst system. We concluded that the electrophilic reagents with different steric and electronic effects have considerable impact on the reactivity of the secondary hydroxy groups which is an important method to evaluate the regioselectivity using TBAB- NaOH catalytic system.

2. Results and Discussion

2.1. Synthesis of *N*-Benzyloxycarbonyl-1,5-dideoxy-1,5-imino-4,6-*O*-isopropylidene-*D*-glucitol

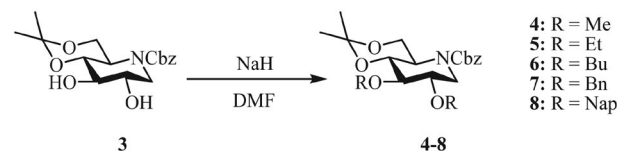
N-Benzyloxycarbonyl-1,5-dideoxy-1,5-imino-4,6-*O*-isopropylidene-*D*-glucitol (**3**) was prepared in two steps from 1-deoxynojirimycin (**1**) in 70% overall yield (Scheme 1). The reaction of 1-deoxynojirimycin (**1**) with benzyl chloroformate in saturated aqueous NaHCO_3 afforded *N*-benzyloxycarbonyl-1,5-dideoxy-1,5-imino-*D*-glucitol (**2**) in 87% yield.^{18,22} Crude compound **2** was directly converted into *N*-benzyloxycarbonyl-1,5-dideoxy-1,5-imino-4,6-*O*-isopropylidene-*D*-glucitol (**3**) (70%) using 2,2-dimethoxypropane and *p*- TsOH in anhydrous DMF (Scheme 1).



Scheme 1. Synthesis of substrate **3**. Reagents and conditions: (a) *N*-benzyloxycarbonyl chloride, DMF, NaHCO_3 , rt, 24 h; (b) 2,2-dimethoxypropane, DMF, rt, 24 h.

2.2. Protection of 2,3-Diol of *N*-Benzyloxycarbonyl-1,5-dideoxy-1,5-imino-4,6-*O*-Isopropylidene-*D*-glucitol and Subsequent Cbz Removal

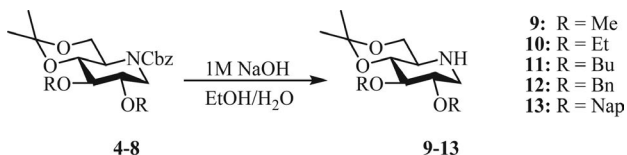
Protection at positions 2- and 3- of compound **3** was carried out using a catalytic amount of NaH as the base in anhydrous DMF with varying alkylating reagents (methyl iodide/ethyl iodide/butyl bromide/benzyl bromide/naphthyl bromide) as shown in Scheme 2.



Scheme 2. Synthesis of 2,3-disubstituted/protected derivatives **4–8** of **3**. Reagents and conditions: NaH , DMF, different alkylating reagents (methyl iodide/ethyl iodide/butyl bromide/benzyl bromide/naphthyl bromide), rt, 6 h.

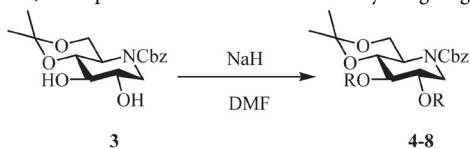
All reactions were conducted at room temperature and the protected products **4–8** were obtained in good yields (67–95%, see Table 1).

Next, we selectively removed the Cbz protecting group from protected iminosugar derivatives to obtain free NH group. Compound **4** was chosen as the model target for Cbz removal and was subjected to different bases (*i.e.* K_2CO_3 , NaOH and I_2) in varying solvents (*i.e.* EtOH, MeOH, DCM). After exploring different conditions with varying bases and solvents, NaOH in EtOH/ H_2O mixture gave the optimum yield of **9** (Scheme 3).



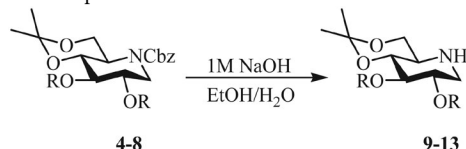
Scheme 3. Cbz deprotection of **4–8**. Reagents and conditions: 1 M NaOH , EtOH/ H_2O , 80 °C, 6–12 h.

Deprotection of compounds **4–8** underwent smoothly under this generalized optimum deprotection conditions at refluxing temperature (6–12 hours) and afforded **9–13** in good yields: 73–83% (Table 2).

Table 1: 2,3-diol protection of **3** with different alkylating reagents.

Entry	Substrate ^a	R	Product	Yield ^b (%)
1.				87
2.				77
3.				67
4.				81
5.				95

^a Conditions: Substrate (0.296 mmol), alkylating reagent (4 eq), NaH (5 eq), DMF (5 mL), 0–25 °C, 6 h; ^b isolated yield.

Table 2: Cbz deprotection of 4–8.

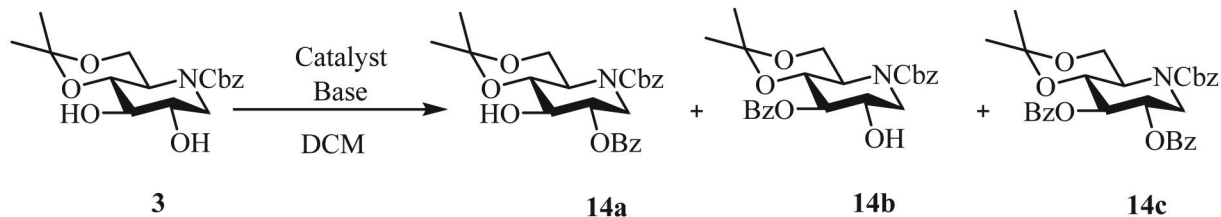
Entry	Substrate ^a	R	Product	Yield ^b (%)
1.				80
2.				77
3.				74
4.				83
5.				73

^a Conditions: Substrate (100 mg), EtOH/H₂O 1:1 (10 mL), NaOH (1 M), 80 °C, 6–12 h; ^b isolated yield.

2. 3. Regioselective Mono-esterification and Alkylation of *N*-Benzyloxycarbonyl-1,5-dideoxy-1,5-imino-4,6-*O*-isopropylidene-*D*-glucitol

2. 3. 1. Benzoylation as the Model Reaction

Selective mono-protection in azasugars/iminosugars scaffold is challenging and demanding. The position of free hydroxy groups in iminosugars has a pronounced effect on enzyme binding. For example, Chery *et al.*¹⁴

**Scheme 4.** Probing optimizing conditions for mono-esterification.

demonstrated the importance of free 2-OH group for enzyme binding for HIV-protease inhibition. It was observed that 4,6-*O*-benzylidene protected iminosugars along with selective mono-pivaloylation at positions 2- or 3- gave promising results when compared to the original drug. The selective mono-esterification and alkylation is very crucial and Bu₂SnO have previously been used for this purpose. However, due to toxicity of this catalyst, there is a need for other mild and less toxic reagents.

For mono protection we have chosen benzoyl chloride as the model electrophile. Compound **3** was reacted

with benzoyl chloride in the presence of the catalyst-base mixture in DCM. Effect of different combinations of the catalyst (*i.e.* DMAP, TBAB) and the base (*i.e.* TEA, K_2CO_3 , NaOH, KI) were observed on product formation (Scheme 4, Table 3).

Compound **3** was converted into 2-benzoylated (**14a**, 45%) and 2,3-di-benzoylated product (**14c**, 20%) completely within two hours upon treatment with DMAP-TEA combination (entry 1, Table 3). Reaction underwent incompletely when TBAB was used as the catalyst in the presence of K_2CO_3 . Even after 48 hours 30% of the starting material was recovered but this combination improved the yield of **14a** upto 55% (entry 2, Table 3). Surprisingly, when the base was switched to NaOH, the reaction time was efficiently reduced to 4 hours and gave **14a** in 70% yield with no recovered starting material (entry 3, Table 3). After experiencing the good results from TBAB-NaOH combination, we switched the catalyst to DMAP and noted the effects. However DMAP-NaOH (entry 4, Table 3) did not prove to be specific for mono esterifica-

tion and gave 2-benzoylated (**14a**, 46%), 3-benzoylated (**14b**, 7%) and 2,3-dibenzoylated (**14c**, 12.36%) products. This reaction condition gave **14a** with improved yield as compared to DMAP-TEA system (entry 1), but prolonged reaction time was a drawback. The combination of DMAP-KI did not give satisfactory results and only traces of **14a** and **14b** were observed (entry 5, Table 3). After probing optimized conditions for esterification, it was concluded that C-2 position is more reactive towards mono-benzoylation when TBAB-NaOH combination was used. Here, NaOH acted as a promoter for the reaction.

2. 3. 2. NMR Spectral Analysis of Mono-benzoylated Product

1H NMR spectra of compounds **14a**, **14b** and **14c** were compared with that of compound **3**. Upon comparison of spectrum of compound **3** with **14c** (Figure 2), two peaks, *i.e.* $\delta = 3.45$ ppm and $\delta = 3.63$ ppm (in spectrum of

Table 3: Optimization of conditions for regioselective benzoylation of **3**.

Entry	Catalyst ^a	Solvent	Base	Time (h)	14a ^b (%)	14b ^b (%)	14c ^b (%)	Recovered starting material ^c (%)
1.	DMAP	DCM	TEA	2	45	–	20	–
2.	TBAB	DCM	K_2CO_3	48	55	–	–	30
3.	TBAB	DCM	NaOH	4	70	–	20	–
4.	DMAP	DCM	NaOH	72	46	7	12.36	–
5.	DMAP	DCM	KI	72	traces	traces	–	–

^a Condition: Catalyst (1.5 eq), base (2 eq), BzCl (1.5 eq), solvent (10 mL), 25 °C, 8–72 h; ^b isolated yield.; ^c recovered starting material.

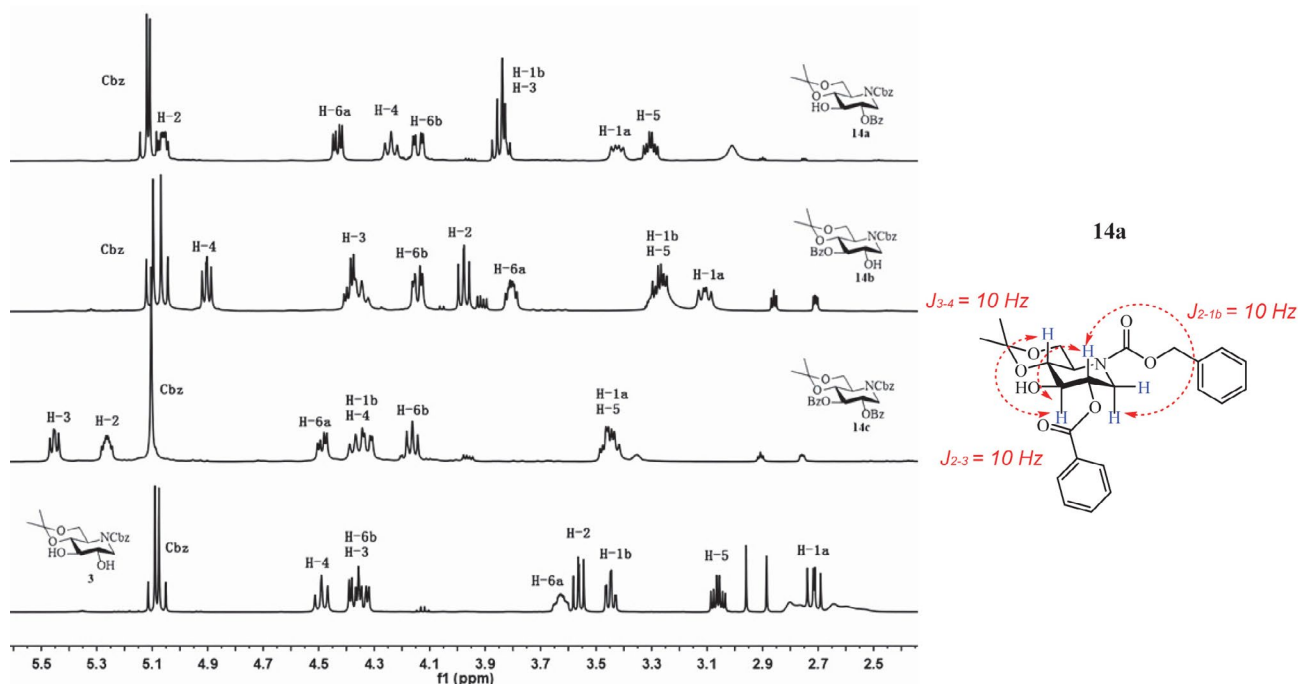


Figure 2. 1H NMR spectra of compounds **3**, **14a**, **14b**, **14c** and corresponding coupling pattern of **14a**.

compound **3**) disappeared and two new peaks appeared at $\delta = 5.26$ ppm and $\delta = 5.45$ ppm in the spectrum of compound **14c**. The chemical shifts of H-2 and H-3 moved towards lower field indicating that both hydroxy groups are protected by benzoyl groups. It was observed that H-3 chemical shift (at $\delta = 3.45$ ppm in the spectrum of **3**) moved towards lower field at $\delta = 4.45$ ppm in the spectrum of compound **14b** indicating that this position is substituted. Similar trend was seen in the spectrum of **14a** where H-2 signal moved to $\delta = 5.06$ ppm from $\delta = 3.63$ ppm (in the spectrum compound **3**) indicating that position 2- is protected. The coupling constants, *i.e.* J_{2-3} , J_{3-4} , J_{2-1b} for compound **14a** were found to be 10 Hz as shown in the Figure 2.

2. 3. 3. Regioselective Alkylation

After probing optimized conditions for mono-esterification, similar conditions were applied for regioselective alkylation by varying electrophiles (*i.e.* benzyl bromide and naphthyl bromide) as shown in Table 4. The reactions proceeded efficiently under these conditions, *i.e.* at 25 °C catalyzed by TBAB-NaOH system. Data summarized in Table 4 clearly indicate the differentiation of reactivity of hydroxy groups towards regioselective alkylation. Both electrophiles gave mono-substituted and di-substituted products in varying ratio. For example, in the case of benzylation (entry 1, Table 4), 2-substituted product **15a** was predominant (70%) as compared to 3-substituted product **15b** (14%). Besides mono-substituted products, fully protected product **7** (10%) was also obtained. However, when more bulky electrophile, *i.e.* naphthyl bromide (entry 2, Table 4) was used, then conversion towards both, mono- and di-substituted products decreased. Decrease in product formation can be explained due to the bulkiness of the electrophile (entry 2) which caused additional steric hindrance.

3. Experimental

3. 1. General

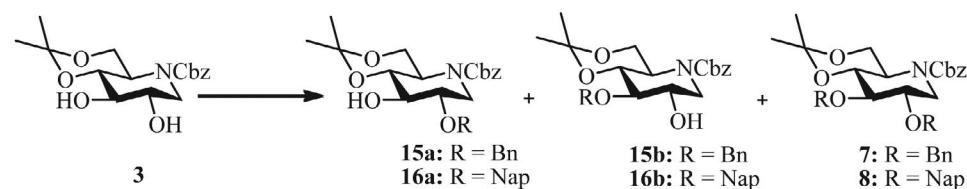
All commercially available chemicals were of analytical grade and were used without further purification. Solvents were dried prior to use according to standard methods. Reactions were performed at ambient temperature unless stated otherwise. Moisture sensitive reactions were carried out under an argon environment. The progression of reactions was monitored by thin layer chromatography (TLC) on silica gel coated plates. Spots were detected under UV-light (254 nm) or visualized via exposure to iodine vapor. Flash chromatography was performed on silica gel (Merk-230 mesh). ^1H and ^{13}C NMR were recorded on a Bruker-500 (at 500 or 126 MHz) in CDCl_3 . Chemical shifts are given in ppm relative to tetramethylsilane as the internal standard ($\delta_{\text{TMS}} = 0$ ppm).

3. 2. Synthesis of *N*-Benzyloxycarbonyl-1,5-dideoxy-1,5-imino-4,6-*O*-isopropylidene-D-glucitol (**3**)

To a stirring solution of *N*-benzyloxycarbonyl-1,5-dideoxy-1,5-imino-D-glucitol (**2**) (7.27 g, 24.45 mmol) in DMF (60 mL) was added catalytic amount of *p*-toluenesulfonic acid monohydrate (PTSA) (140 mg) until pH = 1.5 was obtained. Then, 2,2-dimethoxypropane (2 eq, 6 mL) was added and the reaction mixture was stirred for 24 hours at room temperature until completion. Reaction mixture was quenched with aq. NaHCO_3 solution and extractions were made with ethyl acetate EA (100 mL \times 3). Combined organic layers were washed with brine (100 mL \times 3) and dried over Na_2SO_4 . Purification via flash column chromatography using gradient elution (SiO_2 , petroleum ether/ethyl acetate 1:1, v/v) gave **3** as a colorless oil (4.68 g, 70%).

Yield: 4.68 g, 70%, colorless oil, $R_f = 0.28$ (petroleum ether/ethyl acetate 1:1). ^1H NMR (500 MHz, CDCl_3) δ

Table 4: Regioselective alkylation of **3**.



Entry	Reagent ^a (R)	Catalyst	Base	Solvent	Products	Yield ^b (%)		
						15a–16a	15b–16b	7,8
1.		TBAB	NaOH	DCM	15a, 15b, 7	70	14	10
2.		TBAB	NaOH	DCM	16a, 16b, 8	38	20	4

^a Condition: RBr (1.5 eq), catalyst (1.5 eq), base (2 eq), solvent (10 mL), 25 °C, 24 h; ^b isolated yield.

1.41 (s, 3H, CH₃), 1.49 (s, 3H, CH₃), 2.71 (dd, $J = 13.3, 10.7$ Hz, 1H, H-1a), 3.06 (td, $J = 15.0, 10.4, 5.0$ Hz, 1H, H-5), 3.45 (dd, $J = 8.6, 1.8$ Hz, 1H, H-3), 3.56 (dd, $J = 10.0, 8.8$ Hz, 1H, H-4), 3.62 (ddd, $J = 10.8, 5.7, 2.8$ Hz, 1H, H-2), 4.26–4.43 (m, 2H, H-1b and H-6b), 4.49 (t, $J = 11.3$ Hz, 1H, H-6a), 5.08 (2d, $J = 12.2$ Hz, 2H, CH₂-Ar), 7.23–7.45 (m, 5H, H-Ar). ¹³C NMR (126 MHz, CDCl₃) δ 18.16 (CH₃), 28.26 (CH₃), 48.43 (C-1), 54.78 (C-6), 60.94 (C-5), 66.57 (CH₂-Ar), 68.56 (C-2), 72.25 (C-3), 75.83 (C-4), 98.20 (CH), 127.15, 127.36, 127.67 (CH-Ar), 134.98 (C-Ar), 153.88 (C=O).

3. 3. General Procedure A: 2,3-Dialkylation of *N*-Benzyloxycarbonyl-1,5-dideoxy-1,5-imino-4,6-*O*-isopropylidene-*D*-glucitol (3) to obtain 4–8

Sodium hydride NaH (5 eq, 60 mg, 1.48 mmol) was added to the stirring solution of 3 (100 mg, 0.296 mmol) in dry DMF (5 mL) at 0 °C. Alkylating reagent (4 eq, 1.18 mmol), *i.e.* methyl iodide for 4, ethyl iodide for 5, butyl bromide for 6, benzyl bromide for 7 and naphthyl bromide for 8 was added slowly and the reaction mixture was stirred at room temperature for 6 hours. Reaction progression was monitored by TLC and after completion the reaction was quenched by addition of water. The reaction mixture was poured into water and repeatedly extracted with ethyl acetate EA (100 mL \times 3). Combined organic layers were washed with brine, dried over Na₂SO₄ and concentrated.

N-Benzyloxycarbonyl-2,3-di-*O*-methyl-1,5-dideoxy-1,5-imino-4,6-*O*-isopropylidene-*D*-glucitol (4)

Yield: 95 mg, 87%, yellow oil, $R_f = 0.25$ (petroleum ether/ethyl acetate 6:1). ¹H NMR (500 MHz, CDCl₃) δ 1.41 (s, 3H, CH₃), 1.49 (s, 3H, CH₃), 3.18 (dd, $J = 8.4, 4.2$ Hz, 1H, H-1a), 3.23–3.30 (m, 2H, H-2 and H-1b), 3.36 (s, 3H, OCH₃), 3.51 (s, 3H, OCH₃), 3.61–3.63 (m, 2H, H-5 and H-3), 3.80 (dd, $J = 10.7, 8.5$ Hz, 1H, H-6a), 4.00 (t, $J = 10.6$ Hz, 1H, H-4), 4.37 (dd, $J = 11.3, 4.7$ Hz, 1H, H-6b), 5.09 (d, $J = 12.3$ Hz, 1H, CH₂-Ar), 5.15 (d, $J = 12.3$ Hz, 1H, CH₂-Ar), 7.25–7.38 (m, 5H, H-Ar). ¹³C NMR (126 MHz, CDCl₃) δ 18.25 (CH₃), 28.21 (CH₃), 42.68 (C-1), 51.61 (C-6), 56.16 (OCH₃), 58.04 (OCH₃), 61.97 (C-5), 66.46 (CH₂-Ar), 71.93 (C-2), 78.34 (C-3), 82.70 (C-4), 98.07 (CH), 127.06, 127.24, 127.62, 127.89 (C-Ar), 135.26 (CH-Ar), 155.15 (C=O).

N-Benzyloxycarbonyl-2,3-di-*O*-ethyl-1,5-dideoxy-1,5-imino-4,6-*O*-isopropylidene-*D*-glucitol (5)

Yield: 90 mg, 77%, yellow oil, $R_f = 0.38$ (petroleum ether/ethyl acetate 6:1). ¹H NMR (500 MHz, CDCl₃) δ 1.14 (t, $J = 7.0$ Hz, 3H, CH₃-Ethyl), 1.26 (t, $J = 7.1$ Hz, 3H, CH₃-Ethyl), 1.40 (s, 3H, CH₃), 1.48 (s, 3H, CH₃), 3.22–3.27 (m, 1H, H-1a), 3.32–3.34 (m, 2H, H-2 and H-1b), 3.52–3.59 (m, 2H, H-5 and H-3), 3.67–3.70 (m, 1H, H-3), 3.72–3.80 (m, 5H, 2 \times CH₂-Ethyl and H-6a), 4.07–4.16 (m, 1H,

H-6b), 4.36 (dd, $J = 11.4, 4.8$ Hz, 1H, H-4), 5.07–5.16 (m, 2H, CH₂-Ar), 7.27–7.38 (m, 5H, H-Ar). ¹³C NMR (126 MHz, CDCl₃) δ 14.47 (CH₃-Ethyl), 14.70 (CH₃-Ethyl), 18.28 (CH₃), 28.23 (CH₃), 44.15 (C-1), 52.30 (C-6), 61.90 (C-5), 64.32 (CH₂-Ethyl), 66.22 (CH₂-Ethyl), 72.32 (C-2), 76.81 (C-4), 81.66 (C-3), 97.93 (CH), 127.02, 127.19, 127.59 (C-Ar), 135.33 (CH-Ar), 155.01 (C=O).

N-Benzyloxycarbonyl-2,3-di-*O*-butyl-1,5-dideoxy-1,5-imino-4,6-*O*-isopropylidene-*D*-glucitol (6)

Yield: 90 mg, 67%, colorless oil, $R_f = 0.23$ (petroleum ether/ethyl acetate 10:1). ¹H NMR (500 MHz, CDCl₃) δ 0.90 (t, $J = 10.4$ Hz, 3H, CH₃-Butyl), 0.92 (t, $J = 11.4$ Hz, 3H, CH₃-Butyl), 1.33–1.39 (m, 4H, 2 \times CH₂-Butyl), 1.39 (s, 3H, CH₃), 1.47 (s, 3H, CH₃), 1.49–1.53 (m, 4H, 2 \times CH₂-Butyl), 3.19–3.27 (m, 2H, CH₂-Butyl), 3.28–3.39 (m, 2H, CH₂-Butyl), 3.44–3.54 (m, 2H, H-1a and H-1b), 3.62 (dt, $J = 14.8, 9.5, 6.5$ Hz, 1H, H-5), 3.65–3.73 (m, 2H, H-3 and H-2), 3.77 (dd, $J = 10.6, 8.5$ Hz, 1H, H-6a), 4.08 (t, $J = 10.6$ Hz, 1H, H-6b), 4.37 (dd, $J = 11.4, 4.7$ Hz, 1H, H-4), 5.05–5.20 (m, 2H, CH₂-Ar), 7.23–7.44 (m, 5H, H-Ar). ¹³C NMR (126 MHz, CDCl₃) δ 12.80 (CH₃-Butyl), 12.88 (CH₃-Butyl), 18.26 (2 \times CH₂-Butyl), 28.20 (CH₃), 28.21 (CH₃), 31.03 (CH₂-Butyl), 31.20 (CH₂-Butyl), 44.03 (C-1), 52.19 (C-6), 61.98 (C-5), 66.34 (CH₂-Ar), 68.66 (CH₂-Butyl), 70.56 (CH₂-Butyl), 72.37 (C-2), 77.05 (C-4), 81.58 (C-3), 97.91 (C-H), 127.02, 127.19, 127.59 (C-Ar), 135.32 (CH-Ar), 155.03 (C=O).

N-Benzyloxycarbonyl-2,3-di-*O*-benzyl-1,5-dideoxy-1,5-imino-4,6-*O*-isopropylidene-*D*-glucitol (7)

Yield: 125 mg, 81%, white solid, mp: 40 °C, $R_f = 0.11$ (petroleum ether/ethyl acetate 3:1). ¹H NMR (500 MHz, CDCl₃) δ 1.44 (s, 3H, CH₃), 1.51 (s, 3H, CH₃), 3.31 (td, $J = 14.8, 10.5, 4.8$ Hz, 1H, H-1a), 3.42–3.60 (m, 3H, H-1b, H-2 and H-5), 3.70–3.81 (m, 1H, H-3), 3.92 (dd, $J = 10.7, 8.0$ Hz, 1H, H-6a), 4.12 (t, $J = 10.6$ Hz, 1H, H-4), 4.40 (dd, $J = 11.4, 4.7$ Hz, 1H, H-6b), 4.53–4.60 (m, 2H, CH₂-Ar), 4.70 (d, $J = 11.6$ Hz, 1H, CH₂-Ar), 4.79 (d, $J = 11.6$ Hz, 1H, CH₂-Ar), 5.07–5.14 (m, 2H, CH₂-Ar), 7.24–7.41 (m, 15H, H-Ar). ¹³C NMR (126 MHz, CDCl₃) δ 18.35 (CH₃), 28.28 (CH₃), 43.93 (C-1), 52.19 (C-6), 61.98 (C-5), 66.45 (CH₂-Ar), 70.58 (CH₂-Ar), 72.65 (CH₂-Ar), 72.84 (C-3), 75.02 (C-2), 81.44 (C-4), 98.02 (CH), 126.69, 126.90, 127.08, 127.26, 127.36, 127.45, 127.64 (C-Ar), 135.24 (CH-Ar), 137.03 (CH-Ar), 137.66 (CH-Ar), 155.05 (C=O).

N-Benzyloxycarbonyl-2,3-di-*O*-naphthyl-1,5-dideoxy-1,5-imino-4,6-*O*-isopropylidene-*D*-glucitol (8)

Yield: 175 mg, 95%, colorless oil, $R_f = 0.31$ (petroleum ether/ethyl acetate 6:1). ¹H NMR (500 MHz, CDCl₃) δ 1.56 (s, 3H, CH₃), 1.62 (s, 3H, CH₃), 3.43 (td, $J = 14.8, 10.4, 4.7$ Hz, 1H, H-1a), 3.62 (m, 1H, H-1b), 3.71–3.73 (m, 2H, H-2 and H-5), 3.90 (d, $J = 13.3$ Hz, 1H, H-3), 4.06 (dd, $J = 10.4, 8.0$ Hz, 1H, H-6a), 4.24 (t, $J = 10.7$ Hz, 1H, H-6b), 4.51 (dd, $J = 11.4, 4.6$ Hz, 1H, H-4), 4.76 (d, $J = 11.8$ Hz, 1H, CH₂-

Naph), 4.84 (d, $J = 12.0$ Hz, 1H, CH₂-Naph), 4.95 (d, $J = 11.9$ Hz, 1H, CH₂-Naph), 5.05 (d, $J = 11.9$ Hz, 1H, CH₂-Naph), 5.13 (d, $J = 12.3$ Hz, 1H, CH₂-Ar), 5.21 (d, $J = 12.3$ Hz, 1H, CH₂-Ar), 7.38–7.40 (m, 5H, H-Ar), 7.51–7.56 (m, 6H, H-Naph), 7.72–8.00 (m, 8H, H-Naph). ¹³C NMR (126 MHz, CDCl₃) δ 18.44 (CH₃), 28.39 (CH₃), 44.00 (C-1), 52.30 (C-6), 62.04 (C-5), 66.49 (CH₂-Ar), 70.69 (CH₂-Naph), 72.70 (CH₂-Naph), 72.90 (C-2), 81.50 (C-4), 89.63 (C-3), 98.13 (CH), 124.75, 124.92, 125.08, 125.21, 125.58, 126.04, 126.79, 127.02, 127.10, 127.28, 127.66 (C-Ar and C-Naph), 132.10 (2 \times C-Naph), 132.39 (2 \times C-Naph), 134.52 (CH-Naph), 135.18 (CH-Naph), 135.28 (CH-Ar), 155.09 (C=O).

3. 4. General Procedure B: Removal of *N*-Protecting Group (Cbz) to Obtain 9–13

Substrates 4–8 (100 mg) were dissolved in 1:1 ethanol/water (10 mL) and NaOH (1 M) was added. The reaction mixture was stirred at 80 °C for 6–12 hours. After completion of the reaction as indicated by TLC, the solvents were removed *in vacuo* and extractions were made with ethyl acetate EA (100 mL \times 3). Combined organic layers were dried over Na₂SO₄, filtered and concentrated.

2,3-Di-*O*-methyl-1,5-dideoxy-1,5-imino-4,6-*O*-isopropylidene-D-glucitol (9)

Yield: 51 mg, 80%, yellow oil, $R_f = 0.16$ (petroleum ether/ethyl acetate 1:1). ¹H NMR (500 MHz, CDCl₃) δ 1.39 (s, 3H, CH₃), 1.45 (s, 3H, CH₃), 1.97 (s, 1H, NH), 2.40–2.50 (m, 2H, H-1a and H-1b), 2.53 (td, $J = 14.7, 10.1, 4.8$ Hz, 1H, H-5), 3.10 (t, $J = 8.7$ Hz, 1H, H-2), 3.17 (dd, $J = 9.9, 5.1$ Hz, 1H, H-3), 3.29 (dd, $J = 11.8, 5.1$ Hz, 1H, H-6a), 3.44 (s, 3H, OCH₃), 3.55 (s, 3H, OCH₃), 3.62 (m, 1H, H-4), 3.79 (dd, $J = 10.8, 4.7$ Hz, 1H, H-6b). ¹³C NMR (126 MHz, CDCl₃) δ 18.16 (CH₃), 28.42 (CH₃), 47.23 (C-1), 53.63 (OCH₃), 57.61 (OCH₃), 59.49 (C-6), 62.33 (C-5), 74.63 (C-2), 79.82 (C-3), 83.77 (C-4), 98.09 (CH).

2,3-Di-*O*-ethyl-1,5-dideoxy-1,5-imino-4,6-*O*-isopropylidene-D-glucitol (10)

Yield: 51 mg, 77%, yellow oil, $R_f = 0.44$ (petroleum ether/ethyl acetate 1:1). ¹H NMR (500 MHz, CDCl₃) δ 1.16 (t, $J = 6.2$ Hz, 6H, 2 \times CH₃-Ethyl), 1.37 (s, 3H, CH₃), 1.43 (s, 3H, CH₃), 1.97 (s, 1H, NH), 2.47–2.49 (m, 2H, H-5 and H-1a), 2.85 (s, 1H, H-1b), 3.15–3.21 (m, 3H, H-2, H-3 and H-6a), 3.40 (t, $J = 9.0$ Hz, 1H, H-4), 3.58–3.80 (m, 5H, 2 \times CH₂-Ethyl and H-6b). ¹³C NMR (126 MHz, CDCl₃) δ 12.88 (CH₃-Ethyl), 18.16 (CH₃-Ethyl), 28.46 (CH₃), 28.69 (CH₃), 48.16 (C-1), 53.81 (C-6), 62.67 (C-5), 70.22 (CH₂-Ethyl), 71.65 (CH₂-Ethyl), 75.02 (C-2), 78.79 (C-4), 82.72 (C-3), 97.94 (CH).

2,3-Di-*O*-butyl-1,5-dideoxy-1,5-imino-4,6-*O*-isopropylidene-D-glucitol (11)

Yield: 52 mg, 74%, yellow oil, $R_f = 0.37$ (petroleum ether/ethyl acetate 1:1). ¹H NMR (500 MHz, CDCl₃) δ

0.88 (t, $J = 7.4$ Hz, 6H, 2 \times CH₃-Butyl), 1.37 (s, 3H, CH₃), 1.43 (s, 3H, CH₃), 1.46–1.55 (m, 8H, 4 \times CH₂-Butyl), 1.98 (s, 1H, NH), 2.40–2.55 (m, 2H, H-5 and H-1a), 3.15 (d, $J = 8.7$ Hz, 1H, H-1b), 3.16–3.29 (m, 2H, H-2 and H-3), 3.39 (t, $J = 9.2$ Hz, 1H, H-6a), 3.52–3.69 (m, 4H, 2 \times CH₂-Butyl), 3.70–3.81 (m, 2H, H-6b and H-4). ¹³C NMR (126 MHz, CDCl₃) δ 12.88 (2 \times CH₃-Butyl), 18.16 (2 \times CH₂-Butyl), 28.46 (CH₃), 28.69 (CH₃), 29.18 (CH₂-Butyl), 30.43 (CH₂-Butyl), 48.16 (C-1), 53.81 (C-6), 62.67 (C-5), 70.22 (CH₂-Butyl), 71.65 (CH₂-Butyl), 75.02 (C-2), 78.79 (C-4), 82.72 (C-3), 97.94 (CH).

2,3-Di-*O*-benzyl-1,5-dideoxy-1,5-imino-4,6-*O*-isopropylidene-D-glucitol (12)

Yield: 62 mg, 83%, colorless oil, $R_f = 0.11$ (petroleum ether/ethyl acetate 3:1). ¹H NMR (500 MHz, CDCl₃) δ 1.52 (s, 3H, CH₃), 1.56 (s, 3H, CH₃), 2.07 (s, 1H, NH), 2.61–2.67 (m, 2H, H-1a and H-5), 3.30 (dd, $J = 12.0, 4.6$ Hz, 1H, H-1b), 3.52–3.64 (m, 3H, H-2, H-3 and H-6a), 3.67 (t, $J = 10.7$ Hz, 1H, H-4), 3.89 (dd, $J = 10.9, 4.9$ Hz, 1H, H-6b), 4.74 (d, $J = 11.7$ Hz, 1H, CH₂-Ar), 4.84 (d, $J = 11.7$ Hz, 1H, CH₂-Ar), 4.87 (d, $J = 11.4$ Hz, 1H, CH₂-Ar), 4.98 (d, $J = 11.4$ Hz, 1H, CH₂-Ar), 7.30–7.51 (m, 10H, H-Ar). ¹³C NMR (126 MHz, CDCl₃) δ 18.32 (CH₃), 28.59 (CH₃), 48.28 (C-1), 53.78 (C-6), 62.73 (C-5), 72.38 (CH₂-Ar), 74.00 (CH₂-Ar), 75.52 (C-2), 78.30 (C-4), 82.94 (C-3), 98.07 (CH), 126.50, 126.71, 126.84, 127.01, 127.29, 127.44 (C-Ar), 137.67 (CH-Ar), 138.27 (CH-Ar).

2,3-Di-*O*-naphthyl-1,5-dideoxy-1,5-imino-4,6-*O*-isopropylidene-D-glucitol (13)

Yield: 55 mg, 73%, colorless oil, $R_f = 0.2$ (petroleum ether/ethyl acetate 1:1). ¹H NMR (500 MHz, CDCl₃) δ 1.51 (s, 3H, CH₃), 1.54 (s, 3H, CH₃), 2.18 (s, 1H, NH), 2.63 (m, 2H, H-1a and H-5), 3.28 (m, 1H, H-1b), 3.62–3.70 (m, 4H, H-2, H-3, H-6a and H-4), 3.86 (d, $J = 6.3$ Hz, 1H, H-6b), 4.88 (d, $J = 11.9$ Hz, 1H, CH₂-Naph), 4.96 (d, $J = 11.9$ Hz, 1H, CH₂-Naph), 5.02 (d, $J = 11.7$ Hz, 1H, CH₂-Naph), 5.12 (d, $J = 11.7$ Hz, 1H, CH₂-Naph), 7.45–7.51 (m, 5H, H-Naph), 7.58 (d, $J = 8.4$ Hz, 1H, H-Naph), 7.74–7.90 (m, 8H, H-Naph). ¹³C NMR (126 MHz, CDCl₃) δ 18.37 (CH₃), 28.64 (CH₃), 48.20 (C-1), 53.70 (C-6), 62.66 (C-5), 72.43 (CH₂-Naph), 74.04 (CH₂-Naph), 74.09 (C-2), 78.27 (C-4), 82.87 (C-3), 98.14 (CH), 124.75, 124.96, 125.13, 125.32, 125.54, 125.58, 126.75, 126.99, 127.22 (C-Naph), 132.06 (2 \times C-Naph), 132.35 (C-Naph), 132.42 (C-Naph), 135.13 (CH-Naph), 135.84 (CH-Naph).

3. 5. General Procedure C: Regioselective Mono-Benzoylation and Alkylation to Obtain 14a–16a and 14b–16b

To a suspension of *N*-benzyloxycarbonyl-1,5-dideoxy-1,5-imino-4,6-*O*-isopropylidene-D-glucitol (3) (100 mg, 0.296 mmol) in methylene chloride (DCM) (10 mL), tetrabutylammonium bromide (TBAB) (1.5 eq, 143.13 mg,

0.44 mmol) was added. Sodium hydroxide solution (2 eq, 23.68 mg, 0.59 mmol) 0.5 mL was added to the reaction, followed by the addition of benzoyl chloride (for compounds **14a** and **14b**)/alkylating reagent *i.e.* benzyl bromide for compounds **15a** and **15b** and naphthyl bromide for compounds **16a** and **16b** (1.5 eq, 0.44 mmol). Reaction mixture was stirred at room temperature for 8–24 hours. Upon completion, the reaction mixture was filtered and washed with water (100 mL \times 3) and brine (100 mL \times 3). Organic layer was dried over Na₂SO₄, filtered and concentrated.

N-Benzoyloxycarbonyl-2-O-benzoyl-1,5-dideoxy-1,5-imino-4,6-O-isopropylidene-D-glucitol (14a)

Yield: 99 mg, 70%, colorless oil, R_f = 0.26 (petroleum ether/ethyl acetate 3:1). ¹H NMR (500 MHz, CDCl₃) δ 1.45 (s, 3H, CH₃), 1.54 (s, 3H, CH₃), 3.30 (td, J = 14.8, 10.1, 4.8 Hz, 1H, H-5), 3.42 (dd, J = 13.7, 7.5 Hz, 1H, H-1b), 3.74–3.93 (m, 2H, H-1a and H-3), 4.14 (dd, J = 13.9, 4.0 Hz, 1H, H-6b), 4.24 (t, J = 10.9 Hz, 1H, H-4), 4.43 (dd, J = 11.5, 4.8 Hz, 1H, H-6a), 5.04–5.07 (m, 1H, H-2), 5.08–5.14 (m, 2H, CH₂-Ar), 7.20–7.36 (m, 5H, H-Ar), 7.42–7.45 (m, 2H, H-Bz), 7.58 (dd, J = 10.6, 4.3 Hz, 1H, H-Bz), 7.99–8.00 (m, 2H, H-Bz). ¹³C NMR (126 MHz, CDCl₃) δ 18.23 (CH₃), 28.21 (CH₃), 44.22 (C-1), 52.79 (C-6), 61.39 (C-5), 66.64 (CH₂-Ar), 71.94 (C-3), 72.59 (C-2), 73.48 (C-4), 98.56 (CH), 127.07, 127.29, 127.52, 127.64, 128.48, 128.83 (C-Ar and C-Bz), 132.45 (CH-Bz), 135.00 (CH-Ar), 154.56 (C=O-Ar), 164.95 (C=O-Bz).

N-Benzoyloxycarbonyl-3-O-benzoyl-1,5-dideoxy-1,5-imino-4,6-O-isopropylidene-D-glucitol (14b)

Yield: (see Table 3) 10 mg, 7%, colorless oil, R_f = 0.36 (petroleum ether/ethyl acetate 3:1). ¹H NMR (500 MHz, CDCl₃) δ 1.33 (s, 3H, CH₃), 1.47 (s, 3H, CH₃), 3.11 (dd, J = 14.5, 9.9 Hz, 1H, H-1a), 3.21–3.33 (m, 2H, H-5 and H-1b), 3.77–3.84 (m, 1H, H-6a), 3.98 (t, J = 10.3 Hz, 1H, H-2), 4.11–4.18 (m, 1H, H-6b), 4.32–4.42 (m, 1H, H-3), 4.90 (dd, J = 9.0, 7.2 Hz, 1H, H-4), 5.06 (d, J = 12.2 Hz, 1H, CH₂-Ar), 5.11 (d, J = 12.2 Hz, 1H, CH₂-Ar), 7.29–7.33 (m, 5H, H-Ar), 7.40–7.44 (m, 2H, H-Bz), 7.54–7.57 (m, 1H, H-Bz), 7.99–8.00 (m, 2H, H-Bz). ¹³C NMR (126 MHz, CDCl₃) δ 28.15 (CH₃), 28.78 (CH₃), 47.81 (C-1), 53.95 (C-6), 61.39 (C-5), 66.64 (CH₂-Ar), 69.14 (C-2), 69.75 (C-4), 78.78 (C-3), 98.27 (CH), 124.72, 127.18, 127.36, 127.53, 127.68, 128.95, 132.52 (C-Ar and C-Bz), 135.03 (CH-Bz and CH-Ar), 135.42 (CH-Ar), 154.23 (C=O-Ar), 166.78 (C=O-Bz).

N-Benzoyloxycarbonyl-2,3-di-O-benzoyl-1,5-dideoxy-1,5-imino-4,6-O-isopropylidene-D-glucitol (14c)

Yield: (see Table 3) 20 mg, 12.36%, white solid, mp: 125 °C, R_f = 0.7 (petroleum ether/ethyl acetate 3:1). ¹H NMR (500 MHz, CDCl₃) δ 1.39 (s, 3H, CH₃), 1.51 (s, 3H, CH₃), 3.41–3.45 (m, 2H, H-5 and H-1a), 4.10 (t, J = 10 Hz, 1H, H-4), 4.28–4.41 (m, 2H, H-1b and H-6b), 4.48 (dd, J =

10, 5 Hz, 1H, H-6a), 5.10 (s, 2H, CH₂-Ar), 5.26 (dt, J = 15, 10, 5 Hz, 1H, H-2), 5.45 (dd, J = 10, 5 Hz, 1H, H-3), 7.25–7.35 (m, 5H, H-Ar), 7.39–7.43 (m, 4H, H-Bz), 7.53–7.56 (m, 2H, H-Bz), 7.96–8.01 (m, 4H, H-Bz). ¹³C NMR (126 MHz, CDCl₃) δ 18.12 (CH₃), 28.09 (CH₃), 44.96 (C-1), 53.62 (C-6), 61.46 (C-5), 66.71 (CH₂-Ar), 70.04 (C-2 and C-3), 73.76 (C-4), 98.44 (CH), 127.07, 127.42, 127.50, 127.64, 128.80 (C-Ar and C-Bz), 132.19 (2 \times CH-Bz), 132.41 (2 \times C-Bz), 134.93 (CH-Ar), 154.41 (C=O-Ar), 164.34 (C=O-Bz), 164.67 (C=O-Bz).

N-Benzoyloxycarbonyl-2-O-benzyl-1,5-dideoxy-1,5-imino-4,6-O-isopropylidene-D-glucitol (15a)

Yield: 88.63 mg, 70%, colorless oil, R_f = 0.19 (petroleum ether/ethyl acetate 3:1). ¹H NMR (500 MHz, CDCl₃) δ 1.41 (s, 3H, CH₃), 1.47 (s, 3H, CH₃), 2.90 (dd, J = 9.4, 4.0 Hz, 1H, H-1a), 3.10 (dd, J = 9.6, 3.8 Hz, 1H, H-2), 3.39–3.41 (m, 1H, H-1b), 3.70–3.54 (m, 2H, H-5 and H-6a), 4.15 (dd, J = 13.6, 4.5 Hz, 1H, H-6b), 4.26–4.39 (m, 2H, H-3 and H-4), 4.64 (s, 2H, CH₂-Ar), 5.04–5.06 (m, 2H, CH₂-Ar), 7.25–7.35 (m, 10H, H-Ar). ¹³C NMR (126 MHz, CDCl₃) δ 28.28 (CH₃), 28.48 (CH₃), 45.61 (C-1), 53.82 (C-6), 61.20 (C-5), 66.52 (CH₂-Ar), 71.20 (C-3), 72.26 (CH₂-Ar), 75.15 (C-2), 79.00 (C-4), 98.29 (CH), 124.72, 126.72, 126.84, 126.93, 127.14, 127.35, 127.55, 127.68 (C-Ar), 135.14 (CH-Ar), 136.97 (CH-Ar), 154.15 (C=O-Ar).

N-Benzoyloxycarbonyl-3-O-benzyl-1,5-dideoxy-1,5-imino-4,6-O-isopropylidene-D-glucitol (15b)

Yield: 18.1 mg, 14%, colorless oil, R_f = 0.33 (petroleum ether/ethyl acetate 3:1). ¹H NMR (500 MHz, CDCl₃) δ 1.47 (s, 3H, CH₃), 1.58 (s, 3H, CH₃), 2.62–2.79 (m, 1H, H-1a), 3.09 (ddd, J = 20.9, 12.9, 7.7 Hz, 1H, H-5), 3.30 (t, J = 8.3 Hz, 1H, H-1b), 3.56–3.59 (m, 1H, H-6a), 3.79 (dd, J = 10.1, 8.6 Hz, 1H, H-2), 4.24 (dd, J = 13.4, 4.9 Hz, 1H, H-6b), 4.34 (dd, J = 11.9, 4.9 Hz, 1H, H-3), 4.48 (t, J = 11.3 Hz, 1H, H-4), 4.65 (d, J = 11.6 Hz, 1H, CH₂-Ar), 4.92 (d, J = 11.6 Hz, 1H, CH₂-Ar), 5.04–5.06 (m, 2H, CH₂-Ar), 7.24–7.33 (m, 11H, H-Ar). ¹³C NMR (126 MHz, CDCl₃) δ 28.42 (CH₃), 28.77 (CH₃), 48.13 (C-1), 54.97 (C-6), 61.23 (C-5), 66.47 (CH₂-Ar), 78.27 (C-2), 73.25 (CH₂-Ar), 73.56 (C-4), 83.52 (C-3), 97.75 (CH), 124.71, 126.83, 126.90, 126.93, 127.10, 127.31, 127.57, 127.65 (C-Ar), 135.10 (CH-Ar), 137.68 (CH-Ar), 153.99 (C=O-Ar).

N-Benzoyloxycarbonyl-2-O-naphthyl-1,5-dideoxy-1,5-imino-4,6-O-isopropylidene-D-glucitol (16a)

Yield: 54 mg, 38%, colorless oil, R_f = 0.14 (petroleum ether/ethyl acetate 3:1). ¹H NMR (500 MHz, CDCl₃) δ 1.41 (s, 3H, CH₃), 1.47 (s, 3H, CH₃), 2.96 (d, J = 4 Hz, 1H, H-1a), 3.12 (dd, J = 15.0, 10.0 Hz, 1H, H-3), 3.47 (ddd, J = 9.1, 6.6, 4.6 Hz, 1H, H-1b), 3.58–3.73 (m, 2H, H-5 and H-6a), 4.15 (dd, J = 13.6, 4.3 Hz, 1H, H-2), 4.29–4.33 (m, 2H, H-6b and H-4), 4.81 (s, 2H, CH₂-Naph), 4.99 (d, J = 12.2 Hz, 1H, CH₂-Ar), 5.06 (d, J = 12.2 Hz, 1H, CH₂-Ar),

7.21–7.32 (m, 5H, H-Ar), 7.44–7.46 (m, 3H, H-Naph), 7.69–7.86 (m, 4H, H-Naph). ¹³C NMR (126 MHz, CDCl₃) δ 26.40 (CH₃), 28.32 (CH₃), 49.26 (C-1), 53.84 (C-6), 61.24 (C-5), 66.48 (CH₂-Naph), 67.80 (C-3), 71.34 (CH₂-Naph), 72.34 (C-2), 75.91 (C-4), 98.33 (CH), 125.09, 126.06, 127.00, 127.01, 127.03, 127.12, 127.22, 127.34, 127.41, 127.68, 127.93, 132.34 (C-Naph and C-Ar), 133.82 (C-Ar), 134.48 (C-Ar), 135.18 (C-Naph), 135.36 (C-Naph), 142.71 (CH-Naph), 145.50 (CH-Ar), 154.15 (C=O-Ar).

N-Benzoyloxycarbonyl-3-O-naphthyl-1,5-dideoxy-1,5-imino-4,6-O-isopropylidene-D-glucitol (16b)

Yield: 25 mg, 20%, colorless oil, *R*_f = 0.26 (petroleum ether/ethyl acetate 3:1). ¹H NMR (500 MHz, CDCl₃) δ 1.44 (s, 3H, CH₃), 1.50 (s, 3H, CH₃), 2.78 (dd, *J* = 10.3, 5.0 Hz, 1H, H-2), 3.12 (td, *J* = 14.8, 10.4, 4.9 Hz, 1H, H-1a), 3.37 (t, *J* = 8.2 Hz, 1H, H-1b), 3.63 (ddd, *J* = 10.2, 8.1, 4.9 Hz, 1H, H-5), 3.70 (q, *J* = 7.0 Hz, 1H, H-6a), 3.85 (dd, *J* = 10.0, 8.7 Hz, 1H, H-3), 4.24 (dd, *J* = 13.4, 4.8 Hz, 1H, H-6b), 4.50 (t, *J* = 11.4 Hz, 1H, H-4), 4.84 (d, *J* = 11.8 Hz, 1H, CH₂-Naph), 5.03–5.10 (m, 3H, CH₂-Naph and CH₂-Ar), 7.20–7.38 (m, 5H, H-Ar), 7.43–7.56 (m, 3H, H-Naph), 7.78–7.82 (m, 4H, H-Naph). ¹³C NMR (126 MHz, CDCl₃) δ 26.38 (CH₃), 26.71 (CH₃), 48.14 (C-1), 54.90 (C-6), 61.28 (C-5), 66.51 (CH₂-Ar), 68.36 (C-2), 73.28 (CH₂-Naph), 73.60 (C-4), 83.48 (C-3), 97.81 (CH), 125.04, 125.26, 125.84, 126.05, 126.74, 126.81, 126.96, 127.13, 127.20, 127.33, 127.68 (C-Naph and C-Ar), 129.97 (C-Naph), 132.11 (C-Naph), 132.38 (CH-Naph), 135.10 (CH-Ar), 154.05 (C=O-Ar).

4. Conclusion

To summarize the results, we have demonstrated experiments directed towards selective removal of *N*-protecting group using NaOH as the base. Optimum reaction conditions were probed for regioselective benzylation of *N*-benzyloxycarbonyl-1,5-dideoxy-1,5-imino-4,6-*O*-isopropylidene-D-glucitol. TBAB-NaOH catalytic system gave regioselective mono-alkylated products majorly at the position 2. All newly synthesized compounds were well characterized by spectroscopic means. It was concluded that TBAB-NaOH catalytic system may be considered as an attractive alternative for the regioselective protection of 1-deoxynojirimycin, particularly protection reactions at 2- and 3-hydroxy groups of *N*-benzyloxycarbonyl-1,5-dideoxy-1,5-imino-4,6-*O*-benzylidene-D-glucitol.

5. References

- N. Asano, R. J. Nash, R. J. Molyneux, G. W. J. Fleet, *Tetrahedron: Asymmetry* **2000**, *11*, 1645–1680. DOI:10.1016/S0957-4166(00)00113-0
- E. Danieli, J. Lalot, P. V. Murphy, *Tetrahedron* **2007**, *63*, 6827–6834. DOI:10.1016/j.tet.2007.04.070
- G. J. Davies, T. M. Gloster, B. Henrissat, *Curr. Opin. Struct. Biol.* **2005**, *15*, 637–645. DOI:10.1016/j.sbi.2005.10.008
- S. Chiba, *Biosci. Biotechnol. Biochem.* **2012**, *76*, 215–231. DOI:10.1271/bbb.110713
- G. L. Zhang, C. Chen, Y. Xiong, L. H. Zhang, J. Ye, X. S. Ye, *Carbohydr. Res.* **2010**, *345*, 780–786. DOI:10.1016/j.carres.2010.01.021
- M. Iftikhar, L. Wang, Z. Fang, *J. Chem. Res.* **2017**, *41*, 460–464. DOI:10.3184/174751917X15000341607489
- T. Tsuruoka, H. Fukuyasu, M. Ishii, T. Usui, S. Shibahara, S. Inouye, *J. Antibiot.* **1996**, *49*, 155–161. DOI:10.7164/antibiotics.49.155
- L. Somsak, V. Nagy, Z. Hadady, T. Docsa, P. Gergely, *Curr. Pharm. Des.* **2003**, *9*, 1177–1189. DOI:10.2174/1381612033454919
- D. Durantel, N. B. Nichita, S. C. Durantel, T. D. Butters, R. A. Dwek, N. Zitzmann, *J. Virol.* **2001**, *75*, 8987–8998. DOI:10.1128/JVI.75.19.8987-8998.2001
- W. Yu, T. Gill, L. Wang, Y. Du, H. Ye, X. W. Qu, J. T. Guo, A. Cuconati, K. Zhao, T. M. Block, X. D. Xu, J. Chang, *Med. Chem.* **2012**, *55*, 6061–6075. DOI:10.1021/jm300171v
- A. Mehtaa, N. Zitzmann, P. M. Rudda, T. M. Block, R. A. Dwek, *FEBS Lett.* **1998**, *430*, 17–22. DOI:10.1016/S0014-5793(98)00525-0
- A. Kato, J. Hollinshead, Y. Yamashita, S. Nakagawa, Y. Koike, I. Adachi, C. Y. Yu, G. W. J. Fleet, R. J. Nash, *Phytochem. Lett.* **2010**, *3*, 230–233. DOI:10.1016/j.phytol.2010.08.006
- T. M. Wrodnigg, A. J. Steiner, B. J. Ueberbacher, *Anti-Cancer Agents Med. Chem.* **2008**, *8*, 77–85. DOI:10.2174/187152008783330851
- M. Iftikhar, Z. Fang, *J. Carbohydr. Chem.* **2017**, *36*, 295–306. DOI:10.1080/07328303.2017.1397683
- F. Chery, P. V. Murphy, *Tetrahedron Lett.* **2004**, *45*, 2067–2069. DOI:10.1016/j.tetlet.2004.01.064
- X. M. Zhu, R. R. Schmidt, *Angew. Chem. Int. Ed.* **2009**, *48*, 1900–1934. DOI:10.1002/anie.200802036
- M. Heuckendorff, C. M. Pedersen, M. Bols, *Chem. Eur. J.* **2010**, *16*, 13982–13994. DOI:10.1002/chem.201002313
- D. P. Getma, G. A. DeCrescenzo, R. M. Heintz, *Tetrahedron Lett.* **1991**, *32*, 5691–5692. DOI:10.1016/S0040-4039(00)93531-7
- T. Zhang, T. Wang, Z. Fang, *Synth. Commun.* **2015**, *45*, 2567–2575. DOI:10.1080/00397911.2015.1093143
- M. Matwiejuk, J. Thiem, *Eur. J. Org. Chem.* **2011**, *29*, 5860–5878. DOI:10.1002/ejoc.201100861
- A. M. Schueller, F. R. Heiker, *Carbohydr. Res.* **1990**, *203*, 308–313. DOI:10.1016/0008-6215(90)80030-7
- F. Chery, L. Cronin, J. L. O'Brien, P. V. Murphy, *Tetrahedron* **2004**, *60*, 6597–6608. DOI:10.1016/j.tet.2004.05.080

Povzetek

Zaščitne skupine igrajo pomembno vlogo v kemiji ogljikovih hidratov, saj bistveno vplivajo na reaktivnost substratov. Izvedli smo študijo substitucije različnih zaščitnih skupin v 1-deoksinodžirimycinu. Substrat, *N*-benziloksikarbonil-1,5-dideoksi-1,5-imino-4,6-*O*-izopropiliden-*D*-glucitol smo podvrgli alkiliranju na položajih 2- in 3- in tako pripravili disubstituirane produkte iz katerih smo z uporabo NaOH v EtOH/H₂O selektivno odstranili *N*-Cbz zaščitno skupino. Regioselektivno benzoiliranje in alkiliranje *N*-benziloksikarbonil-1,5-dideoksi-1,5-imino-4,6-*O*-izopropiliden-*D*-glucitola smo izvedli z uporabo katalitskega sistema TBAB-NaOH. Ugotovili smo, da vsi zaščiteni in mono-zaščiteni analogi nastajajo hkrati; njihove strukture smo potrdili s spektroskopskimi metodami. Rezultati kažejo, da igra elektrofilnost pomembno vlogo pri določanju razmerij med različnimi produkti, ki nastanejo.

Scientific paper

Synthesis, Characterization, Crystal Structure and Molecular Docking Studies of a S-methyldithiocarbamate Derivative: Bis[2-hydroxy-benzylidenehydrazono] (methylthio)methyl]disulfide

Winaki P. Sohtun,¹ Arunachalam Kannan,² K. Hari Krishna,³
Dhandayutham Saravanan,^{2,*} Muthuvel Suresh Kumar,³ and Marappan Velusamy^{1,*}

¹ Department of Chemistry, North Eastern Hill University, Meghalaya 793022, India

² Department of Chemistry, National College, Tiruchirappalli 620001, India

³ Centre for Bioinformatics, Pondicherry University, Pondicherry, 605014, India

* Corresponding author: E-mail: mvelusamy@gmail.com

Received: 16-02-2018

Abstract

The title compound bis[2-hydroxybenzylidenehydrazono](methylthio)methyl]disulfide (**1**), an S-methyldithiocarbamate derivative with a disulfide bond has been synthesized by the condensation of 2-hydroxybenzaldehyde with S-methyldithiocarbamate. It has been characterized by elemental analyses, ¹H, ¹³C NMR and FT-IR spectroscopy and mass spectrometry. The single crystal X-ray structure shows that the compound exists in a tautomeric thione form with the dithiocarbamate fragment adopting an *EE* configuration with respect to the C=N bond of the benzylidene moiety. The thermal behaviour of the compound has been studied using thermogravimetric analysis (TGA). The molecular geometry of the compound in the ground state has been optimized using density functional theory (DFT/B3LYP) method with the 6-311++G(d,p) basis sets. Molecular docking of the compound with human carbonic anhydrase II has been performed to probe the nature of interaction.

Keywords: S-methyldithiocarbamate; TGA; Single crystal; Disulphide; Docking studies

1. Introduction

Disulfide compounds are widely distributed in natural bioactive components and show a wide range of potential pharmaceutical applications, such as stabilization and folding of proteins in biological systems.¹ Organic compounds containing S-S bonds play an important role as an intermediate and as protecting groups in organic synthesis.^{2,3} Numerous strategies and reagents have been developed for the synthesis of disulfide bonds including metal based catalytic oxidation, 2,3-dichloro-5,6-dicyanobenzoquinone (DDQ) and peroxides.^{4–6} Currently, the synthesis and characterization of dithiocarbamate based Schiff bases are of great interest because of its potential application in biochemical and pharmacological applications.^{7–9} Schiff bases with carbamate moieties act as strong chelators and can form stable coordination complexes with a variety of metal ions.^{10,11} Due to easy preparation and structural va-

rieties, they have been widely used as chelating ligands in the synthesis of a large variety of metal complexes.^{12,13} Metal complexes derived from dithiocarbamate ligands have been studied not only because of their exciting coordination chemistry, but also their prominent biological activities.^{14,15} These types of Schiff bases facilitate coordination metal ions with different oxidation states through the hard nitrogen and soft sulphur donors. The majority of previous studies were based on Schiff bases of thiosemicarbazones with tridentate N,N,S donor atoms,^{16–18} and only a few reports have been made using Schiff bases of dithiocarbamate derived from S-alkyl moiety. In biological systems, dithiocarbamates are extensively used as inhibitors of enzymes and for the treatment of cancer.^{19,20} In early studies, Bernhardt and co-workers synthesized a series of dithiocarbamate based ligands and their iron(II) complexes and studied their antiproliferative activities.^{21–23} Recently, Crouse et al. reported copper(II) complexes of a series of

dithiocarbazate Schiff base and correlated their structures and their antibacterial activity.²⁴ In this work, the Schiff base bis[2-hydroxybenzylidenehydrazono)-(methylthio)methyl]disulfide has been synthesized and characterized by elemental analyses and ¹H and ¹³C NMR, FT-IR and mass spectrometry. The single crystal X-ray structure of the compound has been determined to assess the conformation of the molecule. The molecular docking of the compound with human carbonic anhydrase II has been also studied to understand the nature of interaction between them.

2. Experimental

2. 1. Materials and Physical Measurements

Solvents were dried and distilled by standard methods before use. Reagents were purchased from commercial suppliers and used without further purification. S-methyldithiocarbazate was prepared according to the published procedure.²⁵ ¹H and ¹³C NMR spectra were recorded on a Bruker AVANCE II 400 MHz NMR spectrometer. IR spectra were recorded using Perkin-Elmer 983 model FT-IR spectrophotometer with compounds being dispersed as KBr discs. The electronic spectra were recorded on an Agilent-8453 diode array spectrophotometer. Mass spectrometry was performed on a Thermo LC-MS spectrometer.

2. 2. Synthesis of Compound 1

A solution of S-methyldithiocarbazate (1.22 g, 10 mmol) in ethanol (20 mL) was added to a stirred solution of 2-hydroxybenzaldehyde (1.22 g, 10 mmol) in ethanol (20 mL). The mixture was stirred for 20 min and refluxed for 12 h. The reaction mixture was then cooled to room temperature and the solid obtained was filtered off, washed several times with cold ethanol and dried under vacuum. Yield: 68 %. The above solid was dissolved in ethanol and refluxed under oxygen atmosphere for 24 h. After cooling the solution at room temperature, the title compound in the form of brown needles was obtained. ¹H NMR (DMSO-*d*₆), δ (ppm) 2.43(s, 6H, S-CH₃), 6.92–6.87 (4H, t, *J* = 10 Hz), 7.34–7.31 (2H, t, *J* = 6.0 Hz), 7.68–7.66 (2H, Ar, d, *J* = 8.0 Hz), 8.74 (2H, s, CH=N), 10.50 (2H, s, Ar-OH). ¹³C NMR (DMSO-*d*₆), δ (ppm): 17.3 (S-CH₃), 116.9, 119.6 (C-C=N, Ar), 120.1, 127.7, 132.7 (4 CH, Ar), 145.0 (HC=N), 157.7(C-S), 197.7 (C-O). ESI-MS (*m/z*): 450.62. UV-vis, λ_{abs}, nm (ε, M⁻¹ cm⁻¹): 350 (54858), 315 (59137), 300 (58055). Anal. found (calcd) for C₁₈H₁₈N₄O₂S₄: C, 47.82 (47.98); H, 4.12 (4.03); N, 12.49 (12.43).

2. 3. Single-crystal X-ray Studies

A single-crystal for X-ray diffraction study was grown by slow evaporation of ethanol solution of **1** at

room temperature. A suitable crystal was mounted on glass fiber for data collection. Data was collected on an Oxford Diffraction Xcalibur Eos Gemini diffractometer. Crystal data were collected at ambient temperature using graphite-monochromated Mo-Kα radiation (λ = 0.71073 Å). The data were solved using direct methods with SHELXS and refined using SHELXL-2013.²⁶ The graphics interface package used was PLATON, and the figures were generated using the ORTEP 3.07 generation package.²⁷ The positions of all atoms were obtained by direct methods. Non-hydrogen atoms were refined anisotropically. The hydrogen atoms were placed in calculated positions, constrained to ride on their parent atom with group *U*_{iso} values assigned, *U*_{iso}(H) = 1.2*U*_{eq} for aromatic carbons and 1.5*U*_{eq} for methyl atoms. The crystallographic data and details of data collection for **1** are given in Table 1.

2. 4. Density Functional Theory Calculations

One of the goals of computational chemistry is to understand the chemical reactivity and to predict the outcome of molecular interactions. Density functional theory (DFT) method has emerged as a powerful tool in studying molecular structure. Among the numerous available DFT methods, we have selected the B3LYP functional which combines the Becke's three-parameter exchange functional (B3) with the Lee-Yang-Parr correlation functional (LYP) with 6-311++G(d,p) basis set calculations^{28–30} were used for predicting the frontier orbitals (HOMO, LUMO) of the title compound. All DFT calculations were carried out using the Gaussian 09 program package.³¹ HOMO-LUMO values are the reliable estimates of reducing and oxidizing properties of the molecules and play an important role in stabilizing the interactions with the receptor.^{32,33}

2. 5. Molecular Docking and Simulation Studies

The biological importance of the synthesized ligand is assessed by performing the docking studies using the Schrödinger Glide software.³⁴ The retrieved pdb file was prepared using the protein preparation wizard³⁵ by removing the water molecules and ligands and the pdb was optimized by assigning the hydrogens, missing atoms, bonds and charges to the atoms. Ligand preparation including the generation of various tautomers, assigning bond orders, ring conformations and stereo chemistries of the ligand were carried out using the LigPrep. All the conformations generated were further minimized using OPLS2005 force field prior to docking study. A receptor grid was generated around the protein active site by selecting the active residues (Gln 92, Thr 199, Zn) with a size of 15 Å using receptor grid generation. The docking calculations were performed using Extra Precision (XP) mode using the Ligand

Docking and the Glide docking score was used to determine the best docked structure from the output.

MD simulations were performed using the GRO-MACS 5.0.6 version (www.gromacs.org)³⁶ using the GRO-MOS 53a6 force field.³⁷ PRODRG server³⁸ was used to generate the topology files for the ligand. The protein was solvated by SPC (Single Point Charge)³⁹ water molecules and the systems were neutralized using two Cl⁻ counter ions. Periodic boundary conditions were implemented in all directions, using a simulation cell with a distance minimum of 1.0 nm from the protein. Electrostatic interactions were computed using the particle mesh Ewald (PME)⁴⁰ simulation method with a 1 nm short-range electrostatic cut-off. The short-range cut-off used for van der Waals interactions during the simulation was also 1 nm. For the temperature coupling, the solvated structure was divided into two groups (protein and non-protein) using velocity rescaling with a stochastic term. The isotropic pressure coupling was employed in the MD simulation by using the Parrinello-Rahman method⁴¹ with a compressibility of $4.5 \cdot 10^{-5} \text{ bar}^{-1}$. During the simulation, constraints were deployed in all bands using the LINC algorithm⁴² with parameters LINC-order of 4. First, each system was energy-minimized for 5,000 steps each using steepest-descent and conjugate gradient algorithms; subsequently, the solvent, and ions were equilibrated for 100 ps in constant volume (NVT) and constant pressure (NPT) ensembles, respectively, while the substrates and cofactors of the protein were restrained harmonically using a force constant of $1000 \text{ kJ mol}^{-1} \text{ nm}^{-2}$. Finally, the two systems were performed for 5 ns MD simulations after removing all the restraints and all the trajectories were stored every 0.002 ps for further analysis. The binding free energies of the ligand were calculated using the *g_mmpbsa* program for the last 1 ns with a reference frame from every 50 ps.

3. Results and Discussion

The disulfide Schiff base was prepared and isolated in good yield which is characterized by spectral and single-crystal X-ray studies. The thermal property of the com-

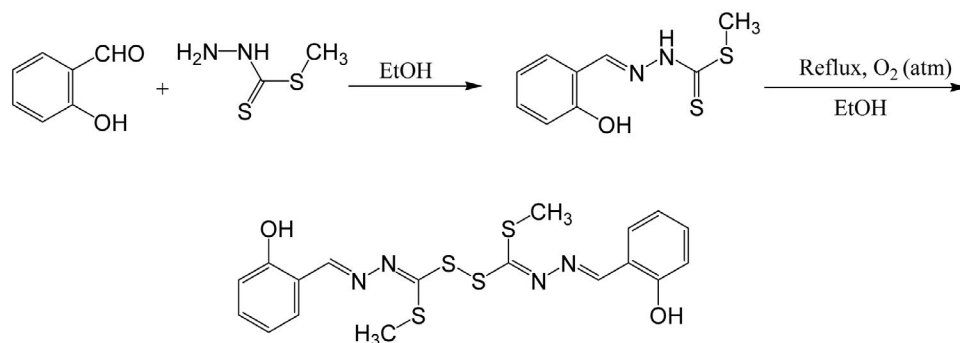
pound was determined by TGA analysis. DFT calculation and molecular docking studies were carried out by Gaussian 09 program package and Schrödinger Glide software respectively.

3. 1. Synthesis and Characterization

The Schiff base containing a disulfide **1** has been prepared by aerial oxidation of *N*'-(2-hydroxybenzylidene)hydrazinecarbodithioic acid methyl ester in ethanol at reflux temperature (Scheme 1). It was isolated as a pale yellow shiny crystalline solid. It is non-hygroscopic, air-stable and is highly soluble in common organic solvents. The compound was purified by recrystallization from ethanol solution and fully characterized by IR, ¹H and ¹³C NMR, mass spectrometry, and electronic spectroscopy. The single-crystal X-ray structure of the compound has been determined.

3. 2. Spectral Studies of the Complex

The ¹H NMR spectrum of compound **1** in DMSO-*d*₆ shows two signals at δ 10.5 and 8.74 ppm due the phenolic OH and azomethine ($-\text{CH}=\text{N}-$) protons respectively. The S-methyl ($-\text{S}-\text{CH}_3$) protons are observed at δ 2.43 ppm. The aromatic protons appear as multiplet in the region of δ 6.87–7.68 ppm. The ¹³C NMR spectrum of **1** shows signals at δ 145.0, 157.7 and 197.7 ppm due to the C=N, C-S and C-O (phenolic) carbons respectively. The S-CH₃ carbon is observed at 17.3 ppm. The phenyl ring carbons appear at δ 116.9, 120.1, 127.7, 132.7 ppm.⁴³⁻⁴⁵ The electronic absorption spectra of the compound have been recorded in acetonitrile and the corresponding spectrum was displayed in Figure 1. The compound showed three intense bands at 300, 315 and 350 nm that can be assigned to $\pi \rightarrow \pi^*$, $\sigma \rightarrow \sigma^*$ transitions of the aromatic rings of benzene and $n \rightarrow \pi^*$ transitions of the azomethine chromophores respectively.⁴⁶ In the IR spectrum, two prominent vibrational bands located at 3110 and 1620 cm^{-1} are characteristics of the OH and C=N stretch, respectively. The peak obtained at 1033 cm^{-1} and 512 cm^{-1} were attributed to N-N and S-S stretching vibrations.



Scheme 1. Synthesis of the compound **1**

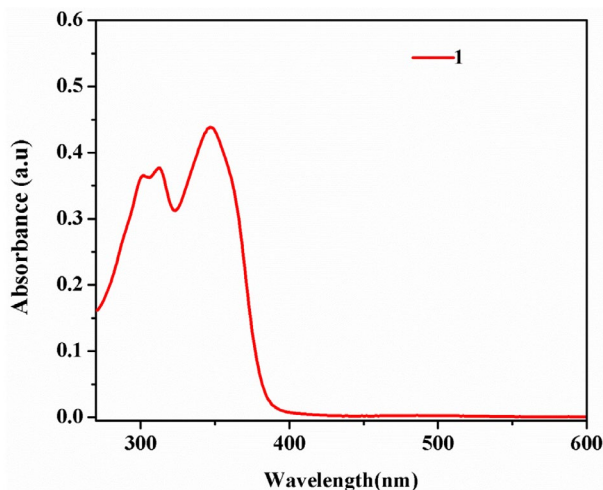


Figure 1. Electronic absorption spectra of **1** in acetonitrile

The IR spectrum of **1** does not display $\nu(\text{S-H})$ at ca. 2570 cm^{-1} indicating that in the solid-state they remain in the thione form.^{47,48} The IR and NMR spectral properties are closely related to those of similar type of disulfide compounds reported already.⁴⁹

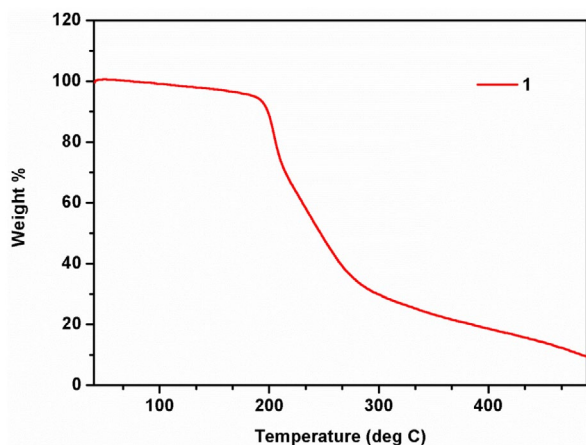


Figure 2. TGA curve for compound **1**.

3. 3. Thermogravimetric Analysis (TGA)

Thermal properties of the compound **1** was evaluated using TGA at a heating rate of $10\text{ }^\circ\text{C}/\text{min}$ under nitrogen atmosphere with temperature range of $30\text{--}900\text{ }^\circ\text{C}$ (Figure 2). The thermogram shows that there was no mass loss occurring below $100\text{ }^\circ\text{C}$ and it was confirmed that the sample does not contain any solvent. Also, the degradation process of **1** starts at around $190\text{ }^\circ\text{C}$.

3. 4. Single-crystal X-ray Structure Analysis

The single crystal of compound **1** was obtained by slow evaporation in an ethanol solution at room temperature. The molecular structure of **1** is shown in Figure 3 with displacement ellipsoids plotted at 50% probability level. Compound **1** crystallizes as monoclinic crystal system in $P2_1/c$ space group, unit cell parameters $a = 12.4489$ (8) \AA , $b = 14.0742$ (9) \AA , $c = 12.0688$ (8) \AA , $\alpha = 90^\circ$, $\beta = 93.403^\circ$ and $\gamma = 90^\circ$. Table S1 shows the selected bond

Table 1. Crystal data for compound **1**.

Empirical formula	$\text{C}_{18}\text{H}_{18}\text{N}_4\text{O}_2\text{S}_4$
Formula weight	450.60
T (K)	293(2)
Crystal system	Monoclinic
Space group	$P2_1/c$
a (\AA)	12.4489(8)
b (\AA)	14.0742(9)
c (\AA)	12.0688(8)
α ($^\circ$)	90
β ($^\circ$)	93.403(5)
γ ($^\circ$)	90
V (\AA^3)	2110.8(2)
Z	4
D_c (g cm^{-3})	1.418
μ (mm^{-1})	0.935
$F(000)$	936
Goof on F^2	1.017
R indices [$I > 2\sigma(I)$]	$R_1 = 0.0456$, $wR_2 = 0.1134$
R indices (all data)	$R_1 = 0.0718$, $wR_2 = 0.0999$

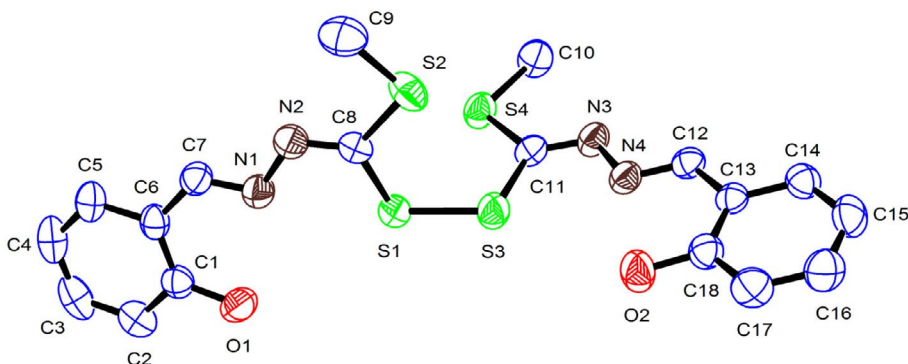


Figure 3. ORTEP diagram and atom labelling scheme for compound **1**. Ellipsoids are plotted at 50% probability level. Hydrogen atoms are omitted for clarity.

lengths and angles of **1**. The bond lengths and angles are within the normal ranges and are comparable to those in related structures.^{50–52} The molecule adopts an *EE* conformation with respect to the C=N bond of the benzylidene moiety. The β -nitrogen and the thioether sulphur are *trans* located with respect to the C11–N3 and C8–N2 bond. The planarity of the molecule is stabilized by a strong intramolecular hydrogen bond O1–H1...N1 = 2.653(9) Å and O2–H2...N4 = 2.631(5) Å. The hydroxyphenyl moiety, which consists of C1–C7, N1, N2, C8 and C12–C18, N3, N4, C11, is nearly perpendicular to the disulfide plane S1–S3–C11 = 105.80(8)° and S1–S3–C8 = 104.63(8)°. However, the observed S–S (2.039 Å), N–N (1.408 Å), C–N (1.280 Å) bond distances and S–C–N (120.80°), S–S–C (104.63°) bond angles are in the range of those reported for other closely related disulfide compounds, particularly, *S,S'*-bis(2-hydroxybenzylidenehydrazono(phenyl)methyl)disulfide, (S–S, 2.050 Å; N–N, 1.406 Å; C–N, 1.279 Å).⁵³

3. 5. Theoretical Results

The ground state energy of compound **1** is calculated as -7.3421×10^4 eV by density functional theory (DFT) methods using B3LYP/6-31G(d,p) level. The Highest Occupied Molecular Orbital (HOMO) localized on half of the molecule that is from benzene ring to one of the sulfur atom in disulfide linkage. The Lowest Unoccupied Molecular Orbital (LUMO) localized on throughout the molecule.

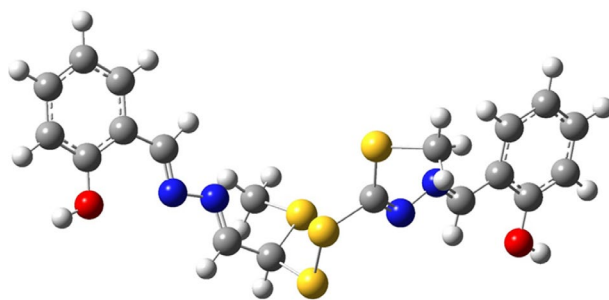


Figure 4. Ground state optimized structure of compound **1** calculated by DFT using B3LYP/6-31G (d, p) level.

The calculated bond lengths and bond angles are similar to that of crystal structure (Figure 4). The excited state calculation also been carried out by Time Dependent-DFT (TD-DFT) methods. The energies of HOMO and LUMO are -5.7007 and -1.6296 eV and its energy gap is 4.0711 eV.

The wavelength corresponding to 4.0711 eV is 304.54 nm and which can be correlated to band at 300 nm obtained from UV-vis spectral study. Along with this transition, it is found that there are three more excited state populated. The excitation energy of the excited state 1 is 3.34 eV with corresponding wavelength of 370.69 nm and the originated transitions are calculated as HOMO-3 to LUMO, HOMO-3 to LUMO+1 and HOMO-4 to LUMO. The excitation energy of the excited state 2 is 3.38 eV with corresponding wavelength of 366.72 nm and the originat-

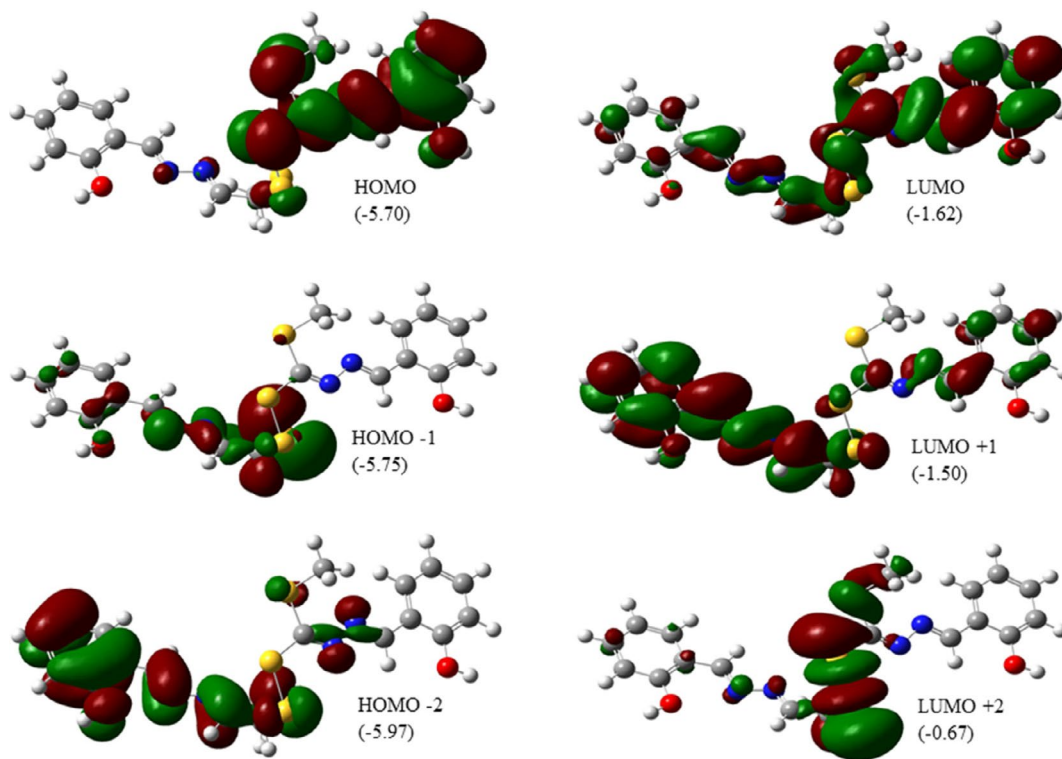


Figure 5. HOMO's and LUMO's of compound **1** calculated by TD-DFT using B3LYP/6-31G(d, p) level; the corresponding energies (in eV) are mentioned in parenthesis.

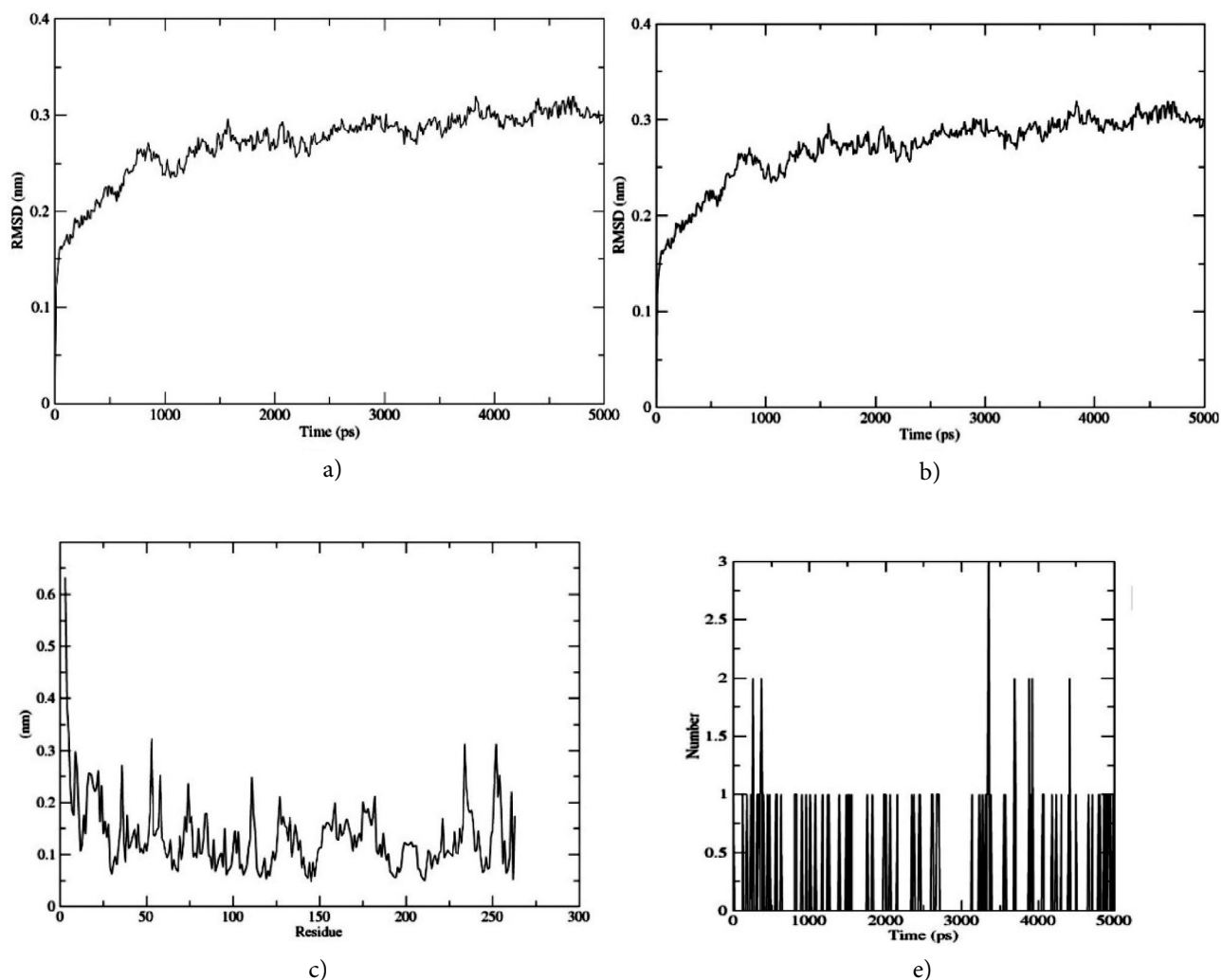


Figure 7. (a) and (b) show the rmsd of the protein and the ligand from the trajectory file. (c) Shows the fluctuation of the protein residues in the course of the simulation. (d) Shows the number of H bonds between the ligand and the protein across the time.

4. Conclusions

In the present study the preparation of the novel compound bis[2-hydroxybenzylidenehydrazono)(methylthio)methyl]disulphide is reported. The compound has been characterized by UV-vis, IR, NMR, and mass spectrometry. It crystallizes in the monoclinic system with the centrosymmetric space group $P2_1/c$. The single crystal X-ray structure determination shows that the compound adopts an *EE* conformation with respect to C=N bond of the benzylidene moiety. The thermal behaviour of the compound has been studied using thermogravimetric analysis (TGA). Theoretical calculations have been performed with DFT/B3LYP/6-31++G(d,p) basis set. The electronic properties have been also calculated (TD-DFT) and compared with the experimental UV-Vis spectrum. The molecular docking studies reveal that the compound can act as a potent inhibitor of carbonic anhydrase II activity.

5. Acknowledgements

We thank DST-PURSE, NEHU-SAIF Shillong, India, for providing XRD and NMR spectral facilities. One of the authors M. V. express his thanks to UGC, MRP-MAJOR-CHEM 2013-5144, (69/2014 F. No. 10-11/12) for financial assistance in the form of a major sponsored project.

6. References

1. Y. Hidaka, S. Shimamoto, *Biomole. Concepts* **2013**, *4*, 597–604. DOI:10.1515/bmc-2013-0022
2. W. Ge, Y. Wei, *Green Chem.* **2012**, *14*, 2066–2070. DOI:10.1039/C2GC35337G
3. G. Saito, J. A. Swanson, K. D. Lee, *Adv. Drug Deliv. Rev.* **2003**, *55*, 199–215. DOI: 10.1016/S0169-409X(02)00179-5
4. Mandala B, Basu B, *RSC Adv.* **2014**, *4*, 13854–13881 DOI: 10.1039/C3RA45997G

5. S. Harusawa, K. Yoshida, C. Kojima, L. Araki, T. Kurihara, *Tetrahedron* **2004**, *60*, 11911–11922. DOI: 10.1016/j.tet.2004.09.109
6. J. K. Vandavasi, W. P. Hu, C. Y. Chen, J. J. Wang, *Tetrahedron* **2011**, *67*, 8895–8901. DOI: 10.1016/j.tet.2011.09.071
7. M. L. Low, L. Maigre, M. I. M. Tahir, E. R. T. Tiekink, P. Dorlet, R. Guillot, T. B. Ravoo, R. Rosli, J. M. Pages, C. Policar, N. Delsuc, K. A. Crouse, *Eur. J. Med. Chem.* **2016**, *120*, 1–12. DOI: 10.1016/j.ejmech.2016.04.027
8. D. B. Lovejoy, D. M. Sharp, N. Seebacher, P. Obeidy, T. Prichard, C. Stefani, M. T. Basha, P. C. Sharpe, P. J. Jansson, D. S. Kalinowski, P. V. Bernhardt, D. R. Richardson, *J. Med. Chem.* **2012**, *55*, 7230–7244. DOI: 10.1021/jm300768u
9. P. Quach, E. Gutierrez, M. T. Basha, D. S. Kalinowski, P. C. Sharpe, D. B. Lovejoy, P. V. Bernhardt, P. J. Jansson, D. R. Richardson, *Mol. Pharmacol.* **2012**, *82*, 105–114. DOI: 10.1124/mol.112.078964
10. E. Zangrando, M. T. Islam, M. A. A. Islam, M. C. Sheikh, M. T. H. Tarafder, R. Miyatake, R. Zahan, M. A. Hossain, *Inorg. Chim. Acta* **2015**, *427*, 278–284. DOI: 10.1016/j.ica.2014.12.014
11. X.-Y. Qiu, C. Zhang, S.-Z. Li, G.-X. Cao, P. Qu, F.-Q. Zhang, J.-G. Ma, B. Zhai, *Inorg. Chem. Commun.* **2014**, *46*, 202–206. DOI: 10.1016/j.inoche.2014.05.015
12. M. X. Li, L. Z. Zhang, C. L. Chen, J. Y. Niu, B. S. Ji, *J. Inorg. Biochem.* **2012**, *106*, 117–125. DOI: 10.1016/j.jinorgbio.2011.09.034
13. M. A. Ali, A. H. Mirza, H. J. H. A. Bakar, P. V. Bernhardt, *Polymhedron* **2011**, *30*, 556–564. DOI: 10.1016/j.poly.2010.11.016
14. P. K. Sasmal, A. K. Patra, A. R. Chakravarty, *J. Inorg. Biochem.* **2008**, *102*, 1463–1472. DOI: 10.1016/j.jinorgbio.2007.12.031
15. M. A. Ali, R. J. Butcher, J. C. Bryan, *Inorg. Chim. Acta* **1999**, *287*, 8–13. DOI: 10.1016/S0020-1693(98)00384-3
16. N. Gokhale, S. Jain, M. Yadav, *Curr. Top. Med. Chem.* **2015**, *15*, 37–42. DOI: 10.2174/1568026615666150112110211
17. B. M. Paterson, P. S. Donnelly, *Chem. Soc. Rev.* **2011**, *40*, 3005–3018. DOI: 10.1039/C0CS00215A
18. T. S. Lobana, R. Sharma, G. Bawa, S. Khanna, *Coord. Chem. Rev.* **2009**, *253*, 977–1055. DOI: 10.1016/j.ccr.2008.07.004
19. M. L. Low, G. Paulus, P. Dorlet, R. Guillot, R. Rosli, N. Delsuc, K. A. Crouse, C. Policar, *Biometals* **2015**, *28*, 553–566. DOI: 10.1007/s10534-015-9831-2
20. A. B. Beshir, S. K. Guchhait, J. A. Gasco, G. Fenteany, *Bioorg. Med. Chem. Lett.* **2008**, *18*, 498–504. DOI: 10.1016/j.bmcl.2007.11.099
21. M. T. Basha, D. Chartres, N. Pantarat, M. A. Ali, A. H. Mirza, D. S. Kalinowski, D. R. Richardson, P. V. Bernhardt, *Dalton Trans.* **2012**, *41*, 6536–6548. DOI: 10.1039/C2DT12387H
22. Z. A. Eisawi, C. Stefani, P. J. Jansson, A. Arvind, P. C. Sharpe, M. T. Basha, G. M. Iskander, N. Kumar, Z. Kovacevic, D. J. R. Lane, S. Sahni, P. V. Bernhardt, D. R. Richardson, D. S. Kalinowski, *J. Med. Chem.* **2016**, *59*, 294–312. DOI: 10.1021/acs.jmedchem.5b01399
23. C. Stefani, P. J. Jansson, E. Gutierrez, P. V. Bernhardt, D. R. Richardson, D. S., *J. Med. Chem.* **2013**, *56*, 357–370. DOI: 10.1021/jm301691s
24. M. L. Low, L. Maigre, P. Dorlet, R. Guillot, J. M. Pagès, K. A. Crouse, C. Policar, N. Delsuc, *Bioconjugate Chem.* **2014**, *25*, 2269–2284. DOI: 10.1021/bc5004907
25. T. B. S. A. Ravoo, K. A. Crouse, M. I. M. Tahir, R. Rosli, D. J. Watkin, F. N. F. How, *J. Chem. Crystallogr.* **2011**, *41*, 491–495. DOI: 10.1007/s10870-010-9907-3
26. G. Sheldrick, 2013. SHELXL2013. Program for Structure Refinement, University of Goettingen, Germany
27. M. N. Burnett, G. K. Johnson, 1996 ORTEP III, Report ORNL-6895, OAK Ridge National Laboratory; Tennessee, USA
28. A. D. Becke, *J. Chem. Phys.* **1993**, *98*, 5648–5652. DOI: 10.1063/1.464913
29. C. Lee, W. Yang, R. C. Parr, *Phys. Rev.* **1988**, *B37*, 785–789. DOI: 10.1103/PhysRevB.37.785
30. J. P. Perdew, Y. Wang, *Phys. Rev. B*, **1986**, *33*, 8800–8802. DOI: 10.1103/PhysRevB.33.8800
31. M. J. Frisch, G. W. Trucks, H. B. Schlegel, G. E. Scuseria, M. A. Robb, J. R. Cheeseman, G. Scalmani, V. Barone, B. Mennucci, G. A. Petersson, H. Nakatsuji, M. Caricato, X. Li, H. P. Hratchian, A. F. Izmaylov, J. Bloino, G. Zheng, J. L. Sonnenberg, M. Hada, M. Ehara, K. Toyota, R. Fukuda, J. Hasegawa, M. Ishida, T. Nakajima, Y. Honda, O. Kitao, H. Nakai, T. Vreven, Jr. J. A. Montgomery, J. E. Peralta, F. Ogliaro, M. J. Bearpark, J. Heyd, E. N. Brothers, K. N. Kudin, V. N. Staroverov, R. Kobayashi, J. Normand, K. Raghavachari, A. P. Rendell, J. C. Burant, S. S. Iyengar, J. Tomasi, M. Cossi, N. Rega, N. J. Millam, M. Klene, J. E. Knox, J. B. Cross, V. Bakken, C. Adamo, J. Jaramillo, R. Gomperts, R. E. Stratmann, O. Yazyev, A. J. Austin, R. Cammi, C. Pomelli, J. W. Ochterski, R. L. Martin, K. Morokuma, V. G. Zakrzewski, G. A. Voth, P. Salvador, J. J. Dannenberg, S. Dapprich, A. D. Daniels, Ö. Farkas, J. B. Foresman, J. V. Ortiz, J. Cioslowski, D. J. Fox, **2009**, Gaussian 09.
32. A. D. Bochevarov, E. Harder, T. F. Hughes, J. R. Greenwood, D. A. Braden, D. M. Philipp, D. Rinaldo, M. D. Halls, J. Zhang, R. A. Friesner, A. Jaguar, *Int. J. Quant. Chem.* **2013**, *113*, 2110–2142. DOI: 10.1002/qua.24481
33. E. Eroglu, H. A. Türkmen, *J. Mol. Graph Model.* **2007**, *26*, 701–708. DOI: 10.1016/j.jmglm.2007.03.015
34. R. A. Friesner, J. L. Banks, R. B. Murphy, T. A. Halgren, J. J. Klicic, D. T. Mainz, M. P. Repasky, E. H. Knoll, M. Shelley, J. K. Perry, D. E. Shaw, P. Francis, P. S. Shenkin, *J. Med. Chem.* **2004**, *47*, 1739–1749. DOI: 10.1021/jm0306430
35. G. M. Sastry, M. Adzhigirey, T. Day, R. Annabhimoju, W. Sherman, *J. Comput. Aided Mol. Des.* **2013**, *27*, 221–234. DOI: 10.1007/s10822-013-9644-8
36. S. Pronk, GROMACS 4.5, **2013**, 29, 845.
37. C. Oostenbrink, A. Villa, A. E. Mark, V. W. F. Gunsteren, *J. Comput. Chem.* **2004**, *25*, 1656–1676. DOI: 10.1002/jcc.20090
38. A. W. Schüttelkopf, D. M. V. Aalten, *Acta Cryst.* **2004**, *D60*, 1355–1363. DOI: 10.1107/S0907444904011679
39. H. J. C. Berendsen, J. P. M. Postma, W. F. V. Gunsteren, J. Hermans, Interaction Models for Water in Relation to Protein Hydration, in Intermolecular Forces, Pullman B, Editor. Springer Netherlands. **1981**, p. 331.

40. T. Darden, D. York, L. Pedersen, *J. Chem. Phys.* **1993**, *98*, 10089–10092. DOI: 10.1063/1.464397
41. M. Parrinello, A. Rahman, *J. Appl. Phys.* **1981**, *52*, 7182–7190. DOI:10.1063/1.328693
42. B. Hess, B. Henk, H. J. C. Berendsen, J. G. E. M. Fraaije, *J. Comput. Chem.* **1997**, *18*, 1463–1472. DOI:10.1002/(SICI)1096-987X(199709)18:12<1463::AID-JCC4>3.0.CO;2-H
43. M. A. A. A. Islam, M. T. H. Tarafder, M. C. Sheikh, M. A. Alam, E. Zangrando, *Trans. Met. Chem.* **2011**, *36*, 531–535. DOI:10.1007/s11243-011-9499-6
44. C. F. Wise, D. Liu, K. J. Mayer, P. M. Crossland, C. L. Hartley, W. R. A. McNamara, *Dalton Trans.* **2015**, *44*, 14265–14271. DOI:10.1039/C5DT02042E
45. M. A. Ali, A. H. Mirza, R. J. Butcher, K. A. Crouse, *Trans. Met. Chem.* **2006**, *31*, 79–87. DOI:10.1007/s11243-005-6305-3
46. K. Chew, M. T. H. Tarafder, K. A. Crouse, A. M. Ali, B. M. Yamin, H.-K. Fun, *Polyhedron*, **2004**, *23*, 1385–1392. DOI:10.1016/j.poly.2004.02.018
47. N. R. Pramanik, M. Chakraborty, D. Biswal, S. S. Mandal, S. Ghosh, S. Chakrabarti, W. S. Sheldrick, M. G. B. Drew, T. K. Mondal, D. Sarkar, *Polyhedron*, **2015**, *85*, 196–207. DOI:10.1016/j.poly.2014.08.010
48. M. T. H. Tarafder, T.-J. Khoo, K. A. Crouse, A. M. Ali, B. M. Yamin, H.-K. Fun, *Polyhedron*, **2002**, *21*, 2691–2698. DOI:10.1016/S0277-5387(02)01272-X
49. S. Kubota, H. K. Misra, M. Shibuya, *Synthesis*, **1982**, *18*, 776–778. DOI:10.1055/s-1982-29941
50. M. Yazdanbakhsha, M. M. Heravib, R. Takjooa, W. Frank, *Z. Anorg. Allg. Chem.* **2008**, *634*, 972–976. DOI:10.1002/zaac.200700521
51. M. A. F. A. Manan, K. A. Crouse, M. I. M. Tahir, R. Rosli, F. N.-F. How, D. J. Watkin, A. M. Z. Slawin, *J. Chem. Crystallogr.* **2004**, *41*, 1630–1641. DOI:10.1007/s10870-011-0151-2
52. A. H. Mirza, M. H. S. A. Hamid, S. Aripin, M. R. Karim, M. Arifuzzaman, M. A. Ali, P. V. Bernhardt, *Polyhedron*, **2014**, *74*, 16–23. DOI: 10.1016/j.poly.2014.02.016
53. D. S. Kalinowski, P. C. Sharpe, P. V. Bernhardt, D. R. Richardson, *J. Med. Chem.* **2007**, *50*, 6212–6225. DOI:10.1021/jm070839q
54. C. A. Behnke, I. L. Trong, J. W. Godden, E. A. Merritt, D. C. Teller, J. Bajorath, R. E. Stenkampa, *Acta Cryst.* **2010**, *D66*, 616–267. DOI:10.1107/S0907444910006554

Povzetek

Spojino bis[2-hidroksibenzilidenhidrazono)(metiltio)metil]disulfid (**1**), ki je derivat S-metilditiokarbazata z disulfidno vezjo smo sintetizirali s kondenzacijo 2-hidroksibenzaldehida in S-metilditiokarbazata. Okarakterizirali smo jo z elementno analizo, ^1H , ^{13}C NMR in FT-IR spektroskopijo in masno spektrometrijo. Rentgenska struktura razkrije, da je spojina v tautomerni obliki tiona z ditiokarbazatnim fragmentom z *EE* konfiguracijo glede na C=N vez benzilidenske skupine. Termične lastnosti spojine smo proučili z termogravimetrično analizo (TGA). Geometrijo spojine v osnovnem stanju smo optimizirali z uporabo teorije gostotnostnega funkcionala (DFT/B3LYP) z uporabo 6-311++G(d,p) baznega seta. Molekularni docking spojine z človeško karbonsko anhidrazo II smo izvedli za določitev interakcij.

Scientific paper

Plate-Like $\text{Bi}_4\text{Ti}_3\text{O}_{12}$ Particles and their Topochemical Conversion to SrTiO_3 Under Hydrothermal Conditions

Alja Čontala,^{1,2} Marjeta Maček Kržmanc^{1,*} and Danilo Suvorov¹¹ Advanced Materials Department, Jožef Stefan Institute Jamova cesta 39, 1000 Ljubljana, Slovenia² International Postgraduate School, Jamova cesta 39, 1000 Ljubljana, Slovenia

* Corresponding author: E-mail: marjeta.macek@ijs.si

Received: 25-05-2018

Abstract

Plate-like $\text{Bi}_4\text{Ti}_3\text{O}_{12}$ particles were synthesized using a one-step, molten-salt method from Bi_2O_3 and TiO_2 nanopowders at 800 °C. The reaction parameters that affect the crystal structure and morphology were identified and systematically investigated. The differences between various $\text{Bi}_4\text{Ti}_3\text{O}_{12}$ plate-like particles were examined in terms of the ferroelectric-to-paraelectric phase transition and the photocatalytic activity for the degradation of Rhodamine B under UV-A light irradiation. The results encouraged us to conduct further testing of the as-prepared $\text{Bi}_4\text{Ti}_3\text{O}_{12}$ plate-like particles as templates for the preparation of plate-like SrTiO_3 perovskite particles using a topochemical conversion under hydrothermal conditions. The characteristics of the $\text{Bi}_4\text{Ti}_3\text{O}_{12}$ plates and the reaction parameters for which the SrTiO_3 preserved the shape of the initial $\text{Bi}_4\text{Ti}_3\text{O}_{12}$ template particles were determined.

Keywords: $\text{Bi}_4\text{Ti}_3\text{O}_{12}$; Aurivillius layered perovskites; Molten-salt synthesis; Plate-like $\text{Bi}_4\text{Ti}_3\text{O}_{12}$; Template plates; Topochemical conversion

1. Introduction

$\text{Bi}_4\text{Ti}_3\text{O}_{12}$ (BIT) is a member of the Aurivillius-type perovskites that have a layered structure in which pseudo-perovskite ($\text{Bi}_2\text{Ti}_3\text{O}_{10}$)²⁻ units are alternating with (Bi_2O_2)²⁺ layers. As a piezoelectric material with a high Curie temperature of 675 °C, $\text{Bi}_4\text{Ti}_3\text{O}_{12}$ has the potential for use in high-temperature piezoelectric applications.^{1,2}

The most common synthesis approaches for the preparation of $\text{Bi}_4\text{Ti}_3\text{O}_{12}$ ceramics and particles are solid-state, molten-salt, hydrothermal and some other methods with lower reaction temperatures, e.g., coprecipitation and sol-gel.^{3,4,5} During the preparation of $\text{Bi}_4\text{Ti}_3\text{O}_{12}$ from Bi_2O_3 and TiO_2 in molten salt or by solid-state reaction, secondary phases such as $\text{Bi}_{12}\text{Ti}_{20}$ or $\text{Bi}_2\text{Ti}_2\text{O}_7$ are commonly formed and must be removed from the product prior to further use due to their detrimental effect on the piezoelectric properties of $\text{Bi}_4\text{Ti}_3\text{O}_{12}$ ceramics.^{6–8} Plate-like $\text{Bi}_4\text{Ti}_3\text{O}_{12}$ particles with a side length of around 1 μm and a thickness of 50 nm were formed in molten NaCl/KCl at 800 °C.⁹ In contrast to the thickness, the side length of the plates was not uniform, varying from 0.25 μm to 3 μm .

He et al. systematically studied the influence of the salt/precursor ratio on the morphology of plate-like $\text{Bi}_4\text{Ti}_3\text{O}_{12}$ particles prepared in molten salt.¹⁰ They observed that the average side length and thickness of the $\text{Bi}_4\text{Ti}_3\text{O}_{12}$ plates decreased with an increase in the amount of salt; however, at high dilutions (molar ratios: NaCl:KCl: $\text{Bi}_4\text{Ti}_3\text{O}_{12}$ \geq 32:32:1) the influence of the salt content was no longer significant. These $\text{Bi}_4\text{Ti}_3\text{O}_{12}$ (001)-oriented plates were also proved to be more effective for the photocatalytic degradation of Rhodamine B (RhB) than irregularly shaped $\text{Bi}_4\text{Ti}_3\text{O}_{12}$ particles obtained using the solid-state method.¹⁰ Thickness, surface defects and faceting of the surface are all parameters that influence the photocatalytic activity (PA). $\text{Bi}_4\text{Ti}_3\text{O}_{12}$ particles prepared with the hydrothermal method usually exhibited smaller dimensions and higher aggregation than those prepared in molten salt.^{11,12} Therefore, a decision has to be taken regarding the preparation method for the specific application of the material.

In contrast to MTiO_3 perovskites ($M = \text{Ba}, \text{Sr}, \text{Pb}$) with their cubic or tetragonal crystal structures, layered perovskites such as Aurivillius ($\text{Bi}_4\text{Ti}_3\text{O}_{12}$ and $\text{MBi}_4\text{Ti}_4\text{O}_{15}$, where $M = \text{Ba}, \text{Sr}, \text{Pb}$) and Ruddlesden-Popper ($\text{Sr}_3\text{Ti}_2\text{O}_7$)

have a tendency to grow in an anisotropic shape due to their large crystal anisotropy.^{13,14}

These layered perovskites are often used as the structural templates for the preparation of anisotropic MTiO_3 perovskites via topochemical conversion.^{15–17} The first use of topochemical conversion for the preparation of (100)-oriented SrTiO_3 tabular particles was demonstrated by Watari et al.¹⁸ This conversion was performed by the reaction of a Ruddlesden-Popper $\text{Sr}_3\text{Ti}_2\text{O}_7$ template and TiO_2 in molten KCl between 1000 °C and 1200 °C. Saito and Takao were the first to use an Aurivillius $\text{SrBi}_4\text{Ti}_4\text{O}_{15}$ template for the preparation of SrTiO_3 (100)-oriented plates with smaller dimensions and a higher aspect ratio (side length 5–10 μm , thickness 0.5 μm).¹⁹ The mechanism of the reaction between SrCO_3 and $\text{SrBi}_4\text{Ti}_4\text{O}_{15}$ in the molten salt was further studied by Chang et al., who optimized the reaction conditions to minimize the Bi remains.¹⁵ Under hydrothermal conditions SrTiO_3 plate-like particles were produced using other templates such as $\text{H}_{1.07}\text{Ti}_{1.73}\text{O}_4 \cdot n\text{H}_2\text{O}$ and sheet-like TiO_2 mesocrystals.^{20,21} $\text{Bi}_4\text{Ti}_3\text{O}_{12}$ particles were already used for a topochemical conversion to BaTiO_3 or SrTiO_3 in molten salt.^{9,22,23}

Based on our previous work $\text{Bi}_4\text{Ti}_3\text{O}_{12}$ is very appropriate template for preparation of BaTiO_3 plate-like particles in the molten salt.⁹ To the best of our knowledge, the topochemical conversion from $\text{Bi}_4\text{Ti}_3\text{O}_{12}$ to BaTiO_3 , SrTiO_3 or CaTiO_3 particles under hydrothermal conditions has not yet been reported. It is well known that the quality and morphology of the initial precursor particles, in addition to the reaction conditions, greatly influence the particle morphology. In this study we report on the preparation of $\text{Bi}_4\text{Ti}_3\text{O}_{12}$ particles with two morphologies and their topochemical transformation to SrTiO_3 under hydrothermal conditions.

2. Methods

2. 1. Experimental

$\text{Bi}_4\text{Ti}_3\text{O}_{12}$ plates were synthesized using the molten-salt method. The salts KCl (Sigma-Aldrich, $\geq 99.0\%$) and NaCl (Merck, $\geq 99.7\%$) were weighed in a 1:1 molar ratio, ground and mixed well in a mortar to achieve a homogeneous mixture. Next, an appropriate amount of Bi_2O_3 nanopowder (99.9% Alfa Aesar) and TiO_2 nanopowder (P25, Degussa) were weighed, added to the salt mixture and mixed well again. A homogeneous mixture of powder was then transferred to the Al_2O_3 crucible, covered and placed in the furnace. The heating rate was 10 °C/min until the temperature reached 800 °C. The morphology and crystal structure for the $\text{Bi}_4\text{Ti}_3\text{O}_{12}$ obtained under different reaction conditions were investigated in order to determine the best reaction conditions for the preparation of well-developed, plate-like $\text{Bi}_4\text{Ti}_3\text{O}_{12}$ particles with a narrow size distribution. The influence of various reaction conditions such as time (20 minutes and 2 hours), Bi:Ti

molar ratio (1.33, 2.0 and 2.67), NaCl:KCl: $\text{Bi}_4\text{Ti}_3\text{O}_{12}$ molar ratio (50:50:1 or 25:25:1) and cooling rate (5 °C/min, 10 °C/min and natural cooling) were examined. In the case of natural cooling, the heating system was turned off after the reaction was performed, and the product was left in the furnace until the furnace reached room temperature. Natural cooling means uncontrolled cooling in a furnace by natural convection, conduction and radiation to room temperature. It was demonstrated that the cooling time from 800 °C to the eutectic temperature of 650 °C in the case of natural cooling was 8 minutes, while for cooling rates of 10 °C/min and 5 °C/min, the cooling times were 15 and 30 minutes, respectively. In this temperature range, where the particle growth still took place, the natural cooling was the fastest. Below 650 °C, the diffusion is expected to be too slow and thus the growth of the particles is negligible. For comparison, $\text{Bi}_4\text{Ti}_3\text{O}_{12}$ was also synthesized under selected conditions (Bi:Ti = 1.33, 800 °C 2 h, natural cooling) using anatase TiO_2 (Sachtleben Pigments Oy, HOMBITAN AFDC 001517011, 99%) μm -sized powder instead of the P25 nanopowder.

After the reaction, the product powders were washed with deionized water by suction filtration in order to remove the salt. Afterwards, they were also washed with 2-M HNO_3 (soaking time 10 minutes) in order to remove the secondary phases and finally with deionized water again (until pH = 7). The product powders were freeze-dried.

In the second part of the study, $\text{Bi}_4\text{Ti}_3\text{O}_{12}$ template plates were tested for the topochemical conversion to SrTiO_3 under hydrothermal conditions. For this reaction $\text{SrCl}_2 \times 6\text{H}_2\text{O}$ (Sigma Aldrich, $\geq 99\%$) was added to the $\text{Bi}_4\text{Ti}_3\text{O}_{12}$ in the molar ratio Sr:Ti = 3. The reaction was performed under hydrothermal conditions in 4-M NaOH (Merck, 99%) with stirring at 200 °C for 12 hours. The product was cooled naturally and washed with deionized H_2O , 1-M HNO_3 and once again with deionized H_2O . The product was freeze-dried.

2. 2. Characterization

The crystal structure was characterized with X-ray powder diffraction (Bruker AXS D4 Endeavor) using Cu-K_α radiation (1.5406 Å). For an estimation of the preferential orientation, a few drops of suspension of the particles in iso-propanol were deposited on a Si single crystal and left for the alcohol to evaporate. The morphology and size of the prepared particles were studied by field-emission scanning electron microscopy (FE-SEM, JSM 7600 F, JEOL). The specific surface area was measured using the BET method with nitrogen adsorption (Gemini 2370 V5.00).

For the PA of the $\text{Bi}_4\text{Ti}_3\text{O}_{12}$ particles, the decomposition of RhB was measured in UV-A light. The concentration of the sample, mixed with RhB and exposed to UV-A light, was 0.2 mg/ml, and the concentration of the RhB was 10 mg/l. Prior to irradiation, the solution was sonicated for

1 minute (pulse:pause was 2:1 seconds) at 80% and afterwards it was stirred in the dark at 500 rpm for 30 minutes. Samples were taken before irradiation and after 1 h, 2 h, 3 h, 4 h and 24 hours of irradiation with UV-A light. The powder was removed after centrifugation. The absorbance was measured at $\lambda = 554$ nm using a Synergy Micro Plate Reader (BIOTEK). Control reactions in the dark for RhB with the sample and a parallel reaction for pure RhB were also performed. Differential scanning calorimetry (DSC) measurements were made on a Jupiter 449 simultaneous thermal analysis (STA) instrument (Netzsch, Selb, Germany). The measurements were made with a heating rate of 20 °C/min in an Ar/O₂ (40/20) atmosphere using a TG/DSC-cp sample holder and platinum crucibles. The temperature and enthalpy calibrations of the STA instrument were made with BaCO₃, CsCl, K₂CrO₄, KClO₄ and RbNO₃ standards.

3. Results and Discussion

3.1. Influence of the Reaction Conditions on the Morphology and Crystal Structure

Bi₄Ti₃O₁₂ was formed in the molten salt by dissolution-precipitation. This means that Bi₂O₃ and TiO₂ firstly dissolved in the molten salt and then Bi₄Ti₃O₁₂ plates precipitated at a high degree of supersaturation. Further growth of the plates occurred by Ostwald ripening. Therefore, the particle size could be tailored with the duration of the reaction. Longer and shorter times were selected for the preparation of larger (μm -sized) and smaller (sub- μm -sized) Bi₄Ti₃O₁₂ plates, respectively.⁹ In particular, sub- μm - and nano-sized anisotropic particles of ferroelectrics (Bi₄Ti₃O₁₂ and BaTiO₃) have recently become of great scientific and technological interest due to their unique shape- and size-dependent functional properties with reduced sub- μm -size dimensions. At first, the phase composition and morphology of the Bi₄Ti₃O₁₂ particles obtained at 800 °C after 2 hours in the first experiment (BIT1) and 20 minutes in the second experiment (BIT2) were examined and compared (Fig. 1, Table 1). In both of these cases

the reaction was performed with surplus Bi₂O₃ (Bi:Ti = 2.67, stoichiometric Bi:Ti = 1.33). The Bi₂O₃ was added in excess in order to provide a high concentration of Bi³⁺ for the formation of Bi₄Ti₃O₁₂ plates. In the case of a shorter synthesis time (20 minutes), the Bi₄Ti₃O₁₂ plates exhibited a smaller average side length as well as a reduced thickness compared to the plates obtained after a longer synthesis time (2 hours), when the particles had more time available for Ostwald-ripening growth. In both cases the XRD analyses showed that a significant amount of Bi₁₂TiO₂₀ secondary phase (PDF #034-0097) was present (Fig. 2, XRD pattern A) in addition to the Bi₄Ti₃O₁₂ (PDF #035-0795). The formation of Bi₁₂TiO₂₀ was a consequence of excess Bi₂O₃ in the reaction mixture. During washing with 2-M HNO₃ the Bi₁₂TiO₂₀ was dissolved and monoclinic Bi₄Ti₃O₁₂ became the only phase in both cases. Reaction conditions for the described Bi₄Ti₃O₁₂ (BIT1 and BIT2) and for the Bi₄Ti₃O₁₂ prepared under other conditions are presented in Table 1. Bi:Ti and NaCl:KCl:Bi₄Ti₃O₁₂ are molar ratios.

In the next step the molar ratio of bismuth to titanium (denoted as Bi:Ti in Table 1) was studied. We selected three values of Bi:Ti: 2.67, 2.0 and 1.33 (stoichiometric) for BIT3, BIT4 and BIT5, respectively. In the experiment using a ratio of 1.33 the plates had a more defined shape and a narrower size distribution (Fig. 1C) than in the other two cases and Bi₄Ti₃O₁₂ was the main phase, observed by XRD after the synthesis. In the other two cases, washing with HNO₃ was necessary to remove the secondary Bi₁₂TiO₂₀ phase.

The influence of the amount of salt on the morphology and crystal structure was also investigated. In accordance with the literature¹⁰ we used a 50:50:1 molar ratio (BIT6) of KCl:NaCl:Bi₄Ti₃O₁₂. However, when the ratio was reduced to 25:25:1 (BIT5) the size distribution of the product particles became more uniform. With a smaller amount of salt, the diffusion distance of the reactant particles is smaller; therefore, the reaction occurs faster and more uniformly. Powder XRD patterns confirmed the dominance of the monoclinic Bi₄Ti₃O₁₂ phase (PDF #035-0795) for both products.

Table 1: Reaction conditions of BIT1-BIT9 for the investigation of the influence of the reaction parameters on the morphology and crystal structure of Bi₄Ti₃O₁₂

Sample	TiO ₂	Bi:Ti	NaCl:KCl:Bi ₄ Ti ₃ O ₁₂	T (°C)	Time	Heating	Cooling
BIT1	P25	2.67	50:50:1	800	2 h	10 °/min	10 °/min
BIT2	P25	2.67	50:50:1	800	20 min	10 °/min	10 °/min
BIT3	P25	2.67	25:25:1	800	2 h	10 °/min	10 °/min
BIT4	P25	2.0	25:25:1	800	2 h	10 °/min	10 °/min
BIT5	P25	1.33	25:25:1	800	2 h	10 °/min	10 °/min
BIT6	P25	1.33	50:50:1	800	2 h	10 °/min	10 °/min
BIT7	P25	1.33	25:25:1	800	2 h	10 °/min	5 °/min
BIT8	P25	1.33	25:25:1	800	2 h	10 °/min	natural
BIT9	anatase	1.33	25:25:1	800	2 h	10 °/min	natural

Cooling rates of 10 °C/min (BIT6), 5 °C/min (BIT7) and natural cooling (BIT8-Fig. 2D) were also compared. Based on SEM observations we concluded that there is no significant difference in the morphology when the cooling rates were 10 °C/min, 5 °C/min or natural cooling.

The most differing BIT products (BIT2 and BIT8) were selected for further analysis. SEM micrographs and

XRD patterns for those plate-like $\text{Bi}_4\text{Ti}_3\text{O}_{12}$ samples are shown in Figures 1 and 2, respectively. The higher degree of aggregation of BIT2 compared to BIT8 is evident from the SEM micrographs as well as from the XRD patterns of the $\text{Bi}_4\text{Ti}_3\text{O}_{12}$ particles deposited on the Si single crystal (Figure 2, XRD patterns C and D). Due to the random orientation of the plate-like $\text{Bi}_4\text{Ti}_3\text{O}_{12}$ particles in the aggre-

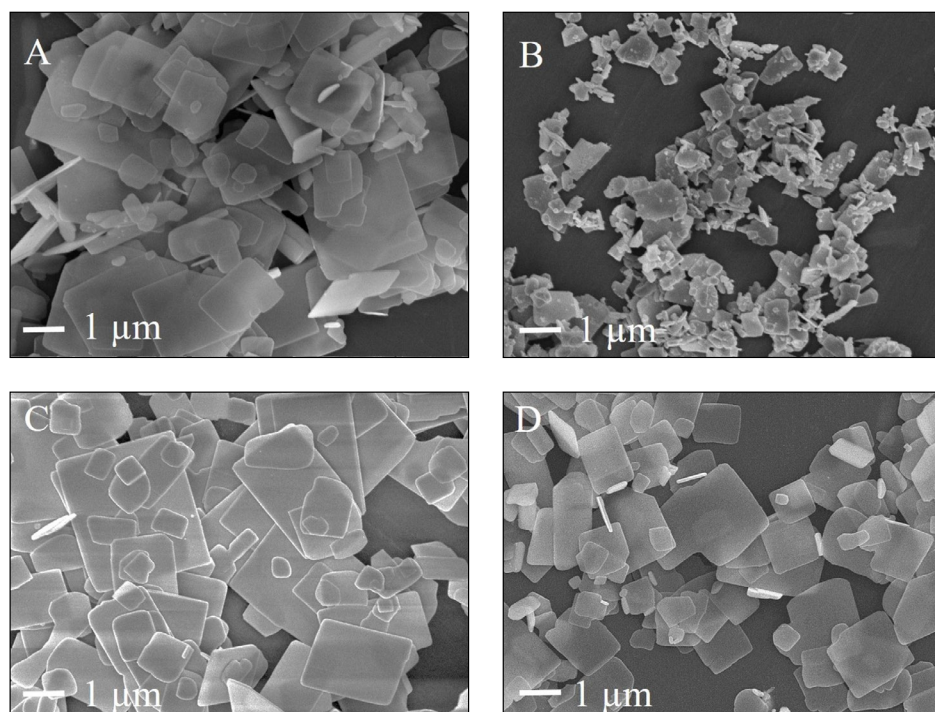


Figure 1: SEM micrographs of the $\text{Bi}_4\text{Ti}_3\text{O}_{12}$ plates that were synthesized at 800 °C for 20 min (B-BIT2) and for 2 h (A-BIT1, C-BIT5, D-BIT8). Other synthesis details are shown in Table 1.

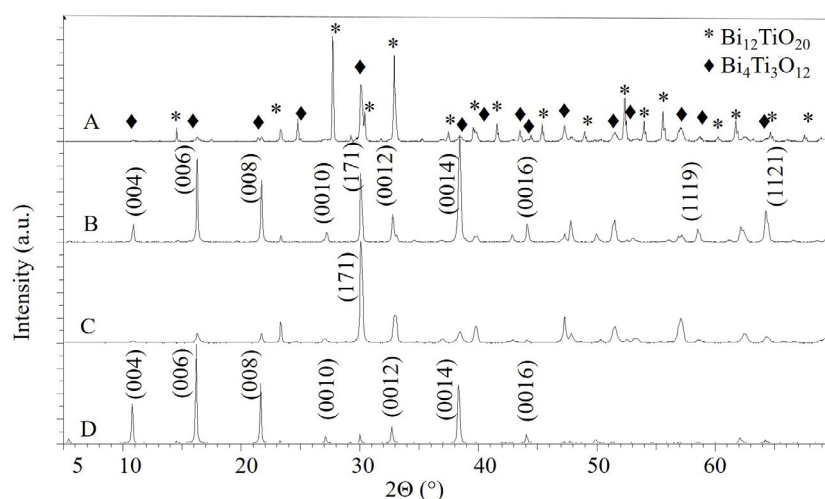


Figure 2: XRD patterns of $\text{Bi}_4\text{Ti}_3\text{O}_{12}$ plates prepared at 800 °C for 20 min (patterns A and C for BIT2) and for 2 h (patterns B and D for BIT8). The A and B patterns represent the XRD patterns of $\text{Bi}_4\text{Ti}_3\text{O}_{12}$ powders washed only by water in order to determine possible secondary phases. The XRD patterns C (for BIT2) and D (for BIT8) were obtained from $\text{Bi}_4\text{Ti}_3\text{O}_{12}$ plates that were cast on the Si single crystal. The $\text{Bi}_4\text{Ti}_3\text{O}_{12}$ plates prepared for examination of their average preferential orientation in these two patterns were washed with 2-M HNO_3 to ensure a single-phase product. In the XRD pattern A, \blacklozenge and $*$ denote the $\text{Bi}_4\text{Ti}_3\text{O}_{12}$ and $\text{Bi}_{12}\text{TiO}_{20}$ phases, respectively. The hkl indexation is given for $\text{Bi}_4\text{Ti}_3\text{O}_{12}$.

gates of BIT2 sample, the relative intensities of the (00*l*)/(117) planes (*l* = even number) were considerably lower in comparison to those of the larger Bi₄Ti₃O₁₂ (BIT8) plates, which oriented during deposition on a Si single crystal in a way that the (00*l*) planes were parallel to the substrate. Based on this we can infer that 1–2- μm -sized Bi₄Ti₃O₁₂ plates exhibited a high (00*l*) preferential orientation (Figure 2, XRD pattern D).

Finally, Bi₄Ti₃O₁₂ was also prepared from μm -sized anatase TiO₂ particles (BIT9) instead of P25 TiO₂ nanopowder, but under the same reaction conditions as for the BIT8. As expected, the plates were less uniform in size. The majority of the plates were much smaller (approx. 100 nm) and the rest were between 1 and 2 microns. This non-uniform particle size distribution was most probably a consequence of the larger anatase particles, which dissolved more slowly and unevenly than the P25 nanoparticles. Also in this case, the XRD pattern confirmed that monoclinic Bi₄Ti₃O₁₂ was the main phase.

For smaller and larger Bi₄Ti₃O₁₂ plates (BIT2 and BIT8) the specific surface area (BET), the photocatalytic activity (PA) and the DSC measurements were performed in order to confirm the significant difference in size and the specific surface area. The BET results were in agreement with the SEM observations. The specific surface area was larger for BIT2 than for BIT8 (Table 2), which is in accordance with the SEM observation and confirmed that the BIT2 particles were smaller and consequently the specific surface area was larger than for BIT8.

Since it is well known that PA is influenced by many factors such as surface defects, particle size, morphology, crystallinity and band gap, we decided to test both types of plates in terms of their capability to degrade organic dye (RhB) under UV-A radiation. A high concentration of defects is not beneficial, neither for the photocatalysis nor for the epitaxial growth of a new phase on the template. Nevertheless, the acceptable level of defects is different for both processes. For photocatalysis, some defects are advantageous when they introduce intermediate surface states that narrow the band gap. In general, a high density of defects, which act as recombination centers for photo-induced electrons and holes, lowered the PA. The photodegradation of RhB in BIT2 was 88% and in BIT8 it was 65% after 4 hours of irradiation with UV-A light. This confirmed our expectations that the PA of BIT2 is larger than that of BIT8. The larger PA of BIT2 can also be ascribed to smaller particles with a higher specific surface area, which provide more active sites for the photocatalytic reaction.

For the DSC measurements both samples (BIT2 and BIT8) were first washed with 2-M HNO₃ to ensure single-phase Bi₄Ti₃O₁₂. The DSC measurements revealed a very similar DSC peak temperature (*T_c*) for the ferroelectric-to-paraelectric phase transition for both types of Bi₄Ti₃O₁₂ plates (643.6 °C for BIT2 and 642.9 °C for BIT8) (Fig. 3). However, the absolute values of the phase-transi-

tion enthalpies ($|\Delta H_{\text{FET}}|$) of the two samples differ significantly. The measured $|\Delta H_{\text{FET}}|$ for BIT2 and BIT8 were 1.457 J/g and 4.555 J/g, respectively (Fig. 3, Table 2). The decrease of the phase-transition enthalpy with a decrease in the particle size was already observed for other ferroelectric particles (BaTiO₃).²⁴ Taking into account that the enthalpy of the phase transition is proportional to the polarization (*P*) ($\Delta H_{\text{FET}} = 2 \pi P^2 T_c / C$ (Eq. 1), where *C* is the Curie-Weiss constant) the decrease of $|\Delta H_{\text{FET}}|$ could be explained by the decrease of *P*. It is also known that the phase-transition enthalpy is related to the domain structure.^{24,25} The larger $|\Delta H_{\text{FET}}|$ of BIT8 could correlate with larger particles and be expected to exhibit a multi-domain structure. Due to the domain clamping the enthalpy of the phase transition was higher for larger particles compared to the single-domain smaller particles. In addition, with a decrease of the particle size, the ratio between the disordered surface and the ordered bulk is increasing, which additionally causes a destruction of the polar state.²⁴

3. 2. Bi₄Ti₃O₁₂ Plates as a Template for Topochemical Conversion to SrTiO₃

Due to the pseudo-perovskite units the Bi₄Ti₃O₁₂ plates are regarded as a suitable template for the preparation of MTiO₃ perovskite plates via topochemical conversion. It was already shown that the transformation from Bi₄Ti₃O₁₂ to BaTiO₃ is possible in the molten salt.⁹ There is great interest in whether this kind of conversion is also

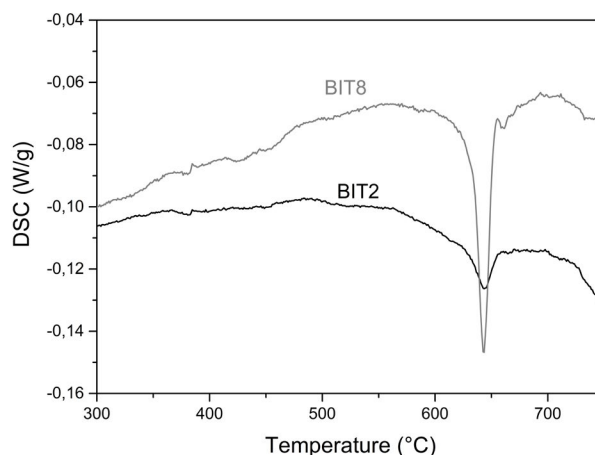


Figure 3: DSC curves of Bi₄Ti₃O₁₂ plates during heating for BIT2 and BIT8 sample.

Table 2: Results for BET, DSC and PA measurements of BIT2 and BIT8

Sample	BET (m ² /g)	<i>T_c</i> (°C)	(J/g)	PA _{4 hours}
BIT2	2.9075	643.6	1.457	88.6%
BIT8	0.4855	642.9	4.555	65.0%

possible under hydrothermal conditions. Kalyani et al. studied the hydrothermal crystallization of SrTiO₃ on anatase nanowires and proved that the formation of SrTiO₃ was driven by the topochemical reaction,²⁶ since the formed SrTiO₃ mesocrystals retain the wire-like shape of the initial anatase particles. To the best of our knowledge there are no literature reports about the topochemical conversion of Bi₄Ti₃O₁₂ to MTiO₃ perovskites under hydrothermal conditions. In the present study we firstly aimed to examine whether under these conditions Bi₄Ti₃O₁₂ plates are an appropriate template for the preparation of SrTiO₃ plates and secondly we wanted to verify how differently sized Bi₄Ti₃O₁₂ template plates (sub- μ m- and above- μ m-sized) influenced the final morphology of the SrTiO₃ particles. From the standpoint of advanced development and the improvement of applications and electronic devices, controlling the shape and size of particles can lead to new or combined and improved properties of existing materials. The miniaturization of electronic devices is also of great interest in nanotechnology; however, it is already well known that materials lose some of their functional properties (i.e., ferroelectricity) below certain small dimensions. Additionally, it is easier to observe the growth of SrTiO₃ on larger plates. For this reason we decided to study the formation of SrTiO₃ from two types of Bi₄Ti₃O₁₂: smaller, sub- μ m-sized, Bi₄Ti₃O₁₂ plate-like particles with a broad particle size distribution (BIT2) and larger, 1–2- μ m-large and well-defined Bi₄Ti₃O₁₂ plates (BIT8). The XRD examination of the reaction products in both cases confirmed the formation of SrTiO₃ (PDF #035-0734) from the Bi₄Ti₃O₁₂ plates under alkaline (4-M NaOH) hydrothermal conditions at 200 °C for 12 hours (Fig. 4, XRD pattern A). The smaller Bi₄Ti₃O₁₂ template particles (BIT2) that were very non-uniform in size, consequently resulted in a non-ideal morphology of the SrTiO₃ particles. This means that the as-prepared SrTiO₃ particles differed in their shape and size. The cube-like particles prevailed, but some of them also exhibited a preferable plate-like shape (Fig. 5A). In contrast, the SrTiO₃ particles prepared from larger Bi₄Ti₃O₁₂ template plates

(BIT8) preserved the shape of the template. The XRD revealed that (00l)-oriented Bi₄Ti₃O₁₂ plates transformed into (h00)-oriented SrTiO₃ plates (Fig. 4, XRD pattern B). However, the morphology of the SrTiO₃ plates was still not perfect. The particles varied in their size, which was most probably the consequence of the non-uniform size distribution of the initial Bi₄Ti₃O₁₂ plates. Figure 5B demonstrates that there were small holes present in some of those SrTiO₃ plates. These holes were also observed when the SrTiO₃ plates were washed only with water after the synthesis. Therefore, the holes were not formed during HNO₃-washing, although HNO₃ is a strong acid and could cause the leaching of Sr and the remains of Bi from the plates. Additionally, the holes were not formed due to the HNO₃ washing of the Bi₄Ti₃O₁₂ template plates, because the holes were also present in the SrTiO₃ plates, which were prepared from the water-washed Bi₄Ti₃O₁₂ plates. Thus, the holes were not a consequence of the etching effect of the HNO₃, although it is known that chemical etching can cause square-shaped holes in Bi₄Ti₃O₁₂ grains.²⁷ These holes were either the consequence of the defective surface of the Bi₄Ti₃O₁₂ plates or originated from the lattice mismatch between the pseudo-perovskite layer of the template and the SrTiO₃ plates. In addition, the removal of the (Bi₂O₂)²⁺ layer during the conversion could also cause exfoliation, the result of which could be those holes. An examination of the morphology of the SrTiO₃ particles prepared from the different Bi₄Ti₃O₁₂ template plates revealed that the completeness of the SrTiO₃ plates strongly depended on both the quality of the Bi₄Ti₃O₁₂ template plates and the reaction conditions. For example, the worst preservation of the initial Bi₄Ti₃O₁₂ template shape during the conversion to SrTiO₃ was observed for the Bi₄Ti₃O₁₂ plates that were prepared from the large, μ m-sized, TiO₂ anatase particles. With this study we confirmed that the μ m-sized Bi₄Ti₃O₁₂ plate-like particles with a rather uniform particle size distribution (i.e. BIT8) can be used as a template for the topochemical transformation to plate-like SrTiO₃ particles with a (h00) preferential orientation.

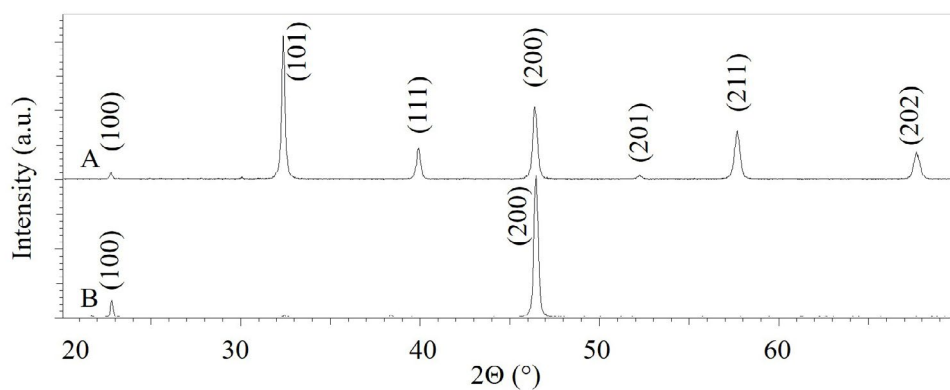


Figure 4: XRD patterns of SrTiO₃ powder prepared from BIT8 (pattern A) and SrTiO₃ plates cast on the Si single crystal (pattern B). XRD pattern of the SrTiO₃ plates deposited on the Si single crystal revealed that their preferential orientation was (100).

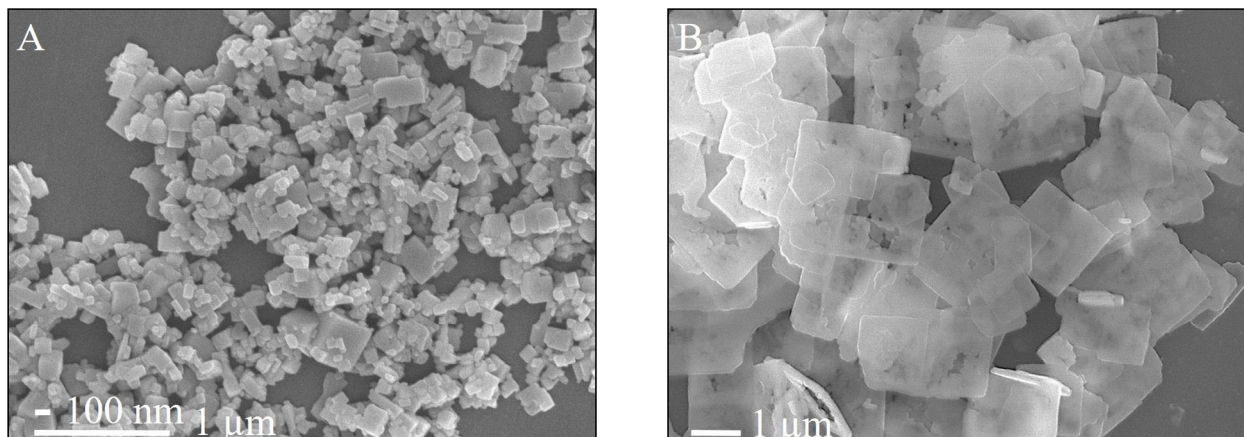


Figure 5: SEM micrographs of SrTiO₃ particles obtained from the topochemical conversion of different Bi₄Ti₃O₁₂ plate-like particles under the same hydrothermal reaction conditions (Sr:Ti molar ratio 3:1, 4-M NaOH, 200 °C for 12 hours). The SrTiO₃ particles A were prepared from the BIT2 template and the SrTiO₃ particles B were prepared from the BIT8 template.

4. Conclusions

In the first part of this research the influence of molten-salt synthesis conditions on the morphology of Bi₄Ti₃O₁₂ plate-like particles was studied. The most appropriate conditions for the growth of μm-sized Bi₄Ti₃O₁₂ plates with a uniform size distribution are as follows: Bi:Ti molar ratio = 1.33 (stoichiometric), molar ratio of NaCl:KCl:Bi₄Ti₃O₁₂ = 25:25:1 and 2-hour reaction time at 800 °C.

In the second part of the study we proved that the as-prepared Bi₄Ti₃O₁₂ plates are an appropriate template for the preparation of plate-like (*h00*)-oriented SrTiO₃ plates using a topochemical conversion under hydrothermal conditions. We also confirmed that the type of TiO₂ precursor (P25 or anatase used for Bi₄Ti₃O₁₂ synthesis) has a great influence on the morphology of the formed Bi₄Ti₃O₁₂ plate-like particles, which, when transformed to SrTiO₃ under hydrothermal conditions, result in even more diverse morphologies. The photodegradation of RhB, BET and DSC measurements confirmed the difference between the used templates. These results also support the choice of template for the topochemical conversion of Bi₄Ti₃O₁₂ to SrTiO₃ under hydrothermal conditions.

5. Acknowledgement

The authors acknowledge the project J2-6753 and the M-era.Net project 3184 HarvEnPiez, which were financially supported by the Slovenian Research Agency and the Ministry of Higher Education Science and Technology, respectively. Alja Čontala is grateful to the Slovenian Research Agency for the financial support of her PhD study. The authors would like to thank Martyrna Durko for performing the photocatalytic measurements.

6. References

- Z. Lazarević, B. D. Stojanović, J. A. Varela, *Sci Sinter*. **2005**, *37*, 199–216. DOI:10.2298/SOS0503199L
- Z. Lazarević, N. Rom, M. Todorović, B. D. Stojanović, *Sci Sinter*. **2007**, *39*, 177–184. DOI:10.2298/SOS0702177L
- F. Zhang, T. Karaki, M. Adachi, *Jpn J Appl Phys*. **2006**, *45*, 7385–7388. DOI:10.1143/JJAP.45.7385
- M. Villegas, C. Moure, J. F. Fernandez, P. Duran, *J Mater Sci*. **1996**, *31*, 949–955. DOI:10.1007/BF00352895
- Y. G. Zhang, H. W. Zheng, J. X. Zhang, et al, *Mater Lett*. **2014**, *125*, 25–27. DOI:10.1016/j.matlet.2014.03.146
- M. G. Navarro-Rojero, J. J. Romero, F. Rubio-Marcos, J. F. Fernandez, *Ceram Int*. **2010**, *36*, 1319–1325. DOI: 10.1016/j.ceramint.2009.12.023
- M. Villegas, A. C. Caballero, C. Moure, P. Duran, J. F. Fernandez JE, *J Am Ceram Soc*. **1999**, *82*, 2411–2416. DOI:10.1111/j.1151-2916.1999.tb02098.x
- T. Zaremba, *J Therm Anal Calorim*. **2008**, *93*, 829–832. DOI:10.1007/s10973-008-9330-6
- M. M. Kržmanc, B. Jančar, H. Uršič, M. Tramšek, D. Suvorov, *Cryst Growth Des*. **2017**, *17*, 3210–3220. DOI:10.1021/acs.cgd.7b00164
- H. He, J. Yin, Y. Li, et al, *Appl Catal B Environ*. **2014**, *156–157*, 35–43. DOI:10.1016/j.apcatb.2014.03.003
- Z. Chen, Y. Yu, J. Hu, A. Shui, X. He, *J Ceram Soc Japan*. **2009**, *117*, 264–267. DOI:10.2109/jcersj.117.264
- Q. Yang, Y. Li, Q. Yin, P. Wang, Y. B. Cheng, *J Eur Ceram Soc*. **2003**, *23*, 161–166. DOI:10.1016/S0955-2219(02)00087-0
- T. Takeuchi, T. Tani, *J Ceram Soc Japan*. **2002**, *110*, 232–236. DOI:10.2109/jcersj.110.232
- R.E. Schaak, T.E. Mallouk, *Chem Mater*. **2002**, *14*, 1455–1471. DOI:10.1021/cm010689m
- Y. Chang, H. Ning, J. Wu, et al, *Inorg Chem*. **2014**, *53*, 11060–11067. DOI:10.1021/ic501604c
- S. F. Poterala, Y. Chang, T. Clark, R. J. Meyer, G. L. Messing, *Chem Mater*. **2010**, *22*, 2061–2068. DOI:10.1021/cm903315u

17. D. Liu, Y. Yan, H. Zhou, *J Am Ceram Soc.* **2007**, *90*, 1323–1326. DOI:10.1111/j.1551-2916.2007.01525.x
18. K. Watari, B. Brahmroutu, G. L. Messing, S. Trolier-McKinstry, S. C. Cheng. *J Mater Res.* **2000**, *15*, 846–849. DOI:10.1557/JMR.2000.0121
19. Y. Saito, H. Takao. *Jpn J Appl Phys.* **2006**, *45*, 7377–7381. DOI:10.1143/JJAP.45.7377
20. D. Hu, H. Ma, Y. Tanaka, L. Zhao, Q. Feng. *Chem Mater.* **2015**, *27*, 4983–4994. DOI:10.1021/acs.chemmater.5b01368
21. P. Zhang, T. Ochi, M. Fujitsuka, Y. Kobori, T. Maima, T. Tachikawa. *Angew Chem Int Ed.* **2017**, *56*, 5299–5303. DOI:10.1002/anie.201702223
22. J. F. Cao, Y. X. Ji, *Chin Phys B.* **2014**, *23*, 128104. DOI:10.1088/1674-1056/23/12/128104
23. J. Cao, X. Huang, Y. Liu, J. Wu, Y. Ji, *Mater Res Express.* **2016**, *3*, 115903. DOI:10.1088/2053-1591/3/11/115903
24. R. Asiaie, W. D. Zhu, S. A. Akbar, P. K. Dutta, *Chem Mater.* **1996**, *8*, 226–234. DOI:10.1021/cm950327c
25. H. I. Hsiang, F. S. Yen, *Jpn J Appl Phys.* **1993**, *32*, 5029–5035. DOI:10.1143/JJAP.32.5029
26. V. Kalyani, B. S. Vasile, A. Ianculescu, M. T. Buscaglia, V. Buscaglia, P. Nanni, *Cryst Growth Des.* **2012**, *12*, 4450–4456. DOI:10.1021/cg300614f
27. T. Jardiel, A. C. Caballero, J. F. Fernández, M. Villegas, *J Eur Ceram Soc.* **2006**, *26*, 2823–2826. DOI:10.1016/j.jeurceramsoc.2005.05.003

Povzetek

$\text{Bi}_4\text{Ti}_3\text{O}_{12}$ delce z obliko, podobno ploščicam smo sintetizirali s pomočjo enostopenjske metode v staljeni soli iz nanodelcev Bi_2O_3 in TiO_2 pri 800 °C. Natančno smo raziskali reakcijske pogoje, ki vplivajo na kristalno strukturo in morfologijo. Razlike med različnimi delci $\text{Bi}_4\text{Ti}_3\text{O}_{12}$ smo preučili z vidika faznega prehoda iz feroelektrične v paraelektrično modifikacijo in fotokatalitske učinkovitosti za razgradnjo Rhodamina B pri svetlobnem obsevanju UV-A. V nadaljevanju smo tako pripravljene $\text{Bi}_4\text{Ti}_3\text{O}_{12}$ ploščice uporabili kot izhodiščne delce za pripravo SrTiO_3 ploščic s topokemijsko pretvorbo pod hidrotermalnimi pogoji. Določili smo značilnosti $\text{Bi}_4\text{Ti}_3\text{O}_{12}$ ploščic in reakcijske pogoje, pri katerih so SrTiO_3 delci ohranili obliko izhodiščnih ploščic $\text{Bi}_4\text{Ti}_3\text{O}_{12}$.

Scientific paper

Enhanced Transport of Nandrolone Decanoate Drug by Human Serum Albumin in Presence of [BMIM]PF₆ and [BMIM]BF₄

Zeyad J. Yasseen,^{1,*} Salman M. Saadeh^{1,*} and Hazem M. Abu Shawish^{2,*}¹ Chemistry Department, The Islamic University, Gaza, Palestine² Faculty of Science, Chemistry Department, Al-Aqsa University, Gaza, Palestine* Corresponding authors: E-mail: zyasseen@iugaza.edu.ps
hazemona1@yahoo.co.uk

Received: 18-05-2018

Abstract

The interaction of nandrolone decanoate drug dissolved in (2%) [BMIM]BF₄ or [BMIM]PF₆ with human serum albumin (HSA) at different temperatures in the range of 285–310 K was examined by fluorescence quenching. Stern-Volmer equation and its modified form were used to determine the interaction parameters *K* and *n*. The results revealed that binding affinities of HSA for nandrolone decanoate drug in 2% [BMIM]BF₄ or [BMIM]PF₆ are in the order of 10⁵ M⁻¹ and the number of bound drug molecules per HSA macromolecule are approximated to 1 at all temperatures studied. The thermodynamic parameters: free energy change (ΔG°), enthalpy change (ΔH°) and entropy change (ΔS°) for HSA–nandrolone decanoate/ionic liquid were calculated according to van't Hoff equation. Data analysis indicated that both electrostatic interactions and hydrophobic interactions played important roles in the interaction of nandrolone decanoate drug with HSA.

Keywords: Nandrolone decanoate; Human serum albumin; Ionic liquids; Fluorescence quenching; electrostatic interaction

1. Introduction

The nature and types of interaction between small molecules and biomacromolecules characterize an active area of research. The circulations, free concentration as well as the metabolism of a variety of drugs in human being are powerfully influenced by drug–protein interactions.^{1–5} These interactions can also regulate the drug stability as well as toxicity for the duration of the chemotherapeutic course of action.¹

Ionic liquids are remarkable for their tunable nature and exceptional properties. They have attracted considerable attention in various areas of chemistry, synthesis and catalysis,¹ electrochemistry,^{5–7} biomass conversion,^{8,9} biotechnology^{10,11} and many other fields. The studies on ionic liquids cover a wide range of topics that include structure and properties as well as advanced chemical transformations.^{12,13} Improvements of separation,¹⁴ electrochemical behavior,¹⁵ analytics, extraction, biocatalytic properties¹⁶ are some established areas. The ecological impact of ionic liquids has been recently recognized.^{17,18}

There are three generations of ionic liquids depending on their chemical structure and properties.¹⁹ Limited water solubility and low dissolution rate are among the major problems of modern drug development. The advantages of using ionic liquids in medicinal chemistry has been recently emphasized.^{20–22} Striking solvent abilities of ionic liquids are widely known and are being exploited in extraction^{23–25} and dissolution of biomolecules.^{26–29} Ionic liquids can enhance water solubility of hydrophobic compounds, possibly due to formation of associates between ionic liquids and biomolecules.³⁰

Nandrolone decanoate (Fig. 1) is a parenteral anabolic steroid. It is primarily used to treat anemia, chronic

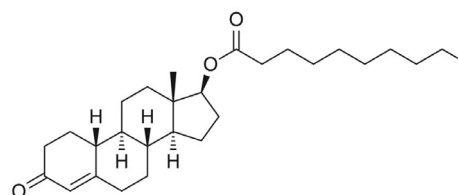


Figure 1. Chemical structure of nandrolone decanoate

renal failure, osteoporosis and AIDS-associated wasting syndrome. It is freely soluble in ethanol, chloroform and acetone but practically insoluble in water (3.09 mg/mL).

Considering limited solubility of the drug in water, it is of interest to study the effect of some ionic liquids, namely 1-butyl-3-methyl-1-imidazolium tetrafluoroborate [BMIM][BF₄] (Fig. 2.a) and 1-butyl-3-methyl-1-imidazolium hexafluorophosphate [BMIM][PF₆] (Fig. 2.b) to increase its solubility in water and to enhance its ability to transfer the drug through the body. Their behaviors were examined by following and analyzing the fluorescence spectra of human serum albumin-nandrolone decanoate mixture in the absence and presence of the selected ionic liquids as solvents. Since the changes in the fluorescence of HSA are indeed related to changes in the fluorescence of tryptophan residue caused by interactions with a variety of quenchers.

In this work, the quenching of HSA fluorescence intensities by the studied drug/2% ionic liquid systems was explored for the first time at different temperatures in the range of 285–310 K.

Binding parameters (K and n) were determined and thermodynamic parameters of HSA– nandrolone decanoate /ionic liquid interaction were calculated. Data analysis indicated that electrostatic interactions and hydrophobic associations played different roles for the two ionic liquids.

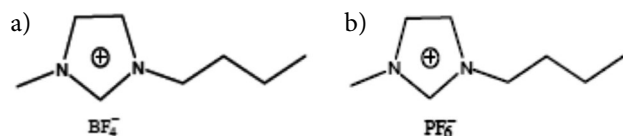


Figure 2. Molecular structure of two ionic liquids: (a) 1-butyl-3-methylimidazolium tetrafluoroborate ([BMIM]BF₄); (b) 1-butyl-3-methylimidazolium hexafluorophosphate ([BMIM]PF₆)

2. Experimental

2.1. Materials and Solutions

Nandrolone decanoate as an ampoule dissolved in oily solution was obtained from Birzeit Pharmaceutical Company (BPC). The ionic liquids; 1-butyl-3-methylimidazolium tetrafluoroborate ([BMIM]BF₄) and 1-butyl-3-methylimidazolium hexafluorophosphate ([BMIM]PF₆) were obtained from Aldrich (mass fraction > 99%). Human serum albumin (HSA, fatty acid free < 0.05%) was purchased from Sigma Chemical Co. and used without further purification. All other reagents of chemically pure grade were commercially available. Doubly distilled water was used throughout. All stock solutions were kept in the dark at 277 K.

Solutions of HSA containing amounts up to 6.5 micromolar were obtained by dilution with buffer containing the ionic liquid and used further with the drug to study its

effect. All HSA solutions were prepared in 50 mM potassium phosphate buffer solutions of pH 7.0 containing 25 mM NaCl to maintain constant ionic strength. Considering large molar absorptivity of HSA, the solutions were properly diluted to give absorbance in the range 0.2 to 0.7 in the linear response covered by the instrument. The HSA stock solution was kept in the dark at 281 K and the pH was checked with a suitably standardized pH meter. During the protein-drug binding experiments, the HSA concentrations were fixed at 2 μM and the drug concentrations were varied from 0 up to 6.5 μM.

2.2. Apparatus

Lambda 20, a Perkin Elmer UV/Vis spectrophotometer, was used for determination of the concentration of HSA using $\epsilon = 35219 \text{ M}^{-1}\text{cm}^{-1}$ at 278 nm as the molar extinction coefficient of HSA.³¹ Fluorescence spectra were obtained using Perkin Elmer luminescence (series no. 70412) spectrometer equipped with a water-jacketed cuvette holder that was maintained at each chosen temperature by means of a circulatory water bath.

2.3. Fluorescence Measurements

Fluorescence spectra (in the range of 280–450 nm upon excitation at 280 nm) were recorded at various temperatures; 285, 293, 303 and 310 K. The reactants were kept at the same temperature before mixing and making fluorescence measurements. The fluorescence intensities were automatically recorded by injecting 20 μL samples of 80 μM drug solution containing 2% ionic liquids into the HSA solution which makes the final concentration of the test solution 0.148% considering the dilution effect. Each titration was made three times.

The inner-filter effect corrections³² were done according to the formula:

$$F_{corr} = F_{obs} 10^{\frac{A_{exc} + A_{em}}{2}} \quad (1)$$

where E_{corr} is the corrected fluorescence value, F_{obs} the measured fluorescence value, A_{exc} and A_{em} the measured absorbance values at the excitation and emission wavelengths, respectively. The interval between every two consecutive sample additions was 2 minutes.

3. Results and Discussion

Fluorescence data were corrected for the inner filter effect caused by attenuation of the excitation beam and emission signal because of absorption by quencher and fluorophore to obtain the proper fluorescence intensity values. The value of the correction factor was 1.05 that incurs a negligible effect to the results.

Nandrolone decanoate drug was selected as a model drug due to its limited solubility in water. In addition, organic solvent may cause denaturation to HSA. Therefore, utilization of selected ionic liquids is justified.

This study is on the effect of ionic liquids on drug-protein interaction. The interaction between nandrolone decanoate and HSA in absence of ionic liquids showed very little quenching in fluorescence intensity which is an indication of marginal interaction. On addition of ionic liquid to the nandrolone decanoate-HSA mixture, a notable drop in fluorescence intensity indicating remarkable effect of ionic liquid on the drug-protein interaction.

3. 1. Interaction of Nandrolone Decanoate Drug with HSA in Presence of Ionic Liquids

Emission spectra of the protein's intrinsic fluorescence was performed to investigate the interaction between the drug (nandrolone decanoate) in 2% ionic liquid ([BMIM]BF₄ or [BMIM]PF₆) and HSA at four different temperatures: 285, 293, 303 and 310 K.

The fluorescence spectra of HSA (2 μ M), obtained in the emission range of 250–450 nm in the absence and the presence of increasing nandrolone decanoate concentrations (0–6.5 μ M) containing 2% ionic liquids ([BMIM]BF₄ or [BMIM]PF₆) were studied in phosphate buffer at pH 7.0 and are shown in Figs. 3 and 4, respectively.

The fluorescence spectrum of HSA produced an emission maximum at 343 nm due to the presence of sole tryptophan (Trp-214) residue which is located in subdomain IIA.³³

Addition of nandrolone decanoate to HSA resulted in a gradual decrease in the fluorescence intensity. However, no shift in the emission maximum was noticed upon nandrolone decanoate addition to HSA. Such quenching in the fluorescence intensity indicated the binding of nandrolone decanoate to HSA, and suggested that the polarity changes in the microenvironment around Trp residue might be responsible for the observed quenching of the fluorescence intensity observed.^{34–37}

Fluorescence quenching of the single tryptophan residue in HSA was used to measure drug-binding affinity. Tryptophan fluorescence is the most frequently examined

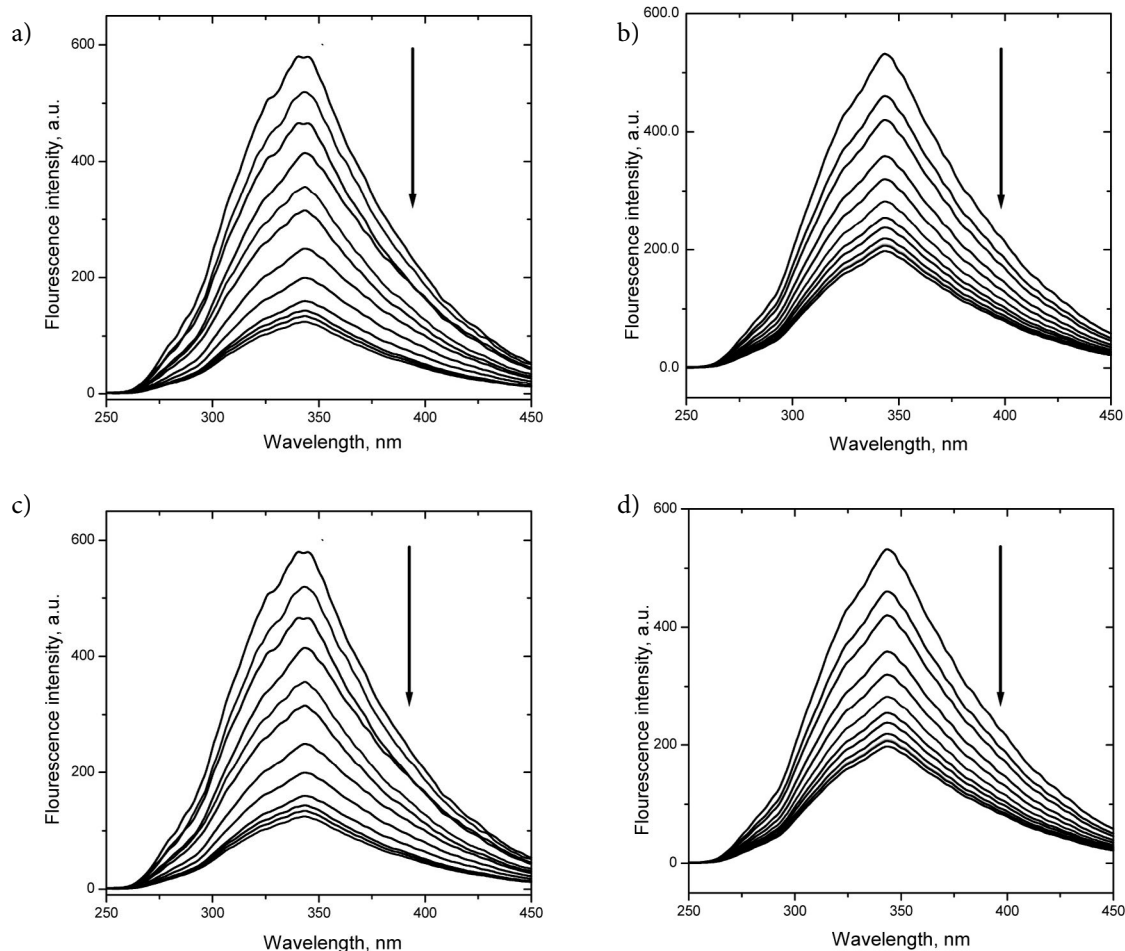


Figure 3. Fluorescence quenching spectra of human serum albumin at various concentrations of nandrolone dissolved in 2% [BMIM]BF₄ ionic liquid, [HSA] = 2 μ M, [nandrolone]/ionic liquid were: 0.00, 0.58, 1.15, 1.72, 2.28, 2.83, 3.37, 3.91, 4.44, 4.96, 5.48, 5.99 and 6.50 μ M all in phosphate buffer solution 50 mM, 25 mM NaCl, pH = 7.0 at different temperatures: (a) 285 K (b) 293 K (c) 303 K and (d) 310 K, λ_{ex} = 280 nm.

among the three intrinsic aromatic fluorophores in HSA molecules to obtain information about conformational changes.

A very small shift (about 3 nm in the wave length of the fluorescence intensity) was observed on addition of increasing amounts of the ionic liquids to the test solution. It is inferred that the protein retains its native three-dimensional structure under the conditions studied in this ex-

periment. In this system, quenching in fluorescence was due to interaction of nandrolone decanoate and HSA but effects of ionic liquids were negligible and the main effect of which was a solubilizing role.

The quenching data were analyzed using the Stern-Volmer equation,

$$F_0/F = 1 + K_{sv} [Q], \quad (2)$$

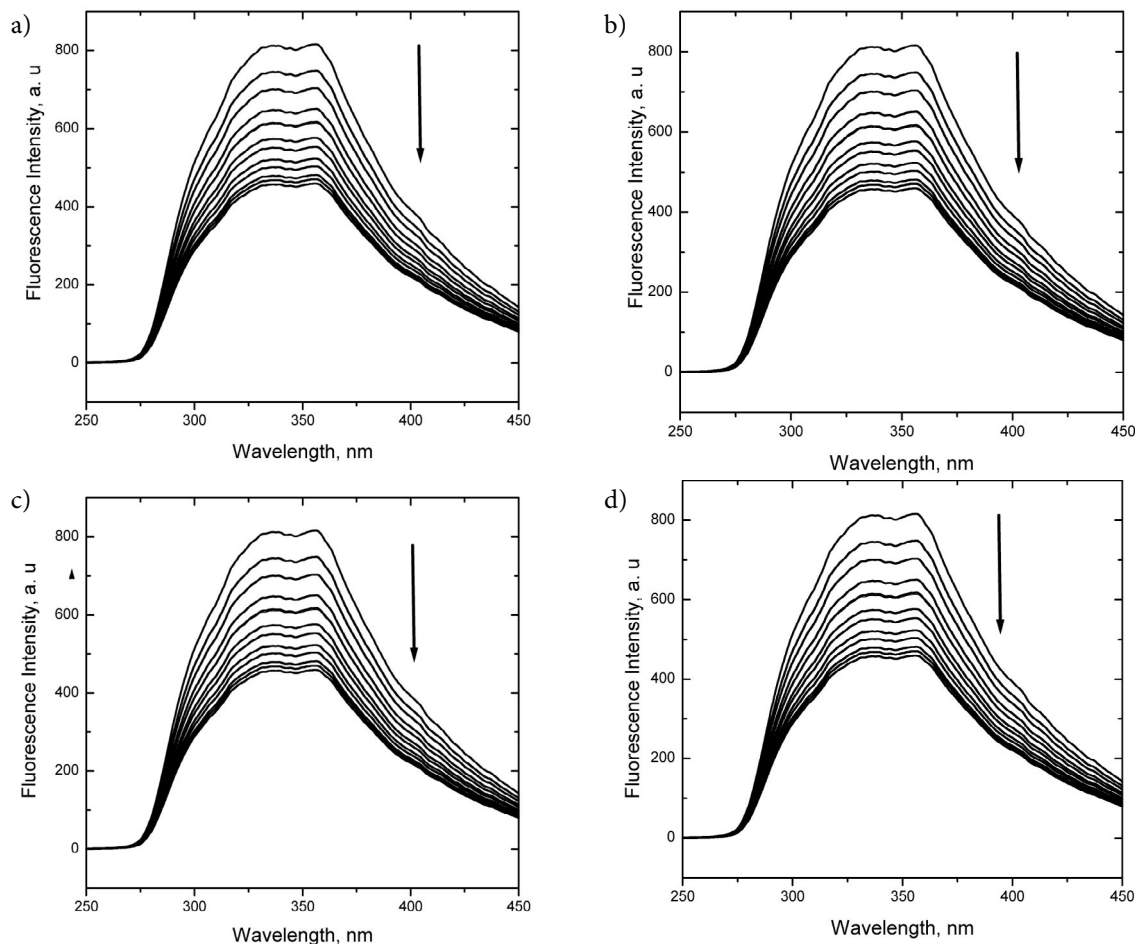


Figure 4. Fluorescence quenching spectra of human serum albumin at various concentrations of nandrolone dissolved in 2% [BMIM]PF₆ ionic Liquid, [HSA] = 2 μM, [nandrolone] were: 0.00, 0.58, 1.15, 1.72, 2.28, 2.83, 3.37, 3.91, 4.44, 4.96, 5.48, 5.99 and 6.50 μM all in phosphate buffer solution 50 mM, 25 mM NaCl, pH = 7.0 at different temperatures: (a) 285K (b) 293 K (c) 303 K and (d) 310 K, λ_{ex} = 280 nm.

Table 1: Results of the binding in the nandrolone decanoate/ionic liquid/HSA systems..

Ionic Liquid	Temperature	$K_{SV} \times 10^5$ (K)	$K_a \times 10^5$ (L mol ⁻¹)	R	Binding sites (n)
[BMIM]BF ₄	285.15	3.50	6.73	0.99162	1.36
	293.15	2.73	5.90	0.99385	1.23
	303.15	1.90	3.72	0.99174	1.16
	310.15	1.30	2.63	0.99961	1.17
[BMIM]PF ₆	285.15	1.75	7.00	0.99992	1.35
	293.15	1.51	6.51	0.99996	1.25
	303.15	1.26	5.44	0.99994	1.28
	310.15	1.08	3.80	0.99986	1.11

and its modified form,

$$\log [(F_0 - F)/F] = \log K + n \log [Q] \quad (3)$$

Where F_0 and F are the relative fluorescence intensities in the absence and presence of quencher drug, $[Q]$ is the concentration of quencher, K_{sv} is the Stern-Volmer quenching constant and K is the binding constant for the accessible fluorophores.³²

3. 2. Stern-Volmer Analysis of HSA Interaction with Nandrolone Decanoate Drug

The fluorescence quenching data for nandrolone decanoate -HSA in presence of the two selected ionic liquids were analyzed by Stern-Volmer equation (equation 2).

The values of K_{SV} constants at different temperatures are listed in Table 1. The patterns of the F_0/F versus $[Q]$ (Stern-Volmer) plots for HSA were shown in Figs. 5 and 6. These plots present good linear relationships between F_0/F versus drug concentration.

The fluorescence intensities were quenched by the interaction of HSA with nandrolone decanoate in the presence of the ionic liquids ([BMIM]BF₄ and [BMIM]PF₆).

This behavior is attributed to nandrolone decanoate binding to HAS, which may be facilitated by both ionic liquids due to their hydrophobicity and enhanced transport of the drug to the binding site.

From table 1, it is noticed that the binding constants for the two systems: nandrolone decanoate -HSA in presence of the studied ionic liquids, [BMIM]BF₄ and [BMIM]PF₆, were of the same order of magnitude, being slightly higher with [BMIM]PF₆ as compared to that with the former. This result is in accordance with expectations based on the similarity in structure of the two compounds. The hydrophobicity of hexafluorophosphate is more than that of tetrafluoroborate anion. Therefore, the

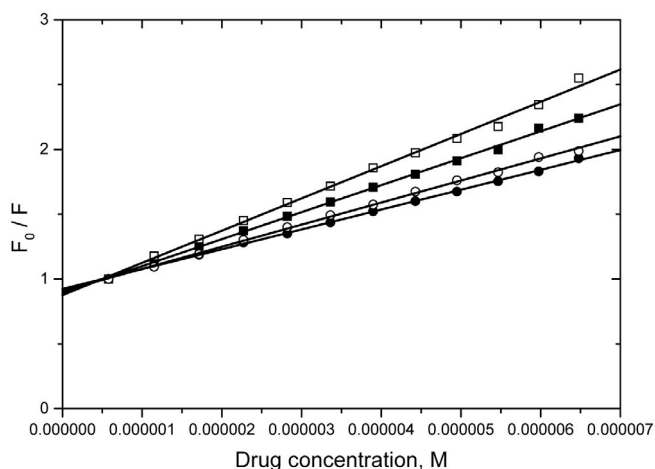


Figure 5. The Stern -Volmer plots for the binding of nandrolone drug with in [BMIM]BF₄ at 285 K (□), 293 K (○), 303 K (■) and 313 K (●). λ_{ex} = 280 nm; λ_{em} = 343 nm and [HSA] = 2 μ M.

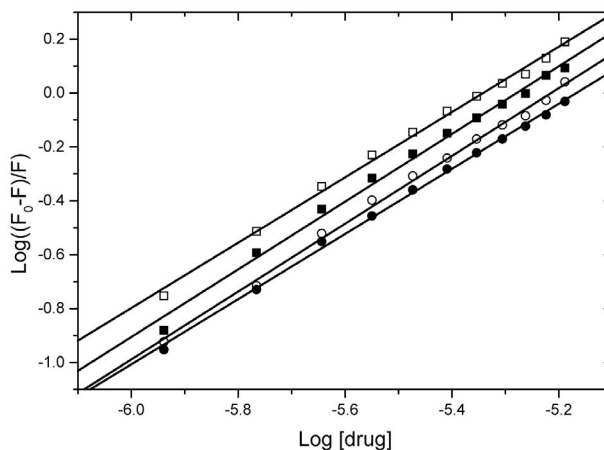


Figure 6. The Stern-Volmer plots for the binding of nandrolone decanoate drug with HSA in presence of [BMIM]PF₆ at 285 K (□), 293 K (○), 303 K (■) and 313 K (●). λ_{ex} = 280 nm; λ_{em} = 343 nm and [HSA] = 2 μ M.

ionic liquid containing hexafluorophosphate can penetrate into the hydrophobic region of HSA making stronger bonding with higher binding constants and explains the observation that this ionic liquid is more effective on the protein.

3. 3. Modified Stern-Volmer Analysis of Binding Equilibria

Quenching data were also analyzed according to the modified Stern-Volmer equation, equation 3. It is shown in Figs. 7 and 8 that the dependence of $\log [(F_0-F)/F]$ versus $\log[\text{quencher}]$ is linear with a slope equal to the value of binding sites (n) and y -intercept corresponding to the \log of the effective quenching constant (K). The corresponding results of the linear regression equations at four different temperatures are shown in Table 1. The decrease

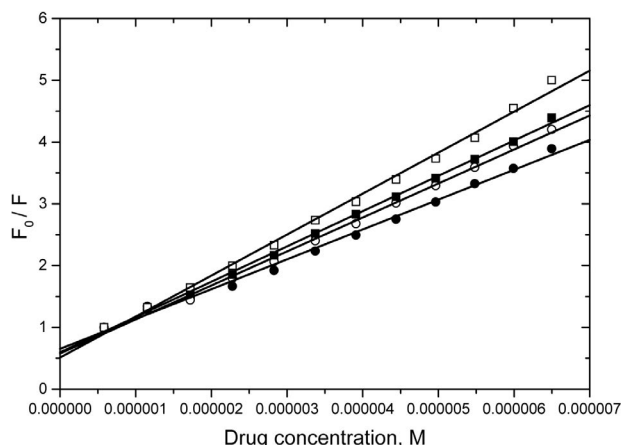


Figure 7. Modified Stern-Volmer plots of $\log [(F_0-F)/F]$ versus $\log[\text{drug}]$ for nandrolone decanoate -ionic liquid-HSA system at different temperatures; the presence of [BMIM]BF₄ or [BMIM]PF₆, [HSA] = 2 μ M.

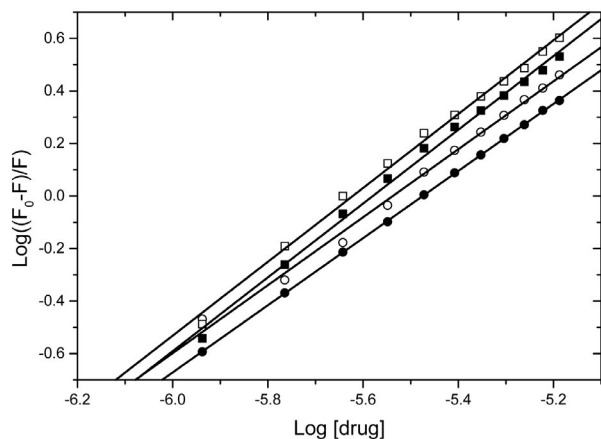


Figure 8. Modified Stern-Volmer plots of $\log [(F_0-F)/F]$ versus $\log[\text{drug}]$ for nandrolone-ionic liquid-HSA system at different temperatures; the presence of [BMIM]BF₄ or [BMIM]PF₆, [HSA] = 2 μM .

ing trend of K with increasing temperature is in accordance with the K_{SV} dependence on temperature resulting in a reduction of the stability of the nandrolone decanoate-HSA complex at higher temperatures.

3. 4. Types of interaction force between HSA and the nandrolone drug

The changes of free energy, enthalpy and entropy were estimated using the Van't Hoff's equation:

$$\ln K_a = -\frac{\Delta H^\circ}{RT} + \frac{\Delta S^\circ}{R} \quad (4)$$

and the relationship,

$$\Delta G^\circ = \Delta H^\circ - T\Delta S^\circ \quad (5)$$

Using van't Hoff equation that can be rewritten as:

$$\left(\frac{\partial \ln K_{eq}}{\partial (1/T)} \right)_P = -\frac{\Delta H^\circ}{R} \quad (6)$$

Integration produces the equation:

$$\ln \left(\frac{K_2}{K_1} \right) = -\frac{\Delta H^\circ}{R} \left(\frac{1}{T_2} - \frac{1}{T_1} \right) \quad (7)$$

Since:

$$\Delta G^\circ = -RT \ln K_{eq} \quad (8)$$

$$\Delta G^\circ = \Delta H^\circ - T\Delta S^\circ$$

Equating the right sides of the equations produces:

$$\ln K_{eq} = -\frac{\Delta H^\circ}{RT} + \frac{\Delta S^\circ}{R} \quad (9)$$

This equation is used for calculation of the equilibrium values obtained for the interaction of drug and HSA.

According to the effective binding constants of nandrolone decanoate drug to HSA obtained at the studied temperatures, the thermodynamic parameters were determined from linear Van't Hoff plot (Fig. 9) and the values are presented in Table 2.

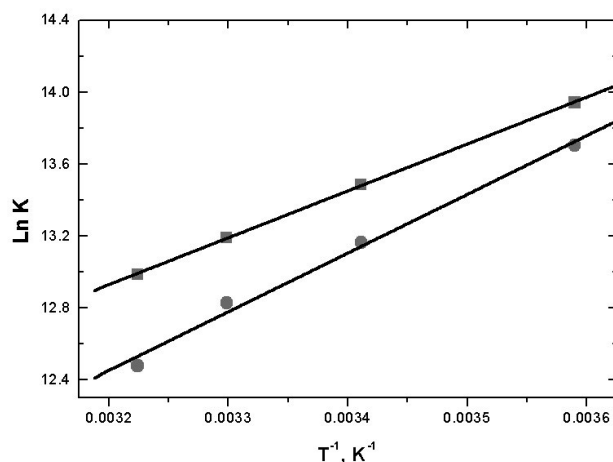


Figure 9. Van't Hoff plot for the interaction of HSA and nandrolone decanoate drug in the presence of ionic liquids; [BMIM]BF₄ (■) (and [BMIM]PF₆) (●)

Table 2: Thermodynamic parameters of the nandrolone decanoate/2% ionic liquid-HSA interaction at different temperatures and pH 7.0.

Ionic Liquid	T, K	$K \times 10^5$ $\text{L} \cdot \text{mol}^{-1}$	ΔG° kJ mol^{-1}	ΔH° kJ mol^{-1}	ΔS° $\text{J mol}^{-1} \text{K}^{-1}$	R
[BMIM]BF ₄	285.15	6.73	-32.55			
	293.15	5.90	-32.86	-21.67	38.16	0.99986
	303.15	3.72	-33.24			
	310.15	2.63	-33.50			
[BMIM]PF ₆	285.15	7.00	-31.90			
	293.15	6.51	-32.04	-27.14	16.70	0.99991
	303.15	5.44	-32.20			
	310.15	3.80	-32.32			

The formation of drug – HSA complexes in presence of the selected ionic liquids were carried out spontaneously through exothermic reaction accompanied by positive ΔS° values. Ross and Subramanian³⁸ have characterized the sign and magnitude of the thermodynamic parameter associated with various kinds of interaction that may take place in protein association processes.

Ionic liquid facilitated binding process of nandrolone decanoate to HSA in aqueous solution is governed by hydrophobic as well as specific interactions (electrostatic and/or hydrogen bond). Binding was characterized by positive entropy and negative enthalpy changes and is more effective in the presence of hexafluorophosphate anions although the size of the anionic part in the [BMIM]BF₄ is smaller and can more easily approaches the hydrophobic core of HSA.

4. Conclusion

The interaction between nandrolone decanoate drug and HSA in presence of ionic liquids [BMIM]BF₄ and [BMIM]PF₆ was investigated through fluorescence quenching methods.

The results indicate that the studied ionic liquids affect the binding of nandrolone decanoate drug to HSA at various temperatures in the range of 285–310 K. It was observed that the binding constants between nandrolone and HSA were decreased with temperature.

In addition, the binding constants in presence of ionic liquid [BMIM]PF₆ is slightly greater than that in presence of [BMIM]BF₄ in the drug solution.

The study opened the door to new avenues in the screening and design of appropriate safe drugs containing ionic liquids that will likely find important applications in modern medical research.

5. Acknowledgement

the authors would like to thank Dr. Ahmad Abu Ismael for a generous gift of the ionic liquids.

6. References

1. Catalysis in Ionic Liquids: From Catalyst Synthesis to Application; Hardacre, C.; Parvulescu, V., Eds.; The Royal Society of Chemistry: Cambridge, 2014.
2. Ionic Liquids (ILs) in Organometallic Catalysis; Dupont, J.; Kollár, L., Eds.; Springer-Verlag: Berlin-Heidelberg, 2015.
3. Environmentally Friendly Syntheses Using Ionic Liquids; Dupont, J.; Itoh, T.; Lozano, P.; Malhotra, S. V., Eds.; CRC Press: Boca Raton-London-New York, 2015.
4. Green Solvents II: Properties and Applications of Ionic Liquids; Mohammad, A.; Inamuddin, Eds.; Springer-Verlag: Berlin-Heidelberg, 2012.
5. V. M. Fedorov, A. A. Kornyshev, *Chem. Rev.* **2014**, 114, 2978–3036. DOI:10.1021/cr400374x
6. Electrochemistry in Ionic Liquids. Vol. 1: Fundamentals; Torriero, A. A. J., Ed.; Springer-Verlag: Berlin-Heidelberg, 2015.
7. Electrochemistry in Ionic Liquids. Vol. 2: Applications; Torriero, A. A. J., Ed.; Springer-Verlag: Berlin-Heidelberg, 2015.
8. S. A. Amarasekara, *Chem. Rev.* 2016, **116**, 6133–6183. DOI:10.1021/acs.chemrev.5b00763
9. L. N. Mai, K. C. Kim, B. Park, J. H. Park, H. S. Lee, M. Y. Koo, *J. Mol. Liq.* **2016**, 215, 541–548. DOI:10.1016/j.molliq.2016.01.040
10. S. Jeong, H. S. Ha, C. M. Lim, M. S. Kim, R. Y. Kim, M. Y. Koo, S. J. So, J. T. Jeon, *Soft Matter* **2012**, 8, 5501–5506. DOI:10.1039/c2sm25223f
11. A. Kumar, P. Venkatesu, *Chem. Rev.*, **2012**, 112 (7), pp 4283–4307. DOI:10.1021/cr2003773
12. F. Giacalone, M. Gruttadauria, *ChemCatChem* **2016**, 8, 664–684. DOI:10.1002/cctc.201501086
13. C. Yue, D. Fang, L. Liu, F. T. Yi, *J. Mol. Liq.* **2011**, 163, 99–121. DOI:10.1016/j.molliq.2011.09.001
14. Ionic Liquids for Better Separation Processes; Rodríguez, H., Ed.; Springer-Verlag: Berlin-Heidelberg, 2016.
15. S. Tang, A. G. Baker, H. Zhao, *Chem. Soc. Rev.* **2012**, 41, 4030–4066. DOI:10.1039/c2cs15362a
16. R. Patel, M. Kumari, B. A. Khan, *A Review Appl. Biochem. Biotechnol.* **2014**, 172, 3701–3720. DOI:10.1007/s12010-014-0813-6
17. Ionic Liquids UnCOILed: Critical Expert Overviews; Seddon, K. R.; Plechkova, N. V., Eds.; John Wiley & Sons, Inc.: Hoboken, NJ, 2013.
18. A. Jordan, N. Gathergood, *Chem. Soc. Rev.* **2015**, 44, 8200–8237. DOI:10.1039/C5CS00444F
19. L. W. Hough, M. Smiglak, H. Rodríguez, P. R. Swatloski, K. S. Spear, T. D. Daly, J. Pernak, E. J. Grisel, D. R. Carliss, D. M. Soutullo, *New J. Chem.* **2007**, 31, 1429–1436. DOI:10.1039/b706677p
20. M. Smiglak, M. J. Pringle, X. Lu, L. Han, S. Zhang, H. Gao, R. D. MacFarlane, D. R. Rogers, *Chem. Commun.* **2014**, 50, 9228–9250. DOI:10.1039/C4CC02021A
21. L. J. Shamshina, S. P. Barber, D. R. Rogers, *Drug Delivery* **2013**, 10, 1367–1381.
22. A. Balk, U. Holzgrabe, L. Meinel, *Eur. J. Pharm. Biopharm.* **2015**, 94, 291–304. DOI:10.1016/j.ejpb.2015.05.027
23. G. M. Freire, F. A. Claudio, M. J. Araujo, A. J. Coutinho, M. I. Marrucho, C. Lopes, P. L. Rebelo, *Chem. Soc. Rev.* **2012**, 41, 4966–4995. DOI:10.1039/c2cs35151j
24. M. M. Seitkalieva, A. A. Grachev, S. K. Egorova, P. V. Ananikov, *Tetrahedron* **2014**, 70, 6075–6081. DOI:10.1016/j.tet.2014.02.025
25. M. M. Seitkalieva, V. V. Kachala, S. K. Egorova, P. V. Ananikov, *ACS Sustainable Chem. Eng.* **2015**, 3, 357–364. DOI:10.1021/sc500770v
26. H. Passos, G. M. Freire, A. J. Coutinho, *Green Chem.* **2014**, 16, 4786–4815. DOI:10.1039/C4GC00236A
27. M. Naushad, A. Z. Allothman, B. A. Khan, M. Ali, *Int. J. Biol. Macromol.* **2012**, 51, 555–560.

- DOI:10.1016/j.ijbiomac.2012.06.020
28. M. F. A. Cláudio, M. A. Ferreira, G. M. Freire, P. A. J. Coutinho, *Green Chem.* **2013**, 15, 2002–2010. DOI:10.1039/c3gc40437d
29. H. Zhao, *J. Chem. Technol. Biotechnol.* **2015**, 90, 19–25. DOI:10.1002/jctb.4511
30. F. A. Cláudio, C. M. Neves, K. Shimizu, N. J. Canongia, N. J. Lopes, G. M. Freire, A. J. Coutinho, *Green Chem.* **2015**, 17, 3948–3963. DOI:10.1039/C5GC00712G
31. U. K. Hansen, T. V. Chuang, M. Otagiri, *Biol. Pharm. Bull.* **2002**, 25(6), 695–704. DOI:10.1248/bpb.25.695
32. Principles of fluorescence spectroscopy. Lakowicz, Joseph R. Springer Science and Business Media, LLC **2006**.
33. T. Peters, All About Albumin: Biochemistry, Genetics, and Medical Applications, Academic Press, San Diego, CA, **1996**.
34. S. R. Feroz, S. B. Mohamad, G. S. Lee, S. N. A. Malek, S. Tayyab, *Phytomedicine* **2015**, 22, 621–630. DOI:10.1016/j.phymed.2015.03.016
35. D. Li, J. Zhu, J. Jin, X. Yao, *J. Mol. Struct.* **2007**, 846, 34–41. DOI:10.1016/j.molstruc.2007.01.020
36. S. Neamtu, N. Tosa, M. Bogdan, *J. Pharm. Biomed. Anal.* **2013**, 85, 277–282. DOI:10.1016/j.jpba.2013.07.032
37. S. Soares, N. Mateus, V.D. Freitas, *J. Agric. Food Chem.* **2007**, 55, 6726–6735. DOI:10.1021/jf070905x
38. D. P. Ross, S. Subramanian, *Biochem.* **1981**, 20, 3096–3102. DOI:10.1021/bi00514a017

Povzetek

Raziskovali smo interakcijo zdravila nandrolon dekanat, raztopljenega v 2 % [BMIM]BF₄ ali [BMIM]PF₆, s človeškim serumskim albuminom (HSA) pri različnih temperaturah v območju 285–310 K. Za določitev interakcijskih parametrov K in n smo uporabili Stern-Volmerjevo enačbo in njeno modificirano obliko. Rezultati so pokazali, da je vezavna afiniteta HSA za nandrolon dekanat v 2 % [BMIM]BF₄ ali [BMIM]PF₆ reda velikosti 10^5 M^{-1} in število vezanih molekul zdravila na vezavno mesto na makromolekuli HSA približno 1 pri vseh preiskovanih temperaturah. Iz van't Hoffove enačbe smo izračunali sledeče termodinamske parametre: spremembo standardne Gibsove proste entalpije (ΔG°), entalpije (ΔH°) in entropije (ΔS°) za sistem HSA– nandrolon dekanat/ionska tekočina. Analiza podatkov je pokazala, da tako elektrostatske kot hidrofobne interakcije igrajo pomembno vlogo v interakciji nandrolon dekanata s HSA.

Scientific paper

Effects of Magnesia Incorporation on Properties of Polystyrene/Magnesia Composites

Salah Eddine Hachani,^{1,*} Abdulmounem Alchekhis,² Zelikha Necira,¹
Nadia Nebbache,¹ Ahmed Meghezzi¹ and Guralp Ozkoc²

¹ Laboratory of Applied Chemistry, Mohamed Khider University, Biskra 07000, Algeria.

² Department of Chemical Engineering, Kocaeli University, Kocaeli 41380, Turkey.

* Corresponding author: E-mail: salaho_hachani@yahoo.fr

Phone number: +213791162887

Received: 02-03-2018

Abstract

In the present study, the effects of magnesia particles on thermal, dynamic mechanical, morphological, and surface properties of polystyrene resin are investigated. In general, the addition of magnesia particles in polystyrene matrix increases the thermal stability, storage modulus, and wettability, on other hand does not affect the molecular mobility. SEM results showed a limited distribution of magnesia particles in the polystyrene matrix at 15 wt.%.

Keywords: Magnesia; polystyrene; Thermal stability; Storage modulus; Wettability; Molecular mobility.

1. Introduction

Thermoplastic polymers are largely used due to their attractive advantages such as recyclability, low process temperature, and low cost.¹ Polystyrene (PS) is one of the most important thermoplastics used today and produced in a huge amount worldwide. This resin has been extensively applied in many fields such as computer industry, foam packaging, toys, and cell-culture wares^{2,3} due to its high modulus, satisfactory tensile strength, transparency, and its low cost.²

The polymers are rarely used in the pure form because of their poor properties; they must be combined with other materials in the form of fibers, particles, and spheres considered as reinforcement, which leads to generate new materials having improved properties, namely polymer composites.⁴ The improvement of polystyrene properties have received great attention from both academia and industry; studies have been conducted in this context including minerals,⁵ glass fibers,⁶ boron nitride,⁷ and nanoparticles such as carbon nanotubes.⁸

Two basic techniques to prepare the PS composites are well known. In solvent casting technique, PS is dissolved in a solvent, such as toluene, and then the filler particles are mixed into solution by means of mechanical or ultrasonic mixing. After casting this solution over a surface, solvent is evaporated and the composite PS film

is obtained.⁹ The other technique is the melt-compounding of PS composites. In this technique, PS is transferred to viscous-melt by heat in an extruder or an internal mixer. Thanks to the shear forces exerted in these devices, the filler particles can be uniformly dispersed in the matrix.¹⁰

Thermoplastic polymers filled with metal oxides are widely used in sensors,¹¹ gas membranes,¹² electronic devices,¹³ optoelectronics, and organic photovoltaic.¹⁴ Magnesia (MgO) is an interesting metal oxide characterized by excellent thermodynamic stability, low dielectric constant, low refractive index, and very large band gap. This metal oxide is largely used in catalysis, refractory, ceramic industry, and toxic waste treatment.¹⁵ Magnesia can be elaborated using different methods such as a combustion process,¹⁶ chemical vapour deposition technique,¹⁷ and ultrasound assisted one pot method.¹⁸

Few studies have treated the use of magnesia in the field of polymer engineering. In a study, it was found that carboxylated nitrile rubbers reinforced with magnesia exhibit better physical properties compared to the ones reinforced with other metallic oxides.¹⁹ Another study demonstrated that the mechanical properties of unsaturated polyester resin have increased after magnesia incorporation.²⁰ A significant improvement of thermal stability of poly (ethylene terephthalate) has achieved at high magnesia amount.²¹ To the best of our knowledge no experimen-

tal background has been proposed to study the effects of magnesia in properties of polystyrene matrix.

The present contribution aims to study the feasibility of magnesia incorporation in the improvement of polystyrene resin properties. Both neat polystyrene and magnesia filled polystyrene composite films prepared by melt-compounding using a single screw extruder have been tested by several techniques to investigate the effects of magnesia on thermal, morphological, dynamic mechanical properties, and wettability of polystyrene matrix.

2. Experimental Part

2.1. Materials

The polystyrene used in the current study was provided by Spanish Petrochemicals Company. Highly pure magnesia powder with an average particle size of 0.447 μm was purchased from BIOCHEM Chemopharma. The polystyrene platelets were grinded using a commercial laboratory milling to ease the mixing between the polystyrene and the magnesia powder during the melt-compounding process.

2.2. Film Preparation

Polystyrene/Magnesia composite films were obtained by extrusion. Both polystyrene and magnesia powders were mixed using a commercial mixer during 5 minutes at room temperature. The resulting mixture was extruded using Plasti-Corder PLE 330 single screw extruder. The extrusion conditions were a barrel temperature of 180 $^{\circ}\text{C}$ and a screw speed of 27 r.p.m. The magnesia loadings were 5, 10, and 15 % by weight.

2.3. Characterisation

2.3.1. DSC Analysis

DSC measurements were carried out using a calorimeter model Mettler Toledo. Samples of 5–6 mg were scanned from 30 to 140 $^{\circ}\text{C}$ under nitrogen atmosphere at heating rate of 10 $^{\circ}\text{C}/\text{min}$.

2.3.2. DMA Analysis

Dynamic mechanical analysis (DMA) was performed using DMA Metravib 50 db machine operating at frequency of 1 Hz. Samples of rectangular form were put in tensile mode, both storage modulus and loss modulus were measured in the temperature range from 40 to 150 $^{\circ}\text{C}$ at a heating rate of 10 $^{\circ}\text{C}/\text{min}$.

2.3.3. Contact Angle Measurement

To measure the contact angle, the photograph of the droplet of distilled water put on the surface of the poly-

meric material was taken by a digital camera. The contact angles were measured on digital photographs using image analysis software (Image J).

2.3.4. Thermogravimetric Analysis

Thermogravimetric analysis (TGA) was conducted using TGA/DTA Mettler Toledo analyser. Samples of 5–6 mg were heated from 30 to 580 $^{\circ}\text{C}$ under air atmosphere at heating rate of 10 $^{\circ}\text{C}/\text{min}$.

2.3.5. Scanning Electron Microscopy (SEM)

Magnesia particles distribution in PS matrix and fractured surface topology were investigated by scanning electron microscopy (SEM) (JEOL JSM-6335F). Samples were coated with gold prior to analysis.

3. Results and Discussions

3.1. DSC Results

Both pure polystyrene and its magnesia filled composites was the subject of differential scanning calorimetric analysis to investigate polystyrene molecular mobility variations after magnesia incorporation. DSC curves of different samples under probe are shown in Figure 1. DSC thermogram of pure polystyrene exhibits only one thermal event, the glass transition temperature T_g ; the temperature at which a polymer transforms from a glassy to a rubbery state. T_g has been determined as the value corresponding to inflection point of onset and end-set temperature profiles. For the neat polystyrene and polystyrene filled with 5, 10, and 15 wt.% of magnesia, T_g values are 95.56, 94.84, 95.61, and 95.12 $^{\circ}\text{C}$, respectively. This indicates that incor-

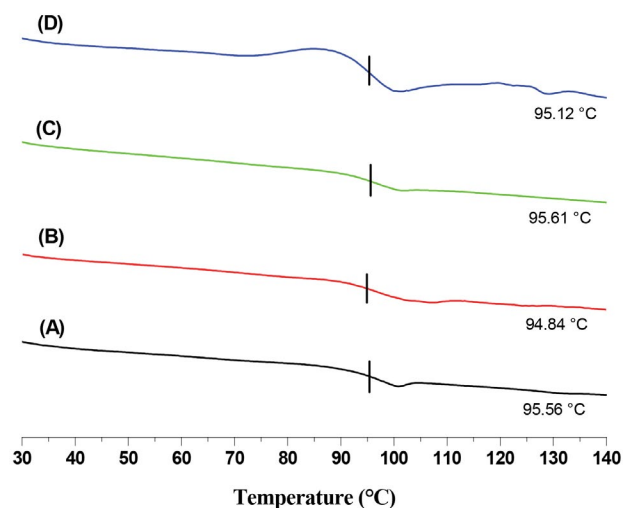


Figure 1: DSC thermograms of (A) neat PS, (B) 5 wt.% magnesia reinforced PS, (C) 10 wt.% magnesia reinforced PS, and (D) 15 wt.% magnesia reinforced PS.

poration of magnesia particles does not affect the glass transition temperature T_g of polystyrene matrix. This experimental finding could be attributed to the weak interactions between magnesia particles and polystyrene matrix, the polystyrene molecular mobility is not modified and no significant variations in glass transition temperature can be registered.

3. 2. DMA Results

Dynamic mechanical analysis (DMA) was used to study the effect of magnesia incorporation on thermo-mechanical properties of polystyrene matrix. The temperature dependence of storage modulus (E') of polystyrene and its magnesia composites is shown in Figure 2. It can be seen that addition of magnesia particles enhanced the storage modulus of the studied composites in the temperature range from 40 to 85 °C, as an example the storage modulus at 60 °C of neat polystyrene increased by 17 % with the addition of 15 wt.% of magnesia. This increase in storage modulus could be attributed to the increase in the stiffness of polystyrene matrix due the reinforcement effect of magnesia particles. Suzhu Yu et al. also have reported amelioration in storage modulus of the neat polystyrene after aluminium powder addition.²²

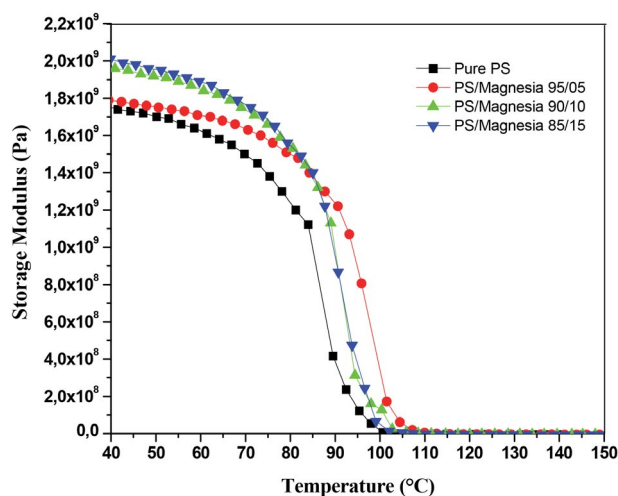


Figure 2: Storage modulus variations of pure PS and PS/Magnesia composites.

Loss modulus curve can be used to determine the glass transition temperature T_g for each studied formulation using the peak maximum in loss modulus and its temperature dependence. Loss modulus variations of neat polystyrene and its magnesia filled composites as a function of temperature are shown in Figure 3. It is evident that the addition of magnesia particles has not a remarkable effect on the glass transition temperature T_g of polystyrene matrix.

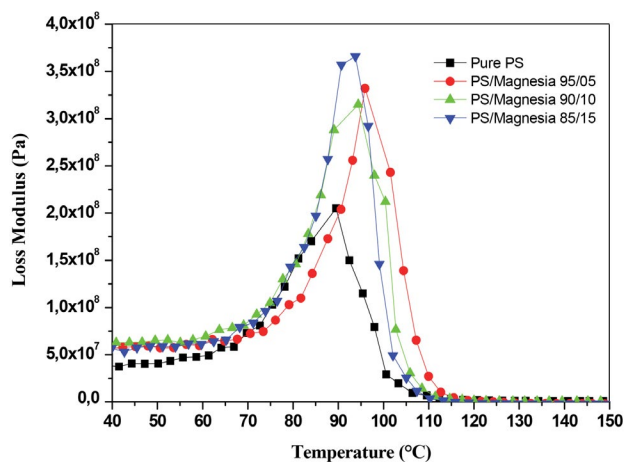


Figure 3: Loss modulus variations of pure PS and PS/Magnesia composites.

3. 3. Contact Angle Measurements Results

Contact angle measurement is a fundamental method used in many scientific and industrial fields such as surface chemistry and biomaterials. Contact angle measurements can inform about surface properties such as surface energy, wettability, and surface modification.²³ In the current study, we adopt this technique to investigate the polystyrene surface wettability which is considered as a key factor to find an appropriate application for a polymer film. Figure 4 shows the appearance of water drops on the

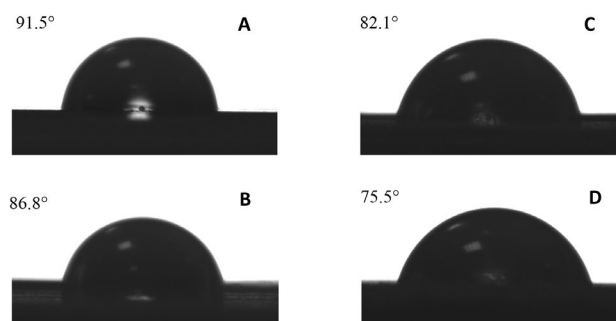


Figure 4: Water contact angles of (A) PS, (B) PS/5 wt.% Magnesia reinforced composite, (C) PS/10 wt.% Magnesia reinforced composite, and (D) PS/15 wt.% Magnesia reinforced composite.

samples indicating the water contact angles. The pure polystyrene has a hydrophobic surface with an average water contact angle of 91.5°. The insertion of 5, 10, and 15 wt.% of magnesia particles in polystyrene matrix decreased significantly the water contact angle to 86.8, 82.1, and 75.5°, respectively. The presence of magnesia in polystyrene composite films tends to reduce the interfacial tension between water and polystyrene interface, which makes the polystyrene surface hydrophilic.

3. 4. Thermogravimetric Analysis (TGA) Results

Thermogravimetric analysis (TGA) was conducted to investigate thermal stability of polystyrene matrix after magnesia incorporation. TGA and DTG thermograms of neat polystyrene and its composites containing 5, 10, and 15 wt.% of magnesia are shown in Figure 5 and 6. Thermal degradation parameters of pure polystyrene and its magnesia composites were extracted from TGA and DTG curves and presented in Table 1. Single phase degradation is observed for the pure polystyrene; this phase is attributed to the decomposition of polystyrene matrix to volatile styrene monomers where mass loss reaches 98 % at 570 °C. When 15 wt.% of magnesia powder added as filler, the thermal stability of the composites under study is ameliorated, where T_{\max} increased from 426.9 to 432.8 °C and the final residue increased from 1.6 to 16.6 %, indicating that magnesia has a retardation effect on the heat transfer in the polystyrene matrix during thermal degradation. On other hand, it can be seen that PS/magnesia 95/05 sample shows the highest IDT value compared with the other formulations, this could be attributed to the good quality of magnesia dispersion and distribution into polystyrene matrix.

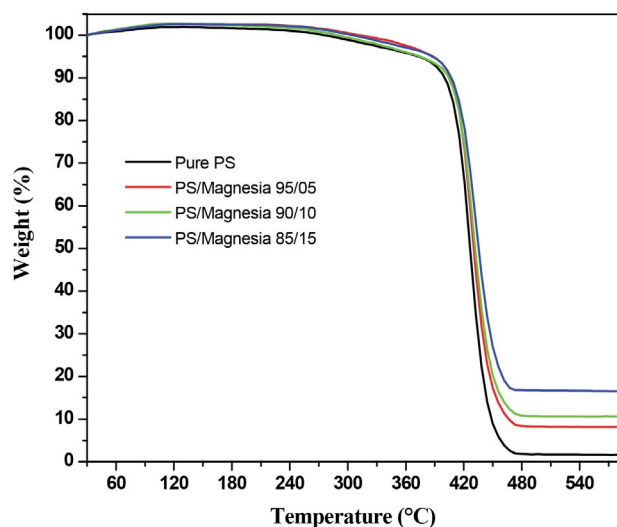


Figure 5: TGA curves of neat polystyrene and PS/Magnesia composites

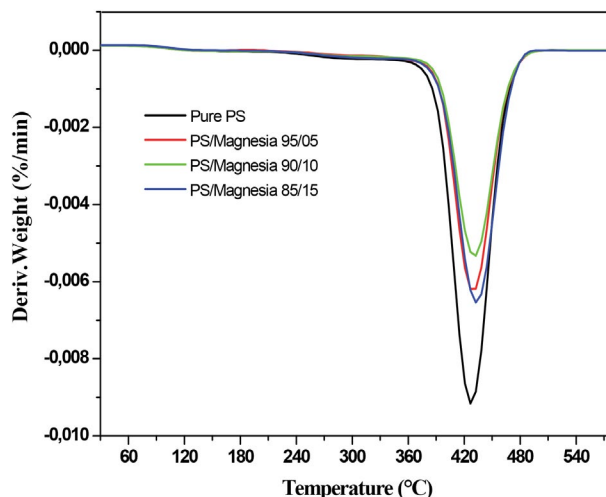


Figure 6: DTG curves of neat polystyrene and PS/Magnesia composites.

3. 5. Morphology of PS/Magnesia Composites

Filler dispersion and distribution in the hosting polymer matrix are two essential parameters which can strongly influence the final properties of the elaborated composite materials. Filler dispersion represents the agglomeration level of filler particles in the polymer matrix whereas filler distribution is filler homogeneity in the resin matrix. Good dispersion and distribution of filler particles in the hosting polymer matrix is desired for maximum properties enhancement. SEM images of selected PS/Magnesia composite samples at different magnifications are shown in Figure 7. SEM images of sample containing 10 wt.% of filler show homogeneous distribution of magnesia particles in polystyrene matrix. In the case of sample containing 15 wt.% of filler, the presence of agglomerations in white colour indicates a difficult dispersion of magnesia particles in polystyrene matrix during the elaboration process.

4. Conclusion

PS/Magnesia composites were investigated as function of magnesia loading level. It is found that magnesia particles are difficult to distributed at 15 wt.%. DSC results

Table 1: Thermal degradation parameters of pure polystyrene and PS/Magnesia composites.

Formulation	IDT (°C)	T_{\max} (°C)	$T_{20\%}$ (°C)	$T_{50\%}$ (°C)	$T_{75\%}$ (°C)	Residue (%)
Pure PS	372.3	426.9	412.4	426.7	437.1	01.6
PS/Magnesia 95/05	388.2	428.9	416.1	430.4	442.6	08.0
PS/Magnesia 90/10	374.8	430.9	416.5	432.0	445.4	10.6
PS/Magnesia 85/15	387.3	432.8	419.0	435.5	452.2	16.6

IDT: initial decomposition temperature: the temperature at 5% of mass loss.²⁴ T_{\max} : the temperature where the maximum weight loss rate occurred, this temperature is determined from DTG thermogram. $T_{20\%}$: the temperature at 20 % of mass loss. $T_{50\%}$: the temperature at 50 % of mass loss. $T_{75\%}$: the temperature at 75 % of mass loss. **Residue**: the final amount after the end of the heating.

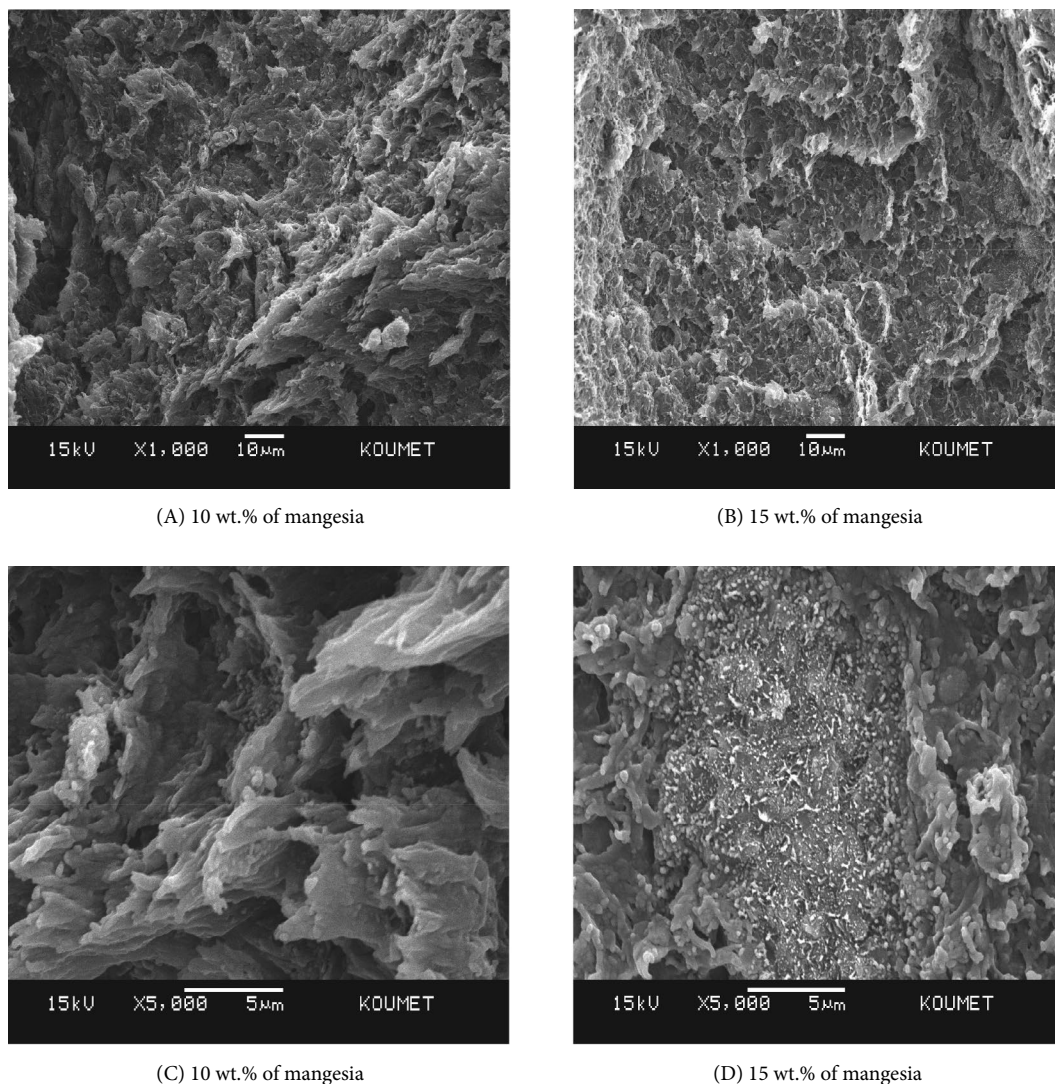


Figure 7: SEM micrographs of PS/Magnesia composites with respect to magnesia loading level (Magnification; $\times 1000, \times 5000$).

revealed that the glass transition temperature T_g of polystyrene matrix was not affected by filler addition. Thermal degradation data showed that the incorporation of magnesia particles has a positive effect on thermal stability of the composites under investigation where T_{max} increased from 426.9 to 432.8 °C and the final residue increased from 1.6 to 16.6 %. DMA results showed that storage modulus increased after introducing magnesia particles. Contact angle measurements indicated that the presence of magnesia particles changed the nature of polystyrene surface from hydrophobic to hydrophilic where the average contact angle decreased from 91.5 to 75.5° after 15 wt.%.

5. References:

1. L. Peng, Y. Deng, P. Yiand, X. Lai, *Micromech. Microeng.* **2014**, *24*, 1–8. DOI:10.1088/0960-1317/24/1/013001
2. E. Youcef, R. Haddad, *SpringerPlus.* **2013**, *2*, 1–32. DOI:10.1186/2193-1801-2-1
3. J. A. Chinn, T. A. Horbett, B. D. Ratner, *Journal of Tissue Culture Methods.* **1994**, *16*, 155–159. DOI:10.1007/BF01540643
4. R. C. Thompson, C. J. Moore, F. S. V. Saal, S. H. Swan, *Philos Trans R Soc Lond B Biol Sci.* **2009**, *364*, 2153–2166. DOI:10.1098/rstb.2009.0053
5. S. E. Hachani, A. Meghezzi, M. Slimani, N. Nebbache, *Int. J. Chem. Sci.* **2016**, *14*, 1236–1242.
6. Q. Zhu, F. Wu, Q. Yang, J. Wang, W. Chen, *Journal of Wuhan University of Technology-Mater. Sci. Ed.* **2010**, *25*, 780–784.
7. K. Kinoshita, N. Matsunaga, M. Hiraoka, H. Yanagimoto, H. Minami, *RSC Adv.*, **2014**, *4*, 8605–8611.
8. Y. Jia, Z. Jiang, J. Peng, X. Gong, Z. Zhang, *Composites Part A.* **2012**, *43*, 1561–1568. DOI:10.1016/j.compositesa.2012.04.011
9. O. Bera, B. Pili, J. Pavličević, M. Jovičić, B. Holló, K. Mészáros

- Szécseyi, M. Špirkova, *Thermochimica Acta*. **2011**, *515*, 1–5. DOI:10.1016/j.tca.2010.12.006
10. S. P. Thomas, S. Thomas, R. Abraham, S. Bandyopadhyay, *EXPRESS Polymer Letters*. **2008**, *2*, 528–538. DOI:10.3144/expresspolymlett.2008.63
11. N. Donato, D. Aloisio, M. Latino, A. Bonavita, D. Spadaro, G. Neri, *Sensors and Microsystems*. **2012**, *109*, 67–71. DOI:10.1007/978-1-4614-0935-9_12
12. A. Michas, P. Millet, *Journal of Membrane Science*. **1991**, *61*, 157–165. DOI:10.1016/0376-7388(91)80012-U
13. A. Malik, A. Sêco, E. Fortunato, R. Martins, *Journal of Non-Crystalline Solids*. **1998**, 227–230, 1092–1095. DOI:10.1016/S0022-3093(98)00248-8
14. O. Pachoumi, C. Li, Y. Vaynzof, K. K. Banger, H. Sirringhaus, *Advanced Energy Materials*. **2013**, *3*, 1428–1436. DOI:10.1002/aenm.201300308
15. R. Kumar, A. Sharma, N. Kishore, *International Journal of Engineering, Applied and Management Sciences Paradigms*. **2013**, *7*, 66–70.
16. F. Gu, C.Z. Li, H.B. Jiang, *J. Cryst. Grow*. **2006**, *289*, 400–404. DOI:10.1016/j.jcrysgro.2005.11.116
17. H. Saitoh, Y. Okada, S. Ohshio, *J. Mater. Sci*. **2002**, *37*, 4597–4602. DOI:10.1023/A:1020696215411
18. S. Gandhi, P. Abiramipriya, N. Pooja, J. Juliat, L. Jeyakumari, A. Y. Arasi, V. Dhanalakshmi, M. R. G. Nair, R. Anbarasan, *Journal of Non-Crystalline Solids*. **2011**, *357*, 181–185. DOI:10.1016/j.jnoncrysol.2010.09.050
19. L. Ibarra, M. Alzorriz, *Journal of Applied Polymer Science*. **2007**, *103*, 1894–1899. DOI:10.1002/app.25411
20. J. Przepiorski, J. Karolczyk, T. Tsumura, M. Toyoda, M. Inagaki, A. W. Morawski, *J Therm Anal Calorim*. **2012**, *107*, 1147–1154. DOI:10.1007/s10973-011-1910-1
21. J. Wang, L. Fan, S. Xu, M. Zeng, Q. Liu, *Acta Materiae Compositae Sinica*. **2011**, *28*, 65–70.
22. S. Yu, P. Hing, *Journal of Applied Polymer Science*. **2000**, *78*, 1348–1353. DOI:10.1002/1097-4628(20001114)78:7<1348::AID-APP50>3.0.CO;2-V
23. G. Lamour, A. Hamraoui, A. Buvailo, Y. Xing, S. Keuleyan, V. Prakash, A. Eftekhari-Bafrooei, E. Borguet, *Journal of Chemical Education*. **2010**, *87*, 1403–1407. DOI:10.1021/ed100468u
24. M. Worzakowska, *J Therm Anal Calorim*. **2015**, *121*, 235–243. DOI:10.1007/s10973-015-4547-7

Povzetek

V tej študiji smo raziskovali učinke delcev MgO na termične, mehanske, morfološke in površinske lastnosti polistirenske smole. Na splošno dodajanje delcev MgO v polistirenski matriks poveča toplotno stabilnost, modul shranjevanja in omočljivost, na drugi strani pa ne vpliva na molekularno mobilnost. Rezultati vrstične elektronske mikroskopije (SEM) so pokazali omejeno porazdelitev delcev MgO v polistirenskem matriksu (masni odstotek MgO = 15 %).

Scientific paper

SR&NI Atom Transfer Radical Random Copolymerization of Styrene and Methyl Methacrylate: Incorporation of Diatomite Platelets

Khezrollah Khezri,¹ Hassan Alijani² and Yousef Fazli³¹ Young Researchers and Elite Club, Central Tehran Branch, Islamic Azad University, Tehran, Iran² Department of Chemistry, Faculty of Science, Shahid Chamran University, Ahvaz, Iran³ Department of Chemistry, Faculty of Science, Arak Branch, Islamic Azad University, Arak, Iran, P.O. Box 14155-6455, Tel: +988633412603

* Corresponding author: E-mail: yousef.fazli75@gmail.com, y-fazli@iau-arak.ac.ir

Received: 10-03-2018

Abstract

Mesoporous diatomite platelets were employed to prepare various random poly (styrene-co-methyl methacrylate)/diatomite composites by *in situ* simultaneous reverse and normal initiation technique for atom transfer radical random copolymerization (SR&NI ATRP) technique. Nitrogen adsorption/desorption isotherm, SEM and TEM were employed for evaluating some inherent properties of the pristine diatomite platelets. Conversion and molecular weight determinations were carried out using GC and SEC respectively. Addition of 3 wt% diatomite platelets leads to increase of conversion from 76 to 92%. Molecular weight of poly (styrene-co-methyl methacrylate) chains increases from 12893 to 14907 g mol⁻¹ by addition of 3 wt% mesoporous diatomite; however, polydispersity index values increases from 1.18 to 1.44. Copolymers composition was evaluated using ¹H NMR spectroscopy. Increasing thermal stability of the nanocomposites is demonstrated by TGA. Differential scanning calorimetry shows an increase in glass transition temperature from 67.6 to 73.4 °C by adding 3 wt% of mesoporous diatomite platelets.

Keywords: Nanocomposite; random poly (styrene-co-methyl methacrylate); mesoporous diatomaceous earth platelets; *In situ* SR&NI ATRP

1. Introduction

During the last decades, polymer based nanocomposites have attracted much attention in the industrial and academia.¹⁻² Addition of low volume of nano-filler in the polymer matrix results in considerable improvements in several properties (such as thermal and mechanical properties).²⁻³ Nanocomposites as a novel class of materials present unique features that are not shared by traditional composites. Nanocomposites can simultaneously present useful properties of organic phase (e.g., flexibility, ductility, and processability) and nano-inorganic phase (e.g., rigidity and thermal stability).⁴⁻⁵ Nanocomposites can be categorized into three main types depending on the number of nanometer regimes of the dispersed filler(s); a) three dimensions are in the order of nanometers such as spherical silica nanoparticles. b) two dimensions are in the nanometer scale such as nanotubes or whiskers.

c) one dimension in the nanometer range such as clay platelets.⁶⁻⁷ Melt intercalation, solution blending, and *in situ* polymerization are three famous pathways to prepare polymer nanocomposites that the latter consists of polymerization of monomer(s) in the presence of nano-fillers.⁸⁻⁹

Diatomite or diatomaceous earth is the fossilised remains of single cell photosynthetic aquatic algae that can be found in large quantities in marine and fresh-water systems. Diatomite is mainly consists of amorphous silica (SiO₂·nH₂O) that is originated from opalescent frustules of diatoms. Diatomite is classified as non-crystalline opal-A according to the mineralogical classification.¹⁰⁻¹² Although amorphous silica is the main component of the diatomite, it contains some impurities such as certain minerals and chemicals (especially alumina and ferric oxide).¹³⁻¹⁴ Diatomite is an insulator and non-inflammable, insoluble in water and contains up to 80–90% voids in its

structure. Diatomite can be easily obtained at a low cost because diatomaceous silica is the most abundant form of silica on the earth.^{12,15–16} Diatomaceous earth possesses highly porous structure, low density, high surface area, suitable stability in chemical property, high permeability and small particle size in which makes it suitable for a wide range of industrial applications such as filter aid, adsorbent, insulating material, catalyst support or carrier, natural insecticide or grain protectant and etc.^{14,16–18}

Controlled radical polymerization (CRP) techniques are investigated to introduce suitable pathways for the preparation of various polymers with predetermined molecular weight, narrow polydispersity index (PDI) values, desired composition and functionalities. Among three most common CRP methods, which are namely nitroxide-mediated polymerization (NMP)¹⁹, reversible addition fragmentation chain transfer (RAFT),²⁰ and atom transfer radical polymerization (ATRP),²¹ ATRP presents some unique benefits such as applicability to a wide variety of monomers and polymerization systems, great industrialization prospects, commercial availability of its reactants and also application of different initiation technique.²¹ These unique features lead to ATRP becomes as a popular producer for polymer chemists.

A review of literatures indicates that application of diatomite as filler to synthesize polymer/diatomite composites have attracted considerable attention. Karaman et al. have prepared polyethylene glycol (PEG)/diatomite composite as a novel form-stable composite phase change material (PCM) in which the PCM was prepared by incorporating PEG in the pores of diatomite.²² Li et al. have synthesized conducting diatomite by polyaniline on the surface of diatomite. Linkage of polyaniline on the surface of diatomite is attributed to the hydrogen bond between the surface of diatomite and polyaniline macromolecules.²³ Li et al. have also prepared fibrillar polyaniline/diatomite composite by one-step in situ polymerization. According to their results, the polyaniline/diatomite composite can be applied as fillers for electromagnetic shielding materials and conductive coatings.²⁴ In addition, other studies such as investigating the effects of extrusion conditions on die-swell behavior of polypropylene/diatomite composite melts and crystallization behaviors and foaming properties of diatomite-filled polypropylene composites have been performed.^{25–26}

In this study, we take unique advantages of simultaneous reverse and normal initiation technique for atom transfer radical polymerization (SR&NI ATRP) method to synthesize random poly (styrene-co-methyl methacrylate)/diatomite nanocomposites. Among different initiation techniques for ATRP, an interesting initiation technique namely SR&NI was employed to prepare tailor-made polymer matrices. SR&NI ATRP is selected for its abundant advantages such as application of transition metal complex in its high oxidation state and decrement of metal concentration in the final products. Moreover, we have

tried to investigate the effect of diatomite platelets loading on the kinetics parameters (conversion, molecular weights, and PDI values) of the SR&NI ATRP of styrene and methyl methacrylate. Evaluation of diatomite platelets as an appropriate replacement of natural clay platelets is also performed by examining thermal properties of the prepared nanocomposites.

2. Experimental

2.1. Materials

Diatomite earth sample was obtained from Kamel Abad-Azerbaijan, Iran. It was dispersed in 100 ml distilled water by magnetic stirring and then it was kept constant until some solid impurities were dispersed. The particles were separated with filter paper and dried at 100 °C for 8 h. Styrene (St, Aldrich, 99%) and methyl methacrylate (MMA, Merck, 99%) were passed through an alumina-filled column, dried over calcium hydride, and distilled under reduced pressure (60 °C, 40 mm Hg). Copper(II) bromide (CuBr₂, Fluka, 99%), N,N,N',N'',N''-pentamethyldiethylenetriamine (PMDETA, Aldrich, 99%), 2,2'-azobisisobutyronitrile (AIBN, Acros), ethyl alpha-bromoisobutyrate (EBiB, Aldrich, 97%), anisole (Aldrich, 99%), tetrahydrofuran (THF, Merck, 99%), and neutral aluminum oxide (Aldrich, 99%) were used as received.

2.2. Simultaneous Reverse and Normal Initiation Technique for Atom Transfer Radical Random Copolymerization of Styrene and Methyl Methacrylate

SR&NI ATRP of styrene and methyl methacrylate was performed in a 200 ml three-neck lab reactor, which equipped with a reflux condenser, nitrogen inlet valve, and a magnetic stir bar that was placed in an oil bath. A typical batch of copolymerization was run at 110 °C with the molar ratio of 150:0.12:0.2:0.2:1 for [M]:[AIBN]:[CuBr₂]:[PMDETA]:[EBiB] giving a theoretical copolymer molecular weight of 15320 g mol⁻¹ at 100% conversion. At first, styrene (8.34 ml, 0.07 mol), methyl methacrylate (6.2 ml, 0.05 mol), CuBr₂ (0.05 g, 0.23 mmol), PMDETA (0.04 ml, 0.23 mmol) and anisole (10 ml) were added to the reactor. Then, it was degassed and back-filled with nitrogen three times, and then left under N₂ with stirring at room temperature. The solution turned green color since the CuBr₂/PMDETA complex was formed. When the majority of the metal complex had formed, reaction temperature was increased to 110 °C during 5 min. Subsequently, predeoxygenated solution of AIBN (0.02 g, 0.14 mmol) in styrene (5 ml, 0.04 mol) and predeoxygenated EBiB (0.17 ml, 1.1 mmol) were injected into the reactor to start the copolymerization reaction. Samples were taken at the end of the reaction to measure the final conversion.

2. 3. Preparation of Random Poly (Styrene-Co-Methyl Methacrylate)/Diatomite Nanocomposites Via *In Situ* SR&NI ATRP

For preparation of nanocomposites, a desired amount of diatomite platelets was dispersed in 5 ml of styrene and the mixture was stirred for 23 h. Then, the remained 3.34 ml of styrene was added to the mixture. Subsequently, copolymerization procedure was applied accordingly. Designation of the samples with the percentage of pristine diatomite platelets is presented in table 1. In this designation, NPSM refers to neat random poly (styrene-co-methyl methacrylate) and RPSMN "X" implies different nanocomposites of random poly (styrene-co-methyl methacrylate) with various percentages of diatomite platelets loading.

Sample	Method of Preparation	Proportion of Pristine Diatomite Platelets (wt%)	Dispersion Time Prior to the Copolymerization (h)
NPSM	SR&NI ATRP	0	–
RPSMN 1	<i>In situ</i> SR&NI ATRP	1	23
RPSMN 2	<i>In situ</i> SR&NI ATRP	2	23
RPSMN 3	<i>In situ</i> SR&NI ATRP	3	23

2. 4. Separation of Random Copolymer Chains from Diatomite Platelets and Catalyst Removal

For separating of random poly (styrene-co-methyl methacrylate) chains from diatomite particles, nanocomposites were dissolved in THF. By high-speed ultracentrifugation (10000 rpm) and then passing the solution through a 0.2 micrometer filter, poly (styrene-co-methyl methacrylate) chains were separated from diatomite particles. Subsequently, copolymer solutions passed through an alumina column to remove catalyst species.

2. 5. Characterization

Materials porosity was characterized by N₂ adsorption/desorption curves obtained with a Quntasurb QS18 (Quntachrom) apparatus. Surface morphology of the pristine diatomite particles was examined by scanning electron microscope (SEM, Philips XL30 and LEO-1455VP) with acceleration voltage of 20 kV and transmission electron microscope (TEM), Philips EM 208 (The Netherlands) with an accelerating voltage of 120 kV. Gas chromatography (GC) is a simple and highly sensitive characterization method and does not require removal of the metal catalyst particles. GC was performed on an Agilent-6890N with a split/splitless injector and flame ionization detector, using a 60 m HP-IN-

NOWAX capillary column for the separation. Size exclusion chromatography (SEC) was used to measure the molecular weight and molecular weight distribution. A Waters 2000 ALLIANCE with a set of three columns of pore sizes of 10000, 1000, and 500 Å was utilized to determine polymer average molecular weight and PDI values. Proton nuclear magnetic resonance spectroscopy (¹H NMR) spectra were recorded on a Bruker 300-MHz ¹H NMR instrument with CDCl₃ as the solvent and tetramethylsilane as the internal standard. Thermal gravimetric analysis (TGA) was carried out with a PL thermo-gravimetric analyzer (Polymer Laboratories, TGA 1000, UK). Thermal analysis were carried out using a differential scanning calorimetry (DSC) instrument (NETZSCH DSC 200 F3, Netzsch Co, Selb/Bavaria, Germany).

3. Results and Discussion

FTIR analysis of the pristine diatomite platelets indicates that although the pristine diatomite platelets are rehydrated, during the preparation process and obtaining the spectrum some water molecules may be re-adsorbed (3434 cm⁻¹). In this spectrum, the strong peak at 1098

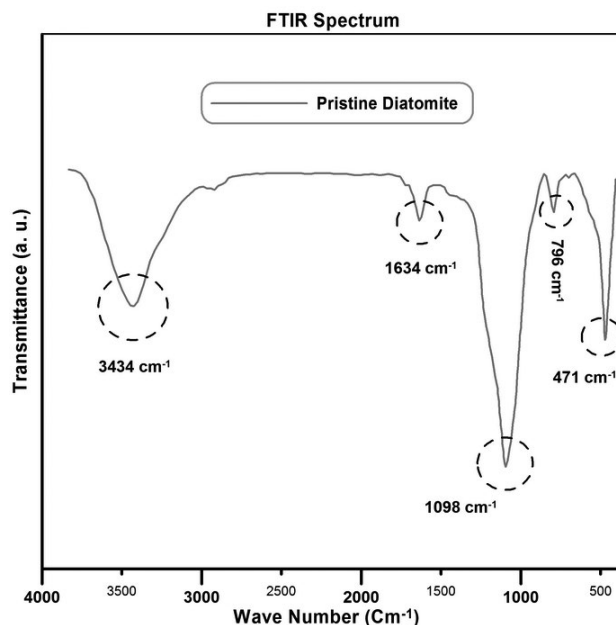


Figure 1: FTIR spectrum of the pristine diatomite sample

cm^{-1} is attributed to the stretching mode of siloxane (Si–O–Si). In addition, the peak at 471 cm^{-1} and 796 cm^{-1} are associated with the asymmetric stretching mode of siloxane bonds the vibration of O–H respectively.^{27–29}

Nitrogen adsorption/desorption isotherm is employed to precise study on the porous structure of the diatomite platelets. Nitrogen adsorption/desorption isotherm of the diatomite platelets is provided in figure 2. According to this figure, the shape of isotherm is similar to the IV type isotherms according to the IUPAC classification and confirms that diatomite platelets have mesoporous structure.^{30–31} The hysteresis is associated with the filling and emptying of the mesopores by capillary condensation. A sharp increase in the nitrogen adsorbed quantity near the relative pressure of 1 demonstrates the existence of macropores in the pure diatomite platelets and therefore non-uniform pore size distribution can be concluded.³²

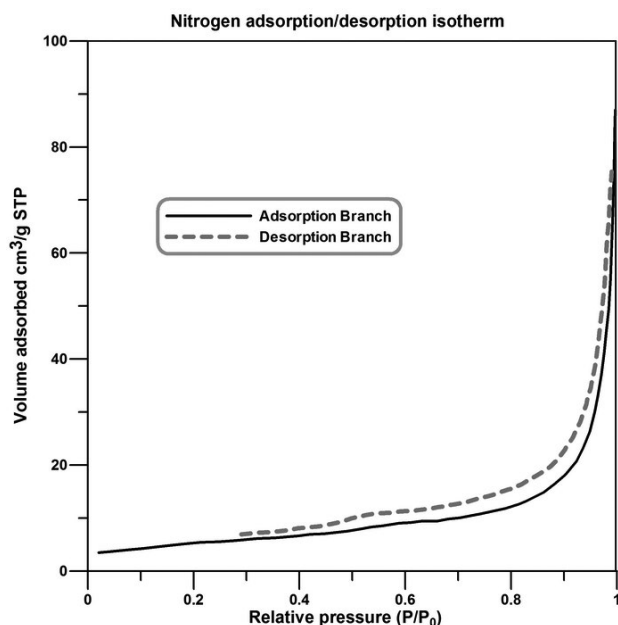


Figure 2: Nitrogen adsorption/desorption isotherm of the pristine diatomite sample

According to extracted data from the nitrogen adsorption/desorption isotherms, surface area of the pristine diatomite platelets is calculated $20.409\text{ m}^2/\text{g}$. Also, average pore diameter is estimated around 28.13 nm .

SEM image of the pristine diatomite platelets is shown in figure 3. According to this image, diatomite sample is composed of plaque plate particles with spherical pores. These plates have regular pores and sometimes are aggregated.

Figure 4 represents TEM image of the pristine diatomite platelets. According to this image, pristine diatomite sample belongs numerous regularly spaced rows of pores in its structure that this observation is confirmed with SEM images. In addition, average pore diameter is estimated around 45 nm .

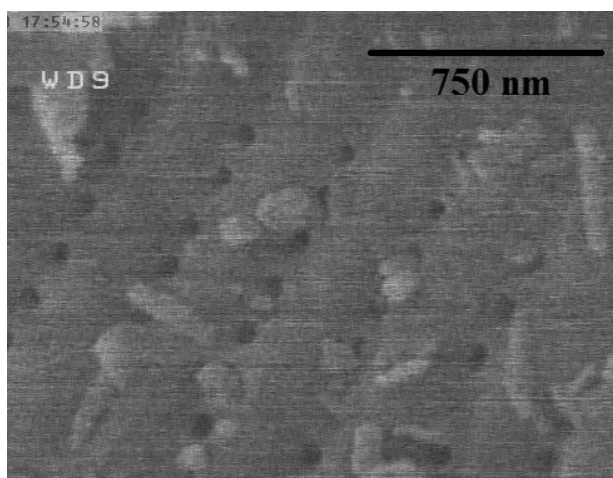


Figure 3: SEM image of the pristine diatomite sample

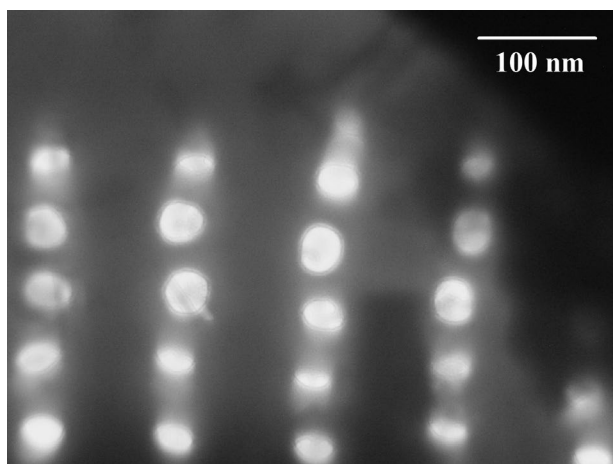


Figure 4: TEM image of the pristine diatomite sample

General mechanism for SR&NI ATRP is illustrated in figure 5. SR&NI ATRP employs transition metal complex in its high oxidation state and therefore by using this initiation technique oxidation problems can be circumvented.

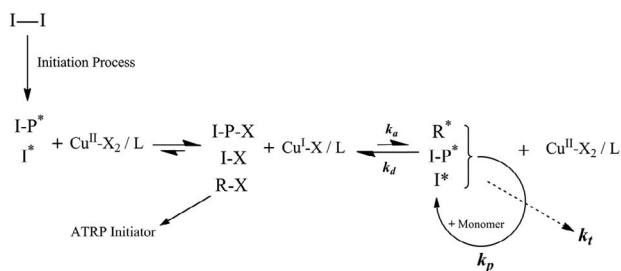


Figure 5: General mechanism for SR&NI ATRP

General procedure for the synthesis of well-defined random poly (styrene-co-methyl methacrylate) chains via SR&NI ATRP in the presence of the diatomite platelets is illustrated in figure 6.

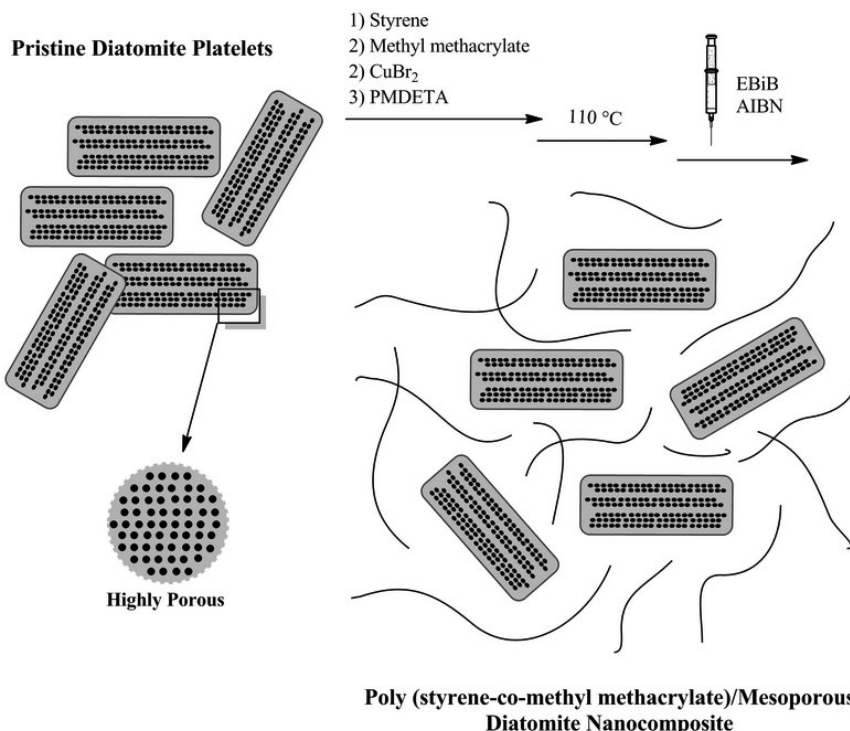


Figure 6: General procedure for the synthesis of well-defined random poly(styrene-co-methyl methacrylate)/diatomite nanocomposites via *in situ* SR&NI ATRP

Although reverse ATRP (RATRP) is a suitable pathway for circumventing oxidation problems (application of transition metal complex in its high oxidation state), SR&NI ATRP presents additional useful properties and therefore can be considered a more appropriate pathway to overcome oxidation problems. SR&NI ATRP applies low-

er metal concentration in its initial components and therefore lower concentration of transition metals will be existed in the final products.³³

SEC traces of the neat random poly(styrene-co-methyl methacrylate) and its different nanocomposites are presented in figure 7. As it can be seen, SEC traces of the neat random poly(styrene-co-methyl methacrylate) and all of the nanocomposites display monomodal peaks corresponding to the molecular weight values predetermined by the molar ratio of monomer to initiator. Neat random poly(styrene-co-methyl methacrylate) reveals narrow distribution and relatively low PDI value in which this result can be employed to demonstrate successful establishment of SR&NI ATRP.

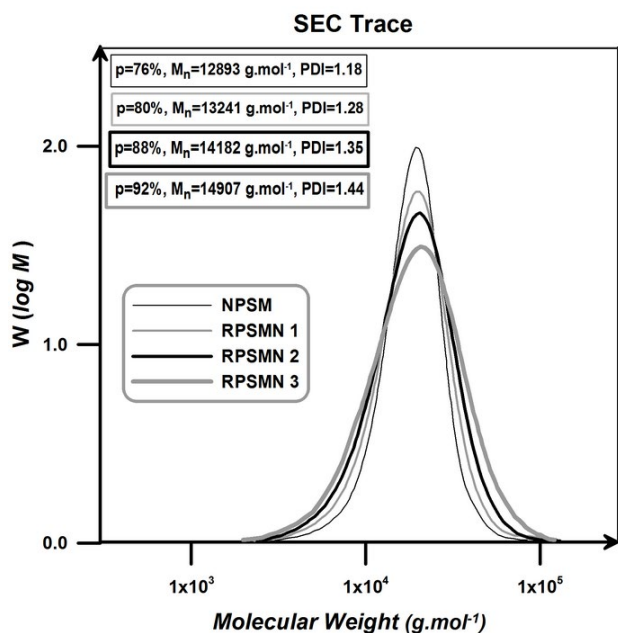


Figure 7: SEC traces of the neat random poly(styrene-co-methyl methacrylate) and its nanocomposites

SR&NI ATRP of styrene and methyl methacrylate without diatomite platelets results in well-defined random copolymer chains with low PDI value. By adding diatomite platelets, conversion and molecular weight were increased. By addition of only 3 wt% of the diatomite platelets, conversion increases from 76 to 92%. Increments of conversion and molecular weight of the products by adding diatomite platelets can be attributed to the pendant hydroxyl groups on the surface (and pores) of the diatomite platelets. In general, polar solvents (especially hydroxyl containing ones like water, phenol, and carboxylic acids) exert a rate acceleration effect on the copolymerization systems for increasing radical activation rate and also reducing radical recombination rate. Pendant hydroxyl groups on the surface (and pores) of the diatomite platelets can possibly cause a polarity change into the reaction medium. In

addition, negatively charged surface (pendant hydroxyl groups on the surface of the diatomite platelets) could absorb and gather positively charged catalyst (Cu ions) and consequently enhances the chain growth rate. Similar effects for adding other nano-fillers such as clay nano-sheets and MCM-41 nanoparticles on polymerization rate were also presented elsewhere.^{34–35} PDI values of the random poly (styrene-co-methyl methacrylate) chains increases by the addition of diatomite platelets loading. This is mainly attributed to the impurity role of the diatomite platelets. These platelets act as an impurity in the copolymerization medium and therefore cause the molecular weight distribution of the resultant copolymers to be increased; PDI value increases from 1.18 to 1.44 by loading of 3 wt% diatomite platelets.³⁶ Extracted data from SEC traces of the neat random poly (styrene-co-methyl methacrylate) and its nanocomposites is summarized in table 2.

By comparing these results with the previous study some useful conclusions can be obtained; *a*) Application of reverse atom transfer radical polymerization (RATRP) results in higher conversion in the same loadings of diatomite platelets. *b*) It is very interesting that variation of the final conversion by addition of 3 wt% of diatomite is equal for both of the systems (16% increment in conversion by adding 3 wt% of diatomite). *c*) Both of the systems present similar behavior in the case of the variation of the molecular weights. *d*) As it expected, application of SR&NI ATRP results in lower PDI values in comparison with RATRP. *f*) According to the PDI values, SR&NI ATRP system results in higher variation in PDI values by addition of diatomite platelets in comparison with the RATRP system.³⁷

Theoretical molecular weight is calculated by using Equation 1:

$$M_n^{Theo} = \frac{[M]_0}{[AIBN]_0} \times Conv. \times M_{monomers} \quad (1)$$

where, $[M]_0$ and $[AIBN]_0$ are initial concentration of the monomers and ATRP initiator, respectively. Conversion is denoted by *Conv.* and the symbol of the average molecular weight of the monomers is $M_{monomers}$.

An appropriate agreement between the theoretical and experimental molecular weights in combination with acceptable PDI values (PDI < 1.5) can be considered as an appropriate evidences for controlled nature of the copolymerization. Also, color change of the reaction media dur-

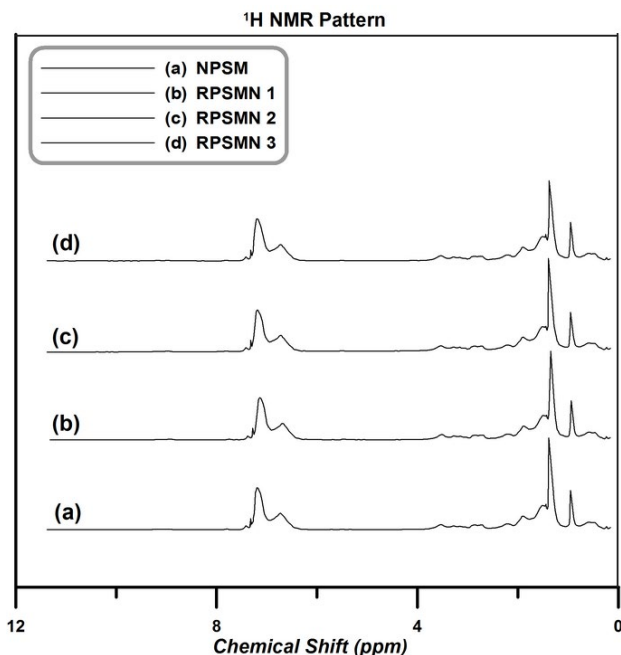


Figure 8: ¹H NMR spectra of the neat poly (styrene-co-methyl methacrylate) and its nanocomposites

ing the copolymerization is an evidence of successful SR&NI ATRP equilibrium establishment.

Evaluation of the structural composition of copolymer chains and determining molar ratio of each monomer in the copolymer chains can be performed by using ¹H NMR spectroscopy. ¹H NMR spectra of the neat poly (styrene-co-methyl methacrylate) and its different nanocomposites are presented in figure 8.

Molar ratio of each monomer in the copolymer chains can be determined by integrating aromatic peaks area (D_{Ph} , 6.6–7.4 ppm, 5H) which corresponds to the phenyl ring of styrene and methoxy group of methyl methacrylate (D_M , 3.4–3.8 ppm, 3H) by using equations (2) and (3):

$$\%St = \frac{D_{Ph}}{\left(\frac{D_{Ph}}{5} + \frac{D_M}{3}\right)} \times 100 \quad (2)$$

$$\%MMA = \frac{D_M}{\left(\frac{D_{Ph}}{5} + \frac{D_M}{3}\right)} \times 100 \quad (3)$$

Table 2: Molecular weights and PDI values of the extracted random poly (styrene-co-methyl methacrylate) chains resulted from SEC traces

Sample	Reaction Time (h)	Conversion (%)	M_n (g mol ⁻¹)		M_w (g mol ⁻¹)	PDI
			Exp.	Theo.		
NPSM	10	76	12893	11643	15214	1.18
RPSMN 1	10	80	13241	12256	16948	1.28
RPSMN 2	10	88	14182	13482	19146	1.35
RPSMN 3	10	92	14907	14094	21466	1.44

The extracted data from ^1H NMR spectrum of the neat poly (styrene-co-methyl methacrylate) and its nanocomposites is summarized in table 3. According to the results, molar ratio of each monomer (styrene and methyl methacrylate) in all the samples is approximately similar to the initial selected mole ratio of the monomers (styrene: ~66.6% and methyl methacrylate: ~33.3%).

Table 3: Extracted data from ^1H NMR spectroscopy analysis of the pure poly (styrene-co-methyl methacrylate) and its nanocomposites

Sample	Mole Ratio (%)	
	St	MMA
NPSM	65	35
RPSMN 1	68	32
RPSMN 2	64	36
RPSMN 3	66	34

Thermal stability of the neat poly (styrene-co-methyl methacrylate) and its various nanocomposites are studied by using TGA analysis. TGA thermograms of weight loss as a function of temperature in the temperature range of 25–700 °C in tow different styles are represented in figure 9. Char values of the samples (at 700 °C) are also provided in this figure. As it is expected, char values increase by increasing diatomite platelets content. In addition, pristine diatomite leaves 92.13% char after complete degradation at 700 °C.

According to the figure 9, thermal stability of the neat poly (styrene-co-methyl methacrylate) is lower than all of the nanocomposites. In addition, by adding diatomite platelets in the poly (styrene-co-methyl methacrylate) matrix, thermal stability of the neat poly (sty-

rene-co-methyl methacrylate) is improved. Moreover, by increasing diatomite platelets content in the nanocomposites samples (RPSMN 1-3), an increase in degradation temperatures was observed. Each TGA thermograms can be divided into three separated degradation steps; *i*) the weight loss at the temperature range of 100–150 °C is attributed to the evaporation of the water molecules. *ii*) the weight loss at the temperature window around 180–350 °C is ascribed by degradation of volatile materials (such as residual monomer and low molecular weight oligomers). *iii*) the final weight loss at the temperatures above 380 °C is attributed to the degradation of the synthesized poly (styrene-co-methyl methacrylate) chains and nanocomposites.^{38–40} Extracted data from TGA curves are summarized in table 4.

Table 4: Extracted data from TGA curves for the neat copolymer and its nanocomposites

Sample	Char (%) at 700 °C	The main decomposition step (°C)	
		Initial point	Final point
NPSM	3.04	331	442
RPSMN 1	4.54	334	446
RPSMN 2	5.81	339	452
RPSMN 3	6.79	345	459
Diatomite	92.13	–	–

Figure 10 graphically illustrates the extracted data from TGA graphs. Degradation temperature of the samples versus amount of degradation is employed to show that addition of diatomite platelets in the poly (styrene-co-methyl methacrylate) matrix, results in an improvement of thermal stabilities of the nanocomposites

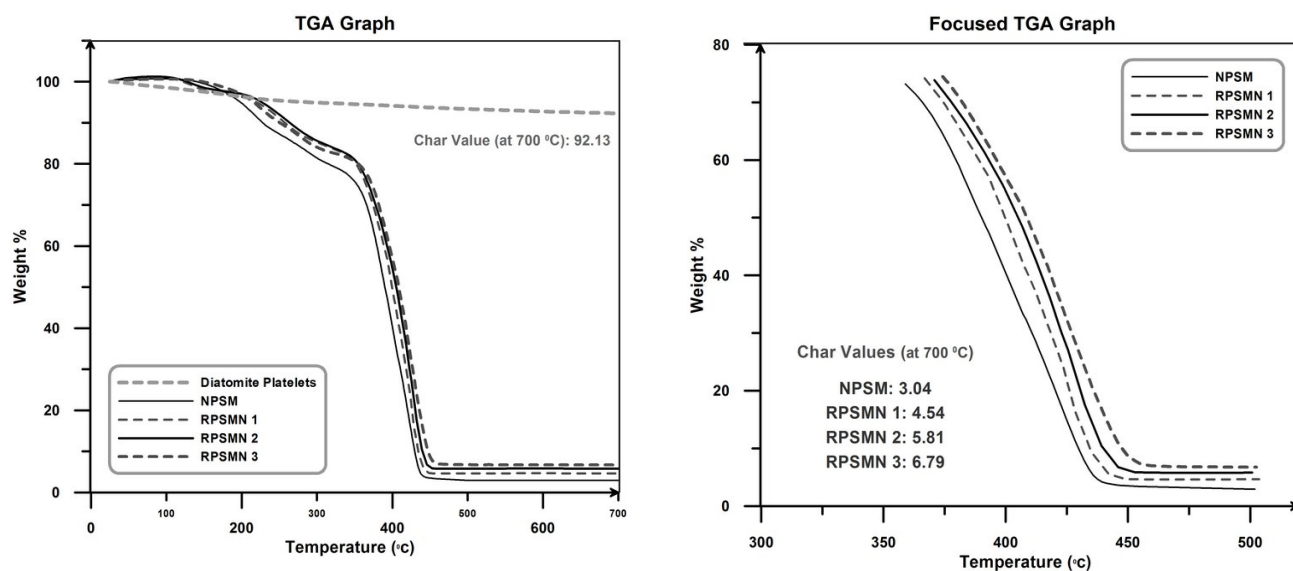


Figure 9: TGA curves of the neat poly (styrene-co-methyl methacrylate) and its nanocomposites in two different styles

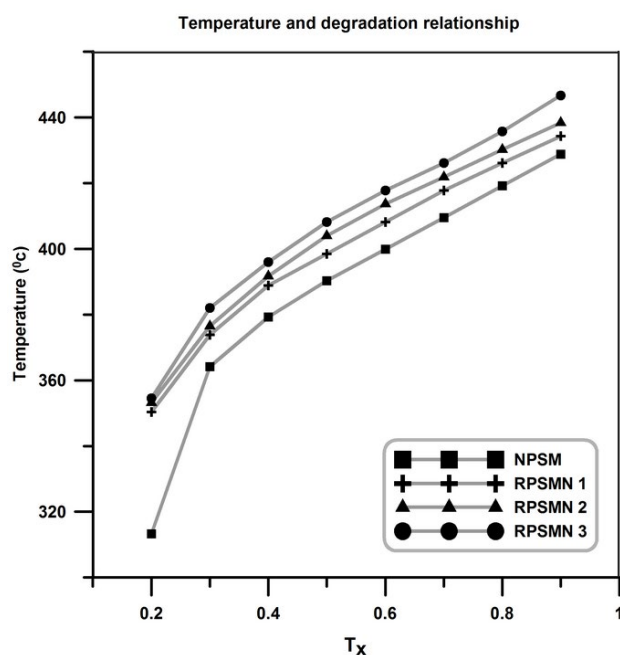


Figure 10: Graphical illustration of temperature and degradation relationship

(T_x : temperature threshold at which X% of poly (styrene-co-methyl methacrylate) and its nanocomposites is degraded).

Improvement in thermal stability of the synthesized sample can be mainly attributed to the high thermal stability of the pristine diatomite platelets and also physical interaction between surface of them and poly (styrene-co-methyl methacrylate) chains. It is clear that by increasing diatomite platelets content, more improvements in thermal stability can be achieved.^{41–42} Moreover, hindrance effect of the diatomite platelets on the copolymer chains movement and restriction of oxygen permeation by these sheets are the other reasons for higher thermal stability of the nanocomposites in comparison with the neat poly (styrene-co-methyl methacrylate). Similar conclusions are also achieved in the case of polymer/clay nanocomposites.^{43–44}

DSC analysis is employed to evaluate the effect of diatomite platelets on the chain confinement of the neat poly (styrene-co-methyl methacrylate) and its nanocomposites and also determination of glass transition temperature (T_g) of the prepared samples. DSC curves of the neat poly (styrene-co-methyl methacrylate) and its different nanocomposites are presented in figure 11. Temperature range of 20–200 °C is used to describe DSC results in the heating path. Diatomite platelets do not bear any transitions in this range of temperature, therefore only thermal transition of random poly (styrene-co-methyl methacrylate) is observed. In these experiments, samples are heated from room temperature to 220 °C to remove their thermal history. Then, they cooled to room temperature to distinguish

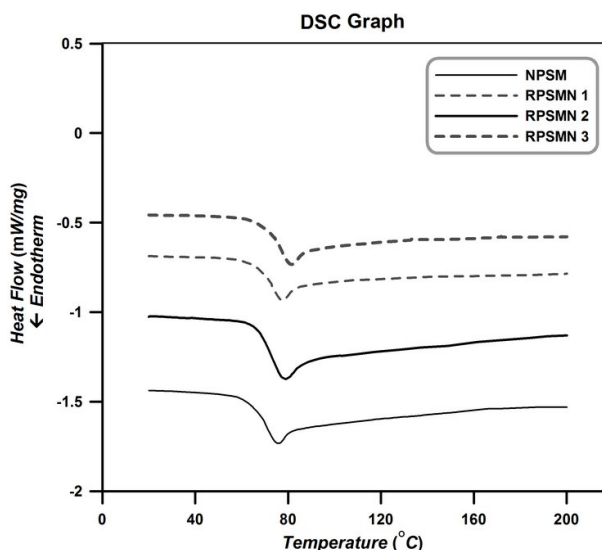


Figure 11: DSC curves of the neat poly (styrene-co-methyl methacrylate) and its nanocomposites

the phase conversion and other irreversible thermal behaviors. Finally, samples are heated from room temperature to 220 °C to obtain T_g values.

As it can be seen in figure 11, an obvious inflection in the heating path is occurred in which shows T_g of the neat random poly (styrene-co-methyl methacrylate) and its various nanocomposites. Corresponding inflection in the cooling path is also appeared. Since there is not another peak in the cooling path, amorphous structure of the synthesized random poly (styrene-co-methyl methacrylate) and its nanocomposites can be concluded. Table 5 summarized the extracted T_g values of the samples from DSC curves.

Table 5: Extracted T_g of the neat random poly (styrene-co-methyl methacrylate) and its nanocomposites

Sample	M_n (g mol ⁻¹)	PDI	T_g (°C)
NPSM	12893	1.18	67.6
RPSMN 1	13241	1.28	69.5
RPSMN 2	14182	1.35	71.1
RPSMN 3	14907	1.44	73.4

According to the table 5, T_g value of the nanocomposites (RPSMN 1-3) is higher than neat poly (styrene-co-methyl methacrylate). In addition, an increase in T_g values is obtained by increasing of diatomite platelets content. Increasing T_g values by adding diatomite platelets content in the copolymer matrix can be attributed to the confinement effect of the diatomite platelets. The rigid two-dimensional diatomite platelets can restrict the steric mobility of the random poly (styrene-co-methyl meth-

acrylate) chains and causes the inflection in the DSC curves starts at higher temperatures. Similar conclusions are also reported in the case of polymer/clay nanocomposites.^{43–44}

4. Conclusions

In situ SR&NI ATRP of styrene and methyl methacrylate in the presence of 3 wt% of mesoporous diatomite platelets leads to increment of conversion and molecular weight from 76 to 92% and 12893 to 14907 g mol⁻¹ respectively. Thus it can be concluded that addition of diatomite platelets results in positive effects on the copolymerization and by addition of diatomite in the copolymerization media, copolymers with higher molecular weight can be achieved. Meanwhile PDI value increases from 1.18 to 1.44. Increment of PDI values indicates that diatomite platelets (such as other nano-fillers) can act as an impurity in the polymerization media. ¹H NMR spectroscopy results show that copolymers composition is approximately similar to the initial feed ratio of each monomers. Improvement in thermal stability of the nanocomposites and increasing T_g values from 67.6 to 73.4 °C was also observed by incorporation of 3 wt% of the mesoporous diatomite platelets. Thermal studies can appropriately demonstrate that diatomite behaves similar natural clay platelets and therefore can be considered as a suitable replacement for clay platelets.

5. References

- H. Du, G. Q. Xu, W. S. Chin, *Chem. Mater.* **2002**, *14*, 4473–4479. DOI:10.1021/cm010622z
- H. Zou, S. Wu, J. Shen, *Chem. Rev.* **2008**, *108*, 3893–3957. DOI:10.1021/cr068035q
- D. R. Paul, L. M. Robeson, *Polymer* **2008**, *49*, 3187–3204. DOI:10.1016/j.polymer.2008.04.017
- D. W. Schaefer, R. S. Justice, *Macromolecules* **2007**, *40*, 8501–8517. DOI:10.1021/ma070356w
- Q. Nguyen, D. Baird, *Adv. Polym. Technol.* **2006**, *25*, 270–285. DOI:10.1002/adv.20079
- S. L. Burkett, N. Ko, N. D. Stern, J. A. Caissie, D. Sengupta, *Chem. Mater.* **2006**, *18*, 5137–5143. DOI:10.1021/cm0614517
- M. Zanetti, S. Lomakin, G. Camino, *Macromol. Mater. Eng.* **2000**, *279*, 1–9. DOI:10.1002/1439-2054(20000601)279:1<1::AID-MAME1>3.0.CO;2-Q
- S. Varghese, J. Karger-Kocsis, *Polymer* **2003**, *44*, 4921–4927. DOI:10.1016/S0032-3861(03)00480-4
- K. Khezri, V. Haddadi-Asl, H. Roghani-Mamaqani, M. Salami-Kalajahi, *J. Appl. Polym. Sci.* **2012**, *124*, 2278–2286. DOI:10.1002/app.35279
- R. B. Vasani, D. Losic, A. Cavallaro, N. H. Voelcker, *J. Mater. Chem. B* **2015**, *3*, 4325–4329. DOI:10.1039/C5TB00648A
- Z. Jian, P. Qingwei, N. Meihong, S. Haiqiang, L. Na, *Appl. Clay Sci.* **2013**, *83–84*, 12–16.
- P. Yuan, D. Liu, D. Tan, K. Liu, H. Yu, Y. Zhong, A. Yuan, W. Yu, H. He, *Micropor. Mesopor. Mater.* **2013**, *170*, 9–19. DOI:10.1016/j.micromeso.2012.11.030
- Y. Jia, W. Han, G. Xiong, W. Yang, *Sci. Technol. Adv. Mater.* **2007**, *8*, 106–109. DOI:10.1016/j.stam.2006.10.003
- W. T. Tsai, K. J. Hsien, Y. M. Chang, C. C. Lo, *Bioresource Technol.* **2005**, *96*, 657–663. DOI:10.1016/j.biortech.2004.06.023
- Y. Wang, J. Cai, Y. Jiang, X. Jiang, D. Zhang, *Appl. Microbiol. Biotechnol.* **2013**, *97*, 453–460. DOI:10.1007/s00253-012-4568-0
- S. Nenadović, M. Nenadović, R. Kovačević, L. Matović, B. Matović, Z. Jovanović, J. Grbović Novaković, *Sci. Sint.* **2009**, *41*, 309–317. DOI:10.2298/SOS0903309N
- X. Qi, M. Liu, Z. Chen, R. Liang, *Polym. Adv. Technol.* **2007**, *18*, 184–193. DOI:10.1002/pat.847
- Y. S. Al-Degs, M. F. Tutunju, R. A. Shawabkeh, *Separ. Sci. Technol.* **2000**, *35*, 2299–2310. DOI:10.1081/SS-100102103
- C. J. Hawker, A. W. Bosman, E. Harth, *Chem. Rev.* **2001**, *101*, 3661–3688. DOI:10.1021/cr990119u
- G. Moad, Y. K. Chong, A. Postma, E. Rizzardo, S. H. Thang, *Polymer* **2005**, *46*, 8458–8468. DOI:10.1016/j.polymer.2004.12.061
- K. Matyjaszewski, J. Xia, *Chem. Rev.* **2001**, *101*, 2921–2990. DOI:10.1021/cr940534g
- S. Karaman, A. Karaipekli, A. Sari, A. Bicer, *Solar Energy Mater. Solar Cells* **2011**, *95*, 1647–1653. DOI:10.1016/j.solmat.2011.01.022
- X. Li, C. Bian, W. Chen, J. He, Z. Wang, N. Xu, G. Xue, *Appl. Surf. Sci.* **2003**, *207*, 378–383. DOI:10.1016/S0169-4332(03)00010-2
- X. Li, X. Li, G. Wang, *Appl. Surf. Sci.* **2005**, *249*, 266–270. DOI:10.1016/j.apsusc.2004.12.001
- S. Hu, X. Zhu, W. Hu, L. Yan, C. Cai, *Polym. Bull.* **2013**, *70*, 517–533. DOI:10.1007/s00289-012-0849-0
- J. Z. Liang, *Polym. Test.* **2008**, *27*, 936–940. DOI:10.1016/j.polymertesting.2008.08.001
- G. Sheng, H. Dong, Y. Li, *J. Environmental Radioactivity* **2012**, *113*, 108–115. DOI:10.1016/j.jenvrad.2012.05.011
- Y. Yu, J. Addai-Mensah, D. Losic, *Sci. Technol. Adv. Mater.* **2012**, *13*, 015008 (11pp).
- K. Khezri, Y. Fazli, *J. Inorg. Organomet. Polym.* **2017**, *27*, 266–274. DOI:10.1007/s10904-016-0469-5
- N. Garderen, F. J. Clemens, M. Mezzomo, C. P. Bergmann, T. Graule, *Appl. Clay Sci.* **2011**, *52*, 115–121. DOI:10.1016/j.clay.2011.02.008
- Y. Du, J. Yan, Q. Meng, J. Wang, H. Dai, *Mater. Chem. Phys.* **2012**, *133*, 907–912. DOI:10.1016/j.matchemphys.2012.01.115
- D. Liu, P. Yuan, D. Tan, H. Liu, T. Wang, M. Fan, J. Zhu, H. He, *J. Colloid Interf. Sci.* **2012**, *388*, 176–184. DOI:10.1016/j.jcis.2012.08.023
- M. Li, N. M. Jahed, K. Min, K. Matyjaszewski, *Macromolecules* **2004**, *37*, 2434–2441. DOI:10.1021/ma035712z
- H. Roghani-Mamaqani, V. Haddadi-Asl, M. Najafi, M. Sala-

- mi-Kalajahi, *Polym. Compos.* **2010**, *31*, 1829–1837.
DOI:10.1002/pc.20975
35. M. Sarsabili, M. Parvini, M. Salami-Kalajahi, A. Asfاده, *Iran. Polym. J.* 2013, *22*, 155–163.
DOI:10.1007/s13726-012-0114-2
36. Y. Fazli, K. Khezri, *Colloid Polym. Sci.* **2017**, *295*, 247–257.
DOI:10.1007/s00396-016-3997-1
37. M. Sarsabili, R. Rahmatolahzadeh, S. A. Shobeiri, M. Hamadani, A. Farazin, K. Khezri, *Polym. Adv. Technol.* **2018**, *29*, 424–432. DOI:10.1002/pat.4131
38. K. Khezri, H. Roghani-Mamaqani, *Mater. Res. Bull.* **2014**, *59*, 241–248. DOI:10.1016/j.materresbull.2014.07.021
39. K. Khezri, H. Mahdavi, *Micropor. Mesopor. Mater.* 2016, *228*, 132–140. DOI:10.1016/j.micromeso.2016.03.022
40. L. D. Perez, J. F. Lopez, V. H. Orozco, T. Kyu, B. L. Lopez, *J. Appl. Polym. Sci.* **2009**, *111*, 2229–2237.
DOI:10.1002/app.29245
41. S. Subramania, S. W. Choia, J. Y. Lee, J. H. Kim, *Polymer* **2007**, *48*, 4691–4703. DOI:10.1016/j.polymer.2007.06.023
42. M. A. Ver Meer, B. Narasimhan, B. H. Shanks, S. K. Mallapragada, *ACS Appl. Mater. Interf.* **2010**, *2*, 41–47.
43. H. Roghani-Mamaqani, V. Haddadi-Asl, M. Najafi, M. Salami-Kalajahi, *J. Appl. Polym. Sci.* 2011, *120*, 1431–1438.
DOI:10.1002/app.33119
44. H. Roghani-Mamaqani, V. Haddadi-Asl, M. Najafi, M. Salami-Kalajahi, *AIChE J.* 2011, *57*, 1873–1881.
DOI:10.1002/aic.12395

Povzetek

Mezoporozne diatomitne ploščice smo uporabili za pripravo poli(stiren-co-metil metakrilat) / diatomitnih kompozitov. Za pripravo smo uporabili tehniko polimerizacije s prenosom atoma (Atom transfer radical polymerization ATRP; simultaneous reverse and normal initiation SR&NI ATRP). Same diatomitne ploščice smo preučili z vrstično elektronsko mikroskopijo (SEM) in presevno elektronsko mikroskopijo, njihovo poroznost pa določili z adsorcijo in desorpcijo dušika. Konverzijo in molekulska masa smo določili s plinsko kromatografijo (GC) in velikostno izključitveno kromatografijo (SEC). Dodatek 3 ut% diatomita je vodil v povečanje pretvorbe s 76 % na 92 %. Molekulska masa verig poli (stiren-co-metil metakrilata) se je povečala od 12893 g mol⁻¹ na 14907 g mol⁻¹. Indeks polidisperznosti se je povečal z 1,18 na 1,44. Sestavo kopolimera smo preučili z uporabo NMR spektroskopije. Povečano termično stabilnost nanokompozita smo dokazali s termogravimetrično analizo (TGA). Rezultati diferenčne dinamične kalorimetrije (DSC) kažejo na zvišanje temperature steklastega prehoda (T_g) s 67,6 °C na 73,4 °C z v primeru dodatka 3 ut% mezoporoznih diatomitnih ploščic.

Scientific paper

Phase Diagram of the Sn–As–Ge System

Galina V. Semenova, Elena Yu. Proskurina, Tatiana P. Sushkova*
and Victor N. Semenov

Department of General and Inorganic Chemistry, Voronezh State University; Universitetskaya pl., 1,
Voronezh, 394018, Russia

* Corresponding author: E-mail: sushtp@yandex.ru

Received: 11-03-2018

Abstract

The paper presents the phase diagram of the Sn–As–Ge system. The diagram of polythermal Sn–GeAs section was constructed using the results of X-ray powder diffraction analysis and differential thermal analysis. We found that in a concentration interval with arsenic content of less than 50 mol%, four-phase peritectic equilibria $L + \text{SnAs} \leftrightarrow \text{GeAs} + \text{Sn}_4\text{As}_3$ (834 K) and $L + \text{GeAs} \leftrightarrow \text{Ge} + \text{Sn}_4\text{As}_3$ (821 K) are present. When the temperature is close to the melting point of pure tin, non-variant equilibrium with tin, germanium and Sn_4As_3 is implemented as well. The study of $\text{Sn}_{0.39}\text{As}_{0.61}$ – $\text{Ge}_{0.28}\text{As}_{0.72}$, SnAs– $\text{Ge}_{0.4}\text{As}_{0.6}$ and SnAs–GeAs₂ sections and elaboration of the type of the SnAs–GeAs phase diagram demonstrated that polythermal sections SnAs–GeAs and SnAs–GeAs₂ can perform phase subsolidus demarcation of the phase diagram of the Sn–As–Ge system. There are also invariant peritectic equilibria $L + \text{GeAs}_2 \leftrightarrow \text{GeAs} + \text{SnAs}$ (840 K) and $L + \text{As} \leftrightarrow \text{SnAs} + \text{GeAs}_2$ (843 K) in the system.

Keywords: Phase diagram; germanium arsenide; tin arsenide; ternary system

1. Introduction

A large number of experimental and theoretical studies of the properties of graphene have provoked considerable scientific interest in layered structures, and compounds of the $A^{IV}B^V$ class in particular. $A^{IV}B^V$ compounds are of great practical value for two reasons: their anisotropic electrophysical characteristics resulting from low-symmetry structure; and their layered crystal structure which allows for the intercalation of ions and molecules into the interlayer space.^{1–5} The presence of volatiles makes it rather difficult to synthesise such compounds, which is why attempts were made to obtain GeP samples in the presence of tin.⁵ In that study, Sn-doped materials with peculiar semiconductor properties were obtained. However, the lack of information about the phase equilibria of A^{IV} – B^V –Sn ternary systems makes further research in this area rather problematic. Therefore, since the synthesis of multicomponent alloys is based on information about phase equilibria, the study of the phase diagram of the Sn–As–Ge system is of great importance.

This paper presents the results of an experimental study of Sn–GeAs, $\text{Sn}_{0.39}\text{As}_{0.61}$ – $\text{Ge}_{0.28}\text{As}_{0.72}$, SnAs– $\text{Ge}_{0.4}\text{As}_{0.6}$,

SnAs–GeAs and SnAs–GeAs₂ polythermal sections, which was performed using differential thermal analysis and X-ray phase analysis methods. *T*-*x* diagrams of the sections were constructed, and the nature of phase equilibria in the ternary Sn–As–Ge system was analysed.

2. Experimental

2.1. Materials and Synthesis

The number of ternary alloys with compositions corresponding to Sn–GeAs, $\text{Sn}_{0.39}\text{As}_{0.61}$ – $\text{Ge}_{0.28}\text{As}_{0.72}$, SnAs– $\text{Ge}_{0.4}\text{As}_{0.6}$, SnAs–GeAs and SnAs–GeAs₂ polythermal sections, were prepared from the preliminary obtained binary compounds using high purity tin Sn-5N (99.999%), arsenic As-5N (99.9997%) and polycrystalline zone purified germanium Ge-5N-6N (99.9999%). Weighing was performed on an AR2140 balance with an accuracy of ± 0.001 g. The preparation of samples was carried out using the one-temperature method in thick-walled quartz ampoules vacuumised up to the residual pressure of 0.05 Pa. During the synthesis of the samples, the temperature was measured using a chromel–alumel thermocouple with a TK–

5.11 contact thermometer. The alloys were subjected to homogenizing annealing for 150 hours at 800–815 K.

2. 2. Research Methods

The study of the samples obtained was carried out on the differential thermal analysis (DTA) setup with a programmable heating of the furnace using OWEN TRM–151 and TRM–202 proportional-integral-differential controllers. The signal received from chromel-alumel thermocouples was digitized and processed by the MasterSCADA software package. In our experiments, the heating rate of DTA-setup was 5 K min⁻¹.

Thermoanalytical studies were carried out using Stepanov's quartz vessels. The experimental substance was ground and placed in the vessels so as to fill the maximum volume, after which the vessels were vacuumised up to the residual pressure of 0.05 Pa. Anhydrous analytically pure aluminum oxide was used as the reference substance. Chromel-alumel thermocouples, used as temperature sensors, were calibrated according to the phase transitions temperatures of pure metals, often used as standards.⁶ Furthermore, Sn, As and Ge were used. Their physical and chemical properties are similar to the properties of the objects we were studying. The precision of determining the temperature of phase transition by the DTA-setup was within the limit of ± 2 K.

X-ray powder diffraction (XRD) analysis of alloy samples of the sections Sn–GeAs, SnAs–Ge_{0.4}As_{0.6}, SnAs–GeAs were performed using a powder diffractometer AR-LX'TRA with the following characteristics: CuK α -radiation, exposure step 0.06°, exposure time 3.0 seconds. The samples of the sections Sn_{0.39}As_{0.61}–Ge_{0.28}As_{0.72} и SnAs–GeAs₂ were performed using a powder diffractometer DRON 4–07 (CoK α -radiation, exposure step 0.1°, exposure time 3.0 seconds). The intermediate phases in the Ge–Sn–As system have the following crystal structure: SnAs – Cubic, space group Fm3m; Sn₄As₃ – Rhombohedral, space group R3m; GeAs – Tetragonal, space group I4mm; GeAs₂ – Orthorhombic, space group Pbam. The recorded X-ray powder diffraction patterns were interpreted using the Powder Diffraction File cards of International Centre for Diffraction Data (ICDD PDF-2 2007).

3. Results and Discussion

In our previous experimental study of polythermal sections Sn₄As₃–GeAs and SnAs–GeAs⁷ it was showed that a peritectic equilibrium $L + \text{SnAs} \leftrightarrow \text{Sn}_4\text{As}_3 + \text{GeAs}$ was achieved in the Ge–As–Sn system at the temperature of 834 K. This conclusion we confirmed by the study of the alloys of the polythermal section Ge–SnAs,⁸ that was based on the results of an X-ray diffraction analysis and differential thermal analysis. The existence of yet another invariant equilibrium $L + \text{GeAs} \leftrightarrow \text{Ge} + \text{Sn}_4\text{As}_3$, which is realized at a temperature of 821 K, was also established.⁸

In this paper, the alloys belonging to the Sn–GeAs section were studied. An X-ray diffraction analysis showed that for all the samples in the solid state, the presence of three phases is detected: irrespective of the composition, the lines of germanium and tin arsenide Sn₄As₃ are fixed. Depending on the third phase contained in the alloys, the samples can be divided into two groups. When the content of germanium arsenide is up to 60 mol.%, the alloys are a heterophasic mixture of tin and germanium, as well as Sn₄As₃ (e.g., the X-ray diffraction pattern in Fig. 1a). For the alloys with germanium arsenide content of 67–94 mol.%, there are no reflexes characteristic of tin; on the contrary, lines indicating the presence of germanium monoarsenide in the solid phase appear, and the intensity of these lines increases with the enrichment of the alloys with this component (Fig. 1b).

The investigation of the alloys by differential thermal

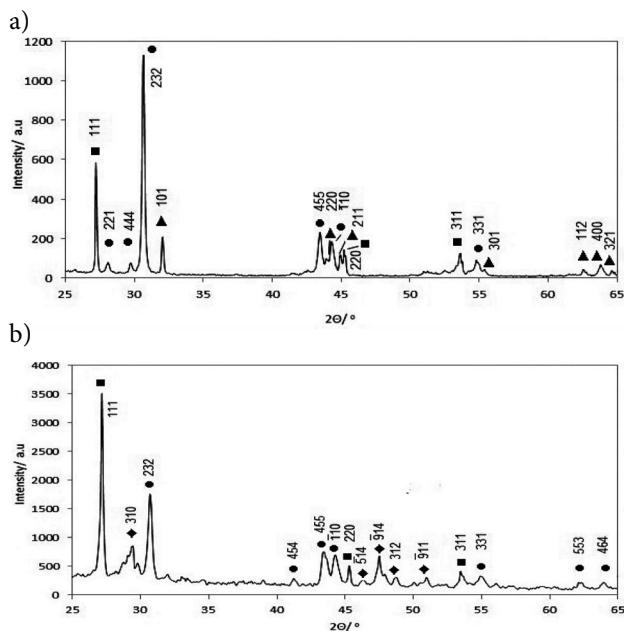


Figure 1. XRD patterns of the alloys of the polythermal section Sn–GeAs: a – 0.33; b – 0.82 mol. f. GeAs. The symbols denote: ● – Sn₄As₃; ■ – Ge; ▲ – Sn; ◆ – GeAs.

analysis showed that when the content of germanium arsenide is more than 60 mol. % three endothermic effects were fixed, and the low-temperature effect was observed at the same temperature of 821 K. According to our data obtained from the study of the polythermal cross section of Ge–SnAs,⁸ this corresponds to the four-phase process $L + \text{GeAs} \leftrightarrow \text{Ge} + \text{Sn}_4\text{As}_3$. The second effect at 939 K was noted for the samples in the range of 82–94 mol.% GeAs compositions. The high-temperature effect corresponding to the liquidus on the heating curves was not very distinct, but was well reproduced on the cooling curves. For samples with a monoarsenide germanium content of less than 60 mol.%, the effect at 821 K was absent, for all the alloys

of a given concentration interval, an endothermic effect is realized at 505 K.

Fig. 2 shows phase equilibria in the Sn–As–Ge system within the concentration interval of less than 50 mol.% As. This allows for correct interpretation of the experimental results of studying the T-x diagram of the Sn–GeAs section.

The presence of a horizontal section on the T-x cut chart (the first effect on heating curves) corresponds to a invariant four-phase equilibrium in the ternary system. According to an X-ray diffraction analysis in the composition range of less than 60 mol.% GeAs, there are three solid phases: tin, germanium and Sn_4As_3 . Thus, we can assume the existence of a four-phase equilibrium $L \leftrightarrow \text{Sn}_4\text{As}_3 + \text{Ge} + \text{Sn}$ in the system, which is realized at a temperature of 505 K. Tin is absent in the region of compositions rich in GeAs, but three solid phases are still recorded: Ge, Sn_4As_3 and GeAs.

The alloys the compositions of which correspond to the concentration region *ab* (Fig. 2) of the polythermal section lie in the region of primary crystallization of the germanium monoarsenide $L \leftrightarrow \text{GeAs}$. Secondary crystallization is connected with the three-phase equilibrium line e_3U_4 , along which the process $L \leftrightarrow \text{GeAs} + \text{Ge}$ is carried out. The crystallization ends at U_4 point: $L + \text{GeAs} \leftrightarrow \text{Ge} + \text{Sn}_4\text{As}_3$. The segment *cd* intersects the field of primary crystallization of germanium. After the primary crystallization, the figurative point of the liquid falls on the curve U_4E_1 . The process ends with eutectic crystallization at the point E_1 (the temperature of this four-phase transformation noted by the DTA method is 505 K). The sequence of processes will be as follows: $L \leftrightarrow \text{Ge}$; $L \leftrightarrow \text{Ge} + \text{Sn}_4\text{As}_3$; $L \leftrightarrow \text{Ge} + \text{Sn}_4\text{As}_3 + \text{Sn}$. The segment *cd* also crosses the field of primary crystallization of tin. However, taking into account the degenerate nature of the eutectic processes e_1E_1 and e_2E_1 , it should be assumed that the four-phase and preceding three-phase processes will occur in a narrow concentration interval (p. E_1 – is degenerated) and it is not possible to investigate them. The presented reasoning makes it possible to interpret the data of differential thermal analysis and construct the T-x diagram of the polythermal section of Sn–GeAs (Fig. 3).

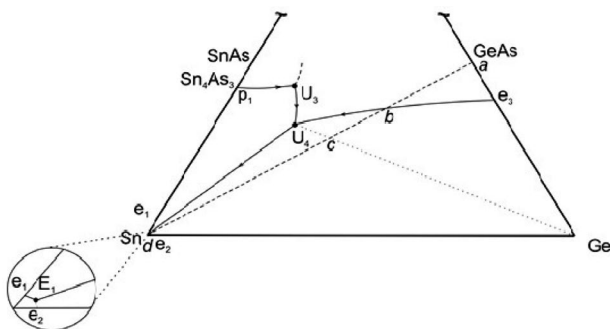


Figure 2. Crystallization processes of the alloys of the polythermal section Sn – GeAs.

While studying the SnAs–GeAs polythermal section⁷ it was suggested that this section is quasibinary and can be presented as a eutectic phase diagram with coordinates of the eutectic point 840 K and 20 mol% GeAs. The results of the experimental study of the polythermal section SnAs– $\text{Ge}_{0.4}\text{As}_{0.6}$ allowed us to elaborate the T-x diagram of SnAs–GeAs. The polythermal section SnAs– $\text{Ge}_{0.4}\text{As}_{0.6}$ starts from the figurative point of tin monoarsenide and from the double eutectic point (GeAs₂+GeAs) in the

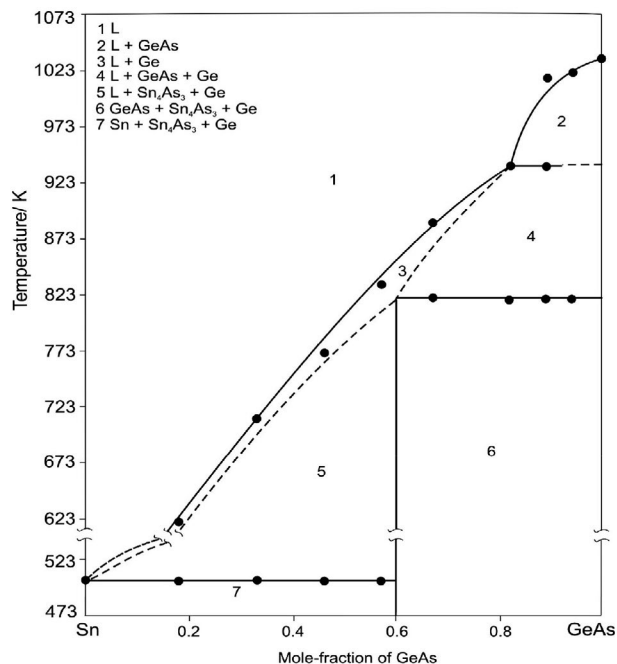


Figure 3. T-x diagram of the polythermal section Sn–GeAs.

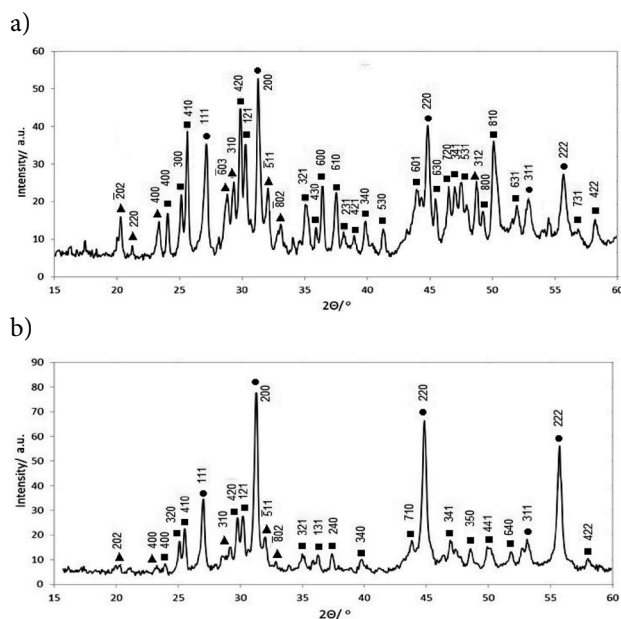


Figure 4. XRD patterns of the alloys of the polythermal section SnAs– $\text{Ge}_{0.4}\text{As}_{0.6}$: a – 0.15; b – 0.75 mol.f. SnAs. The symbols denote: ● – SnAs; ■ – GeAs₂; ▲ – GeAs.

Ge–As system. The alloys of the polythermal section SnAs–Ge_{0.4}As_{0.6} are the mixtures of GeAs, GeAs₂ and SnAs. XRD patterns of some of the alloys are given as an example in Fig. 4 a, b.

The results of the differential thermal analysis showed that the first endothermic effect for all the samples of the SnAs–Ge_{0.4}As_{0.6} section was observed at the temperature of 840 K. In Fig. 5 as an example, thermograms of alloys of two sections are presented: SnAs–GeAs and SnAs–Ge_{0.4}As_{0.6}. For the alloys of the section SnAs–GeAs (Fig. 5a), two endothermic effects are observed, and for the cut SnAs–Ge_{0.4}As_{0.6}, there are three effects, which can be clearly seen on the cooling curves. The beginning of the first endothermic effect is the same for both samples - 840 K. For greater clarity, on Fig. 6 the thermograms in the coordinates ΔT -T are compared.

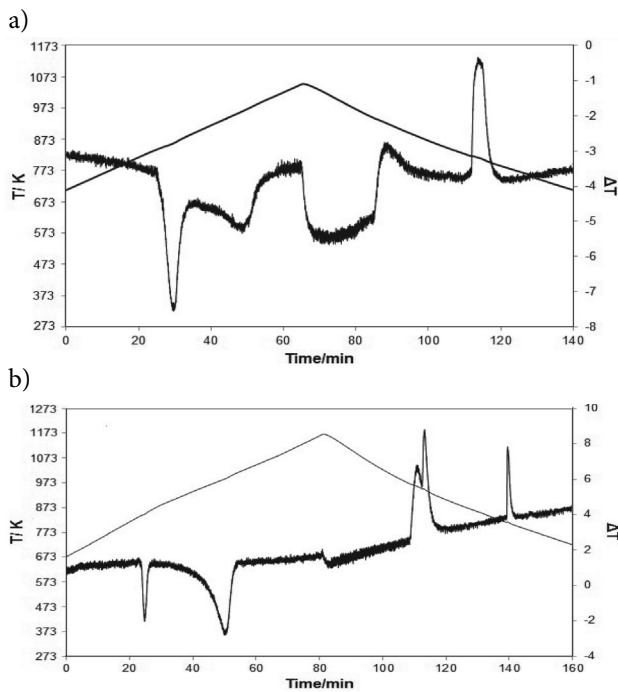


Figure 5. Thermograms for (SnAs)_{0.4}(GeAs)_{0.6} (a) and (SnAs)_{0.15}(Ge_{0.4}As_{0.6})_{0.85} (b) alloys

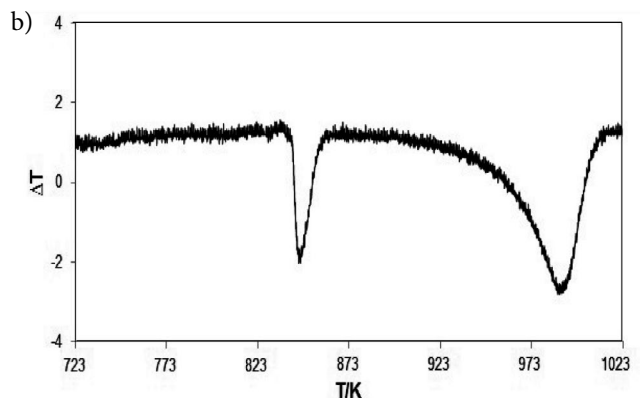
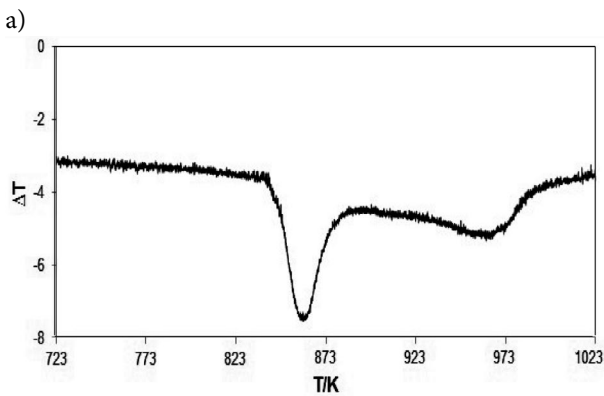


Figure 6. The DTA results in ΔT - T coordinates for (SnAs)_{0.4}(GeAs)_{0.6} (a) and (SnAs)_{0.15}(Ge_{0.4}As_{0.6})_{0.85} (b) alloys

If there is an eutectic equilibrium with three solid phases SnAs + GeAs + GeAs₂, a lower temperature corresponding to the melting of the triple eutectic should be expected. The results obtained can be explained, if we assume that the ternary Sn–As–Ge system includes a peritectic four-phase equilibrium $L + \text{GeAs}_2 \leftrightarrow \text{GeAs} + \text{SnAs}$. Taking this into account, a T - x diagram of the polythermal section SnAs–Ge_{0.4}As_{0.6} was constructed, and the form of the polythermal section SnAs–GeAs was specified (Fig. 7 a, b).

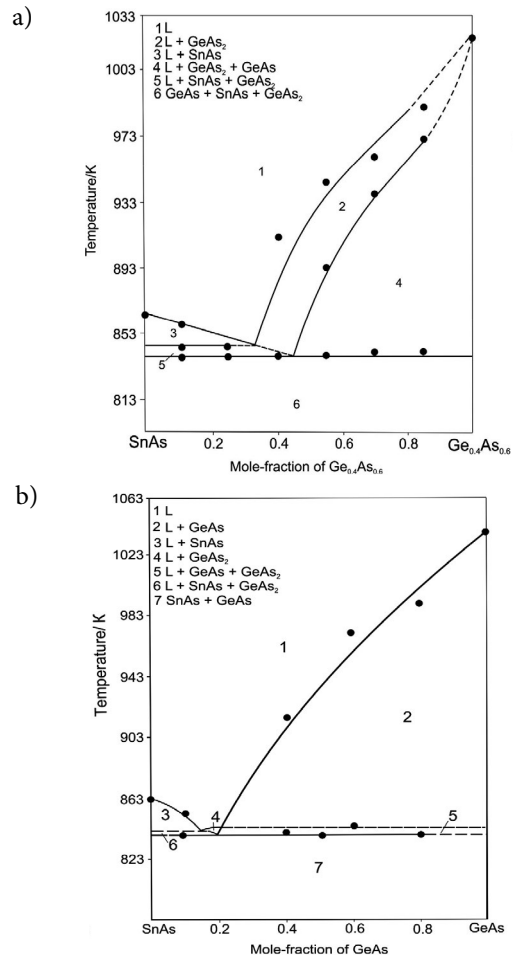


Figure 7. T - x diagrams of polythermal sections SnAs–Ge_{0.4}As_{0.6} (a) and SnAs–GeAs (b).

In order to establish the nature of phase equilibria in the Sn–As–Ge system within the concentration interval of more than 50 mol% of arsenic, an experimental study of the polythermal sections $\text{Sn}_{0.39}\text{As}_{0.61}\text{–Ge}_{0.28}\text{As}_{0.72}$ and SnAs–GeAs_2 was carried out. The X-ray diffraction analysis of the alloys belonging to the polythermal section SnAs–GeAs_2 allowed us to detect a heterophasic mixture of two phases – tin monoarsenide and germanium diarsenide (Fig. 8 a, b).

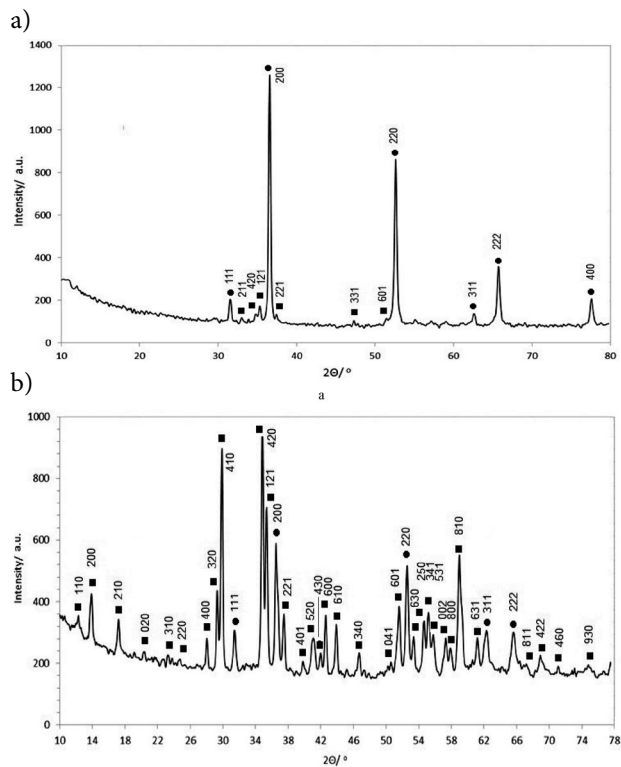


Figure 8. XRD patterns of the alloys of the polythermal section SnAs–GeAs_2 : a – 0.25; b – 0.85 mol.f. GeAs_2 . The symbols denote: ● – SnAs; ■ – GeAs_2 .

Using differential thermal analysis allowed us to detect the endothermic effect in the samples of all concentration range at the same temperature of 843 K. The polythermal section $\text{Sn}_{0.39}\text{As}_{0.61}\text{–Ge}_{0.28}\text{As}_{0.72}$ goes through the

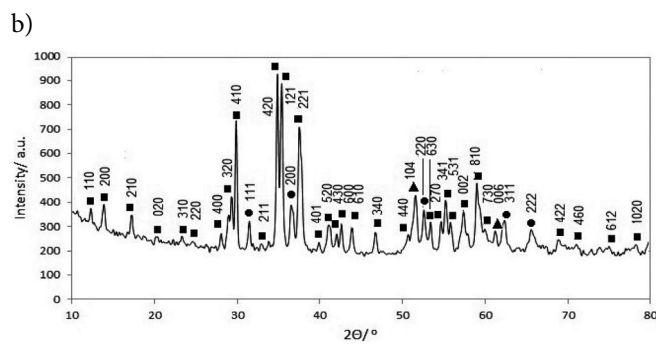
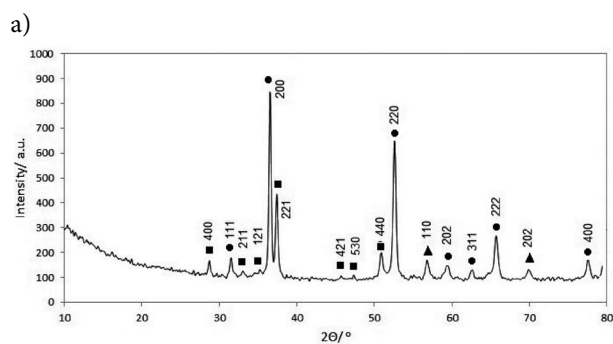


Figure 9. XRD patterns of the alloys of the polythermal section $\text{Sn}_{0.39}\text{As}_{0.61}\text{–Ge}_{0.28}\text{As}_{0.72}$: a – 0.10; b – 0.90 mol.f. $\text{Ge}_{0.28}\text{As}_{0.72}$. The symbols denote: ● – SnAs; ■ – GeAs_2 ; ▲ – As.

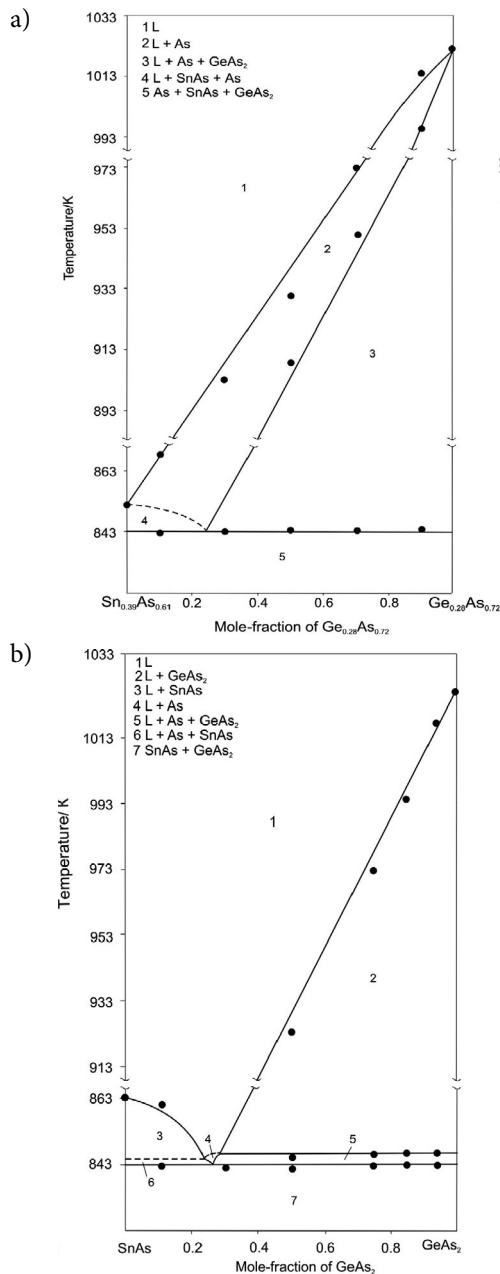


Figure 10. T-x diagrams of polythermal sections $\text{Sn}_{0.39}\text{As}_{0.61}\text{–Ge}_{0.28}\text{As}_{0.72}$ (a) and SnAs–GeAs_2 (b).

double eutectic point ($\text{GeAs}_2 + \text{As}$) in the binary system Ge–As and through the eutectic point ($\text{SnAs} + \text{As}$) in the Sn–As system. The alloys whose compositions belong to the polythermal section $\text{Sn}_{0.39}\text{As}_{0.61}\text{–Ge}_{0.28}\text{As}_{0.72}$ represent a heterophasic mixture of arsenic, germanium diarsenide and tin monoarsenide (Fig. 9 a, b).

Phase diagram of the $\text{Sn}_{0.39}\text{As}_{0.61}\text{–Ge}_{0.28}\text{As}_{0.72}$ section is shown in Fig. 10a. Differential thermal analysis demonstrated that in all the samples the first endothermic effect was observed at the same temperature of 843 K (Fig. 11, 12). Implementation of the same temperature at the section SnAs– GeAs_2 (Fig. 10b) allows us to conclude that there exists a peritectic invariant equilibrium $\text{L} + \text{As} \leftrightarrow \text{SnAs} + \text{GeAs}_2$.

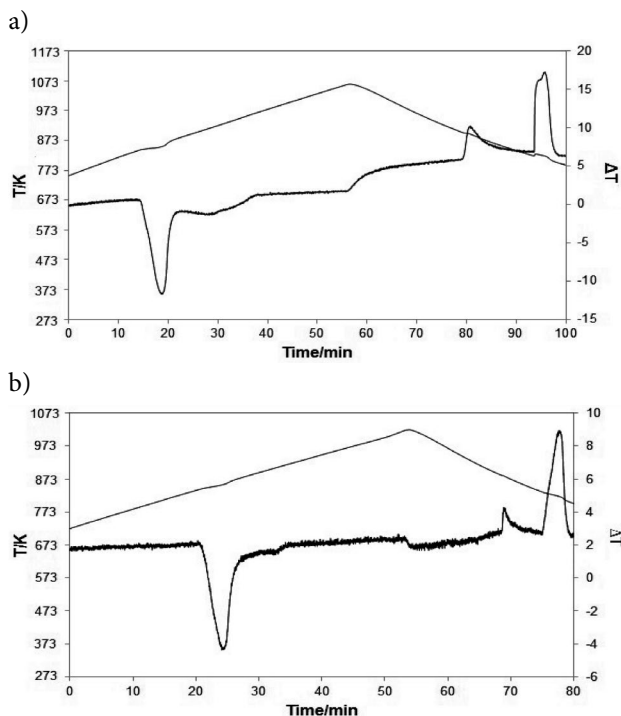


Figure 11. Thermograms for $(\text{SnAs})_{0.5}(\text{GeAs}_2)_{0.5}$ (a) and $(\text{Sn}_{0.39}\text{As}_{0.61})_{0.7}(\text{Ge}_{0.28}\text{As}_{0.72})_{0.3}$ (b) alloys.

Thus, there are four equilibria of peritectic character in the ternary system of Sn–As–Ge:

1. $\text{L} + \text{As} \leftrightarrow \text{SnAs} + \text{GeAs}_2$
2. $\text{L} + \text{GeAs}_2 \leftrightarrow \text{GeAs} + \text{SnAs}$
3. $\text{L} + \text{SnAs} \leftrightarrow \text{Sn}_4\text{As}_3 + \text{GeAs}$
4. $\text{L} + \text{GeAs} \leftrightarrow \text{Ge} + \text{Sn}_4\text{As}_3$

Given that the eutectic points on the tin side are degenerate in the Ge–Sn and Sn–As systems, we can expect that the coordinate of the four-phase equilibrium point E_1 will be implemented in the tin-rich area of the alloys. Eutectic crystallization of three solid phases $\text{L} \leftrightarrow \text{Ge} + \text{Sn} + \text{Sn}_4\text{As}_3$ takes place at the E_1 point (Fig. 13).

The analysis of the nature of phase equilibria in the ternary Sn–As–Ge system, as well as the experimental study of polythermal sections Sn–GeAs, $\text{Sn}_4\text{As}_3\text{–GeAs}$,

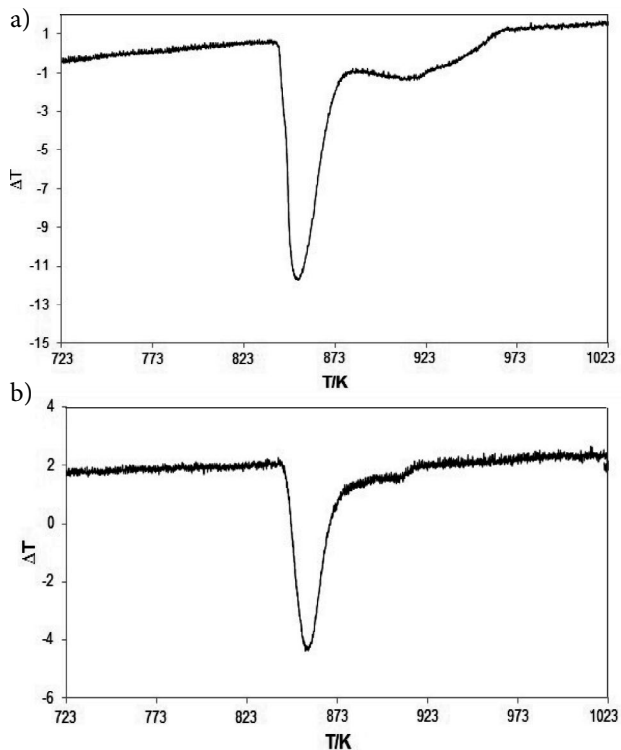


Figure 12. The DTA results in $\Delta T\text{–}T$ coordinates for $(\text{SnAs})_{0.5}(\text{GeAs}_2)_{0.5}$ (a) and $(\text{Sn}_{0.39}\text{As}_{0.61})_{0.7}(\text{Ge}_{0.28}\text{As}_{0.72})_{0.3}$ (b) alloys.

$\text{Sn}_{0.39}\text{As}_{0.61}\text{–Ge}_{0.28}\text{As}_{0.72}$, SnAs– $\text{Ge}_{0.4}\text{As}_{0.6}$, SnAs–GeAs and SnAs– GeAs_2 using the methods of differential thermal and X-ray diffraction analysis, allowed us to construct a $T\text{–}x\text{–}y$ diagram of the Sn–As–Ge system (Fig. 13).

It seemed impractical to use a 3D chart, whereas Sheila's scheme turned out to be quite informative and, most importantly, convenient for the analysis of the phase states and the processes of melting and crystallization, as well as for calculations and cross-sections building (Fig. 14).

The main objective was to reduce the three-dimensional diagram of the triple system to a one-dimensional scheme, which would give a clear idea of the phase equilibria in the system. We performed this reduction by taking into account nonvariant and monovariant transformations only, leaving out the concentration of phases and using only the temperature axis. The scheme shown in Fig. 14 illustrates phase equilibria and successive (with decreasing temperature) crystallization processes in the ternary Sn–As–Ge system.

4. Conclusions

The polythermal sections of the phase diagram of the Sn–As–Ge ternary system were studied by differential thermal and X-ray analysis methods, which made it possible to represent the nature of phase equilibrium $\text{L} + \text{GeAs} \leftrightarrow \text{Ge} + \text{Sn}_4\text{As}_3$ ($T = 821 \text{ K}$) in the system established ear-

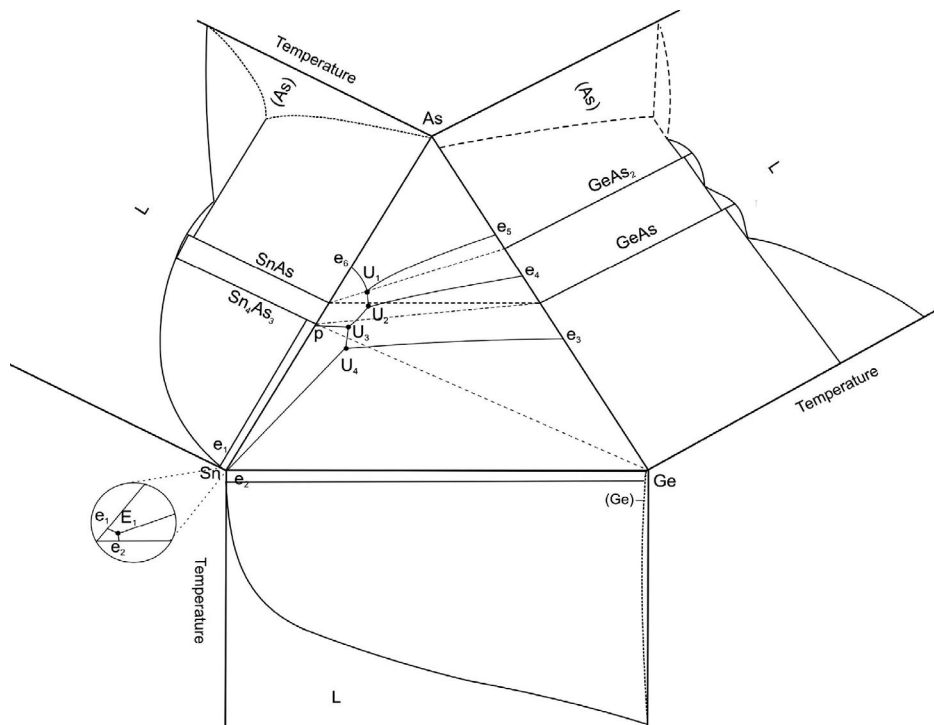


Figure 13. Sn–As–Ge phase diagram.

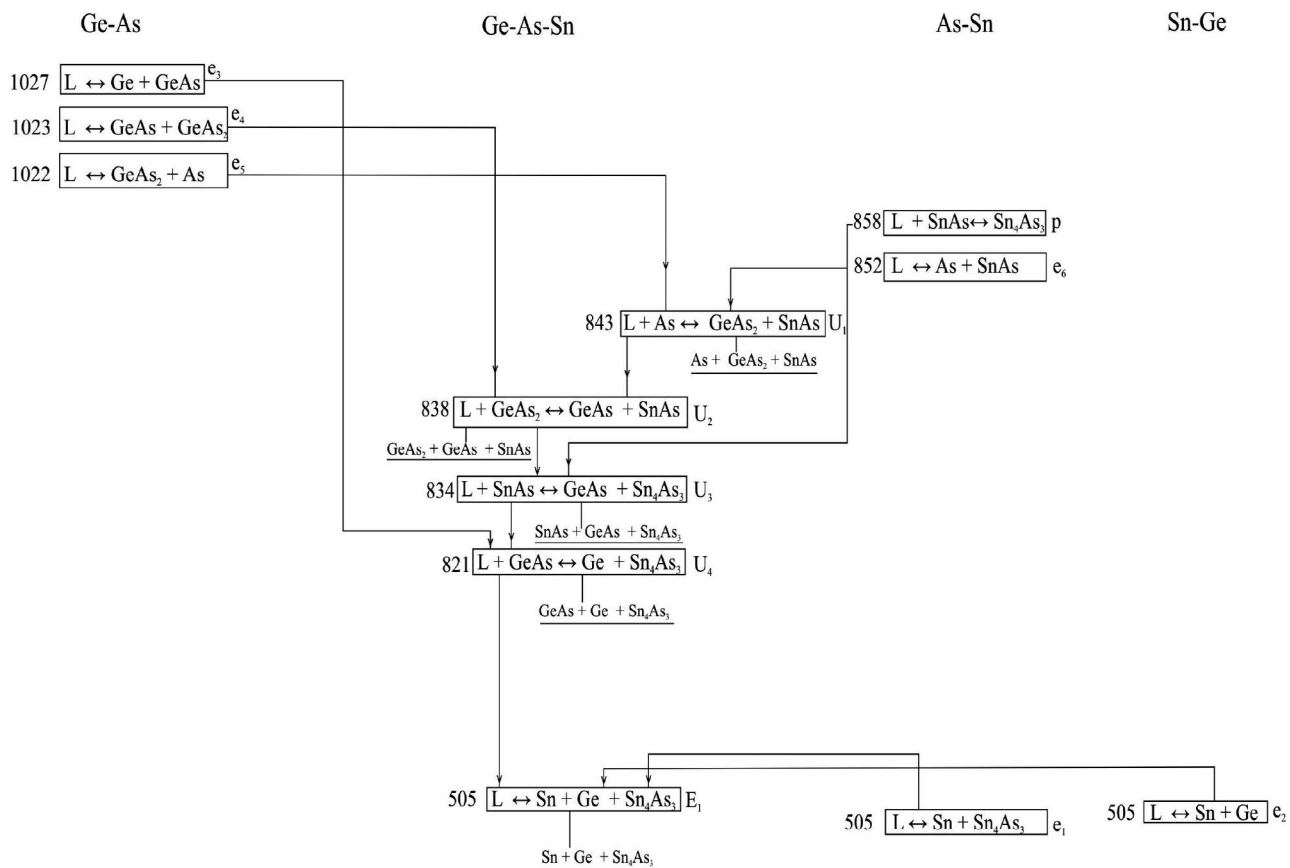


Figure 14. Flow diagram of the Sn–As–Ge system.

lier during the study of the Ge–SnAs and Sn₄As₃–GeAs sections. It is also shown that, at a temperature close to the melting point of tin, an invariant equilibrium is realized involving a melt and three solid phases: tin, germanium monoarsenide and Sn₄As₃. This fact is not surprising, since in the binary systems Ge–Sn and Sn–As the eutectic points are degenerate. Investigation of alloys in the concentration region with an arsenic content of more than 50 mol. % allowed to establish the presence of two more invariant processes. For samples whose compositions correspond to the concentration triangle formed by the figurative points GeAs, GeAs₂ and SnAs, the temperature of the first endoeffect equal to 840 K was recorded by differential thermal analysis. This value coincides with the temperature of the first effect for alloys of the GeAs–SnAs cross section. This can be explained by the existence at a given temperature of the peritectic invariant equilibrium $L + \text{GeAs}_2 \leftrightarrow \text{GeAs} + \text{SnAs}$, since the triple eutectic with these phases should have a lower temperature than for the GeAs–SnAs section. Investigation of the SnAs–GeAs₂ cross section and comparison of the results obtained with DTA data for samples with a high arsenic content made it possible to conclude that the equilibrium $L + \text{As} \leftrightarrow \text{SnAs} + \text{GeAs}_2$ takes place at 843 K. Thus, in the Sn–As–Ge ternary system there are five invariant equilibria, which are presented in the paper as a flow diagram.

Povzetek

V prispevku predstavljamo fazni diagram sistema Sn–As–Ge. Diagram v sistemu Sn–GeAs smo izdelali z uporabo rezultatov rentgenske praškovne difrakcijske analize in diferencialne termične analize. Ugotovili smo, da so v koncentracijskem intervalu z vsebnostjo arzena manj kot 50 mol% prisotne štiri fazne v peritektičnem ravnotežju $L + \text{SnAs} \leftrightarrow \text{GeAs} + \text{Sn}_4\text{As}_3$ (834 K) in $L + \text{GeAs} \leftrightarrow \text{Ge} + \text{Sn}_4\text{As}_3$ (821 K). Ko je temperatura blizu tališča čistega kositra, pride do invariantnega ravnotežja s kositrom, germanijem in Sn₄As₃. Podrobneje smo raziskali tudi sekcije Sn_{0,39}As_{0,61}–Ge_{0,28}As_{0,72}, SnAs–Ge_{0,4}As_{0,6} in SnAs–GeAs₂ in preučevali fazna diagrama SnAs–GeAs in SnAs–GeAs₂ v sistemu Sn–As–Ge. V sistemu smo tudi opazili invariantna peritektična ravnotežja $L + \text{GeAs}_2 \leftrightarrow \text{GeAs} + \text{SnAs}$ (840 K) in $L + \text{As} \leftrightarrow \text{SnAs} + \text{GeAs}_2$ (843 K).

5. Acknowledgment

The authors are grateful for the conduct of X-ray studies Center for collective use of scientific equipment of Voronezh State University.

6. References

1. C. Barreteau, B. Michon, C. Besnard, E. Giannini, *J. Cryst. Growth*. **2016**, *443*, 75–80. DOI:10.1016/j.jcrysgro.2016.03.019
2. F. Shojaei, HS Kang, *J. Phys. Chem. C*. **2016**, *120*, 23842–23850. DOI:10.1021/acs.jpcc.6b07903
3. K. Lee, S. Kamali, T. Ericsson, M. Bellard, K. Kovnir, *Chem. Mater.* **2016**, *28*(8), 2776–2785. DOI:10.1021/acs.chemmater.6b00567
4. M. Khatun, A. Mar, Z. *Naturforsch.* **2016**, *71*(5), 375–380. DOI:10.1515/znb-2015-0203
5. K. Lee, S. Synnestvedt, M. Bellard, K. Kovnir, *J. Solid State Chem.* **2015**, *224*, 62–70. DOI:10.1016/j.jssc.2014.04.021
6. G. Klancnik, J. Medved, A. Nagode, G. Novak, D. Steiner Petrovic, *J. Therm. Anal. Calorim.* **2014**, *116*, 295–302. DOI:10.1007/s10973-013-3536-y
7. E. Kononova, S. Sinyova, G. Semenova, T. Sushkova, *J. Therm. Anal. Calorim.* **2014**, *117*(3), 1171–1177. DOI:10.1007/s10973-014-3883-3
8. G. V. Semenova, E. Yu. Kononova, T.P. Sushkova, *Russian J. Inorgan. Chem.* **2014**, *59*(12), 1517–1521. DOI:10.1134/S0036023614120225

Scientific paper

Optical Response of Two Azo Ligands Containing Salicyaldimine-based Ligand as Side Chains Towards Some Divalent Metal Ions and Their Antioxidant Behavior

Zohreh Shaghghi^{1,*} and Gholamreza Dehghan²¹ Department of Chemistry, Faculty of Science, Azarbaijan Shahid Madani University, Tabriz, Iran² Department of Biology, Faculty of Natural Science, University of Tabriz, Tabriz, Iran

* Corresponding author: E-mail: shaghghi@azaruniv.ac.ir

Phone: +98 4131452092; Fax: +984134327541

Received: 18-03-2018

Abstract

According to applicability of azo-azomethine compounds in chemical sensors and biological activities, two receptors: 1,2-[1-(3-imino-4-hydroxyphenylazobenzene)]-4-nitrobenzene (**1**) and 1,2-[1-(3-imino-4-hydroxyphenylazo-4-nitrobenzene)]-4-nitrobenzene (**2**) are investigated for detection of nickel, cobalt, copper, lead, mercury, zinc and cadmium divalent metal ions by UV-vis spectroscopy. With the addition of all metal ions to the DMSO solution of ligands, the peaks at 558 and 549 nm increase in intensity with hypsochromic or bathochromic shifts except Zn²⁺ ions and **2**, while the peaks at 388 and 391 nm dramatically decrease in intensity. In both cases, the largest shift is observed after addition of copper ions. In solution, both receptors produce a cation blue shift from 558 and 549 nm to 503 and 497 nm with the sensible color change of solutions from purple-red to orange. Therefore, both compounds can highly recognize copper ions in DMSO solution. In the next step, Benesi-Hildebrand plot and Job's method are used for determination of binding constant (K_a) and stoichiometry of formed complexes, respectively. Also, the investigation of solvent effect in the UV-vis spectra of ligands shows that the generation of hydrazine and enamionone tautomers increases in highly polar solvents such as DMF and DMSO. Finally, the antioxidant activity of ligands is studied by DPPH method. The results show that NO₂ withdrawing groups in 1,2-[1-(3-imino-4-hydroxyphenylazo-4-nitrobenzene)]-4-nitrobenzene probably affect keto-enol equilibrium. As a result, this ligand reduces free radicals to non-reactive species by donating hydrogen.

Keywords: Azo-Azomethine ligands; UV-vis spectroscopy; Optical response; DPPH method; Molecular receptors

1. Introduction

Schiff bases are common organic compounds which can be easily synthesized. Among Schiff base derivatives, azo dyes are very important. Azo-azomethine compounds contain both azo and imine units. These compounds are produced by condensation of an azo dye containing aldehyde groups with primary amines.¹ Schiff bases and azo dyes have found applications in several fields such as medicinal, pharmaceutical and coordination chemistry. Some biological activities such as antifungal, antibacterial, anti-tumor, pesiticial, antiviral and anti-inflammatory has been known for Schiff-bases²⁻⁷ and azo compounds.⁸⁻¹¹ Because of the excellent donor properties of azo groups they are extensively used in coordination chemistry.¹²⁻¹⁴ Additionally, azomethine compounds can be used as chemosensors for metal ions and anions. They bind as ligands

to cations or interact with anions and therefore change color of the solution or maxima of absorbance band.¹⁵⁻¹⁸

Copper ions are important in metabolic processes, but in excess they can cause the imbalance of homeostasis leading to severe diseases such as Alzheimer's, Parkinson's, Mekne's, and Wilson's diseases.^{19,20} Also copper ions are one of the materials that pollute environment and produce some problems in industry. Cobalt ions are dangerous pollutants. Cobalt can irritate respiratory system and cause lung diseases.²¹ Therefore, the development of simple and selective chemosensors for copper and cobalt ions is necessary.^{22,23} Previously, we reported easy methods for designing low cost sensors based on azo- azomethine ligands for recognition of copper and cobalt ions.^{24,25} In progress, here we report synthesis, characterization and optical response of one new azo-salicyaldimine based ligand **1** (1,2-[1-(3-imino-4-hydroxyphenylazobenzene)]-4-ni-

trobenzene) for detection of copper, lead, mercury, cobalt, nickel, cadmium and zinc divalent metal ions by spectrophotometry technique. Then, the response of azo-azomethine groups of compound **1** is compared with compound **2** (1,2-[1-(3-imino-4-hydroxyphenylazo-4-nitrobenzene)]-4-nitrobenzene). Moreover, the antioxidant activity of both ligands is investigated against DPPH method.

2. Experimental

2.1. General

1-(3-formyl-4-hydroxyphenylazo)-4-nitrobenzene and 1-(3-formyl-4-hydroxyphenylazobenzene) were prepared according to previous methods.^{1,26} Elemental analyses were performed on ElementarVario ELIII. IR spectra were recorded on a FT-IR Spectrometer Bruker Tensor 27 in the region 4000–400 cm⁻¹ using KBr pellets. Electronic absorption spectra in the UV-vis region were obtained with T 60 UV/vis Spectrometer PG Instruments Ltd. NMR spectra were obtained on Bruker Avance 400 in DMSO with SiMe₄ as internal standard at room temperature.

2.2. Synthesis of Ligands

2.2.1. 1,2-[1-(3-imino-4-hydroxyphenylazobenzene)]-4-nitrobenzene (**1**)

1-(3-formyl-4-hydroxyphenylazobenzene) (1.84 mmol, 0.416 g) in ethanol (30 mL) was added drop wise over one hour to an ethanol solution (15 mL) of 4-nitro-1,2-diaminobenzene (0.920 mmol, 0.141 g), the color of solution changed quickly and brown precipitation appeared. After refluxing for 4h, the mixture was filtrated. The residue solid was washed with ethanol, recrystallized in CH₂Cl₂/C₂H₅OH and dried (red-brown powder). Yield (0.314 g, 60%). IR (KBr, cm⁻¹) 3363 (OH group), 1617 (–C=N– imine), 1519 and 1489 (–N=N– *cis* and *trans*), 1343 and 1313 (NO₂ group), 1273 (CO phenolic), 1150, 1106, 858, 747, 688, 643. ¹H NMR (400 MHz, DMSO-*d*₆): 12.60 (s, 2H, OH), 9.09 (s, 1H, ArH), 8.56 (s, 2H, –HC=N–), 8.41 (d, 4H, *J* = 8.69 Hz, ArH), 8.01–8.05 (m, 6H, ArH), 7.96 (d, 4H, *J* = 9.01 Hz, ArH), 7.20 (d, 1H, *J* = 8.90 Hz, ArH), 6.82 (d, 1H, *J* = 8.90 Hz, ArH), 6.76 (s, 2H, ArH),

Elem. Anal. Calcd for C₃₂H₂₃O₄N₇: C, 67.48; H, 4.04; N, 17.22. Found: C, 67.27; H, 3.91; N, 17.40.

2.2.2. 1,2-[1-(3-imino-4-hydroxyphenylazo-4-nitrobenzene)]-4-nitrobenzene (**2**)

This ligand was prepared from condensation reaction between 1-(3-formyl-4-hydroxyphenylazo-4-nitrobenzene) and 4-nitro-1,2-diaminobenzene in ethanol according to literature.²⁷ Yield (0.394 g, 65%). IR (KBr, cm⁻¹) 3364 (OH group), 1609 (–C=N– imine), 1520 and 1489 (–N=N– *cis* and *trans*), 1342 (NO₂ group), 1286 (CO phenolic), 1147, 1105, 1102, 857, 747, 688. ¹H NMR (400 MHz, DMSO-*d*₆): 12.60 (s, 2H, OH), 9.09 (s, 1H, ArH), 8.54 (s, 2H, –HC=N–), 8.41 (d, 4H, *J* = 8.05 Hz, ArH), 8.03 (d, 6H, *J* = 8.06 Hz, ArH), 7.95 (d, 2H, *J* = 9.1 Hz, ArH), 7.21 (d, 1H, *J* = 9.2 Hz, ArH), 6.81 (d, 1H, *J* = 9.2 Hz, ArH), 6.76 (s, 2H, ArH), Elem. Anal. Calcd for C₃₂H₂₁O₈N₉: C, 58.27; H, 3.19; N, 19.12. Found: C, 58.82; H, 2.91; N, 19.32.

2.3. Measurement of Radical Scavenging Activity

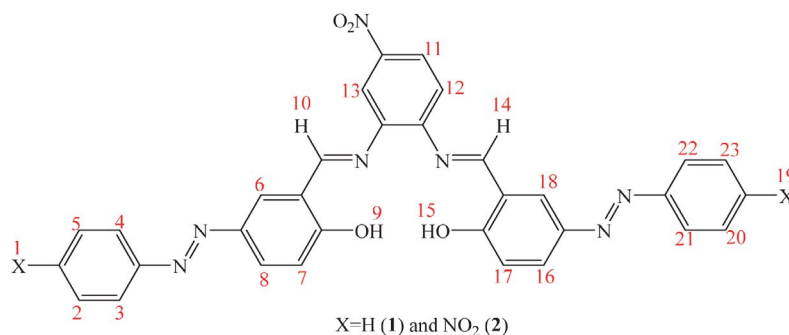
The ability of compounds **1** and **2** was investigated for removing free radicals by DPPH (1,1-diphenyl-2-picrylhydrazyl) using the method of literature.²⁸ The solutions of **1** or **2** in DMSO with concentrations of 10 to 60 μg/mL were added to a methanol solution of DPPH (0.1 mM). The mixtures were shaken seriously. Then the absorption of solutions was measured at λ = 517 nm after 10 minutes. Finally, the percentage of radical scavenging was determined by the following equation: (A_C is the absorbance of free DPPH and A_S is the absorbance of DPPH after reaction with **1** or **2**.)

$$\text{RSA}\% = 100 (A_C - A_S) / A_C \quad (1)$$

3. Results and Discussion

3.1. Synthesis and Characterization

Receptors **1** and **2** were synthesized from the condensation reaction of 1-(3-formyl-4-hydroxyphenylazobenzene) or 1-(3-formyl-4-hydroxyphenylazo-4-ni-



Scheme 1: Structures of azo-azomethine receptors

trobenzene) with 1,2-diamino-4-nitrobenzen benzene in ethanol and characterized by standard methods.

3. 1. 1. FT-IR and ^1H NMR Spectra

In the IR spectra of ligands, imine stretching vibration appears at 1617 cm^{-1} for **1** and 1609 cm^{-1} for **2**. The NO_2 symmetric and asymmetric stretching vibrations occur as sharp and strong bands at 1313 cm^{-1} and 1343 cm^{-1} . Moreover, the vibrations of ($-\text{N}=\text{N}-$) groups as *cis* and *trans* forms are present at 1519 cm^{-1} and 1489 cm^{-1} respectively.

The structure of **1** and **2** are fully characterized by ^1H NMR spectroscopy. The formation of imine group is established by the appearance of the signal at 8.56 ppm in **1** and 8.54 ppm in **2**, depending on the substituent attached to the imine nitrogen atom. The OH proton signals appear as one singlet at 12.64 in **1** and 12.61 ppm in **2**. The aromatic proton signals appear in the range of 6.76–9.09 ppm (Scheme 1 and Table 1).

An antioxidant acts *via* two mechanisms: one of them depends on the benzyl hydrogen atom and other follows the route of keto-enol form.²⁹ As shown in Fig. 1, compound **2** reveals high antioxidant activity against DPPH method (78% for $60\text{ }\mu\text{g/mL}$), while compound **1** display low activity (less than 13% for $20\text{ }\mu\text{g/mL}$). It seems that the possible mechanism for both compounds is the keto-enol route (Scheme 3). Several factors such as structure, temperature and solvent can affect the keto-enol equilibrium. The structure factors involve steric bulk, conjugation, electron-withdrawing/donating groups and resonance.³⁰ The structure of both compounds is similar (the only difference between two structures is the existence of NO_2 groups at the *para* position of azo units in **2**) (Scheme 1). These NO_2 withdrawing groups in compound **2** probably affect keto-enol equilibrium. As a result, ligand **2** reduces free radicals to non-reactive species by donating hydrogen.

Table 1: ^1H NMR chemical shifts of ligands **1** and **2**

Chemical shifts, δ TMS (ppm)	Assignments ^a	<i>J</i> (Hz)	Chemical shifts, δ TMS (ppm)	Assignments ^a	<i>J</i> (Hz)
Compound 1			Compound 2		
12.64	[s, 2H] (9, 15)		12.61	[s, 2H] (9, 15)	
9.10	[s, 1H] (13)		9.09	[s, 1H] (13)	
8.56	[s, 2H] (10, 14)		8.54	[s, 2H] (10, 14)	
8.42	[d, 4H] (3, 4, 21, 22)	8.69	8.41	[d, 4H] (3, 4, 21, 22)	8.05
8.01–8.05	[m, 6H] (2, 5, 7, 17, 20, 23)		8.03	[d, 6H] (2, 5, 7, 17, 20, 23)	8.06
7.96	[d, 4H] (1, 8, 16, 19)	9.01	7.95	[d, 2H] (8, 16)	9.01
7.20	[d, 1H] (12)	8.90	7.21	[d, 1H] (12)	9.20
6.82	[d, 1H] (11)	8.90	6.81	[d, 1H] (11)	9.20
6.76	[s, 2H] (6, 18)		6.76	[s, 2H] (6, 18)	

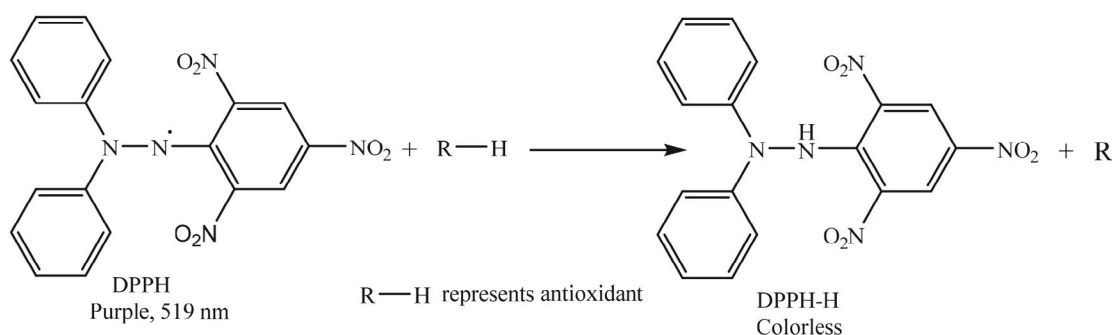
3. 2. Antioxidant Activity

The antioxidant activity of compounds **1** and **2** is investigated by DPPH radical scavenging method. In this method, radical DPPH reduces to its non-radical form in the presence of hydrogen-donating material that named antioxidant (Scheme 2).

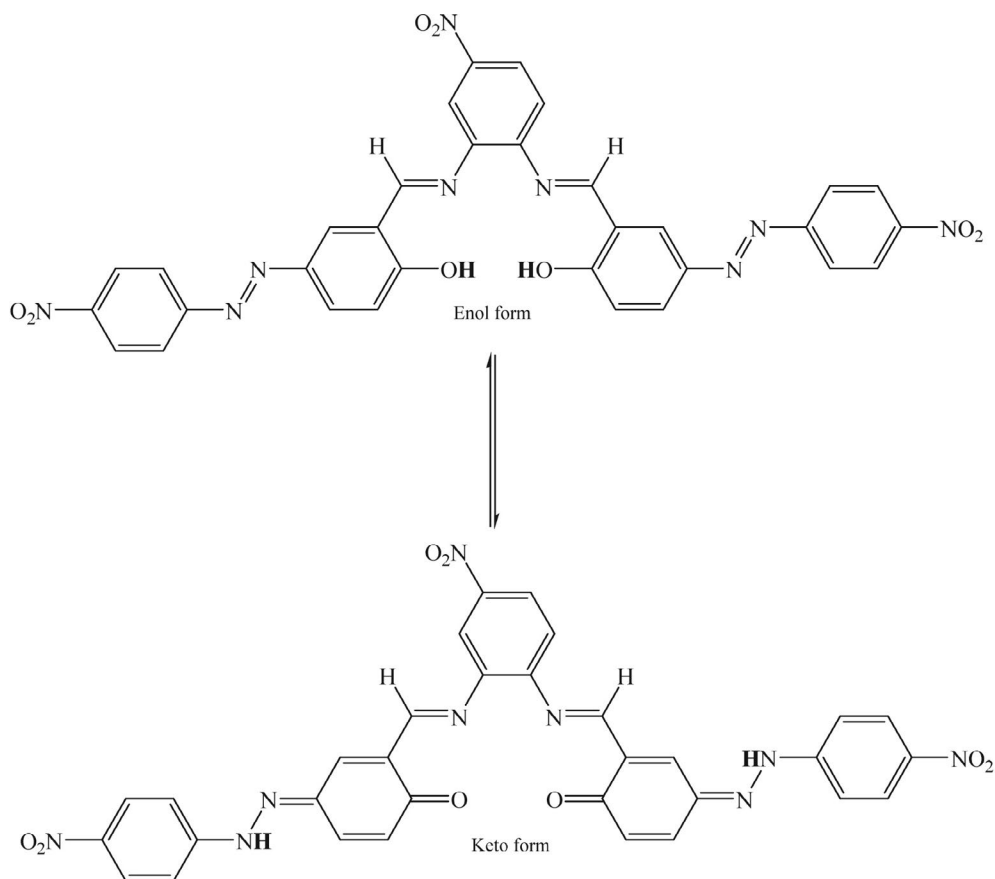
3. 3. UV-vis Spectroscopy Experiments

3. 3. 1. UV-vis Spectra of Ligands

Figs. 2 and 3 show the UV-vis spectra of receptors **1** and **2** in DMSO solution. Both compounds show one strong absorption band at $\lambda = 278\text{ nm}$ corresponding to



Scheme 2: DPPH radical and its stable form (DPPH= 1,1-diphenyl-2-picrylhydrazyl)



Scheme 3. Suggested mechanism for 1,2-[1-(3-imino-4-hydroxyphenylazo)-4-nitrobenzene]-4-nitrobenzene as antioxidant

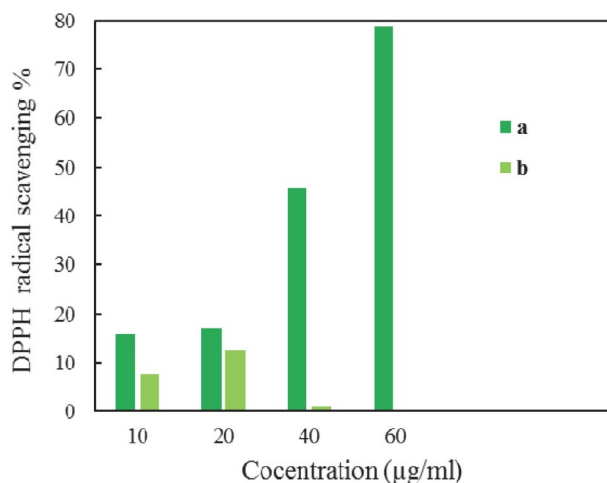


Fig. 1. Effects of 1,2-[1-(3-imino-4-hydroxyphenylazo)-4-nitrobenzene]-4-nitrobenzene (a) and 1,2-[1-(3-imino-4-hydroxyphenylazo)-4-nitrobenzene]-4-nitrobenzene (b) against DPPH after 10 min

the $\pi \rightarrow \pi^*$ transition of aromatic rings, one broad absorption band at $\lambda = 388$ nm for **1** and 391 nm for **2** attributable to the $\pi \rightarrow \pi^*$ transition of azo groups and $\pi \rightarrow \pi^*$ or $n \rightarrow \pi^*$ transition of imine groups³¹ and the strong and broad absorption band at $\lambda = 558$ nm for **1** and 549 nm for **2** corresponding to the $n \rightarrow \pi^*$ transition of ($-N=N$) units.³²

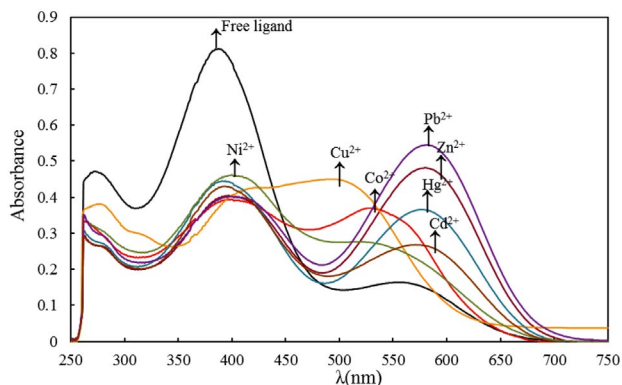


Fig. 2. UV-vis spectra of ligand **1** (0.02 mM) before and after adding a 0.02 mM concentration of various metal acetates in a DMSO solution

The UV-vis absorption spectra of azo Schiff-base ligands **1** and **2** in CH_2Cl_2 , CHCl_3 , CH_3OH and $\text{C}_2\text{H}_5\text{OH}$ show main band at 364–382 nm which can be assigned to $\pi \rightarrow \pi^*$ transition of azo groups. However, in DMSO and DMF solution, the first band that located at 388–391 nm, similar to other solvents, is because of $\pi \rightarrow \pi^*$ transition of azo groups, while the second one which appeared at 549–558 nm can be assigned to an intramolecular charge transfer $n \rightarrow \pi^*$ transition of azo-aromatic chromophore (Fig. 4).^{33,34} In general, the absorption bands of **1** and **2** at 364–

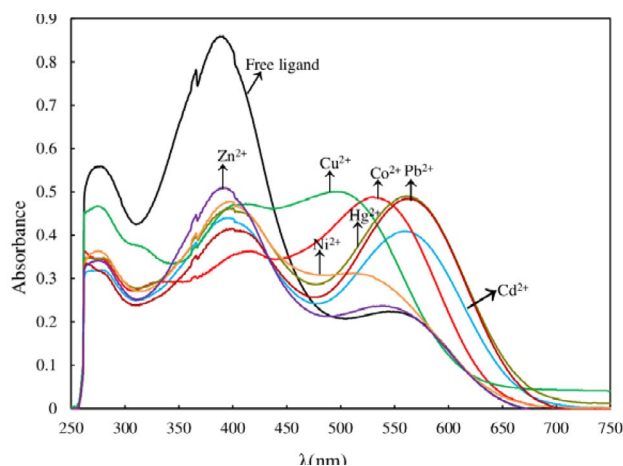


Fig. 3. UV-vis spectra of ligand **2** (0.01 mM) before and after adding a 0.01 mM concentration of various metal acetates in a DMSO solution.

391 nm show bathochromic shift with polarity change of solvents.^{35,36} Also, the solvatochromism that exhibited by azo ligands may be to the effect of proton transfer or dipole moment changes in various solvents (in DMSO and DMF an additional absorption maximum is observed at 549–558 nm. This absorption is attributed to the existence of tautomeric form on highly polar solvents).^{37,38}

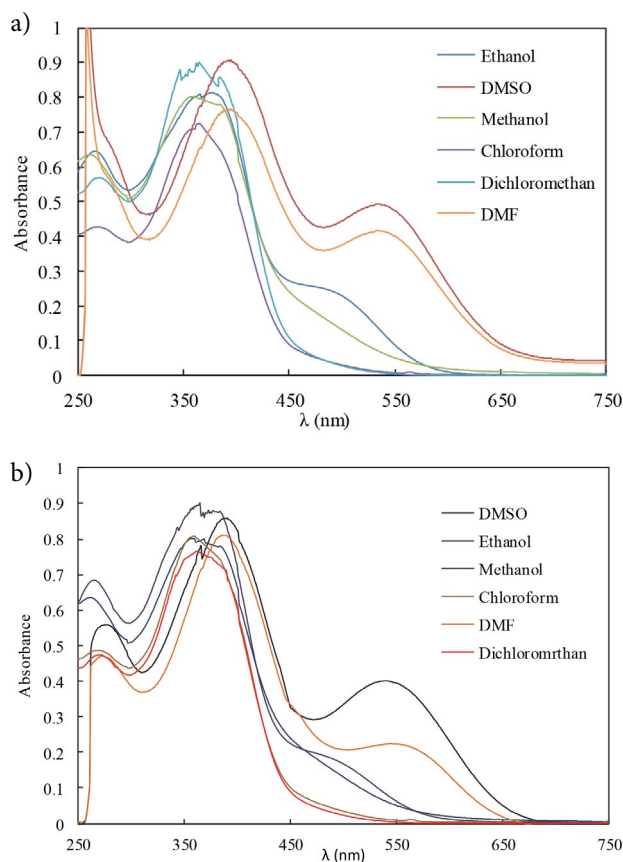


Fig. 4. UV-vis spectra of azo Schiff-bases **1** (a) and **2** (b) in various solvents ($\sim 10^{-4}$ M)

3. 3. 2. Cation Binding Studies

The optical response of **1** (2×10^{-5} mol L⁻¹) for Cu²⁺, Cd²⁺, Co²⁺, Zn²⁺, Ni²⁺, Pb²⁺ and Hg²⁺ as their acetate salts (2×10^{-5} mol L⁻¹) in DMSO is studied. As shown in Fig. 2, the broad band at 558 nm rises in intensity after addition of Pb²⁺, Zn²⁺, Hg²⁺ and Cd²⁺ ions to the DMSO solution of **1** with a bathochromic shift (+29 nm). The intensity of the band at 558 nm increases as follow: Pb²⁺ > Zn²⁺ > Hg²⁺ > Cd²⁺. Upon the addition of Cu²⁺ and Co²⁺ ions to **1** the peak at 558 nm increases in intensity and shifts to shorter wavelengths. The largest hypsochromic shift is seen after addition of copper ions (-55 nm) with the sensible color change of solution to orange. The peak at 388 nm shrinks in intensity with the addition of all studied cations. As shown in Fig. 2, no significant change is observed in the UV-vis spectrum of **1** after adding nickel ions.

The recognition ability of **2** (2×10^{-5} mol L⁻¹) for Cu²⁺, Cd²⁺, Co²⁺, Zn²⁺, Ni²⁺, Pb²⁺ and Hg²⁺ as acetate salts (2×10^{-5} mol L⁻¹) in DMSO is shown in Fig. 3. Upon addition of Pb²⁺, Cd²⁺ and Hg²⁺ ions to **2**, the peak at 549 nm increases in intensity with a bathochromic shift (almost +20 nm). Addition of Cu²⁺, Co²⁺ and Ni²⁺ ions to the DMSO solution of **2** exhibits significant increase in peak intensity at 549 nm with a hypsochromic shift. Similarity to **1**, the largest blue shift is obtained after addition of Cu²⁺ ions (-52 nm). As expected, addition of all metal ions to **2** shows decrease in peak intensity at 391 nm. It is notable that no significant change is observed in the UV-vis spectra of **2** after addition of Zn²⁺ ions.

In both cases, the changing in the UV-vis Spectra can be explained that: there is likely a fine balance between enol and keton forms of ligands in DMSO solution and the complexation of ligands with metal ions probably affect it. In additional, decreasing of $n \rightarrow \pi^*$ transition of imine groups in intensity shows nitrogen atoms of imine units coordinate to the metal ion center.^{39–41}

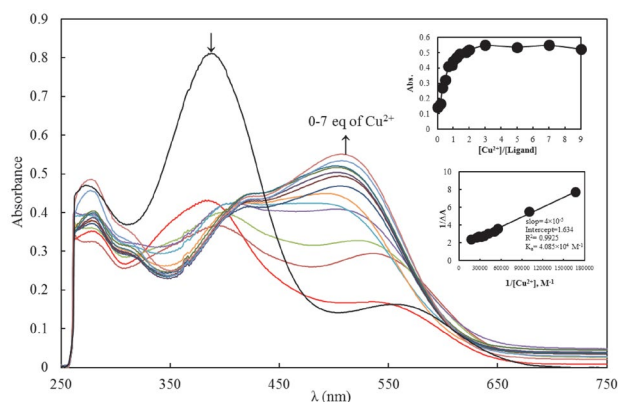


Fig. 5. Changes in the UV-vis spectra of **1** (0.020 mM) upon titration by Cu(CH₃COO)₂ in a DMSO solution, where the concentration of Cu(CH₃COO)₂ varies from 0.004–0.14 mM. Insets: above: Absorption at selected wavelength versus equivalents of cation added, down; Benesi–Hildebrand plot of the receptor with Cu²⁺ ion.

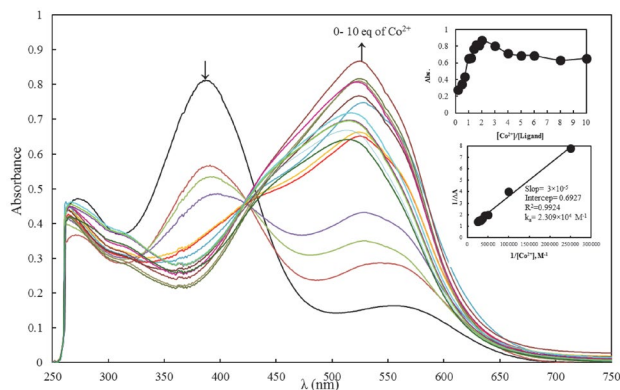


Fig. 6. Changes in the UV-vis spectra of **1** upon titration by $\text{Co}(\text{CH}_3\text{COO})_2$ in a DMSO solution, where the concentration of $\text{Co}(\text{CH}_3\text{COO})_2$ varies from 0.004–0.2 mM. Insets: above: Absorption at selected wavelength versus equivalents of cation added, down; Benesi-Hildebrand plot of the receptor with Co^{2+} ion.

2. 3. 3. Titrations with UV-vis Spectroscopy

Upon gradual addition of Cu^{2+} ions to DMSO solution of **1**, the absorption at 558 nm gradually increases in intensity with hypsochromic shift to 503 nm and the peak at 388 nm strongly decreases in intensity (Fig. 5). Similarity to **1**, with the progressive addition of Cu^{2+} ions to **2**, the peak at 549 nm shifts to 497 nm and increases in intensity, while the peak at 391 nm dramatically decreases and finally disappears (Fig. 7). In both case, the color solution change from purple-red to orange after addition of copper ions.

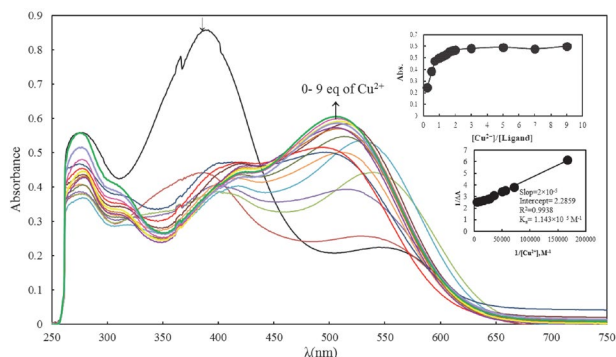


Fig. 7. Changes in the UV-vis spectra of **2** (0.020 mM) upon titration by $\text{Cu}(\text{CH}_3\text{COO})_2$ in a DMSO solution, where the concentration of $\text{Cu}(\text{CH}_3\text{COO})_2$ varies from 0.004–0.18 mM. Insets: above: absorption at selected wavelength versus equivalents of cation added, down; Benesi-Hildebrand plot of the receptor with Cu^{2+} ion.

Upon successive addition of Co^{2+} to **1**, a hypsochromic shift is observed from 558 to 525 nm. The peak at 525 nm rises with the gradual addition of cobalt ions to **1**. The peak at 388 nm dramatically decreases in intensity and disappears after extra addition of Co^{2+} ions (Fig. 6). Finally, upon incremental addition of Co^{2+} to **2**, $n \rightarrow \pi^*$ transition shifts from 549 nm to 537 nm. The peak at 537 nm gradu-

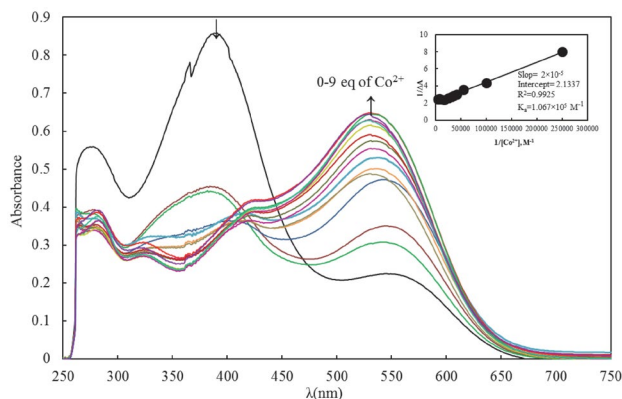


Fig. 8. Changes in the UV-vis spectra of **2** (0.020 mM) upon titration by $\text{Co}(\text{CH}_3\text{COO})_2$ in a DMSO solution, where the concentration of $\text{Co}(\text{CH}_3\text{COO})_2$ varies from 0.004–0.18 mM. Inset: Benesi-Hildebrand plot of the receptor with Co^{2+} ion.

ally increases in intensity while the peak at 391 nm decreases in intensity (Fig. 8).

The Job's plot results show a 1:1 binding stoichiometry for **1** and **2** with Cu^{2+} . (the proposed structure of **1** and **2** with Cu^{2+} is shown in Scheme 4) while the 2:1 binding stoichiometry for **1** and **2** with Co^{2+} is determined by Job's plot experiments (Fig. 9).

In the next step, 1:1 association constants of **1** and **2** with Cu^{2+} are determined on the Benesi-Hildebrand plots⁴² at $\lambda = 503$ and 497 nm, respectively (Figs. 5 and 7). Correspondingly, assuming a 2:1 (**1** or **2**: cobalt ion) complex, the binding constants (K_a) are also calculated using the Benesi-Hildebrand method (Figs. 6 and 8). The resulting values are summarized in Tables 3 and 4. As shown, the ability of both receptors for recognition of Cu^{2+} metal ion is similar while the tendency of **1** for detection of Co^{2+} ion is higher than **2**.

Table 2: UV-vis spectra data upon titration of compound **1** with cations in DMSO

Ligand + cation	Ligand, λ_{max} (nm)	Complex, λ_{max} (nm)	Hypsochromic shift, $\Delta\lambda_{\text{max}}$ (nm)	K_a (M^{-1})
Ligand- Cu^{2+}	558	503	-55	4.085×10^4
Ligand- Co^{2+}	558	525	-33	2.309×10^4

Table 3: UV-vis spectra data upon titration of compound **2** with cations in DMSO

Ligand + cation	Ligand, λ_{max} (nm)	Complex, λ_{max} (nm)	Hypsochromic shift, $\Delta\lambda_{\text{max}}$ (nm)	K_a (M^{-1})
Ligand- Cu^{2+}	549	497	-52	1.143×10^5
Ligand- Co^{2+}	549	537	-12	1.067×10^5

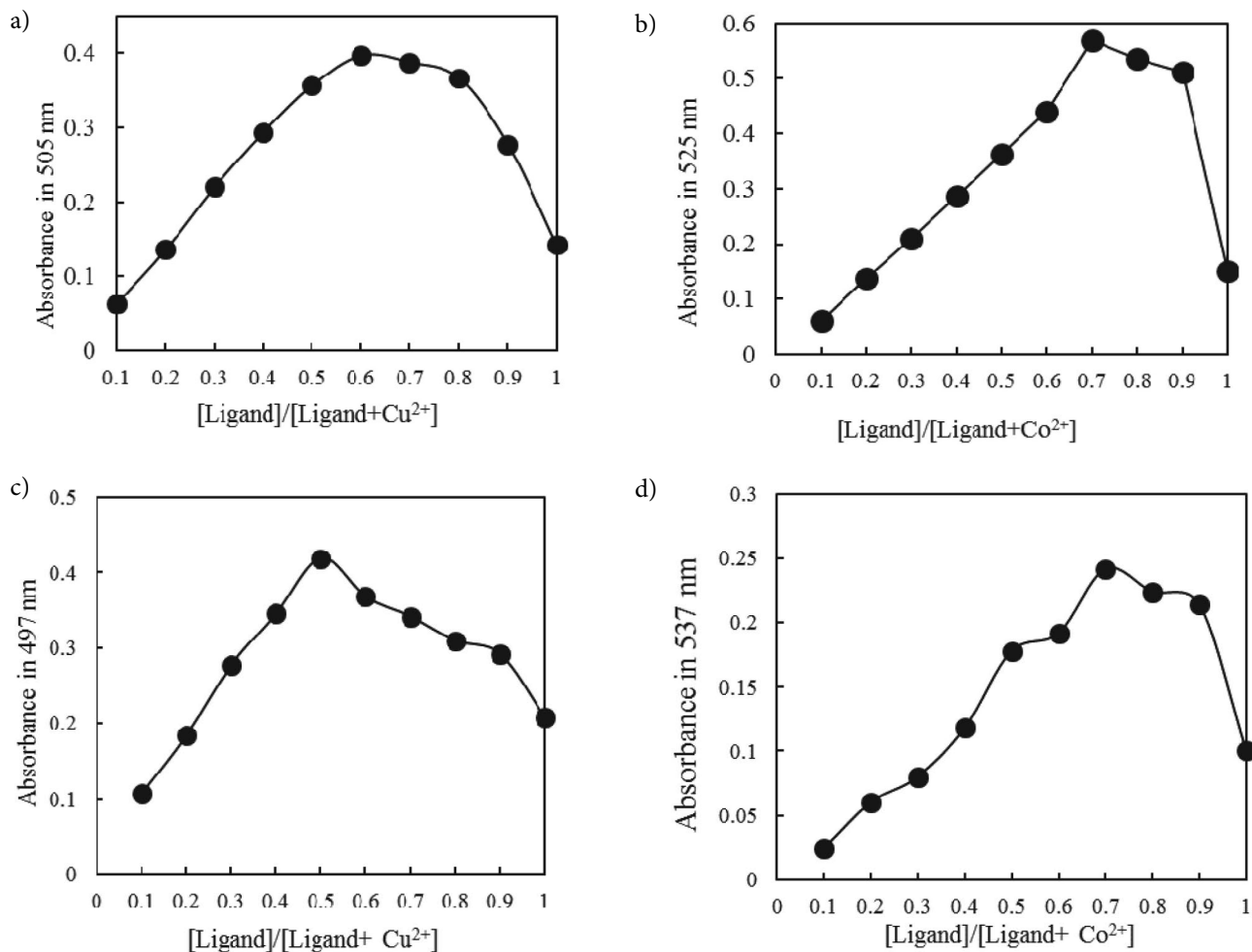
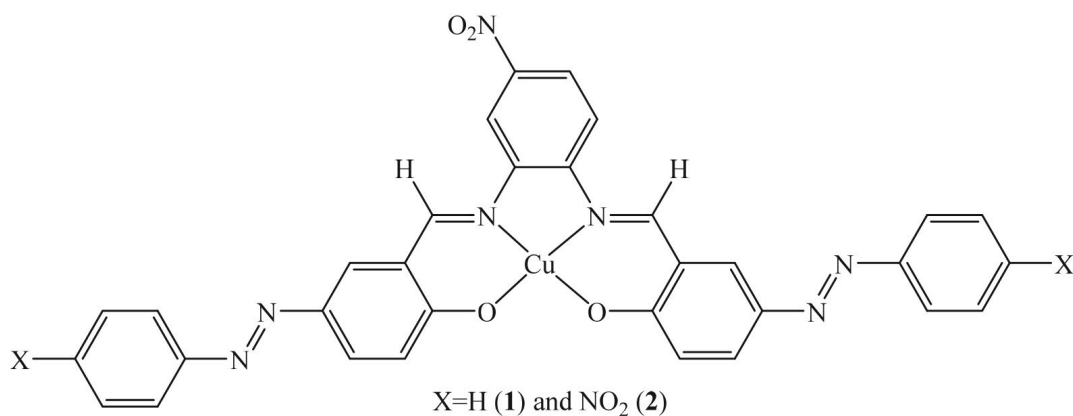


Fig. 9. Job plots for ligand 1 with Cu^{2+} (a) and Co^{2+} (b) and ligand 2 with Cu^{2+} (c) and Co^{2+} (d), where the absorptions are plotted against the mole fractions of ligands at an invariant total concentration of 2×10^{-5} M in DMSO.



Scheme 4. Suggested structure for ligands with Cu^{2+}

4. Conclusion

At first new azo-azomethin derivative **1** was synthesized and characterized with some standard methods. Then the optical response of azo units of the synthesized compound was investigated for detection of some divalent met-

al ions by spectrophotometry technique. In the next step, the results of cation recognition by 1,2-[1-(3-imino-4-hydroxyphenylazo)benzene]-4-nitrobenzene (**1**) was compared with 1,2-[1-(3-imino-4-hydroxyphenylazo)-4-nitrobenzene]-4-nitrobenzene (**2**) (the only difference of

between two structures is the existence of nitro groups at the *para* positions of azo units in **2**). Study revealed the ability of both receptors for recognition of Cu²⁺ metal ion to be similar while the tendency of **1** for detection of Co²⁺ ion is higher than **2** (the binding constant of **1** with copper and cobalt ions is larger than **2**). Also, the investigation of solvent effect in the UV-vis spectra shows that the generation of hydrazine and enaminone tautomers increase in highly polar solvents such as DMF and DMSO. Moreover, the investigation of antioxidant activity of ligands with DPPH method indicates NO₂ withdrawing groups in compound **2** probably affect keto–enol equilibrium. As a result, ligand **2** strongly reduced free radicals to non-reactive species while compound **1** showed low activity.

5. Appendix

FT-IR and ¹H NMR spectra of compounds **1** and **2** are available in Appendix.

6. Acknowledgments

This work was supported by Azarbaijan Shahid Madani University (Project NO. 217/d/9401).

7. References

- H. Dincalp, F. Toker, I. Durucasu, N. Avciyasi, S. Icli, *Dyes Pig.* **2007**, *75*, 11–24. DOI:10.1016/j.dyepig.2006.05.015
- E. Gungor, S. Celen, D. Azaz, H. Kara, *Spectrochim. Acta A.* **2012**, *94*, 216–221. DOI:10.1016/j.saa.2012.03.034
- S. A. Hudson, P. M. Maitlis, *Chem. Rev.* **1993**, *93*, 861–885. DOI:10.1021/cr00019a002
- A. Halve, A. Goyal, *Orient. J. Chem.* **2001**, *12*, 87–88.
- E. H. Saffa, D. M. Etaiw, E. A. Abd, H. A. E. Z. Eman, A. A. Elham, *Spectrochim. Acta A.* **2011**, *79*, 1331–1337. DOI:10.1016/j.saa.2011.04.064
- V. E. Kuzmin, V. P. Lozitsky, G. L. Kamalov, R. N. Lozitskaya, A. I. Zheltvay, A. S. Fedtchouk, D. N. Kryzhanovskiy, *Acta Biochim. Pol.* **2000**, *47*, 867–875.
- G. Ceyhan, M. Kose, M. Tumer, I. Demirtas, A. S. Yağlioğlu, V. McKee, *J. Lumin.* **2013**, *143*, 623–634. DOI:10.1016/j.jlumin.2013.06.002
- M. Sarigul, P. Deveci, M. Kose, U. Arslan, T. H. Dagi, M. Kurtoglu, *J. Mol. Struct.* **2015**, *1096*, 64–73. DOI:10.1016/j.molstruc.2015.04.043
- D. Mahata, S. M. Mandal, R. Bharti, V. K. Gupta, M. Mandal, A. Nag, G. B. Nando, *Int. J. Biol. Macromol.* **2014**, *69*, 5–11. DOI:10.1016/j.ijbiomac.2014.05.017
- S. N. Pandeya, D. Sriram, G. Nath, E. DeClercq, *Eur. J. Pharm. Sci.* **1999**, *9*, 25–31. DOI:10.1016/S0928-0987(99)00038-X
- D. Das, N. Sahu, S. Mondal, S. Roy, P. Dutta, S. Gupta, T. K. Mondal, C. Sinha, *Polyhedron*, **2015**, *99*, 77–86. DOI:10.1016/j.poly.2015.06.027
- M. Sarigul, A. Sari, M. Kose, V. McKee, M. Elmastas, I. Demirtas, M. Kurtoglu, *Inorg. Chim. Acta.* **2016**, *444*, 166–175. DOI:10.1016/j.ica.2016.01.042
- C. Anitha, C. D. Sheela, P. Tharmaraj, S. Sumathi, *Spectrochim. Acta A.* **2012**, *96*, 493–500. DOI:10.1016/j.saa.2012.05.053
- M. Al-Noaimi, A. Hammoudeh, M. El-khateeb, F. F. Awwadi, D. Taher, A. Mansi, O. S. Abdel-Rahman, *Inorg. Chim. Acta.* **2017**, *454*, 222–228. DOI:10.1016/j.ica.2016.04.029
- V. Reena, S. Suganya, S. Velmathi, *J. Fluor. Chem.* **2013**, *153*, 89–95. DOI:10.1016/j.jfluchem.2013.05.010
- A. K. Mahapatra, S. K. Manna, P. Sahoo, *Talanta*, **2011**, *85*, 2673–2680. DOI:10.1016/j.talanta.2011.08.040
- M. Orojloo, S. Amani, *Talanta*, **2016**, *159*, 292–299. DOI:10.1016/j.talanta.2016.06.042
- N. Kaur, S. Kumar, *Tetrahedron*, **2011**, *67*, 9233–9264. DOI:10.1016/j.tet.2011.09.003
- E. L. Que, D. W. Domaille, C. Chang, *J. Chem. Rev.* **2008**, *108*, 1517–1549. DOI:10.1021/cr078203u
- D. Pramanik, C. Ghosh, S. G. Dey, *J. Am. Chem. Soc.* **2011**, *133*, 15545–15552. DOI:10.1021/ja204628b
- A. Shahat, M. Awual, M. Naushad, *Chem. Eng. J.* **2015**, *271*, 155–163. DOI:10.1016/j.cej.2015.02.097
- J. Cheng, L. Yang, X. Zeng, H. D. Zhao, D. Tian, *Sens. Actuators B.* **2016**, *237*, 495–500. DOI:10.1016/j.snb.2016.06.106
- G. Wang, H. Chen, Y. Chen, N. Fu, *Sens. Actuators B.* **2016**, *233*, 550–558. DOI:10.1016/j.snb.2016.04.119
- B. Shaabani, Z. Shaghaghi, A. A. Khandar, *Spectrochim. Acta A.* **2012**, *98*, 81–85. DOI:10.1016/j.saa.2012.07.097
- Z. Shaghaghi, *Spectrochim. Acta A.* **2014**, *131*, 67–71. DOI:10.1016/j.saa.2014.04.026
- A. A. Khandar, Z. Rezvani, *Polyhedron* **1999**, *18*, 129–133. DOI:10.1016/S0277-5387(98)00275-7
- K. Hamidian, M. Irandoust, E. Rafiee, M. Joshaghani, *Z. Naturforsch.* **2012**, *57b*, 159–164.
- G. Dehghan, Z. Khoshkam, *Food Chem.* **2012**, *131*, 422–426. DOI:10.1016/j.foodchem.2011.08.074
- A. A. H. Kadhum, A. A. Al-Amiery, A. Y. Musa, A. B. Mohamad, *Int. J. Mol. Sci.* **2011**, *12*, 5747–5761. DOI:10.3390/ijms12095747
- K. T. Smith, S. C. Young, G. W. DeBlasio, C. S. Hamann, *J. Chem. Educ.* **2016**, *93*, 790–794. DOI:10.1021/acs.jchemed.5b00170
- A. Arab Ahmadi, S. Amani, *Molecules*, **2012**, *17*, 6434–6448. DOI:10.3390/molecules17066434
- H. Galen, G. Hennrich, J. D. Mendoza, P. Prados, *Eur. J. Org. Chem.* **2010**, 1249–1297. DOI:10.1002/ejoc.200901394
- A. Kakanejadifard, F. Azarbani, A. Zabardasti, A. Rezayat, M. Ghasemian, S. Kakanejadifard, *Spectrochim. Acta A.* **2013**, *114*, 404–409. DOI:10.1016/j.saa.2013.05.027
- M. Ghasemian, A. Kakanejadifard, F. Azarbani, A. Zabardasti, S. Kakanejadifard, *Spectrochim. Acta A.* **2014**, *124*, 153–158. DOI:10.1016/j.saa.2014.01.005
- G. Kurtoglu, B. Avar, H. Zengin, M. Kose, K. Sayin, M. Kurtoglu, *J. Mol. Liquids* **2014**, *200*, 105–114.

- DOI:10.1016/j.molliq.2014.10.012
36. M. Ghasemiana, A. Kakanejadifarda, F. Azarbani, A. Zabardasti, S. Shirali, Z. Saki, S. Kakanejadifard, *Spectrochim. Acta A*. **2015**, *138*, 643–647. DOI:10.1016/j.saa.2014.11.048
37. H. Khanmohammadi, M. Pass, K. Rezaeian, G. Talei, *J. Mol. Struct.* **2014**, *1072*, 232–237. DOI:10.1016/j.molstruc.2014.05.014
38. H. Khanmohammadi, A. Abdollahi, *Dyes Pigm.* **2012**, *94*, 163–168. DOI:10.1016/j.dyepig.2011.12.013
39. T. H. Kim, S. H. Kim, L. V. Tan, Y. G. Seo, S. Y. Park, H. Kim, J. S. Kim, *Talanta*, **2007**, *71*, 1294–1297. DOI:10.1016/j.talanta.2006.06.035
40. Y. Dong, T. H. Kim, H. J. Kim, M. H. Lee, S. Y. Lee, R. K. Mahajan, H. Kim, J. S. Kim, *J. Electroanal. Chem.* **2009**, *628*, 119–124. DOI:10.1016/j.jelechem.2009.01.015
41. T. H. Kim, S. H. Kim, L. Y. Tan, Y. Dong, H. Kim, J. S. Kim, *Talanta*, **2008**, *74*, 1654–1658. DOI:10.1016/j.talanta.2007.10.033
42. T. L. Kao, C. C. Wang, Y. T. Pan, Y. J. Shiao, J. Y. Yen, C. M. Shu, G. H. Lee, S. M. Peng, W. S. Chung, *J. Org. Chem.* **2005**, *70*, 2912–2920. DOI:10.1021/jo047880a

Povzetek

Glede na uporabo azo-azometinov v kemijskih senzorjih in zaradi njihove biološke aktivnosti smo raziskovali dva receptorja, 1,2-[1-(3-imino-4-hidroksifenilazobenzen)]-4-nitrobenzen (**1**) in 1,2-[1-(3-imino-4-hidroksifenilazo-4-nitrobenzen)]-4-nitrobenzen (**2**) za detekcijo nikljevih, kobaltovih, bakrovih, svinčevih, živosrebrih, cinkovih in kadmijevih dvovalentnih ionov z UV-vis spektroskopijo. Z dodatkom kovinskih ionov v raztopino ligandov v DMSO se vrhovom pri 558 in 549 nm poveča intenziteta s hipokromnim ali batokromnim premikom, razen v primeru Zn^{2+} iona in **2**, medtem ko se vrhovom pri 388 in 391 nm znatno zmanjša intenziteta. V obeh primerih se po dodatku bakrovih ionov pojavi največji premik. V raztopinah oba receptorja povzročita premik vrhov pri 558 in 549 nm na 503 in 497 nm z zaznavno barvno spremembo raztopin od vijolično-rdeče do oranžne barve. Obe spojini zelo dobro zaznavata bakrove ione v raztopini DMSO. V naslednjem koraku smo uporabili Benesi-Hildebrandove diagrame in Jobovo metodo za določanje konstant stabilnosti (K_a) in stehiometrije nastalih kompleksov. Proučevanje vpliva topliva na UV-vis spektre ligandov kaže, da je pri polarnih topilih, kot sta DMF in DMSO, večji delež hidrazinskega in enaminonskega tautomera. Nadalje smo določili antioksidativno aktivnost ligandov z metodo DPPH. Rezultati kažejo, da NO_2 elektronakceptorske skupine na 1,2-[1-(3-imino-4-hidroksifenilazo-4-nitrobenzen)]-4-nitrobenzenu verjetno vplivajo na keto-enol ravnotežje. Rezultat tega je, da ligand pretvori proste radikale v nereaktivne zvrsti z doniranjem vodika.

Scientific paper

Room-Temperature Synthesis and Optical Properties of NdVO₄ Nanoneedles

Mirela Dragomir^{1,3,*} and Matjaž Valant^{1,2}¹ Materials Research Laboratory, University of Nova Gorica, Slovenia² University of Electronic Sciences and Technology of China, Institute of Fundamental and Frontier Science, North Jianshe Road No. 4 Section 2, Chengdu, China³ Present address: Department of Chemistry and Chemical Biology, McMaster University, Hamilton, Ontario, L8S 4M1, Canada

* Corresponding author: E-mail: mirela85.dragomir@gmail.com

Received: 25-03-2018

Abstract

Tetragonal NdVO₄ nanoneedles were prepared via a simple room-temperature precipitation method in the absence of any surfactant or template, starting from simple inorganic salts, NdCl₃ and Na₃VO₄, as raw materials. The nanoneedles were characterized by XRPD, SEM, Raman, PL, and lifetime spectroscopy. The particles have a length of about 100 nm and a diameter of 20 nm and grow along <112> direction. The advantages of this method lie in the high yield, non-toxic solvents, mild reaction conditions, and that it can potentially be employed for the preparation of other 1D lanthanide vanadates.

Keywords: Nanostructures; Chemical synthesis; Optical properties; Raman spectroscopy; X-ray diffraction

1. Introduction

The interesting optical properties of lanthanides such as luminescence, up-conversion, wide optical transparency, or large birefringence originate primarily from the multitude of transitions within the 4fⁿ electronic states of the lanthanide ion. Thus, lanthanide-containing materials find applications as laser host matrices, optical polarizers, thermophosphors, sensors, solar cells, scintillators for γ -rays detection, in nuclear waste storage, ionic conductors, catalysts or photocatalysts.^{1–5} The efficiency of the 4fⁿ excitations in a lanthanide ion can be enhanced through a charge transfer from a host material with a higher absorption coefficient. The orthovanadate group, VO₄^{3–}, is a good host for the trivalent ion because it can excite most of the lanthanide ions via the charge transfer transition within the VO₄^{3–} group, followed by an energy transfer to the emissive lanthanide ion. Choosing a crystal site with a very low symmetry for the lanthanide ion further increases the rate of absorption and emission, which can result in higher quantum yields.

In a tetragonal ABO₄ structure type, the A-site ion has a D_{4h} symmetry. Thus, a lanthanide ion sitting on this crystal site has a low symmetry which favours the elec-

tric dipole transitions resulting in higher radiative rate constants and less quenching processes. Neodymium vanadate, NdVO₄, is one of the most studied orthovanadate from the lanthanide orthovanadate family with the ABO₄-type structure. Numerous investigations have been made on optical materials based on NdVO₄ due to their good optical properties.^{3,6,7} For example, Y-doped NdVO₄ is a well-known laser material with five times higher absorption coefficient at 808 nm (the standard wavelength of the currently available laser diodes) than the Nd:YAG laser diode.⁶ The catalytic properties of NdVO₄ have also been investigated, i.e. for oxidative dehydrogenation of propane.² Additionally, it has been found that NdVO₄ exhibits a photocatalytic activity for degradation of dyes and organic pollutants comparable or even higher than that of the commercial TiO₂.^{8,9} Another study indicated that Mo-doping increased the photocatalytic activity of NdVO₄ for the degradation of different dyes (e.g., methylene blue, rhodamine B, remazol brilliant blue).⁴

At ambient conditions, NdVO₄ adopts a zircon-type structure in the I4₁/amd (Z = 4) space group with the lanthanide ion located in a polyhedron coordinated by eight oxygen ions. Under an applied pressure of about 6 GPa,

the zircon-type NdVO_4 undergoes a phase transformation to a metastable monazite-type structure with the space group $P2_1/n$ ($Z = 4$) where the Nd atoms are located in a eight-coordinate site (with eight unique Nd–O bond distances).^{10,11} At around 11.4 GPa, NdVO_4 further transforms to a scheelite-type phase and so to a denser packing. All these phase transformations are accompanied by a decrease of the band gap by 0.5 eV (measured on a single crystal).¹⁰

Due to large specific surface areas and quantum size effects, nanocrystalline materials exhibit properties that are usually not observed in the bulk. Accordingly, the lanthanide orthovanadates in the form of nanocrystals show properties that make them potential multiphoton fluorescent materials, biochemical labels, solar cells, light emitting diodes (LEDs), oxidant sensors, and contrast agents in magnetic resonance imaging.^{12–16} Therefore, the design and synthesis of the nanosized NdVO_4 opens up many opportunities for applications. Several methods have been developed for the synthesis of 0D, 1D or 2D NdVO_4 nanostructures such as: microwave synthesis, co-precipitation followed by thermal treatment, hydrothermal, metathesis reactions, or sonochemical synthesis.^{8,17–21} Each of these methods has certain drawbacks – the requirement of either thermal treatment at high temperatures, long reaction time (up to several days), expensive equipment or the use of toxic solvents.

A new and simple method to obtain crystalline NdVO_4 nanoparticles at room temperature through a precipitation method, using a cheap and non-toxic solvent is reported in this study. In addition of being a very convenient and fast method, this route also conserves energy because it does not involve any thermal treatment.

2. Experimental Part

2.1. Synthesis

The precipitation procedure for the synthesis of NdVO_4 nanoparticles employed in this study is summarized in the scheme depicted in Fig. 1.

In this method, $\text{NdCl}_3 \cdot 6\text{H}_2\text{O}$ (99.9%, Alfa Aesar) and Na_3VO_4 (99.9%, Alfa Aesar), were used as precursors and $\text{NH}_3(\text{aq})$ (25%) was the precipitating agent. Firstly, a NdCl_3 aqueous solution was prepared by adding 0.05 mol $\text{NdCl}_3 \cdot 6\text{H}_2\text{O}$ to 2 mL of distilled H_2O , while a Na_3VO_4 solution was prepared by dissolving 0.05 mol Na_3VO_4 in 3 mL of distilled H_2O . The pH of the final solution was adjusted to < 1 with a few mL of $\text{HCl}(\text{aq})$ (32%). Secondly, the two solutions were mixed slowly until a clear yellow solution resulted. $\text{NH}_3(\text{aq})$ (25%) was then added fast and under vigorous stirring to the above solution until the pH reached a value of ~ 11 . A blueish-green precipitate formed. Then the obtained mixture was stirred for five more minutes before the precipitate was filtered, washed thoroughly with $\text{NH}_3(\text{aq})$ and then dried at room temperature over-

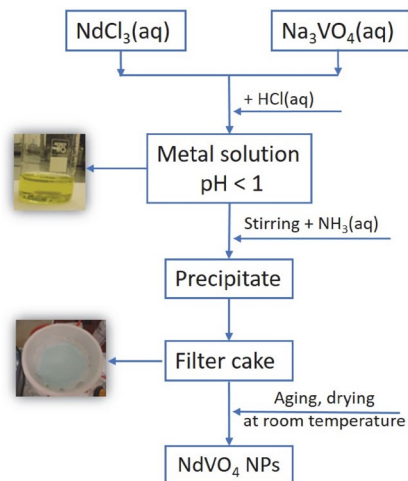
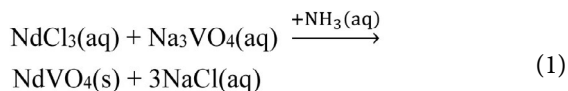


Fig. 1. A schematic representation of the synthetic procedure to obtain NdVO_4 nanoparticles.

night. The reaction that leads to the formation of NdVO_4 can be summarized as follows:



2.2. Characterisation

The phase composition was analysed by X-ray powder diffraction (XRPD) using a PANalytical X'Pert PRO diffractometer with $\text{Cu K}\alpha_1$ radiation ($\lambda = 1.54056 \text{ \AA}$). The X-ray powder diffraction pattern was collected over the 2θ range $5\text{--}80^\circ$ with a step size of 0.017° . A structure refinement was conducted using *Topas* (version 6, Bruker, AXS, Karlsruhe, Germany). A fundamental parameters approach was used for the profile fitting.²² A profile refinement was conducted in which the background (6th order Chebyshev polynomial), the unit cell parameters, the scale factor, the crystallite size, the sample displacement, and preferred orientation were stepwise refined to obtain a calculated diffraction profile that best fit the experimental pattern. All the occupancies were fixed at nominal composition and kept constant during refinement. Finally, the quality of the fit was assessed from the fit parameters such as R_{wp} , R_p and χ^2 .

The morphology of the NdVO_4 nanopowders was examined with a Scanning Electron Microscope (SEM) model JEOL JSM 7100F, operating at an accelerating voltage of 10 kV (in secondary electron mode). The samples were first dispersed in ethanol, then few drops of this dispersion were added onto a Si wafer and air dried. The Si wafer was fixed on the SEM sample holder using a carbon tape.

Raman spectroscopy was used for identification and structural characterisation of the NdVO_4 nanoparticles. Room temperature Raman spectra were collected in

a 180° backscattering geometry, with a microprobe Raman system type Horiba Jobin-Yvon Lab RAM HR spectrometer equipped with a holographic notch filter and a CCD detector, using a 632.81 nm excitation line of a 25 mW He-Ne laser. The samples were placed and oriented on an Olympus BX 40 microscope equipped with 50× objective and the spectra were recorded in the 50–1000 cm^{-1} range with a resolution of 1 μm . To test the phase purity, the spot resolution of were recorded on different regions of the sample.

Diffuse reflectance spectroscopy (DRS) measurements were performed to obtain the band gap energies. The DRS spectra were recorded in the 250–800 nm range, with a UV-Vis spectrophotometer (Perkin Elmer, model λ 650S) equipped with a 150 mm integrated sphere and using Spectralon as a reference material. The DRS data were converted to absorbance coefficients according to Kubelka-Munk method where NdVO_4 was considered a direct band gap semiconductor.²³ The details of the determination of band gap energies by using the Kubelka-Munk theory are described elsewhere.²⁴ The photoluminescence (PL) emission spectra were collected with an Edinburgh Instruments Spectrometer (model FLS920) using a steady state 450 W xenon arc lamp. The experimental setup was equipped with a blue-sensitive high speed photomultiplier (Hamamatsu H5773-03 detector) tube. The emission spectra were collected at room temperature, in a 400–700 nm range, using an excitation wavelength of 371 nm ($\lambda_{\text{em}} = 524$ nm).

Information on the electron relaxation and recombination mechanisms were obtained by monitoring the PL intensity at a specific wavelength as a function of time delay after an exciting laser pulse. The time-resolved PL spectra were recorded at room temperature on a pico-second diode laser EPL 375 with an excitation wavelength of 371 nm, in the time range 0 to 50 ns. The analysis of the fluorescence decays was performed using the F900 analysis software. The measured (convoluted) data was fitted using the “Reconvolution Fit method”.²⁵ This method fits the sample response to the data over the rising edge, to match the theoretical sample response, $R(t)$. The Reconvolution Fit procedure extracts the raw data (fluorescence decay) and eliminates both the noise and the effects of the exciting light pulse.

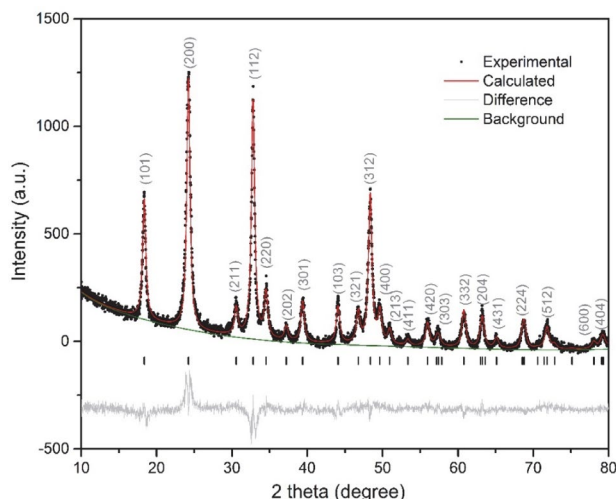


Fig. 2. X-ray powder diffraction pattern of the NdVO_4 nanopowder. The black full circles represent raw data and, red solid line is the Rietveld fit, the black vertical bars are the Bragg reflections, while the grey line shown below is the difference between observed and calculated intensity.

3. Results and Discussion

3. 1. X-ray and SEM Studies

Fig. 2 shows the XRPD patterns of the as-obtained NdVO_4 sample, which was indexed as a tetragonal NdVO_4 phase with the space group $I4_1/amd$ (ICSD code 78077). No impurities were detected. Additionally, the Rietveld refinement indicated that the (112) reflection appears with higher intensity due to the preferred directional growth of the nanoneedles along $\langle 112 \rangle$. The unit cell parameters obtained after the Rietveld refinement are presented in Table 1. The agreement factors were: $R_p = 6.59$, $R_{wp} = 7.78$, and $\chi^2 = 1.26$. As it can be seen, the refined cell parameters are in good agreement with the literature reported values.

The particle size and morphology were examined by SEM. From Fig. 3 it can be seen that the NdVO_4 particles prepared in this study have a needle-like shape with a length of about 100 nm and a diameter of about 20 nm. A schematic representation showing the NdVO_4 nanoneedles grown along $\langle 112 \rangle$ is depicted in Fig. 4. The SEM study also showed that the nanoparticles tend to agglomerate leading to formation of larger clusters.

Table 1. The unit cell parameters obtained after Rietveld refinement of the NdVO_4 nanoneedles and a comparison with the literature-reported values.

Unit cell parameters Space group: $I4_1/amd$	This study (nanoneedles)	Yuvaraj et al. ²⁶ (27 nm particles)	Fuess et al. ²⁷ (polycrystalline)	Panchal et al. ¹¹ (polycrystalline)
a (Å)	7.3397(6)	7.3571	7.3290	7.334(1)
b (Å)	7.3397(6)	7.3571	7.3290	7.334(1)
c (Å)	6.4128(6)	6.4227	6.4356	6.436(1)
c/a	0.8737(6)	0.8729	0.7878	0.8776(1)
V (Å ³)	346.332(65)	347.641	345.683	346.177

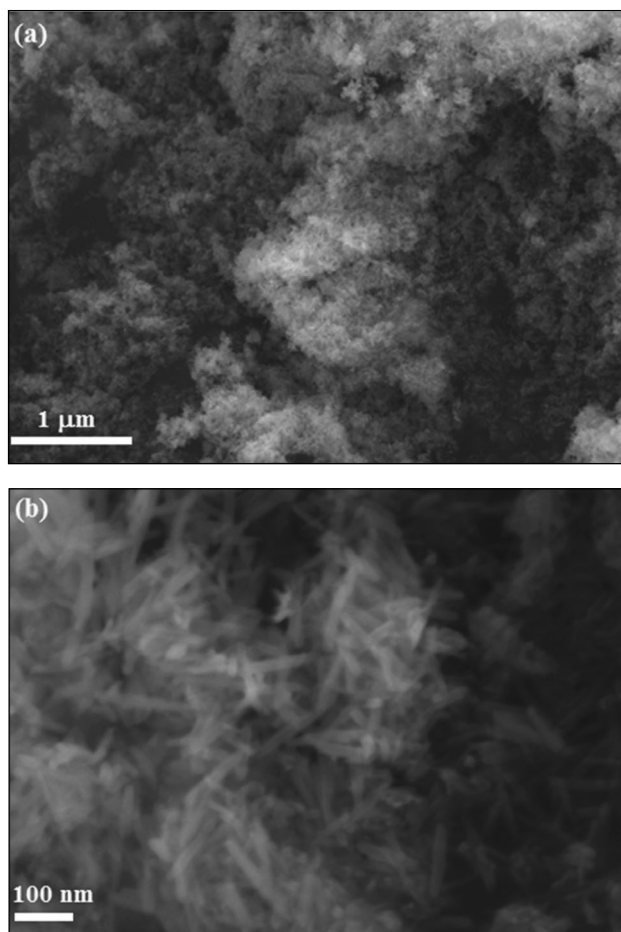


Fig. 3. SEM images of the NdVO_4 nanopowders. (a) Low magnification, (b) High magnification.

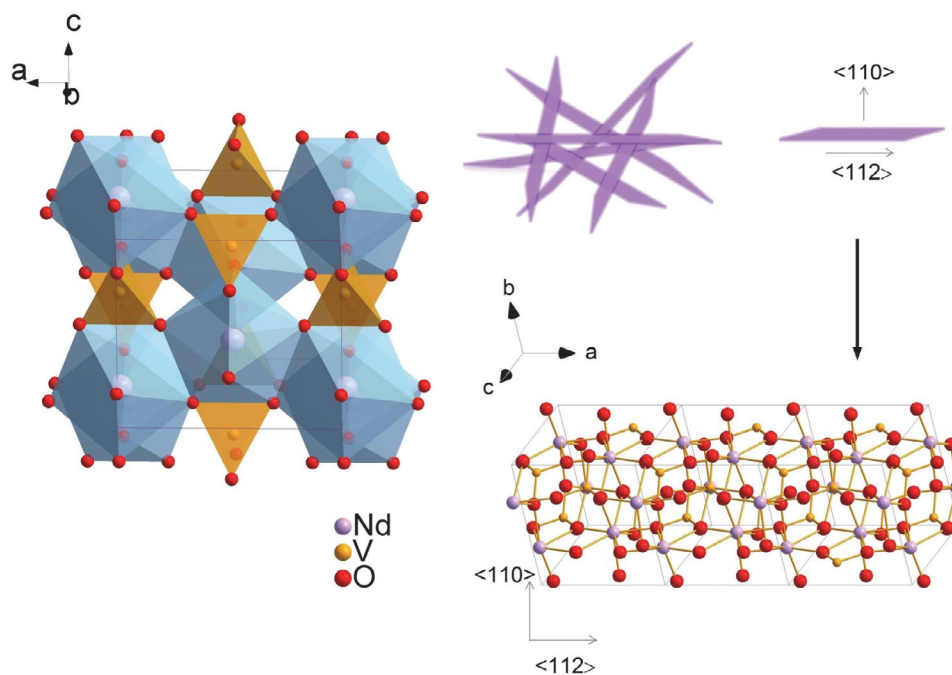


Fig. 4. (a) Crystal structure of NdVO_4 ; (b) Schematic representation of the as-grown NdVO_4 nanoneedles; (c) Ball-and-stick model showing a tetragonal NdVO_4 nanoneedle grown along $\langle 112 \rangle$.

3. 2. Raman Analysis

Raman analysis was performed on the as-obtained NdVO_4 nanopowders to study finer structural details (Fig. 5). As the XRPD analysis already suggested, the NdVO_4 synthesised in this study is adopting the zircon-type structure. From a group theory consideration NdVO_4 adopting this structure has 12 Raman active modes: $2A_{1g}$, $4B_{1g}$, B_{2g} , and $5E_g$.²⁸ From these 12 modes, 7 are internal modes associated with vibrations in the VO_4 structural unit ($2A_{1g}$, $2B_{1g}$, $1B_{2g}$, $2E_g$), and 5 are external vibrations ($3E_g$, $2B_{1g}$). So far, the Raman spectra of NdVO_4 have been measured on single crystals and polycrystalline samples by several

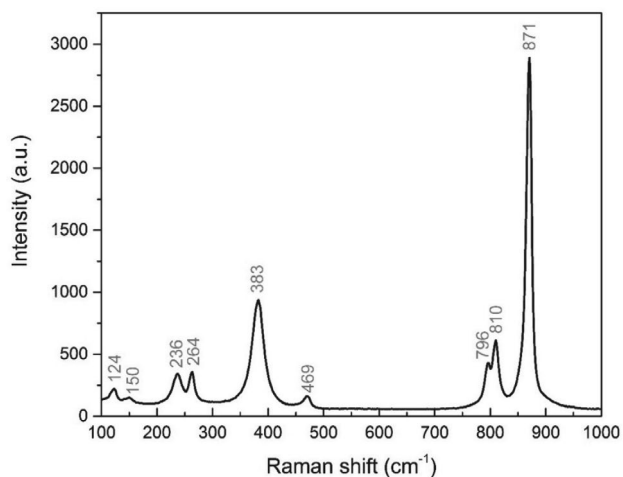


Fig. 5. Raman spectrum of the NdVO_4 nanoparticles prepared in this study.

Table 2. The Raman modes of NdVO₄ reported in the literature and the Raman modes observed in this study.

Study	Sample type	Peak position (cm ⁻¹)											Temp.
This study	Nanoneedles	871	810	796	469	383	–	264	236	150	124	–	297 K
Panchal et al. ¹¹	Polycrystalline	871	808	794	472	381	373	260	243	151	124	113	297 K
Yuvaraj et al. ²⁶	Nano rods	876	–	770	–	–	–	–	–	–	–	–	297 K
Jandl et al. ²⁹	Single crystal	873	810	797	472	381	–	259	242	151	122	–	10 K
Nguyen et al. ²⁸	Single crystal	871	808	795	472	381	375	260	237	148	123	113	297 K
Antic-Fidancev et al. ³⁰	Polycrystalline	873	810	797	473	380	378	259	242	151	121	111	4.2 K
		868	805	790	471	380	375	262	235	151	122	112	4.2 K
Santos et al. ³¹	Single crystal	871	808	795	472	381	375	260	237	148	123	113	297 K

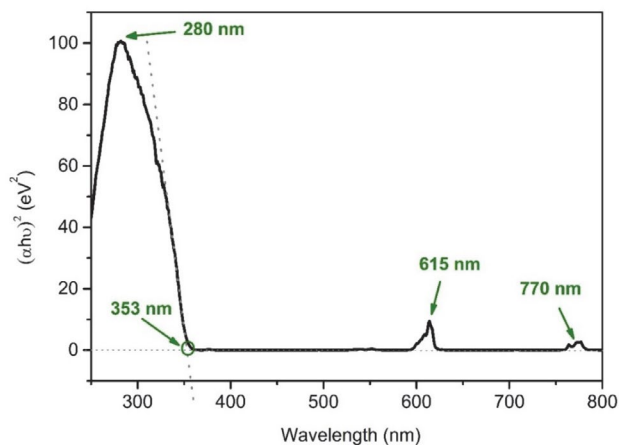
research groups. A comparison of our results with the literature reports is shown in Table 2.

It can be seen that the observed Raman modes in this study are in good agreement with the literature data. The only modes that were not observed are the modes located at 113, 225, and 373 cm⁻¹ (these modes are rarely observed). In the 100–1000 cm⁻¹ region, the Raman spectrum of NdVO₄ shows 9 modes that are separated in two regions. The high frequency region includes the internal modes in the VO₄ units, whereas the external modes occur at lower frequency and correspond to motions of the Nd–O bonds in the NdO₈ polyhedron. The symmetry annotations were made in accordance with the previous assignments reported in the literature.^{10,11,27}

3. 3. Optical Studies

Fig. 6 shows the UV-Vis diffuse reflectance spectrum of the NdVO₄ nanoneedles prepared in this study.

The light absorption was observed at a wavelength of about 770 nm, followed by another absorption at about 615 nm. A third absorption peak started at about 353 nm, increased sharply and reached a maximum at about 280 nm (associated with the O²⁻–V⁵⁺ charge transfer within the VO₄³⁻ group).^{32,33} The sharp increase at about 353 nm corresponds to the band gap transition in NdVO₄. The additional absorption peaks observed in the UV-Vis

**Fig. 6.** The UV-Vis diffuse reflectance spectrum of the NdVO₄ nanopowder prepared in this study.

spectrum of NdVO₄ at about 615 and 770 nm have been described in the literature and they are summarized in Table 3.

From the plot of the absorbance versus the energy (Fig. 7) the band gap of the NdVO₄ nanopowders was calculated to be 3.50 eV, which is in the UV region of the electromagnetic spectrum. This value falls well in the range of values reported by other research groups.^{8,10}

The electronic structure of zircon-type NdVO₄ has also been investigated by Panchal et al.¹⁰ They observed

Table 3. Characteristic peaks observed in the 500–800 nm range in the UV-Vis absorption spectra of NdVO₄.

Peak position (nm)			Synthesis method and particle size	Study	Comments/ Assignment From ⁴ I _{9/2} to:
(1)	(2)	(3)			
–	615	770	Co-precipitation, needles of ~100 nm length and 20 nm diameter	This study	(1) / (2) ⁴ G _{5/2} and (3) ⁴ F _{7/2}
–	590	750	Solid-state reactions, ~1 μm.	Dragomir et al., ^{24,34} Singh et al.	(1) / (2) ⁴ G _{5/2} , (3) ⁴ F _{7/2}
532	582	744	Templated sol-gel Nanotubes with the diameter of about 40 nm	Peng et al. ³⁵	(1) ⁴ G _{7/2} and ⁴ G _{9/2} (2) ⁴ G _{7/2} , (3) ⁴ F _{7/2} and ⁴ S _{3/2}
538	590	752	Nanowires, 100 nm diameter and 3 μm length	Xu et al. ³⁶	(1) ² G _{7/2} , (2) ⁴ G _{5/2} , (3) ⁴ F _{7/2}
~525	593	753	Hydrothermal, nanorods, length: 400–700 nm.	Wu et al. ³⁷	(1) ⁴ G _{7/2} and ⁴ G _{9/2} , (2) ⁴ G _{5/2} , (3) ⁴ F _{7/2}

that NdVO_4 shows similar band shape with LuVO_4 and YVO_4 ; the upper part of the valence band and the lower part of the conduction band is mainly comprised of the V $3d$ and O $2p$ states, whereas the Nd $6s$ states contribute to a decrease in the band gap due to their hybridization with the antibonding conduction band states.

Under UV excitation (Fig. 8) the NdVO_4 nanoneedles show green, yellow, and orange emissions. The NdVO_4 spectrum consists of a broad peak centred at about 500 nm with three small shoulders at about 523, 545, and 600 nm. Several researchers have reported the photoluminescence spectra of nanosized NdVO_4 (excited with UV light). Wu et al. reported the PL emission spectrum of single crystalline nanorods (of ~ 200 nm in diameter and 400–700 nm in length).³⁷ The spectrum shows a strong emission around 490 nm followed by two less intense peaks at ~ 525 and 550 nm and a triplet at about 600–615 nm.

The NdVO_4 nanoneedles prepared in this study show similar peaks. Similar results were also obtained for 1 μm NdVO_4 particles prepared by a solid-state method and described by Dragomir et al.²⁴ Briefly, the emission at about 500 nm can be assigned to the ${}^4G_{11/2} \rightarrow {}^4I_{11/2}$ transition, whereas the shoulders at ~ 525 , 545, and 600 nm can be attributed to the ${}^4G_{7/2} \rightarrow {}^4I_{9/2}$, ${}^4G_{7/2} \rightarrow {}^4I_{9/2}$, and ${}^4G_{5/2} \rightarrow {}^4I_{9/2}$ transitions, respectively.

Fig. 9 shows the time-resolved photoluminescence spectrum of the NdVO_4 nanoneedles excited by a 371 nm laser wavelength and monitored at 524 nm. This decay curve could only be simulated by a third-order exponential function with the three lifetimes: $\tau_1 = 0.16$ ns, $\tau_2 = 1.70$

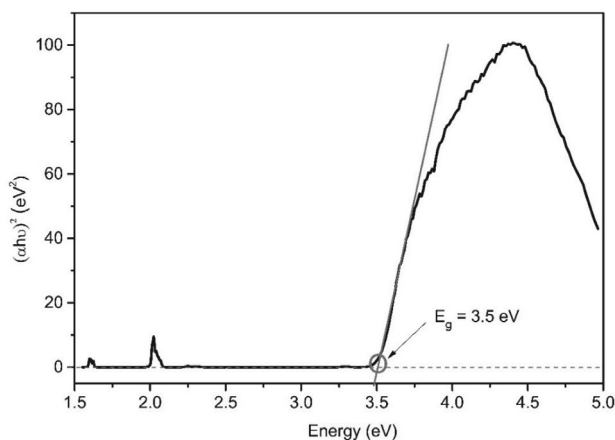


Fig. 7. Optical band gap of NdVO_4 nanoparticles.

ns and $\tau_3 = 4.74$ ns. The fitting parameters of the photoluminescence decay curves are presented in Table 4. These results suggest that the PL decay processes were dominated by third order kinetics. To the authors' knowledge, this is the first report on the dynamics of photo-excited carriers in NdVO_4 .

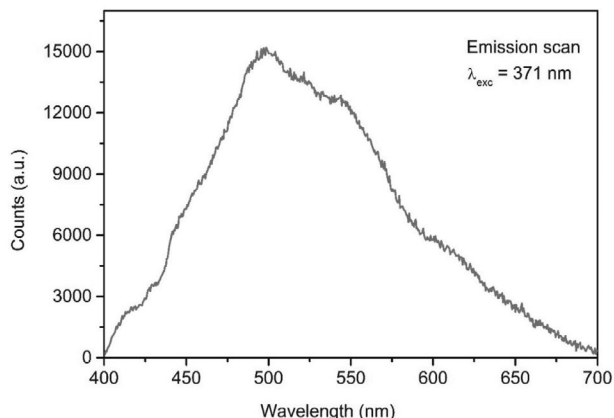


Fig. 8. The emission spectrum of NdVO_4 nanoneedles, measured at room temperature.

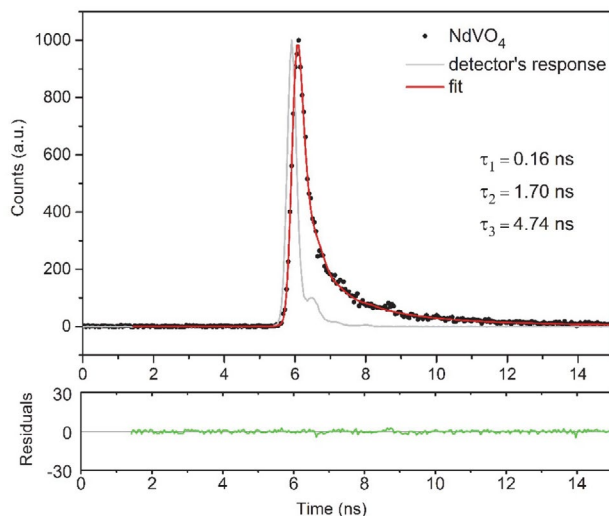


Fig. 9. Photoluminescence lifetime measured on the NdVO_4 nanoneedles, $\lambda_{\text{em}} = 524$ nm. The black dots represent the time-domain intensity decay. The red line is the fitting curve, while the grey line is the response of the detector. The green line below represents the difference between the fitted curve and the measured data. The goodness of fit, χ^2 , is 1.418.

Table 4. Fitting parameters of the photoluminescence decay curves of the NdVO_4 nanoneedles ($\lambda_{\text{ex}} = 371$ nm, $\lambda_{\text{em}} = 524$ nm).

Sample	Lifetime (ns)	Standard deviation (ns)	χ^2	B_1	B_2	B_3
NdVO_4 nanoparticles	$\tau_1 = 0.16$ (50.61%)	0.01	1.418	0.35	0.03	0.00
	$\tau_2 = 1.70$ (30.64%)	0.15				
	$\tau_3 = 4.74$ (18.75%)	0.59				

4. Conclusions

A facile room-temperature precipitation method was employed for the synthesis of NdVO₄ nanoneedles. This approach utilizes aqueous solutions of NdCl₃, Na₃VO₄ and NH₃(aq) as a precipitating agent. The synthesis yielded impurity-free, crystalline NdVO₄ nanoneedles with a tetragonal structure, space group *I*₄*1*/*amd*. The Rietveld refinement study indicated a preferential growth of the nanoparticles along the <112> direction. The Raman analysis further supported the fact that the nanoparticles are single phase NdVO₄ with a zircon-type structure, while SEM analysis showed that the as-synthesised particles have a needle-like morphology with a length of about 100 nm and a width of about 20 nm. The UV-Vis absorption spectrum showed an absorption band located at 353 nm (3.5 eV) which corresponds to the band gap transition. The room-temperature PL spectrum of the NdVO₄ nanoneedles shows green, yellow, and orange emissions. The lifetimes of the nanoneedles were monitored for the 524 nm emission and were found to be 4.74 nanoseconds.

In addition to its simplicity, the synthetic method employed in this study also conserves energy since it does not require any thermal treatment. This method could potentially be tailored for the facile preparation of other 1D lanthanide vanadate structures.

5. Acknowledgements

This work was supported by the Slovenian Research Agency under the Young Researchers Programme and the Research Programme P2-0337.

6. References

- J. A. Baglio, O. J. Sovers. *J. Solid State Chem.* **1971**, *3*, 458–465. DOI:10.1016/0022-4596(71)90085-5
- C.-T. Au, W.-D. Zhang. *Faraday Trans.* **1997**, *93*, 1195–1204. DOI:10.1039/a607565g
- X. Wu, Y. Tao, L. Dong, J. Zhu, Z. Hu. *J. Phys. Chem. B* **2005**, *109*, 11544–11547. DOI:10.1021/jp0503922
- S. Mahapatra, G. Madras, T. N. G. Row. *J. Phys. Chem. C* **2007**, *111*, 6505–6511. DOI:10.1021/jp069007e
- M. Eghbali-Arani, A. Sobani-Nasab, M. Rahimi-Nasrabadi, F. Ahmadi, S. Pourmasoud. *Ultrason. Sonochem.* **2018**, *43*, 120–135. DOI:10.1016/j.ultsonch.2017.11.040
- R. A. Fields, M. Birnbaum, C. L. Fincher. *Appl. Phys. Lett.* **1987**, *51*, 1885–1887. DOI:10.1063/1.98500
- H. Zhang, H. Kong, S. Zhao, J. Jiu et al. *J. Cryst. Growth* **2003**, *256*, 292–297. DOI:10.1016/S0022-0248(03)01356-3
- S. Mahapatra, G. Madras, T. N. G. Row. *Ind. Eng. Chem. Res.* **2007**, *46*, 1013–1017. DOI:10.1021/ie060823i
- A. Di Paola, E. Garcia-Lopez, G. Marci, L. Palmisano. *J. Hazard. Mater.* **2012**, *211–212*, 3–29. DOI:10.1016/j.jhazmat.2011.11.050
- V. Panchal, D. Errandonea, A. Segura, P. Rodriguez-Hernandez, A. Muñoz, S. Lopez-Moreno, M. Bettinelli. *J. Appl. Phys.* **2011**, *110*, 043723. DOI:10.1063/1.3626060
- V. Panchal, D. Errandonea, F. J. Manjon, A. Munoz, P. Rodriguez-Hernandez, S. N. Achary, A. K. Tyagi. *J. Phys. Chem. Solids* **2017**, *100*, 123–133. DOI:10.1016/j.jpcs.2016.10.001
- X. Huang, S. Han, W. Huang, X. Liu. *Chem. Soc. Rev.* **2013**, *42*, 173–201. DOI:10.1039/C2CS35288E
- C. Che Lin, R.-S. Liu. *J. Phys. Chem. Lett.* **2011**, *2*, 1268–1277. DOI:10.1021/jz2002452
- Y. Liu, D. Tu, H. Zhu, X. Chen. *Chem. Soc. Rev.* **2013**, *42*, 6924–6958. DOI:10.1039/c3cs60060b
- C. Yao, Y. Ton. *TrAC, Trends Anal. Chem.* **2012**, *39*, 60–71. DOI:10.1016/j.trac.2012.07.007
- M. Abdeselem, M. Schoeffel, I. Maurin, R. Ramodiharilafy, G. Autret, O. Clément, P.-L. Tharaux, J.-P. Boilot, T. Gacoin, C. Bouzigues, A. Alexandrou. *ACS Nano*, **2014**, *8*, 11126–11137. DOI:10.1021/nn504170x
- S. Mahapatra, S. K. Nayak, G. Madras, T. N. G. Row. *Ind. Eng. Chem. Res.* **2008**, *47*, 6509–6516. DOI:10.1021/ie8003094
- J. Liu, Y. Li. *J. Mater. Chem.* **2007**, *17*, 1797–1803. DOI:10.1039/b617959b
- Z. Xu, C. Li, Z. Hou, C. Peng, J. Lin. *CrystEngComm* **2011**, *13*, 474–482. DOI:10.1039/C0CE00161A
- M. Jang, K. M. Doxsee. *CrystEngComm* **2011**, *13*, 1210–1214. DOI:10.1039/C0CE00590H
- R. Kalai Selvan, A. Gedanken, P. Anilkumar, G. Manikandan, C. J. Karunakaran. *J. Cluster. Sci.* **2009**, *20*, 291–305. DOI:10.1007/s10876-008-0229-y
- R. W. Cheary, A. Coelho. *J. Appl. Crystallogr.* **1992**, *25*, 109–121. DOI:10.1107/S0021889891010804
- P. Kubelka, F. Munk. *Z. Tech. Phys.* **1931**, *12a*, 593–601.
- M. Dragomir. Ph.D. thesis, **2013**, University of Nova Gorica.
- Manual of the fluorescence lifetime. Edinburgh Instruments, **2000**, UK.
- S. Yuvaraj, R. K. Selvan, V. Kumar, I. Perelshtein, A. Gedanken, S. Isakkimuthu, S. Arumugam. *Ultrason. Sonochem.* **2014**, *21*, 599–605. DOI:10.1016/j.ultsonch.2013.08.015
- H. Fuess, A. Kallel. *J. Solid State Chem.* **1972**, *5*, 11–14. DOI:10.1016/0022-4596(72)90002-3
- A.-D. Nguyen, K. M. Murdoch, N. M. Edelstein, L. A. Boatner, M. M. Abraham. *Phys. Rev. B* **1997**, *56*, 7974–7987. DOI:10.1103/PhysRevB.56.7974
- S. Jandl, Y. Lévesque, V. Nekvasil, M. Bettinelli. *Opt. Mater.* **2010**, *32*, 1549–1552. DOI:10.1016/j.optmat.2010.07.004
- E. Antic-Fidancev, J. Holsa, M. Lemaitre-Blaise, P. Porcher. *J. Phys.: Condens. Matter.* **1991**, *3*, 6829–6843. DOI:10.1088/0953-8984/3/35/012
- C. C. Santos, E. N. Silva, A. P. Ayala, I. Guedes, P. S. Pizani, C.-K. Loong, L. A. Boatner. *J. Appl. Phys.* **2007**, *101*, 053511. DOI:10.1063/1.2437676
- Y.-S. Chang, F.-M. Huang, Y.-Y. Tsai, L.-G. Teoh. *J. Lumin.* **2009**, *129*, 1181–1185. DOI:10.1016/j.jlumin.2009.05.020

33. N. S. Singh, R. S. Ningthoujam, G. Phaomei, S. D. Singh, A. Vinu, R. K. Vatsa. *Dalton Trans.* **2012**, 41, 4404–4412. DOI:10.1039/c2dt12190e
34. M. Dragomir, I. Arçon, S. Gardonio, M. Valant. *Acta Mater.* **2013**, 61, 1126–1135. DOI:10.1016/j.actamat.2012.10.020
35. X. N. Peng, X. Zhang, L. Yu, L. Zhou. *Mod. Phys. Lett. B* **2009**, 23, 2647–2653. DOI:10.1142/S021798490902076X
36. J. Xu, C. Hu, G. Liu, H. Liu, G. Du, Y. Zhang. *J. Alloys Compd.* **2011**, 509, 7968–7972. DOI:10.1016/j.jallcom.2011.05.051
37. X. Wu, Y. Tao, L. Dong, J. Zhu, Z. Hu. *J. Phys. Chem. B* **2005**, 109, 11544–11547. DOI:10.1021/jp0503922

Povzetek

Tetragonalni NdVO_4 v obliki nanoiglic je bil pripravljen s preprosto reakcijo obarjanja pri sobni temperaturi, brez uporabe surfaktantov ali predlog in le iz enostavnih anorganskih soli (NdCl_3 in Na_3VO_4). Za karakterizacijo produkta v obliki nanoiglic so bile uporabljene sledeče metode: PXRD, SEM, Ramanska in fotoluminiscenčna spektroskopija ter fotoluminiscenčna dinamika. Dolžina delcev, ki rastejo vzdolž $\langle 112 \rangle$ smeri, znaša približno 100 nm, njihov premer pa okoli 20 nm. Opisana metoda, katere prednosti so visok izkoristek, uporaba netoksičnih topil in blagi reakcijski pogoji, je potencialno uporabna tudi za pripravo drugih 1D lantanidnih vanadatov.

Scientific paper

Amperometric Enzyme-Free Glucose Sensor Based on Electrodeposition of Au Particles on Polyaniline Film Modified Pt Electrode

Shveta Malhotra,^{1,2} Yijun Tang^{1,*} and Pradeep K. Varshney²¹ Department of Chemistry, University of Wisconsin Oshkosh, USA, 54901² Department of Chemistry, Faculty of Engineering & Technology, Manav Rachna International Institute of Research & Studies (a deemed-to-be-University), Faridabad, India, 121004

* Corresponding author: E-mail: tangy@uwosh.edu

Tel: +1 (920) 424-7097

Received: 29-03-2018

Abstract

An amperometric non-enzymatic glucose sensor of high sensitivity was developed by modification of Pt electrode with electrodeposition of Au particles on polyaniline film. The Au particles were deposited under optimum growth conditions for maximum dispersion on polymer film to achieve highly sensitive glucose sensor. The characterization of the electrode and the analytical parameters were evaluated using chronoamperometry and cyclic voltammetry techniques. The sensor showed wide linear range from 0.01–8 mM along with swift response time of less than 5 s. Moreover, a high sensitivity of 113.6 $\mu\text{A mM}^{-1} \text{cm}^{-2}$ is obtained along with low detection limits of 0.5 μM . The sensor also showed high stability, reproducibility, and repeatability. Furthermore, the sensor has shown high selectivity towards glucose exclusively in the presence of interferents such as sucrose, uric acid, and ascorbic acid. The practical applicability of the proposed sensor was confirmed from successful analysis of glucose in different juice samples and these results were comparable to the commercial glucose meter. Thus, our sensor stands promising non-enzymatic sensor for routine analysis of glucose.

Keywords: Non-enzymatic, Glucose sensor, Polyaniline, Cyclic Voltammetry, Chronoamperometry

1. Introduction

The detection of glucose is not limited to clinical diagnosis but also used in the other fields such as pharmaceutical, food, and biotechnology.¹ The research in the fabrication of glucose sensors is tremendous due to the need of highly stable and sensitive sensors.² The amperometric glucose sensors are either enzymatic or non-enzymatic.^{3,4} The development of former sensors took a leap after development of first enzyme-based sensor in 1962. In spite of the tremendous research in the field of enzyme-based sensors still the need remains for development of highly stable sensors.⁵ One of the reasons is that enzyme loses their activity due to change in the environmental conditions and thereof these sensors are not stable for long term use. While in the case of non-enzymatic sensors, direct electron transfer for oxidation of glucose takes place without the activity of enzymes.⁶ The catalytic behavior in these sensors has been attained by the presence of metals or alloys.

Researchers are focusing on development of an ideal glucose sensor that is highly stable, sensitive, reproducible and has a fast response.⁷ All these analytical parameters can be attained in a single electrode by modification of the existing electrodes with conducting polymer-metal nanoparticles composites.⁸ In such composites, the role of conducting polymer is to provide mechanical stability and high conductivity while the dispersion of metal nanoparticles is responsible for the catalytic action of the sensor. Conducting polymers such as polyaniline (PANI), poly(*o*-phenylenediamine) (PoPD), polythiophenes, poly(3, 4-ethylenedioxythiophene) (PEDOT), polyvinylferrocenium, and polypyrrole (PPY) have been researched in the fabrication of ideal sensors.^{9–15} These polymers make available active sites for the dispersion of metal nanoparticles. The contribution of PANI is the greatest as it has a wide range of conductance (over 11 orders), excellent polymerization yield, and is stable to environmental conditions.¹⁶ Three oxidizable forms of PANI exist in an

acid solution. These are emeraldine salt (ES), pernigraniline salt (PS), and leucoemeraldine salt (LS). The ES-PANI can either be reduced to PS-PANI or oxidized to LS-PANI. The ES-PANI is the only conductive form of PANI and hence used in the development of sensors.¹⁷

The surface area of the electrode is increased with maximum dispersion of metal particles on the polymer film that contributes towards the increased electrocatalytic behavior. The immobilization of metal particles on the polymer matrix is greatly affected by certain factors such as analyte concentration, electrodeposition time, temperature, and method of preparation.¹⁸ Different noble metals are being researched for development of glucose sensors such as Pd, Pt, and Au. The gold particles were our source of interest in this study due to its better electrocatalytic behavior and maximum dispersion on polymer matrix. Moreover, Au particles have advanced biocompatibility, anti-poisoning characteristic and wide range of oxidation potential.⁸

Herein, we report the development of amperometric non-enzymatic sensor with electrodeposition of Au particles on PANI film modified Pt electrode for detection of glucose. The Au particles were electrodeposited from KAuCl_4 solution. The optimum concentration of the analyte and deposition time was evaluated for maximum dispersion of Au particles. The current response of as-prepared sensor (Au/PANI/Pt) was studied under different concentrations of glucose using CV technique. The analytical parameters such as sensitivity, selectivity, limit of detection, linear range of concentration, and response time was also studied using chronoamperometry technique. The sensor was evaluated for its practical applicability in analysis of glucose in juice samples and these results were compared with commercial glucose meter.

2. Experimental

2.1. Chemicals & Apparatus

Potassium chloride (KCl, Fisher Scientific, 100.2%), potassium tetrachloroaurate(III) (KAuCl_4 , Aldrich, 98%), aniline ($\text{C}_6\text{H}_5\text{NH}_2$, Oakwood Chemicals, $\geq 99.0\%$), sodium hydroxide (NaOH) (Fisher Scientific, 99.4%), uric acid (UA, Nutritional Biochemicals Corporation), ascorbic acid (AA, Acros Organics), sucrose (Aldrich), D-glucose (Macron Fine Chemicals). All the chemicals were used as received. The KAuCl_4 solution was prepared in 0.01 M KCl. All the water-based solutions were prepared in deionized water and glucose solutions in 0.1 M NaOH. In all the experiments, 3-electrode system was used with modified Pt electrode (working electrode), Pt wire electrode (counter electrode), and calomel electrode (SCE) (reference electrode). The CV and CA techniques were performed using electrochemical analyzer (CHI750C Electrochemical Workstation), purchased from CH Instruments, Inc., USA. Scanning electron microscopy (SEM) was used to study the morphological properties of the sensor using Hitachi Scanning Electron Microscope SN-

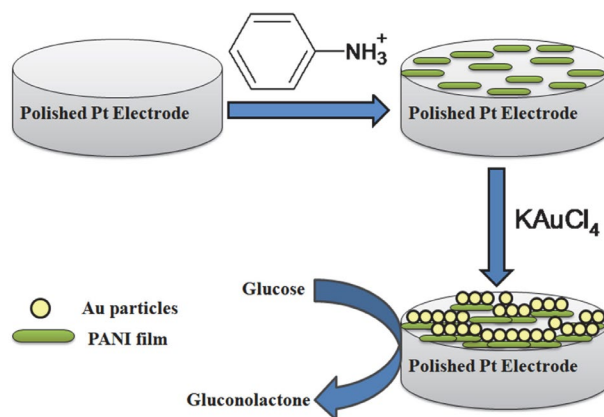
2460. When not in use, the working modified Pt electrode was stored at room temperature. Also, all the experiments in this report were carried out at room temperature.

2.2. Preparation of Au/PANI/Pt Electrode

The bare Pt electrode was mirror polished with the alumina slurries (in order: 0.1, 0.3 and 0.05 μm) then rinsed and ultrasonicated in deionized water for 10 min. The polished electrode was dipped in 1 M H_2SO_4 and potential sweep applied between -0.2 V and $+0.7$ V to obtain clean Pt electrode (scan rate: 50 mVs^{-1}). The shiny cleaned electrode was dried in air for the electrodeposition of PANI film.

The electrodeposition of PANI film on the Pt electrode was done from 50 mM aniline in 1 M HCl solution by sweeping potential in the range of -0.2 V to $+0.1$ V for 20 cycles at 50 mVs^{-1} . The green color coating of PANI film on Pt electrode was observed. Then the electrode was rinsed with deionized water and over-oxidation of PANI film was done by applying potential of $+0.1$ V for 300 s in 0.1 M NaOH.¹⁹ This electrode was labeled as PANI/Pt.

For the dispersion of the Au particles on PANI film, the as-prepared PANI/Pt electrode was immersed in KAuCl_4 solution for 3600 s then the Au particles were electrodeposited in potentiostatic mode for 600 s at a potential of -0.5 V.²⁰ Then the electrode was rinsed with deionized water and dried in air. This electrode was labeled as Au/PANI/Pt. The entire scheme for preparation of the proposed sensor is shown in Scheme 1.



Scheme 1. Preparation of Au particles immobilized on PANI film modified Pt electrode.

3. Results and Discussions

3.1. Characterization of Au/PANI/Pt Electrode

SEM images of PANI/Pt and Au/PANI/Pt modified electrodes were obtained to study the surface morphology

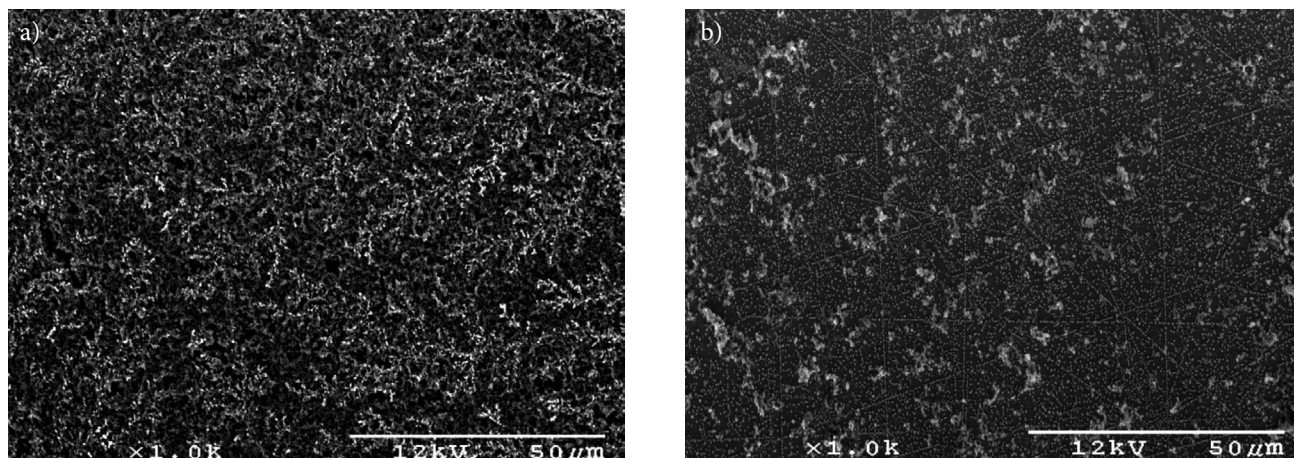


Figure 1. SEM images of (a) PANI/Pt (b) Au/PANI/Pt electrodes.

of the sensor. A network of PANI film is observed on PANI/Pt electrode (Fig. 1a) that provides appropriate surface area for the immobilization of the Au particles. Fig. 1b indicates that Au particles are distributed all over the surface of the PANI film with an average size of 130 nm.

The polyaniline film was electrodeposited on Pt electrode through *in-situ* electro polymerization of aniline done using CV technique at scan rate of 50 mVs^{-1} . As shown in Fig. 2a, the current increases with the increase in number of cycles and reaches maximum at 20 scan cycles. Precisely, with cycles higher than 20 the current becomes constant and a decrease in current response is also observed (Fig. 2b). Thus, we carried out the polymerization of aniline at 20 scan cycles.

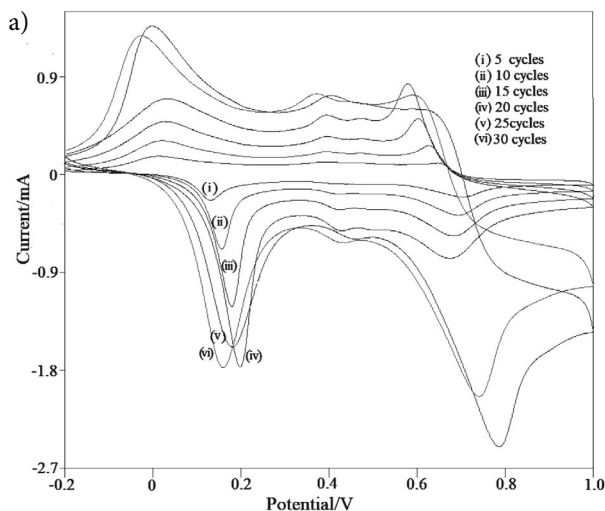
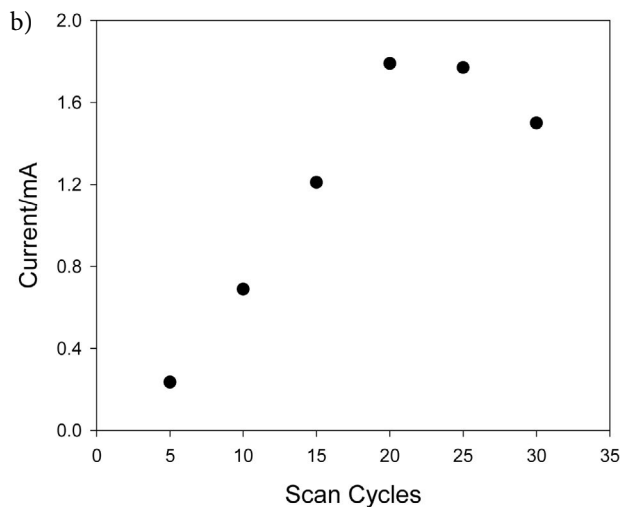


Figure 2. (a) Cyclic voltammogram of polymerization of aniline on Pt electrode at (i) 5 cycles, (ii) 10 cycles, (iii) 15 cycles, (iv) 20 cycles, (v) 25 cycles (vi) 30 cycles. (b) Plot of anodic peak current with number of scan cycles for polymerization of aniline.

The voltammogram obtained (Fig. 3a) shows well defined two redox couples at potential $+0.24 \text{ V}$ and $+0.81 \text{ V}$ confirming the formation of PANI film. The peak at $+0.20 \text{ V}$ is ascribed to the transition from the leucoemeraldine (LS) \rightarrow emeraldine (ES) oxidation state while the

peak at $+0.81 \text{ V}$ is attributed to the oxidation from the emeraldine (ES) \rightarrow pernigraniline (PS) oxidation state.¹⁹ The increase in current with increase in subsequent number of cycles indicates that the thickness of the polymer film increases with each cycle. After the complete polymerization, the surface of the modified electrode is coated with green color indicating the formation of conductive ES-PANI. The deposition of Au particles on PANI matrix is performed based on selection of optimum growth conditions for better performance of our sensor.

A typical voltammogram for Au/PANI composite is shown in Fig. 3b. The peak at $+0.22 \text{ V}$ is to some extent restrained in presence of Au(0) as compared to PANI film (Fig. 3a). This can be due to the ejection of protons.²¹ The



peak at $+0.48 \text{ V}$ corresponds to the intermediate complex $[\text{PANI}^+\text{AuCl}_4^-]$ formed during the reaction between anilinium ion and KAuCl_4 (Eq. 1). The reduction of the complex at this potential yields Au(0). This intermediate complex is not affected by the change of composition of the

electrolyte. The peak at +0.76 V is attributed to absorption of anions by the polymer.²² The conductivity of the PANI/Au composite sensor is maintained due to the presence of oxidized and reduced species in equal number as well as high levels of proton doping.²³

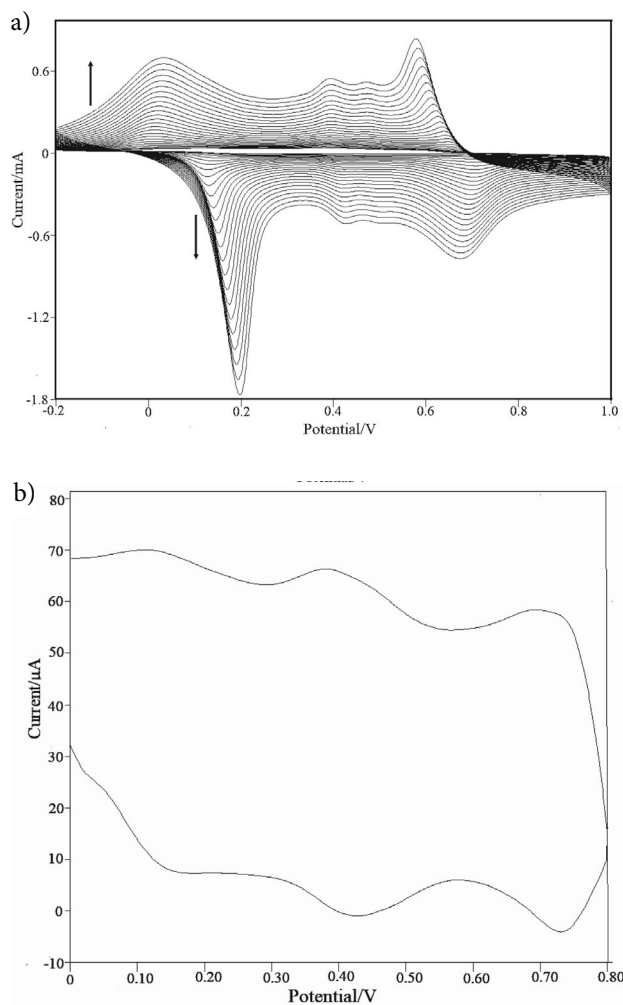
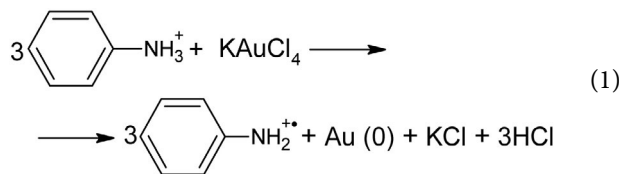


Figure 3. Cyclic voltammogram of (a) electropolymerization of PANI film on Pt electrode in 50 mM aniline in 1 M HCl (b) Au deposited on PANI film modified Pt electrode in 1 M HCl. Scan rate: 50 mVs⁻¹.

3. 2. Optimization of Conditions

3. 2. 1. Growth of Au Particles

It is an essential criterion to select the optimum concentration of KAuCl₄ solution for maximum dispersion of

Au particles on polymer. To achieve this, we prepared different concentrations of KAuCl₄ solution (0.25–1.5 mM) in 0.01 M KCl and recorded the response current towards oxidation of 1 mM glucose solution. Fig. 4a displays the variation of anodic peak current with different KAuCl₄ concentrations. As observed, the anodic peak current increases up to 0.5 mM KAuCl₄ after which the catalytic action of Au decreases and peak current gradually falls. This can be attributed to the fact that concentration >0.5 mM results in aggregation of Au particles that causes decrease in electrocatalytic performance of the electrode. Thus, we selected 0.5 mM KAuCl₄ concentration for deposition of Au particles.

Furthermore, deposition time required for Au particles was also considered during the fabrication process of the sensor. The Au particles were allowed to deposit on the PANI/Pt electrode for different time periods (1200–4800 s) and the current was observed towards oxidation of 1 mM glucose. As evident from Fig. 4b, the maximum anodic peak current is observed at 3600 s and afterwards it decreases. Hence, the optimum growth time for Au particles was selected as 3600 s.

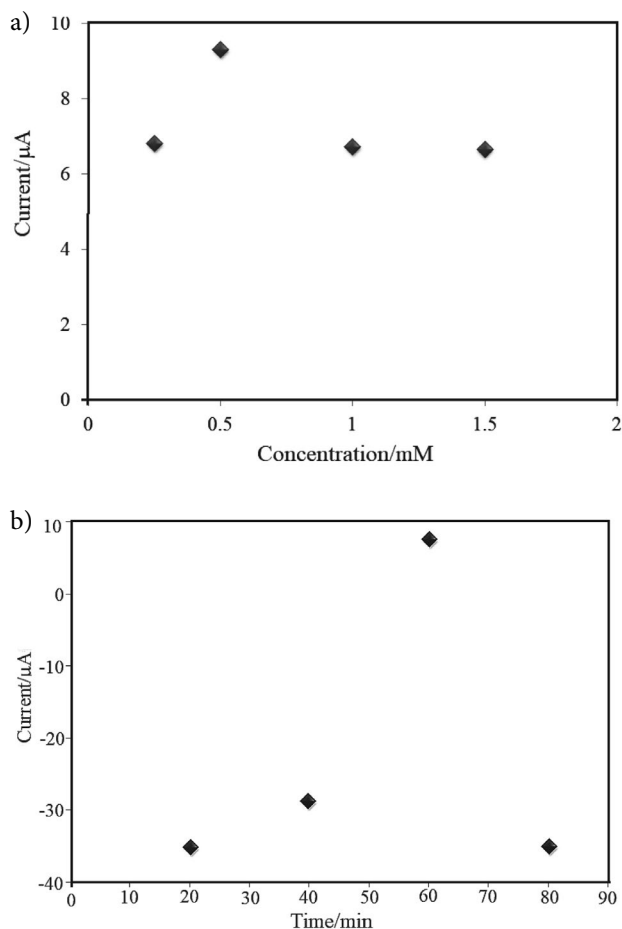


Figure 4. Variation of anodic peak current towards oxidation of 1 mM glucose in 0.1 M NaOH with different (a) KAuCl₄ concentrations (b) Deposition time.

3.2. 2. Optimum NaOH Concentration

The mechanism behind the electro-oxidation process of glucose to gluconolactone in the presence of Au particles is understood with the formation of active Au hydroxides (AuOH_{ads}). The presence of OH^- directly influences the formation of AuOH that is essential for the oxidation process of glucose on surface of Au. The active AuOH_{ads} acts as catalyst and initiates the process of adsorption of dehydrogenated intermediates during oxidation process of glucose. The formation of AuOH_{ads} on Au occurs readily in alkaline medium rather than neutral or acidic medium.^{24,25} Thus we prefer to study the performance of our sensor in strong alkaline medium.

The protons generated from dehydrogenation intermediate steps of glucose are neutralized by the OH^- . This is greatly affected by increasing the alkalinity of the solution. Hence, we also evaluated the performance of the sensor in different concentrations of NaOH (0.01 M – 0.2 M). As evident from Fig. 5, the maximum current is observed for oxidation of glucose in 0.1 M NaOH solution. The increase in anodic current response with increasing concentration of NaOH might be due to the rapid formation of AuOH_{ads} that catalyses the glucose oxidation. While at higher NaOH concentrations Au is transformed to water-soluble ion HAuO_3^- .^{24,26}

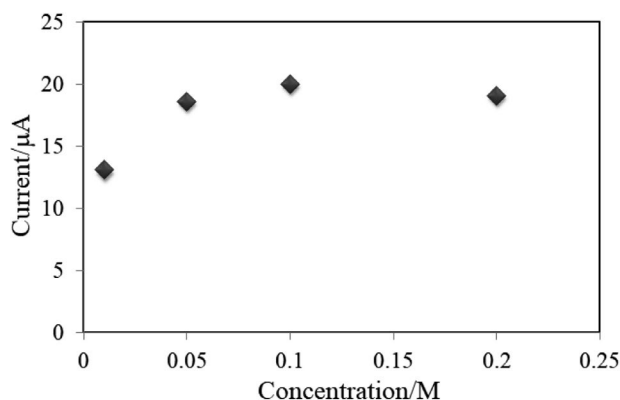


Figure 5. Variation of anodic peak current with 10 mM glucose in different concentrations of NaOH.

3.3. Electrocatalytic Behavior Towards Glucose

Fig. 6a shows the oxidation of 1 mM glucose in 0.1 M NaOH with bare Pt, PANI/Pt and Au/PANI/Pt electrodes. As observed, no obvious peak of glucose oxidation is observed with bare Pt and PANI/Pt electrode while the prominent oxidation peak is observed in case of Au/PANI/Pt electrode. The presence of AuNPs on the surface of Au/PANI/Pt electrode leads to formation of AuOH_{ads} which catalyzes the oxidation of glucose to gluconolactone. Thus, a sharp increase in the anodic current response towards glucose is observed with Au/PANI/Pt electrode. The voltammograms in Fig. 6a are observed to cross each other

due to the fact that in Au/PANI/Pt curve the presence of AuNPs enhances the anodic peak current for glucose oxidation. The AuNPs are dispersed all over the surface of the PANI film and hence promote electron transfer for redox process. Thus, Au/PANI/Pt curve crosses bare Pt and PANI/Pt curves where the anodic peak current is negligible or low. The prominent current response with Au/PANI/Pt electrode in comparison to the current response of bare Pt and PANI/Pt electrodes enables us to detect glucose. This confirms that the oxidation of glucose is initiated by the presence of Au particles in Au/PANI/Pt sensor. Thus, the oxidation of glucose is significantly improved because of the electrocatalytic behavior of Au particles.

Furthermore, Fig. 6b represents the current response of Au/PANI/Pt electrode in the absence and presence of 16 mM glucose. A broader anodic peak for the oxidation of

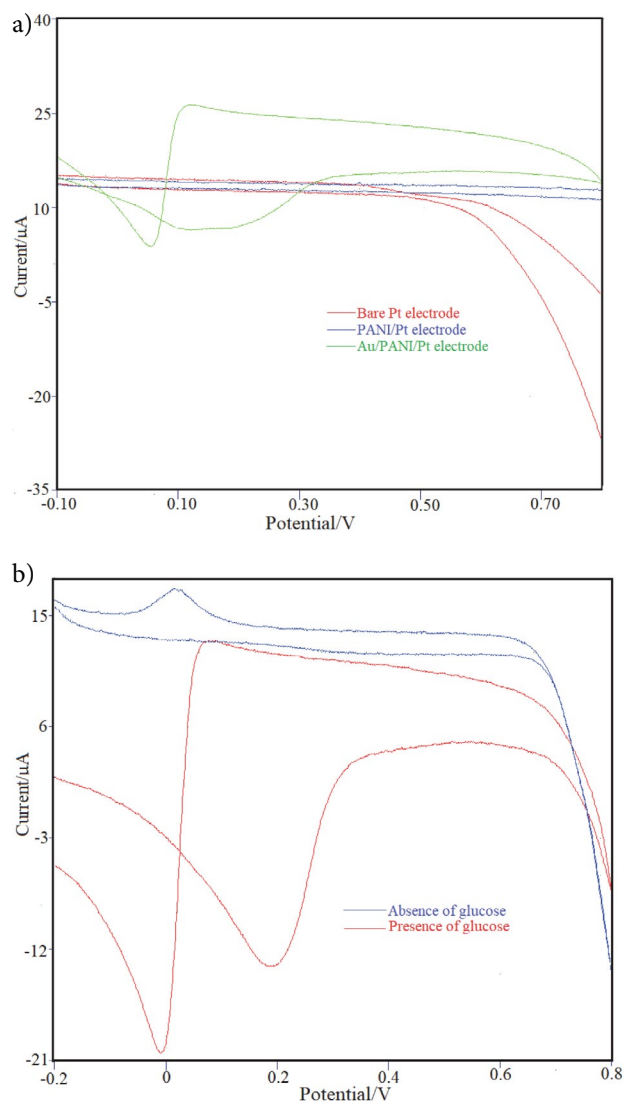


Figure 6. (a) CVs of bare Pt electrode, PANI/Pt electrode, and Au/PANI/Pt electrode towards oxidation of 1 mM glucose in 0.1 M NaOH. (b) Current response of Au/PANI/Pt sensor in absence and presence of 16 mM glucose in 0.1 M NaOH (scan rate: 50 mVs⁻¹).

glucose can be observed in presence of glucose while no obvious peak is observed in blank solution. This further confirms that our sensor shows prominent oxidation of glucose.

3. 4. Effect of Scan Rate

The Au/PANI/Pt sensor was evaluated for the oxidation of glucose at different scan rates in CV. As observed from Fig. 7a, the current response increases with increase in scan rate towards oxidation of 1 mM glucose. A linear graph is obtained for the plot of anodic peak current (I_p) vs scan rate (v) with linear regression coefficient, $R^2 = 0.9932$ (Fig. 7b). This confirms that process of glucose oxidation is a surface controlled phenomenon with adsorption of glucose on surface of electrode.²⁷

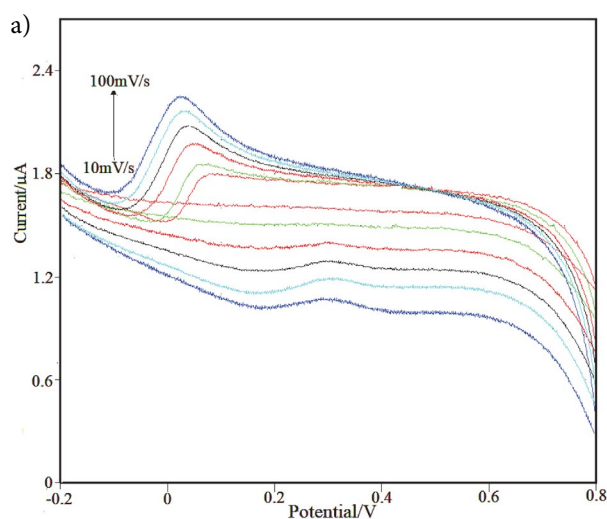
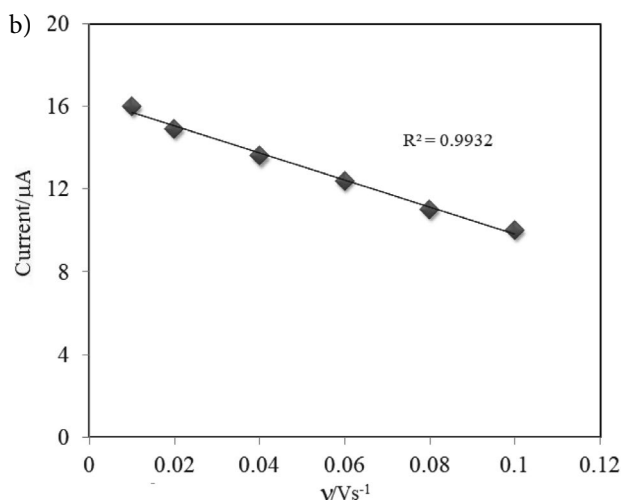


Figure 7. (a) CVs of Au/PANI/Pt electrode studied at various scan rates: 10, 20, 40, 60, 80, and 100 mVs^{-1} with 1 mM glucose in 0.1 M NaOH. (b) Plot of I_p vs. scan rate.

technique. First, the applied potential was selected where the substantial current is observed due to oxidation of glucose. We studied the effect of applied potential using Hydrodynamic Modulation Voltammetry (HMV) technique. Fig. 8 shows the voltammogram obtained for oxidation of 10 mM glucose. The current gradually increases to maximum at potential +0.067 V after which it gradually decreases. Hence, all the chronoamperometric experiments of Au/PANI/Pt were performed at +0.067 V.

For chronoamperometric measurement various concentrations of glucose were successively added to 0.1 M NaOH at an interval of 50 s. The solution was constantly stirred during the run of the experiment. Fig. 9a shows the chronoamperometric current response obtained for successive additions of glucose. As evident from figure, the



3. 5. Evaluation of Analytical Parameters

3.5.1 Chronoamperometric Response of Au/PANI/Pt Sensor

After optimizing the conditions for the fabrication of sensor, its analytical parameters were evaluated using CA

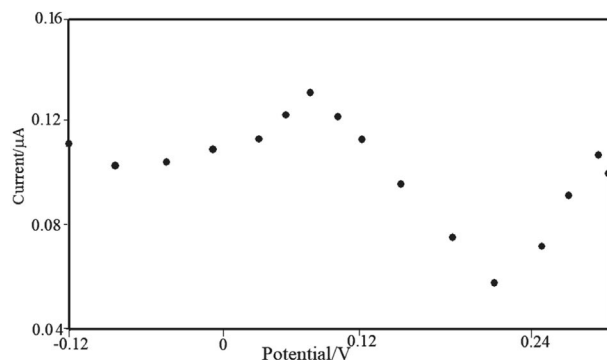


Figure 8. Variation of applied potential with Au/PANI/Pt electrode towards 10 mM glucose in 0.1 M NaOH.

response current increases with increasing concentrations of glucose. As observed from the insert of the Fig. 9a, the sensor achieved 95% of the steady-state current response in less than 5 s. The calibration plot observed for the wide glucose concentrations from 0.01 mM – 8 mM is linear with regression coefficient, $R^2 = 0.9946$ (Fig. 9b). The sensitivity of the sensor is calculated as $113.6 \mu\text{A mM}^{-1} \text{cm}^{-2}$ from Eq. (2)

$$\text{Sensitivity} = \frac{\text{Slope of the Chronoamperometric Calibration Curve}}{\text{Active Surface Area}} \quad (2)$$

The active surface area is calculated from Randles-Sevcik Equation (Eq. 3) as the method described by Chaiyo et al²⁸,

$$I_p = 268600 n^{(3/2)} A D^{(1/2)} C v^{(1/2)} \quad (3)$$

where, I_p – peak current (A), n – number of electron transfer, D – diffusion coefficient (cm^2/s), C – bulk concentra-

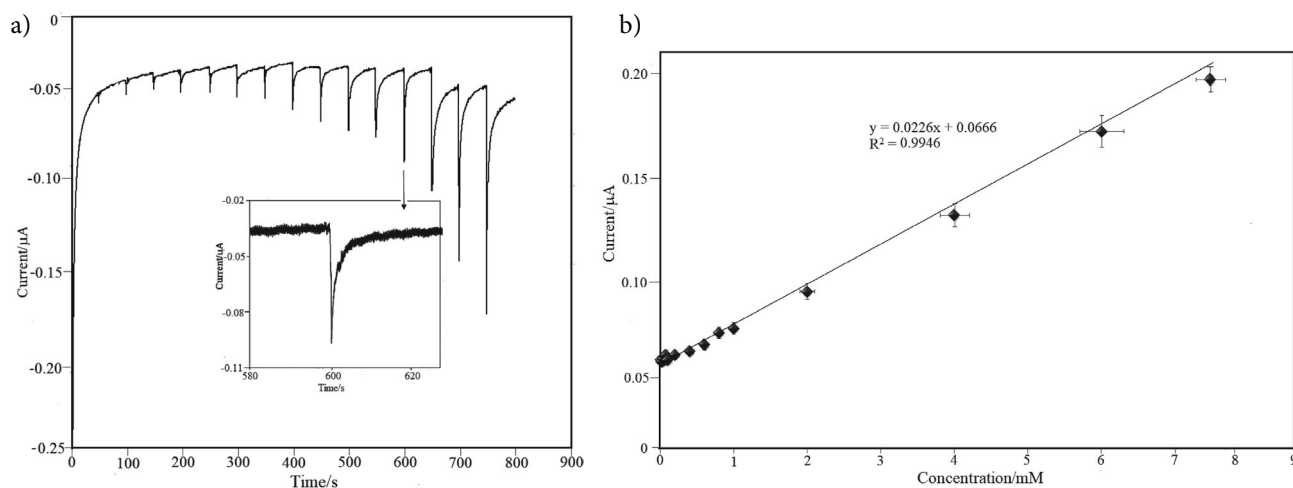


Figure 9. (a) Chronoamperometric response of Au/PANI/Pt modified electrode in 0.1 M NaOH (applied potential: + 0.067 V). Insert shows the enlarged image of response time at 600 s. (b) Calibration plot between current and glucose concentrations.

tion (mol/cm^3), A – surface area of the electrode (cm^2), and v – scan rate (V/s).²⁶ Briefly, the voltammograms of the modified electrode were recorded in 0.01 mM of potassium ferrocyanide [$\text{K}_4\text{Fe}(\text{CN})_6$] redox couple at different scan rates (10, 20, 40, 60, 80 and 100 V/s). The slope obtained from linear calibration curve of I_p vs $v^{1/2}$ is substituted in Eq. (3). From this, the active surface area of the modified electrode is calculated as 0.000278 cm^2 . This value is very low and seems to be contradictory to the actual geometrical surface area of the electrode. However, it should be observed here that that concentration of Au and PANI used in this experiment is very low and have resulted in smaller active surface area available for oxidation. However, even with such small area we were able to get high sensitivity for our sensor.

The low detection limits calculated for our sensor is $0.5 \mu\text{M}$ ($S/N = 3$) with the help of Eq. (4)

$$\text{LOD} = \frac{3\sigma}{S} \quad (4)$$

Where, σ – standard deviation of blank solution (10 readings) and s – slope of the calibration curve.

The performance parameters of our sensor are comparable to other Au particles based enzyme-free glucose sensors reported recently, listed in Table 1.

3. 5. 2 Selectivity & Stability

Many interfering species such as AA, UA, and sucrose have activities similar to glucose and thus inter-

Table 1. Comparison of performance parameters of Au/PANI/Pt sensor to recently reported non-enzymatic glucose sensors based on Au particles

Electrode	LOD	Linear Range	Sensitivity ($\mu\text{A mM}^{-1} \text{cm}^{-2}$)	References
AuNPs-MWCNTs-Chitosan/Au	$0.5 \mu\text{M}$	0.001 mM–1.0 mM	27.7	[24]
AuNP/GONR/Carbon sheet	$0.5 \mu\text{M}$	$0.5 \mu\text{M}$ –10 mM	57.1	[29]
AuNPs/GC	0.05 mM	0.1 mM–25 mM	87.5	[30]
Pd-Au cluster/GC	$50 \mu\text{M}$	0.1 mM–30 mM	75.3	[31]
GNPs/PANI/GCE	0.1 mM	0.3 mM–10 mM	NA	[32]
AuNP/GPE	$12 \mu\text{M}$	0.05 mM–5.0 mM	52.61	[33]
Au-NTAs/GCE	$2.1 \mu\text{M}$	$5 \mu\text{M}$ –16.4 mM	44.2	[34]
AuNPs/SPCE	$200 \mu\text{M}$	0.5 mM–8.5 mM	9.12^*	[35]
GCE/PAPBA–Au NC	$23.4 \mu\text{M}$	0.5 mM–11.0 mM	34.6	[36]
GCE/TiO ₂ NW/ PAPBA–Au TNC	$9.3 \mu\text{M}$	0.5 mM–11.0 mM	66.8	
NiO/Au/PANI/rGO/GCE	$0.23 \mu\text{M}$	$90 \mu\text{M}$ –6000 μM	NA	[19]
Au/PANI/Pt	$0.5 \mu\text{M}$	0.01 mM–8 mM	113.6	This work

MWCNTs: Multiwalled carbon nanotubes; GONRs: Graphene oxide nanoribbons; Au-NTAs: gold nanotube arrays; SPCE: screen-printed carbon electrode; TiO₂ NW: titanium dioxide nanowire; PAPBA: poly(3-aminophenyl boronic acid); AuNC: gold nanocomposite; TNC: ternary nanocomposite; rGO: reduced graphene oxide nanocomposites (NiO/Au/PANI/); *unit: $\mu\text{A}/\text{mA}\cdot\text{cm}^2$.

ferre in the oxidation of glucose. Thus, it is required to fabricate a sensor that can show selectivity to glucose exclusively in the presence of many interferents. The level of glucose found in food and human blood is much higher than interfering species.³⁷ We studied the selectivity behavior of Au/PANI/Pt sensor in presence of AA, UA, and sucrose by CA technique. In this process, 0.1 mM AA, 0.1 mM UA, 0.1 mM sucrose, and 1mM glucose were added successively in 0.1 M NaOH at an interval of 50 s (applied potential: +0.067 V). It is very clear from Fig. 10a that the current response for glucose is much higher than for other interferents. This validates that the proposed Au/PANI/Pt sensor shows selectivity to glucose.

The stability of a sensor is its performance over a period of time. The stability of our Au/PANI/Pt sensor was studied by recording the current response towards oxidation of 10 mM glucose once in 7 days for a period of 3

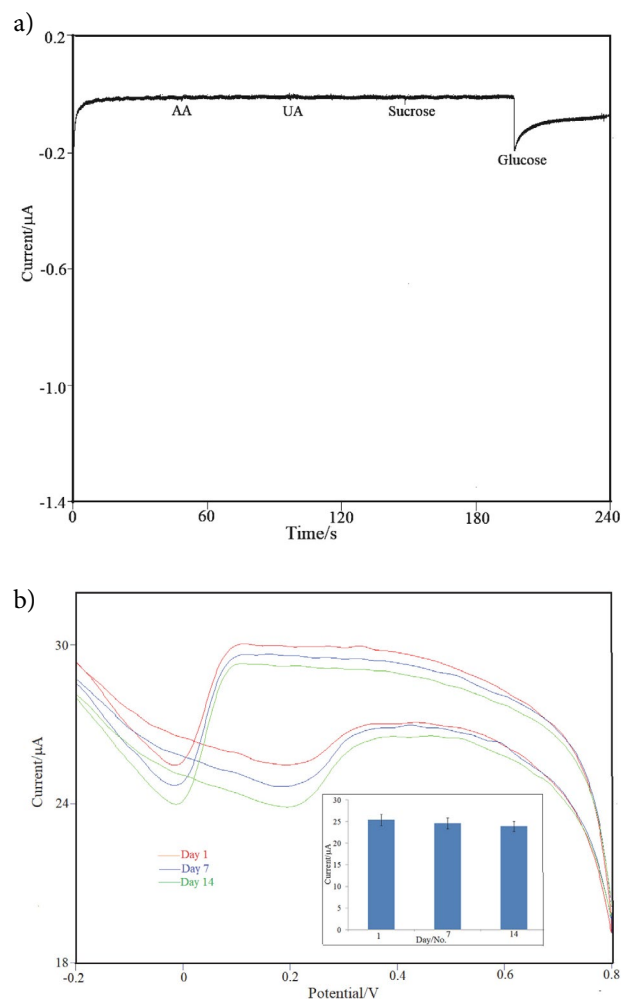


Figure 10. (a) Effect of interfering species on Au/PANI/Pt electrode in presence of 1 mM glucose in 0.1 M NaOH. (b) The current response of Au/PANI/Pt electrode recorded on Day 1, Day 7, and Day 14. Insert shows bar graph plotted for response current obtained over 3 weeks (with SD error bars).

weeks. When not in use, the sensor was stored at room temperature. From Fig. 10b, it was calculated that the response current decreases for only 5.9% of its initial value. Hence, we can confirm that our sensor shows excellent stability.

3.5.3. Reproducibility & Repeatability

Reproducibility is defined as the similarity among current responses from identical electrodes for same analyte. The reproducibility of the Au/PANI/Pt sensor was studied by fabricating five identical Au/PANI/Pt sensors with same procedure. These sensors were used to study the current response against 10 mM glucose in 0.1 M NaOH and RSD of only 2.97% was observed (Fig. 11a).

Repeatability is the agreement between the succeeding current responses recorded for the same analyte. The repeatability of the proposed sensor was considered by recording successive fifteen current responses with 10 mM glucose (Fig. 11b). The sensor showed RSD of only 3.92% for repeated measurements. From these data, we can confirm that our Au/PANI/Pt sensor shows excellent reproducibility and repeatability.

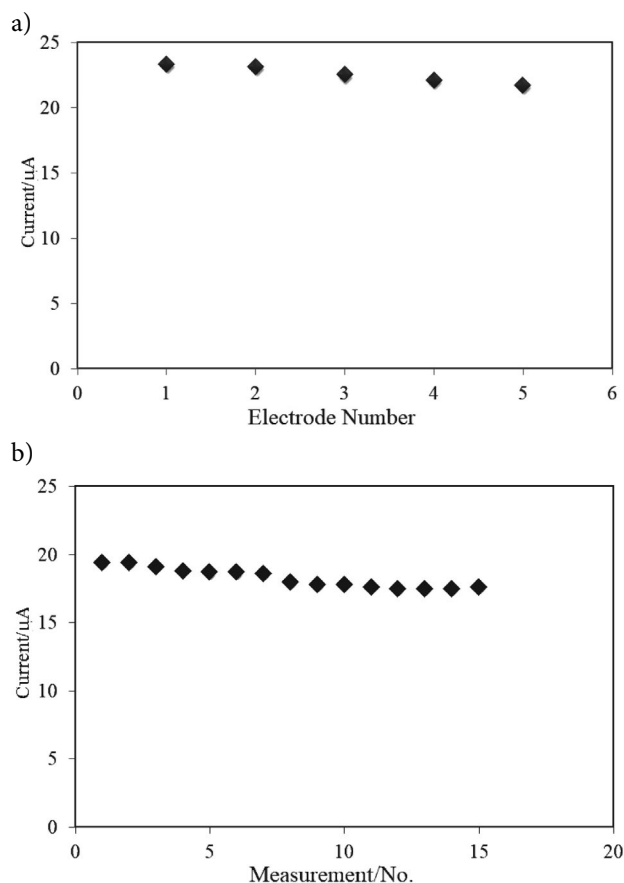


Figure 11. Current response towards 10 mM glucose in 0.1 M NaOH (a) with five identical Au/PANI/Pt sensors (b) for 15 successive measurements with Au/PANI/Pt electrode.

4. Detection of Glucose in Juice With Au/PANI/Pt Sensor

The as-prepared Au/PANI/Pt sensor was used to detect glucose in boxed juice samples and the results obtained were compared to the commercial glucose meter (TRUEtrack®). Three different varieties of boxed juices (mango, pineapple, and orange) were taken from local store and each of them was diluted to 1:100 for performing standard addition method. Equal volumes of the diluted juice samples were spiked with different concentrations of glucose viz, 1 mM, 2 mM, 3 mM, and 4 mM and the

as-prepared solutions were marked as Std 1, Std 2, Std 3, and Std 4 respectively. Figs. 12 a, b and c show the chronoamperometric response of Au/PANI/Pt electrode when equal volumes of each of the samples were added sequentially at an interval of 50 s at an applied potential +0.067 V. The concentration of the glucose was determined from extrapolating the standard addition plot between the response current and glucose concentration in standard solutions. A linear regression coefficient ($R^2 \sim 0.99$) is obtained for each of the samples. Table 2 indicates that the concentrations of the glucose obtained from our Au/PANI/Pt sensor are in good agreement with reference glucose meter. These results confirm that our sensor is reliable for accurate measurements of glucose in practical use.

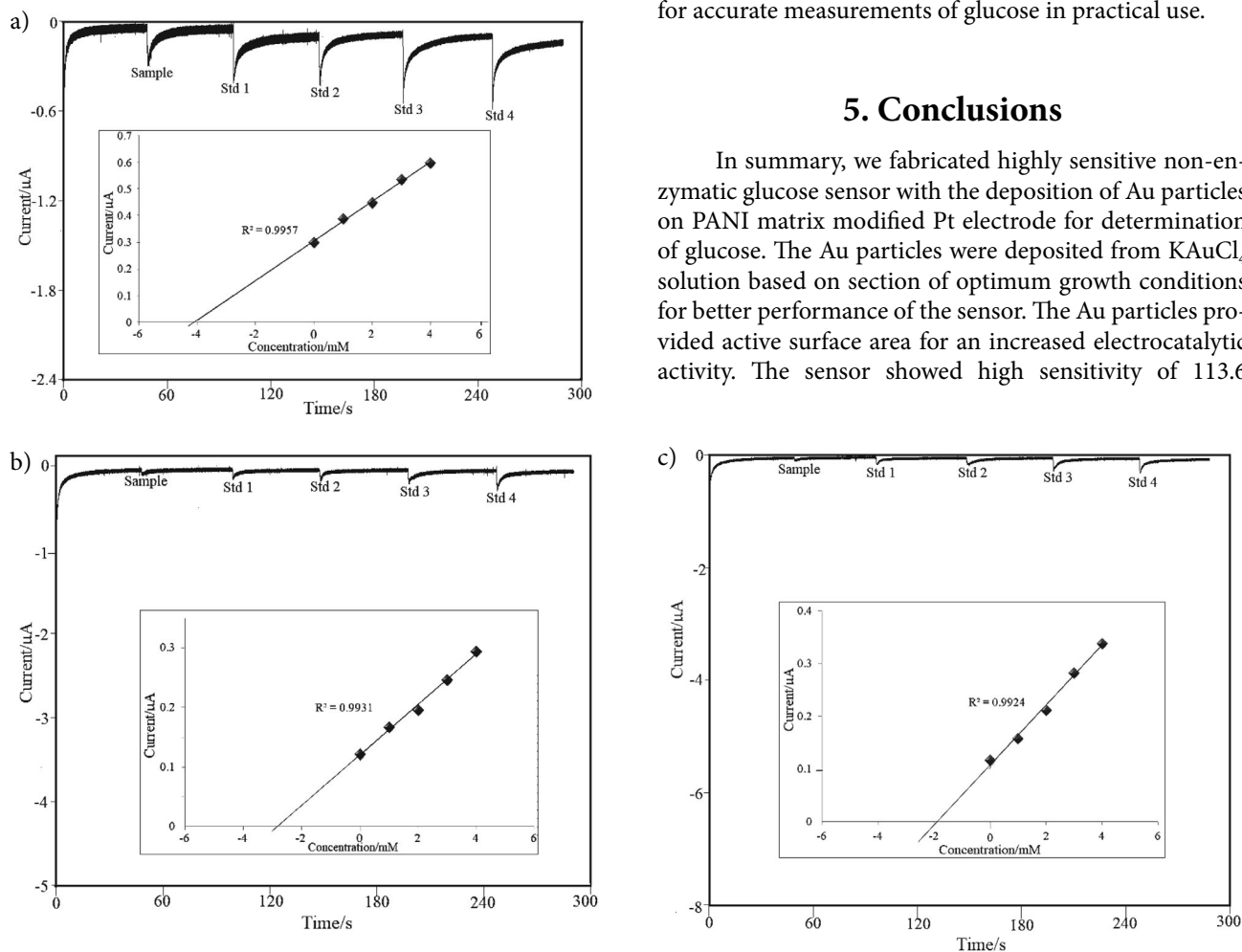


Figure 12. Chronoamperometric response of Au/PANI/Pt electrode in determination of glucose in (a) mango juice, (b) pineapple juice, and (c) orange juice. Std1:1 mM, Std2: 2 mM, Std3: 3 mM, Std4: 4 mM glucose. Insert shows the respective standard addition graph.

Table 2. Concentration of glucose recorded in various boxed juice samples

Juice Sample	Glucose determined by Au/PANI/Pt sensor (mmol/L)	Glucose shown by Glucose meter (mmol/L)	Bias
Mango	20.4	19.5	0.9
Pineapple	14.0	15.0	-1.0
Orange	8.7	8.8	-0.1

5. Conclusions

In summary, we fabricated highly sensitive non-enzymatic glucose sensor with the deposition of Au particles on PANI matrix modified Pt electrode for determination of glucose. The Au particles were deposited from KAuCl_4 solution based on section of optimum growth conditions for better performance of the sensor. The Au particles provided active surface area for an increased electrocatalytic activity. The sensor showed high sensitivity of 113.6

$\mu\text{A mM}^{-1}\text{cm}^{-2}$ with low detection limits of $0.5 \mu\text{M}$. Also, the response time of the sensor was much less than 5 s. Apart from these performance parameters, the proposed Au/PANI/Pt sensor has shown excellent stability, reproducibility and repeatability. The sensor was able to show selectivity to only glucose in presence of many other interfering species (AA, UA, and sucrose). The applicability of the sensor was verified with detection of glucose in a variety of boxed juice samples and these results were comparable to commercial glucose meter. The excellent performance parameters of our sensor verify that it is a promising non-enzymatic glucose sensor for routine examination of glucose.

6. Acknowledgements

We gratefully acknowledge financial support from the University of Wisconsin Oshkosh Faculty Development Program. We would like to thank Dr. Todd Kostman of Biology Department of UW Oshkosh for conducting SEM work. Also, we are thankful to Dean, Faculty of Engineering and Technology, Manav Rachna International Institute of Research & Studies (formerly as MRIU), Faridabad, for his kind support.

7. References

- G. Wang, X. He, L. Wang, A. Gu, Y. Huang, B. Fang, B. Geng and X. Zhang, *Microchim. Acta* **2013**, *180*, 161–186. DOI:10.1007/s00604-012-0923-1
- Z. Wang, H. Lei and L. Feng, *Spectrochim. Acta A* **2013**, *114*, 293–297. DOI:10.1016/j.saa.2013.05.089
- J. Anojčić, V. Guzsvány, O. Vajdle, D. Madarász, A. Rónavári, Z. Kónya, K. Kalcher, *Sens. Actuators B Chem.* **2016**, *233*, 83–89. DOI:10.1016/j.snb.2016.04.005
- J. Mohapatra, B. Ananthoju, V. Nair, A. Mitra, D. Bahadur, N. V. Medhekar, M. Aslam, *Appl. Surf. Sci.* **2018**, *442*, 332–341. DOI:10.1016/j.apsusc.2018.02.124
- S. A. Rothwell, S. J. Killoran and R. D. O'Neill, *Sensors* **2010**, *10*, 6439–6462. DOI:10.3390/s100706439
- K. Tian, M. Prestgard and A. Tiwari, *Mater. Sci. Eng. C* **2014**, *41*, 100–118. DOI:10.1016/j.msec.2014.04.013
- Q. Wang, X. Cui, J. Chen, X. Zheng, C. Liu, T. Xue, H. Wang, Z. Jin, L. Qiao and W. Zheng, *RSC Adv.* **2012**, *2*, 6245–6249.
- H. Çiftçi, E. Alver, F. Çelik, A. Ü. Metin and U. Tamer, *Microchim. Acta* **2016**, *183*, 1479–1486. DOI:10.1007/s00604-016-1782-y
- S. Ameen, M. S. Akhtar and H. S. Shin, *Appl. Catal. A* **2016**, *517*, 21–29. DOI:10.1016/j.apcata.2016.02.023
- X. Zhuang, C. Tian, F. Luan, X. Wu and L. Chen *RSC Adv.* **2016**, *6*, 92541–92546.
- L. Liu, Y. Chen, H. Lv, G. Wang, X. Hu and C. Wang, *J. Solid State Electrochem.* **2015**, *19*, 731–738. DOI:10.1007/s10008-014-2659-9
- M. A. Hocevar, G. Fabregat, E. Armelinb, C. A. Ferreira and C. Alemán, *Eur. Polym. J.* **2016**, *79*, 132–139. DOI:10.1016/j.eurpolymj.2016.04.032
- M. Mazloum-Ardakani, E. Amin-Sadrabadi and A. Khoshroo, *J. Electroanal. Chem.* **2016**, *775*, 116–120. DOI:10.1016/j.jelechem.2016.05.044
- O. G. Sahin, H. Gulce and A. Gulce, *J. Electroanal. Chem.* **2013**, *690*, 1–7. DOI:10.1016/j.jelechem.2012.11.021
- J. Yang, M. Cho, C. Pang and Y. Lee, *Sens. Actuators B Chem.* **2015**, *211*, 93–101. DOI:10.1016/j.snb.2015.01.045
- A. G. Mac Diarmid and A. J. Epstein, *Synth. Met.* **1995**, *69*, 85–92. DOI:10.1016/0379-6779(94)02374-8
- C. Dhand, N. Dwivedi, S. Mishra, P.R. Solanki, V. Mayandi, R. W. Beurman, S. Ramakrishna, R. Lakshminarayanan and B.D. Malhotra, *Nanobiosensors in Disease Diagnosis*, **2015**, *4*, 25–46.
- G. H. Wu, X. H. Song, Y. F. Wu, X. M. Chen, F. Luo and X. Chen, *Talanta* **2013**, *105*, 379–385. DOI:10.1016/j.talanta.2012.10.066
- Kh. Ghanbari and Z. Babaei, *Anal. Biochem.* **2016**, *498*, 37–46. DOI:10.1016/j.ab.2016.01.006
- A. J. Wang, J. J. Feng, Y. F. Li, J. L. Xi and W. J. Dong, *Microchim. Acta* **2010**, *171*, 431–436. DOI:10.1007/s00604-010-0452-8
- D. W. Hatchett, M. Josowicz and J. Janata, *J. Phys. Chem. B* **1999**, *103*, 10992–10998. DOI:10.1021/jp991110z
- A. Saheb, J. A. Smith, M. Josowicz, J. Janata, D.R. Baer and M. H. Engelhard, *J. Electroanal. Chem.* **2008**, *621*, 238–244. DOI:10.1016/j.jelechem.2007.11.025
- J. M. Kinyanjui, J. Hanks, D.W. Hatchett, A. Smith and M. Josowicz, *J. Electrochem. Soc.* **2004**, *151*, D113–D120. DOI:10.1149/1.1808593
- T. Kangkamano, A. Numnuam, W. Limbut, P. Kanatharana and P. Thavarungku, *Sens. Actuators B Chem.* **2017**, *246*, 854–863. DOI:10.1016/j.snb.2017.02.105
- V. E. Coyle, A. E. Kandjani, Y. M. Sabri and S. K. Bhargava, *Electroanalysis* **2017**, *29*, 294–304. DOI:10.1002/elan.201600138
- F. Matsumoto, M. Harada, N. Koura and S. Uesugi, *Electrochem. Commun.* **2003**, *5*, 42–46. DOI:10.1016/S1388-2481(02)00529-5
- Md. M. Hasan, Md. E. Hossain, M. A. Mamun and M.Q. Ehsan, *J. Saudi Chem. Soc.* **2012**, *16*, 145–151.
- S. Chaiyo, E. Mehmeti, W. Siangproh, T. L. Hoang, H. P. Nguyen, O. Chailapakul and K. Kalcher, *Biosens. Bioelectron.* **2018**, *102*, 113–120. DOI:10.1016/j.bios.2017.11.015
- N. S. Ismail, Q. H. Le, H. Yoshikawa, M. Saito and E. Tamiya, *Electrochimica. Acta* **2014**, *146*, 98–105. DOI:10.1016/j.electacta.2014.08.123
- G. Chang, H. Shu, K. Ji, M. Oyama, X. Liu and Y. He, *Appl. Surf. Sci.* **2014**, *288*, 524–529. DOI:10.1016/j.apsusc.2013.10.064
- C. Shen, J. Su, X. Li, J. Luo and M. Yang, *Sens. Actuators B Chem.* **2015**, *209*, 695–700. DOI:10.1016/j.snb.2014.12.044
- A. J. S. Ahammad, A. Al Mamun, T. Akter, M. A. Mamun, S. Faraezi and F. Z. Monira, *J. Solid State Electrochem.* **2016**, *20*, 1933–1939. DOI:10.1007/s10008-016-3199-2

33. A. N. Kawde, M. A. Aziz, M. El-Zohri, N. Baig and N. Odewunmi, *Electroanalysis*, **2017**, *29*, 1214–1221. DOI:10.1002/elan.201600709
34. T. Tian, J. Dong and J. Xu, *Microchim. Acta* **2016**, *183*, 1925–1932. DOI:10.1007/s00604-016-1835-2
35. N. X. Viet and Y. Takamura, *Journal of Science: Natural Sciences and Technology* **2016**, *32*, 83–89.
36. N. Muthuchamy, A. Gopalan and K. P. Lee, *RSC Adv.* **2018**, *8*, 2138–2147.
37. K. M. El Khatib and R. M. Abdel Hameed, *Biosens. Bioelectron.* **2011**, *26*, 3542–3548. DOI:10.1016/j.bios.2011.01.042

Povzetek

Razvili smo visoko občutljivi amperometrični neencimatski senzor za glukozo z modifikacijo Pt elektrode z elektrodepozicijo Au delcev na polianilinski film. Depozicija Au delcev je potekala pod optimalnimi ravnimi pogoji, s čimer smo dobili maksimalno disperzijo na polimernem filmu in pridobili visoko občutljiv senzor za glukozo. Karakterizacijo elektrode in določitev analitskih parametrov smo naredili s kronoamperometrijo in ciklično voltometrijo. Senzor je pokazal široko linearno območje od 0,01 – 8 mM ter hiter čas odgovora v manj kot 5 s, hkrati z visoko občutljivostjo 113,6 $\mu\text{A mM}^{-1} \text{cm}^{-2}$ in nizko mejo zaznave 0,5 μM . Senzor je pokazal tudi visoko stabilnost, obnovljivost in ponovljivost. Nadalje je senzor pokazal visoko selektivnost za glukozo v prisotnosti interferentov, kot so saharoza, sečna kislina in askorbinska kislina. Praktično uporabnost predlaganega sensorja smo potrdili z uspešno določitvijo glukoze v različnih vzorcih soka in ti rezultati so bili primerljivi z rezultati komercialnega glukozometra. Naš senzor je torej obetaven neencimatski senzor za rutinsko določanje glukoze.

Scientific paper

Surface Modifications of the Biodegradable Magnesium Based Implants with Self-Assembled Monolayers Formed by T-BAG Method

Ivana Škugor Rončević,* Nives Vladislavić and Marijo Buzuk

Department of General and Inorganic Chemistry, Faculty of Chemistry and Technology, University of Split,
R. Boškovića 35, 21000 Split, Croatia

* Corresponding author: E-mail: skugor@ktf-split.hr
Tel.: +385-213-29472; Mobile: +385-987-09455

Received: 13-04-2018

Surface modifications with SAM formed T-BAG method

Abstract

In this paper, magnesium based materials (Mg and Mg-alloy (AZ91D)) were surface modified using various organic acids (carboxylic and phosphonic), in order to improve corrosion resistance and enhance their biocompatibility. Formations of surface layer were performed by tethering by aggregation and growth (T-BAG) method. Organization and bond mode of these layers were examined by Fourier transform infrared spectroscopy (FTIR). Additionally, semiempirical quantum molecular modeling calculation methods were used for getting insight into their structural and electronic properties, as also as corrosion resistance in the physiological solution (Hanks' solution). Corrosion resistance of modified materials were investigated by electrochemical impedance spectroscopy (EIS) in the physiological solution (Hanks' solution) and obtained results reveal a beneficial effect of the modification by forming organic acids self-assembled monolayer (SAM) on the corrosion properties of magnesium based materials, especially layers of octadecylphosphonic acid. The maximum corrosion inhibition efficiency of 87% for magnesium and of 93% for Mg-alloy (AZ91D) are achieved by the formation of octadecylphosphonic acid (ODPA) SAM.

Keywords: Magnesium based materials; electrochemical impedance spectroscopy (EIS); self-assembling monolayer (SAM); tethering by aggregation and growth (T-BAG).

1. Introduction

Biodegradability and similar mechanical properties to human bone make magnesium and its alloys a promising candidate for implantable materials used in medical devices.¹ As a potential biodegradable material, magnesium shows many advantages over current metallic materials and biodegradable plastics and ceramics. Therefore, Mg and its alloys have been successfully applied as scaffolds, load bearing and biodegradable orthopedic implants in the physiological environment. Considerable literature is available on the corrosion behavior and electrochemical properties of magnesium and its alloys and Xiaodong et al. have published an excellent article on microstructure and bio-corrosion behavior of as-cast Mg-2Zn-0.5Ca-Y series alloys for biomedical application.² Several Mg alloys, such as Mg-Al-Zn, Mg-Al-Mn, LAE442, Al-free WE43, Mg-Zn and Mg-Ca, were investigated and developed as biodegrad-

able metallic materials.³ Nevertheless, several problems such as inadequate strength when used at load-bearing sites, rapid corrosion characterized by hydrogen evolution must be solved before using this metal in biomedical purposes.⁴ In the human body, these hydrogen bubbles can be accumulated in gas pockets next to the magnesium based implant and can slow tissue recovery or even cause necrosis of tissue.⁵ For improving the lifetime of Mg alloys, their surface can be modified by introducing various organic coatings. Different chemical treatments, such as deposition of chemical conversion layers,⁶ treatments based on the sol-gel application⁷ and the surface modification by formation of self-assembling monolayers (SAMs) of non-toxic organic molecules on the native oxide surfaces by a simple immersion process, were used.^{8,9} As one of the important factor enhancing corrosion resistance (thus improving durability and performability) of implantable materials, is adhesion of organic coatings on implantate surface.¹⁰

In a corrosion system containing the aggressive anions and the inhibitor anions, oxidized metal acts as a hard Lewis acid and anions act as Lewis bases. Hence, the inhibitor anions should be harder bases than the aggressive anions, since they must preferentially bind to the highly oxidized metal ions on the film surface. In particular, compounds containing carboxylic group have been reported to be effective inhibitors, thus hampering chloride –induced breakdown oxide film of various metals and alloys. This can be done Surface Modification of Biodegradable Magnesium Alloys by adsorption of carboxylate on the oxide film, since the carboxylate ions are harder bases than chloride.¹¹

The self-assembling monolayers (SAMs) provide a convenient method for modifying surfaces and producing organized adherent films, which acts as effective barriers to the penetration of corrosive species like oxygen and aggressive ions.¹² Self-assembled monolayer (SAM)-forming monomers consist of three domains: a terminal functional group that ultimately defines the exposed surface functionality, a hydrocarbon chain (typically oligomethylene) to promote monolayer packing and organization, and an anchoring group responsible for the specific chemical interactions with the substrate.⁹ The main characteristics of the SAMs are: (1) the film forms spontaneously through a simple chemical adsorption and strongly adheres to the metal surface; (2) film formation is conformal allowing objects of any shape to be coated; (3) the thickness of the film can be controlled at the nanolevel by selecting adsorbates; (4) the films are densely packed and crystalline; (5) the chemical composition of the film can be tailored by design and synthesis of adsorbates.¹³ The facile use and intrinsic versatility of SAMs have made them a key ingredient of surface science. Self-assembly on a surface results from the interplay of (i) the affinity of the head group for the surface, which imparts the orientation of the adlayer and templates the structure in the case of crystalline surfaces, (ii) the non-covalent lateral interactions between the chains, that stabilize the structure and yield molecular order, and (iii) the intramolecular interactions which determine the fine details of the super-lattice structure (e.g. tilt-angle, surface lattice reconstruction).¹⁴ SAM surface functionalisation is convenient for defining the chemistry of surfaces that are far from ideal, like the technological surfaces that are either polycrystalline or amorphous, often exposed to ambient contamination (SAM molecules will “clean” out physisorbed and even strongly adsorbed contaminants), or processed and used in environments less controlled than ultra-high vacuum conditions.¹⁵ Modification of oxide surfaces has typically been performed using silanes, carboxylic acids, and phosphonic acids.¹⁶ The preparation of alkylphosphonic acid SAMs on magnesium alloys by vapor deposition and simple immersion methods and by an immersion method followed with heat treatment has been reported by Ishizaki et al^{17,18} and by Grubač et al¹⁹, respectively. Organic phosphonic acids form a strong bond with metal oxides, and the ad-

sorption rate and stability strongly depends on the density of hydroxyl groups.³ The interaction (bonding mode) varies among surfaces, and may be monodentate, bidentate or tridentate.²⁰ The Langmuir-Blodgett method²¹ and the tethering by aggregation and growth (T-BAG) method²² are two typical SAMs techniques used for modification of inorganic materials surface.

The advantage of T-BAG method is that the organic functional groups can be directly transverse to the substrates without promoting surface activation or applying of pressure.³ The purpose of this study is to improve the surface chemical stability and enhance the corrosion resistance of biodegradable magnesium and magnesium AZ91D alloy within physiological environments. The corrosion resistance of the surface coated AZ91D alloy was investigated in a standard simulated body fluid (Hanks' solution). Here we report the formation and characterization of covalently bounded SAMs of organic acids on the native oxide surface of Mg and Mg alloy (AZ91D).

2. Experimental

The AZ91D alloy (wt.%: Al 8.6, Mn 0.19, Zn 0.51, Si 0.05, Cu 0.025, and Fe 0.004) and commercial pure magnesium (wt.%: Mn 0.1, Cu 0.02, Pb 0.01, Sn 0.01, and Na 0.006) were used in this study. The working electrodes, with surface area of 0.235 cm², were sealed into glass tubes with Polirepar S. They were abraded with fine emery paper, polished with alumina powder down to 0.05 μm, degreased in ethanol in an ultrasonic bath, rinsed with distilled water, and dried in a stream of nitrogen. The ethanolic solutions of each organic acids used to form the SAM by T-BAG method were: 1.0 mM palmitic acid (PA, CH₃(CH₂)₁₄COOH), 1.0 mM stearic acid (SA, CH₃(CH₂)₁₆COOH), 0.7 mM dodecylphosphonic acid (DDPA, CH₃(CH₂)₁₁PO(OH)₂) and 0.7 mM octadecylphosphonic acid (ODPA, CH₃(CH₂)₁₇PO(OH)₂).

Schematic T-BAG method is shown in Figure 1. The freshly prepared electrode is held vertically in an alcoholic solution of the corresponding acid temperature 60 °C. During self-assembling, during 2 h, ethanol is allowed to evaporate slowly, as long as the level of alcoholic solution did not fall below the level of the electrode, or until the electrode did not stay at the “dry”. After SAM forming electrodes were rinsed with distilled water and air dried. The treated sample was then heated at 140 °C for 24 hours. For comparison of the impedance spectra, electrode materials were kept during 2 hours in alcohol and equally thermally treated (blanc probe).

Molecular modeling of organic acid molecules was performed by using the Semiempirical program from the HyperChem 6.0.3. The FTIR spectra were recorded in the 4000–650 cm⁻¹ region using Horizontal Attenuated Total Reflectance (HATR) method on a Perkin-Elmer Spectrum One FTIR spectrometer.

The corrosion resistance of Mg and AZ91D alloy was investigated at 37 °C in a Hanks' solution, pH 6.67, with following composition (g L⁻¹): NaCl 8.00, KCl 0.40, NaHCO₃ 0.35, NaH₂PO₄ × H₂O 0.25, Na₂HPO₄ × 2H₂O 0.06, CaCl₂ × 2H₂O 0.19, MgCl₂ 0.19, MgSO₄ × 7H₂O 0.06, and glucose 1.00. All chemicals were of p.a. purity. The experiments were carried out in a standard three-electrode cell. The counter electrode was a large area platinum electrode and the reference electrode, to which all potentials are referred, was Ag/AgCl/3 M KCl (209 mV vs. SHE). Before measurements the electrodes were stabilized for 30 min in the Hanks' solution.

The electrochemical impedance spectroscopy (EIS) measurements were performed at the open circuit potential (OCP) with an ac voltage amplitude of ±10 mV in the frequency range from 100 kHz to 0.1 Hz. Measurements were carried out using a Solartron SI 1287 electrochemical interface and a Solartron SI 1255 frequency response analyzer. The EIS data were fitted using the complex non-linear least squares fit analysis software Zview.²³ The numerical values of impedance parameters were determined with a standard deviation χ^2 of the order of 10⁻⁵, and the relative error of each element was less than 5 %.

3. Results and Discussion

3.1. Preparation of Self-Assembled Monolayers

T-BAG is a simple technique of self-organization of amphiphilic molecules at the air solvent interface performed under ordinary laboratory conditions at atmospheric pressure and at lower temperatures. SAMs bound directly to the spontaneously formed oxide film whose growth is not limited by surface OH content (as in the case of the silylation process), and densely packed surface bound monolayer films can be obtained. Amphiphilic molecules are transferred from an alcoholic solution to the metal substrate surface in inverse analogy to Langmuir-Blodgett methods which contributes the organized aggregation of the dissolved polar parts of amphiphilic molecules at the air alcohol interface.²⁴ When the self-assembling process substrate is heated at 140 °C the surface adsorbed amphi-

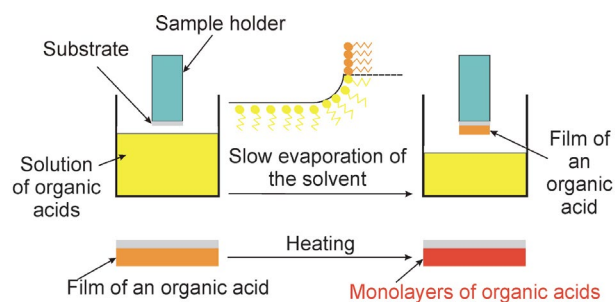


Figure 1. The T-BAG method setup.²²

philic molecules converts to the surface-bound, thus monolayers become stable.^{22,24–26}

3.2. EIS Measurements – Carboxylic Acids SAM

The AZ91D alloy surface was modified with carboxylic acids SAM using the T-BAG method²² and the corrosion resistance of the modified electrodes was tested with EIS. Impedance spectra for the unmodified and modified AZ91D alloy are shown in Figure 2.

In Nyquist's diagram of the impedance spectra shown in Figure 2 it can be seen that the fatty acid SAMs formed by the T-BAG method increase the polarization resistance of the AZ91D alloy and thus increase its corrosion resistance in the Hanks' solution. AZ91D alloy samples modified with carboxylic acids SAM in Bode diagram in the low frequency region have higher overall impedance in compared to the unmodified sample. In Nyquist's diagram, an increase in the diameter of the capacitive semicircle with an increase in the length of the alkyl chain is observed. The increase of the polarization resistance value refers to the better protective properties of stearic acid SAM formed by the T-BAG method compared to the palmitic acid SAM

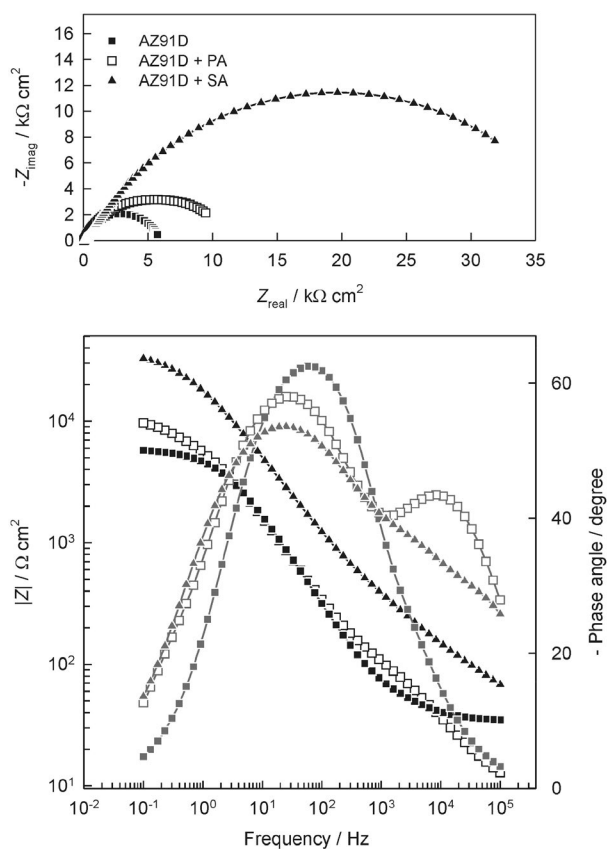


Figure 2. Nyquist and Bode plots of the unmodified AZ91D alloy and AZ91D alloy modified with the carboxylic acids SAM recorded in Hanks' solution at the open circuit potential.

formed under the same conditions. The phase angle vs. $\log f$ dependence indicates the capacitance behavior that is expressed in a much wider medium frequency range for electrodes modified with carboxylic acids SAM.

By modifying the AZ91D alloy with carboxylic acids SAM formed by T-BAG method third time constant becomes more pronounced. Therefore, the impedance spectra of the AZ91D alloy electrode modified with carboxylic acids SAM are fitted with an equivalent circuit which consists of three time constants. The total impedance, Z of the investigated electrochemical system is described by the transfer function:

$$Z(j\omega) = R_{el} + \{Q_1(j\omega)^{n_1} + \{R_1 + \{Q_2(j\omega)^{n_2} + \{R_2 + [Q_3(j\omega)^{n_3} + R_3^{-1}]^{-1}\}^{-1}\}^{-1}\}^{-1}\}^{-1} \quad (1)$$

The first parallel R_1 - CPE_1 combination describes the process of dissolving magnesium at the magnesium/electrolyte interface. R_1 is a charge transfer resistance; CPE_1 is a double layer capacity. The second parallel R_2 - CPE_2 combination is associated with the surface film, where R_2 is the surface film resistance, and CPE_2 is its capacity. The third parallel R_3 - CPE_3 combination represents carboxylic acid SAM (Figure 3).²⁷

The constant phase element (CPE) was used instead of capacitance because the associated distribution of time constants provides an improved fit.²⁸ Its impedance is equal to $Z(CPE) = [(Q(j\omega)^n)^{-1}]^{-1}$; where Q is the constant, ω is the angular frequency, and n is the CPE power. When $n = 1$, Q represents the pure capacitance, while for $n \neq 1$ the system shows behavior that has been attributed to the surface heterogeneity²⁹ or to the continuously distributed time constants for charge transfer reactions.³⁰ The numerical values of impedance parameters obtained by fitting procedure are listed in Table 1. The value of polarization resistance (R_p), which represents the corrosion resistance, is equal to the sum of R_1 and R_2 for spontaneously passivated specimens and to the sum $R_1 + R_2 + R_3$ for specimens modified with SAM. The values of the inhibition efficiency of magnesium corrosion in Hanks' solution are also presented in the Table 1. The inhibition efficiency (η %) of modified surface layers were calculate using the numerical values of R_p according to the expression:

$$\eta(\%) = \left[\frac{(R_p^p - R_p^s)}{R_p^p} \right] \times 100 \quad (2)$$

where R_p^p and R_p^s are the polarization resistance values of specimens modified with SAMs and those spontaneously passivated, respectively.

The protection efficiency of the AZ91D alloy modified with the palmitic acid SAM is 47 %, while the protection efficiency of the AZ91D alloy modified with stearic acid SAM is 85 %.

These obtained values indicate that increasing of the length of the alkyl chain increases the barrier properties of

the carboxylate film and the efficacy of the AZ91D alloy protection in Hanks' solution. The AZ91D alloy modified with stearic acid SAM has almost the four times higher polarization resistance than the alloy modified with palmitic acid SAM. In addition to increases of the polarization resistance, increasing the length of alkyl chain decreases the capacitance of the film. Low capacity values and increased resistance of carboxylate SAM by prolongation of the alkyl chain result in denser packing and greater regulation of SAM due to the reorganization of the alkyl chains with the van der Waals forces.¹³

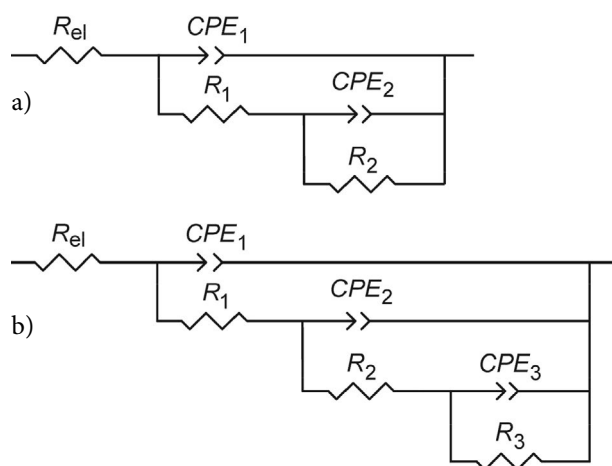


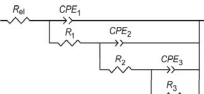
Figure 3. EECs used to fit impedance data.

The corrosion resistance of the unmodified magnesium and magnesium modified with carboxylic acids SAM using the T-BAG method was also tested with EIS. The impedance spectra which had a very similar shape to those of unmodified AZ91D alloy and which are therefore fitted with the same EECs (Figure 3a) are not shown here.

3. 3. EIS Measurements – Phosphonic Acids SAM

Figure 4 and Figure 5 represent Nyquist and Bode plots of AZ91D alloy and magnesium modified with DDPA and ODPA SAM formed by T-BAG method, respectively. For comparison, spectra of electrodes without SAM were recorded and shown. By modifying the AZ91D alloy with phosphonic acids SAM the third time constant becomes more apparent. The impedance spectra of modified AZ91D alloy shown in Figure 4 are therefore fitted with an electric equivalent circuit having three time constants (Figure 3b). In Nyquist plots shown in Figures 4 and 5, there are two clearly separated capacitive semicircles, small in the high frequency region and large in

Table 1. The protection efficiency (η %) of modified surface layers and optimal values of the equivalent circuit parameters wherewith the fitting of the impedance spectra of the unmodified AZ91D alloy and AZ91D alloy modified with palmitic acid (PA) SAM and stearic acid (SA) SAM formed by the T-BAG method in Hanks' solution, pH 6.67 are performed.

	$10^5 \times Q_1 /$	n_1	$R_1 /$	$10^6 \times Q_2 /$	n_2	$R_2 /$	$10^5 \times Q_3 /$	n_3	$R_3 /$	η / %
	$\Omega^{-1} \text{ cm}^{-2} \text{ s}^n$		$\Omega \text{ cm}^2$	$\Omega^{-1} \text{ cm}^{-2} \text{ s}^n$		$\text{k} \Omega \text{ cm}^2$	$\Omega^{-1} \text{ cm}^{-2} \text{ s}^n$		$\text{k} \Omega \text{ cm}^2$	
AZ91D	2.1	0.75	131	1.5	0.96	5.8	–	–	–	–
AZ91D PA	0.3	0.82	100	6.9	0.85	0.1	2.6	0.56	10.9	47
AZ91D SA	0.2	0.69	141	3.7	0.69	0.6	0.6	0.67	38.1	85

$$R_{el} = 26 \Omega \text{ cm}^2$$

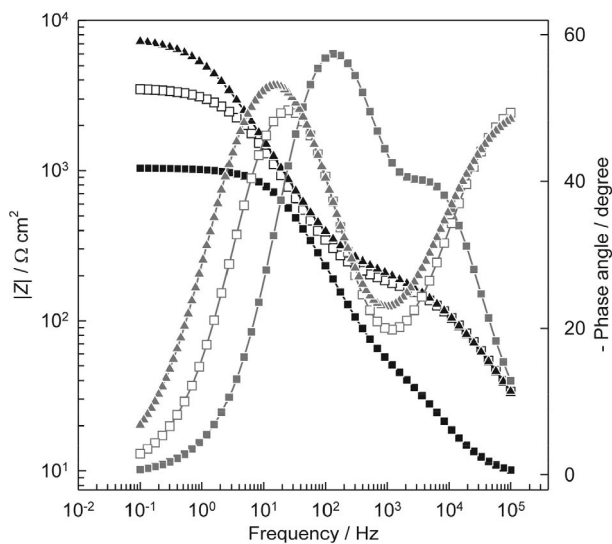
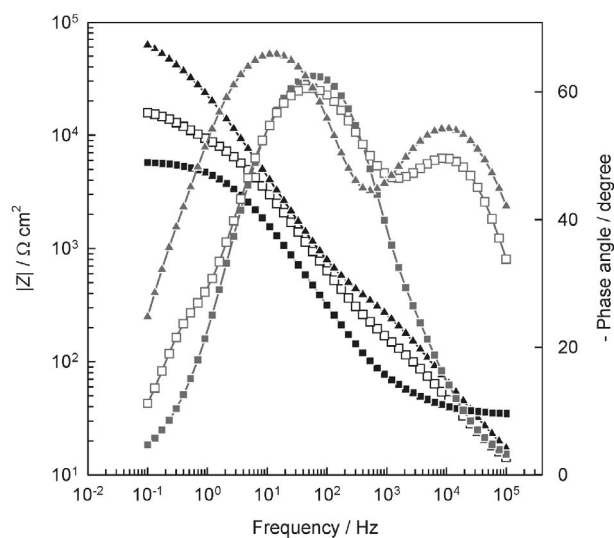
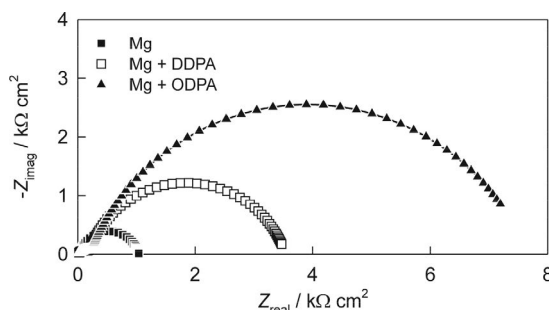
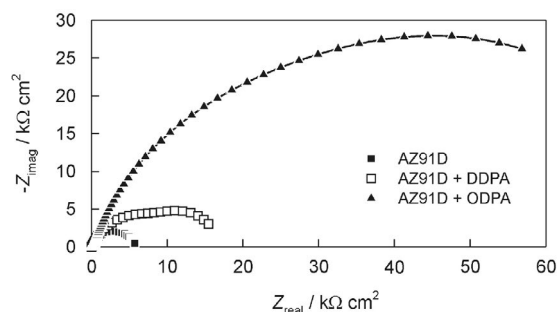


Figure 4. Nyquist and Bode plots of unmodified AZ91D alloy and AZ91D alloy modified with phosphonic acids SAM recorded in the Hanks' solution at the open circuit potential.

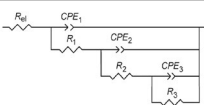
Figure 5. Nyquist and Bode plots of unmodified magnesium and magnesium modified with phosphonic acids SAM recorded in the Hanks' solution at the open circuit potential.

the medium and low frequencies region. As a result of the adsorption of phosphonic acid, the capacitive semicircles (Nyquist plot) increases while the capacitance behavior and the phase angle maxima (Bode plot) move to lower frequencies region and occur in a wider frequency range indicating an increase in polarization resistance. In Figures 4 and 5 in the medium frequency region of the Bode plot, it can be seen the maxima and linear dependence $\log |Z|$ vs $\log f$ with a slope close to -1 which is the result of the capacitive behavior of the protected electrode. In the high frequency region, the dependence $\log |Z|$ vs $\log f$ does not

achieve frequency independence, *i.e.* flattening, and the phase angle contains an additional maximum. In Nyquist plot, it can also be seen that the polarization resistance of the electrodes modified with SAMs is greater than the polarization resistance of the unprotected electrodes.

Values of the impedance parameters are given in Table 2 (Figure 4) and Table 3 (Figure 5). The R_p values for spontaneously passivated alloy specimens equal to $5.9 \text{ k} \Omega \text{ cm}^2$ and very low R_p value for Mg ($\sim 1 \text{ k} \Omega \text{ cm}^2$) can be observed. The AZ91D alloy has two phase microstructure typically consisting of a matrix of a grains with

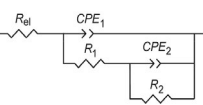
Table 2. The protection efficiency (η %) of modified surface layers and optimal values of the equivalent circuit parameters wherewith the fitting of the impedance spectra of the unmodified AZ91D alloy and AZ91D alloy modified with dodecylphosphonic acid (DDPA) SAM and octadecylphosphonic acid (ODPA) SAM formed by the T-BAG method in Hanks' solution, pH 6.67 are performed.



	$10^6 \times Q_1 /$ $\text{k} \Omega \text{ cm}^2$	n_1	$R_1 /$ $\Omega^{-1} \text{ cm}^{-2} \text{ s}^n$	$10^6 \times Q_2 /$ $\Omega \text{ cm}^2$	n_2	$R_2 /$ $\Omega^{-1} \text{ cm}^{-2} \text{ s}^n$	$10^5 \times Q_3 /$ $\text{k} \Omega \text{ cm}^2$	n_3	$R_3 /$ $\Omega^{-1} \text{ cm}^{-2} \text{ s}^n$	$\eta / \%$
AZ91D	20.7	0.75	100	1.5	0.96	5.8	–	–	–	–
AZ91D DDPA	6.4	0.73	300	5.4	0.80	11.9	9.2	1.00	5.0	66
AZ91D ODPA	5.4	0.72	600	3.4	0.87	65.6	4.2	1.00	17.1	93

$$R_{cl} = 10 \Omega \text{ cm}^2$$

Table 3. The protection efficiency (η %) of modified surface layers and optimal values of the equivalent circuit parameters wherewith the fitting of the impedance spectra of the unmodified magnesium and magnesium modified with dodecylphosphonic acid (DDPA) SAM and octadecylphosphonic acid (ODPA) SAM formed by the T-BAG method in Hanks' solution, pH 6.67 are performed.



	$10^6 \times Q_1 /$ $\Omega^{-1} \text{ cm}^{-2} \text{ s}^n$	n_1	$R_1 /$ $\Omega \text{ cm}^2$	$10^6 \times Q_2 /$ $\Omega^{-1} \text{ cm}^{-2} \text{ s}^n$	n_2	$R_2 /$ $\text{k} \Omega \text{ cm}^2$	$\eta / \%$
Mg	10.9	0.79	67	8.9	0.88	1.0	–
Mg DDPA	3.0	0.68	197	21.2	0.81	3.3	71
Mg ODPA	5.6	0.64	246	20.9	0.79	7.4	87

$$R_{cl} = 9 \Omega \text{ cm}^2$$

the β phase (the intermetallic $\text{Mg}_{17}\text{Al}_{12}$) along the α grain boundaries.³¹ The β -phase is cathodic with the respect to the matrix α phase and exhibits a passive behavior over a wider pH range than either of its components Al and Mg.³² It has been found that $\text{Mg}_{17}\text{Al}_{12}$ is inert in chloride solutions and, if spread over the α matrix, it acts as an effective corrosion barrier.^{32,33} This is the main reason why alloy specimens show a highest corrosion resistance in the Hanks' solution in comparison to that unmodified magnesium. The R_p values for specimens additionally modified with DDPA SAM are $17.2 \text{ k} \Omega \text{ cm}^2$ (Table 2) and $3.5 \text{ k} \Omega \text{ cm}^2$ (Table 3) respectively, while those for specimens additionally modified with ODPA SAM are equal to $83.3 \text{ k} \Omega \text{ cm}^2$ (Table 2) and $7.6 \text{ k} \Omega \text{ cm}^2$ (Table 3), respectively. Protection efficiencies of DDPA SAM on the AZ91D alloy surface and magnesium surface equal to 66% and 71%, respectively while those for ODPA SAM on the AZ91D alloy surface and magnesium surface equal to 93% and 87%, respectively.

The greatest value of polarization resistance (*i.e.*, the best protective properties) shows AZ91D alloy modified with ODPA SAM formed by T-BAG method. Therefore, an influence of time exposed to the Hanks' solution and usage of the different surface modification methods on the electrochemical behavior of the AZ91D alloy modified with the ODPA SAM formed by T-BAG method was investigated by electrochemical impedance spectroscopy. Impedance spectra were recorded in a Hanks' solution of pH 6.67 at 37 °C at an open circuit potential in the time

interval of 10 minutes to 240 minutes. Nyquist and Bode plot of the modified AZ91D alloy after different exposure times to the Hanks' solution is shown in Figure 6. In Nyquist plot, two capacitive semicircles can be observed, small in the high frequency region and large in the medium and low frequencies region. The polarization resistance of the electrode is increased by increasing of the time exposed to the Hanks' solution up to 120 minutes of electrode stay within Hanks' solution. For longer periods of exposure times, the polarization resistance decreases, indicating the decrease of ODPA SAM protective behavior. In medium frequencies region, the expressed capacitance behavior of the electrodes is represented by the linear dependence $\log |Z|$ vs. $\log f$ with a slope of less than -1 and a phase angle of about 70° . The deviation from the ideal capacitive behavior to which the inclination slope less than -1 is particularly pronounced for longer periods of exposure times (over 120 minutes) to Hanks' solution and is most likely due to the disruption of phosphonate SAM due to accumulation of corrosive products on the surface of the electrode causing the appearance of a third time constant.³⁴ Therefore, the impedance spectra up to the exposure times of 120 minutes are analyzed with EEC which contains two time constants, and the impedance spectra obtained for longer exposure times with EEC which contains three time constants.

As can be seen from Figure 7 the T-BAG method as well as the immersion method results in the formation of stable phosphonate SAMs on the surface of AZ91D alloys which are an effective barrier between AZ91D alloys and

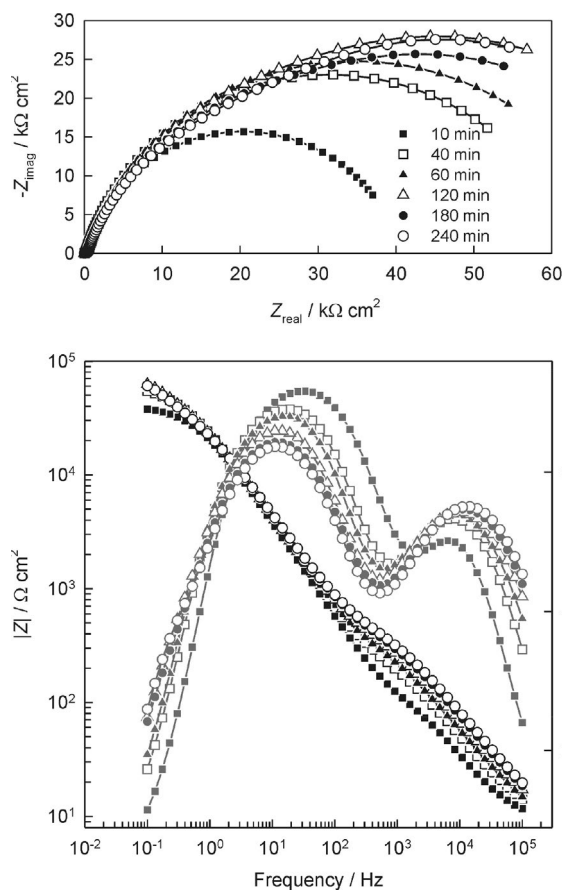


Figure 6. Nyquist and Bode plot of the AZ91D alloy modified with ODPa SAM recorded in Hanks' solution at the open circuit potential during its stay within the electrolyte.

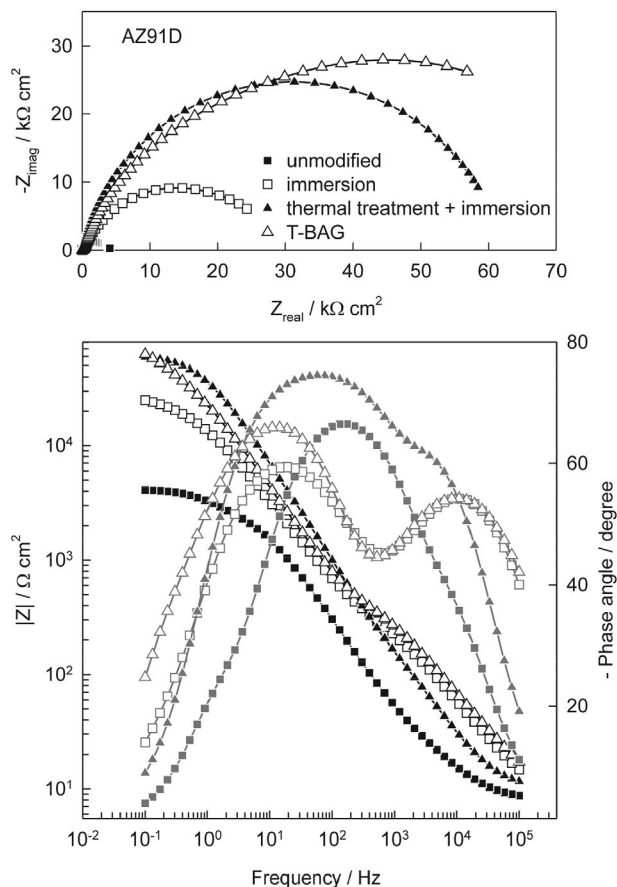


Figure 7. Nyquist and Bode plots of unmodified AZ91D alloy and AZ91D alloy modified with ODPa SAM recorded in Hanks' solution at the open circuit potential. (Three different surface modification methods are indicated.)

electrolytes. The highest values of the polarization resistance of the AZ91D|oxide|SAM system were obtained for ODPa SAM formed on the AZ91D alloy by the T-BAG method.

Therefore, with the T-BAG method a better structural reorganization of phosphonate films which cause arrangeous and homogeneous structure with a smaller number of defects is achieved.²²

3. 4. Molecular Modeling

The stability of the adsorption bond is related to Pearson's HSAB principle.^{35–37} Soft-soft and hard-hard interactions are favored with respect to crossed interactions. The hard-hard and soft-soft bond character relates to ionic (charge controlled) and covalent (frontier controlled) reactions, respectively.³⁸ Acidity or basicity of the metal and the adsorbent molecule should be considered as acidic sites that favor adsorption of basic adsorbents, and as basic sites that favor adsorption of acidic adsorbents. In terms of Lewis acidity, metal ions at a high oxidation state or coordinatively unsaturated, as well as anionic vacancies

can be considered as acidic centers. On the other hand, oxygenated anions and hydroxyl groups are basic sites. The outer sphere complexes (the ligand weakly interacts with surface groups) and the inner sphere complexes (the ligand is coordinated with the metal) may form between organic acids and oxidized metal surface. The principle of electroneutrality implies that in the bulk of the oxide, charge of the metal ion is compensated by the charge of the surrounding oxygen atoms.¹¹ Negative charge of a carboxylate group (COO^-) is distributed over oxygen atoms (Figure 8) Hence, the charge is almost neutralized by the Pauling charge of magnesium and equally distributed over the ligands, which is favorable for adsorption. The absolute hardness, η defined by Pearson is associated with the ionization potential, I and the electron affinity A , and is given by the expression:^{36–38}

$$\eta = \frac{(I - A)}{2} \quad (3)$$

According to the Koopman's theorem,³⁹ the I and A are connected to the frontier orbital energies:

$$I = E_{\text{HOMO}} \text{ and } A = -E_{\text{LUMO}} \quad (4)$$

For anions, A is a large negative number consequently, η is also quite large. Because it's known that the hardness is independent of charge the approximation can be made for a number of ions of interest. Proportionality can be assumed between for an anion and for the corresponding radical that allow rating of anions in order of increasing chemical hardness in the absence of added interelectronic repulsion.¹¹

Table 4 lists the chemical hardness, η of the investigated acids. Between the oxidized Mg alloy surface and the inhibitors hard acid-hard base interactions were found.

In a corrosion system containing an inhibitor, the molecular structure of the inhibitor also plays an important role in determining its mode of adsorption on the corroded surface. Hydrophobicity, solubility, molecular spatial structure and molecular electronic structure can be related to corrosion inhibitor properties. Quantum chemical methods enable the definition of a large number of molecular quantities characterizing such as reactivity, shape, and binding properties of a molecule.⁴⁰

Carboxylic and phosphonic acids were molecular modeled by using Semi-empirical program from the HyperChem package in order to obtain the relationship between inhibition efficiency and their electronic properties. Geometry optimizations of organic acids were performed by theoretical calculations of semi-empirical method; AM1, PM3 and MNDO level. The highest occupied molecular orbital (HOMO) and the lowest unoccupied molecular orbital (LUMO) are performed. The optimized molecular structures of compounds are shown in Figure 8. The calculated quantum chemical parameters E_{HOMO} , E_{LUMO} , ΔE and μ (dipole moment) are listed in Table 4. It has been reported in the literature that high values of E_{HOMO} are likely to indicate a tendency of the molecule to donate electrons to appropriate acceptors with low energy and the higher the corrosion inhibition efficiency. In addition, the energy of the lowest unoccupied molecular orbital (E_{LUMO}) indicates the easier the acceptance of electrons from metal surface, as the energy gap ($\Delta E = E_{\text{LUMO}} - E_{\text{HOMO}}$) decreased and the efficiency of inhibitor improved.^{41,42} The results of Table 4 show that the E_{LUMO} for ODPa (for all method) is lower than DDPA, SA and PA has the lowest energy gap. The results are agreed with the experimental results (EIS) which indicate that ODPa could have better performance as corrosion inhibitor. Some authors showed that an increase of the dipole moment leads to decrease of inhibition and vice versa, suggesting that lower values of the dipole moment will favor accumulation of the inhibitor in the surface layer. In contrast, the increase of the dipole moment can lead to increase of inhibition and vice versa, which could be related to the dipole-dipole interaction of molecules and metal surface.⁴³ The lower value of μ obtained for ODPa is coherent with the first explanation indicating

accumulation of the inhibitor in the surface layer in comparison to other organic acids. The results of Table 4 show that the calculated quantum chemical parameter obtained with different methods has the same trends. The regions of highest electron density (HOMO) are the sites at which electrophiles attack with the superlative ability to bond to the metal surface.⁴³ The results show that the highest occupied molecular orbital (HOMO) density is oriented towards the electrode and that HOMO and LUMO orbitals for investigated organic acids are localized and saturated on a carboxyl, *i.e.*, phosphonic head group. Hence it should be expecting that the carboxylate group *i.e.* phosphonate head group is attached by its oxygen atoms to Mg ions. The circumstances of adsorption of these acids are shown in Figure 8.

Table 4. Quantum chemical parameters of used compounds obtained from quantum method.

Method	Compound	Parameters				
		E_{HOMO} (eV)	E_{LUMO} (eV)	ΔE (eV)	η (eV)	μ (D)
AM1	PA	-4.666	0.821	3.844	1.922	3.616
	SA	-7.981	1.948	6.033	3.016	2.210
	DDPA	-7.531	1.401	6.130	3.065	1.208
	ODPA	-8.132	0.425	7.706	3.853	0.535
PM3	PA	-6.582	1.035	5.546	2.773	3.396
	SA	-8.053	2.237	5.817	2.908	1.624
	DDPA	-6.861	0.906	5.955	2.977	1.044
	ODPA	-7.423	0.037	7.386	3.694	0.490
MNDO	PA	-8.296	1.605	6.691	3.345	1.774
	SA	-8.325	1.562	6.763	3.381	1.744
	DDPA	-8.424	-0.015	8.409	4.204	0.636
	ODPA	-8.907	-0.245	8.658	4.329	0.581

3.5. FTIR Characterization

For obtaining information about a nature of attraction between acids and an oxide/hydroxide film on the surface, FTIR spectroscopy measurements were performed. The obtained spectra are presented in Figure 9.

Both FTIR spectra contain the stretching values $\nu(\text{C-H})_{\text{asymm.}} \leq 2918 \text{ cm}^{-1}$ and $\nu(\text{C-H})_{\text{symm.}} \leq 2850 \text{ cm}^{-1}$ which indicates the existence of a well organized monolayer, which is characterized by alkyl chains in an all-trans configuration that are all tilted from the normal to the surface at the same angle.⁴⁴ FTIR spectra of the AZ91D alloy modified with SA SAM contains the peaks at 1558 cm^{-1} and at 1454 cm^{-1} correspond to the asymmetric and symmetric COO^- stretching, respectively. The presence of these peaks and the lack of peaks corresponding to the $\nu(\text{C=O})$ stretching and C-O-H stretching indicate that the carboxylic head group is attached to the surface layer in a bidentate configuration.^{27,45,46}

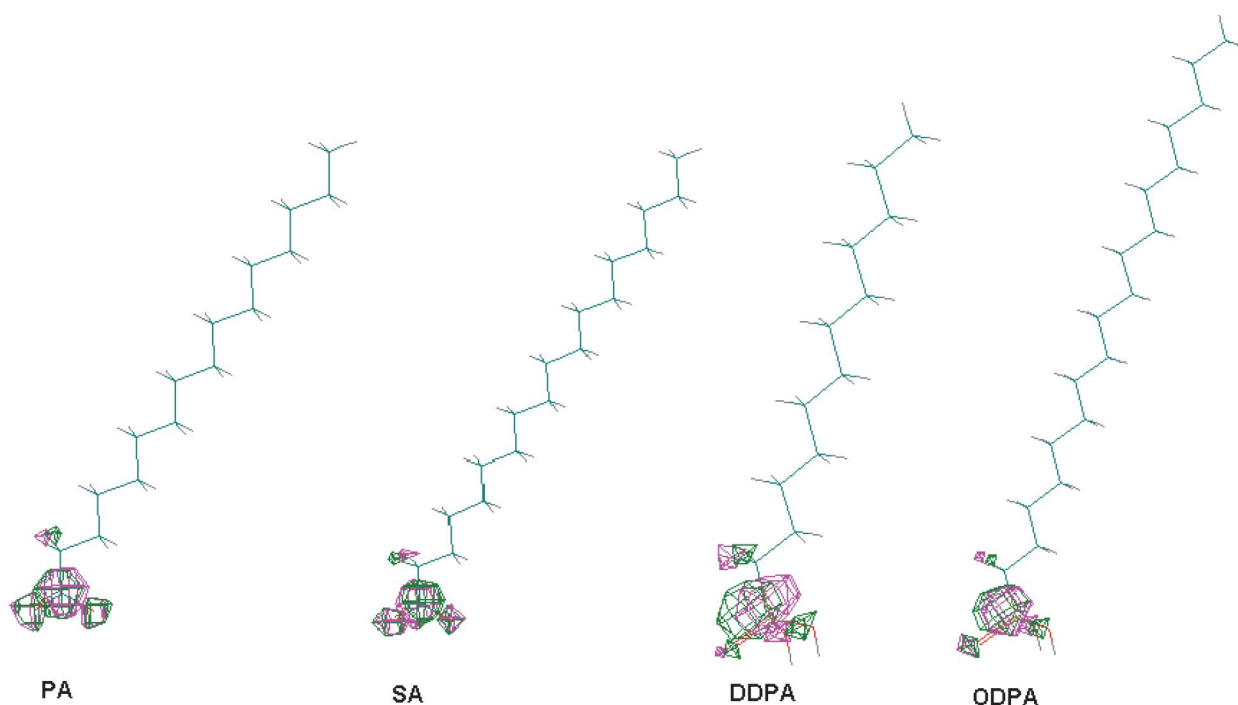


Figure 8. Geometry optimization of organic acids calculated by semi empirical method.

The PO region of the AZ91D alloy, on whose surface DDPA SAM was formed, contains peaks at 1105.1 cm^{-1} and 1019.1 cm^{-1} that can be attributed to the stretching vibration of the P–O bond, which indicates that the phosphonic acid is on the oxidized AZ91D alloy surface, bond-

ed through head group.⁴⁷ However, the FTIR spectrum of AZ91D alloy surface modified with DDPA SAM contains peaks of weak intensity at 954 cm^{-1} and 937 cm^{-1} (corresponding to stretching vibration of the P–OH bond) and a peak of weak intensity around 1224 cm^{-1} (corresponding to stretching vibration of the P=O bond), which suggest the presence of a number of different binding modes in DDPA monolayers.⁴⁸ The peak of low intensity at a wavenumber of about 2300 cm^{-1} in the FTIR spectrum of AZ91D alloy modified with DDPA SAM confirms the presence of free P–OH groups in DDPA SAM.⁴⁷

The AZ91D alloy modified with PA SAM and AZ91D alloy modified with ODPA SAM were also characterized by FTIR spectroscopy. The FTIR spectra of the AZ91D alloy modified with PA (ODPA) SAM contain all significant peaks and the obtained wavenumber values agree well with the values for AZ91D alloy modified with SA (DDPA) SAM, respectively. These spectra due to a small percentage of transmittance are not shown here.

These results (compare the Figure 2 and Figure 4 and the Table 1 and Table 2) indicated that phosphonates allow the formation of more stable monolayers on oxide surfaces because phosphonic acids may form additional P–O–M bonds (bidentate or tridentate) with hydroxyl groups on the surface, leading to a higher stability compared to carboxylate monolayers on metal oxides.⁹

Phosphonic acids form robust monolayers without the need to resort to cross-linking, as is common, for example, in silane surface modification.⁴⁹

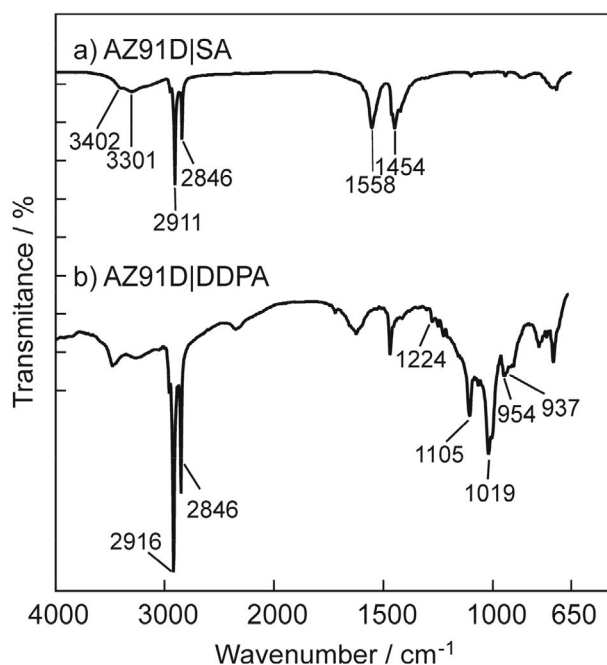


Figure 9. The FTIR spectra of AZ91D alloy modified with the SAM of: a) stearic acid (SA) and b) dodecylphosphonic acid (DDPA).

4. Conclusions

In this work we presented surface modification of magnesium based materials, by self-assembled layer using T-BAG method, using four organic acids (two carboxylic and two phosphonic acids), in order to enhance the corrosion resistance.

Layers of these organic acids on magnesium based materials are investigated with FTIR and obtained results suggest that are organized as self-assembled monolayer by electrostatic attraction of functional groups of organic acids and MgO/Mg(OH)₂ film.

Corrosion resistance of SAMs formed on magnesium based materials are investigated by EIS in simulated body fluid electrolyte (Hanks' solution).

Obtained results reveal that most promisingly potential for corrosion inhibition of magnesium based materials has ODPa, due to longest chain and to the conversion of phosphonic group to phosphonate during preparation of SAM (formation of additional P-O-Metal bond).

Inhibiting potentials of used organic acids are evaluated by semiempirical methods computations of quantum chemical parameters and obtained results are in agreement with experimental data.

5. References

1. Y. Jang, B. Collins, J. Sankar, Y. Yun, *Acta Biomater.* **2013**, *9*, 8761–8770. DOI:10.1016/j.actbio.2013.03.026
2. R. Xiaodong, L. Xuesong, Y. Yue, Y. You, W. Hua, *Rare Metal Mat. Eng.* **2017**, *46*(1), 45–50.
3. C-W. Yang, C. Liu, D-J. Lin, M-L. Yeh, T-M. Lee, *Sci. Rep-Uk.* **2017**, *7*:16910, 1–13.
4. Y. Wan, G. Xiong, H. Luo, F. He, Y. Huang, X. Zhou, *Materials and Design* **2008**, *29*, 2034–3067. DOI:10.1016/j.matdes.2008.04.017
5. G. Song, *Corros. Sci.* **2007**, *49*, 1696–1701. DOI:10.1016/j.corsci.2007.01.001
6. K. Brunelli, M. Dabalà, I. Calliari, M. Magrini, *Corros. Sci.* **2005**, *47*, 989–1000. DOI:10.1016/j.corsci.2004.06.016
7. Y. Tamar, D. Mandler, *Electrochim. Acta* **2008**, *53*, 5118–5127. DOI:10.1016/j.electacta.2008.02.029
8. Z. Grubač, I. Škugor-Rončević, M. Metikoš-Huković, R. Babić, M. Petravić, R. Peter, *J. Electrochem. Soc.* **2012**, *159*, C253–C258. DOI:10.1149/2.047206jes
9. N. S. Bhairamadgi, S. P. Pujari, F. G. Trovela, A. Debrassi, A. A. Khamis, J. M. Alonso, A. A. Zahrani, T. Wennekes, H. A. Al-Turaif, C. van Rijn, Y. A. Alhamed, H. Zuilhof, *Langmuir* **2014**, *30*, 5829–5839. DOI:10.1021/la500533f
10. M. F. Montemor, M. G. S. Ferreira, *Electrochim. Acta* **2007**, *52*, 7486–7495. DOI:10.1016/j.electacta.2006.12.086
11. S. Martinez, L. Valek, I. Stipanović Oslaković, *Journal of The Electrochem. Soc.* **2007**, *154* (11), C671–C677. DOI:10.1149/1.2777882
12. P. E. Laibinis, G. M. Whitesides, *J. Am. Chem. Soc.* **1992**, *114* (6), 1990–1995. DOI:10.1021/ja00032a009
13. Ž. Petrović, M. Metikoš-Huković, R. Babić, *Prog. Org. Coat.* **2008**, *61*, 1–6. DOI:10.1016/j.porgcoat.2007.08.006
14. J. C. Love, L. A. Estroff, J. K. Kriebel, R. G. Nuzzo, G. M. Whitesides, *Chem. Rev.* **2005**, *105*, 1103–1169. DOI:10.1021/cr0300789
15. S. Casalini, C. A. Bortolotti, F. Leonardi, F. Biscarini, *Chem. Soc. Rev.* **2017**, *46*, 40–71. DOI:10.1039/C6CS00509H
16. S. P. Pujari, L. Scheres, A. T. M. Marcelis, H. Zuilhof, *Angew. Chem., Int. Ed.* **2014**, *53*, 6322–6336. DOI:10.1002/anie.201306709
17. T. Ishizaki, K. Teshima, Y. Masuda, M. Sakamoto, *J. Colloid Interface Sci.* **2011**, *360*, 280–288. DOI:10.1016/j.jcis.2011.04.039
18. T. Ishizaki, M. Okido, Y. Masuda, N. Saito, M. Sakamoto, *Langmuir* **2011**, *27*, 6009–6017. DOI:10.1021/la200122x
19. Z. Grubač, M. Metikoš-Huković, R. Babić, I. Škugor Rončević, M. Petravić, R. Peter, *Mater. Sci. Eng.* **2013**, *C 33*, 2152–2158.
20. A. Raman, M. Dubey, I. Gouzman, E. S. Gawal, *Langmuir* **2006**, *22*, 6469–6472. DOI:10.1021/la060636p
21. I. Langmuir, *J. Am. Chem. Soc.* **1917**, *39*, 1848–1906. DOI:10.1021/ja02254a006
22. E. L. Hanson, J. Schwartz, B. Nickel, N. Koch, M. F. Danisman, *J. Am. Chem. Soc.* **2003**, *125*, 16074–16080. DOI:10.1021/ja035956z
23. <http://www.scribner.com/products> (accessed on 23 March 2018)
24. G. L. Gaines, *Insoluble Monolayers at Liquid-Gas Interfaces*, New York (John Wiley & Sons Inc), **1966**.
25. E. S. Gawalt, M. J. Avaltroni, N. Koch, J. Schwartz, *Langmuir* **2001**, *17*, 5736–5738. DOI:10.1021/la010649x
26. E. S. Gawalt, M. J. Avaltroni, M. P. Danahy, B. M. Silverman, E. L. Hanson, K. S. Midwood, J. E. Schwarzbauer, J. Schwartz, *Langmuir* **2003**, *19*, 200–204. DOI:10.1021/la0203436
27. M. Metikoš-Huković, R. Babić, I. Škugor Rončević, Z. Grubač, *ECS Trans.* **2012**, *41*, 81–91.
28. J. R. Macdonald, *Impedance Spectroscopy: Emphasizing Solid Materials and Systems*, New York (John Wiley & Sons Inc), **1987**, pp. 301.
29. Z. Lukasc, *J. Electroanal. Chem.* **1999**, *464*, 68–75. DOI:10.1016/S0022-0728(98)00471-9
30. J. R. Macdonald, *J. Electroanal. Chem.* **1994**, *378*, 17–29. DOI:10.1016/0022-0728(94)87053-5
31. G. Song, A. Atrens, M. Dargusch, *Corros. Sci.* **1998**, *41*, 249–273. DOI:10.1016/S0010-938X(98)00121-8
32. G. Song, A. Atrens, *Adv. Eng. Mater.* **2003**, *5*, 837–858. DOI:10.1002/adem.200310405
33. N. Pebere, C. Riera, F. Dabosi, *Electrochim. Acta* **1990**, *35*, 555–561. DOI:10.1016/0013-4686(90)87043-2
34. Y. Jang, B. Collins, J. Sankar, Y. Yun, *Acta Biomater.* **2013**, *9*, 8761–8770. DOI:10.1016/j.actbio.2013.03.026
35. R. G. Pearson, *Inorg. Chem.* **1988**, *27*, 734–740. DOI:10.1021/ic00277a030
36. R. G. Pearson, *J. Chem. Sci.* **2005**, *117*, 369–377. DOI:10.1007/BF02708340

37. F. H. Walters, *J. Chem. Educ.* **1991**, *68*, 29–31.
DOI:10.1021/ed068p29
38. G. Klopman, *J. Am. Chem. Soc.* **1968**, *90*, 223–234.
DOI:10.1021/ja01004a002
39. T. A. Koopmans, *Physica* **1933**, *1*, 104–113.
DOI:10.1016/S0031-8914(34)90011-2
40. G. Gece, *Corros. Sci.* **2008**, *50*, 2981–2992.
DOI:10.1016/j.corsci.2008.08.043
41. A. Y. Musa, A. A. H. Kadhum, A. B. Mohamad, A. A. B. Rahoma, H. Mesmari, *J. Mol. Struct.* **2010**, *969*, 233–237.
DOI:10.1016/j.molstruc.2010.02.051
42. M. Behpour, S. M. Ghoreishi, M. Khayatkashani, N. Soltani, *Mater. Chem. and Phys.* **2012**, *131*, 621–633.
DOI:10.1016/j.matchemphys.2011.10.027
43. L. Herrag, B. Hammouti, S. Elkadiri, A. Aouniti, C. Jama, H. Vezin, F. Bentiss, *Corros. Sci.* **2010**, *52*, 3042–3051.
DOI:10.1016/j.corsci.2010.05.024
44. M. D. Porter, T. B. Briht, D. L. Allara, C. E. D. Chidsey, *J. Am. Chem. Soc.* **1987**, *109*, 3559–3568.
DOI:10.1021/ja00246a011
45. M. A. Szymański, M. J. Gillan, *Surf. Sci.* **1996**, *367*, 135–148.
DOI:10.1016/S0039-6028(96)00870-9
46. A. Raman, E. Gawalt, *Langmuir* **2007**, *23*, 2284–2288.
DOI:10.1021/la063089g
47. I. Škugor Rončević, M. Buzuk, N. Vladislavić, *Metals* **2016**, *6* 316, 1–16.
48. G. Fonder, I. Minet, C. Volcke, S. Devillers, J. Delhalle, Z. Mekhalif, *Appl. Surf. Sci.* **2011**, *257*, 6300–6307.
DOI:10.1016/j.apsusc.2011.02.071
49. P. B. Paramonov, S. A. Paniagua, P. J. Hotchkiss, S. C. Jones, N. R. Armstrong, S. R. Marder, J.-L. Brédas, *Chem. Mater.* **2008**, *20*, 5131–5133. DOI:10.1021/cm8014622

Abstract

V tem prispevku smo materiale na osnovi magnezija (Mg in Mg-zlitina (AZ91D)) površinsko modificirali z uporabo različnih organskih kislin (karboksilnih in fosfonskih), da bi izboljšali protikorozijsko zaščito in povečali njihovo biokompatibilnost. Površinski sloj smo vezali z metodo agregacije in rasti (tethering by aggregation and growth (T-BAG)). Razporeditev in način vezave teh plasti smo preučili z infrardečo spektroskopijo (FTIR). Poleg tega smo s semiempiričnimi kvantnokemijskimi metodami poskusili pridobiti boljši vpogled v njihove strukturne in elektronske lastnosti ter preučili korozijsko odpornost v fiziološki raztopini. Korozijsko odpornost modificiranih materialov smo raziskali z elektrokemijsko impedančno spektroskopijo (EIS) v fiziološki raztopini. Rezultati modifikacije magnezija in materialov na osnovi magnezija z nanosom strukturno urejenih monoplasti organskih kislin (self-assembled monolayer (SAM)) kažejo na izboljšanje korozijskih lastnosti teh materialov. Najboljšo protikorozijsko zaščito (87 % za magnezij in 93 % za Mg zlitino (AZ91D)) dosežemo z uporabo oktadecilfosfonske kisline (ODPA).

Scientific paper

Adsorptive Removal of Cationic and Anionic Dyes from Aqueous Solutions by Using Eggshell Household Waste as Biosorbent

Eszter Rápó,¹ Robert Szép,² Ágnes Keresztesi,² Maria Suciú³ and Szende Tonk^{1,*}

¹ Faculty of Sciences and Arts, Sapientia Hungarian University of Transylvania, Calea Turzii no. 4, RO-400193, Cluj-Napoca, Romania (corresponding author: tonkszende@gmail.com Tel.: +40 744 767 794)

² Faculty of Economics, Sapientia Hungarian University of Transylvania, Piața Libertății no. 1, RO-530104, Miercurea-Ciuc, Romania

³ National Institute for Research and Development of Isotopic and Molecular Technologies, Electron Microscopy Integrated Laboratory, 67-103 Donath Str., 400293, Cluj Napoca, Romania

* Corresponding author: E-mail: tonkszende@gmail.com

Received: 14-04-2018

Abstract

In the last years, the adsorption processes were proven effective and easy to use techniques to clean polluted wastewater. The purpose of this research is to examine the biosorption method on organic indicators (Methylene Blue, Malachite Green, Congo Red and Bromphenol Blue) in aqueous medium by using chicken eggshell. The adsorption process was investigated in static circumstance. We examined the initial change of concentration (10–50 mg/l), the pH effect on the adsorption process, the equilibrium process, and the sorption kinetics. With scanning electron microscope, we examined the morphology and texture of the eggshell; furthermore, we conducted EDX microanalysis and ecotoxicological tests. Our results support the influence of the parameters on the sorption process.

Keywords: Adsorption; eggshell; cationic dye; anionic dye

1. Introduction

The World Economic Forum has consecutively assessed the water crisis as one of the major global risks over the past five years. In 2016, the water crisis was determined as the global risk of highest concern for people and economies for the next ten years.¹ In global scale it is estimated that 80% of wastewater is released to the environment without adequate treatment.² Water pollution is highly affected by industrial development. Textile industry uses dyes to color their products producing wastewater containing organic matter with strong color.³ Due to low level dye-fiber fixation, approximately 15% of the total dyestuff produced annually is lost during the dyeing process and comes out with waste water.^{4,5} The removal of dyes from water becomes environmentally important because small quantities can be toxic to natural waters causing allergic reactions, skin irritation, cancer, mutations, its color is highly visible and inhibits sunlight penetration into waters like streams, rivers, lakes.⁶ For this reason, the effective removal of these dyes by using clean-up technologies is an

outstanding task. Adsorption is a well-known equilibrium separation process and an effective method for water decontamination applications.⁷ Eggshell could be a low-cost adsorbent for dye removal from wastewater because dye molecules can bind to the porous structure of eggshell (17000 pores) having large surface area.^{8–10} Eggs are the most common and widely used natural food on Earth; only in the US 50 billion eggs are consumed per year.¹¹

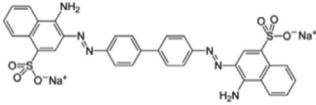
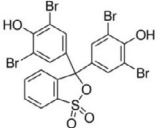
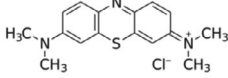
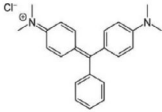
2. Materials and Methods

2. 1. Preparation of Dye

Methylene Blue (MB) and Malachite Green (MG) cationic dyes were purchased from Loch-Ner.s.r.o., Czech Republic and Loba Chemie, Wien-Fischamend, Austria, respectively and were used without any further purification treatment. Anionic dyes Congo Red and Bromphenol Blue (BPB) were purchased from Merck KGaA, Germany and Loba Chemie Wien-Fischamend respectively. Chemical structures and characteristics of all four dyes are summarized in Table 1.

Table 1. Description of indicators used in the experiment

Characteristics	Congo Red	Bromphenol Blue	Methylene Blue	Malachite Green
Chemical formula	C ₃₂ H ₂₂ N ₆ Na ₂ O ₆ S ₂	C ₁₉ H ₁₀ Br ₄ O ₅ S	C ₁₆ H ₁₈ ClN ₃ S	C ₂₃ H ₂₅ ClN ₂
M (g/mol)	696.66	669.96	373.91	364.91
anionic/cationic	anionic	anionic	cationic	cationic
Previous biosorption study	12,13	14,15	16,17	7,18

Stock solutions of dyes were prepared by dissolving 1 g of each dye in 1 L deionized water. During the adsorption experiments, 1g/L stock solution was diluted to obtain the needed concentration.

2. 2. Preparation of Adsorbent

The chicken eggshell used as biosorbent was gathered from household, kitchen waste. The shells were firstly washed in tap water, then in deionized (MilliQ) water. The cleaned eggshell was dried in drying cabinet (Memmert UN75 PLUS) at 80 °C, then powdered and sieved at 160 μm size fraction geologist sieve. During the biosorption experiments 3–3 g of powdered shell was used without any chemical or physical treatment.

2. 3. Effect of Initial Dye Concentration

The sorption of indicator dyes on chicken eggshell's surface was studied in aqueous solutions using 250 mL Erlenmeyer flasks, where 100 mL dye solutions were constantly mixed (VARIOMAG Electronisher MULTIPOINT HP multi-magnetic shaker) with 3 g of biosorbent (160 μm particle size) at 750 rpm, room temperature (T = 20 ± 1 °C), and without initial pH adjustment. Spectrophotometer (Agilent Cary 60 UV-Vis spectrophotometer) was used to periodically measure dye concentrations at λ_{max} = 497,580,664,619, respectively for Congo Red, BPB, MB, MG using calibration curve as measuring technique for quantitative analysis.

In each case the samples supernatant were centrifuged (Hettick Zentrifugen Mikro 20) for 5 minutes at 10000 rotation/min, after which the maximum absorption was measured by spectrophotometer.

In order to investigate the effect of concentration on adsorption, 100 mL of Congo Red, BPB, MB, MG solutions were mixed with 3 g of powdered eggshell at different initial concentrations between 10–50 mg/L. In each case, three parallel experiments were executed.

2. 4. Effect of pH

Due to the fact that the solutions' pH highly affects not only the aqueous chemistry but also the biosorbents'

active sites, the removal of Congo Red, BPB, MB, MG from aqueous solution was investigated at different pH values between 2–10. pH was adjusted with 0.1 mol/L NaOH and 0.1 mol/L HCl. During the experiment, constant parameters were: c = 30 mg/L, 3 g of 160 μm particle sized biomass, 750 rpm, T = 20 ± 2 °C.

2. 5. SEM and EDX Analytical Measurement

The texture and morphology of chicken eggshell before and after treatment with dyes was analyzed using Scanning electron microscopy (JEOL(USA)JSM5510 LV SEM). Elemental studies were also carried out using Energy dispersive spectroscopy.

2. 6. Bioconcentration Factor

BCF is a value that gives the dyes' accumulation efficiency in eggshell. It was calculated based on the dye concentrations in the eggshell and the dissolved dye concentration of aquatic solution.

$$BCF = \frac{C_{\text{indicator on eggshell}}}{C_{\text{indicator in water}}} \quad (1)$$

2. 7. Ecotoxicological Tests – the Effect of Dyes on Seedling Growth

Based on Hungarian standard MSZ 21978/8-85 the toxicological effect of Congo Red, BPB anionic and MB, MG cationic dyes was studied on lettuce and mustard seeds. During the experiments, 25 seeds were placed in autoclaved (at 120 °C) Petri-dishes and 5–5 mL dye solution was added at different concentrations (0, 10, 30, 50, 1000 mg/L). The two simultaneous set of samples were put in a dark chamber for 3 days, where the temperature was kept constant T = 20 ± 2 °C. After the passing days the length of the seeds roots were measured and the number of seedling was also examined. With the help of the equation below, by knowing the length of the seeds (using the averages of the 25 seed length) the root growth inhibition was calculated.

$$X = \frac{K-M}{K} * 100 \quad (2)$$

Where: X – Root growth inhibition, K – root length of control seeds (mm), M – root length of dye-contaminated seeds (mm).

3. Results and Discussions

3. 1. Effects of Initial Indicator Dye Concentration

During our research the effect of Congo Red, BPB anionic and MB, MG cationic indicators uptake by chicken eggshell household waste was examined using different initial dye concentrations between 10–50 mg/L. Figure 1 shows the efficiency and quantity in equilibrium of various dyes at different initial concentration, where 3 g eggshell powder of 160 μm particle size was constantly shaken at 75 0rpm with 100 mL solution at room temperature ($T = 20 \pm 2$ °C) without pH adjustment ($\text{pH}_{\text{CR}} = 8.05$, $\text{pH}_{\text{BPB}} = 2.7$, $\text{pH}_{\text{MB}} = 3.95$, $\text{pH}_{\text{MG}} = 2.76$). With the increase of initial dye concentration in case of Congo Red, MB and MG, the adsorption capacity also increased, whereas in case of BPB there was no such trend.

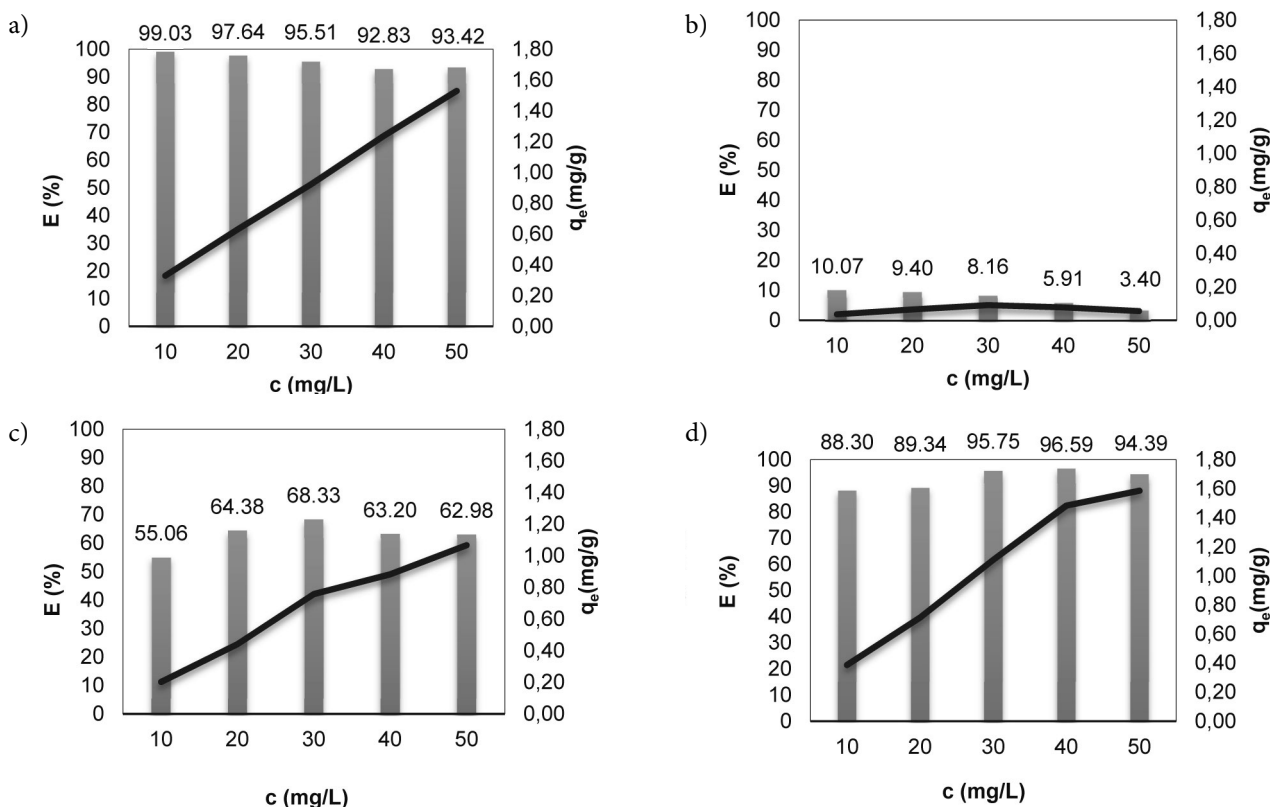


Figure 1. Effect of initial dye concentration for Congo Red (a), BPB (b), MB (c), MG (d) ($C_i = 0\text{--}50$ mg/L, 3 g biomass, 160 μm , 700 rpm, $\text{pH}_{\text{Congo}} = 8.05$; $\text{pH}_{\text{BPB}} = 2.70$; $\text{pH}_{\text{MB}} = 3.95$; $\text{pH}_{\text{MG}} = 2.76$, $T = 20 \pm 1$ °C)

3. 2. Effect of Solution pH

The pH of aqueous solution can highly affect the biosorbents' (eggshell) surface charge. In acidic media, the surface of the adsorbent is protonated, while in a basic medium its surface deprotonates. During our research, the adsorption processes were studied by varying the aqueous solutions' pH, ranging between 2–10. As seen in figure 2. Congo Red dyes' highest adsorption efficiency was obtained at pH

= 2, but in all cases E was above 93%. BPB dyes' highest efficiency was also at pH = 2 ($E = 67\%$). For MB the adsorption was most efficient at pH = 10, achieving 75% efficiency, while the lowest was at pH = 2 where $E = 14\%$. MG is similar to Congo Red dye, with a high percentage efficiency at all pHs. Thus, it can be said that BPB anionic dye preferred acidic medium, while MB cationic dye preferred the basic medium, whereas there was no significant change in case of Congo Red and MG, because the efficiency was high at all pHs. Similar results were obtained by Zeroual et al., 2006; Iqbal and Ashiq, 2010; Salleh et al., 2011; Zulfikar and Setiyanto, 2013; Tiwari et al., 2015; El-Dars et al., 2015.^{3,14,19–22}

3. 3. SEM and EDX

Scanning electron microscopy photographs were taken in order to examine the shape of the samples' parti-

cle, size of appeared aggregates, porosity and texture before and after adsorption with eggshell biomass. Figure X shows the SEM of the control sample (160 μm sized eggshell without adsorption) and four dye treated samples with 50 mg/L dye solutions. It can be seen that the porous, cross-linked structure of eggshell disappears in comparison to the control sample (Figure 3.a) in case of MB, MG, Congo Red; this is due to the fact that the eggshell has incorporated the color into its "caverns". On the other hand,

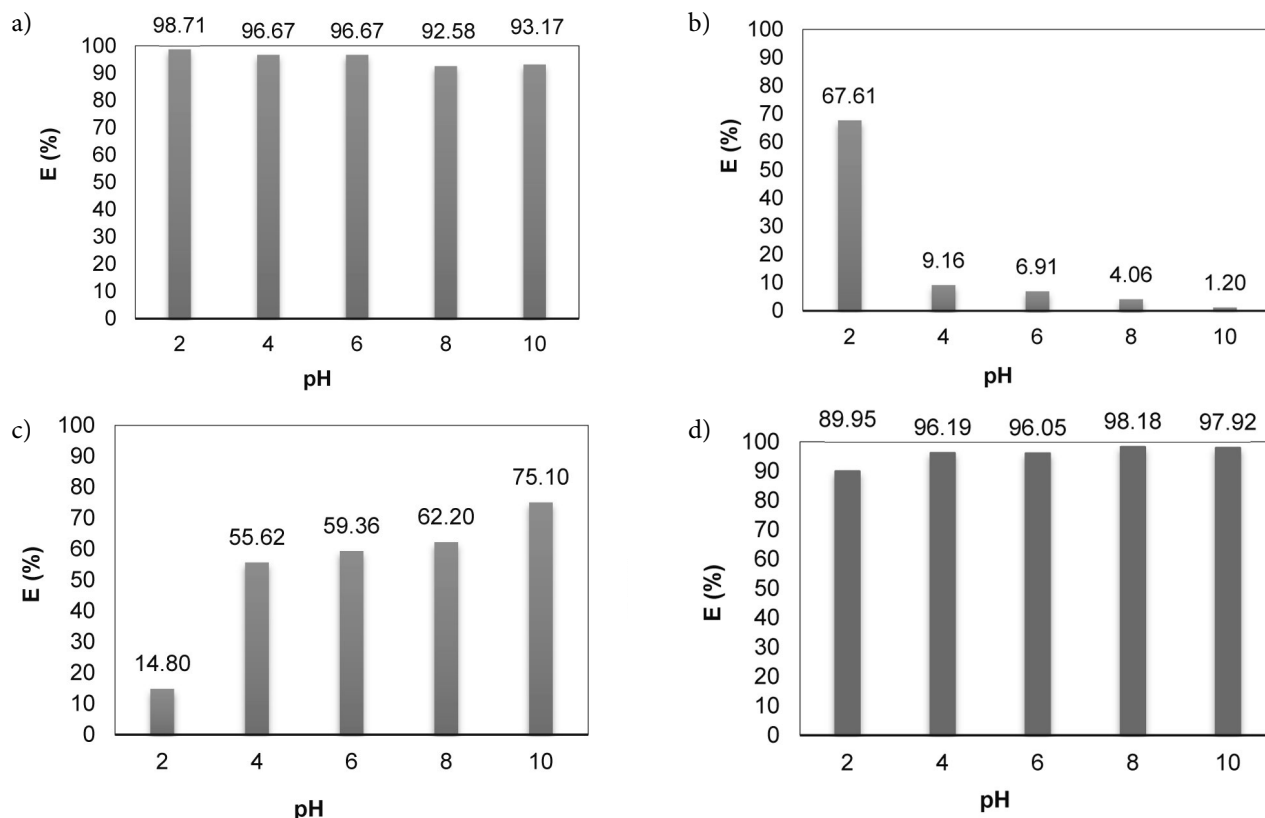


Figure 2. Effect of pH for indicators: Congo Red (a), BPB (b), MB (c), MG (d) ($C_i = 30$ mg/L, 1.5 g biomass, 160 μ m, 700 rpm, $T = 20 \pm 1$ °C)

in case of BPB (Figure 3.e) some of the cross-linked structure is saturated, in other parts smaller or larger aggregates have appeared, but the cross-linked structure, characteristic to eggshell structure, is still visible. This can be explained in the following way: when comparing the result with the amount of bounded material, we can see that BPB has the smallest value ($c_i = 50$ mg/L, $q_e = 0.06$ mg/g), so we can conclude that there are still free binders and the eggshells' crystal grid structure is still visible.

In order to examine the elemental composition of

the eggshell both for control and dye adsorbed samples X-ray spectroscopy (EDX) was carried out. From Table 2 it can be assumed that the control sample contains mostly carbon, oxygen and calcium. This was expected because eggshell is made of calcium carbonate (approx. 94%). Samples contaminated with dye not only contain elements specific to eggshell but also elements gained from the dye they were adsorbed with, we can see that new elements appeared, some completely disappeared while others only decreased.

Table 2. Eggshells' elemental composition, results obtained were computed from 9 data ($C_{\text{dye}} = 50$ mg/L, 160 μ m)

Elements	Wt(%) control eggshell	Wt(%) MB	Wt(%) MG	Wt(%) Congo Red	Wt(%) BPB
C	22.944 \pm 9.144	25.169 \pm 2.617	24.662 \pm 6.016	23.504 \pm 5.877	25.092 \pm 6.607
N	0.314 \pm 0.735	0	0	0	0
O	43.990 \pm 10.782	46.110 \pm 1.241	47.633 \pm 6.553	45.058 \pm 2.076	47.050 \pm 8.348
Na	0.063 \pm 0.108	0.046 \pm 0.044	0.063 \pm 0.067	0.096 \pm 0.046	0.050 \pm 0.079
F	0	0.870 \pm 0.688	1.763 \pm 1.693	2.390 \pm 0.805	1.520 \pm 1.726
Mg	0.445 \pm 0.237	0.328 \pm 0.036	0.312 \pm 0.040	0.358 \pm 0.034	0.192 \pm 0.217
Al	0.429 \pm 0.541	0.340 \pm 0.072	0.403 \pm 0.180	0.366 \pm 0.111	0.690 \pm 0.720
Si	0	0	0.008 \pm 0.020	0.018 \pm 0.040	0
P	0.084 \pm 0.219	0.084 \pm 0.051	0.107 \pm 0.045	0.096 \pm 0.026	0.085 \pm 0.069
S	0.175 \pm 0.328	0.236 \pm 0.030	0.2370 \pm 0.213	0.238 \pm 0.058	0.385 \pm 0.196
Ca	29.245 \pm 9.553	26.750 \pm 1.265	28.765 \pm 5.136	27.864 \pm 3.337	28.973 \pm 5.117
Cu	0	0.020 \pm 0.020	0.015 \pm 0.023	0.008 \pm 0.018	0
K	0.015 \pm 0.048	0	0	0	0
Br	0	0	0	0	0.130 \pm 0.162

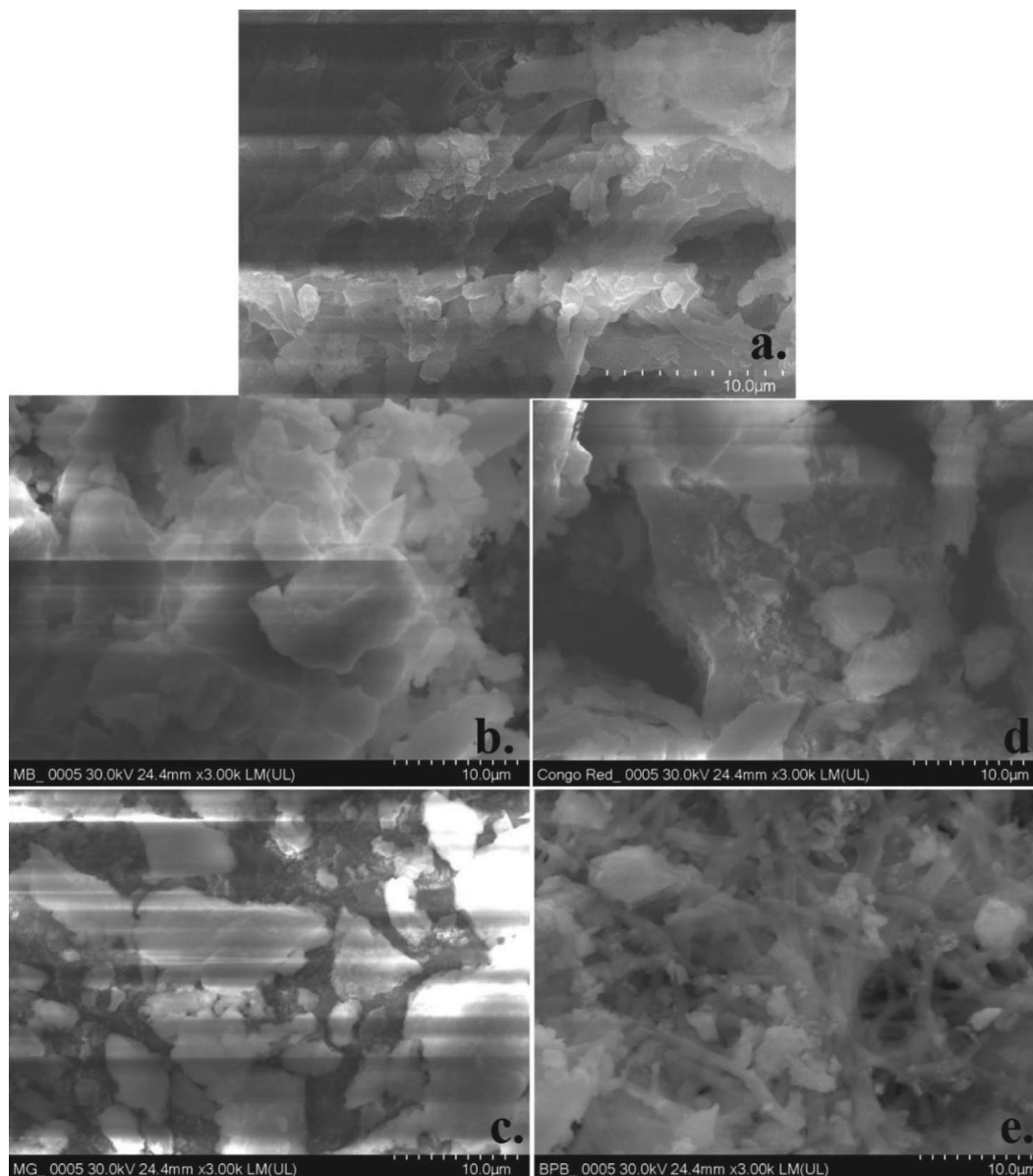


Figure 3. a. control eggshell, 50 mg/L b. MB, c. MG, d. Congo Red, e. BPB adsorbed eggshell household waste.

Figure 4 is a graphical representation of the distribution of trace elements summarized in Table 2. We can see clearly the decrease of Mg while the increase of Sulphur. Furthermore, Sulphur as keystone of dyes can be seen in each sample, while nitrogen is eliminated. In the case of BPB, the presence of bromine proves the eggshells' adsorption ability. Results obtained demonstrate that even in small concentrations (50 mg/L) the elemental composition of the eggshell can change when is used for dye adsorption.

3. 4. Bioconcentration Factor

Figure 5 shows that BCF decreases with the increase of dye concentration in case of Congo Red while BCF increases in case of MG, clearly demonstrating that eggshell

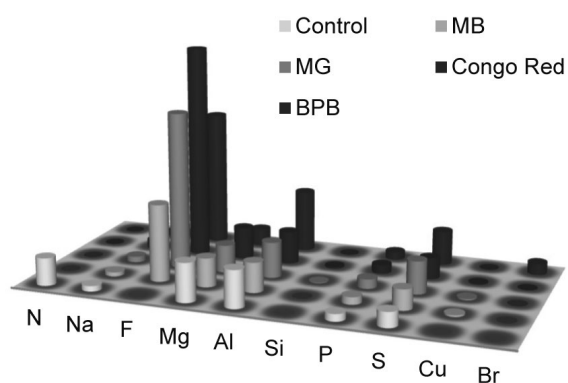


Figure 4. Appearance of trace elements in eggshell before and after adsorption

is a promising biosorbent to remove indicators.¹⁰ On the other hand, there is no significant change in the presence of BPB and MB.

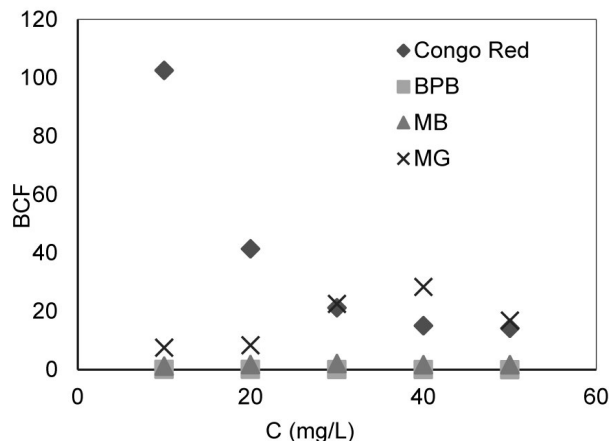


Figure 5. Bioconcentration factor

3. 5. Ecotoxicological Test

During research the toxicity of each indicator was studied by carrying out seed germination, seedling growth test for salad (lettuce) and mustard seeds. Four different concentrations were used beside the control sample. After 72 h. the length of each seeds' root was measured and 2×25 measurements' arithmetic mean was calculated and summarized in tables.

For Congo Red in Table 3 it is obvious that for lettuce seed the inhibition of germination can reach 80%, while for mustard seed negative values were obtained. The growth of the seed roots can be explained by the presence of nitrogen in the dye. Moreover, from the 25 seeds more were germinated in case of mustard than in case of lettuce.

Table 3 shows that the degree of germination is increased by increasing the concentration in case of BPB. The inhibition grows with concentration increase, in high concentrations (1 g/L) for lettuce reaches 100% and for mustard 99.85%.

In case of MB for lettuce seed the inhibition is around 30% for 10 mg/L concentration, the inhibition increases with the increase of dye concentration. For mustard seed, the values are much lower. During the experiments the mustard seed became blue and the seeds also discolored.

Both for the mustard and lettuce seed the inhibition was high in case of MG, more than 88% was obtained even at low concentration (10 mg/L) for mustard seed, whereas in case of lettuce seed more seeds germinated. Mustard seeds have become colored and around them (in the inhibition zone) the dye was discolored.

Figure 5 shows mustard and lettuce seed sprouts. On the left (Figure 6.a,d) side seeds were in control solution while on the right (Figure 6.b,c) side seeds were placed in 50 mg/L MG solution. It can be seen that the sprouts are healthy and long (lettuce 40 mm, mustard 70 mm), while in the dye solution the seeds were colorful and small (barely 10 mm). It is also noteworthy that the control had at least 20 sprouts out of 25 seeds, while in the dye solution it was much less. These observations apply in each case. All



Figure 6. Mustard (a, b) and lettuce (c, d) seeds before (a, d) and after (b, c) seed growth test

Table 3. Seedling growth test containing root growth inhibition data, as the standard method required results obtained were computed from 2 parallel experiments ($C_1 = 0-1000$ mg/L, $T = 20$ °C, $t = 72$ h)

Dye Concentration (mg/L)	Congo Red		BPB		MB		MG	
	Lettuce (%)	Mustard (%)	Lettuce (%)	Mustard (%)	Lettuce (%)	Mustard (%)	Lettuce (%)	Mustard (%)
10	-35.75	-5.31	24.84	45.75	30.37	20.25	88.68	63.36
30	68.88	-25.74	43.43	69.42	49.09	10.81	93.67	83.44
50	82.62	-21.87	54.97	78.79	79.66	17.43	97.17	83.16
1000	36.83	18.28	100	99.85	99.19	74.14	100	97.25

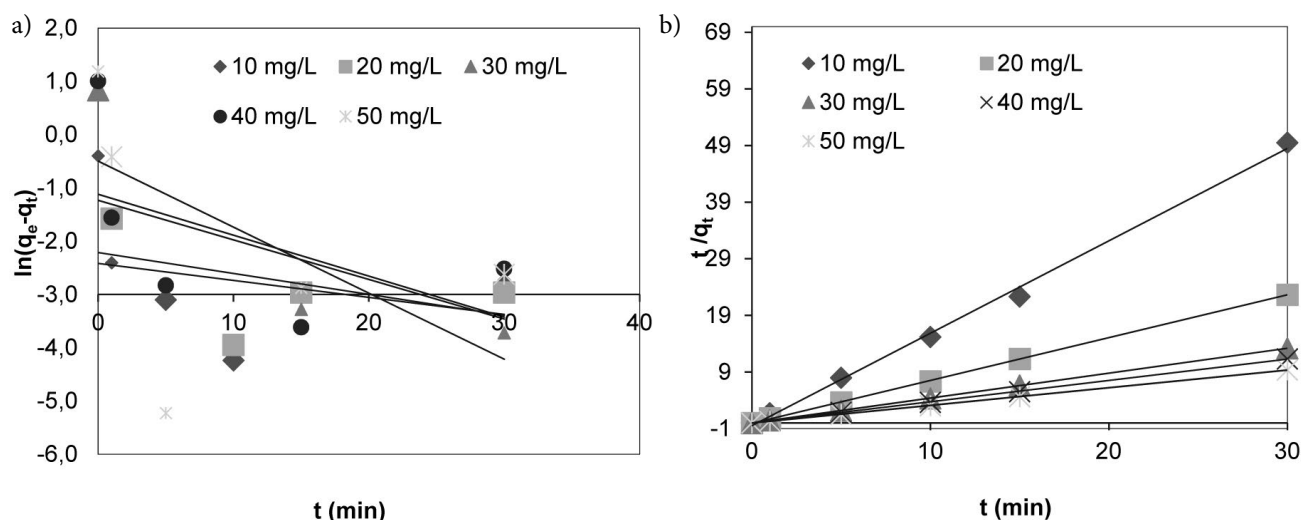


Figure 7. Pseudo-first (a) and pseudo-second (b) order kinetic models in case of MB

in all, we can conclude that seed germination is dye and plant dependent.

3. 6. Adsorption Kinetic Models

Experimental data were analyzed using various kinetic models to describe the mechanism of adsorption process of Congo Red, BPB anionic and MB, MG cationic dyes on chicken eggshell household waste. Linearized graphics are only present in case of MB, but the others show similar trends. The pseudo-first-order (Lagergen) plot is shown in Figure 6.a. From the intercept and slope of the straight lines' plot q_e (quantity in equilibrium) and k_1 (Lagergen rate constant) was calculated and listed in table 4 for all four indicators.

Pseudo-second-order (Ho&McKay) plot is shown in figure 6. b. as in case of pseudo-first- order kinetic model q_e (quantity in equilibrium) and k_2 (equilibrium rate constant) was calculated from straight lines' intercepts and slopes. Table 4 not only shows the kinetic models' specific parameters but also the linear regression coefficients. Based on received data in all cases pseudo-second-order kinetic model describes the adsorption process.

Similar results were obtained by Rani et al. where they studied Congo Red biosorption on coconut residual fiber.¹² Mudyawabikwa et al. studied MB removal by activated carbon made from tobacco stems.²³ They affirm that the study of kinetics of this process is really important "since it is a depiction of adsorbate uptake rate and also controlling parameter to the adsorption process residual time".

Table 4. Adsorption kinetics ($C_i = 10\text{--}50$ mg/L, 3 g biomass, 160 μm , 700 rpm, $T = 20 \pm 2$ °C)

MB		Pseudo-first-order				Pseudo-second-order				CongoRed		Pseudo-first-order				Pseudo-second-order			
C	q_e	k_1	q_e	R^2	k_2	q_e	R^2	C	q_e	k_1	q_e	R^2	k_2	q_e	R^2	k_2	q_e	R^2	
(mg/L)	(exp)	(1/t)	(calc)		(g/mg	(calc)		(mg/L)	(exp)	(1/t)	(calc)		(g/mg	(calc)		(g/mg	(calc)		
	(mg/g)		(mg/g)		$\times t$)	(mg/g)			(mg/g)		(mg/g)		$\times t$)	(mg/g)		$\times t$)	(mg/g)		
10	0.20	-0.04	0.11	0.118	-5.59	0.61	0.997	10	0.33	-0.06	0.36	0.604	0.71	0.99	0.996				
20	0.44	-0.03	0.09	0.159	0.42	1.91	0.999	20	0.63	-0.04	0.53	0.847	0.42	1.91	0.999				
30	0.76	-0.12	0.61	0.714	0.24	2.75	0.999	30	0.92	-0.02	0.65	0.742	0.24	2.75	0.999				
40	0.88	-0.08	0.33	0.292	0.18	3.73	0.999	40	1.24	-0.03	0.91	0.844	0.18	3.73	0.999				
50	1.07	-0.07	0.29	0.144	0.12	4.67	0.999	50	1.53	-0.01	0.77	0.555	0.12	4.67	0.999				
MG		Pseudo-first-order				Pseudo-second-order				BPB		Pseudo-first-order				Pseudo-second-order			
C	q_e	k_1	q_e	R^2	k_2	q_e	R^2	C	q_e	k_1	q_e	R^2	k_2	q_e	R^2	k_2	q_e	R^2	
(mg/L)	(exp)	(1/t)	(calc)		(g/mg	(calc)		(mg/L)	(exp)	(1/t)	(calc)		(g/mg	(calc)		(g/mg	(calc)		
	(mg/g)		(mg/g)		$\times t$)	(mg/g)			(mg/g)		(mg/g)		$\times t$)	(mg/g)		$\times t$)	(mg/g)		
10	0.39	0.03	0.05	0.022	-5.92	1.07	0.999	10	0.04	-0.02	0.06	0.731	2.45	0.11	0.995				
20	0.71	-0.02	0.12	0.137	-36.46	2.14	0.999	20	0.07	-0.03	0.29	0.262	0.21	0.42	0.919				
30	1.11	-0.08	0.25	0.276	8.89	3.30	0.999	30	0.09	-0.07	0.55	0.935	0.25	0.68	0.991				
40	1.48	-0.03	0.28	0.050	-18.53	4.31	0.999	40	0.08	-0.03	0.61	0.946	0.11	0.73	0.997				
50	1.59	-0.05	0.18	0.073	-34.70	4.71	0.999	50	0.06	-0.06	0.39	0.978	0.40	0.52	0.976				

Table 5. Adsorption isotherm models calculated constants for indicator adsorption onto eggshell surface ($C_i = 10\text{--}100$ mg/L, 3 g biomass, 160 μm , 700 rpm, $T = 20 \pm 2$ °C)

	Langmuir			Freundlich			Dubinin-Radushkevich			Temkin		
	K_L (L/mg)	q_{\max} (mg/g)	R^2	n	K_f ($\text{mg}^{(1-1/n)}\text{L}^{1/n}/\text{g}$)	R^2	β ($\text{mol}^2 \text{kJ}^2$)	E (kJ/mol)	R^2	A_T (L/g)	B (J/mol)	R^2
MB	0.04	0.87	0.911	0.78	36.90	0.930	9×10^{-6}	0.24	0.990	2.36	2×10^{-5}	0.989
MG	0.33	2.13	0.856	2.09	1.46	0.965	3×10^{-7}	1.29	0.955	2.53	7×10^{-5}	0.961
CongoRed	3.75	1.22	0.999	2.50	1.02	0.996	4×10^{-8}	3.54	0.854	2.66	2×10^{-6}	0.917
BPB	0.59	0.04	0.827	1.02	1.23	0.811	8×10^{-7}	2.89	0.755	2.13	2×10^{-7}	0.803

Pseudo-second-order kinetic model described the adsorption process in case of MG using nanowires loaded activated carbon as biosorbent and in case of BPB using bentonite carbon composite material.^{14,24}

3. 7. Adsorption Isotherm Models

Equilibrium processes can be characterized by adsorption isotherm models. In order to characterize the adsorption process and to determine the amount of adsorption, four different isotherm models (Langmuir, Freundlich, Temkin, Dubinin-Radushkevich) were used for all four dyes' equilibrium data, obtained after adsorption with eggshell.

Table 5 contains the calculated parameters characteristic to each isotherm model. Due to the fact that $B - \text{Temkin}$ constant is less than 20 kJ/mol and $E - \text{energy}$ is less than 8 kJ/mol the adsorption is mostly physical in nature.

As shown in Table 5 MB fits the Dubinin-Radushkevich isotherm model more closely, which indicates that chemical adsorption also occurs, ion exchange happens, similar results were obtained using walnut as biosorbent for MB removal.²⁵ In case of MG the linear regression coefficients are very near values but it aligned closer to Freundlich isotherm model, Santhi et al. got Freundlich isotherm as well by studying MG adsorption on prawn waste.²⁶ In case of BPB and Congo Red the adsorption process can be described by Langmuir isotherm model. Similar results to Congo Red:^{27,28} and to BPB:^{19,29,15}

4. Conclusions

The present study compared two anionic (Congo Red, Bromphenol Blue) and two cationic (Methylene Blue Malachite Green) dyes' adsorption properties on eggshell surface. By studying the effect of pH, results demonstrate that anionic dyes adsorb better in acidic while cationic dyes in basic medium. Highest efficiency occurred at pH = 2 for Congo Red and BPB (98.71, 67.61%) while for MB and MG in basic medium (75.10, 98.18%). SEM images show that the porous, cross-linked structure of eggshell disappeared after dye adsorption in case of Congo Red, MB, MG. From EDX measurements it is obvious that egg-

shell is mostly made of CaCO_3 and after adsorption process the amount of sulphur, chromium and bromine increased in samples. With the help of seed germination test, the different effect of each dye on lettuce and mustard seed growth was investigated, where the phytotoxic test was plant and dye dependent. For all four dyes the adsorption mechanism was best described by pseudo-second-order kinetic model. In case of MB Dubinin-Radushkevich, MB-Freundlich, BPB, Congo Red Langmuir isotherm model fitted better the adsorption data.

5. References

1. The United Nations World Water Development Report – Facts and figures.
<http://unesdoc.unesco.org/images/0024/002475/247553e.pdf>
2. The United Nations World Water Development Report – Executive summary,
<http://unesdoc.unesco.org/images/0024/002475/247552e.pdf>.
3. M. A. M. Salleh, D. K. Mahmoud, W. A. W. A. Karim, A. Idris, *Desalination* **2011**, 280, 1–13.
DOI: 10.1016/j.desal.2011.07.019.
4. R. Dutta, T. V. Nagarjuna, S. A. Mandavgane, J. D. Ekhe, *Ind. Eng. Chem. Res.* **2014**, 53, 18558–18567.
DOI: 10.1021/ie5030003.
5. R. B. Arfi, S. Karoui, K. Mougin, A. Ghorbal, *Euro-Mediterr. J. Environ. Integr.* **2017**, 2, 20.
DOI: 10.1007/s41207-017-0032-y.
6. M.-S. Chiou, P.-Y. Ho, H.-Y. Li, *Dyes Pigments* **2004**, 60, 69–84, **DOI:** 10.1016/S0143-7208(03)00140-2.
7. C. Indolean, S. Burcă, A. Măicăneanu, *Acta Chim. Slov.* **2017**, 64, 513–521, **DOI:** 10.17344/acsi.2017.3271.
8. W. T. Tsai, J. M. Yang, C. W. Lai, Y. H. Cheng, C. C. Lin, C. W. Yeh, *Bioresour. Technol.* **2006**, 97, 488–493.
DOI: 10.1016/j.biortech.2005.02.050.
9. P. S. Guru, S. Dash, *Adv. Colloid Interface Sci.* **2014**, 209, 49–67. **DOI:** 10.1016/j.cis.2013.12.013.
10. S. Tonk, C. Majdik, S. Robert, M. Suci, E. Rápó, B. Nagy, A. Gabriela Niculae, *Rev. Chim.-Buchar.- Orig. Ed.* **2017**, 68, 1951.
11. How many chickens are there in the United States? How many eggs do they produce? Just the facts here., <http://www.ansc.purdue.edu/faen/poultry%20facts.html>, accessed November 26, 2017.

12. K. C. Rani, A. Naik, R. S. Chaurasiya, K. S. M. S. Raghavarao, *Water Sci. Technol.* **2017**, *75*, 2225–2236. DOI: 10.2166/wst.2017.109.
13. N. F. El-Harby, S. M. A. Ibrahim, N. A. Mohamed, *Water Sci. Technol.* **2017**, *76*, 2719–2732. DOI: 10.2166/wst.2017.442.
14. F. El-Dars, H. M. Ibrahim, H. A. B. Farag, M. Zakaria Abdelwahhab, M. Shalabi, *Int. J. Sci. Eng. Res.* **2015**.
15. S. Dhananasekaran, R. Palanivel, S. Pappu, *J. Adv. Res.* **2016**, *7*, 113–124. DOI: 10.1016/j.jare.2015.03.003.
16. O. Hamdaoui, M. Chiha, *Acta Chim. Slov.* **2007**, *54*, 407–418.
17. D. Caparkaya, L. Cavas, *Acta Chim. Slov.* **2008**, *55*, 547–553.
18. H. Mei Chen, J. Liu, X. Zhong Cheng, Y. Peng, *Adv. Mater. Res.* **2012**, *573–574*, 63–67. DOI: 10.4028/www.scientific.net/AMR.573-574.63.
19. Y. Zeroual, B. S. Kim, C. S. Kim, M. Blaghen, K. M. Lee, *Water. Air. Soil Pollut.* **2006**, *177*, 135–146. DOI: 10.1007/s11270-006-9112-3.
20. M. J. Iqbal, M. N. Ashiq, *J. Chem. Soc. Pak.* **2010**, *32*, 419–428.
21. M. A. Zulfikar, H. Setiyanto, 'Study of the adsorption kinetics and thermodynamic for the removal of Congo Red from aqueous solution using powdered eggshell', **2013**.
22. D. P. Tiwari, S. K. Singh, N. Sharma, *Appl. Water Sci.* **2015**, *5*, 81–88. DOI: 10.1007/s13201-014-0171-0.
23. B. Mudyawabikwa, H. H. Mungondori, L. Tichagwa, D. M. Katwire, *Water Sci. Technol.* **2017**, *75*, 2390–2402. DOI: 10.2166/wst.2017.041.
24. M. Ghaedi, E. Shojaeipour, A. M. Ghaedi, R. Sahraei, *Spectrochim. Acta. A. Mol. Biomol. Spectrosc.* **2015**, *142*, 135–149. DOI: 10.1016/j.saa.2015.01.086.
25. Removal of Methylene Blue from Aqueous Solution Using Agricultural Residue Walnut Shell: Equilibrium, Kinetic, and Thermodynamic Studies, <https://www.hindawi.com/journals/jchem/2017/8404965/>, accessed October 13, **2017**.
26. D. T. S. Dr. T. Santhi, S. Manonmani, T. Smitha, K. Mahalakshmi, *Rasayan J. Chem.* **2009**, *2*, 813–824.
27. P. D. Saha, S. Chowdhury, M. Mondal, K. Sinha, *Sep. Sci. Technol.* **2011**.
28. J. Liu, X. Z. Cheng, P. Qin, M. Y. Pan, *Adv. Mater. Res.* **2012**, *599*, 391–399. DOI: 10.4028/www.scientific.net/AMR.599.391.
29. A. A. El-Zahhar, N. S. Awwad, E. E. El-Katori, *J. Mol. Liq.* **2014**, *199*, 454–461. DOI: 10.1016/j.molliq.2014.07.034.

Povzetek

V zadnjih letih se je adsorpcija izkazala kot učinkovit in enostaven način čiščenja onesnaženih odpadnih vod. Namen predstavljene študije je preučitev uporabe biosorpcije s pomočjo kokošjih jajčnih lupin za odstranitev organskih indikatorjev (metilensko modro, malahitno zeleno, kongo rdeče in bromfenol modro) in vodnih raztopin. Proces adsorpcije je bil preučevan pod statičnimi pogoji. Preučevali smo vpliv začetne koncentracije (10–50 mg/L), vpliv pH vrednosti, doseženo ravnotežje in kinetiko adsorpcije. S pomočjo vrstične elektronske mikroskopije smo preučili morfologijo in teksturo jajčnih lupin, prav tako pa smo izvedli EDX mikroanalizo in ekotoksikološke teste. Rezultati potrjujejo vpliv preučevanih parametrov na sorpcijski proces.

Scientific paper

Synthesis and Characterization of New Photoresponsive, Ortho and Para Oriented Azomethine Polymers

Farah Qureshi,* Muhammad Yar Khuhawar and Taj Muhammad Jahangir

Institute of Advanced Research Studies in Chemical Sciences, University of Sindh, Jamshoro, Sindh-Pakistan

* Corresponding author: E-mail: farahqureshi94@yahoo.com

Tel: +92-229213213, +92-3313534844

Received: 20-04-2018

Abstract

Five new azomethine polymers having aliphatic-aromatic moieties were synthesized by polycondensation reaction of dialdehydes and diamines. The dialdehyde monomers differ only in the orientation of the aromatic ring (ortho or para) and were synthesized by condensation reaction between aromatic aldehyde and 1,6-dibromohexane. The molecular mass of the monomers was recorded through E.I mass spectrum. The polymers structures were confirmed by elemental microanalysis, FT-IR, ¹HNMR and UV-Vis Spectroscopy. The morphology of monomers and polymers was evaluated by scanning electron microscopy (SEM). All the polymers were soluble in DMSO (on heating) and somewhat in other solvents. Thermal stability of polymers was analyzed by thermogravimetry (TG) and differential thermal analysis (DTA), all the polymers showed good thermal stability higher than their corresponding monomers. The TG of polymers indicated maximum rate of weight loss (T_{max}) within 412–708 °C. Fluorescence emission spectra of polymers were recorded and the results indicated that all the polymers were photo-responsive and indicated 1 to 4 emission bands with maximum within 349–606 nm. The limit of detection of polymers was within 0.625–1.25 µg/ml. The polymers were also examined for their antimicrobial activities against bacteria and fungi.

Keywords: Polyazomethines, thermal stability, fluorescence, antimicrobial activities, morphology

1. Introduction

The conjugated azomethine polymers also called Schiff base polymers are reported and studied since last several decades¹. These are generally synthesized by polycondensation reaction between dialdehydes or diketones with diamines.^{2–4} However, an interest in preparation of new Schiff base polymers and their applications in different field keep on increasing.⁵ The researchers are focusing their attention toward conjugated azomethine polymers during recent years^{6,7} because of their useful properties such as electrical conductivity, optoelectronic and thermal stability.^{8,9} They also exhibit liquid crystalline behavior.^{10–14} Poly(azomethines) containing (-N=C) functional group have been applied successfully to some extent as transporting materials in organic solar cells^{15–17} and their application.¹⁸ They can act as antimicrobial agents and these are proving interesting, because these are nonvolatile and thermally stable and cannot penetrate through human skin.^{19,20} They could protect losses through skin by volatilization.^{21,22} The conjugated polyazomethines indicate fluorescence properties, they can be applied in the

manufacture of chemical sensors, photoluminescence devices and light emitting diodes.^{23,24} The Schiff base polymers derived from aromatic aldehydes with ortho-hydroxy group (salicylaldehyde) can act as chelate polymers with transition metal ions for their removal from industrial contaminated and waste water.²⁵ The polymeric Schiff bases having aliphatic-aromatic groups indicate better thermal stabilities, but they are difficult to process as they have high melting/ decomposition points and are insoluble in common organic materials.²⁶ To improve their solubility different arrangements are made in their structure, which includes ether and ester linkages, introducing solution enhancing groups²⁷ copolymerization and blending.^{28–30} Flexible spacers have also been introduced to enhance their solubility without affecting their thermal stability.³¹ In the present work five new photo-responsive polyazomethines were synthesized, they differ in orientation of ether groups attached with the aromatic rings and also various types of aromatic or alicyclic rings were incorporated in the polymer chain, the purpose of these structural modifications was to investigate their effects on the properties (solubility, thermal stability and

fluorescence) of polymers. The monomers and their polymers are characterized by different spectroscopic techniques, thermal analysis, scanning electron microscopy (SEM), solubility, spectrofluorimetry and antimicrobial activities.

2. Materials and Methods

2.1. Materials

2-hydroxybenzaldehyde (Merck, Germany), 4-hydroxybenzaldehyde (Fluka, Switzerland), 1,6-dibromohexane (Sigma Aldrich, St.Louis USA), 2,6-diaminopyridine (Sigma-Aldrich, Germany), 1,4-phenylenediamine (Alfa-Aesar, UK), 1,5-naphthalenediamine (Toshima, Kita-ka, Tokyo, Japan), 1,2-cyclohexanediamine (E.Merck, Germany), dimethylsulfoxide (DMSO) (Daejung, Korea), dimethylformamide (BDH AnalAR, England), anhydrous sodium carbonate (Sigma-Aldrich, Germany), *p*-toluenesulfonic acid (Daejung, Korea), ethanol (E. Merck, Germany), potassium hydroxide (E. Merck, Germany), chloroform, tetrahydrofuran (THF) (E. Merck, Germany) and distilled water from all glass were used.

2.2. Synthesis of Monomers

Two dialdehyde monomers 2,2'-hexamethylenebis(oxybenzaldehyde) (*o*-HOB) and 4,4'-hexamethylenebis(oxybenzaldehyde) (*p*-HOB) were prepared through the reaction of 2-hydroxybenzaldehyde or 4-hydroxybenzaldehyde with 1,6-dibromohexane by following the reported procedure.^{26,31} The preparation of related compounds is also reported^{32,33} but in present work procedure reported by Catanescu et al.²⁶ gave better results and was followed. The mass, FT-IR, ¹HNMR and UV spectra of both monomers agreed with the structure assigned and the results are given in Section 3.4, 3.5 and 3.6 respectively. The monomer *o*-HOB indicated *m/z* (Relative intensity %), M⁺ 326 (3.7), 189 (8.9), 147 (14.6), 135 (26.3), 121 (75), 83 (43.8), 55 (100), the mass spectral data of *p*-HOB is already reported.³¹

2.3. Synthesis of Polymers

The polymers were synthesized by slightly modified general procedure as reported^{26,31} as under: A 250 ml round bottom flask equipped with condenser and magnetic stirrer was charged with equimolar mixture (5mmol) of different diamines and dialdehydes, both were dissolved separately in DMF solvent, then *p*-toluenesulfonic acid was added as catalyst. The mixture was refluxed under nitrogen with continuous stirring for 6h. The mixture was poured into 250 ml of water and allowed to form precipitate. The product was collected by filtration, washed with ethanol and dried.

2.3.1. Poly-4,4'-hexamethylenebis(oxybenzaldehyde) 1,5-naphthalenediimine (PpHOBND)

Mp. 280 °C (decomposed), yield 78%, elemental microanalysis calculated for (C₃₀H₂₈N₂O₂)_n, (observed %) %C= 80.35(80.68), %H= 6.25 (6.58), %N= 6.25 (5.42), FT-IR, cm⁻¹ (Relative intensity), 2938 (w), 2863 (w), 1668 (m), 1598 (s), 1511 (m), 1472 (w), 1395 (w), 1303 (w), 1249 (s), 1161 (s), 1108 (w), 1015 (w), 925(w), 893 (w), 831(m), 780 (w), 739 (w), 659 (w).¹HNMR (DMSO), δ ppm 1.483, 1.764, 4.090 (t), 7.106 (d), 7.841 (d), 9.850. UV (DMSO), λ-max nm (1% absorptivity) 284 (292.4) 340 (60.8).

2.3.2. Poly-4,4'-hexamethylenebis(oxybenzaldehyde)1,4-phenylenediimine (PpHOBPD)

Mp. 310 °C (decomposed), yield 76 %, elemental microanalysis calculated for (C₂₆H₂₆N₂O₂)_n, (observed %) %C=78.39 (78.29), %H= 6.53 (6.69), %N=7.03 (7.95). FT-IR, cm⁻¹ (Relative intensity), 2240(w), 1598 (m), 1570 (w), 1510 (w), 1472 (w), 1422 (w), 1393 (w), 1300 (w), 1242 (s), 1163 (m), 1110 (w), 1017 (m), 950 (w), 883 (w), 835 (m), 766 (w), 724 (w), 655 (w).¹HNMR (DMSO), δ ppm 1.227, 1.485, 1.765, 2.720, 2.880, 4.091 (t), 7.106 (d), 7.523, 7.842 (d), 9.851. UV (DMSO), λ-max nm (1% absorptivity) 278 (466.8), 595 (17.2).

2.3.3. Poly-4,4'-hexamethylenebis(oxybenzaldehyde)1,2-cyclohexanediimine (PpHOBcy)

Mp. 100–200 °C (becomes liquid crystalline at 100 °C and melted at 200 °C), yield 79%, elemental microanalysis calculated for (C₂₆H₃₂N₂O₂)_n (observed %) %C= 77.22 (78.30), %H= 7.92 (8.18), %N= 6.93 (5.58). FT-IR, cm⁻¹ (Relative intensity), 2934 (w), 2860 (w) 1683 (m), 1640 (m) 1601 (m), 1511 (m), 1470 (w), 1389 (w), 1306 (w), 1246 (s), 1160 (m), 1111 (w), 1084 (w), 1013 (m), 946 (w), 839 (m), 746 (w), 712 (w), 683 (w), 658 (w). ¹HNMR (DMSO), δ ppm 1.208, 1.238, 1.270, 1.295, 1.319, 1.346, 1.386, 1.482, 1.539, 1.568, 1.602, 1.755 (d), 1.839, 3.998, 4.089 (t), 6.854 (d), 6.945 (d), 7.104 (d), 7.501 (d), 7.601 (t), 7.758 (d), 7.841 (d), 8.168 (d), 9.850. UV (DMSO), λ-max nm (1% absorptivity) 275 (434.2)

2.3.4. Poly-2,2'-hexamethylenebis(oxybenzaldehyde)1,4-phenylenediimine (PoHOBPD)

Mp. 150 °C (decomposed), yield 75%, elemental microanalysis calculated for (C₂₆H₂₆N₂O₂)_n (observed %) %C= 78.39 (78.34), %H= 6.53 (6.63), %N= 7.03 (6.97). FT-IR, cm⁻¹ (Relative intensity), 2943 (w), 2868 (w), 1685 (w), 1611 (m), 1595 (s), 1497 (m), 1485 (w), 1479 (w), 1456 (m), 1396 (w), 1364 (w), 1301 (w), 1286 (w), 1249 (s), 1187 (w), 1160 (w), 1102 (m), 1043 (w), 1021 (m), 980 (w), 887 (w), 839 (m), 780 (w), 750 (s), 730 (w). ¹HNMR (DMSO), δ ppm 1.228, 1.534, 1.802, 2.722, 2.882, 4.132 (d), 7.050,

7.214 (d), 10.379. UV (DMSO), λ -max nm (1% absorptivity) 262 (660.8), 321 (542.4), 373 (465.6)

2. 3. 5. Poly-2,2'-hexamethylenebis(oxybenzaldehyde)2,6-diiminopyridine (PoHOBP)

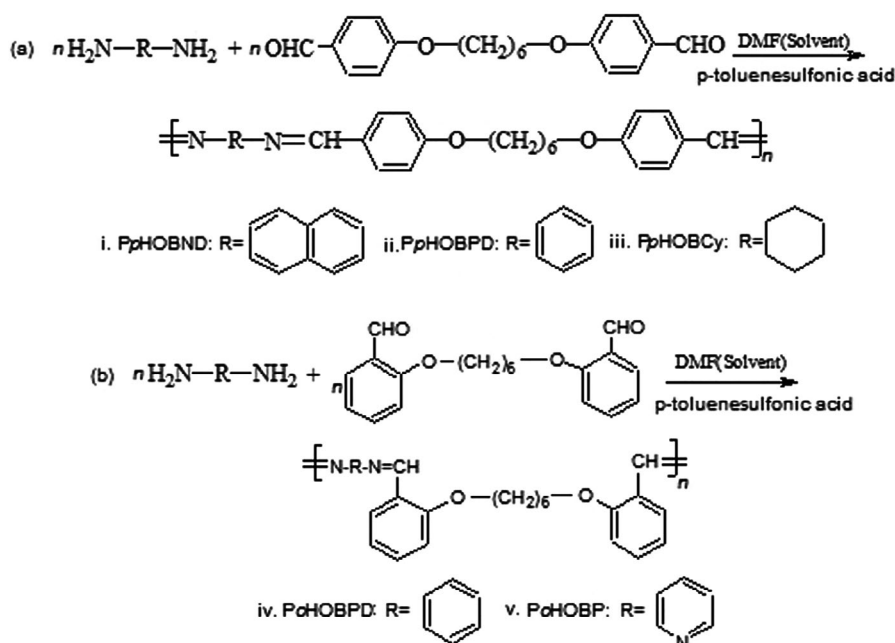
Melting/decomposition above 360 °C, yield 76 %, elemental microanalysis calculated for $(C_{25}H_{25}N_3O_2)_n$ (observed %) %C= 75.18 (75.02), %H= 6.26 (6.70), %N= 10.52 (10.22). FT-IR, cm^{-1} (Relative intensity), 3620 (w), 2940 (w), 2862 (w), 2219 (w), 1681(w), 1596 (m), 1483 (w), 1449 (s), 1284(w), 1233 (s), 1160 (w), 1102 (w), 1044 (w), 999 (w), 930 (w), 869 (w), 833 (w), 800 (w), 834 (m), 751 (s), 720 (w), 683 (w), 647 (w). 1H NMR (DMSO), δ ppm 1.225, 1.532, 1.799, 1.815, 2.720, 2.879, 4.136 (t), 7.029, 7.048, 7.067, 7.202, 7.224, 7.610, 7.629, 7.658 (d), 7.677 (d), 7.941, 10.377. UV (DMSO), λ -max nm (1% absorptivity) 261 (122.4), 320 (80.8).

2. 4. Analysis of Monomers and Polymers.

The elemental microanalysis of polymers was performed by elemental microanalysis Ltd, Devon, United Kingdom. E.I mass spectra of the monomers were recorded on JEOL JMS 600 mass spectrometer (USA) at HEJ Research Institute of Chemistry, University of Karachi, Sindh-Pakistan. UV-Vis spectra of monomers and polymers were recorded in DMSO solvent within 500–200 nm on Perkin Elmer double beam Lambda 35 spectrophotometer (Perkin Elmer, Singapur) using dual 1 cm quartz cuvette. Spectrophotometer was controlled by the computer with software. FT-IR spectra of the synthesized compounds were recorded within 4000–600 cm^{-1} on Nicolet

Avatar 330 FT-IR with Attenuated total reflectance (ATR) accessory (smart partner) (Thermo Scientific, USA). 1H -NMR spectra of the compounds were recorded on Bruker AVANCE-NMR spectrophotometer (UK) at 400 MHz using tetramethylsilane (TMS) as internal standard and DMSO as solvent at HEJ Research Institute of Chemistry, University of Karachi Sindh-Pakistan. Fluorescence measurement was performed on Spectrofluorophotometer RF-5301 PC Series (Shimadzu Corporation, Kyoto, Japan) using 1cm quartz cuvette. Thermogravimetry (TG) and Differential thermal analysis (DTA) were performed at Centralized Resource Laboratory, University of Peshawar, Peshawar-Pakistan on thermogravimetric thermal analyzer Pyris Diamond TG/DTA (Perkin Elmer, USA) in nitrogen atmosphere with a flow rate of 50 ml/min and heating rate of 20 °C/min from 50 °C to 800 °C using 5 to 9 mg of sample placed on ceramic pan. In order to determine the morphologies of polymers they were also characterized by Scanning electron microscopy using JEOL JSM-6490LV Scanning Electron Microscope (USA) at Center for Pure and Applied Geology, University of Sindh, Jamshoro, Sindh-Pakistan. The accelerating voltage for taking images was 15 KV.

The antibacterial activity of the polymers was measured through 96 well plate method by using microplate alamar blue assay. The antibacterial activity was tested against bacterial species: Escherichia coli, Shigella flexneri, Staphylococcus aureus, and Pseudomonas aeruginosa using standard drug Ofloxacin. For measuring antifungal activity of the polymers agar tube dilution method was used. The antifungal activity was tested against fungal species: Trichophyton rubrum, Candida albicans, Aspergillus niger, Microsporium canis, Fusarium lini, Canadida gla-



Scheme 1. Reaction scheme (a) synthesis of para oriented polymers (b) synthesis of ortho oriented polymers.

brata using standard drug Amphotericin B for *Aspergillus niger* and drug Miconazole for other species. Percent inhibition of the polymers was compared with the percent inhibition of the standard drug. For antibacterial assay 2 mg of polymer was dissolved in DMSO solvent to get concentration of 50 µg/ml. For antifungal assay the concentration of polymers was 200 µg/ml in DMSO. Incubation period was 7 days at 28 °C ± 1 °C.

3. Results and Discussion

3.1. Synthesis of Monomers and Polymers

The dialdehyde monomers (*p*-HOB or *o*-HOB) were prepared by condensation of *p*-hydroxybenzaldehyde or *o*-hydroxybenzaldehyde with 1,6-dibromohexane. The monomers were obtained in good yield, *p*-HOB = 92% and *o*-HOB = 81%. The aliphatic spacers of *n*-hexane are common in both the (dialdehyde) monomers. The variation is only in the ortho and para linkages. The polycondensation

of an equimolar mixture of dialdehyde (*p*-HOB or *o*-HOB) with diamines (1,5-naphthalenediamine, 1,4-phenylenediamine, 1,2-cyclohexanediamine, 2,6-diaminopyridine) results into polymers (*Pp*HOBND, *Pp*HOBPD, *Pp*HOBcy, *Po*HOBPD or *Po*HOBP) containing aliphatic-aromatic groups in the main chain following the reaction Scheme 1. The polymers were also obtained in good yield (76–79%). The structure of the polymers was confirmed by different techniques and the results supported their formation. Salih İlhan et al. have reported the formation of Schiff base by the condensation of monomer *o*-HOB with 2,6-diaminopyridine.³⁴ Similar reactants were used for the synthesis of polymer *Po*HOBP, the melting/decomposition point of the polymer (*Po*HOBP) was above 360 °C while the reported Schiff base decomposed at 280 °C, the mass spectrum of the polymer (*Po*HOBP) obtained through E.I mass spectroscopy did not show the mass corresponding to Schiff base, the polymer (*Po*HOBP) had higher mass than the reported Schiff base which supported the formation of the polymer (*Po*HOBP).

Table 1. Solubility of monomers and polymers in different solvents at the concentration of 5mg/ 5 ml

S. No	Compound	Solubility in different solvents					
		H ₂ O	Ethanol	Chloroform	THF	DMF	DMSO
1.	<i>p</i> -HOB	IS ^e	S ^a	S	S	S	S
2.	<i>Pp</i> HOBND	IS	IS	IS	PS ^c	PS	S(Δ) ^b
3.	<i>Pp</i> HOBPD	IS	IS	IS	IS	IS	S(Δ)
4.	<i>Pp</i> HOBcy	IS	PS	IS	IS	PS	S
5.	<i>o</i> -HOB	IS	S	S	S	S	S
6.	<i>Po</i> HOBPD	IS	IS	SS ^d	IS	IS	S(Δ)
7.	<i>Po</i> HOBP	IS	IS	IS	IS	PS	S(Δ)

^a(soluble), ^b(soluble on heating), ^c(partially soluble), ^d(slightly soluble), ^e(insoluble)

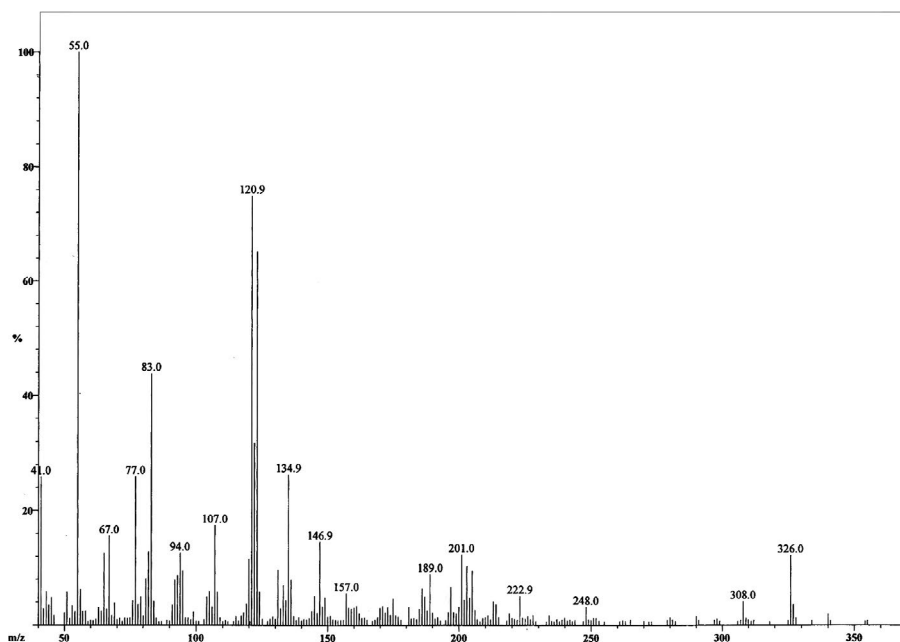


Figure 1. E.I mass spectrum of the monomer *o*-HOB

3. 2. Solubility of Monomers and Polymers

The solubility of monomers and polymers is summarized in Table 1. The monomers were soluble in organic solvents and insoluble in water. The polymers were soluble in DMSO on heating but the PpHOBCy was soluble in DMSO without heating also. The better solubility of PpHOBCy is because of the presence of more flexible cyclohexane ring while other synthesized polymers have rigid aromatic rings.

3. 3. E.I Mass Spectrum of Monomers

The mass spectrum of *p*-HOB is already reported³¹ and the mass spectrum of *o*-HOB showed M^+ at m/z 326, and other main fragments at m/z 205, 189, 177, 147, 135 and 121 corresponding to $[M-(O.C_6H_4.CHO)]^+$, $[CHO.C_6H_4.O.(CH_2)_3.CH=CH]^+$, $[CHO.C_6H_4.O.(CH_2)_4]^+$, $[CHO.C_6H_4.O.CH=CH]^+$, $[CHO.C_6H_4.O.CH_2]^+$ and $[CHO.C_6H_4.O]^+$. The peaks at 83(43%) and 55(100%) corresponded to C_6H_{11} and C_4H_7 as shown in Figure 1.

3. 4. FT-IR of Monomers and Polymers

FT-IR of *p*-HOB is reported³¹ and the FT-IR of *o*-HOB also agreed with the reported values³⁴. The comparative FT-IR of *p*-HOB and *o*-HOB showed as under: monomer *p*-HOB and *o*-HOB showed strong band at 1685 cm^{-1} and 1678 cm^{-1} for ν C=O respectively, *p*-HOB shows bands at 1595 , 1507 cm^{-1} and *o*-HOB at 1595 , 1484 cm^{-1} for ν C=C aromatic rings. The *p*-HOB showed bands at

1250 , 1069 cm^{-1} and *o*-HOB at 1244 , 1072 cm^{-1} for C-O-C vibrations. The polymers PpHOBNND, PoHOBD and PoHOBP showed weak band while PpHOBCy indicated medium intensity band within 1668 – 1682 cm^{-1} due to ν C=O of end on groups but this band was not visible in PpHOBD. The polymers indicated band of strong to medium intensity within 1596 – 1640 cm^{-1} due to ν C=N. One to two bands were visible within 1601 – 1482 cm^{-1} due to aromatic rings of the polymers. The polymers show band within 1233 – 1249 due to C-O-C asymmetric vibrations and a band within 999 to 1021 due to C-O-C symmetric vibrations. The polymers spectra showed number of band within 980 – 646 cm^{-1} due to in plane and out of plane C-H vibration of aromatic rings as shown in Figure 2. Similar assignments have been indicated for FT-IR of polyazomethines⁸.

3. 5. ¹HNMR Spectroscopy of Monomers and Polymers

The ¹HNMR of monomer *p*-HOB³¹ and ¹³C-NMR of *o*-HOB³⁴ are reported. The comparative ¹HNMR (DMSO) spectra of monomers indicated δ ppm for *p*-HOB at 9.850 and *o*-HOB at 10.375 for CHO, *p*-HOB indicated two doublets at 7.840 and 7.103 while *o*-HOB indicated multiplet at 7.641, doublet at 7.208, and triplet at 7.044 due to C-H aromatic protons. The *p*-HOB indicated triplet at 4.089 while *o*-HOB indicated triplet at 4.130 for O-CH₂ groups. *p*-HOB indicated triplet at 1.746 and singlet at 1.482 while *o*-HOB indicated doublet at 1.803 and

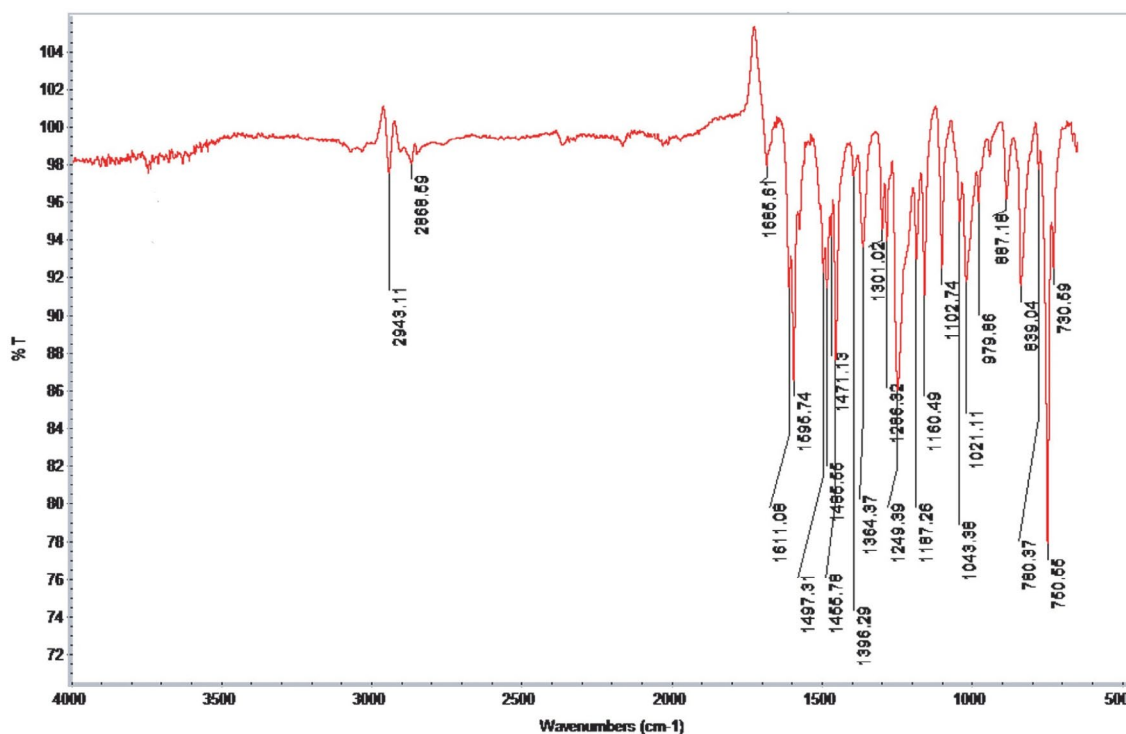


Figure 2. FT-IR spectrum of polymer PoHOBD, conditions as experimental

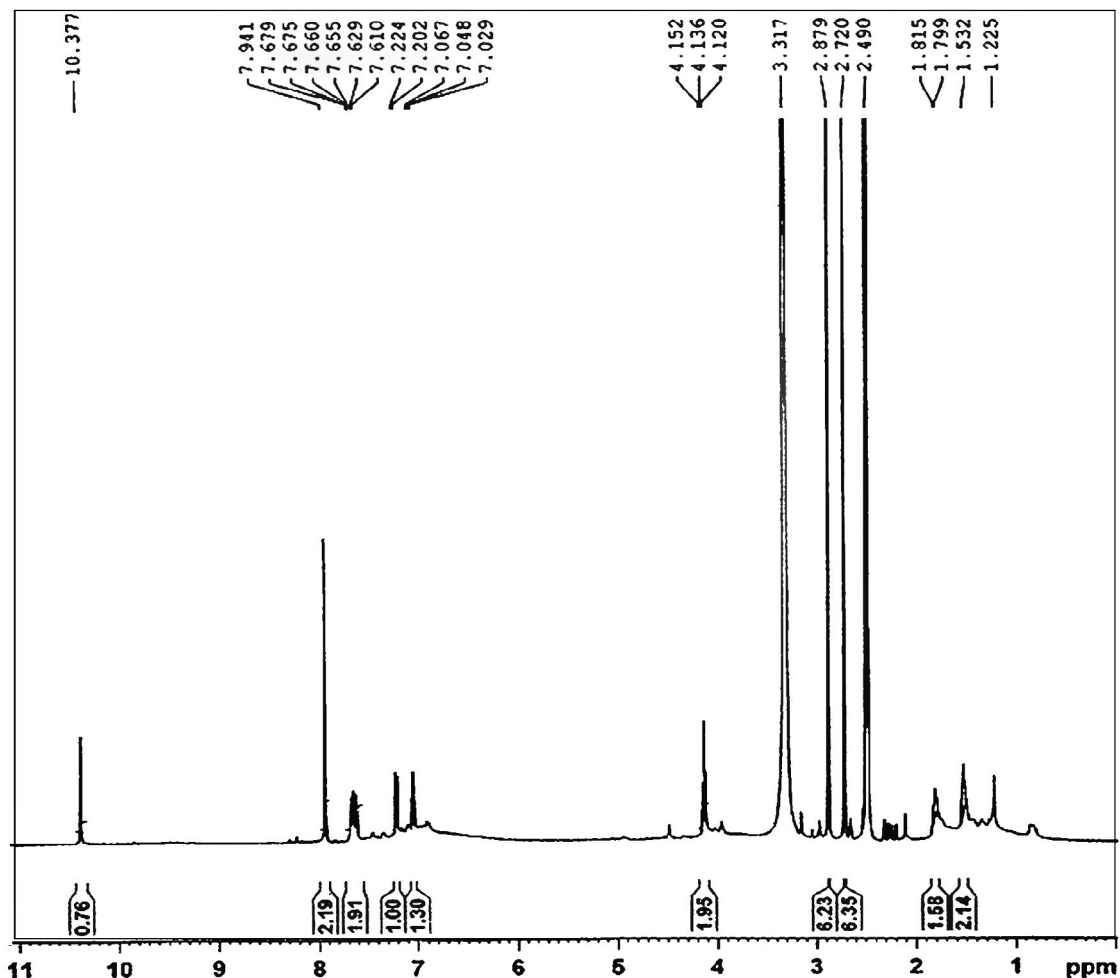


Figure 3. ^1H NMR spectrum of polymer PoHOBP

singlet at 1.527 for CH_2 groups, Catanescu et al have reported a similar assignments for related monomer.²⁶ ^1H NMR in DMSO of the polymer PpHOBNND showed singlet at δ ppm 9.850 for $\text{N}=\text{CH}/\text{HC}=\text{O}$, two doublets at 7.106 and 7.841 for C-H aromatic protons, triplet at 4.090 for O- CH_2 and singlet at 1.764 and 1.483 for CH_2 groups. PpHOBNPD indicated singlet at 9.851 for $\text{N}=\text{CH}/\text{HC}=\text{O}$, doublet at 7.106, singlet at 7.523 and doublet at 7.842 for aromatic C-H protons, triplet at 4.091 for O- CH_2 and singlets at 2.880, 2.720, 1.765, 1.485, 1.227 for CH_2 groups. PpHOBNCy indicated singlet at δ ppm 9.850 for $\text{N}=\text{CH}/\text{HC}=\text{O}$, doublets at 8.168, 7.841, 7.758, triplet at 7.601 and doublets at 7.501, 7.104, 6.945, 6.854 for aromatic C-H protons, triplet at 4.089 for O- CH_2 groups, singlet at 3.998 was for cyclohexane, singlet at 1.839, doublet at 1.755 and singlets at 1.602, 1.568, 1.539, 1.482, 1.386, 1.346, 1.319, 1.295, 1.270, 1.238, 1.208 for CH_2 groups (n-hexane or cyclohexane CH_2 protons). PoHOBNPD showed singlet at 10.379 for $\text{N}=\text{CH}$, doublet at 7.214 and singlet at 7.050 for C-H aromatic protons, doublet at 4.132 for O- CH_2 and singlet from 2.882 to 1.228 for CH_2 groups. PoHOBNP indicated singlet at 10.377 for $\text{N}=\text{CH}$,

singlet at 7.941, doublets at 7.677, 7.658, singlets from 7.629 to 7.029 for C-H aromatic protons, triplet at 4.136 for O- CH_2 , singlets from 2.879, 2.720, 1.815, 1.799, 1.532, 1.225 for CH_2 groups (Figure 3).

3. 6. UV-Vis Spectroscopy of Monomers and Polymers

UV-Vis spectra of monomers and polymers were obtained in DMSO. The monomer *p*-HOB shows a broad band at 283 nm and its molar absorptivity was $3.2 \times 10^4 \text{ L}\cdot\text{mole}^{-1} \text{ cm}^{-1}$. The monomer *o*-HOB shows two bands at 258 nm and 322 nm with molar absorptivities 1.5×10^4 and $8.8 \times 10^3 \text{ L}\cdot\text{mole}^{-1} \text{ cm}^{-1}$. The polymers PpHOBNND, PpHOBNPD and PoHOBNP showed two bands while polymer PoHOBNPD showed three bands (Figure 4), the increase in the number of bands in the absorption spectra is due to π - π^* transition in conjugated azomethine with naphthalene, phenyl and pyridine rings. The polymer PpHOBNCy showed only one band because extension of conjugation was not possible with cyclohexane ring. The results are summarized in Table 2.

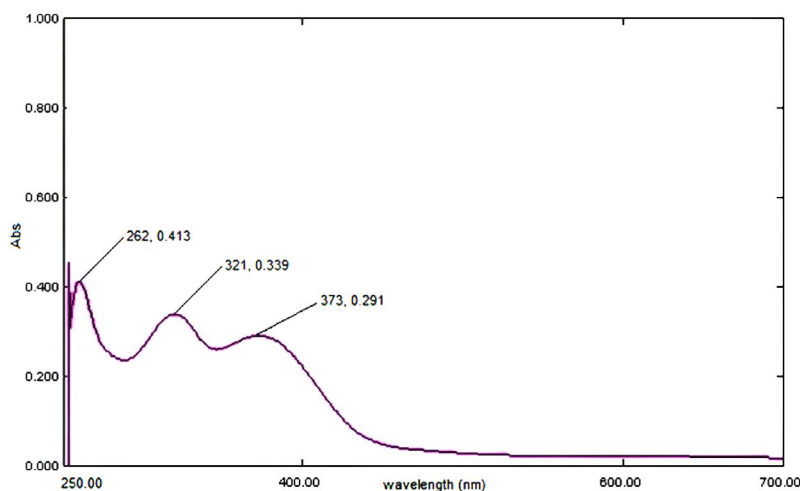


Figure 4. UV/Vis spectrum of the polymer PoHOBPD conditions as experimental

Table 2. Results of spectrophotometric studies of monomers and polymers in DMSO Solvent

S. No	Compound	λ nm (ϵ 1%)	Possible transition
1.	<i>p</i> -HOB	283(32500) ^a	$\pi - \pi^*$ transition within aromatic ring system
2.	<i>o</i> -HOB	258(15987) ^a	$\pi - \pi^*$ transition within aromatic ring system
		322(8867) ^a	$\pi - \pi^*$ transition involving aromatic ring and conjugated C=C-C=O π -electron system
3.	P <i>p</i> HOBND	284(292)	$\pi - \pi^*$ transition within aromatic ring system
		340(61)	$\pi - \pi^*$ transition involving aromatic ring and conjugated C=C-N=C π -electron system
4.	P <i>p</i> HOBPD	278(467)	$\pi - \pi^*$ transition within aromatic ring system
		595(17)	$\pi - \pi^*$ transition in conjugated azomethine group
5.	P <i>p</i> HOB <i>Cy</i>	275(434)	$\pi - \pi^*$ transition within aromatic ring system
6.	P <i>o</i> HOBPD	262(661)	$\pi - \pi^*$ transition within aromatic ring system
		321(542)	$\pi - \pi^*$ transition involving aromatic ring and conjugated C=C-N=C π -electron system
		373(466)	$\pi - \pi^*$ transition in conjugated azomethine group
7.	P <i>o</i> HOB <i>P</i>	261(122)	$\pi - \pi^*$ transition within aromatic ring system
		320(81)	$\pi - \pi^*$ transition involving aromatic ring and conjugated C=C-N=C π -electron system

^a(molar absorptivity (ϵ) L. mol⁻¹ cm⁻¹)

3. 7. Fluorescence Spectroscopy of Monomers and Polymers

The monomers and polymers contained conjugated chromophoric groups which could indicate fluorescence intensity within UV-Vis region. Choi et al.²⁴ have reported fluorescence from poly(azimethines). Fluorescence emission of the monomers and polymers were examined in DMSO solvent. The monomer *p*-HOB showed a emission band at 378 (at excitation 275 nm) and *o*-HOB shows two emission bands 354 nm (excitation 258 nm) and 374 nm (excitation 322 nm). The polymers indicated two to four emission bands (Figure 5), except P*p*HOB*Cy* which indicated one emission band at 349 nm (excitation 275 nm). The results of spectrofluorometric studies are summarized in Table 3, and the results showed that all the monomers and the polymers were fluorescence materials. The polymer P*p*HOBND indicated highest fluorescence intensity and P*p*HOB*Cy* indicated lowest intensity. There was a shift in wavelength of emission and excitation of the polymers as compared to their corresponding monomers

p-HOB and *o*-HOB due to polymerization. The number of emission bands observed were higher (3 and 4) for the polymers P*o*HOBPD and P*o*HOB*P* derived from *o*-HOB as compared to the polymers P*p*HOBND, P*p*HOBPD and P*p*HOB*Cy* (1 to 2 emission bands) derived from the mon-

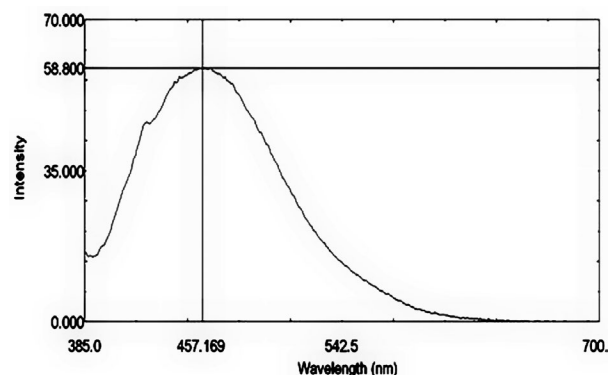


Figure 5. Fluorescence emission spectrum of polymer PoHOBPD (λ_{ex} : 373 nm, λ_{em} : 457 nm)

Table 3: Spectrofluorometric determination of monomers and polymers using DMSO solvent

S. No	Compound	Concentration in $\mu\text{g/ml}$	Excitation wavelength in nm	Emission wavelength in nm (color)	Relative Intensity of emission
1.	<i>p</i> -HOB	20	283	375	948
2.	<i>o</i> -HOB	12.5	258	354	76.2
			322	374	178.1
3.	PpHOBND	25	284	372	409
			340	399 (violet)	1018
4.	PpHOBPD	25	278	351	355
			595	688 (red)	18.1
5.	PpHOBCy	50	275	349	5.45
6.	PoHOBPD	6.25	262	354	204.2
			321	388 (violet)	261.4
			373	457 (blue)	58.80
7.	PoHOBP	25	261	353	232
				434 (violet)	105.6
				526 (green)	29.5
			320	357	273.5

omer *p*-HOB due to ortho group effect. All the polymers showed 1 or 2 color emissions except PpHOBCy, the emission colors include violet, blue, green and red. The limit of detection (LODs) of the polymers in DMSO were calculated, at least signal to noise ratio 3:1 at the emission band of higher sensitivity and were observed within 0.625–1.25 $\mu\text{g/ml}$.

3. 8. Thermal Analysis of Monomers and Polymers

Thermal behavior of monomer and polymers was evaluated by TG (Thermogravimetry) and DTA (Differential thermal analysis) in nitrogen atmosphere. TG and DTA of monomer *p*-HOB is reported.³¹ TG of *o*-HOB showed three stages of weight loss with 73% weight loss within 216–465 °C, 6% weight loss within 466–542 °C and 15% weight loss within 543–625 °C with maximum rate of weight loss (T_{max}) at 357 °C, DTA showed melting endotherm at 93 °C, followed by vaporization/decomposition exotherms at 403, 464 and 532 °C and large decomposition exotherm at 603 °C. TG of PpHOBND showed four stages

of weight loss with 6% weight loss within 300–426 °C, 37% weight loss within 427–520 °C, 6% weight loss within 521–605 °C and 48% weight loss within 606–795 °C, T_{max} indicated at 708 °C, DTA showed two exotherms at 416 and 466 °C due to vaporization/decomposition and large decomposition exotherm at 714 °C. TG of PpHOBPD showed two stages of weight loss with 28% weight loss within 363–500 °C and 66% weight loss within 501–705 °C with T_{max} at 628 °C, DTA showed two large decomposition exotherms at 398 and 615 °C. TG of PpHOBCy showed four stages of weight loss with 22% weight loss within 280–425 °C, 40 % weight loss within 426–500 °C, 8 % weight loss within 501–555 °C and 22% weight loss within 556–626 °C with T_{max} at 469 °C (the lower T_{max} value was may be due to the presence of cyclohexane ring), DTA showed two decomposition exotherms at 366 and 470 °C, and a large decomposition exotherm at 596 °C. TG of PoHOBPD showed three stages of weight loss with 44% weight loss within 346–477 °C, 9% weight loss within 478–558 °C and 38% weight loss within 559–674 °C, T_{max} value showed at 412 °C, DTA indicated three vaporization/decomposition exotherms at 395, 463 and 517 °C, followed by large decompo-

Table 4. Thermal analysis data of monomers and polymers

Compound	TG analysis				Thermal stability T_{max} °C	DTA analysis	
	I	Weight loss stages II III		IV		Endo °C	Exo °C
	Wt. loss % (temperature range °C)						
<i>p</i> -HOB	95 (250–500)	–	–	–	362	112, 365, 475	
<i>o</i> -HOB	73 (216–465)	6 (466–542)	15 (543–625)	–	357	93	403, 464, 532, 603
PpHOBND	6 (300–426)	37 (427–520)	6 (521–605)	48 (522–795)	708	–	416, 466, 714
PpHOBPD	28 (363–500)	66 (501–705)	–	–	628	–	398, 615
PpHOBCy	22 (280–425)	40 (426–500)	8 (501–555)	22 (556–626)	469	–	366, 470, 596
PoHOBPD	44 (346–477)	9 (478–558)	38 (559–674)	–	412	–	395, 463, 517, 661
PoHOBP	8 (99–338)	28 (339–480)	11 (481–574)	49 (575–743)	655	–	358, 448, 514, 684

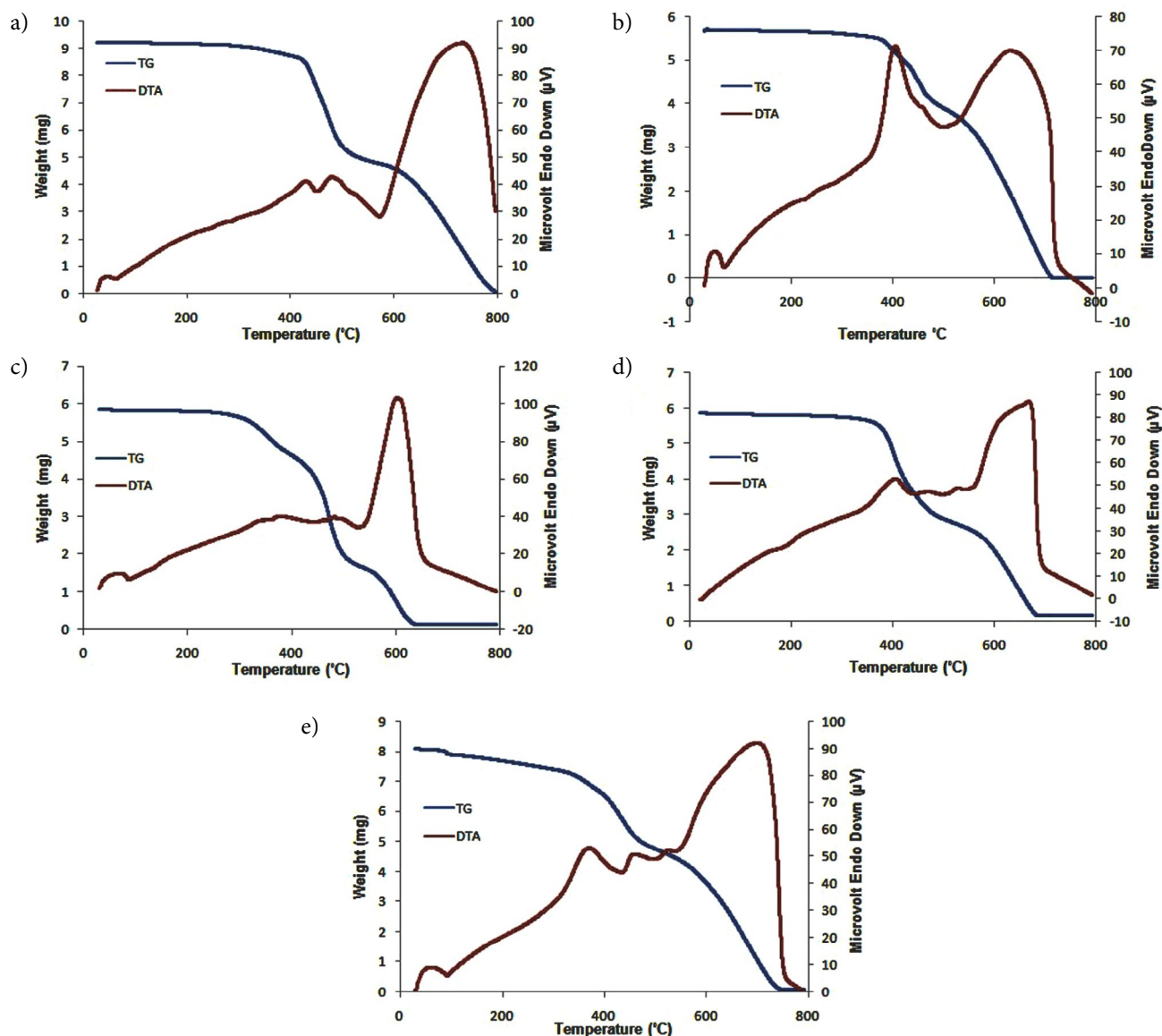


Figure 6. TG/DTA graphs of polymers (a) PpHOBND (b) PpHOBPD (c) PpHOBCy (d) PoHOBPD and (e) PoHOBP conditions as experimental

sition exotherm at 661 °C. TG of PoHOBP indicated four stages of weight loss with 8% weight loss within 99–338 °C, 28% weight loss within 339–480 °C, 11% weight loss within 481–574 °C and 49% weight loss within 575–743 °C with T_{\max} at 655 °C, DTA showed three vaporization/decomposition exotherms at 358, 448 and 514 °C and a large decomposition exotherm at 684 °C. The TG/DTA graphs of all the polymers are given in Figure 6. The polymers indicated high thermal stability as compared to monomers because their T_{\max} values were higher than their corresponding monomers. The thermal analysis results are given in Table 4.

3. 9. Biological Activities of Polymers

The polymers were tested for their biological activities against bacteria and fungi. The polymer PpHOBND

showed 40% antifungal activity against *Aspergillus niger*, PpHOBPD showed 30% inhibition against *Fusarium Lini*, PpHOBCy indicated 20% inhibition against *Candida albicans*, PoHOBPD showed 15% inhibition against *Microsporum canis* while the polymer PoHOBP did not show inhibition against fungi, the results of antifungal activities are summarized in Table 5. The polymer PpHOBCy indicated 22% antibacterial activity against *Staphylococcus aureus* and 3.24% inhibition against *Escherichia Coli*, PoHOBPD showed 18.6% inhibition against *Staphylococcus aureus*, PpHOBND showed 11% inhibition against *Escherichia Coli* and 9% inhibition against *Staphylococcus aureus*, PpHOBPD showed 7.18% inhibition against *Escherichia Coli* and 4.53% inhibition against *Staphylococcus aureus* and the polymer PoHOBP showed 8.86% inhibition against *Escherichia Coli*, the results of antibacterial activities are summarized in Table 6.

Table 5: Results of antifungal activities of polymers in DMSO solvent

Name of Fungus	% inhibition of Polymers				Standard Drug
	PpHOBND	PpHOBPD	PpHOBCy	PoHOBPD	
Trichphyton rubrum	–	–	–	–	Miconazole
Candida albicans	–	–	20%	–	Miconazole
Aspergillus nigar	40%	–	–	–	Amphotericin B
Microsporium canis	–	–	–	15%	Miconazole
Fusarium Lini	–	30%	–	–	Miconazole

The (–) sign indicates no inhibition against fungi

Table 6: Results of antibacterial activities of polymers in DMSO Solvent

Bacteria	% inhibition of polymers compared with the % inhibition of standard drug Ofloxacin				
	PpHOBND	PpHOBPD	PpHOBCy	PoHOBPD	PoHOBP
Escherichia Coli	10.936	7.180	3.249	–	8.865
Shigella flexeneri	–	–	–	–	–
Staphylococcus aureus	8.952	4.526	21.944	18.601	–
Psuedomonas aeruginosa	–	–	–	–	–

The (–) sign indicates no inhibition against bacteria

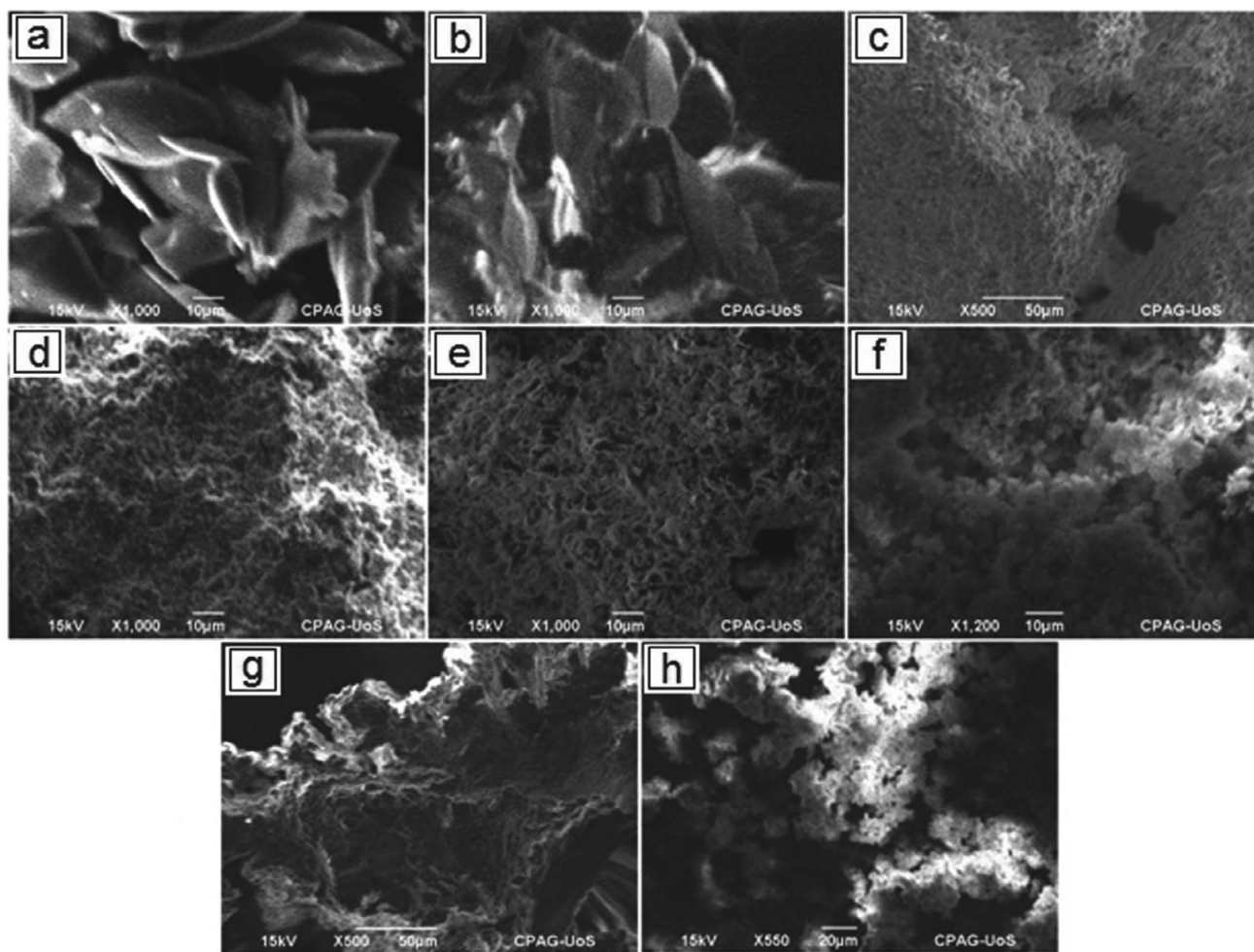


Figure 7. SEM Images of (a) *p*-HOB (b) *o*-HOB (c) PpHOBND (d) PpHOBPD (e) PpHOBCy (f) PoHOBPD (g) PoHOBP and (h) Schiff base reported³⁴ conditions as experimental.

3. 10. Scanning Electron Microscopy of Monomers and Polymers

The SEM images of the monomers and polymers were recorded at 100, 50, 20 and 10 μm . The polymer PpHOBND and PpHOBPD had sponge like morphology (Figure 7c and 7d). The polymer PpHOBcy had fibrous like clusters with porous surface (Figure 7e). The morphology of polymer PoHOBPD was agglomerated and this agglomerated structure was due to inter-particle attraction of monomers (Figure 7f). PoHOBP had nanoscale roughness (Figure 7g) while the reported Schiff base derived from *o*-HOB³⁴ had agglomerated clusters (Figure 7h). The monomer *p*-HOB had seeds like morphology (Figure 7a) and the monomer *o*-HOB had leaves like appearance (Figure 7b). The results support that the morphology of the polymers was different from their corresponding monomers.

4. Conclusion

Five new photo-responsive polyazomethines with flexible spacers of *n*-hexane were synthesized by one step polycondensation between dialdehydes and diamines. The polymers were characterized by elemental microanalysis, UV-Vis, fluorescence, FT-IR, ¹HNMR, TG/DTA and SEM. The polymers indicated fluorescence emissions within visible region with LODs of polymers at 0.625–1.25 $\mu\text{g}/\text{ml}$ levels and high thermal stabilities within the range of 412–708 °C. The polymers were also tested for their antimicrobial activities against bacteria and fungi, the polymer PpHOBND indicated moderate antifungal activity against *Aspergillus niger*.

5. References

- G. F. D'Alelio, in: N. M. Bikales (Ed.): Encyclopedia of Polymer Science and Technology, Vol.10, Interscience, New York, **1969**, pp. 659.
- S. Banerjee, C. Saxena, *J. Polym. Sci. A Polym. Chem.* **1996**, *34*, 3565–3572. DOI:10.1002/(SICI)1099-0518(199612)34:17<3565::AID-POLA11>3.0.CO;2-C
- A. G. El-Shakeil, M. K. H. Saad-Addin, A. A. Dheya, *Polymer Bulletin.* **1997**, *39*, 1–7. DOI:10.1007/s002890050112
- M. Y. Khuhawar, M. A. Mughal, A. H. Channar, *Eur. Polym. J.* **2004**, *40*, 805–809. DOI:10.1016/j.eurpolymj.2003.11.020
- A. Iwan, *Sustainable Energy Rev.* **2015**, *52*, 65–79. DOI:10.1016/j.rser.2015.07.078
- M. L. Petrus, R. K. M. Bouwer, U. Lafont, D. H. K. Murthy, R. J. P. Kist, M. L. Böhm, Y. Olivier, T. J. Savenije, L. D. A. Siebeles, N. C. Greenham, T. J. Dingemans, *Polym. Chem.* **2013**, *4*, 4182–4191. DOI:10.1039/C3PY00433C
- A. Iwan, M. Palewicz, A. Sikoran, J. Chmielowiec, A. Hreniak, G. Pasciak, P. Bilski, *Synth Met.* **2010**, *160*, 1856–1867. DOI:10.1016/j.synthmet.2010.06.029
- D. Sek, B. Jarzabek, E. Grabiak, B. Kaczmarczyk, H. Janeczek, A. Sikora, A. Hreniak, M. Palewicz, M. Lapowski, K. Karon, A. Iwan, *Synth Met.* **2010**, *160*, 2065–2076. DOI:10.1016/j.synthmet.2010.07.026
- P. K. Dutta, P. Jain, P. Sen, R. Trivedi, P. K. Sen, J. Dutta, *Eur. Polym. J.* **2003**, *39*, 1007–1011. DOI:10.1016/S0014-3057(02)00328-2
- V. Cozan, E. Butuc, A. Stoleriu, M. Rusa, M. Rusu, Y. Ni, M. DING, *J. Macromol. Sci.-Pure Appl. Chem.* **1995**, *32*, 1243–1262.
- V. Cozan, L. Marin, in: M. Cazacu (Ed.): Thermotropic Liquid Crystalline Polyazomethines, in Advances in Functional Heterochain Polymers, Chapter 3, Nova Publishers Inc., New York, **2008**, ISBN 978-1-60456-598-0, pp. 67–115.
- S. Ogiri, M. Ikeda, A. Kanazawa, T. Shiono, T. Ikeda, *Polymer.* **1999**, *40*, 2145–2150. DOI:10.1016/S0032-3861(98)00421-2
- C.-H. Li, T.-C. Chang, *J. Polym. Sci. A Polym. Chem.* **1990**, *28*, 3625–3638. DOI:10.1002/pola.1990.080281309
- A. Iwan, E. Schab-Balcerzak, D. Pocięcha, M. Krompiec, M. Grucela, P. Bilski, M. Klosowski, H. Janeczek, *A Polym. Chem.* **2011**, *34*, 61–74. DOI:10.1016/j.optmat.2011.07.004
- A. Iwan, B. Boharewicz, I. Tazbir, M. Malinowski, M. Filapek, T. Kłęb, B. Luszczynska, I. Glowacki, K. P. Korona, M. Kaminaska, J. Wojtkiewicz, M. Lewandowska, A. Hreniak, *Solar Energy.* **2015**, *117*, 246–259. DOI:10.1016/j.solener.2015.03.051
- A. Iwan, B. Boharewicz, I. Tazbir, M. Filapek, *Electrochim. Acta.* **2015**, *159*, 81–92. DOI:10.1016/j.electacta.2015.01.215
- A. Iwan, B. Boharewicz, I. Tazbir, A. Sikora, M. Maliński, Ł. Chrobak, W. Madej, *Chem. Sci Rev. Lett.* **2015**, *4*, 597–608
- A. Iwan, E. Schab-Balcerzak, K. P. Korona, S. Grankowska, M. Kamińska, *Synth Met.* **2013**, *185–186*, 17–24. DOI:10.1016/j.synthmet.2013.10.008
- M. A. Mughal, A. H. Mughal, Z. M. Ali, G.Z. Memon, M. Y. Khuhawar, H. Saleem, *IOSR, Journal of Engineering (IOSR-JEN).* **2013**, *3*, 48–55
- N. Nishat, R. Rasool, S. Parveen, S.A. Khan, *J. Appl. Polym. Sci.* **2011**, *122*, 2756–2756. DOI:10.1002/app.34100
- I. A. Alkskas, A. M. Alhubge, F. Azam, *Chin. J. Polym. Sci.* **2013**, *31*, 471–480. DOI:10.1007/s10118-013-1237-4
- N. Y. Baran, M. Karakşla, H. Ö Demir, M. Saçak, *J Mol Struct.* **2016**, *1123*, 153–161. DOI:10.1016/j.molstruc.2016.06.028
- L. Guo, S. Wu, F. Zeng, J. Zhao, *Eur. Polym. J.* **2006**, *42*, 1670–1675. DOI:10.1016/j.eurpolymj.2006.01.025
- M. K. Choi, H. L. Kim, D. H. Suh, *J. Appl. Polym. Sci.* **2006**, *101*, 1228–1233. DOI:10.1002/app.24209
- A. Shah, M. Y. Khuhawar, A. A. Shah, *J. Appl. Polym. Sci.* **2012**, *21*, 325–334. DOI:10.1007/s13726-012-0033-2
- O. Catanescu, M. Grigoras, G. Colotin, A. Dobreanu, N. Hurduc, C.I. Simionescu, *Eur. Polym. J.* **2001**, *37*, 2213–2216. DOI:10.1016/S0014-3057(01)00119-7
- O. Thomas, O. Inganäs, M. R Andersson, *Macromolecules.* **1998**, *31*, 2676–2678. DOI:10.1021/ma9701090
- P. K. Gutch, S. Banerjee, D. C. Gupta, D. K. Jaiswal, *Polym. Chem.* **2001**, *39*, 383–388. DOI:10.1002/1099-0518(20010201)39:3<383::AID-POLA1005>3.0.CO;2-3

29. Y-l. Wang, G. Zhang, M-l. Zhang, Y. Fan, B-y. Liu, J. Yang, *Chin. J. Polym. Sci.* **2012**, *30*, 370–377.
DOI:10.1007/s10118-012-1124-4
30. S. Shi, Z. Li, J. Wang, *J POLYM RES*, **2007**, *14*, 305–312.
DOI:10.1007/s10965-007-9111-0
31. F. Qureshi, M. Y. Khuhawar, T. M. Jahangir, A. H. Channar, *Acta Chim. Slov.* **2016**, *63*, 113–120.
DOI:10.17344/acsi.2015.1994
32. H. B. Donahoe, L. E. Benjamin, L. V. Fennoy, D. Greiff, *J. Org. Chem.* **1961**, *26*, DOI:10.1021/jo01061a047
33. R. W. Date, C. T. Imrie, G. R. Luckhurst, J. M. Seddon, *Liquid Crystals*, **1992**, *12*, 203–238.
DOI:10.1080/02678299208030393
34. S. İlhan, H. Temel, M. Sunkur, İ. Teğın, *Indian Journal of Chemistry*, **2008**, *47A*, 560–564.

Povzetek

Pet novih azometinskih polimerov, ki imajo alifatsko-aromatske dele, smo sintetizirali s polikondenzacijo dialdehidov in diaminov. Dialdehidni monomeri se razlikujejo le po orientaciji aromatskega obroča (orto ali para) in so bili sintetizirani s kondenzacijsko reakcijo med aromatskim aldehydom in 1,6-dibromoheksanom. Molekulska masa monomerov smo določili z masno spektroskopijo z ionizacijo z elektroni (EI). Strukture polimerov smo potrdili z elementarno mikroanalizo, infrardečo spektroskopijo (FTIR), NMR spektroskopijo (1HNMR) in UV-VIS spektroskopijo. Morfologijo monomerov in polimerov smo ocenili z vrstično elektronsko mikroskopijo (SEM). Vsi polimeri so bili topni v DMSO (pri segrevanju) in nekoliko v drugih topilih. Termično stabilnost polimerov smo analizirali s termogravimetrično analizo (TG) in diferenčno termično analizo (DTA). Toplotna stabilnost polimerov je bila višja od njihovih ustreznih monomerov. TG polimerov je pokazala najvišjo stopnjo izgube mase (T_{max}) v območju od 412 °C do 708 °C. S fluorescenčno emisijsko spektroskopijo polimerov smo pokazali, da vsi polimeri fluorescirajo in določili od enega do štirih emisijskih vrhov v območju od 349 nm do 606 nm. Meja detekcije polimerov je bila v območju od 0,625 µg/ml do 1,25 µg/ml. Polimerom smo določali tudi njihovo protimikrobno aktivnost napram bakterijam in glivam.

Scientific paper

Structural Requirements for Molecular Recognition by fMLP Analogs Receptors: Comparative Conformational Analysis of (for-Met-Leu-Phe-OMe) and its Thioamide Analog (for-Met-Leu ψ [CSNH]Phe-OMe)

Chakib Ameziane Hassani,^{1,*} Mourad Houssat,¹ Jamal Eddine Hazm² and Ahmed Harrach³

¹ Laboratory of Applied Chemistry LCA, Faculty of Sciences and Technology, Sidi Mohamed Ben Abdellah University PB 2202, Fez, Morocco.

² Laboratory of Mechanical Engineering, Faculty of Sciences and Technology, Sidi Mohamed Ben Abdellah University PB 2202, Fez, Morocco.

³ Laboratory of Condensed Matter Chemistry, Faculty of Sciences and Technology, Sidi Mohamed Ben Abdellah University PB 2202, Fez, Morocco.

* Corresponding author: E-mail: chakib-ameziane@hotmail.com
Telephone Number: +212-663503010

Received: 09-07-2018

Abstract

In order to determine the structural requirements of fMLP analogs receptors, this work presents the results of a comparative conformational analysis of the active chemotactic peptide (formyl-Met-Leu-Phe-OMe) and its inactive analog (formyl-Met-Leu ψ [CSNH] Phe-OMe) using the theoretical method PEPSEA. This study showed that a γ turn structure centered on the central residue is the native structure of the chemotactic peptide fMLP analogs, where both CO(formyl) and NH(central residue) groups are available and ready to interact with the receptor. The inactive analog fML^SP-OMe prefers instead a γ turn structure centered on the Met residue, where the two groups cited above are not available for this interaction. Our results and those of literature enable us to propose the “induced fit” model of Burgen for the molecular recognition process. Consequently, the activity of fMLP analogs chemotactic peptides would not be related to a specific secondary structure (β turn, γ turn or extended....) but rather to the freedom and the availability of the CO(formyl) and the NH group at position 2.

Keywords: Chemotactic peptide; fMLP analogs; Conformational analysis; Molecular recognition.

1. Introduction

The chemotactic peptide fMLP has received much interest in recent years, due to the key role that it plays in our body, particularly in the immune system, it induces the release of the polymorphonuclear leukocytes, the superoxide O₂⁻ and the lysozyme enzyme of the neutrophil.¹⁻⁴ It is considered to be a very active agent.⁵ The structure-activity relationship was established as well as the specificity of the receptors located on the neutrophil cell surface.⁶⁻⁹

The studies carried out by Freidinger et al,¹⁰⁻¹³ which consist to create Lactam bridges in peptide structures and

by Perdih et al to synthesis of α -amino-organometallic acids,¹⁴ have shown the success of peptidomimetic in the field of the design of new therapeutic agents. The aim of these modifications is to limit the degrees of freedom and capture the bioactive conformation of a native peptide. In the case of fMLP analogs, several modifications have been made.¹⁵⁻¹⁹ The influence of the terminal groups has been studied, and it has been demonstrated that esterification of the carboxylic C-terminal does not affect the biological activity of the molecule.²⁰ On the other hand, the substitution of the formyl group at N-terminal by the tert-butyl-carbonyl group (Boc) results in a total loss of activity.^{21,22} In 1985 Sauvé et al tried to introduce changes at the back-

bone by replacing amide bonds by thioamide ones which are more resistant to enzymatic hydrolysis.¹⁵ The synthesized analogs were tested and the biological activities were evaluated using the release of lysozyme from human neutrophils. The replacement of the amide bond at the Methionine by a thioamide bond was carried out and resulted in a dramatic loss of activity.³ The comparative conformational study of the two molecules formyl-Met-Leu-Phe-OMe and formyl-Metψ(CSNH)Leu-Phe-OMe showed that the active chemotactic peptide must have the formyl group free of any intramolecular interaction in order to be available for the formation of the complex with the receptor.¹⁶ The substitution of the central residue with disubstituted α-α residues such as aminocyclohexanecarboxylic acid (Acc6) and aminocyclopentanecarboxylic acid (Acc5) resulted in an increase in activity.²³ Using a theoretical method, our comparative conformational studies of the parent peptide with these lathers have revealed that the native conformation of fMLP chemotactic peptides is the β-turn structure, despite the unavailability of the CO(-formyl).^{24,25}

In order to continue our investigations on the structural requirements of the fMLP chemotactic receptors,^{16,24,25} we present, through this work, a comparative conformational study of the parent active peptide (formyl-Met-Leu-Phe-OMe) and its thioamide analog (formyl-Met-Leuψ(CSNH)-Phe-OMe) devoid of any activity.³ The main objective is to explain the difference in activity between the two tripeptides (fig. 1), to propose the native conformation of fMLP analogs and to determine the structural requirements for molecular recognition by their receptors.

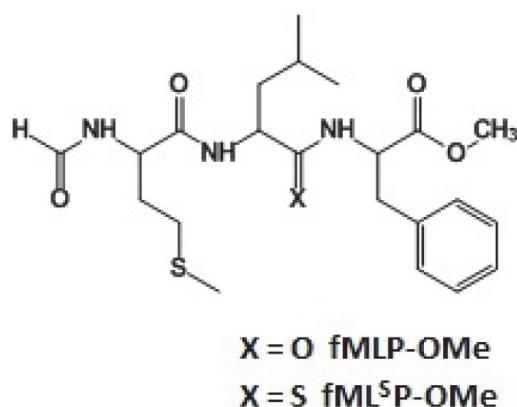


Fig 1. Structure of fMLP-OMe and fML⁵P-OMe.

2. Methods and Materials

The method used in this study is called PEPSEA (PEPtidic SEArch). It was developed by Michel et al in the structural chemistry laboratory of the Sherbrooke University,²⁶ and it has shown its effectiveness in the theoretical

conformational studies of several peptide molecules and their structure-activity relationship.^{16,24–32} This approach is based on the fact that the structural thermodynamic and statistical properties of a molecular system can be deduced only from a population presenting its conformational space. The principle of PEPSEA consists of generating a population of conformations that characterize a particular peptidic sequence. Rather than striving for global minima, the population of conformers is randomly generated using the subtractive method,³³ which generates numbers between 0 and 1. These numbers are then converted into values between -180° and $+180^\circ$ and assigned to different torsional angles that define a starting structure of the analyzed molecule. After the random generation step, a minimization of energy to the closest minimum is performed using the conjugate gradient algorithm.³⁴ The convergence criterion was set to 10^{-4} , terminating the calculation when the module of the vector constituted by the first derivatives becomes less than this value. Finally, a statistical analysis is applied to this population of minima to deduce the thermodynamic and structural properties of the peptides studied; this new approach is applied with the PEPSEA program.

The force field used by the PEPSEA program to compute the conformational energy is ECEPP/2 “Empirical Calculation Energy Program for Peptide”.³⁵ This force field uses rigid geometry to represent the amino acid residues of the polypeptidic chain. The conformational energy function is the sum of four terms: Electrostatic term E_{ele} , 12–6 Lennard–Jones term E_{LJ} , hydrogen-bond term E_{hb} and the torsion term E_{tor} .

$$E_{\text{conf}} = E_{\text{ele}} + E_{\text{LJ}} + E_{\text{hb}} + E_{\text{tor}} \quad (1)$$

The PEPSEA program uses the specific parameters of each residue (atomic coordinates, geometrical and energy parameters...) to describe the geometry of the peptidic molecules. The force field ECEPP/2 possesses the parameters of the 26 amino acid residues and of terminal protecting groups commonly found in proteins. However, for the thioleucyl residue that is not included in the database, we used the parameters proposed by Michel et al to consider the thioamide bond.¹⁶

It is worth noting that the dielectric constant used by PEPSEA is $D = 2$ (Different of that in vacuum). According to Momany et al,³⁶ this effective dielectric constant $D = 2$ is equivalent to the experimental dielectric constant (set between 4 and 8) similar to that of proteins in a polar medium.

As all endogenous peptides, the tripeptides under investigation in this study are constituted by the sequence of amino acids, all in L configuration.

2. 1. Experimental Procedure

The PEPSEA program described above carried out the conformational search and the localization of the most

stable conformers. For each two considered tripeptides, 20.000 conformers were randomly generated and energy minimized to the closest minima. During this generation, all torsion angles are allowed to vary except the amide bonds; ω (Met), ω (Leu) and ω (Phe) which are fixed at 180° . We have carefully ensured that the 20.000 generated conformations subjected to minimization are the same for both molecules. For each tripeptide, the first 100 conformers of lower conformational energies were submitted to a second energy minimization allowing all dihedral angles to be modified. For each of those 100 minima, the Hessian matrix was calculated and the free energy was evaluated.³⁷ The resulting conformers were sorted by increasing values of the free energies, and then clustered into groups of conformers having the same structural characteristics (β turn, γ turn or extended....).

The calculation of energy and minimization were performed on station HP pro-Intel (R) Core(TM) i3-3240 CPU @3.40 GHz at the faculty of sciences and techniques of Fez.

3. Results

For the evaluation of the minimization efficiency, we have studied the energy distributions of the 20.000 conformers of the 2 molecules: fMLP-OMe and fML^SP-OMe. The next figure (Fig 2) represents these distributions.

Of these graphs, it can be seen that the conformers generated and minimized are grouped in a single distribution having a Gaussian form for the 2 molecules studied. This observation confirms the effectiveness of the minimization process.

Tables 1 and 2 give the conformational characteristics of the fifty most stable conformers obtained after the second minimization for each tripeptide. Conformers were numbered by increasing free energy values. The conformational energies (ΔE) are given relative to the global minima: conformer 7 ($E_0 = -5.65$ Kcal/mol) for fMLP-OMe and conformer 3 ($E_0 = -4.65$ Kcal/mol) for fML^SP-OMe. Free energy values (ΔG) have been computed relative to the same conformers at $T = 300$ K, the entropic contributions ($-T\Delta S$) and statistical weights (W_i) are also presented. The structural characteristics have been given for each conformer indicating the presence or not of an intramolecular hydrogen bond between the different donors and acceptors. The torsion angles for the fifty conformers of the parent peptide and the thioamide analog are listed in Appendices 1 and 2 respectively, with their conformational energies in Kcal/mol.

The conformational analysis of the fifty most stable conformers of the parent peptide fMLP-OMe (table 1) shows that it can adopt varied conformational structures, which the majority can be distributed into four classes:

The first class is represented by seventeen conformers adopting a β turn structure centered on Met and Leu.

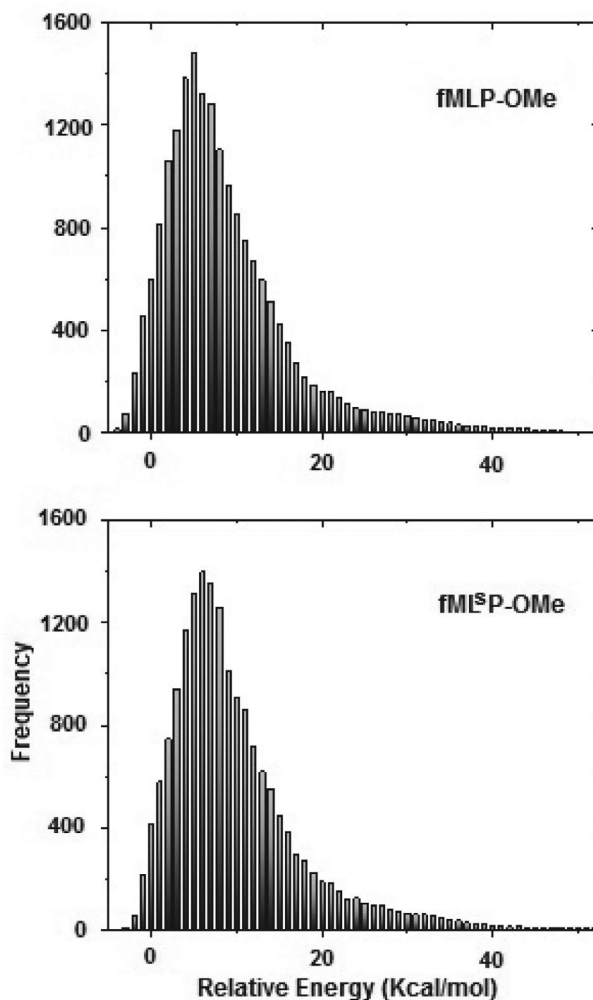


Fig 2: Energy distributions of minimized conformers of fMLP-OMe and fML^SP-OMe.

Five of them are stabilized by a hydrogen bond between the CO formyl and NH of Phe: conformers (2, 4, 28, 42 and 43), and twelve adopt this structure but without that the hydrogen bond being established: conformers (3, 5, 6, 11, 12, 13, 15, 18, 23, 29, 36 and 37). Fig.3a gives a stereoscopic superposition view of the conformers belonging to this class, from which we can see that they are similar, mainly at the backbone level. The Met and Leu side chains are oriented in two different ways, while the Phe residue can rotate more freely. It is worth noting that several authors have suggested this structure for many fMLP-OMe analogs, using spectroscopic X-ray and NMR methods as well as molecular modeling studies.^{21,23–25,38–42} Fig.4a shows a stereoscopic view of the superposition of our β turn structure (conformer 2, table 1) with those found by Bardi for the Boc-Met-Aib-Phe-OMe analog²¹, Rathore for the f-Met-AC8C-Phe-OMe³⁸ and Zecchini for the f-Met- Δ^2 Leu-Phe-OMe³⁹. This figure shows that there is a great similarity at the backbone level and that the only differences with our structure lie just at the side chains orientation of Methionine and Phenylalanine.

Table 1. Conformational characteristics of fMLP^a:

	Conf	ΔG ^b	ΔE ^c	$-T\Delta S$ ^d	WI ^e	Formyl	Met	Leu	Phe
1 st class	2	-0.77	1.76	-2.54	0.1035	CO			NH
	3	-0.39	0.59	-0.98	0.0543				
	4	-0.15	1.56	-1.71	0.0363	CO			NH
	5	-0.02	1.63	-1.66	0.0294				
	6	-0.01	2.42	-2.44	0.0289				
	11	0.15	2.63	-2.49	0.0221				
	12	0.17	1.71	-1.54	0.0211				
	13	0.18	2.61	-2.43	0.0210				
	15	0.30	2.13	-1.83	0.0172				
	18	0.41	1.53	-1.12	0.0142				
	23	0.53	2.14	-1.61	0.0116				
	28	0.74	1.15	-0.41	0.0081	CO			NH
	29	0.77	1.91	-1.14	0.0078				
	36	0.93	2.66	-1.73	0.0059				
37	0.95	2.15	-1.20	0.0057					
42	1.03	2.67	-1.64	0.0050	CO			NH	
43	1.06	2.11	-1.05	0.0048	CO			NH	
2 nd class	1	-0.81	1.43	-2.24	0.1103		CO		NH
	16	0.34	2.34	-2.00	0.0159		CO		NH
	19	0.45	2.68	-2.23	0.0133		CO		NH
	20	0.46	1.73	-1.27	0.0131		CO		NH
	21	0.48	1.54	-1.06	0.0126				
	33	0.87	1.97	-1.09	0.0065		CO		NH
	38	0.95	2.78	-1.83	0.0057				
	41	1.01	1.41	-0.39	0.0052		CO		NH
	44	1.06	2.79	-1.73	0.0048		CO		NH
	46	1.11	2.49	-1.38	0.0044		CO		NH
48	1.18	2.59	-1.42	0.0039		CO		NH	
49	1.29	2.34	-1.05	0.0033		CO		NH	
3 rd class	8	0.11	2.43	-2.32	0.0236	CO		NH	
	10	0.14	2.08	-1.94	0.0224	CO		NH	
	17	0.36	1.37	-1.01	0.0154	CO		NH	
	26	0.63	1.96	-1.34	0.0099	CO		NH	
	31	0.82	2.46	-1.64	0.0072	CO		NH	
	34	0.89	1.68	-0.80	0.0064	CO		NH	
45	1.10	2.57	-1.47	0.0045	CO		NH		
4 th	7	0.00	0.00	0.00	0.0283	CO	CO	NH	NH
	27	0.72	1.51	-0.80	0.0085	CO	CO	NH	NH
	32	0.86	2.07	-1.21	0.0067	CO	CO	NH	NH
Other conformers	9	0.14	2.06	-1.92	0.0224				
	14	0.29	2.01	-1.72	0.0173				
	22	0.52	2.56	-2.04	0.0119				
	24	0.54	2.72	-2.18	0.0114				
	25	0.62	2.71	-2.09	0.0101				
	30	0.81	2.32	-1.51	0.0072				
	35	0.90	2.56	-1.66	0.0062				
	39	0.96	1.87	-0.91	0.0057				
	40	1.00	2.08	-1.07	0.0052				
	47	1.15	2.23	-1.08	0.0041				
50	1.31	2.44	-1.13	0.0031					

a. First 50 minimum energy conformations are listed. b. Free energy: $\Delta G = G - G_0$. G_0 is the free energy of the conformation having $E = E_0$. c. Conformational energy: $\Delta E = E - E_0$. E_0 (fMLP) = -5.65 Kcal/mol. d. Entropic contribution: $-T\Delta S = \Delta G - \Delta E$. e. Statistical weight of conformers: W_i .

 β turn structure  γ turn structure centered on Met
 γ turn structure centered on Leu  double γ turn

Table 2. Conformational characteristics of fML^{SP} ^a:

	Conf	ΔG ^b	ΔE ^c	$-T\Delta S$ ^d	WI ^e	Formyl	Met	Thio-Leu	Phe
1 st class	2	-0,77	1,76	-2.54	0.1035	CO			NH
	2	-0.43	1.78	-2.21	0.0817	CO			NH
	4	-0.01	1.78	-1.79	0.0400	CO			NH
	5	0.10	2.61	-2.51	0.0336				
	6	0.19	1.96	-1.77	0.0290				
	8	0.22	1.81	-1.59	0.0276				
	12	0.50	2.46	-1.96	0.0170				
	16	0.83	1.98	-1.15	0.0098				
	18	0.90	1.38	-0.48	0.0088	CO			NH
	19	0.90	2.06	-1.16	0.0088				
	20	0.90	2.13	-1.23	0.0088	CO			NH
	21	0.95	2.23	-1.28	0.0081	CO			NH
	23	1.07	1.34	-0.27	0.0066				
	24	1.09	2.30	-1.21	0.0064				
	25	1.12	2.81	-1.7	0.0061	CO			NH
	26	1.12	3.00	-1.88	0.0060	CO			NH
	31	1.44	2.01	-0.57	0.0036	CO			NH
41	1.81	2.20	-0.39	0.0019	CO			NH	
47	2.08	3.15	-1.07	0.0012					
49	2.16	3.10	-0.94	0.0011					
2 nd	1	-0.87	1.42	-2.3	0.1719		CO		NH
	13	0.83	1.98	-1.15	0.0098		CO		NH
3 rd class	9	0.24	3.04	-2.8	0.0265	CO		NH	
	10	0.26	2.67	-2.41	0.0258	CO		NH	
	14	0.69	1.03	-0.34	0.0124	CO		NH	
	17	0.88	2.63	-1.74	0.0090	CO		NH	
	22	1.02	3.65	-2.63	0.0071	CO		NH	
	27	1.20	3.24	-2.04	0.0053	CO		NH	
	28	1.29	2.92	-1.63	0.0045	CO		NH	
	30	1.34	3.30	-1.97	0.0042	CO		NH	
	32	1.48	3.63	-2.15	0.0033	CO		NH	
	33	1.53	3.00	-1.47	0.0031	CO		NH	
	36	1.61	2.09	-0.48	0.0026	CO		NH	
	38	1.69	3.47	-1.77	0.0023	CO		NH	
	42	1.85	2.78	-0.93	0.0018	CO		NH	
	43	1.86	3.79	-1.93	0.0017	CO		NH	
	44	2.00	3.87	-1.87	0.0014	CO		NH	
48	2.13	2.55	-0.42	0.0011	CO		NH		
50	2.29	2.84	-0.55	0.0008	CO		NH		
4 th	3	0.00	0.00	0.00	0.0403	CO	CO	NH	NH
	37	1.69	2.68	-0.99	0.0023	CO	CO	NH	NH
	39	1.74	2.91	-1.17	0.0021	CO	CO	NH	NH
	45	2.03	1.50	0.53	0.0013	CO	CO	NH	NH
Other conformers	7	0.20	2.58	-2.39	0.0285				
	11	0.39	2.33	-1.95	0.0206				
	15	0.74	3.03	-2.3	0.0115				
	29	1.29	3.21	-1.91	0.0045				
	34	1.53	3.26	-1.73	0.0031				
	35	1.54	2.92	-1.39	0.0030				
	40	1.79	3.38	-1.6	0.0020				
46	2.03	4.20	-2.17	0.0013					

a. First 50 minimum energy conformations are listed. b. Free energy: $\Delta G = G - G_0$. G_0 is the free energy of the conformation having $E = E_0$.
c. Conformational energy: $\Delta E = E - E_0$. E_0 (fMLP) = -5,65Kcal/mol. d. Entropic contribution: $-T\Delta S = \Delta G - \Delta E$. e. Statistical weight of conformers: Wi.

 β turn structure
 γ turn structure centered on Leu
 γ turn structure centered on Met
 double γ turn

The second class includes twelve conformers characterized by conformations adopting a γ turn structure centered on Leu, ten of them are stabilized by an intramolecular hydrogen bond involving the CO of Met and NH of Phe (1, 16, 19, 20, 33, 41, 44, 46, 48 and 49). It is interesting to note that the most stable conformer regarding the free energy belongs to this class. Fig.3b presents the stereoscopic superposition view of the conformers of this class, showing that the major variability is at the Met side chain. Using NMR studies, this structure was found for the analogs formyl-Met-Aib-Phe-OH, formyl-Met-Aib-Phe-OMe, and formyl-Met-Pro-Phe-OMe.^{15,17,43} Following IR and Circular Dichroism studies this structure was also found for fMLP-OH, fMLCha-OMe, and fMLP-OMe.⁴⁴ The stereoscopic superposition view of the minimized structure of this latter using the Metropolis Montecarlo

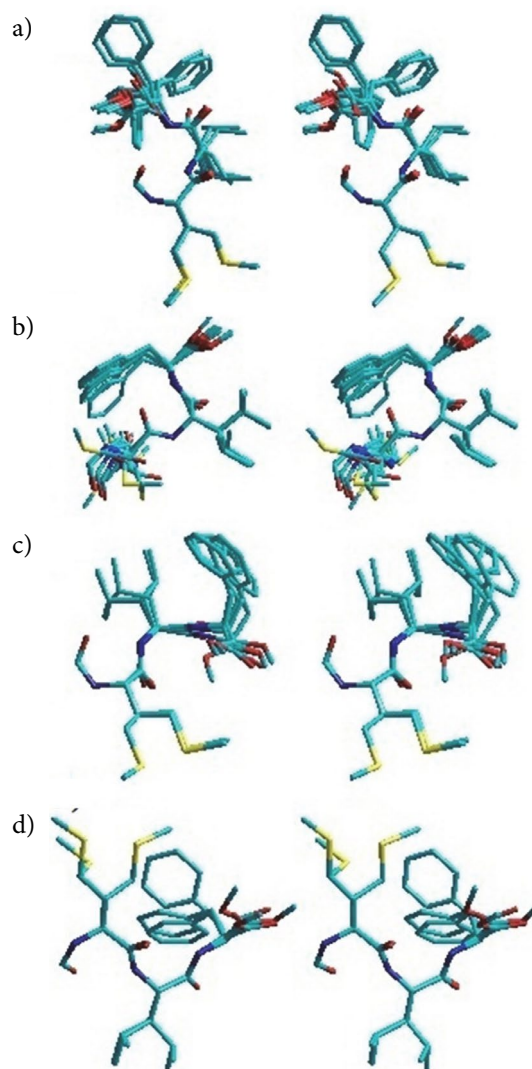


Fig 3: Stereoscopic superposition views of conformers of different classes obtained for fMLP-OMe. **a-** β turn involving CO formyl and NH Phe. **b-** γ turn centered on Leu involving CO of Met and NH of Phe. **c-** γ turn centered on Met involving CO formyl and NH of Leu. And **d-** Double γ turns cited above.

procedure,⁴⁵ with our γ turn structure centered on Leu (conformer 1, table 1) is presented in Fig.4b and shows the great similarity between both structures.

The third class is that of the conformers characterized by the presence of another γ turn structure centered this time on the Met residue, and represented by seven conformers (8, 10, 17, 26, 31, 34 and 45). Such structure is stabilized by an intramolecular hydrogen bond involving the CO formyl and NH of Leu. The stereoscopic superposition view of the conformers belong to this class is presented in Fig.3c.

The fourth class gathers structures in a double γ turns (a γ turn centered on Met and a γ turn centered on Leu at the same time) and include three conformers (7, 27, and 32). The stereoscopic superposition view of the three conformers of this group is given in Fig.3d. Using NMR studies Lucente et al have proposed this structure for the for-Met-Dag-Phe-OMe and for-Met-Cpg-Phe-OMe analogs.⁴⁶ However, by molecular modeling, Michel et al proposed it as the rigidified precursor for extended conformation after the release of the intramolecular H-bond by external interactions.¹⁶ The eleven remaining conformers, not belonging to any of the classes above, are mainly stabilized by hydrophobic interactions and characterized by favorable entropic terms, leading to lower

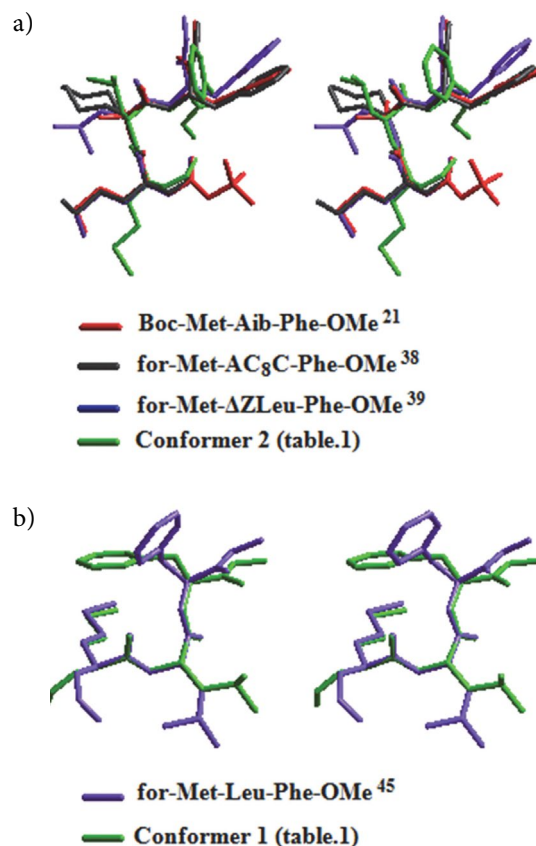


Fig 4: Stereoscopic superposition views of the conformers of this study with those of the literature. **a-** β turn structures **b-** γ turn centered on Leu.

values of free energies. This observation is exemplified by conformer 9.

For the thioamide analog fML^SP-OMe, the table 2 shows that preferred structures are distributed on the same classes found previously for fMLP-OMe: 19 for the first class (β turn centered on Met and Leu), 2 for the second (γ turn structures centred on Leu), 17 for the third (γ turn structures centred on Met), and 4 for the fourth class (double γ turns structures). The stereoscopic superposition views of structures of different classes obtained for this molecule (fML^SP-OMe) are presented in Appendix 3.

4. Discussion

The main structural difference that can explain the dramatic fall in fML^SP-OMe activity compared to that of the potent peptide fMLP-OMe can be deduced directly from the comparison of Tables 1 and 2, and considering the number of times where the two pharmacophores, CO(formyl) and NH(Leu), are involved in intramolecular hydrogen bonds in both cases. For fML^SP-OMe, the CO(formyl) group acts as H acceptor 30 times: C¹⁰ β turns in 9 cases and C⁷ γ turns in 21 cases. On the contrary for the parent peptide fMLP-OMe, the situation is very different: This group is involved in intramolecular hydrogen bonds only 15 times: C¹⁰ β turns in 5 cases and C⁷ γ turns in 10 cases. Likewise, the NH(Leu) is involved in hydrogen bonds 21 times for the fML^SP-OMe and only 10 times for the fMLP-OMe. This result is in perfect agreement with the literature which emphasizes the importance of the availability of these two groups in the formation of the substrate-receptor complex.^{7,16,39,47–54}

The determination of the native structure of the fMLP analogs can be deduced by comparing the conformational preferences of the two tripeptides for the conformers that we have presented in Table 1 and Table 2.

The fact that we found almost the same number of conformers adopting the β turn structure (1st class, Fig. 3a) for the active peptide fMLP-OMe (17 times), and for its inactive analog fML^SP-OMe (19 times), rejects the proposition that this structure may be the native structure of chemotactic peptides. Indeed, if this structure was native, the thioamide analog would also have been active.

The double γ turns structure (4th class, Fig. 3d) will also be rejected for the same reason, the fMLP-OMe adopts this structure 3 times and the fML^SP-OMe, devoid of any activity, adopts it 4 times.

The γ turn structure centered on Met (3rd class, Fig. 3c) is more preferred by the inactive thioamide analog (17 times, table 2) compared to the parent peptide (7 times, table 1), consequently, its chance to be native becomes weak. We note here that in this structure the two groups CO(formyl) and NH(Leu) are involved in an intramolecular hydrogen bond which decreases their availability to participate in the process of molecular recognition and

justify the inactivity of the thionated analog. It is very important to remember that the large preference of the fML^SP-OMe to adopt this structure over than fMLP-OMe is not a stroke of luck, since the generated departure conformations were identical for the two molecules.

The γ turn structure centered on Leu (2nd class, Fig. 3b) seems to be the native structure of fMLP analogs; firstly, because it is more preferred by the active parent peptide fMLP-OMe (12 times) than for its inactive analog fML^SP-OMe (2 times). Secondly, it confirms the importance of the CO(formyl) and NH(Leu) that has been mentioned above. Indeed in this structure, the two groups are not involved in any intramolecular hydrogen bond, which allows us to suggest them as pharmacophores responsible for the formation of the substrate-receptor complex.

Since several structures (β turns, γ turns and extended) have been proposed for active fMLP analogs, and given the great importance of the two pharmacophores CO(formyl) and NH at position 2 demonstrated in this study, we can suggest that in the molecular recognition process it is the “Induced fit” model of Burgen which applies.^{55,56} According to this model, there is no requirement for a molecule to take a specific secondary structure (β turn, γ turn or extended...), because any conformer, within reasonable limits, can be extracted from the solution and bound by the receptor. For the fMLP active analogs, we suggest that the substrate binds in a first step with the receptor proposing the CO formyl (necessary but not sufficient condition), after several conformational changes for both receptor and substrate, this latter proposes the determinant NH group at position 2 for the constructive interaction with the receptor. The absence of structural data from studies of the interaction of fMLP with its receptors makes a docking study necessary to validate the proposed model and confirm the importance of these two groups in the molecular recognition process.

5. Conclusion

The comparative conformational study of fMLP-OMe and its analog fML^SP-OMe described in present work allowed us to deduce three fundamental aspects concerning the structural requirements of fMLP analogs receptors.

- The γ turn structure centered on the central residue seems to be the native structure of the chemotactic peptide analogs.
- The CO(formyl) and NH at position 2 must be free of any intramolecular hydrogen bond and available for a constructive interaction with the receptor.
- The inactive analog fML^SP-OMe prefers a γ turn structure centered on the Met residue.

Our results and a careful examination of the recent literature enable us to suggest the “Induced-fit” model of

Burgen in the molecular recognition process, and that the fMLP analogs activity is not related to the adoption of a specific secondary structure (β turn, γ turn or extended....), but rather to the freedom and availability of the CO (formyl) and NH group at position 2 to form the substrate-receptor complex.

Conflict of interest: The authors declare that they have no conflict of interest.

6. References

- R. Snyderman, Reviews of Infectious Diseases, *Fed. Proc.* **1985**, *7*, 390–394.
- S. Spisani, M. C. Pareschi, M. Buzzi, M. L. Colamussi, C. Bondi, S. Traniello, G. P. Zecchini, M. P. Paradisi, I. Torrini, M. E. Ferretti, *Cell. Signal.* **1996**, *8*, 269–277. DOI:10.1016/0898-6568(96)00049-6
- B. Belleau, G. Lajoie, G. Sauve, V. S. Rao, A. di Paola, *Int. J. Immunopharmacol.* **1989**, *11*, 467–471. DOI:10.1016/0192-0561(89)90175-6
- G. Cavicchioni, M. Turchetti, K. Varani, S. Falzarano, S. Spisani, *Bioorg. Chem.* **2003**, *31*, 322–330. DOI:10.1016/S0045-2068(03)00070-1
- M. Sukumar, P.A. Raj, P. Balam, E.L. Becker, *Biochem. Biophys. Res. Commun.* **1985**, *128*, 339–344. DOI:10.1016/0006-291X(85)91684-5
- H. J. Showell, R. J. Freer, H. S. Zigmond, E. Schiffmann, S. Aswanikumar, B. Corcoran, E. L. Becker, *J. Exp. Med.* **1976**, *143*, 1154–1169. DOI:10.1084/jem.143.5.1154
- R. J. Freer, A. R. Day, N. Muthukumaraswamy, D. Pinon, A. Wu, H. J. Showell, E. L. Becker, *Biochemistry.* **1982**, *21*, 257–263. DOI:10.1021/bi00531a009
- S. Aswanikumar, B. Corcoran, E. Schiffmann, A. R. Day, R. J. Freer, H. J. Showell, E. L. Becker, *Biochem. Biophys. Res. Commun.* **1977**, *74*, 810–817. DOI:10.1016/0006-291X(77)90375-8
- F. Boulay, M. Tardif, L. Brouchon, P. Vignais, *Biochemistry.* **1990**, *29*, 11123–11133. DOI:10.1021/bi00502a016
- R. M. Freidinger, D. S. Veber, R. Hirschman, L. M. Paegge, *Int. J. Pept. Protein Res.* **1980**, *16*, 464–470. DOI:10.1111/j.1399-3011.1980.tb02970.x
- R. M. Freidinger, D. S. Perlow, D. S. Veber, *J. Org. Chem.* **1982**, *47*, 104–109. DOI:10.1021/jo00340a023
- R. M. Freidinger, *J. Med. Chem.* **2003**, *46*, 5553–5566. DOI:10.1021/jm030484k
- A. Perdih, D. Kikelj, *Current Medicinal Chemistry.* **2006**, *13*, 1525–1556. DOI:10.2174/092986706777442066
- A. Perdih, M. S. Dolenc, *Current Organic Chemistry.* **2011**, *15*, 3750–3799. DOI:10.2174/138527211797884566
- G. Sauve, V. S. Rao, G. Lajoie, B. Belleau, *Can. J. Chem.* **1985**, *63*, 3089–3101. DOI:10.1139/v85-511
- A. G. Michel, G. Lajoie, C. Ameziane Hassani, *Int. J. Pept. Protein. Res.* **1990**, *36*, 489–498. DOI:10.1111/j.1399-3011.1990.tb00987.x
- H. Dugas, M. Laroche, M. Ptak, H. Labbé, *Int. J. Pept. Protein. Res.* **1993**, *41*, 595–605. DOI:10.1111/j.1399-3011.1993.tb00482.x
- G. Vertuani, M. Boggian, A. Breveglieri, G. Cavicchioni, S. Spisani, A. Scatturin, *Amino Acids.* **1995**, *9*, 375–383. DOI:10.1007/BF00807274
- G. Cavicchioni, A. Breveglieri, M. Boggian, G. Vertuani, E. Reali, S. Spisani, *J. Pept. Sci.* **1996**, *2*, 135–140.
- M. Iqbal, P. Balam, H. J. Showell, R. J. Freer, E. L. Becker, *FEBS Lett.* **1984**, *165*, 171–174. DOI:10.1016/0014-5793(84)80163-5
- R. Bardi, A. Piazzesi, C. Toniolo, P. A. Raj, S. Raghothama, P. Balam, *Int. J. Pept. Protein.Res.* **1986**, *27*, 229–238. DOI:10.1111/j.1399-3011.1986.tb01815.x
- C. K. Derian, H. F. Solomon, J. D. Higgins, M. J. Beblavy, R. J. Santulli, G. J. Bridger, M. C. Pike, D. J. Kroon, A. J. Fischman, *Biochemistry.* **1996**, *35*, 1265–1269. DOI:10.1021/bi952087k
- C. Toniolo, M. Crisma, G. Valle, G. M. Bonora, S. Polinelli, E. L. Becker, R. J. Freer, R. Balaji Rao, P. Balam, M. Sukuma, *Pept.Res.* **1989**, *2*, 275–281.
- Y. Wazady, C. Ameziane Hassani, M. Lakhdar, A. Ezzamarty, *Int. J. Mol. Sci.* **2001**, *2*, 1–9. DOI:10.3390/i2010001
- Y. Wazady, C. Ameziane Hassani, M. Lakhdar, A. Ezzamarty, *Acta Chim. Slov.* **2002**, *49*, 55–65.
- G. Michel, C. Ameziane Hassani, B. Natalie, *Can. J. Chem.* **1992**, *70*, 596–603. DOI:10.1139/v92-083
- C. Ameziane Hassani, La Génération et l'Analyse des Populations de Structures Peptidiques en Vue d'Etudier les Hyper-surfaces d'Energie Conformationnelle en Mécanique Classique. Ph.D. Thesis, Université de Sherbrooke. Canada, **1991**.
- F. Lemay, C. Ameziane Hassani, A. G. Michel, *Can. J. Chem.* **1990**, *68*, 1186–1191. DOI:10.1139/v90-183
- G. Michel, C. Jeandenans, *Comput. Chem.* **1993**, *17*, 49–59. DOI:10.1016/0097-8485(93)80028-C
- H. Meirovitch, E. Meirovitch, A. Michel, M. Vásquez, *J. Phys. Chem.* **1994**, *98*, 6241–6243. DOI:10.1021/j100076a002
- A. Khat, M. Lamoureux, Y. Boulanger, *J. Med. Chem.* **1996**, *39*, 2492–2498. DOI:10.1021/jm9503254
- C. Ameziane Hassani, M. Houssat, J. E. Hazm, *Struct. Chem.* **2017**, *29*, 481–489. DOI:10.1007/s11224-017-1045-5
- D. E. Knuth, In “Semi-numerical algorithms.” 2nd ed. Vol. 2. The art of computer programming. Addison-Wesley, Reading Mass. **1981**, 3.2–3.3.
- M. J. D. Powell. *Math. Program.* **1977**, *12*, 241–254. DOI:10.1007/BF01593790
- G. Nemethy, M. S. Pottle, H. A. Scheraga, *J. Phys. Chem.* **1983**, *87*, 1883–1887. DOI:10.1021/j100234a011
- F. A. Momany, R. F. McGuire, A. W. Burgess, H. A. Scheraga, *J. Phys. Chem.* **1975**, *79*, 2361–2381. DOI:10.1021/j100589a006
- S. S. Zimmerman, M. S. Pottle, G. Némethy, H. A. Scheraga, *Macromolecules.* **1977**, *10*, 1–9. DOI:10.1021/ma60055a001
- R. S. Rathore, *Biopolym. Pept. Sci. Sect.* **2005**, *80*, 651–664. DOI:10.1002/bip.20231

39. G. P. Zecchini, M. P. Paradisi, I. Torrini, G. Lucente, E. Gavuzzo, F. Mazza, G. Pochetti, M. Paci, M. Sette, A. Di Nola, G. Veglia, S. Traniello, S. Spisani, *Biopolymers*. **1993**, 33, 437–451. DOI:10.1002/bip.360330310
40. E. Morera, G. Lucente, G. Ortari, M. Nalli, F. Mazza, E. Gavuzzo, S. Spisani, *Bioorganic Med. Chem.* **2002**, 10, 147–157. DOI:10.1016/S0968-0896(01)00256-5
41. S. Spisani, S. Traniello, G. Cavicchioni, F. Formaggio, M. Crisma, C. Toniolo, *J. Pept. Sci.* **2002**, 8, 56–65. DOI:10.1002/psc.369
42. S. Prasad, R. B. Rao, H. Bergstrand, B. Lundquist, E. L. Becker, P. Balam, *Int. J. Pept. Protein Res.* **1996**, 48, 312–318. DOI:10.1111/j.1399-3011.1996.tb00847.x
43. P. A. Raj, P. Balam, *Biopolymers*. **1985**, 24, 1131–1146. DOI:10.1002/bip.360240703
44. G. Vertuani, S. Spisani, M. Boggian, S. Traniello, A. Scatturin, *Int. J. Pept. Protein Res.* **1987**, 29, 525–532. DOI:10.1111/j.1399-3011.1987.tb02280.x
45. E. Gavuzzo, F. Mazza, G. Pochetti, A. Scatturini, *J. Peptide Protein Res.* **1989**, 34, 409–415. DOI:10.1111/j.1399-3011.1989.tb00710.x
46. G. Lucente, M. P. Paradisi, C. Giordano, A. Sansone, D. Torino, S. Spisani, *Amino Acids*. **2008**, 35, 329–338. DOI:10.1007/s00726-007-0621-1
47. R. J. Freer, A. R. Day, J. A. Radding, E. Schiffmann, S. Aswan-ikumar, H. J. Showell, E. L. Becker, *Biochemistry*. **1980**, 19, 2404–2410. DOI:10.1021/bi00552a019
48. C. Bismara, G. M. Bonora, C. Toniolo, E. L. Becker, R. J. Freer, *Int. J. Pept. Protein Res.* **1985**, 26, 482–492. DOI:10.1111/j.1399-3011.1985.tb01015.x
49. G. Cavicchioni, A. Fraulini, M. Turchetti, K. Varani, S. Falzarano, B. Pavan, S. Spisani, *Eur. J. Pharmacol.* **2005**, 512, 1–8. DOI:10.1016/j.ejphar.2005.02.013
50. G. Cavicchioni, A. Fraulini, S. Falzarano, S. Spisani, *Bioorg. Chem.* **2006**, 34, 298–318. DOI:10.1016/j.bioorg.2006.07.001
51. C. Giordano, G. Lucente, A. Masi, M. P. Paradisi, A. Sansone, S. Spisani, *Bioorganic Med. Chem.* **2006**, 14, 2642–2652. DOI:10.1016/j.bmc.2005.11.043
52. S. Spisani, G. Cavicchioni, *Bioorg. Chem.* **2000**, 28, 252–259. DOI:10.1006/bioo.2000.1175
53. R. Selvatici, A. Siniscalchi, S. Spisani, *Rev. Med. Chem.* **2013**, 13, 553–564. DOI:10.2174/1389557511313040008
54. G. Cavicchioni, G. Vertuani, A. Scatturin, S. Spisani, *Bioorganic Med. Chem. Lett.* **1994**, 4, 1551–1554. DOI:10.1016/S0960-894X(01)80564-3
55. S. V. Burgen, G. Feeny, G. C. K. Roberts, *Nature*. **1975**, 253, 753–755. DOI:10.1038/253753a0
56. T. Nogrady, Medicinal chemistry, A biochemical approach, Oxford. University. Press. **1988**, chapter 1, pp. 47–49.

Povzetek

To delo predstavlja rezultate primerjalne konformacijske analize aktivnega kemotaktičnega peptida (formil-Met-Leu-Phe-OMe) in njegovega reaktivnega analoga (formil-Met-Leu ψ [CSNH] Phe-OMe) z uporabo teoretičnega modela PEP-SEA, katerega namen je določitev strukturnih zahtev fMLP. Študija je pokazala, da je struktura z γ zavojem, centrirana na centralnem preostanku, nativna za analoge kemotaktičnega peptida fMLP, v katerem sta obe skupini, tako CO (formil) kot NH (centralni preostanek), na razpolago za interakcijo z receptorjem. Neaktivni analog fMLP^S-OMe pa ima namesto tega raje strukturo z γ zavojem, ki je centrirana na preostanku Met, kjer zgoraj omenjeni skupini nista dostopni za interakcijo. Naši rezultati in tisti iz literature omogočajo, da za molekularni proces prepoznavanja predlagamo »induced fit« model po Burgenu. Aktivnost fMLP analogov kemotaktičnega peptida ni povezana s specifično sekundarno strukturo (β zavoj, γ zavoj ali iztegnjena...), ampak z dostopnostjo CO in NH skupin na položaju 2.

Scientific paper

Third-Order Nonlinear Optical Properties of a Carboxylic Acid Derivative

Clodoaldo Valverde,^{1,2,3,*} Sizelizio Alves de Lima e Castro,^{4,2}
Gabriela Rodrigues Vaz,¹ Jorge Luiz de Almeida Ferreira,⁴ Basílio Baseia,^{5,7}
and Francisco A. P. Osório^{5,6}

¹ Campus de Ciências Exatas e Tecnológicas, Universidade Estadual de Goiás, 75001-970, Anápolis, GO, Brazil.

² Universidade Paulista, 74845-090, Goiânia, GO, Brazil.

³ Centro Universitário de Anápolis, 75083-515, Anápolis, GO, Brazil.

⁴ Engenharia Mecânica – Universidade de Brasília, Brasília, DF, Brazil

⁵ Instituto de Física, Universidade Federal de Goiás, 74.690-900, Goiânia, GO, Brazil.

⁶ Escola de Ciências Exatas e da Computação, Pontifícia Universidade Católica de Goiás, 74605-10, Goiânia, GO, Brazil.

⁷ Departamento de Física, Universidade Federal da Paraíba, 58.051-970, João Pessoa, PB, Brazil.

* Corresponding author: E-mail: valverde@ueg.br

Received: 14-05-2018

Abstract

We report a study of the structural and electrical properties of a carboxylic acid derivative (CAD) with structural formula $C_5H_8O_2$ ((*E*)-pent-2-enoic acid). Using the Møller-Plesset Perturbation Theory (MP2) and the Density Functional Theory (DFT/CAM-B3LYP) with the 6-311++G(*d,p*) basis set the dipole moment, the linear polarizability and the first and second hyperpolarizabilities are calculated in presence of static and dynamic electric field. Through the supermolecule approach the crystalline phase of the carboxylic acid derivative is simulated and the environment polarization effects on the electrical parameters are studied. Static and dynamic estimation of the linear refractive index and the third-order nonlinear susceptibility of the crystal are obtained and compared with available experimental results. The characteristic vibrational modes and functional groups present in CAD were analyzed by Fourier Transform Infrared Spectrum (FT-IR) in the region of 400–4000 cm^{-1} . Through the Hirshfeld surface analysis the molecular structure and the vibrational modes properties of the CAD crystal are explored. The effects of solvent medium on the molecular properties are taken into account through the Polarizable Continuum Model (PCM). Also, the frontiers molecular orbitals, the band gap energy, and the global chemical reactivity descriptors are discussed. All the properties studied suggest that the present material may be considered for nonlinear optical material.

Keywords: First and second hyperpolarizabilities; Hirshfeld surface analysis; third-order susceptibility

1. Introduction

In recent decades, organic compounds have attracted great attention motivated by their potential applications in chemistry of materials such as nonlinear optical materials (NLO),¹ solar cell materials,² photonic materials,³ photonic devices,⁴ optical devices,⁵ electrochemical sensors,⁶ in ultra-fast optical signal processing.^{7–11} Due to architectural flexibility and ease of manufacturing the NLO devic-

es, organic materials with extensively delocalized π electrons have attracted significant attention due to their large NLO susceptibility.^{12–15} The advantage of the organic compounds over the inorganic materials is that NLO properties can be manipulated, by changing the substituents and the functional groups on the starting reactants. The NLO response of the organic compounds to the action of an applied electric field is related to the relocation of the π -electron.

Finding new organic crystals that present efficient NLO properties is the challenge of the present days and a great number of experimental and theoretical works has been addressed to this end. In this context, here we present an investigation of the electric and optical properties of a carboxylic acid derivative. Carboxylic acid derivatives have various applications in textile treatment, in the production of cellulose plastics and ester; as an example the ester of salicylic acid is prepared from acetic acid. The use of unsaturated fatty acids and fatty acids in general have been used with great interest in nutrition and health sciences,^{16,17} due to their great role in biological processes, especially as an antibiotic against many bacteria and fungi.^{18,19} Fatty acids and their derivatives act as a receptor ligand in the cerebral cortex and hippocampus and elevated concentrations can be found in patients with Alzheimer's and Parkinson's disease.²⁰ Determinations of the crystal structure of α,β -unsaturated carboxylic acids are still scarce in the literature, but in recent years it has been gaining great interest from researchers.^{21–25} Our motivation for the study of α,β -unsaturated carboxylic acid crystal came from the fact that we not found works in the literature that treat of the NLO properties of this material.

The constituent units of an organic crystal may possess (or not) a center of symmetry, which is responsible for nonlinear optical effects, as well as by the generation of the second and third susceptibility governed respectively by the first and second hyperpolarizabilities. Density functional theory (DFT) and other methods in quantum chemistry have proved to be highly successful in describing structural and electronic properties, as the molecular polarizabilities and hyperpolarizabilities, static and dynamic in a vast class of materials from atoms and molecules to simple crystals.^{10,11,26–37}

The carboxylic acid derivative (CAD) studied in this work is the (*E*)-pent-2-enoic acid with structural formula $C_5H_8O_2$ (Figure 1); it was synthesized and structurally characterized by Tim Peppel et al.²³ Through an ab initio approach the dipole moment, the linear polarizability and the first and second hyperpolarizabilities have been calculated. The effect of an applied electric field (static and dynamic) was considered in our calculation. Also, the influence of the crystalline environment on the electric and optical properties was studied. Moreover the highest occupied molecular orbital (HOMO) and the lowest unoccupied molecular orbital (LUMO) were calculated including the gap energies calculated in presence of several solvent media.

2. Methodology

2.1. Hirshfeld Surface

The CAD compound was crystallized,²³ in a triclinic centrosymmetric space group $P\bar{1}$ with the following crystallographic data: $a = 6.7336$ (13) Å, $b = 6.7821$ (13) Å, $c =$

7.2349 (14) Å, $\alpha = 67.743$ (2)°, $\beta = 75.518$ (2)°, $\gamma = 64.401$ (2)°, unit cell volume $V = 274.29$ (9) Å³ with 2 molecules in the unit cell. The (*E*)-pent-2-enoic acid is essentially planar.

The intermolecular interactions and their quantitative contributions to the stability of supramolecular assembly in organic crystals of CAD can be explored by Hirshfeld surface analysis and the associated 2D-fingerprint plots was calculated using Crystal Explorer software.^{38,39} These tools allow us to examine the context of the whole system through the color mapping identifying specific regions where the intermolecular interactions occur; these tools also allow to quantify percentage of areas related to each contact. Fingerprint plots can summarize all contact distances to the Hirshfeld surface and express their contributions in terms of a percentage share.

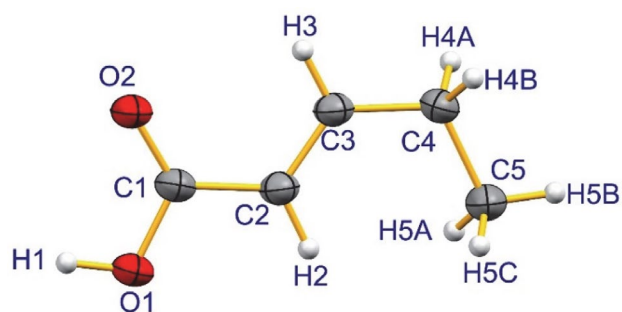


Figure 1: A view of the asymmetric unit of the compound $C_5H_8O_2$ with the atom-numbering scheme

2.2. Computational Details

The theoretical method used to calculate the static linear polarizability and the dipole moment was the Møller-Plesset Perturbation Theory (MP2). The other parameters as the hyperpolarizabilities were calculated via the Density Functional Theory (DFT) with CAM-B3LYP functional. In all calculations the 6-311++G(*d,p*) basis set was used. The SM approach taken into account the crystallographic geometry obtained by X-ray by Tim Peppel et al.²³ Previous studies have shown that this basis set provide a realistic description of the electrical properties.⁴⁰

The crystalline environment polarization was simulated by the supermolecule (SM) approach, where the atoms of the surrounding molecules are considered as point charge. The approach operates with a bulk consisting of a set of $11 \times 11 \times 11$ unit cells, with 2 asymmetric units in each unit cell, totalizing 1331 unit cells generating a bulk with 39,930 atoms. A schematic representation of this bulk is shown in Figure 2, where the CAD isolated molecule is highlighted in blue in the center of the image.

The SM approach have been used in several works, in Ref.⁴¹ the authors showed that this method can represent the dipole moment and the first hyperpolarizability with results close to those of the experimental ones. In Ref.⁴²

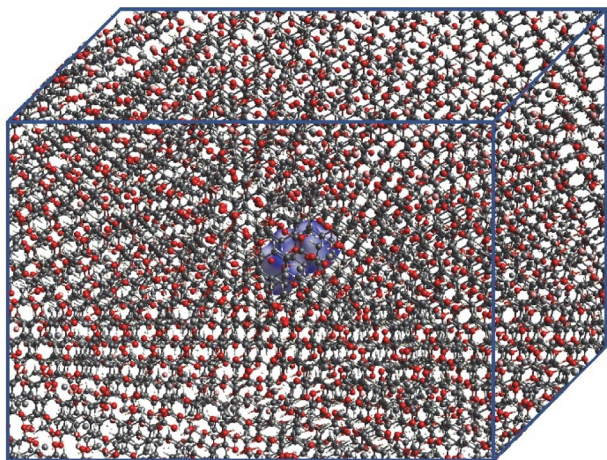


Figure 2: A schematic of the bulk is displayed.

the authors have shown that the SM can represent macroscopic properties of the crystal as the linear susceptibility, $\chi^{(1)}$, and for the nonlinear second-order susceptibility, $\chi^{(2)}$, in this case they worked with urea and thiurea and their theoretical results were close to those of experiments, after using a scale factor. In Ref.⁴⁰ the authors also simulated the properties of $\chi^{(1)}$ and $\chi^{(2)}$ of the molecule 3-methyl-4-nitropyridine-1-oxide with results again close to the experimental ones.

The iterative process of the SM approach is carried out in several steps: first we determined the electric charge of the isolated molecule, by adjusting the molecular electrostatic potential (ChelpG), considering the electric charges distribution in vacuum, through the MP2 method. The partial atomic charges of the single isolated molecule of an asymmetric unit are calculated (ChelpG). Then we replace each corresponding atom in the generated unit cells by the partial atomic charge, previously obtained, and the static electric properties (dipole moment (μ), linear polarizability (α) and first (β) second (γ) hyperpolarizabilities) and the new partial atomic charges of the asymmetric unit were calculated. The iterative process continues with the substitution of the partial atomic charges in each calculation step, until the convergence of the electric dipole moment be reached.

The applicability of the supermolecule approach and the scheme of electrostatic polarization is advantageous due to the rapid convergence of the dipole moment of CAD throughout the process, in which six iterations were considered. The convergence of iterative series for this electrical property can be seen in Figure 3.

In the present study the electronic dipole moment, molecular mean polarizability ($\langle\alpha\rangle$), anisotropy of polarizability ($\Delta\alpha$) and first (β_{total}), and second molecular hyperpolarizabilities ($\langle\gamma\rangle$) of the title compounds has been calculated using the following expressions,

$$\mu = (\mu_x^2 + \mu_y^2 + \mu_z^2)^{\frac{1}{2}}, \quad (1)$$

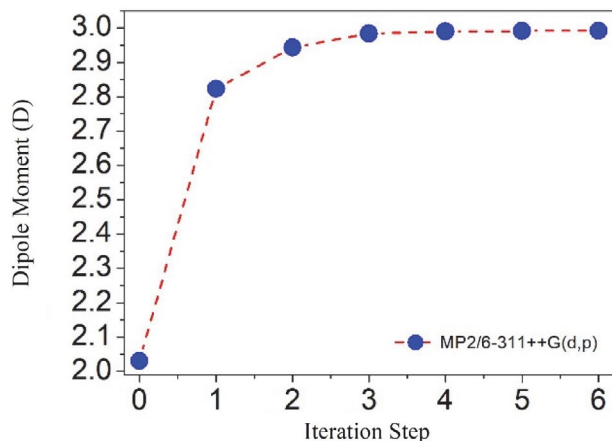


Figure 3: Evolution of values of the dipole moment of the CAD with the respective iteration numbers. A $11 \times 11 \times 11$ unit cell assembly was considered (step 0 indicates the isolated molecule and the other steps indicate the embedded molecule).

$$\langle\alpha\rangle = \frac{\alpha_{xx} + \alpha_{yy} + \alpha_{zz}}{3}, \quad (2)$$

$$\Delta\alpha = 2^{-1/2} \left[(\alpha_{xx} - \alpha_{yy})^2 + (\alpha_{yy} - \alpha_{zz})^2 + (\alpha_{zz} - \alpha_{xx})^2 + 6\alpha_{xz}^2 + 6\alpha_{xy}^2 + 6\alpha_{yz}^2 \right]^{1/2}, \quad (3)$$

and,

$$\langle\gamma\rangle = \frac{1}{15} \sum_{i,j=x,y,z} (\gamma_{iijj} + \gamma_{ijij} + \gamma_{ijji}). \quad (4)$$

In the present work as the optical dispersion in the medium was not taken into account, the average (or absolute value) of static second hyperpolarizability can be simplified via the Kleinmann,⁴³ approach and calculated through the expression,

$$\langle\gamma\rangle = \frac{1}{5} \left[\gamma_{xxxx} + \gamma_{yyyy} + \gamma_{zzzz} + 2(\gamma_{xxyy} + \gamma_{xxzz} + \gamma_{yyzz}) \right]. \quad (5)$$

The average linear polarizability $\langle\alpha\rangle$ can be related with the linear refractive index (n) of the crystal by the Clausius-Mossotti relation, which is given by,⁴⁴

$$\frac{n^2 - 1}{n^2 + 2} = \frac{4\pi N}{3} \langle\alpha\rangle, \quad (6)$$

where N is the number of molecules per unit cell volume. The experimental quantity, the third-order electric susceptibility $\chi^{(3)}$, is related to the second hyperpolarizability by the expression,^{44,45}

$$\chi^{(3)} = f^4 N \langle\gamma\rangle, \quad (7)$$

where f is the Lorentz local field correction factor given by,

$$f = \frac{(n^2 + 2)}{3}. \quad (8)$$

All the numerical results for the tensors polarizability and hyperpolarizabilities were obtained from the Gaussian-09 output file and converted by the electronic units (esu), where the molecular environment were taken into account through the SM method.

3. Results and Discussion

3. 1. FT-IR Computational Studies

The characteristic vibrational modes and functional groups present in CAD were analyzed by Fourier Transform Infrared Spectrum (FT-IR). The spectrum was recorded in the range of 400–4000 cm^{-1} . From Figure 4 we observed that a transmittance peak appears at 3806 cm^{-1} which is due to OH stretching vibration. The C-H stretching vibration is observed at 3128 and 3055 cm^{-1} . The stretching vibration O-C occurs in 1829, 1387 and 1178 cm^{-1} respectively. The peak 1301 cm^{-1} is attributed to H-C-C stretching vibration; peak 702 cm^{-1} is the H-C-C bending, and the 586 cm^{-1} peak is attributed to the H-O-C-C torsion movements. Thus, all functional groups present in the crystalline structure of CAD were confirmed.

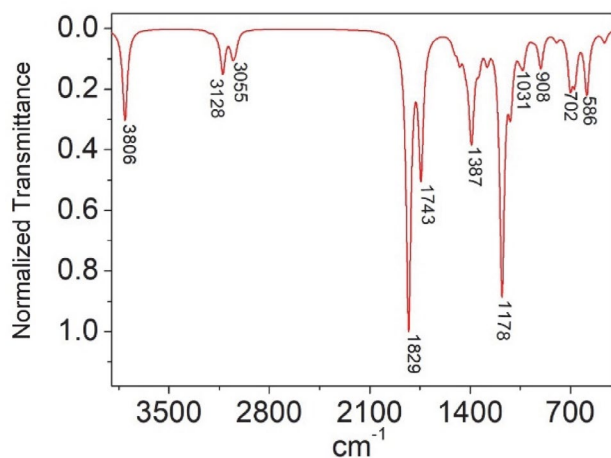


Figure 4: CAM-B3LYP/6-311++G(d,p) used to calculate FT-IR spectrum of $\text{C}_5\text{H}_8\text{O}_2$.

3. 2. Hirshfeld Surface Analysis

The molecular structure CAD, $\text{C}_5\text{H}_8\text{O}_2$, previously studied by Tim Peppel et al.,²³ was analyzed in this work using the Hirshfeld surface (HS) and its associated 2D-fingerprint plot. The calculate were made using in Density Functional Theory (DFT) at level Becke88/LYP/6-311G(d,p) to experimental X-ray diffraction data via Tonto.^{46,47} The HS and its 2D-fingerprint figures allow us visualizing, exploring and quantifying the intermolecular interactions in the crystalline network of the compound CAD. The surface was generated on the basis of the normalized contact distances, which are defined in terms of d_i

(the distance to the nearest nucleus within the surface) and d_e (the distance from the point to the nearest nucleus external to the surface) related to van der Waals radii,^{48,49} of the atoms. The high resolution default of d_{norm} surface was mapped over the colour scale, ranging from -0.369 (red) to 1.201 Å (blue), with the fingerprint plots using the expanded 0.6 – 2.8 Å view of d_e vs. d_i . Figure 5, where a surface with a blue-white-red scheme is showed. The blue spots are devoid of close contacts, the white areas represent contacts around the van der Waals radius and the red regions evidence shorter contacts. The Hirshfeld surface analysis of CAD confirms that the molecules are linked into centrosymmetric dimers via pairs of O—H...O hydrogen bonds in the crystals. The distance O...H is 1.635 Å (see Figure 5). The 2D-fingerprint plots (Figure 6) derived from d_i and d_e from pairs measured on each individual point of the calculated HS summarize the contributions of intermolecular contacts to the total surface area of Hirshfeld. The intermolecular contacts that can be explored in CAD are as follows: C...C, C...H, C...O, H...H and H...O. The intercontacts H...O the figure 6 (fingerprint) presents characteristic peaks that provide evidence of non-classical hydrogen bonding, including reciprocal contacts with 34.3% of the total surface. The contacts of type H...H show the highest contributions with a total of 52.5% followed by C...H (8.7%), C...C (2.5%) and C...O (1.6%).

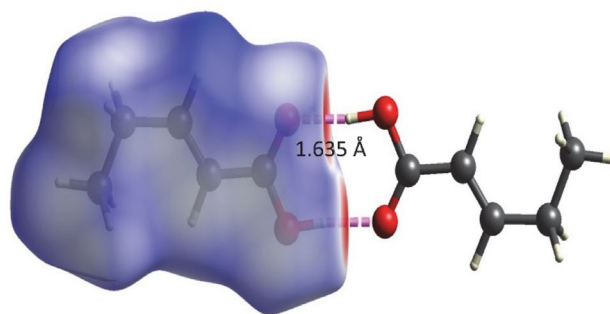


Figure 5: The Hirshfeld surface d_{norm} mapped of $\text{C}_5\text{H}_8\text{O}_2$ for visualizing the intercontacts, showing molecules are linked into centrosymmetric dimers via pairs of O—H...O hydrogen bonds.

3. 3. Static Electrical Parameters Computational Calculation

In Table 1 our results for the components and average values of the dipole moment and the linear polarizability for the isolated molecule and embedded molecule of the CAD are presented.

From Table 1 can be seen that the value of the average dipole moment is found to be 2.03D and 2.99D for the isolated and embedded molecule respectively, showing that the environment polarization effect in this case is substantial and causes an increases of 47.29% in the average dipole moment. The major contribution to the average di-

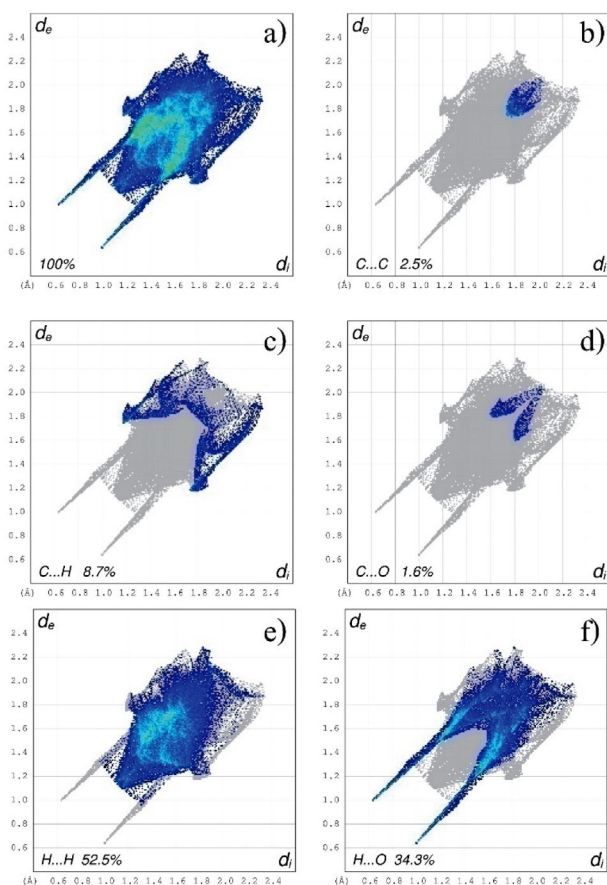


Figure 6: The Fingerprint plot for $C_5H_8O_2$ a) 100% of contacts; b) C...C; c) C...H; d) C...O; e) H...H; and f) H...O, produced from d_e and d_i function mapped in color showing the percentage contribution of each type of interaction in total interactions verified; d_e is the distance from the surface to the nearest atom exterior to the surface and d_i is the distance from the surface to the nearest atom interior to the surface.

Table 1: MP2/6-311++G(d,p) results for the components and the average values of the dipole moment (in D) and the linear polarizability (in 10^{-24} esu).

	Isolated	Embedded		Isolated	Embedded
α_{xx}	9.28	9.36	μ_x	-1.82	-2.76
α_{xy}	1.81	1.91	μ_y	-0.88	-1.10
α_{yy}	8.78	8.80	μ_z	-0.21	-0.36
α_{xz}	-0.25	-0.29	$\langle\mu\rangle$	2.03	2.99
α_{yz}	-2.18	-2.18			
α_{zz}	9.11	9.10			
$\langle\alpha\rangle$	9.06	9.09			
$\Delta\alpha$	3.21	2.62			

Table 2: CAM-B3LYP/6-311++G(d,p) results for the second hyperpolarizability (in 10^{-36} esu) in the static case.

$C_5H_8O_2$	γ_{xxxx}	γ_{yyyy}	γ_{zzzz}	γ_{xxyy}	γ_{yyzz}	γ_{xxzz}	$\langle\gamma\rangle$
Isolated	4.80	5.04	4.52	2.71	1.87	1.70	5.39
Embedded	4.50	4.44	3.69	2.56	1.50	1.56	4.77
$\Delta\%$	-6.25	-11.90	-18.36	-5.54	-19.79	-8.24	-11.50

pole moment is given by the μ_x component, mainly for the embedded molecule. However the values of the average linear polarizability and the linear polarizability components are practically insensible to the crystalline environment polarization. As consequence of this fact a small value of the linear polarizability anisotropy can be observed in **Table 1**, and Δ value are smaller for the embedded molecule (2.6×10^{-24} esu) than for the isolated molecule (3.2×10^{-24} esu). And as can be seen the diagonal component dominates the polarizability and are the elements responsible by the calculation of the average linear polarizability (equation 2).

In **Table 2** the CAM-B3LYP/6-311++G(d,p) results for the second hyperpolarizability (in units of 10^{-36} esu) for the static case are presented for CAD isolated and embedded molecules. As shown in the **Table 2** the values of the average second hyperpolarizability (in units of 10^{-36} esu) are 5.39 and 4.77 for isolated molecule and embedded molecule respectively. Although the values of the average dipole moment and average linear polarizability for the CAD were two and three times the urea values respectively,^{50–52} the values of average second hyperpolarizability are found almost similar to urea (4.16×10^{-36} esu) and smaller than the value for the L-arginine phosphate monohydrate crystal (14.16×10^{-36} esu).³⁴

The calculations for the linear refractive index (n) via Eq. (6) and $\chi^{(3)}$ through Eq. (7) were calculated using the DFT/CAM-B3LYP functional and 6-311++G(d,p) basis set. In these calculations we have used the static value of the electric parameters (Table 2). In a more recent work the SM approach was used to simulate the linear refractive index and the third-order electric susceptibility of the (2E)-3-(3-methylphenyl)-1-(4-nitrophenyl)prop-2-en-1-one (3MPNP) crystal⁵³ with results close to the experimental ones. The CAM-B3LYP results for the linear refractive index and the static third-order non-linear susceptibility, $n = 1.47$ and $\chi^{(3)} = 17.84 \times 10^{-22} \frac{m}{V}$. It is worth noting that this approach is an approximation to estimate the NLO properties and other factors can also affect the NLO responses. Also, in **Table 2** the percentage variation of the second hyperpolarizabilities tensor components is shown: note that all values are reduced due to the influence of the environment polarization.

The Table 3 shows the influence of environment polarization on the electron density of the CAD molecule due to the field of punctual charges of neighboring molecules that can also be qualitatively analyzed in terms of partial atomic charges. The results of the charges fit via

CHELPG for the isolated and embedded molecules show a small charge transfer between H1-O1-C1-O2 of the isolated molecule (0.026e) for the embedded molecule (-0.022e). The compound methyl (C5-H5A-H5B-H5C) reduced its charge by around 161%.

Table 3: MP2/6-311++G(d,p) results for the CHELPG atomic charges of isolated and embedded CAD.

Number	Atom	Isolated	Charge (e) Converged	$\Delta\%$
1	C1	0.821	0.886	7.88
2	C2	-0.348	-0.345	-0.71
3	H2	0.176	0.168	-4.30
4	C3	-0.103	-0.099	-3.25
5	H3	0.115	0.155	34.89
6	C4	0.229	0.178	-22.62
7	H4A	-0.024	-0.008	-66.43
8	H4B	-0.038	-0.014	-63.54
9	C5	-0.054	-0.032	-41.75
10	H5A	0.010	0.019	100.00
11	H5B	0.015	0.010	-29.69
12	H5C	-0.005	-0.010	118.39
13	O1	-0.644	-0.641	-0.55
14	O2	-0.587	-0.747	27.30
15	H1	0.436	0.480	9.94

4. Dynamic Effects

In this section the dynamic effects of an applied electric field with frequency ω is taken into account in the calculation of the dynamic properties of the carboxylic acid derivative (CAD). Using the CAM-B3LYP/6-311+G(d) we calculate the second hyperpolarizability $\gamma(-\omega; \omega_1, \omega_2, \omega_3)$, where by convention the first frequency in the parenthesis denoted by the negative signal, is the emitted radiation frequency; the other frequencies (positive) concern the absorbed radiation, where $\omega = \omega_1 + \omega_2 + \omega_3$.

Figure 7 shows the calculated values for the average linear polarizability $\langle\alpha(-\omega; \omega)\rangle$ and for the average second hyperpolarizabilities $\langle\gamma(-\omega; \omega, 0, 0)\rangle$ (Kerr effect) and $\langle\gamma(-2\omega; \omega, \omega, 0)\rangle$ (dc-second harmonic generation (SHG)) as function of the applied electric field frequencies for both cases, isolated and embedded molecules. The results in Figure 7 (a,b,c) show that the dispersion relations are practically insensitive to the environment polarization, and present a similar behavior, i.e., all curves increase smoothly and continuously.

In order to make a more accurate estimative of the dynamic third-order susceptibility ($\chi^{(3)}$) we have used two different models for the $\langle\gamma\rangle$ -dynamic: (1) the frequency-dependent second hyperpolarizability ($\langle\gamma(-\omega; \omega, \omega, -\omega)\rangle$) associated to the nonlinear optical process of the intensity dependent refractive index (IDRI) from dc-Kerr result, and (2) the third harmonic generation hyperpolarizability ($\langle\gamma(-3\omega; \omega, \omega, \omega)\rangle$). Following a previous work⁵⁴, for small frequencies⁵⁵ average hyperpolarizabilities can be written as,

$$\langle\gamma(-\omega; \omega, \omega, -\omega)\rangle \cong 2\langle\gamma(-\omega; \omega, 0, 0)\rangle - \langle\gamma(0; 0, 0, 0)\rangle. \quad (9)$$

$$\langle\gamma(-3\omega; \omega, \omega, \omega)\rangle \cong 6\langle\gamma(-\omega; \omega, 0, 0)\rangle - 5\langle\gamma(0; 0, 0, 0)\rangle. \quad (10)$$

Table 4 shows the results for the linear refractive index, the second hyperpolarizabilities IDRI ($\gamma(\text{IDRI})$) and THG ($\gamma(\text{THG})$), defined by equations (9) and (10) respectively and the respective third-order nonlinear susceptibilities $\chi^{(3)}$ (IDRI) and $\chi^{(3)}$ (THG), for two values of the electric field frequencies $\omega = 0.0428$ a.u. and $\omega = 0.06$ a.u..

Table 4: CAD embedded molecules linear refractive index and the IDRI and THG results for γ (10^{-36} esu) and the $\chi^{(3)}$ (10^{-22} m²/V²).

ω (a.u)	n	$\gamma(\text{IDRI})$	$\chi^{(3)}(\text{IDRI})$	$\gamma(\text{THG})$	$\chi^{(3)}(\text{THG})$
0.0428	1.48	5.31	20.54	6.39	24.72
0.06	1.49	5,81	22.86	7.89	31.05

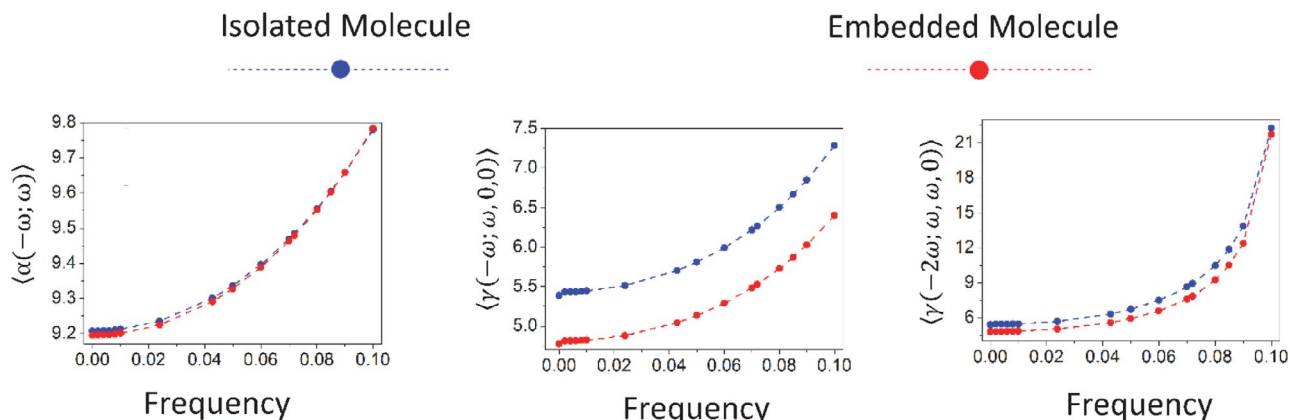


Figure 7: Dynamic evolution of the calculated values for: a) average linear polarizability $\langle\alpha(-\omega; \omega)\rangle$ (10^{-24} esu); b) average second hyperpolarizability $\langle\gamma(-\omega; \omega, 0, 0)\rangle$ (10^{-36} esu); c) average second hyperpolarizability $\langle\gamma(-2\omega; \omega, \omega, 0)\rangle$ (10^{-36} esu) for the compound CAD ($\text{C}_5\text{H}_8\text{O}_2$).

The values of the $\chi^{(3)}$ for the CAD embedded molecule (Table 4) in both frequencies are high when compared with the results obtained for chalcone derivatives studied by the Z-scan technique by D'Silva et al. (2012).⁵⁶ The value of the third-order electric susceptibility (in units of $(10^{-22} \text{ m}^2/\text{V}^2)$) of the chalcone derivatives 4Br4MSP, 3Br4MSP and 4N4MSP are 2.30, 1.99 and 2.37 respectively,⁵⁶ the CAD $\chi^{(3)}$ -value is 22.86 ($\omega = 0.06 \text{ a.u.}, \lambda = 759 \text{ nm}$), therefore 9.94, 11.49 and 9.65 times higher than these values respectively. The typical $\chi^{(3)}$ -value reported in the literature is of order of $10^{-22}(\frac{\text{m}}{\text{V}})$.⁵⁷

5. Solvent Media

The solvent media may change the properties of the molecules, as the displacements of electronic absorption bands, the reaction rates, the NLO properties, among others. Thus an adequate description of the solvent medium is necessary. There are two models that simulate the solvent medium: the continuous model and the discrete model. In this work we use the method of Polarizable Continuum Model (PCM), in which the dielectric properties of the solvent medium are used for the solvation of the system. A PCM advantage is the possibility of making a purely quantum treatment of the solute-solvent interaction. The calculations were performed numerically based on finite field method, include the optimization of the structure using the PCM-CAM-B3LYP/6-311++G(d,p) level of theory. We selected Chloroform, Dichloromethane, Acetone, Ethanol, Methanol, Dimethyl Sulfoxide (DMSO), and Water as the solvent media, and the gas-phase results are included by comparison.

When in a solvent medium the electrical properties of the organic compounds change, one of the changes is the loss of the centrosymmetry conformation which causes a not null value for the first hyperpolarizability. Here we consider the first hyperpolarizability component parallel to the dipole moment (taken as z-direction) given by,

$$\beta_{\parallel z} = \frac{1}{5} \sum_{i=1}^3 (\beta_{zii} + \beta_{izi} + \beta_{iiz}) \quad (11)$$

Table 5: PCM-CAM-B3LYP/6-311++G(d,p) results for the dynamic linear polarizability (in 10^{-24} esu), first hyperpolarizability (in 10^{-30} esu) and second hyperpolarizability (in 10^{-36} esu) of $\text{C}_5\text{H}_8\text{O}_2$ in various solvent media for the frequency $\omega = 0.0428 \text{ a.u.}$

Dielectric Constant (ϵ)	$\text{C}_5\text{H}_8\text{O}_2$	$\langle \alpha(-\omega; \omega) \rangle$	$\beta_{\parallel z}(-\omega; \omega, 0)$	$\beta_{\parallel z}(-2\omega; \omega, \omega)$	$\langle \gamma(-\omega; \omega, 0, 0) \rangle$	$\langle \gamma(-2\omega; \omega, \omega, 0) \rangle$
1.00	Gas-Phase	10.21	-0.95	-1.13	6.55	7.27
4.71	Chloroform	11.31	-0.66	-0.78	9.56	10.11
8.93	Dichloromethane	11.27	-0.67	-0.78	9.96	10.24
20.49	Acetone	11.16	-0.68	-0.77	10.13	10.13
24.85	Ethanol	11.16	-0.68	-0.77	10.18	10.16
32.61	Methanol	11.16	-0.68	-0.77	10.18	10.16
46.70	Dimethyl Sulfoxide	12.90	-0.70	-0.79	10.45	10.44
78.36	Water	11.10	-1.77	-1.87	10.27	10.11

The dynamical electric parameter $\beta_{\parallel z}(-\omega; \omega_1, \omega_2)$ is an experimentally relevant quantity because it is closely related to the direction of the ground state charge transfer. In the specific cases we consider $\beta_{\parallel z}(-\omega; \omega, 0)$ and $\beta_{\parallel z}(-2\omega; \omega, \omega)$ that correspond to the Pockels effect and to the SHG respectively.

Table 5, shows the values for average linear polarizability, first hyperpolarizability and second hyperpolarizability for various solvent media. Figure 8 shows that the average linear polarizability increases to a value close to 26.3% when comparing the DMSO medium with the gas-

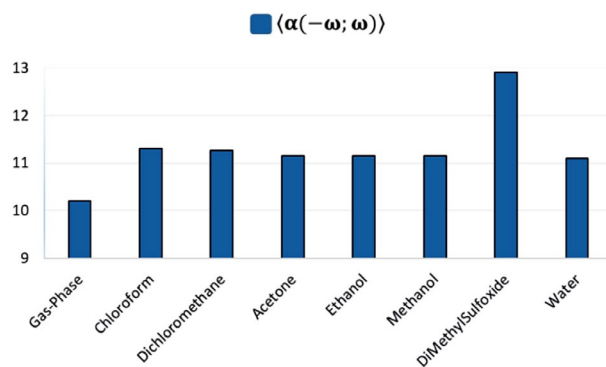


Figure 8: PCM-CAM-B3LYP/6-311++G(d,p) results for average linear polarizability $\langle \alpha(-\omega; \omega) \rangle$ (10^{-24} esu) for $\omega = 0.04282$ of compound $\text{C}_5\text{H}_8\text{O}_2$ in a solvent medium.

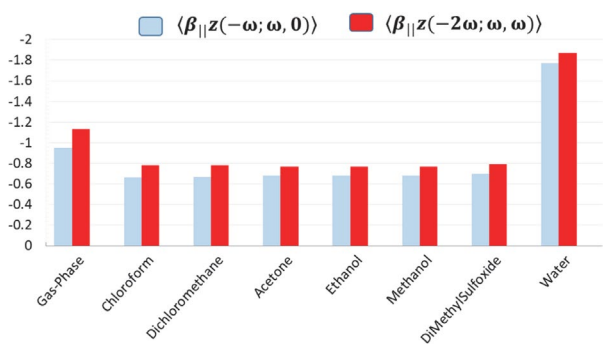


Figure 9: PCM-CAM-B3LYP/6-311++G(d,p) results for first hyperpolarizabilities (10^{-30} esu) $\langle \beta_{\parallel z}(-\omega; \omega, 0) \rangle$ and $\langle \beta_{\parallel z}(-2\omega; \omega, \omega) \rangle$ for $\omega = 0.04282 \text{ a.u.}$ of compound $\text{C}_5\text{H}_8\text{O}_2$ in a solvent medium.

phase. The first hyperpolarizability $\langle\beta_{||z}(-\omega; \omega, 0)\rangle[\langle\beta_{||z}(-2\omega; \omega, \omega)\rangle]$ increases around 86.3% [65.5%] when comparing the gas-phase with water, see Figure 9, and the second hyperpolarizability $\langle\gamma(-\omega; \omega, 0, 0)\rangle[\langle\gamma(-2\omega; \omega, \omega, 0)\rangle]$ increases around 59.5% [43.6%] when comparing the DMSO medium with the gas-phase, see Figure 10. The choice of the solvent medium allows us to control the NLO properties; in other words, the first hyperpolarizability is more sensitive in water whereas the second hyperpolarizability is more sensitive in DMSO solvent medium.

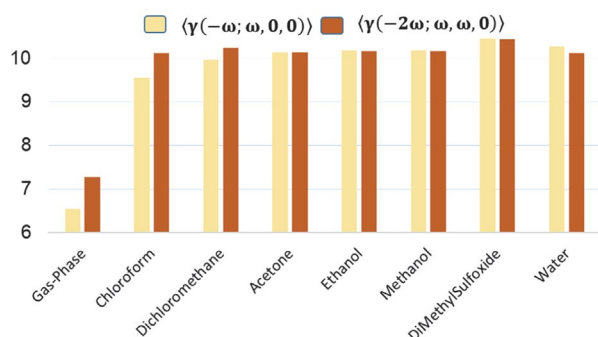


Figure 10: PCM-CAM-B3LYP/6-311++G(d,p) results for second hyperpolarizabilities (10^{-36} esu) $\langle\gamma(-\omega; \omega, 0, 0)\rangle$ and $\langle\gamma(-2\omega; \omega, \omega, 0)\rangle$ for $\omega = 0.04282$ a. u. of compound $C_5H_8O_2$ in a solvent medium.

Figure 11 shows the overlap of the structure of the crystal molecule with the molecule in the gas phase of the compound $C_5H_8O_2$; the anchorage point occurs in the O2-C1-O1-H1 geometry (see Figure 1). The X-ray geometry of the theoretical structure was analyzed in terms of root mean square deviation (RMSD) calculated for non H-atoms. The H-atoms were neglected in view of their uncertainties in X-ray position refinement. The compound $C_5H_8O_2$ presents in RMSD = 0.0328 max. d = 0.0571 Å. The RMSD parameter indicates no significant deviation between the theoretical and experimental data.

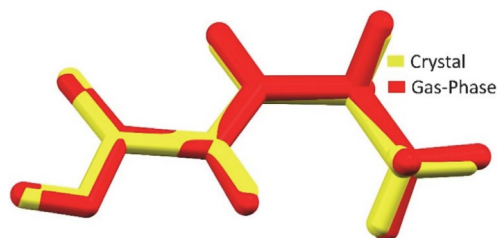


Figure 11: Compound $C_5H_8O_2$ overlap of compound yellow (crystal), red (gas-phase). The anchorage point occurs in the O₂-C₁-O₁-H₁ geometry.

6. HOMO and LUMO Analysis

The PCM-CAM-B3LYP/6-311+G(d) level of theory has been used to obtain the energies of the highest occu-

ried molecular orbital (HOMO) and lowest unoccupied molecular orbital (LUMO). These quantum chemical parameters, HOMO and LUMO energies, play the same role of electron donor and electron acceptor, respectively; therefore they determine the molecular reactivity and the ability of a molecule to absorb light. Also they can be used for predicting the most reactive position in π -electron systems and explain several types of reactions in conjugated systems. The HOMO-LUMO separation energy is called the gap energy, and a small value of this parameter implies a charge transfer interaction within the molecule, which influences the NLO activity of the molecule. In Table 5 the HOMO and LUMO energies for the CAD in several solvent media are presented, showing that the values present a small variation in different solvent media.

Table 6: PCM-CAM-B3LYP/6-311+G(d) results for the energy HOMO-LUMO (in eV) of compound $C_5H_8O_2$ in a solvent medium.

$C_5H_8O_2$	HOMO	LUMO
Acetone	-9.22	-0.27
Chloroform	-9.22	-0.25
Dichloromethane	-9.23	-0.26
DiMethylSulfoxide	-9.23	-0.28
Ethanol	-9.23	-0.28
Gas-Phase	-9.23	-0.17
Methanol	-9.23	-0.28
Water	-9.23	-0.28

It is clear from Figure 12 that the HOMO is largely located on C2-C3 atoms and moderately on H4A-C4-H4B atoms whereas the LUMO is mainly present on C2-C3 atoms and moderately on C3 atom. Also the band gap energies in different solvent media are presented in Figure 12, where we note a small variation of this parameter is, of order of 0.1 eV. Through the HOMO and LUMO energies the global chemical reactivity descriptors (GCRD) such the electronic chemical potential (μ_{cp}), the chemical hardness (η), softness (S), and the global electrophilicity index (ω) can be calculated through the equations

$$\mu_{cp} = \frac{1}{2}(E_{HOMO} + E_{LUMO}), \quad (12)$$

$$\eta = \frac{1}{2}(E_{LUMO} - E_{HOMO}), \quad (13)$$

$$S = \frac{-E_{HOMO}}{2\eta}, \quad (14)$$

$$\omega = \frac{\mu_{cp}^2}{2\eta}. \quad (15)$$

Calculations for the GCRD can be seen in Table 6 for various solvent media. The obtained GCRD results reveal that the CAD molecule offers good chemical strength and stability.

Table 7: PCM-CAM-B3LYP/6-311+G(d) results for the electronic chemical potential (μ_{cp}), the chemical hardness (η), softness (S), and the global electrophilicity index (ω) (in eV) of compound $C_5H_8O_2$ in a solvent medium.

$C_5H_8O_2$	μ_{cp}	η	S	ω
Acetone	-4.75	4.48	1.03	2.52
Chloroform	-4.74	4.49	1.03	2.50
Dichloromethane	-4.75	4.49	1.03	2.51
DiMethylSulfoxide	-4.76	4.48	1.03	2.53
Ethanol	-4.76	4.48	1.03	2.53
Gas-Phase	-4.70	4.53	1.02	2.44
Methanol	-4.76	4.48	1.03	2.53
Water	-4.76	4.48	1.03	2.53

The effect of the solvent on the GCRD is not significant.

When we observed the effect of the transition between non-polar solvents (Chloroform) and polar solvents (DMSO) the Band-Gap between Chloroform-DMSO does not exceed 0.03 eV, indicating that this property is not significantly affected by the solvent.

7. Conclusion

Studies of the structural and electrical properties of (*E*)-pent-2-enoic acid (CAD) with structural formula $C_5H_8O_2$ have been performed by the Hirshfeld surface analysis and the DFT/CAM-B3LYP and MP2 theory both with the 6-311++*G(d,p)* basis set. The SM approach was used to simulate crystalline environment of the CAD crystal. The dipole moment, linear polarizability and second hyperpolarizabilities were calculated for CAD isolated and

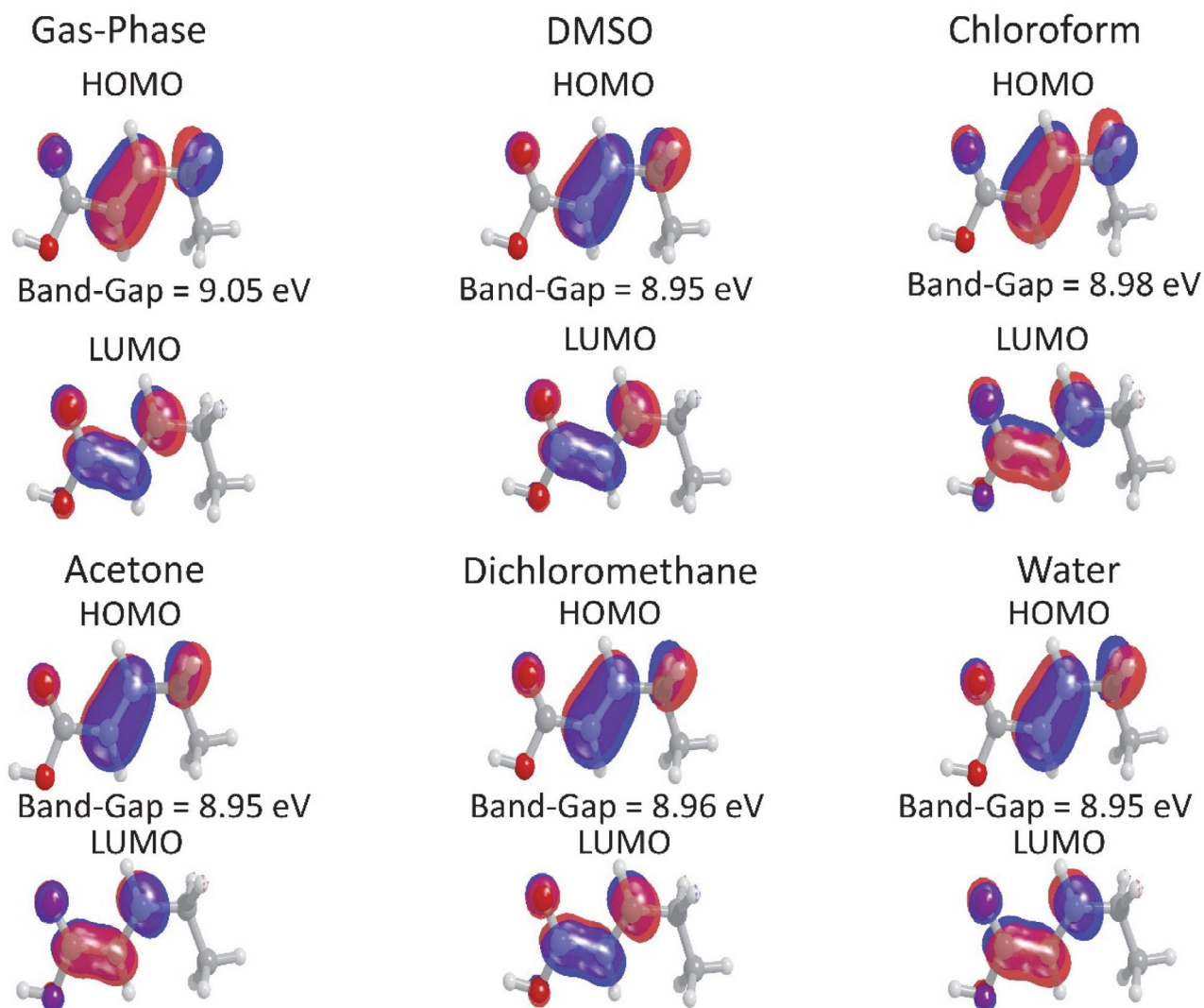


Figure 12: The HOMO-LUMO frontier orbital for the compound $C_5H_8O_2$ in different solvent media.

embedded molecules. For CAD embedded molecule an estimation of the linear refractive index and the third-order nonlinear susceptibility, both static and dynamic, are performed and the results compared with available experimental results. Also the effects of solvent medium on the molecular properties were considered through the PCM method, and the HOMO and LUMO energies were calculated. The band gap energies ranged from 8.95eV (DMSO) to 9.05eV (gas-phase). In addition, the global chemical reactivity descriptors were calculated and the results reveal that the CAD molecule possesses good chemical strength and stability.

The molecular structure of the CAD crystal were explored by Hirshfeld surface analysis and the associated 2D-fingerprint plots calculated using Crystal Explorer software.^{38,39}The intermolecular contacts that were explored are as follows: C...C, C...H, C...O, H...H and H...O. The intercontacts H...O shown in figure 6 (fingerprint) presents characteristic peaks that provide evidence of non-classical hydrogen bonding, including reciprocal contacts with 34.3% of the total surface. The contacts of type H...H show the highest contributions with a total of 52.5% followed by C...H (8.7%), C...C (2.5%) and C...O (1.6%). The vibrational modes behavior and the functional groups present in CAD were studied by FT-IR.

Our theoretical results show that the crystalline environment polarization effect on the average linear polarizability and average second hyperpolarizability is small, in the static and dynamic situation, but the third-order electric susceptibility (IDRI) of the CAD crystal is 9.94, 11.49, and 9.65 times greater than the chalcone derivatives 4Br4MSP, 3Br4MSP and 4N4MSP respectively,⁵⁶ and near 10 times larger than the fused silica,⁴⁵ this latter usually being taken as reference. As consequence, the CAD exhibits a good nonlinear optical effect.

8. References

- I. SHEIKHSOAE and W. FABIAN, *Dye. Pigment.*, **2006**, *70*, 91–98. DOI: 10.1016/j.dyepig.2005.04.011.
- V. Jeux, O. Segut, D. Demeter, T. Rousseau, M. Allain, C. Dalinot, L. Sanguinet, P. Leriche and J. Roncali, *Dye. Pigment.*, **2015**, *113*, 402–408. DOI: 10.1016/j.dyepig.2014.09.012.
- A. Iwan and D. Sek, *Prog. Polym. Sci.*, **2011**, *36*, 1277–1325. DOI: 10.1016/j.progpolymsci.2011.05.001.
- H.-J. Niu, Y.-D. Huang, X.-D. Bai and X. Li, *Mater. Lett.*, **2004**, *58*, 2979–2983. DOI: 10.1016/j.matlet.2004.05.007.
- L.-Y. Kong, Z.-W. Li, T. Okamura, G.-H. Ma, Q. Chu, H.-F. Zhu, S.-H. Tang, W.-Y. Sun and N. Ueyama, *Chem. Phys. Lett.*, **2005**, *416*, 176–181. DOI: 10.1016/j.cplett.2005.09.074.
- İ. Kaya, M. Yıldırım and A. Avcı, *Synth. Met.*, **2010**, *160*, 911–920. DOI: 10.1016/j.synthmet.2010.01.044.
- A. L. Briseno, S. C. B. Mannsfeld, C. Reese, J. M. Hancock, Y. Xiong, S. A. Jenekhe, Z. Bao and Y. Xia, *Nano Lett.*, **2007**, *7*, 2847–2853. DOI: 10.1021/nl071495u.
- L. Tan, W. Jiang, L. Jiang, S. Jiang, Z. Wang, S. Yan and W. Hu, *Appl. Phys. Lett.*, **2009**, *94*, 153306. DOI: 10.1063/1.3120769.
- M. Jazbinsek, L. Mütter and P. Gunter, *IEEE J. Sel. Top. Quantum Electron.*, **2008**, *14*, 1298–1311. DOI: 10.1109/JSTQE.2008.921407.
- C. Polisseni, K. D. Major, S. Boissier, S. Grandi, A. S. Clark and E. A. Hinds, *Opt. Express*, **2016**, *24*, 5615. DOI: 10.1364/OE.24.005615.
- L. Zhang, E. Pavlica, X. Zhong, F. Liscio, S. Li, G. Bratina, E. Orgiu and P. Samori, *Adv. Mater.*, **2017**, *29*, 1605760. DOI: 10.1002/adma.201605760.
- W. Sun, M. M. McKerns, C. M. Lawson, G. M. Gray, C.-L. Zhan and D.-Y. Wang, **2000**, p. 280 DOI: 10.1117/12.408515.
- A. Ronchi, T. Cassano, R. Tommasi, F. Babudri, A. Cardone, G. M. Farinola and F. Naso, *Synth. Met.*, **2003**, *139*, 831–834. DOI: 10.1016/S0379-6779(03)00274-1.
- A. J. Kiran, D. Udayakumar, K. Chandrasekharan, A. V. Adhikari and H. D. Shashikala, *J. Phys. B At. Mol. Opt. Phys.*, **2006**, *39*, 3747–3756. DOI: 10.1088/0953-4075/39/18/005.
- Y. Gao, Q. Chang, H. Ye, W. Jiao, Y. Song, Y. Wang and J. Qin, *Appl. Phys. B*, **2007**, *88*, 255–258. DOI: 10.1007/s00340-007-2687-6.
- B. Lands, *Nutrients*, **2012**, *4*, 1338–1357. DOI: 10.3390/nu4091338.
- A. A. Spector, H. Kim and E. Century, *J. Lipid Res.*, **2015**, *56*, 11–21. DOI: 10.1194/jlr.R055095.
- M. S. BLUM, A. F. NOVAK and S. TABER, *Science (80-.)*, **1959**, *130*, 452–453. DOI: 10.1126/science.130.3373.452.
- S. R. TOWNSEND GE, MORGAN JF, TOLNAI S, HAZLETT B, MORTON HJ, *Cancer Res.*, **1960**, *20*, 503–510.
- T. C. Murphy, C. Poppe, J. E. Porter, T. J. Montine and M. J. Picklo Sr, *J. Neurochem.*, **2004**, *89*, 1462–1470. DOI: 10.1111/j.1471-4159.2004.02442.x.
- M. Sonneck, T. Poppel, A. Spannenberg and S. Wohlrab, *Crystals*, **2015**, *5*, 466–474. DOI: 10.3390/cryst5040466.
- T. Poppel, M. Sonneck, A. Spannenberg and S. Wohlrab, *Acta Crystallogr. Sect. E Crystallogr. Commun.*, **2015**, *71*, o323–o323. DOI: 10.1107/S2056989015007380.
- T. Poppel, M. Sonneck, A. Spannenberg and S. Wohlrab, *Acta Crystallogr. Sect. E Crystallogr. Commun.*, **2015**, *71*, o316–o316. DOI: 10.1107/S2056989015007203.
- M. Sonneck, T. Poppel, A. Spannenberg and S. Wohlrab, *Acta Crystallogr. Sect. E Crystallogr. Commun.*, **2015**, *71*, o426–o427. DOI: 10.1107/S2056989015009469.
- M. Sonneck, T. Poppel, A. Spannenberg and S. Wohlrab, *Acta Crystallogr. Sect. E Crystallogr. Commun.*, **2015**, *71*, o528–o529. DOI: 10.1107/S2056989015011937.
- A. N. Castro, L. R. Almeida, M. M. Anjos, G. R. Oliveira, H. B. Napolitano, C. Valverde and B. Baseia, *Chem. Phys. Lett.*, **2016**, *653*, 122–130. DOI: 10.1016/j.cplett.2016.04.070.
- T. L. Fonseca, M. A. Castro, H. C. B. de Oliveira and S. Cunha, *Chem. Phys. Lett.*, **2007**, *442*, 259–264. DOI: 10.1016/j.cplett.2007.06.020.
- T. L. Fonseca, H. C. B. de Oliveira, O. A. V. Amaral and M. A. Castro, *Chem. Phys. Lett.*, **2005**, *413*, 356–361. DOI: 10.1016/j.cplett.2005.08.007.

29. H. C. B. de Oliveira, T. L. Fonseca, M. A. Castro, O. A. V. Amaral and S. Cunha, *J. Chem. Phys.*, **2003**, *119*, 8417–8423. DOI: 10.1063/1.1612474.
30. L. R. Almeida, M. M. Anjos, G. C. Ribeiro, C. Valverde, D. F. S. Machado, G. R. Oliveira, H. B. Napolitano and H. C. B. de Oliveira, *New J. Chem.*, **2017**, *41*, 1744–1754. DOI: 10.1039/C5NJ03214H.
31. D. F. S. Machado, T. O. Lopes, I. T. Lima, D. A. da Silva Filho and H. C. B. de Oliveira, *J. Phys. Chem. C*, **2016**, *120*, 17660–17669. DOI: 10.1021/acs.jpcc.6b01567.
32. B. Baseia, F. Osório, L. Lima and C. Valverde, *Crystals*, **2017**, *7*, 158. DOI: 10.3390/cryst7060158.
33. A. N. Castro, F. A. P. Osório, R. R. Ternavisk, H. B. Napolitano, C. Valverde and B. Baseia, *Chem. Phys. Lett.*, **2017**, *681*, 110–123. DOI: 10.1016/j.cplett.2017.05.066.
34. C. Valverde, R. F. N. Rodrigues, D. F. S. Machado, B. Baseia and H. C. B. de Oliveira, *J. Mol. Model.*, **2017**, *23*, 122. DOI: 10.1007/s00894-017-3274-3.
35. R. F. N. Rodrigues, L. R. Almeida, F. G. dos Santos, P. S. Carvalho Jr, W. C. de Souza, K. S. Moreira, G. L. B. de Aquino, C. Valverde, H. B. Napolitano and B. Baseia, *PLoS One*, **2017**, *12*, e0175859. DOI: 10.1371/journal.pone.0175859.
36. G. C. Ribeiro, L. R. Almeida, H. B. Napolitano, C. Valverde and B. Baseia, *Theor. Chem. Acc.*, **2016**, *135*, 244. DOI: 10.1007/s00214-016-1999-1.
37. W. F. Vaz, J. M. F. Custodio, R. G. Silveira, A. N. Castro, C. E. M. Campos, M. M. Anjos, G. R. Oliveira, C. Valverde, B. Baseia and H. B. Napolitano, *RSC Adv.*, **2016**, *6*, 79215–79227. DOI: 10.1039/C6RA14961H.
38. S. K. Wolff, D. J. Grimwood, J. J. McKinnon, M. J. Turner, D. Jayatilaka and M. A. Spackman, **2012**.
39. D. Jayatilaka, S. K. Wolff, D. J. Grimwood, J. J. McKinnon and M. A. Spackman, *Acta Crystallogr. Sect. A*, **2006**, *62*, s90.
40. O. L. Santos, J. R. Sabino, H. C. Georg, T. L. Fonseca and M. A. Castro, *Chem. Phys. Lett.*, **2017**, *669*, 176–180. DOI: 10.1016/j.cplett.2016.12.042.
41. T. L. Fonseca, J. R. Sabino, M. A. Castro and H. C. Georg, *J. Chem. Phys.*, **2010**, *133*, 144103. DOI: 10.1063/1.3501237.
42. O. L. Santos, T. L. Fonseca, J. R. Sabino, H. C. Georg and M. A. Castro, *J. Chem. Phys.*, **2015**, *143*, 234503. DOI: 10.1063/1.4937481.
43. D. A. Kleinman, *Phys. Rev.*, **1962**, *126*, 1977–1979. DOI: 10.1103/PhysRev.126.1977.
44. K. Senthil, S. Kalainathan, A. R. Kumar and P. G. Aravindan, *RSC Adv.*, **2014**, *4*, 56112–56127. DOI: 10.1039/C4RA09112D.
45. U. Gubler and C. Bosshard, *Phys. Rev. B*, **2000**, *61*, 10702–10710. DOI: 10.1103/PhysRevB.61.10702.
46. D. Jayatilaka, D. J. Grimwood, J. J. McKinnon, A. Lee, A. Lemay, A. J. Russel, C. Taylo, S. K. Wolff, Cassam-Chenai and A. Whitton, **2005**.
47. D. Jayatilaka and D. J. Grimwood, eds. P. M. A. Slood, D. Abramson, A. V. Bogdanov, Y. E. Gorbachev, J. J. Dongarra and A. Y. Zomaya, Springer Berlin Heidelberg, Berlin, Heidelberg, **2003**, pp. 142–151. DOI: 10.1007/3-540-44864-0_15.
48. S. S. Batsanov, *Inorg. Mater.*, **2001**, *37*, 871–885. DOI: 10.1023/A:1011625728803.
49. A. Bondi, *J. Phys. Chem.*, **1964**, *68*, 441–451. DOI: 10.1021/j100785a001.
50. N. K. Nkungli and J. N. Ghogomu, *J. Theor. Chem.*, **2016**, *2016*, 1–19. DOI: 10.1155/2016/7909576.
51. T. Pluta and A. J. Sadlej, *J. Chem. Phys.*, **2001**, *114*, 136. DOI: 10.1063/1.1328398.
52. X. Song and S. O. Farwell, *J. Anal. Appl. Pyrolysis*, **2004**, *71*, 901–915. DOI: 10.1016/j.jaap.2003.12.002.
53. C. Valverde, F. A. P. Osório, T. L. Fonseca and B. Baseia, *Chem. Phys. Lett.*, **2018**, *706*, 170–174. DOI: 10.1016/j.cplett.2018.06.001.
54. S. Marques, M. A. Castro, S. A. Leão and T. L. Fonseca, *Chem. Phys. Lett.*, **2016**, *659*, 76–79. DOI: 10.1016/j.cplett.2016.07.009.
55. D. M. Bishop and D. W. De Kee, *J. Chem. Phys.*, **1996**, *104*, 9876–9887. DOI: 10.1063/1.471752.
56. E. D. D'silva, G. K. Podagatlapalli, S. Venugopal Rao and S. M. Dharmaparakash, *Mater. Res. Bull.*, **2012**, *47*, 3552–3557. DOI: 10.1016/j.materresbull.2012.06.063.
57. P. Günter, *Nonlinear Optical Effects and Materials*, Springer Berlin Heidelberg, Berlin, Heidelberg, **2000**, vol. 72. DOI: 10.1007/978-3-540-49713-4.

Povzetek

V tem prispevku poročamo o strukturnih in električnih lastnostih derivata karboksilne kisline (CAD) s strukturno formulo $C_5H_8O_2$ (*E*-pent-2-enojske kisline). Z uporabo perturbacijske teorije Møller-Plesset (MP2) in teorije gostotnega funkcionala (DFT/CAM-B3LYP) z baznim setom 6-311++G(*d,p*) smo izračunali dipolni moment, linearno polarizabilnost ter prvo in drugo hiper-polarizabilnost v prisotnosti statičnega in dinamičnega električnega polja. S super-molekularnim pristopom smo simulirali kristalno fazo CAD in vplive polarizacije okolja na njene električne parametre. Dobili smo statično in dinamično oceno linearnega lomnega količnika in nelinearne susceptibilnosti tretjega reda za kristal in jih primerjali z razpoložljivimi eksperimentalnimi rezultati. Značilni vibracijski načini in funkcionalne skupine, ki so prisotne v CAD, so bili analizirani s Fourier Transform infrardečo spektroskopijo (FT-IR) v območju 400–4000 cm^{-1} . S Hirshfeldovo analizo površine smo raziskali molekularno strukturo in lastnosti vibracijskih načinov kristala CAD. Vpliv topila na molekularne lastnosti je upoštevan s pomočjo modela polarizabilnega kontinuuma (PCM). Hkrati smo obravnavali mejne molekularne orbitale, energije in globalno kemijsko reaktivnost deskriptorjev. Vse študirane lastnosti kažejo, da lahko predstavljeni material smatramo za nelinearen optičen material.

Scientific paper

Synthesis of Fe₃O₄ Nanoparticles Modified by Oak Shell for Treatment of Wastewater Containing Ni(II)

Seyyed Mojtaba Mousavi,¹ Seyyed Alireza Hashemi,¹ Hossein Esmaili,^{2,*}
Ali Mohammad Amani³ and Fatemeh Mojoudi⁴

¹ Department of Medical Nanotechnology, School of Advanced Medical Sciences and Technologies, Shiraz University of Medical Sciences, Shiraz, Iran

² Department of Chemical Engineering, Bushehr Branch, Islamic Azad University, Bushehr, Iran

³ Department of Medical Nanotechnology, School of Advanced Medical Sciences and Technologies, Shiraz University of Medical Sciences, Shiraz, Iran

⁴ Department of Environment, Faculty of Natural Resources, College of Agriculture & Natural Resources, University of Tehran, Karaj, Iran

* Corresponding author: E-mail: esmaeli.hossein@gmail.com & esmaeli.hossein@iaubushehr.ac.ir

Received: 13-06-2018

Abstract

In present study, removal of nickel ions (Ni (II)) from synthetic wastewater using Fe₃O₄ nanoparticles modified by oak shell was investigated. The FTIR analysis of the adsorbent suggested the occurrence of interaction between the carboxyl group on oak shell modified magnetic nanoparticles (OSMMN) surface and Ni (II). Also, the morphology and size of the adsorbent were observed by SEM and TEM. Additionally, the effect of different parameters such as contact time, adsorbent dose, solution pH and initial concentration of nickel (II) ions were investigated on the adsorption of nickel. The adsorption experiments showed that the maximum Ni(II) adsorption was obtained as contact time = 15 min, temperature = 25 °C, adsorbent dosage = 2.6 g/L, and pH = 4.5. In these conditions, 93.88% Ni(II) was removed from aqueous solution. Moreover, in order to study equilibrium behavior of adsorption, Langmuir and Freundlich isotherm models were applied. The results showed that the experimental data were fitted well with the Langmuir isotherm model, and the maximum adsorption capacity of the adsorbent using Langmuir model was determined to be 454.54 mg/g which was a considerable amount.

Keywords: Oak shell; magnetic nanoparticles; adsorption; synthetic wastewater; nickel

1. Introduction

Heavy metal contamination of water is a common phenomenon. The effluent of a number of industrial and metallurgical processes like plating, photography, aerospace, atomic energy and petrochemical facilities can result heavy metals pollution in the water resources, if the metal content is not treated.^{1,2} So, the discharge of heavy metals into an aquatic ecosystem has become a matter of concern over the last decades because of their extreme toxicity and tendency for bioaccumulation in the food chain even in relatively low concentrations.³ Pollutants of serious concern include lead, chromium, mercury, uranium, selenium, zinc, arsenic, cadmium, gold, copper and nickel.⁴ Nickel is a toxic heavy metal that is widely used in silver

refineries, electroplating, zinc base casting and storage battery industries.⁵ The chronic toxicity of nickel to humans and the environment has been well documented. For example, high concentration of nickel (II) causes cancer of the lungs, nose and bone. It is essential to remove Ni (II) from industrial wastewater before being discharged.

There are a number of methods for removal of heavy metals from aqueous solutions and industrial wastewater. Common removal techniques of heavy metals from industrial wastewaters are chemical precipitation, ion change, solvent extraction, reverse osmosis, ultrafiltration, electro-dialysis and adsorption. Adsorption technique is an attractive method for water treatment, especially if the adsorbent is costly efficient, convenient to separate and easy to regenerate.^{6,7} Nowadays, bio-adsorption is used for

heavy metals ions removal and is highly favorable. In such biologic adsorption processes, many biomaterials are employed. Using agricultural residues or industrial by-products having biological activities has received a considerable attention.⁸ In recent years, a number of agricultural materials such as moss peat,^{5,9} banana peels,^{10,11} orange peel,¹² peanut hulls,¹³ activated charcoal,¹⁴ almond husk,¹⁵ eggshell¹⁶ and other unimportant agricultural wastes have been used to remove heavy metals contaminants. Recently, magnetic particles have also gained special attention in water treatment.¹⁷ In terms of simplicity, high potential, high surface area and high efficiency to removal heavy metal ions from waste water. Of these particles, Fe₃O₄ is the traditional particle that is extensively used in wastewater treatment; because of their high activities, hydrophilic, chemically stable, non-toxic and magnetic. Also, it's an environment-friendly adsorbent, cheap and available.^{18,19,20}

The purpose of this study was to determine the potential and adsorption capacity of Fe₃O₄ nanoparticles modified by oak shell (OSMMN) for the removal of Ni (II) from aqueous solution. The effect of various parameters such as namely contact time, adsorbent dose, pH, and the initial concentration of Ni(II) ions was studied. Also, the equilibrium behavior of adsorbent was investigated. To the best of author's knowledge, this is the first report of the application of OSMMN for attenuation of Ni ions from aqueous solution.

2. Materials and Methods

2.1. Chemicals and Devices

All chemicals and reagents were analytical grade. FeCl₂·4H₂O (99.9%), FeCl₃·6H₂O (96%), KCl salt, citrate, hydrochloric acid (37%) and ammonia (NH₃OH) solution (25%), were purchased from Merck company (Darmstadt, Germany) and used without further purification. Nickel was also purchased from Sigma-Aldrich (Germany) and oak shell was collected from local trees. The amount of Ni (II) in aqueous solutions was measured by using Cintra 101 spectrophotometer (GBC Specific Equipment, Australia) at a wavelength of 546 nm before and after adsorption process. Also, the citrate buffer solution with pH 4.5 was prepared using citric acid (0.1 M), NaOH and HCL (0.1 M). In addition, a transmission electron microscope (TEM, 906E, LEO, Germany), Scanning electron microscope (SEM, VEGA, TESCAN), pH-meter (632Metrohm, Herisau, Switzerland) and a super magnet (1.2 T, 10 cm × 5 cm × 2 cm) were used in the experiments. Moreover, Dynamic Light Scattering (HORIBA Jobin Yvon, SZ-100) is applied for measuring the particle size distribution of the adsorbent.

2.2 Preparation of Fe₃O₄ Nanoparticles Modified by Oak Shell

Magnetic oak shell nanoparticles was prepared by co-precipitation method. To do so, Fe₃O₄ nanoparticles

were synthesized by co-precipitation of 4 mmol ferric (FeCl₃·6H₂O) and 2 mmol ferrous salts (FeCl₂·4H₂O) in distilled water. After stirring for 1 h, chemical precipitation was achieved at 80 °C under vigorous stirring by adding 40 ml of NH₄OH solution. During the reaction process, the pH was maintained approximately at 10. After adding ammonia solution, it was stirred for 1 h. Afterwards, the precipitate was washed with distilled water for removal of all existing in the effluents. Next, using a magnet, the magnetic adsorbent was collected at the bottom of the balloon and the solution was discarded. After preparing Fe₃O₄, one gram of oak shell was added to the solution and stirred for 20 min. Then, in order to oxidize the mixture, NH₄OH solution added as dropwise and stirring continued for 50 min, and stirring was then stopped. After, the product was separated from the solution using a magnetic field and washed with distilled water. The solution was then heated in an oven at 105 °C for 24 h until dry. After cooling, the adsorbent was pulverized by a mill.

2.3. Adsorption Experiments

The adsorption experiments were done using batch method. 0.03 g of magnetic oak shell nanoparticles were equilibrated with 50 ml of solution containing nickel. The pH value of the samples was adjusted by using diluted solutions of NaOH and HCl (0.1 M). After addition of magnetic oak shell nanoparticles, the resulting solution was stirred for 5 min. Then, the suspension was allowed to settle by a magnet and the supernatant was analyzed to measure the remaining nickel by atomic absorption apparatus.

In all experiments, bio-adsorption percentage of Ni ions (R%) was calculated with equation 1:

$$R(\%) = \left(\frac{C_o - C_f}{C_o} \right) * 100 \quad (1)$$

Where C₀ and C_f represent the initial and final ion concentrations, respectively. Also, all experiments were done duplicate.

2.4. Desorption Process

For the desorption test, the adsorbed nickel ions on the adsorbent were transferred to a flask containing 100 mL of desorbing agent such as HNO₃. The mixture was stirred at 200 rpm using a magnetic stirrer at room temperature for 2 h and the desorbed nickel(II) concentration in the solution were determined by spectrophotometer. The desorption process was done consecutively six cycles.

3. Results and Discussion

3.1. Characterization of Biosorbent

To characterize the functional groups in bio-adsorbent, FTIR analysis was applied. The FT-IR spectra of

Fe_3O_4 nanoparticles in the range of $400\text{--}4000\text{ cm}^{-1}$ is represented in Fig. 1-a. An adsorption band at 593 cm^{-1} is belonged to the vibrations of the Fe-O functional group. The bands appearing at 3447 cm^{-1} can be attributed to O-H group that cover iron oxide surfaces in an aqueous environment. Modification of oak shell onto the Fe_3O_4 MNPs was also ascertained by FTIR. As shown in Fig. 1-b, the sharp peak at 612 cm^{-1} corresponds to Fe-O vibration in magnetite. The peak at 3412 cm^{-1} belongs to the N-H bond of oak shell that indicates the presence of oak shell onto magnetic iron oxide nanoparticles. Also, several peaks have been viewed in this Figure which can be related to the groups of C=C, N-H and etc.

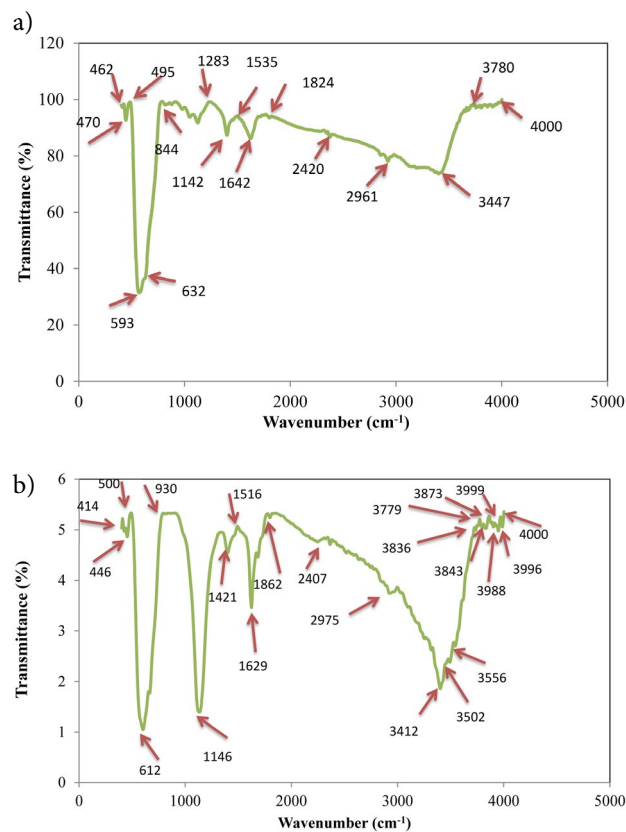


Fig. 1: (a) FT-IR spectra of Fe_3O_4 nanoparticles and (b) FT-IR spectra of OSMMN

Furthermore, SEM and TEM images provide information about morphology and size of oak shell magnetic nanoparticles. Figs. 2 and 3 are shown SEM and TEM images, respectively. It can be observed that the magnetic nanoparticles with the average size of 40 nm have a high surface area and abundant pore for adsorption of ions.

Also, particle size distribution of a material can be important to understand the average particle size. Particle size distribution of adsorbent is displayed in Fig. 4. As shown in this Fig., the average size of particles is about 10 nm which shows the particle size of the adsorbent is on a nano scale.

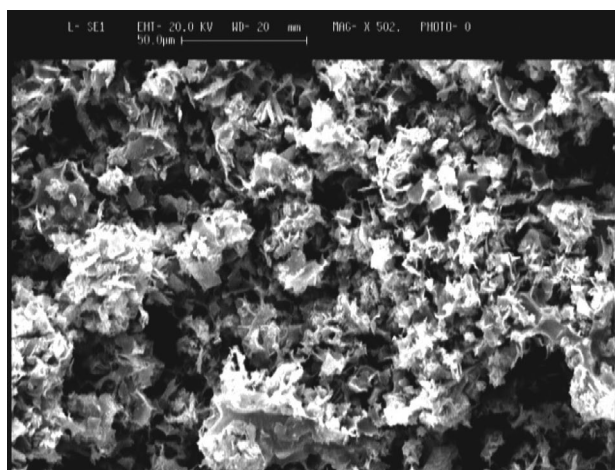


Fig. 2: SEM image of OSMMN

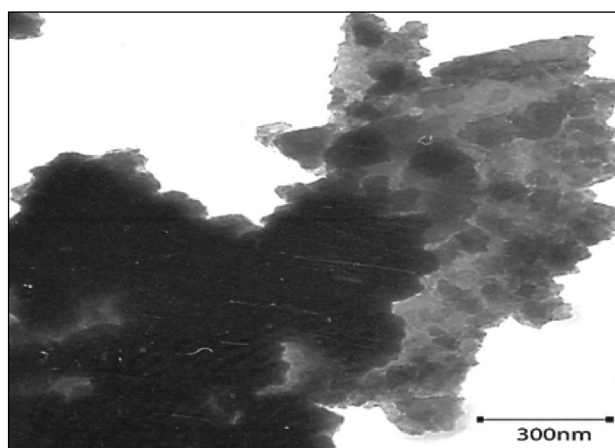


Fig. 3: TEM image of OSMMN

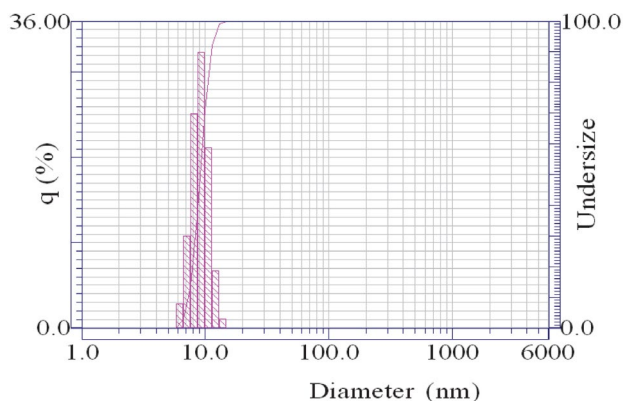


Fig. 4: Particle size distribution of Fe_3O_4 nanoparticles modified by oak shell

3. 2. Effect of Solution pH and Buffer Volume

Initial solution pH is one of the effective parameters in adsorption of metal ions, because hydrogen ion competes with metal ion to relocate active sites of the

adsorbent.²¹ The effect of pH was conducted by mixing 0.03 g (0.6 g/L) of adsorbent in 50 ml Ni (II) solution with the concentration of 20 mg/L. HCl and NaOH was used for the purpose of keeping pH in the range of 4–7 throughout the experiments. The effect of pH on the removal of Ni²⁺ from aqueous solution is presented in Fig. 5. It can be observed that the removal of nickel ions increased with increasing pH and reached a maximum value at pH 4.5. At lower pH values, Ni (II) ion removal was inhibited, because at low pHs the medium contains a high concentration of hydrogen ions, therefore competition between H⁺ and Ni²⁺ ions for the available adsorption sites could be possible. The percentage removal of Ni was observed to be sharp between pH value of 4.5 to 7 (from the percentage removal of 92.2% to 66.38%). At pH values greater than 4.5, the adsorption of Ni (II) ions decreases because of the precipitation of nickel hydroxide resulting from Ni (II) ions reacting with hydroxide ions. In further works, the pH of the solutions was adjusted by using citrate buffer volume. The effect of buffer volume on the removal efficiency is displayed in Fig. 6. As shown in this Fig., the removal yield was increased with increasing buffer volume and the maximum efficiency was obtained at 3 ml of buffer solution with the adsorption of 92.8%.

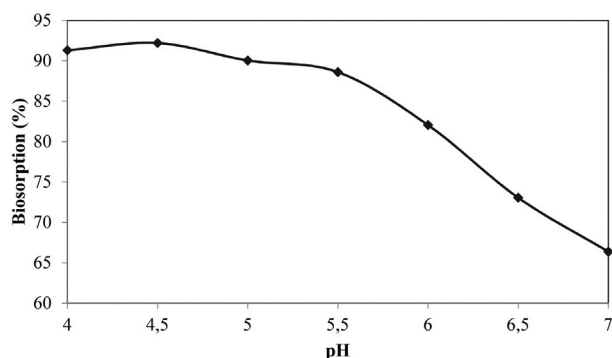


Fig. 5: Effect of solution pH on Ni (II) removal (Conditions: temperature of 25 °C, initial ion concentration of 20 mg/L, contact time 5 min, adsorbent dose of 0.6 g/L).

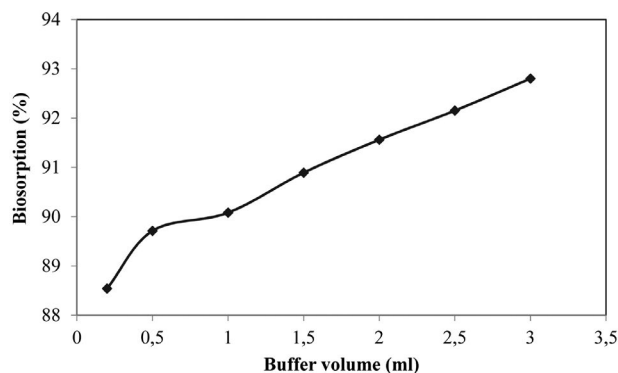


Fig. 6: Effect of buffer volume (ml) of solution on Ni (II) removal.

3. 3. Effect of Electrolyte

The effect of electrolyte concentration (adjusted by KCl) on the adsorption of Ni (II) is illustrated in Fig. 7. As shown in this Figure, the adsorption efficiency of Ni (II) decreased within the concentration range of 0–1 mol/L of KCl in the test solution. At higher concentration, the Ni ion removal efficiency was decreased. So, it is concluded that the presence of KCl electrolyte has negative effect on bio-adsorption of Ni (II) ions using oak shell magnetic nanoparticles and a concentration of 0.0 mol/L (93.52% removal) was used for further works.

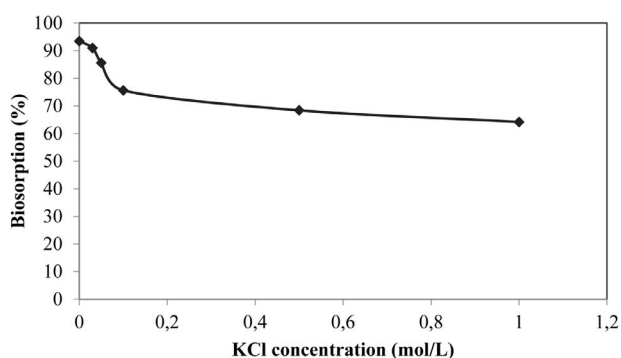


Fig. 7: Effect of electrolyte concentration (adjusted by KCl) on the removal of Ni (II)

3. 4. Effect of Temperature

The effect of temperature on the adsorption of Ni (II) from synthetic wastewater was examined within the temperature range of 5–25 °C. The effect of temperature on nickel (II) removal using OSMMN is illustrated in Fig. 8. The results showed that the adsorption of Ni (II) using 0.6 g/L of OSMMN at the pH of 4.5 is increased versus variation of temperature. At 25 °C, the adsorption efficiency was 93.6% that the highest adsorption rate was obtained.

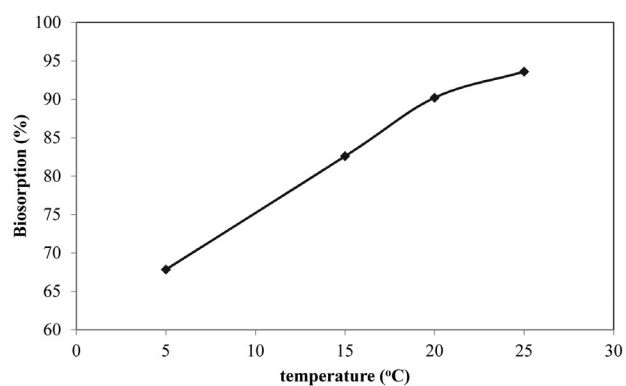


Fig. 8: Effect of temperature on Ni (II) removal from aqueous solution using OSMMN (Conditions: initial ion concentration 20 mg/L, contact time 5 min, adsorbent dosage 0.6 g/L and pH of 4.5).

3. 5. Bio-Adsorbent Dosage Effect

Adsorbent dosage is considered as an important parameter, because this parameter defines the capacity of ad-

sorbent.²² The effect of bioadsorbent dose on the removal of Ni (II) from aqueous solution was investigated in a batch system by adding various amounts of adsorbent (0.6–3 g/L) into a flask containing 50 mL of Ni (II) solution. The initial ion concentration and pH value of the solutions were fixed at 20 mg/L and 4.5 for all batch experiments, respectively. Also, the suspension was stirred for 5 min. After that time, the solution was coagulated and settled and the supernatant was analyzed for the remaining Ni (II). The results are shown in Fig. 9. The results revealed that as adsorbent dosage went up, the bio-adsorption also increased owing to rise in the number of active sites of bio-adsorbent. The optimum dosage of oak shell magnetic nanoparticles for removing Ni (II) was obtained 2.6 g/L with the maximum removal of 93.66%.

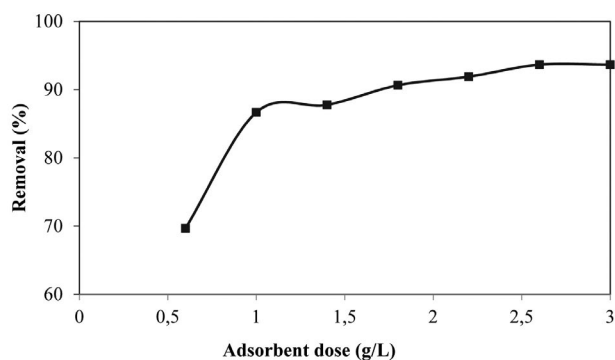


Fig. 9: Effect of OSMMN dosage on the removal of Ni (Conditions: temperature of 25 °C, initial ion concentration of 20 mg/L, contact time 5 min and pH of 4.5)

3. 6. Effect of Contact Time

Contact time is one of the important parameters in bio-adsorption process.^{23,24} The effect of stirring time on the performance of OSMMN in adsorbing Ni (II) was investigated. The solution pH and oak shell magnetic nanoparticles dosage were fixed at their obtained optimum values. Fig. 10 shows removal efficiencies for Ni (II) as a

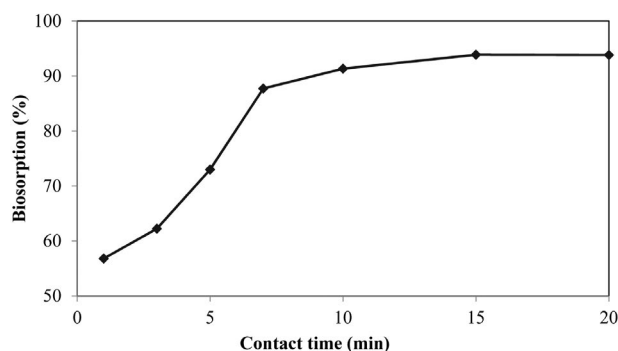


Fig. 10: Effect of contact time on Ni (II) removal (Conditions: temperature of 25 °C, initial ion concentration of 20 mg/L, pH of 4.5 and adsorbent dose of 2.6 g/L)

function of stirring times (1–20 min). These data elucidate that adsorption started immediately upon adding the magnetic oak shell particles to nickel solution. The removal efficiency of Ni (II) was rapidly increased from 56.81 % to 93.88 % as the stirring time was increased from 1 to 15 min. After 15 min, no change in biosorption was observed. So, according to these results, the optimum stirring time for removing nickel obtained 15 min.

3. 7. Modeling of Isothermal Adsorption

Adsorption isotherms are useful for the description of adsorption process and its mechanisms and also adsorption isotherms provide the basic requirements for designing adsorption process. Two important isotherm models were selected in this study, Langmuir and Freundlich isotherm models.^{20,23,25}

Freundlich model is an empirical model and can describe adsorption capability of adsorbents. This model is applied for non-ideal adsorption on heterogeneous surfaces. The linear form of this model is expressed by Equation 2.²³

$$\ln q_e = \ln K_F + \frac{1}{n} \ln C_e \quad (2)$$

In Eq. (2) K_F (Lg^{-1}) and n (dimensionless) are Freundlich isotherm constants and the degree of nonlinearity between solution concentration and adsorption, respectively. The plot of $\ln q_e$ versus $\ln C_e$ for the adsorption was employed to generate K_F and n from the intercept and the slope values, respectively (Fig. 11-a).

Also, the Langmuir model describes the monolayer bio-sorption process onto the adsorbent surface with specific binding sites. The linear form of Langmuir model is written as follows:²³

$$\frac{C_e}{q_e} = \frac{1}{K_L q_m} + \frac{C_e}{q_m} \quad (3)$$

In Eq. (3), q_m is the monolayer adsorption capacity (mg/g); and K_L is the Langmuir constant (L/mg), and is related to the free energy of adsorption. A plot of C_e/q_e versus C_e for the adsorption of Ni onto bio-adsorbent shows a straight line of slope, $1/q_m$, and intercept, $1/K_L q_m$ (Fig. 11 (b)). In order to determine the variability of adsorption, a dimensionless constant called as separation parameter ' R_L ' was used and defined as in the Equation (4).

$$R_L = \frac{1}{1 + K_L C_o} \quad (4)$$

Where C_o is the highest initial Ni concentration (mg/L). The value of separation parameter indicates the shape of isotherm to be either favorable ($0 < R_L < 1$), unfavorable ($R_L > 1$), linear ($R_L = 1$) or irreversible ($R_L = 0$).^{23,24}

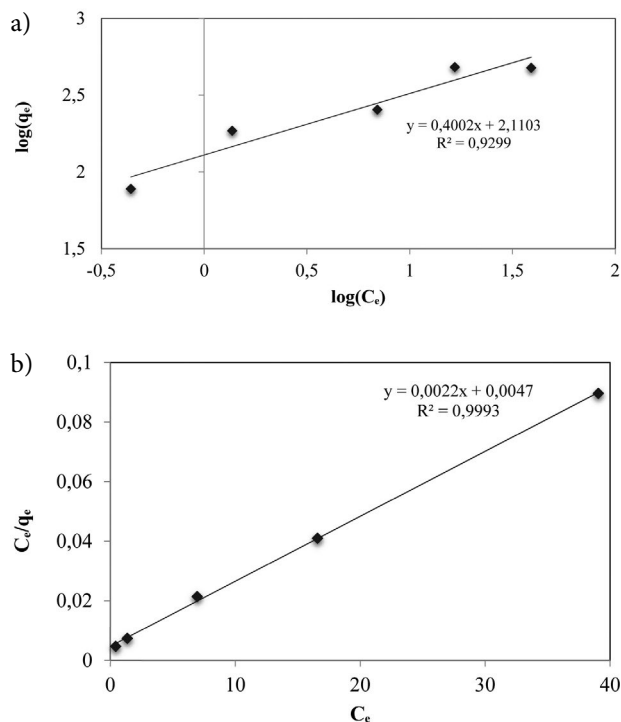


Fig. 11: The adsorption isotherm curves related to a) Freundlich and b) Langmuir models for adsorption of Ni (II) on oak shell modified by magnetic nanoparticle.

The capacities of magnetic oak shell nanoparticles to adsorb Ni (II) were examined by measuring the initial and the final concentration of Ni (II) at the pH of 4.5 and the temperature of 25 °C in a batch system. Both Langmuir and Freundlich adsorption isotherms were used to normalize the adsorption data. The correlation of ion adsorption data with the Langmuir isotherm model was higher (with R^2 values of 0.9993) than the Freundlich model ($R^2 = 0.9299$). Summarizes the models, constants, and coefficients are listed in Table 1. According to this table, the maximum predictable adsorption capacity of Ni (II) is 454.54 mg ion/g adsorbent. K_L represents the equilibrium biosorption constant and therefore, higher values of K_L led to an optimal adsorption process.

Table 1: Parameters and constants of Langmuir and Freundlich isotherm models for the removal of Ni(II) by means of OSMMN.

Langmuir	
Parameters	Values
q_{max} (mg/g)	454.54
K_L (L/mg)	0.46
R^2	0.9993
Freundlich	
K_F (mg/g)	8.24
n	5.75
R^2	0.9299

3. 8. Recycling of the Adsorbent

The ability of recovering and reusing of the adsorbent was tested in several steps of adsorption and desorption. The result is shown in Figure 12. As shown in Figure 12, 78% of nickel was desorbed from the adsorbent after first cycle and after 6 cycles, there were slight changes in nickel desorption. So, it was concluded that the desired removal of 90% can be achieved after 6 cycles.

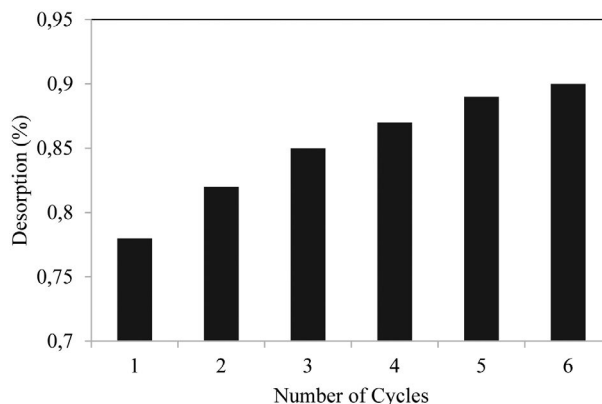


Fig. 12: Desorption of Ni(II) from the adsorbent after six cycles

4. Conclusions

Fe_3O_4 nanoparticles modified by oak shell was used as an applicatory bio-adsorbent for Ni (II) removal from aqueous solution. The effect of pH, adsorbent dosage, temperature, buffer volume, electrolyte and time were studied. The maximum removal of Ni (II) is found to be 93.88% at pH 4.5, temperature of 25 °C, adsorbent dose of 2.6 g/L and contact time of 15 min. The experimental data fitted well with the Langmuir model. Based on Langmuir model, the maximum adsorption capacity of Ni (II) was determined 454.54 mg/g. The capability of adsorbent to remove Ni (II) from aqueous solution efficiently after long cycles (e.g. 6 cycles) was acceptable. In General, resulting tests on the nickel ion removal from effluent using the OSMMN showed the potential applicability of this adsorbent in industrial wastewater treatment.

Conflict of Interests Statement

The authors declare that there is no conflict of interests.

5. References

1. M. Kobya, E. Demirbas, E. Senturk, M. Ince. *Bioresour. Technol.* **2005**, *96*, 1518–1521.
DOI:10.1016/j.biortech.2004.12.005.
2. S. Congeevaram, S. Dhanarani, J. Park, M. Dexilin, K. Thamaraiselvi.. *J. Hazard. Mater.* **2007**, *146*, 270–277.

- DOI:10.1016/j.jhazmat.2006.12.017.
3. M. Bansal, D. Singh, V. K. Garg, P. Rose, *Int. J. Civ. Environ. Eng.* **2009**, *1*, 108–114.
 4. P. E. Aikpokpodion, R. R. Ipinmoroti, S. M. Omotoso, *Am.-Eurasian J. Toxicol. Sci.* **2010**, *2*, 72–82.
 5. K. Kadirvelu, K. Thamaraiselvi, C. Namasivayam, *Sep. Purif. Technol.* **2001**, *24*, 497–505.
DOI:10.1016/S1383-5866(01)00149-6.
 6. F. M. Mohammed, E. P. L. Roberts, A. Hill, A. K. Campen, N. W. Brown, *Water Res.* **2011**, *45*, 3065–3074.
DOI:10.1016/j.watres.2011.03.023.
 7. F. Ahmadi, H. Esmaeili, *Desalin. Water Treat.* **2018**, *110*, 154–167. DOI:10.5004/dwt.2018.22228.
 8. T. W. Tee, A. R. M. Khan, *Environ. Technol. Lett.* **1988**, *9*, 1223–1232. DOI:10.1080/09593338809384685.
 9. L. Bulgariu, D. Bulgariu, M. Macoveanu, *Environ. Eng. Manag. J.* **2010**, *9*, 667–674.
 10. M. R. Mehrasbi, Z. Farahmandkia, B. Taghibeigloo, A. Taromi, *Water Air Soil Pollut.* **2009**, *199*, 343–351.
DOI:10.1007/s11270-008-9883-9.
 11. R. S. D. Castro, L. E. G. Caetano, P. M. Ferreira, M. Padilha, J. Margarida, L. F. Saeki, M. Zara, U. Antonio, G. Martinez, R. Castro, *Ind. Eng. Chem. Res.* **2011**, *50*, 3446–3451.
DOI:10.1021/ie101499e.
 12. L. Xiaomin, Y. Tang, X. Cao, D. Lu, F. Lu, W. Shao, *Colloids Surf. A Physicochem. Eng. Asp.* **2008**, *317*, 512–521.
DOI:10.1016/j.colsurfa.2007.11.031
 13. F. D. Oliveira, A. C. Soares, O. Freitas, S. A. Figueiredo, *Global NEST Journal* **2010**, *12*, 206–214.
 14. M. C. S. Minello, A. L. Paco, R. S. D. Castro, L. Caetano, P. M. Padilha, G. Ferreira, M. A. U. Martinez, G. R. Castro, *Fresen. Environ. Bull.* **2010**, *19*, 2210–2214.
 15. H. Hasar, *J. Hazard. Mater.* **2003**, *97*, 49–57.
DOI:10.1016/S0304-3894(02)00237-6.
 16. B. S. Zadeh, H. Esmaeili, R. Foroutan, *Indones. J. Chem.* **2018**. DOI:10.22146/ijc.28789.
 17. S. Lunge, S. Singh, A. Sinha, *J. Magn. Magn. Mater.* **2014**, *356*, 21–31. DOI: 10.1016/j.jmmm.2013.12.008
 18. R. Taman, M. E. Ossman, M. S. Mansour, H. A. Farag, *J. Ad. Chem. Eng.* **2015**, *5*, 125–132.
DOI:10.4172/2090-4568.1000125.
 19. M. Kumari, C. U. Pittman, D. Mohan, *J. colloid interface sci.* **2015**, *442*, 120–132. DOI:10.1016/j.jcis.2014.09.012.
 20. F. S. Khoo, H. Esmaeili, *J. Serb. Chem. Soc.* **2018**, *83*, 237–249.
DOI:10.2298/JSC170704098S.
 21. M. Rafatullah, O. Sulaiman, R. Hashim, A. Ahmad, *J. Hazard. Mater.* **2009**, *170*, 969–977.
DOI:10.1016/j.jhazmat.2009.05.066.
 22. R. Foroutan, H. Esmaeili, M. Abbasi, M. Rezakazemi, M. Mesbah., *Environ. Technol.* **2017**.
DOI:10.1080/09593330.2017.1365946
 23. F. S. Sarvestani, H. Esmaeili, B. Ramavandi, *3 Biotech.* **2016**, *6*, 251. DOI:10.1007/s13205-016-0570-z.
 24. R. Foroutan, H. Esmaeili, S. M. Derakhshandeh Rishehri, F. Sadeghzadeh, S. R. Mirahmadi, M. Kosarifarad, B. Ramavandi, *Data Brief.* **2017**, *12*, 485–492.
DOI:10.1016/j.dib.2017.04.031.
 25. R. Mahini, H. Esmaeili, R. Foroutan, *Turk. J. Biochem.* **2018**.
DOI:10.1515/tjb-2017-0333.

Povzetek

Študija preučuje odstranjevanje Ni (II) ionov iz odpadnih voda s pomočjo nanodelcev modificiranih z zmletimi želodovimi lupinami (OSMMN). FTIR analiza je pokazala interakcije med karboksilnimi skupinami prisotnimi na OSMMN in Ni (II) ioni. Morfologija magnetnih nanodelcev prekritih s prahom želodovih lupin je bila analizirane s pomočjo TEM. Preučevan je bil tudi vpliv kontaktnega časa, količine adsorbenta, pH vrednosti raztopine in začetne koncentracije Ni (II) ionov na učinkovitost adsorpcije. Eksperimenti so pokazali, da je maksimalna, 93.88 % adsorpcija dosežena pri pH vrednosti 4.5, koncentraciji adsorbenta 2.6 g/L, temperaturi 25 °C in kontaktnem času 15 min. Ravnotežne vrednosti adsorpcije so poskusili opisati tako z Langmuirjevo kot tudi s Freundlichovo izotermo, pri čemer se je izkazalo, da je boljše ujemanje doseženo z Langmuirjevo izotermo. Maksimalna ocenjena kapaciteta OSMMN s pomočjo Langmuirjeve izoterme je znašala 454.54 mg/g, kar je znatna količina.

Scientific paper

Multicomponent Solvent-Free Synthesis, Antibacterial Evaluation and QSAR Study of 2-(Bis(benzylthio)methylene) malononitriles

Hamid Beyzaei,* Parviz Baranipour, Reza Aryan, Pouya Karimi, Mahmood Sanchooli and Hojat Samareh Delarami

Department of Chemistry, Faculty of Science, University of Zabol, Zabol, Iran

* Corresponding author: E-mail: hbeyzaei@yahoo.com and hbeyzaei@uoz.ac.ir
Tel: +98 5431232186 / Fax: +98 5431232180

Received: 19-07-2018

Abstract

Multicomponent reaction of malononitrile, carbon disulphide and various benzyl halides was developed as an efficient strategy for the synthesis of 2-(bis(benzylthio)methylene)malononitrile derivatives *via* two different procedures: (a) in the presence of K_2CO_3 as a base in acetonitrile and (b) under solvent-free conditions in the presence of triethylamine. Higher yields with shorter reaction times were obtained from the latter procedure. Inhibitory activity of all derivatives was evaluated against 22 pathogenic bacteria including both Gram-negative and Gram-positive strains. Thioether **4b** showed broad-spectrum antibacterial activities according to the antibiogram tests. DFT calculations (B3LYP/6-311++G**) were performed to determine the type of drug–receptor interactions. It was found that reversible dipole–dipole forces play a key role in most interactions.

Keywords: Multicomponent reaction; solvent-free; thioether; antimicrobial activity; QSAR

1. Introduction

Organic compounds containing C–S–C bonds are known as sulfides or thioethers. These functional groups exist alone or alongside others in various pharmaceutical and biologically active molecules (Figure 1.). L-Methionine is a proteinogenic amino acid that plays an essential role in the growth of new blood vessels. It is a beneficial

supplement to treat schizophrenia, asthma, alcoholism, Parkinson's disease, drug withdrawal, copper poisoning, allergies and depression diseases. Bithionol is a diarylthioether that is used against trematode and cestode infestations, especially in animals.¹ It should be consumed with caution in human infections due to its photosensitizing effects on the skin.² Cefotiam belongs to a class of

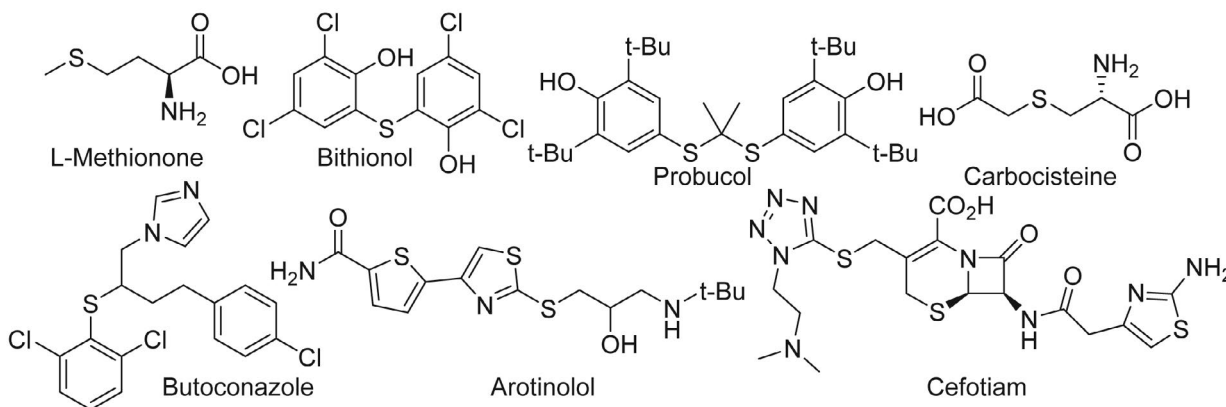


Figure 1. Some approved thioether-based drugs.

antibiotics known as cephalosporins.³ Butoconazole nitrate (Gynazole-1) is used for treatment of vulvovaginal yeast infections.⁴ Arotinolol is prescribed for the treatment of hypertension and essential tremor.^{5,6} Probucole as a potent antioxidant drug lowers the level of cholesterol (mainly LDL) in the blood.⁷ Carbocysteine (*S*-carboxymethylcysteine), prepared by alkylation of cysteine using chloroacetic acid, improves the symptoms of chronic obstructive pulmonary disorder (COPD) and bronchiectasis.⁸

New methods and procedures were developed to synthesize organic sulfides. For this purpose, metal-catalyzed reactions,^{9–11} Sandmeyer and Leuckart reactions,^{12,13} coupling of thiols with Grignard reagents in the presence of *N*-chlorosuccinimide,¹⁴ photocatalytically initiated thiol-ene reaction,¹⁵ free radical displacement on alkynes,¹⁶ regioselective conjugate addition of thiols to acyclic $\alpha,\beta,\gamma,\delta$ -unsaturated dienones,¹⁷ *in situ* nucleophilic substitution of aryl bromides with potassium iodomethyltrifluoroborates,¹⁸ displacement reaction of halogens by sulfur,¹⁹ Stevens rearrangement of thioethers with arynes,²⁰ and synthesis of thiiranes *via* reaction of epoxides with thiourea in DES²¹ were proposed by researchers. Alkylation of thiols or their salts is a well-developed method for the preparation of thioether derivatives.^{22,23} Furthermore, these compounds were successfully synthesized *via* a variety of one-pot multistep^{24–26} and multicomponent^{27,28} alkylation reactions.

Theoretical studies can guide chemists to design and discover new medicines as well as to predict their action mechanisms. Some thioether-ester crown ethers were synthesized as potential inhibitors of *Klebsiella pneumoniae*.²⁹ QSAR calculations including Moriguchi octanol–water partition coefficient, polar surface area, hydrophilic factor, Ghose–Crippen molar refractivity, unsaturation index and weighted holistic invariant molecular descriptors were in compliance with the MIC value of the synthetic compounds.²⁹ Antiplatelet activities of some synthesized 2-(arylmethylthio)-3-phenylquinazolin-4-ones were evaluated on ADP and arachidonic acid-induced platelet aggregation in human plasma.³⁰ Theoretical calculations showed a fairly parabolic correlation between IC₅₀ values of derivatives and their related molecular volume and surface area. Recently, a connection was determined between thioether pleuromutilin derivatives and bacterial 50S ribosomal protein L3 using 3D-QSAR and Topomer CoMFA analysis and ADMET prediction.³¹

In this project, some 2-(bis(benzylthio)methylene) malononitrile derivatives were synthesized *via* two pathways, namely in the presence of a solvent and under solvent-free conditions. Inhibitory properties of these symmetric thioethers were assessed against different genera of bacterial pathogens. QSAR studies were applied to predict the correlation between biological activities of synthesized thioethers and physicochemical descriptors.

2. Experimental

2. 1. Chemicals

All yields refer to isolated products. Melting points were recorded on a Kruss type KSP1N melting point apparatus and are corrected. The reaction progress was monitored by aluminium TLC plates pre-coated with silica gel with fluorescent indicator F254 using *n*-hexane/ethyl acetate (9:1, v/v) as the desired mobile phase. The resulted TLC plates were visualized under UV radiation (254 nm). The IR spectra of the products were recorded on a Bruker Tensor-27 FT-IR spectrometer using KBr disks. The ¹H and ¹³C NMR spectra of compounds in DMSO-*d*₆ or CDCl₃ were recorded on a Bruker FT-NMR Ultra Shield-400 spectrometer (400 and 100 MHz, respectively). CHNS/O analyses were performed on a Thermo Finnigan Flash EA microanalyzer. Initial bacterial or fungal suspensions were adjusted with a Jenway 6405 UV/Vis spectrophotometer.

2. 1. 1. General Procedure for the Synthesis of Thioethers 4a–h

2. 1. 1. 1. The Classical Conditions

0.66 g malononitrile (1) (10 mmol), 0.76 g carbon disulfide (2) (10 mmol), 2.76 g potassium carbonate (20 mmol) and benzylhalides **3a–h** (20 mmol) in 20 mL acetonitrile were mixed well. The mixture was heated under reflux for 5–9 h. *The end of the reaction* was indicated by TLC. The reaction mixture was cooled to room temperature. The contents were added to 20 mL water and extracted with diethyl ether (2 × 10 mL). The extract was washed with water (3 × 15 mL), and the organic phase was separated, dried over anhydrous MgSO₄, filtered and concentrated under reduced pressure. The solid residues were recrystallized from different mixtures of ethanol and water to give colorless needles.

2. 1. 1. 2. The Solvent-Free Conditions

0.66 g malononitrile (1) (10 mmol), 0.76 g carbon disulfide (2) (10 mmol), 2.02 g triethylamine (20 mmol) and benzylhalides **3a–h** (20 mmol) were vigorously stirred to form a macroscopically homogeneous mixture. The mixture was heated at 80 °C for 4–7.5 h. The progress of the reaction was monitored by TLC. After cooling to room temperature, the contents were added to 20 mL water. The procedures of extraction and purification proceeded similarly to the classical conditions.

2. 1. 1. 3. 2-(Bis(benzylthio)methylene)malononitrile (4a).

Light orange needles; m.p. 87–88 °C (Ref.³² 85–86 °C); IR (KBr) ν 2924, 2214 (C≡N), 1588, 1502, 1449 (CH₂), 1248, 1091, 831, 711 cm⁻¹.

2.1.1.4. 2-(Bis((2-nitrobenzyl)thio)methylene) malononitrile (4b).

Dark brown needles; m.p. 82–84 °C; IR (KBr) ν 2925, 2360, 2176 (C≡N), 1635, 1558 (asymmetric NO₂ stretch-

ing), 1448 (CH₂), 1312 (symmetric NO₂ stretching), 1236, 1008, 833, 703 cm⁻¹; ¹H NMR (400 MHz, CDCl₃) δ 7.38 (s, 2H, H-3'), 7.26–7.30 (m, 4H, 2 H-5';6'), 7.20 (m, 2H, 2 H-4'), 3.74 (s, 4H, 2 CH₂) ppm; ¹³C NMR (100 MHz, CDCl₃) δ 33.1 (2 CH₂), 119.4 (NC–C=C), 121.4 (2 C≡N), 127.1 (2 C-6'), 129.5 (2 C-4'), 130.2 (2 C-5'), 131.3 (2 C-3'), 134.8 (2 C-1'), 147.3 (2 C-2'), 166.2 (NC–C=C) ppm. Anal. Calcd. for C₁₈H₁₂N₄O₄S₂: C, 52.42; H, 2.93; N, 13.58; S, 15.55. Found: C, 52.37; H, 2.94; N, 13.62; S, 15.50.

2. 1. 1. 5. 2-(Bis((4-nitrobenzyl)thio)methylene) malononitrile (4c).

Light brown needles; m.p. 93–94 °C; IR (KBr) ν 2924, 2360, 2189 (C≡N), 1635, 1558 (asymmetric NO₂ stretching), 1456 (CH₂), 1345 (symmetric NO₂ stretching), 1312, 1236, 1008, 833, 703 cm⁻¹; ¹H NMR (400 MHz, DMSO-*d*₆) δ 8.10 (d, *J* = 7.3 Hz, 4H, 2 H-3';5'), 7.50 (d, *J* = 7.3 Hz, 4H, 2 H-2';6'), 3.79 (s, 4H, 2 CH₂) ppm; ¹³C NMR (100 MHz, DMSO-*d*₆) δ 34.9 (2 CH₂), 120.6 (NC–C=C), 123.9 (2 C-2';6'), 124.1 (2 C≡N), 130.5 (2 C-3';5'), 141.7 (2 C-1'), 146.9 (2 C-4'), 170.1 (NC–C=C) ppm. Anal. Calcd. for C₁₈H₁₂N₄O₄S₂: C, 52.42; H, 2.93; N, 13.58; S, 15.55. Found: C, 52.36; H, 2.92; N, 13.63; S, 15.53.

2. 1. 1. 6. 2-(Bis((2,4-dinitrobenzyl)thio)methylene) malononitrile (4d).

Dark brown needles; m.p. 157–159 °C (decomp.); IR (KBr) ν 2924, 2360, 2218 (C≡N), 1604, 1532 (asymmetric NO₂ stretching), 1457 (CH₂), 1346 (symmetric NO₂ stretching), 1067, 853, 777 cm⁻¹; ¹H NMR (400 MHz, DMSO-*d*₆) δ 8.77 (s, 2H, 2 H-3'), 8.58 (d, *J* = 8.2 Hz, 2H, 2 H-5'), 8.18 (d, *J* = 8.2 Hz, 2H, 2 H-6'), 3.48 (s, 4H, 2 CH₂) ppm; ¹³C NMR (100 MHz, DMSO-*d*₆) δ 30.2 (2 CH₂), 120.8 (2 C≡N), 127.7 (NC–C=C), 128.4 (2 C-3'), 130.2 (2 C-6'), 130.7 (2 C-5'), 137.0 (2 C-1'), 147.4 (2 C-4'), 148.2 (2 C-2'), 168.2 (NC–C=C) ppm. Anal. Calcd. for C₁₈H₁₀N₆O₈S₂: C, 43.03; H, 2.01; N, 16.73; S, 12.76. Found: C, 43.09; H, 2.02; N, 16.68; S, 12.80%.

2. 1. 1. 7. 2-(Bis((2-chlorobenzyl)thio)methylene) malononitrile (4e).

Dark brown needles; m.p. 87–88 °C; IR (KBr) ν 2922, 2224 (C≡N), 1746, 1572, 1444 (CH₂), 1377, 1237, 1162, 1052 (C–Cl), 823, 760 cm⁻¹; ¹H NMR (400 MHz, CDCl₃) δ 7.36 (m, 2H, 2 H-3'), 7.22 (m, 6H, 2 H-4';5';6'), 3.76 (s, 4H, 2 CH₂) ppm; ¹³C NMR (100 MHz, CDCl₃) δ 41.0 (2 CH₂), 121.8 (2 C≡N), 126.7 (NC–C=C), 128.4 (2 C-4'), 128.9 (2 C-3'), 129.7 (2 C-5'), 130.7 (2 C-2'), 130.9 (2 C-6'), 131.5 (2 C-1'), 162.4 (NC–C=C) ppm. Anal. Calcd. for C₁₈H₁₂Cl₂N₂S₂: C, 55.25; H, 3.09; N, 7.16; S, 16.39. Found: C, 55.27; H, 3.08; N, 7.14; S, 16.43.

2. 1. 1. 8. 2-(Bis((2,4-dichlorobenzyl)thio)methylene) malononitrile (4f).

Dark brown needles; m.p. 88–90 °C; IR (KBr) ν 2926, 2220 (C≡N), 1739, 1587, 1453 (CH₂), 1237, 1050 (C–Cl),

867, 727 cm⁻¹; ¹H NMR (400 MHz, DMSO-*d*₆) δ 7.56 (s, 2H, 2 H-3'), 7.32–7.45 (m, 4H, 2 H-5';6'), 3.78 (s, 4H, 2 CH₂) ppm; ¹³C NMR (100 MHz, DMSO-*d*₆) δ 33.1 (2 CH₂), 122.4 (2 C≡N), 125.9 (NC–C=C), 127.7 (2 C-5'), 129.3 (2 C-3'), 132.6 (2 C-1'), 133.5 (2 C-6'), 134.4 (2 C-4'), 135.2 (2 C-2'), 163.7 (NC–C=C) ppm. Anal. Calcd. for C₁₈H₁₀Cl₄N₂S₂: C, 46.98; H, 2.19; N, 6.09; S, 13.93. Found: C, 47.04; H, 2.18; N, 6.08; S, 13.89.

2. 1. 1. 9. 2-(Bis((2-cyanobenzyl)thio)methylene) malononitrile (4g).

Dark yellow needles; m.p. 94–96 °C; IR (KBr) ν 2925, 2176 (C≡N), 1652, 1488 (CH₂), 1373, 1008, 869, 703 cm⁻¹; ¹H NMR (400 MHz, DMSO-*d*₆) δ 7.67 (m, 6H, 2 H-3';4';5'), 7.46 (m, 2H, 2 H-6'), 3.81 (s, 4H, 2 CH₂) ppm; ¹³C NMR (100 MHz, DMSO-*d*₆) δ 34.9 (2 CH₂), 115.4 (2 C-2'), 120.6 (NC–C=C), 122.1 (2 C-4'), 123.9 (2 C-6'), 124.1 (2 C≡N), 124.7 (C≡N-2'), 129.2 (2 C-3'), 130.5 (2 C-5'), 146.9 (2 C-1'), 170.1 (NC–C=C) ppm. Anal. Calcd. for C₂₀H₁₂N₄S₂: C, 64.49; H, 3.25; N, 15.04; S, 17.22. Found: C, 64.52; H, 3.26; N, 15.02; S, 17.20.

2. 1. 1. 10. 2-(Bis(((perfluorophenyl)methyl)thio)methylene)malononitrile (4h).

Cream needles; m.p. 97–99 °C; IR (KBr) ν 2927, 2199 (C≡N), 1715, 1522, 1474 (CH₂), 1311, 1125 (C–F), 993, 965, 752 cm⁻¹; ¹H NMR (400 MHz, DMSO-*d*₆) δ 3.92 (s, 2 CH₂) ppm; ¹³C NMR (100 MHz, DMSO-*d*₆) δ 23.2 (2 CH₂), 112.9 (NC–C=C), 115.5 (2 C≡N), 118.0 (2 C-1'), 139.3 (2 C-2';6'), 143.0 (2 C-4'), 146.9 (2 C-3';5'), 162.1 (NC–C=C) ppm. Anal. Calcd. for C₁₈H₄F₁₀N₂S₂: C, 43.04; H, 0.80; N, 5.58; S, 12.76. Found: C, 43.01; H, 0.80; N, 5.60; S, 12.78.

2. 2. *In vitro* Antibacterial Activity

Gram-negative bacterial strains including *Acinetobacter baumannii* (PTCC 1855), *Pseudomonas aeruginosa* (PTCC 1310), *Klebsiella pneumoniae* (PTCC 1290), *Escherichia coli* (PTCC 1399), *Shigella flexneri* (PTCC 1234), *Shigella dysenteriae* (PTCC 1188), *Proteus mirabilis* (PTCC 1776), *Proteus vulgaris* (PTCC 1079), *Salmonella enterica subsp. enterica* (PTCC 1709) and *Salmonella typhi* (PTCC 1609), and Gram-positive bacterial strains including *Enterococcus faecalis* (PTCC 1778), *Streptococcus pyogenes* (PTCC 1447), *Streptococcus agalactiae* (PTCC 1768), *Streptococcus equinus* (PTCC 1445), *Streptococcus pneumoniae* (PTCC 1240), *Listeria monocytogenes* (PTCC 1297), *Staphylococcus aureus* (PTCC 1189), *Staphylococcus epidermidis* (PTCC 1435), *Bacillus cereus* (PTCC 1665), *Bacillus subtilis subsp. spizizenii* (PTCC 1023), *Bacillus thuringiensis subsp. kurstaki* (PTCC 1494), *Rhodococcus equi* (PTCC 1633) were prepared from the Persian Type Culture Collection (PTCC), Karaj, Iran. IZD, MIC and MBC values were determined by using broth disk diffusion, microdilution and time-kill methods, according to CLSI (Clinical and Laboratory Standards Institute) guide-

Table 2. Inhibitory activities of thioethers 4a–h against Gram-negative pathogenic bacteria.

Bacteria		Products								Antibiotic Gentamicin
		4a	4b	4c	4d	4e	4f	4g	4h	
1855	IZD	–	22.76	–	–	13.10	15.40	12.11	–	19.63
	MIC	–	64	–	–	512	128	512	–	16
	MBC	–	128	–	–	1024	256	1024	–	32
1310	IZD	–	12.56	–	–	–	–	11.65	–	25.90
	MIC	–	512	–	–	–	–	512	–	0.063
	MBC	–	1024	–	–	–	–	1024	–	0.063
1290	IZD	–	13.11	–	–	–	–	14.56	–	21.78
	MIC	–	512	–	–	–	–	256	–	4
	MBC	–	1024	–	–	–	–	512	–	4
1399	IZD	–	11.80	–	–	10.12	8.90	–	–	23.60
	MIC	–	256	–	–	512	1024	–	–	8
	MBC	–	512	–	–	1024	2048	–	–	8
1234	IZD	7.39	30.45	–	9.80	6.89	9.90	16.11	10.62	19.46
	MIC	512	16	–	256	1024	256	128	256	2
	MBC	1024	64	–	512	2048	512	256	512	8
1188	IZD	–	12.65	–	–	–	–	–	–	21.16
	MIC	–	128	–	–	–	–	–	–	0.031
	MBC	–	256	–	–	–	–	–	–	0.063
1776	IZD	11.60	10.40	–	–	–	–	10.80	–	21.82
	MIC	512	512	–	–	–	–	512	–	0.063
	MBC	1024	1024	–	–	–	–	1024	–	1
1079	IZD	–	7.80	–	–	–	–	–	–	30.26
	MIC	–	512	–	–	–	–	–	–	4
	MBC	–	1024	–	–	–	–	–	–	4
1709	IZD	–	21.67	–	–	–	–	13.34	–	23.84
	MIC	–	64	–	–	–	–	256	–	8
	MBC	–	128	–	–	–	–	512	–	8
1609	IZD	–	21.80	–	–	–	–	11.67	–	21.29
	MIC	–	64	–	–	–	–	512	–	0.063
	MBC	–	128	–	–	–	–	1024	–	0.125

QSAR studies were used to correlate biological activities of compounds into their physicochemical parameters. It is well known that the antibacterial activity of antibiotics is related to intermolecular interactions between the drug and receptor. Identification of the type of forces involved is necessary to adequately explore drug–receptor interactions. Intermolecular interactions are mainly divided into reversible dipole–dipole forces, weak London dispersion forces and stronger irreversible covalent bonding. The challenge of determining these interactions particularly in antibacterial agents has been the subject of a vast amount of both theoretical and experimental studies.

In this investigation, the IZD values of synthesized thioethers 4a–h were computationally related to their physicochemical descriptors. For this purpose, all three classes of intermolecular interactions have been considered. Figure 2 shows the typical structure of studied ligands.

S_N2 , Schiff base formation and Michael addition are chemical interactions involved in drug–receptor complexes. Covalent bonds can be usually formed *via* nucleophilic attack on electron-deficient sites of biological macromolecules. The Pearson's Hard and Soft, Acids and Bases (HSAB)

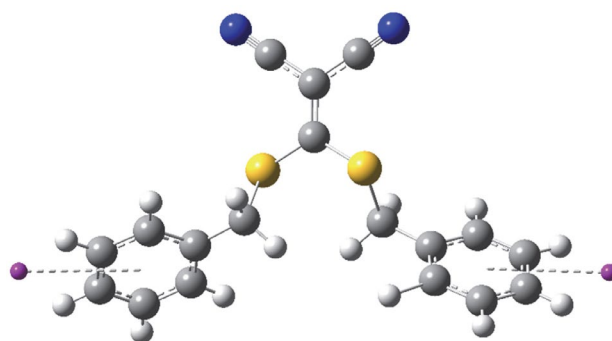


Figure 2. Typical structure of thioethers 4a–h.

theory predicts a significant degree of selectivity that occurs in such nucleophile–electrophile interactions.^{37–39} Accordingly, important electronic descriptors including hardness (HD), softness (SOF), electronegativity (EN) and electrophilicity (EPH), which are obtained from energies of HOMO and LUMO, were used to characterize irreversible covalent interactions. They, respectively, describe stability, reactivity, electron affinity and a measure of energy lowering due to maximal electron flow between the donor and acceptor.⁴⁰ They can be calculated as:⁴¹

Table 3. Inhibitory activities of thioethers **4a–h** against Gram-positive pathogenic bacteria.

Bacteria	Products	Products								Antibiotic Gentamicin
		4a	4b	4c	4d	4e	4f	4g	4h	
1778	IZD ^a	–	13.90	–	–	14.80	–	–	14.80	15.64
	MIC ^b	–	128	–	–	128	–	–	128	0.5
	MBC ^c	–	256	–	–	256	–	–	256	1
1447	IZD	–	10.46	–	–	–	7.40	11.81	–	14.19
	MIC	–	1024	–	–	–	2048	512	–	2
	MBC	–	2048	–	–	–	4096	1024	–	2
1768	IZD	–	15.56	7.24	8.60	–	7.12	–	7.89	–
	MIC	–	256	1024	1024	–	1024	–	1024	–
	MBC	–	512	2048	2048	–	2048	–	2048	–
1445	IZD	–	9.95	–	9.40	8.67	–	–	17.67	19.87
	MIC	–	128	–	256	512	–	–	64	2
	MBC	–	256	–	512	1024	–	–	128	2
1240	IZD	–	10.80	–	–	–	–	–	–	24.74
	MIC	–	256	–	–	–	–	–	–	1
	MBC	–	512	–	–	–	–	–	–	1
1297	IZD	–	24.12	–	–	–	9.67	–	9.90	18.71
	MIC	–	16	–	–	–	1024	–	1024	2
	MBC	–	32	–	–	–	2048	–	2048	2
1189	IZD	–	10.89	–	–	–	–	7.49	–	22.19
	MIC	–	512	–	–	–	–	1024	–	1
	MBC	–	1024	–	–	–	–	2048	–	1
1435	IZD	8.55	17.67	14.97	–	9.70	9.23	–	7.34	27.20
	MIC	1024	256	256	–	512	512	–	1024	1
	MBC	2048	512	512	–	1024	1024	–	2048	2
1665	IZD	–	17.55	–	8.50	–	8.66	10.56	–	25.51
	MIC	–	128	–	1024	–	1024	512	–	0.25
	MBC	–	256	–	2048	–	2048	1024	–	4
1023	IZD	–	9.11	7.50	–	8.13	6.12	–	8.29	27.20
	MIC	–	512	1024	–	1024	1024	–	1024	1
	MBC	–	1024	2048	–	2048	2048	–	2048	2
1494	IZD	–	22.89	–	–	–	10.48	–	–	26.82
	MIC	–	16	–	–	–	512	–	–	1
	MBC	–	32	–	–	–	1024	–	–	1
1633	IZD	–	11.53	–	–	–	–	–	8.94	20.17
	MIC	–	128	–	–	–	–	–	1024	2
	MBC	–	256	–	–	–	–	–	2048	2

–: No noticeable antibacterial effect at the initial concentrations; ^a Values reported as mm; ^b Values reported as $\mu\text{g mL}^{-1}$; ^c Values reported as $\mu\text{g mL}^{-1}$.

$$\text{HD} = \frac{\text{LUMO} - \text{HOMO}}{2}; \text{SOF} = \frac{1}{\text{HD}}; \text{EN} = -\frac{\text{LUMO} + \text{HOMO}}{2}; \text{EPH} = -\frac{\text{EN}^2}{2\text{HD}}$$

Moreover, maximum and minimum local electrostatic surface potential (Max.LESP, Min.LESP) as well as average positive and average negative electrostatic potential (AESP(+), AESP(–)) were applied to characterize relatively strong dipole–dipole interactions, namely hydrogen and halogen bonds in ligand–receptor complexes.⁴² Furthermore, the weak intermolecular dispersion forces have been outlined by molecular volume (MV), molecular surface area (MSA), and polarizability (PL). The numerical values of the molecular descriptors were calculated and are presented in Table 4.

The information mathematical models obtained from four Gram-negative (1855, 1234, 1399, 1776) and five Gram-positive (1447, 1297, 1665, 1768, 1435) bacteria are shown in Table 5. The inhibitory activity of thioethers **4a–h** against Gram-negative strains were correlated to their both chemical and reversible physical descriptors, and are presented in Figures 3 and 4.

In Figure 3-A, the IZD values of compounds **4b,e,f,g** against bacterium 1855 were reasonably related to covalent bond descriptors including HLG (HOMO-LUMO gap), HD, SOF and EPH. This implies that covalent bonds

Table 4. The numerical values of the calculated descriptors.

Products	4a	4b	4c	4d	4e	4f	4g	4h
HOMO ^a	-0.2533	-0.2561	-0.2721	-0.2766	-0.2515	-0.2570	-0.2650	-0.2709
LUMO ^a	-0.1046	-0.1227	-0.1281	-0.1482	-0.0982	-0.1050	-0.1123	-0.1196
HLG ^a	0.1487	0.1334	0.1441	0.1284	0.1533	0.1520	0.1527	0.1512
HD ^a	0.0743	0.0667	0.0720	0.0642	0.0766	0.0760	0.0764	0.0756
SOF ^b	13.45	15.00	13.88	15.57	13.05	13.16	13.09	13.23
EN ^a	-0.1790	-0.1894	-0.2001	-0.2124	-0.1748	-0.1810	-0.1886	-0.1953
EPH ^a	-0.2155	-0.2689	-0.2779	-0.3511	-0.1994	-0.2155	-0.2330	-0.2521
AESP(+) ^c	13.13	14.79	19.53	20.76	11.96	12.41	14.71	15.38
AESP(-) ^c	-13.38	-16.27	-15.55	-12.44	-12.52	-12.61	-17.37	-8.29
Max.LESP ^c	32.67	30.56	42.30	43.18	31.50	39.62	33.10	33.77
Min.LESP ^c	-37.66	-35.96	-31.52	-29.63	-38.29	-36.12	-33.64	-32.87
MV ^d	969.0	1045.1	1078.5	1181.6	1033.0	1120.4	1021.2	1034.3
MSA ^e	570.4	589.0	662.6	712.7	607.8	672.0	556.9	619.0
PL ^f	37.49	41.17	41.17	44.60	41.35	45.20	42.28	36.58

^a Values reported as hartree; ^b Values reported as hartree⁻¹; ^c Values reported as kcal.mol⁻¹; ^d Values reported as Å³; ^e Values reported as Å²; ^f Values reported as a.u.

Table 5. The correlation coefficient (r^2) and rate of change sign (+) or (-) of QSAR calculations.

Descriptors	Bacteria								
	1855	1234	1399	1776	1447	1297	1665	1768	1435
HOMO	-	0.9909: (-)	-	0.9927: (+)	-	-	-	-	-
LUMO	-	0.9982: (-)	-	-	-	-	0.9540: (-)	-	-
HLG	0.9384: (-)	0.9998: (-)	0.7779: (-)	-	-	0.9995: (-)	0.9435: (-)	-	0.8253: (-)
HD	0.9384: (-)	0.9998: (-)	0.7779: (-)	-	-	0.9995: (-)	0.9435: (-)	-	0.8253: (-)
SOF	0.9362: (+)	0.9999: (+)	0.7840: (+)	-	-	0.9997: (+)	0.9456: (+)	-	0.8215: (+)
EN	-	0.9963: (-)	-	-	0.8611: (-)	-	-	-	-
EPH	0.6554: (-)	0.9958: (-)	0.6281: (-)	-	-	-	0.9853: (-)	-	-
AESP(+)	-	0.9985: (+)	0.6973: (+)	-	0.8931: (+)	-	-	-	-
AESP(-)	-	-	0.8084: (-)	0.8007: (+)	0.9938: (-)	0.6947: (-)	0.9984: (-)	0.7188: (-)	0.7278: (-)
Max.LESP	0.7828: (+)	0.9951: (+)	-	-	0.7027: (-)	0.6088: (-)	0.9202: (-)	0.8041: (+)	-
Min.LESP	-	0.9990: (-)	-	0.9854: (-)	0.5978: (+)	-	-	-	-
MV	0.9647: (+)	-	-	-	0.9953: (-)	-	0.9024: (-)	0.8740: (-)	-
MSA	0.9749: (+)	-	-	-	0.9992: (-)	0.6159: (-)	0.9663: (-)	0.9995: (-)	-
PL	0.7474: (+)	-	-	0.7617: (-)	0.7074: (-)	-	0.9311: (-)	0.8883: (-)	-

are formed because of a charge transfer process from the nucleophilic centers to the electrophilic sites. Furthermore, moderate to weak correlations were observed against reversible physical descriptors (Max.LESP, MV, MSA and PL), removal of **4b** strikingly improved them. It can be deduced that less effective ligands (molecules with lesser IZD values) preferably act *via* establishing dipole-dipole and short distance dispersion forces. Inhibitory activity against strain 1234 was observed with all thioethers, except compound **4c**. However, as indicated in Figure 3-B, their action mechanism is not the same. Different trends against irreversible covalent descriptors were found in series **4b,f,g,h** and **4a,d,e**. The former series, except ligand **4f**, behaved differently from the latter one toward the dipole-dipole descriptors. No reasonable relationship was found between antibacterial activities of synthesized compounds against species 1234 and the dispersion forces de-

scriptors, it reflects the dominant contribution of dipole-dipole and covalent interactions. Similar weak correlations on dispersion forces descriptors were observed against bacterial species 1399 and 1776, as shown in Figure 4.

The antibacterial effects of thioethers **4a-h** on five Gram-positive strains have been correlated to their physicochemical descriptors in Figures 5 and 6. Moderate to good relationships were established between the IZD values of ligands **4b,f,g** and all reversible descriptors against bacterium 1447, EN was the only irreversible parameter that can make a meaningful correlation (Figure 5-A). This probably represents a more prominent role of reversible interactions in observed effects.

The irreversible descriptors including HLG, HD and SOF show better correlations with the inhibitory properties of ligands **4b,f,h** on bacterium 1297 than reversible ones including AESP(-), Max.LESP and MSA, as illustrated in

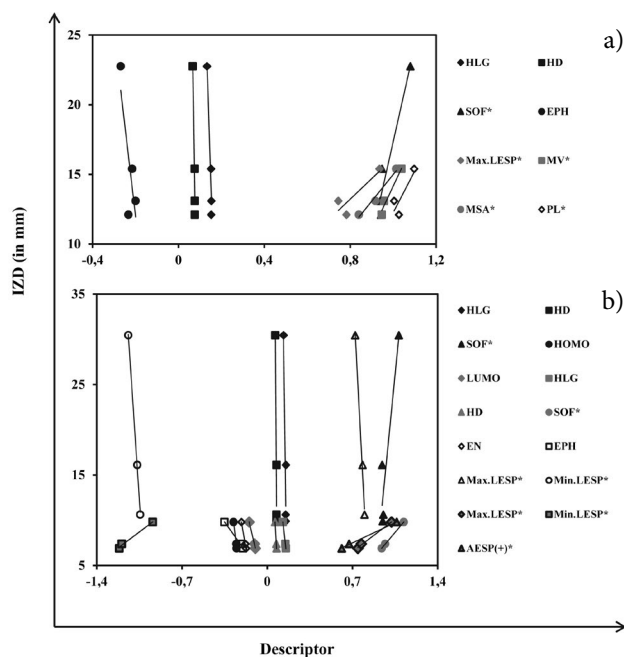


Figure 3. The correlation between descriptors and the IZD values of the ligands **4b,e-g** and **4a,b,d-h** against Gram-negative bacteria 1855 (a) and 1234 (b), respectively. Descriptors with large outlying numerical values (superscripted by *) are divided by them of ligand **4c** for the charts to be able to cover all the numbers.

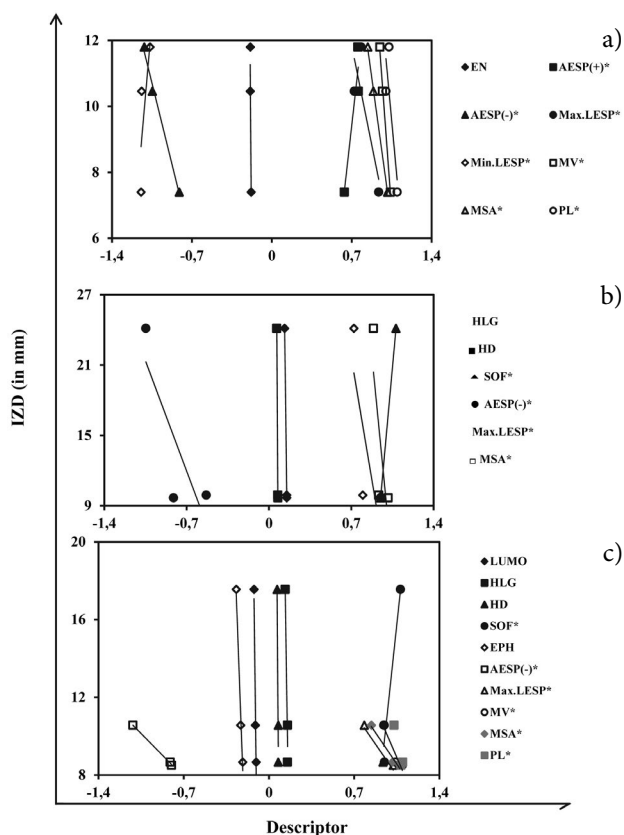


Figure 5. The correlation between descriptors and the IZD values of the ligands **4b,f,g** and **4b,f,h** and **4b,d,f,g** against Gram-positive bacteria 1447 (a), 1297 (b) and 1665 (c), respectively.

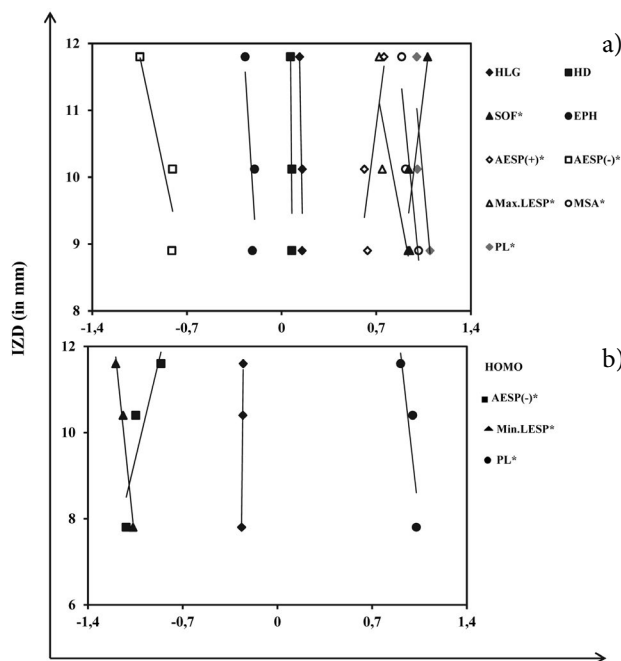


Figure 4. The correlation between descriptors and the IZD values of the ligands **4b,e,f** and **4a,f,g** against Gram-negative bacteria 1399 (a) and 1776 (b), respectively.

Figure 5-B. The orbital overlapping is the most probable type of interactions occurring between ligands and micro-organisms. The same results can be seen in the Figure 5-C. While the antimicrobial activities of the ligands **4b,f,g** on

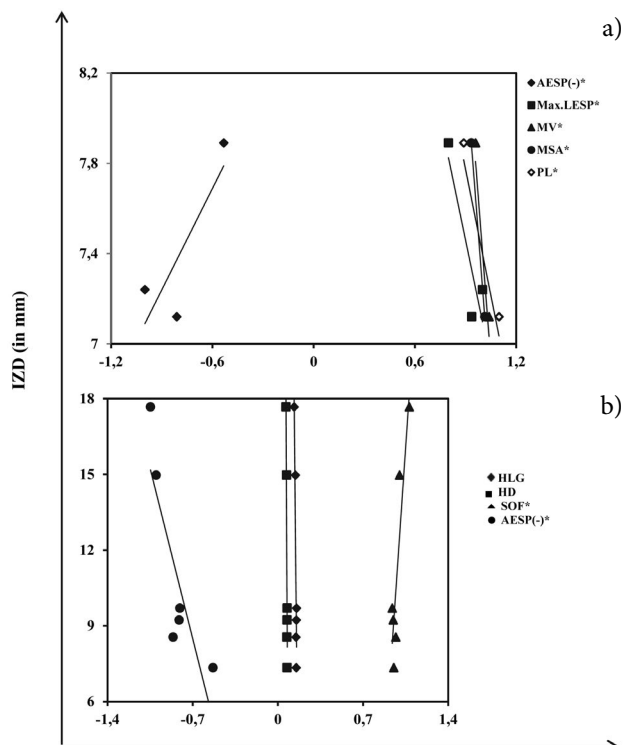


Figure 6. The correlation between descriptors and the IZD values of the ligands **4c,f,h** and **4a-c,e,f,h** against Gram-positive bacteria 1768 (a) and 1435 (b), respectively.

strain 1665 have been strongly correlated to irreversible descriptors, any clear relationship was observed on the reversible dipole–dipole and London dispersion descriptors. Acceptable correlations were found with reversible interactions when compounds **4d,f,g** without considering molecule **4b** were included in calculations. This indicates that the action mechanism of the highly active ligand **4b** against bacterium 1665 is preferably through covalent interactions. Two Gram-positive bacteria 1768 and 1435 exhibited quite different behavior. As indicated in Figure 6, while the former strain is affected by a few ligands (**4c,f,h**) with relatively low activities, all ligands, except thioether **4d**, could more efficiently inhibit the growth of the latter strain. Low activities of the ligands **4c,f,h** against bacterium 1768 *via* only reversible interactions can be seen in Figure 6-A. However, covalent descriptors such as HLG, HD and SOF were dominant interactions in thioethers **4a,b,c,e,f,g,h** against bacterium 1435, as shown in Figure 6-B.

The resulting data presented in Table 5 show that the inhibitory activity of the ligands on 4 Gram-negative bacteria, was mainly related both to irreversible chemical and reversible physical (dipole–dipole and short distance dispersion forces) interactions. However, no logical correlation was observed between short distance descriptors of ligands and their antibacterial activities against microorganisms 1234 and 1399. In contrast, acceptable relationships were established on Gram-positive bacteria when only dipole–dipole interactions were considered. There is no such relation between the IZD values on bacteria 1768 and 1435, and covalent and London dispersion interactions, respectively. As a result, associations between Gram-positive bacterial receptors and host ligands were interpreted by dipole–dipole interactions including hydrogen and halogen bonding rather than the chemical bonding and dispersion forces. The presence or absence of interactions contributing to our QSAR calculations are summarized in Table 6.

The numerical values of some descriptors associated with inhibitory activity of ligands **4a–c,e–g** against bacteria 1855, 1234, 1297, 1665 and 1435 were compared with each other to elucidate the basis for the significantly highest activity of the ligand **4b** (Figure 7). Information of ligand **4d** was not considered because of lack of its correlation with **4b**. The minimum HD, the maximum SOF and the minimum Max.LESP belonging to thioether **4b** is illustrated in Figure 7-A, -B and -C, respectively. As a result, it is predicted that derivative **4b** should have the least stability and the most reactivity toward the nucleophile–electrophile chemical interactions.

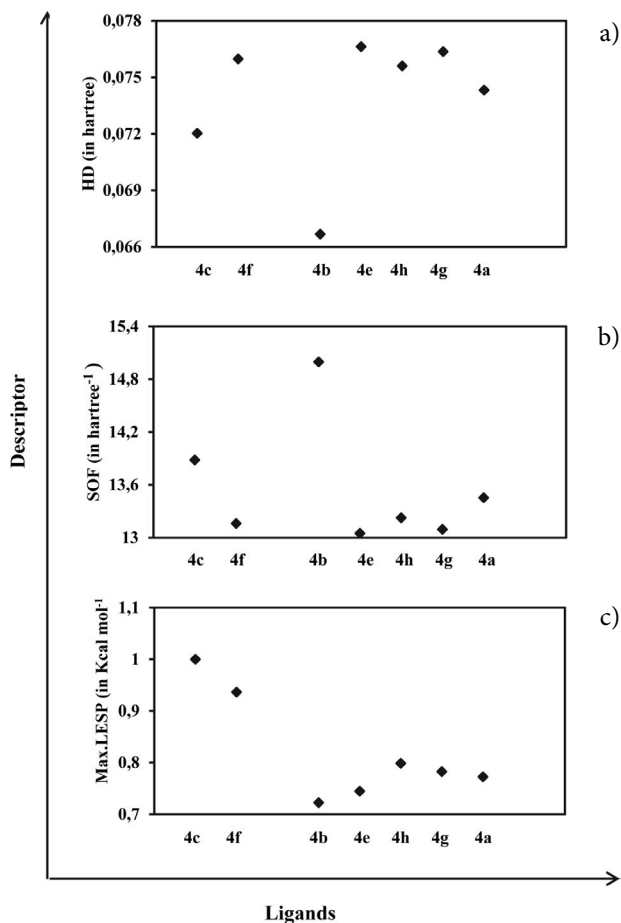


Figure 7. Comparison of HD (a), SOF (b) and Max.LESP (c) of all ligands, except **4d**, with them values of the highly active ligand **4b**.

4. Conclusions

Thioether derivatives **4a–h** were synthesized *via* two procedures. The antimicrobial activity of all synthesized ligands was evaluated against a variety of both Gram-negative and Gram-positive pathogenic bacteria. Theoretical calculations were conducted to correlate inhibitory activity of these ligands into their physico-chemical descriptors. It was found that highly active ligands could affect both Gram-positive and Gram-negative bacteria *via* covalent bonding interactions. Less active ligands preferably bound bacteria through both hydrogen bond and short distance London dispersion forces. Relatively strong dipole–dipole interactions of hydrogen and halogen bonding contribute in all ligand–receptor interactions. Furthermore, the same

Table 6. The presence (P) or absence (A) of interactions contributing to QSAR calculations.

Interactions	Bacteria								
	1855	1234	1399	1776	1447	1297	1665	1768	1435
Covalent bonding	P	P	P	P	P	P	P	A	P
Dipole–dipole	P	P	P	P	P	P	P	P	P
Dispersion forces	P	A	A	P	P	P	P	P	A

rate of change of sign was observed at both classes of bacteria for irreversible covalent descriptors (Table 5). However, signs in descriptors including Max.LESP, Min.LESP, MV, MSA and PL were opposite to each other. These models convey that calculations must be focused on short distance dispersion forces and dipole–dipole interactions rather than covalent bonding to find differences in the mechanisms of action of ligands against Gram-negative and Gram-positive bacteria. The models propose that high softness of ligand **4b** is probably the main cause of its widespread and strong antibacterial activities. Indeed, it efficiently links to targets *via* chemical covalent bonding.

5. Acknowledgements

This work was supported by the University of Zabol under Grant number UOZ-GR-9517-15.

6. References

1. Y. Sanada, H. Senba, R. Mochizuki, H. Arakaki, T. Gotoh, S. Fukumoto, H. Nagahata, *J. Vet. Med. Sci.* **2009**, *71*, 617–620. DOI:10.1292/jvms.71.617
2. W. Leonardi, L. Zilbermintz, L. W. Cheng, J. Zozaya, S. H. Tran, J. H. Elliott, K. Polukhina, R. Manasherob, A. Li, X. Chi, D. Gharaibeh, T. Kenny, R. Zamani, V. Soloveva, A. D. Haddow, F. Nasar, S. Bavari, M. C. Bassik, S. N. Cohen, A. Levitin, M. Martchenko, *Sci. Rep.* **2016**, *6*, 34475. DOI:10.1038/srep34475
3. R. Muller, C. Bottger, G. Wichmann, *Arzneimittelforschung* **2003**, *53*, 126–132. DOI:10.1055/s-0031-1297083
4. L. S. Seidman, C. K. Skokos, *Infect. Dis. Obstet. Gynecol.* **2005**, *13*, 197–206. DOI:10.1155/2005/453239
5. H. Wu, Y. Zhang, J. Huang, Y. Zhang, G. Liu, N. Sun, Z. Yu, Y. Zhou, *Hypertens. Res.* **2001**, *24*, 605–610. DOI:10.1291/hypres.24.605
6. K. -S. Lee, J. -S. Kim, J. -W. Kim, W. -Y. Lee, B. -S. Jeon, D. Kim, *Parkinsonism Relat. Disord.* **2003**, *9*, 341–347. DOI:10.1016/S1353-8020(03)00029-4
7. S. Yamashita, Y. Matsuzawa, *atherosclerosis* **2009**, *207*, 16–23. DOI:10.1016/j.atherosclerosis.2009.04.002
8. A. Esposito, M. R. Valentino, D. Bruzzese, M. Bocchino, A. Ponticiello, A. Stanziola, A. Sanduzzi, *Pulm. Pharmacol. Ther.* **2016**, *37*, 85–88. DOI:10.1016/j.pupt.2016.03.003
9. M. S. Oderinde, M. Frenette, D. W. Robbins, B. Aquila, J. W. Johannes, *J. Am. Chem. Soc.* **2016**, *138*, 1760–1763. DOI:10.1021/jacs.5b11244
10. M. Jouffroy, C. B. Kelly, G. A. Molander, *Org. Lett.* **2016**, *18*, 876–879. DOI:10.1021/acs.orglett.6b00208
11. F. Santoro, M. Mariani, F. Zaccheria, R. Psaro, N. Ravasio, Beilstein *J. Org. Chem.* **2016**, *12*, 2627–2635. DOI:10.3762/bjoc.12.259
12. Y. Li, J. Pu, X. Jiang, *Org. Lett.* **2014**, *16*, 2692–2695. DOI:10.1021/ol5009747
13. S. M. M. Elshafie, *Org. Prep. Proc. Int.* **1983**, *15*, 225–231. DOI:10.1080/00304948309356646
14. J.-H. Cheng, C. Ramesh, H.-L. Kao, Y.-J. Wang, C.-C. Chan, C.-F. Lee, *J. Org. Chem.* **2012**, *77*, 10369–10374. DOI:10.1021/jo302088t
15. O. O. Fadeyi, J. J. Mousseau, Y. Feng, C. Allais, P. Nuhant, M. Z. Chen, B. Pierce, R. Robinson, *Org. Lett.* **2015**, *17*, 5756–5759. DOI:10.1021/acs.orglett.5b03184
16. V. J. Gray, J. Cuthbertson, J. D. Wilden, *J. Org. Chem.* **2014**, *79*, 5869–5874. DOI:10.1021/jo500814y
17. S. Shaw, J. D. White, *Org. Lett.* **2015**, *17*, 4564–4567. DOI:10.1021/acs.orglett.5b02280
18. G. A. Molander, J. Ham, *Org. Lett.* **2006**, *8*, 2031–2034. DOI:10.1021/ol060375a
19. G. Turkoglu, M. E. Cinar, T. Ozturk, *Synthesis* **2016**, *48*, 3618–3624. DOI:10.1055/s-0035-1561673
20. X.-B. Xu, Z.-H. Lin, Y. Liu, J. Guo, Y. He, *Org. Biomol. Chem.* **2017**, *15*, 2716–2720. DOI:10.1039/C7OB00277G
21. N. Azizi, Z. Yadollahy, A. Rahimzadeh-Oskooee, *Synlett* **2014**, *25*, 10851088. DOI:10.1055/s-0033-1341050
22. Y. Nishimoto, A. Okita, M. Yasuda, A. Baba, *Org. Lett.* **2012**, *14*, 1846–1849. DOI:10.1021/ol300450j
23. N. Sakai, T. Miyazaki, T. Sakamoto, T. Yatsuda, T. Moriya, R. Ikeda, T. Konakahara, *Org. Lett.* **2012**, *14*, 4366–4369. DOI:10.1021/ol302109v
24. V. Padmavathi, G. Dinneswara Reddy, S. Nagi Reddy, K. Mahesh, *Eur. J. Med. Chem.* **2011**, *46*, 1367–1373. DOI:10.1016/j.ejmech.2011.01.063
25. Q. Huang, P. F. Richardson, N. W. Sach, J. Zhu, K. K. -C. Liu, G. L. Smith, D. M. Bowles, *Org. Process Res. Dev.* **2011**, *15*, 556–564. DOI:10.1021/op100286g
26. I. Yavari, E. Sodagar, M. Nematpour, *Helv. Chim. Acta* **2014**, *97*, 420–425. DOI:10.1002/hlca.201300345
27. G. C. Patra, S. Pal, S. C. Bhunia, N. K. Hazra, S. C. Pal, *Indian J. Chem.* **2016**, *55B*, 471–477.
28. V. D. Dyachenko, V. N. Nesterov, I. V. Dyachenko, *Russ. J. Gen. Chem.* **2011**, *81*, 751–755. DOI:10.1134/S1070363211040232
29. A. Sadeghian, S. M. Seyedi, H. Sadeghian, A. Hazrathoseyni, M. Sadeghian, *J. Sulfur Chem.* **2007**, *28*, 597–605. DOI:10.1080/17415990701670718
30. Z. Eskandariyan, M. Esfahanizadeh, K. Haj Mohammad Ebrahim Tehrani, V. Mashayekhi, F. Kobarfard, *Arch. Pharmacol. Res.* **2014**, *37*, 332–339. DOI:10.1007/s12272-013-0192-5
31. Z. Wang, Z. Wang, L. Ping Cheng, *Lett. Drug Des. Discovery* **2017**, *14*, 869–879. DOI:10.2174/157018081466617011154331
32. J. J. D'Amico, P. G. Ruminski, L. A. Suba, J. J. Freeman, W. E. Dahl, *Phosphorus Sulfur Relat. Elem.* **1985**, *21*, 307–314. DOI:10.1080/03086648508077673
33. H. Beyzaei, Z. Motraghi, R. Aryan, B. Ghasemi, M. M. Zahedi, A. Samzadeh-Kermani, *Acta Chim. Slov.* **2017**, *64*, 911–918. DOI:10.17344/acsi.2017.3609
34. M. J. Frisch, G. W. Trucks, H. B. Schlegel, G. E. Scuseria, M. A. Robb, J. R. Cheeseman, G. Scalmani, V. Barone, B. Men-

- nucci, G. A. Petersson, H. Nakatsuji, M. Caricato, X. Li, H. P. Hratchian, A. F. Izmaylov, J. Bloino, G. Zheng, J. L. Sonnenberg, M. Hada, M. Ehara, K. Toyota, R. Fukuda, J. Hasegawa, M. Ishida, T. Nakajima, Y. Honda, O. Kitao, H. Nakai, T. Vreven, J. A. Montgomery, J. E. Peralta, F. Ogliaro, M. Bearpark, J. J. Heyd, E. Brothers, K. N. Kudin, V. N. Staroverov, R. Kobayashi, J. Normand, K. Raghavachari, A. Rendell, J. C. Burant, S. S. Iyengar, J. Tomasi, M. Cossi, N. Rega, J. M. Millam, M. Klene, J. E. Knox, J. B. Cross, V. Bakken, C. Adamo, J. Jaramillo, R. Gomperts, R. E. Stratmann, O. Yazyev, A. J. Austin, R. Cammi, C. Pomelli, J. W. Ochterski, R. L. Martin, K. Morokuma, V. G. Zakrzewski, G. A. Voth, P. Salvador, J. J. Dannenberg, S. Dapprich, A. D. Daniels, O. Farkas, J. B. Foresman, J. V. Ortiz, J. Cioslowski, D. J. Fox, Gaussian 09, Revision A 02, Gaussian, Inc., Wallingford CT, USA, 2009.
35. R. F. W. Bader, *Atoms in Molecules - A Quantum Theory*, 1nd ed., Oxford University Press, Oxford, England, 1990.
36. E. D. Glendening, A. E. Reed, J. E. Carpenter, F. Weinhold, NBO 3.1, Gaussian, Inc., Pittsburgh PA, USA, 2001.
37. R. M. LoPachin, D. S. Barber, T. Gavin, *Toxicol. Sci.* **2008**, *104*, 235–249. DOI:10.1093/toxsci/kfm301
38. R. M. LoPachin, T. Gavin, D. R. Petersen, D. S. Barber, *Chem. Res. Toxicol.* **2009**, *22*, 1499–1508. DOI:10.1021/tx900147g
39. R. G. Pearson, *Coord. Chem. Rev.* **1990**, *100*, 403–425. DOI:10.1016/0010-8545(90)85016-L
40. R. G. Parr, P. K. Chattaraj, *J. Am. Chem. Soc.* **1991**, *113*, 1854–1855. DOI:10.1021/ja00005a072
41. P. Thanikaivelan, V. Subramanian, J. R. Rao, B. U. Nair, *Chem. Phys. Lett.* **2000**, *323*, 59–70. DOI:10.1016/S0009-2614(00)00488-7
42. F. A. Bulat, A. Toro-Labbé, T. Brinck, J. S. Murray, P. Politzer, *J. Mol. Model.* **2010**, *16*, 1679–1691. DOI:10.1007/s00894-010-0692-x

Povzetek

Razvili smo večkomponentno reakcijo malononitrila, ogljikovega disulfida in različnih benzil halidov ter jo uporabili kot učinkovito strategijo za sintezo serije 2-(bis(benziltio)metilen)malononitrilnih derivatov. Sinteze smo izvedli na dva načina: (a) v prisotnosti K_2CO_3 kot baze v acetonitrilu in (b) pod pogoji brez topil v prisotnosti trietilamina. Višji izkoristki in krajši reakcijski časi so bili odlika pristopa (b). Inhibitorne aktivnosti vseh spojin smo ugotovili za 22 različnih patogenih bakterij, ki so vključevale tako Gram-negativne kot tudi Gram-pozitivne seve. Tioeter **4b** je v antibiogramskih testih izkazal široko antibakterijsko aktivnost. Da bi ugotovili vrsto interakcij med učinkovinami in receptorji, smo izvedli tudi DFT izračune (B3LYP/6-311++G**); izkazalo se je, da reverzibilne dipol–dipol interakcije v večini primerov igrajo ključno vlogo.

DRUŠTVENE VESTI IN DRUGE AKTIVNOSTI
SOCIETY NEWS, ANNOUNCEMENTS, ACTIVITIES

Vsebina

Mednarodna kemijska olimpijada 2018	S73
Koledar važnejših znanstvenih srečanj s področja kemije, kemijske tehnologije in kemijskega inženirstva	S79
Navodila za avtorje	S84

Contents

International Chemistry Olympiad 2018	S73
Scientific meetings – chemistry, chemical technology and chemical engineering	S79
Instructions for authors	S84

Mednarodna kemijska olimpijada 2018

Andrej Godec
UL, FKKT

Letošnja mednarodna kemijska olimpijada je bila jubilejna. Vse skupaj se je namreč začelo leta 1968 v takratni Čehoslovaški republiki. Zato sta se za organizacijo letošnje, 50. mednarodne kemijske olimpijade, skupaj prijaviili Češka in Slovaška Republika.

Olimpijada je potekala od 19. do 29.7.2018; začeli smo v Bratislavi, in se kasneje preselili še v Prago. Olimpijade se je udeležila naslednja ekipa: Vid Kermelj, Martin Rihtaršič (oba srebrna medalja, in oba iz gimnazije Škofja Loka), Jože Gašperlin (bronasta medalja, gimnazija Kranj) in Nastja Medle (gimnazija Novo mesto). Vsem štirim čestitamo za res lep uspeh!

Ekipo sva vodila mentorja dr. Berta Košmrlj in dr. Andrej Godec, oba iz Fakultete za kemijo in kemijsko tehnologijo v Ljubljani.

Priprave na olimpijado in izbirna tekmovanja potekajo v Ljubljani. Letos je pri tem sodelovala naslednja ekipa FKKT: dr. Berta Košmrlj, dr. Helena Prosen, dr. Alojz Demšar, dr. Darko Dolenc, dr. Andrej Godec in dr. Jernej Markelj. Pomagali sta še Branka Miklavčič in Mojca Žitko.

Pri organizaciji udeležbe na olimpijadi sodelujemo z

Zvezo za tehniško kulturo Slovenije. Vsem se za pomoč najlepše zahvaljujemo.

Letošnje olimpijade se je udeležilo 300 tekmovalcev iz 76 držav. Vsaka država ima lahko največ štiri tekmovalce, in dva mentorja. Zastopani so pravzaprav že vsi kontinenti. Vsako leto pa pridejo tudi države opazovalke, ki potem že naslednje leto lahko pripeljejo tudi tekmovalce. Letos so to bile Gana, Luksemburg, Mali, Katar, Šrilanka in Združeni arabski emirati, tako da lahko že naslednje leto pričakujemo še več tekmovalcev.

Absolutni zmagovalec letošnje olimpijade je bil Qingyu Chen iz Kitajske (dosežek zaokroženih 94%), drugi je bil Rus Aleksej Konoplev (90%), in tretji Korejec Raymond Eugene Bahng (89%). Vsega skupaj je bilo podeljenih 35 zlatih, 65 srebrnih in 95 bronastih medalj. Naš dosežek je bil odličen: Vid je v absolutni konkurenci zasedel 67. mesto (73%), Martin 94. (66%) in Jože 140. (58%).

Na olimpijadi sta dva tekmovalna dneva: najprej je na vrsti praktično delo v laboratoriju, in kasneje še teoretični test. Vsak traja po pet ur.

Vloga mentorjev je usklajevanje in prevajanje besedil



Slovenska ekipa na 50. mednarodni kemijski olimpijadi. Z leve so Andrej Godec, Berta Košmrlj, Nastja Medle, Martin Rihtaršič, Jože Gašperlin, Vid Kermelj, in Eliška Lieberzeitová, vodička naše ekipe.

nalog, kar nam vzame večino časa. Na koncu naloge svoje ekipe popraviva, in ocene usklajujeva z organizatorjevimi na arbitraži.

Otvoritev letošnje olimpijade je bila 21.7. v dvorani Stará Tržnica v centru Bratislave. Gre za dogodek najvišjega ranga v državi organizatoriki, zato so tam predstavniki politike, stroke in medijev, otvoritev pa je tudi priložnost, da država organizatorica predstavi svoje dosežke in kulturo. Udeležence so letos najprej pozdravili predstavniki ministrstev Slovaške in Češke republike, ter zatem še rektorja obeh univerz, organizatorik olimpijade. Na Slovaškem je to bila Univerza Comenius (CU, *Univerzita Komenského*), največja in najstarejša v tem delu sveta. Tradicija te univerze temelji na Akademiji Istropolitana, ki jo je leta 1465 v Bratislavi ustanovil madžarski kralj Matthias Corvinus. Soorganizatorica na češki strani je bila Vysoká škola chemicko-technologická (UCT) v Pragi.

Po uvodni slovesnosti smo mentorji odšli na ogled centra Bratislave in popoldne na večerjo in srečanje z dijaki na gradu Červený Kameň. Center Bratislave je podoben ljubljanskemu, le da je večji, v njem pa v glavnem prevladujejo turisti, tako da je kar nekam prazen.

Slovaška je sicer geografski center Evrope. Krasi jo lepa narava, pa naprimer 1600 mineralnih vrelcev, v katerih se je namakal tudi Ludwig van Beethoven. Ima najstarejše in največje rudnike opala na svetu; tukaj je bil najden najtežji, Harlekýn, ki ima kar 607 gramov. Oboje, dragi kamni in mineralna voda, je nastopalo tudi v nalogah, ki so jih reševali dijaki.



Slovaki radi šahirajo.

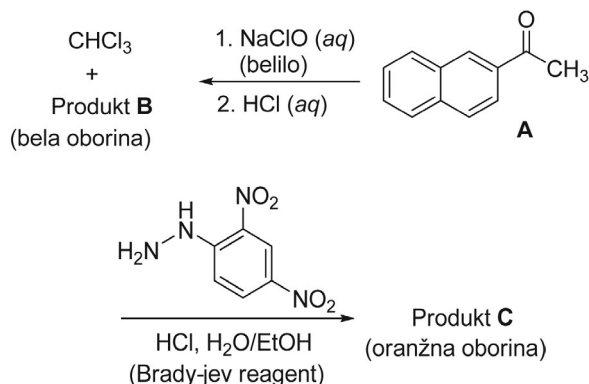


Laboratorijski pult tekmovalca.

Hrana je podobna naši, in tako kot naša tudi zelo dobra. Marija Terezija je kljub odporu prebivalcev tukaj uvedla sajenje krompirja, kar je rešilo takratni problem lakote, krompir pa je danes postal nacionalno živilo številka 1. Iz krompirjevega testa delajo razne cmoke in piroške, naprimer izvrstne *bryndzové pirohy*, ki so napolnjeni z ovčjo skuto. Ponudbo hrane dopolnjuje zelo popularno zelje, ter različno meso, od tega še največ govedina.

Mentorji smo drugi dan dopoldne opravili pregled laboratorijev na Univerzi Comenius, kjer bodo dijaki izvajali tri poskuse. Prvi tekmovalni dan na olimpijadi namreč pomeni praktično delo, mentorji pa moramo preveriti, ali je na pultih vsa oprema, ki jo bodo potrebovali.

Prva naloga v praktičnem delu je bila organska sinteza; sledila je izolacija produktov in analiza čistoče, ki je potekala s tankoplastno kromatografijo. Izhodna spojina reakcije je bil (2-naftil)etanon (na shemi A, 2-acetonafton), s katerim so izvedli haloformsko reakcijo (produkt B), ter potem še reakcijo z Bradyjevim reagentom (produkt C).



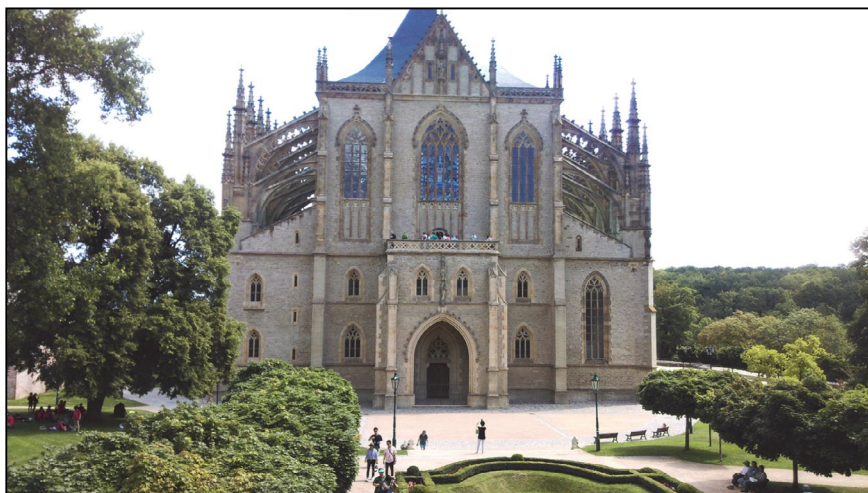
Pri tej nalogi so morali dijaki med drugim izvesti ekstrakcijo, ter vakuumsko filtracijo produktov.

Druga naloga je bila iz fizikalne kemije. Dijaki so določali kinetiko oscilirajoče reakcije; izhodna spojina je bil luminol, ki je vir kemoluminiscence. V prisotnosti primerne katalizatorja, npr. Cu^{2+} , lahko reagira z oksidanti, najbolj pogosto z H_2O_2 , pri čemer nastanejo produkti v vzbujenem elektronskem stanju. Ti produkti sprostitjo presežno energijo z oddajanjem modre svetlobe. Celoten postopek lahko z dodatkom cisteina spremenimo v oscilirajočo reakcijo, pri kateri se pojavi svetloba po določenem indukcijskem času. Ko se ves cistein porabi, postane baker ponovno katalitično aktiven, kar se pokaže z bliskom modre svetlobe. Čas, ki je potreben, da se pojavi blisk, so dijaki uporabili pri študiju hitrosti oksidacije cisteina, ki jo katalizira baker. S spreminjanjem koncentracij in reakcijskih pogojev so na koncu določili konstanti reakcijskih hitrosti v hitrostnem zakonu: $v = k_1[\text{H}_2\text{O}_2][\text{Cu}] + k_2[\text{Cu}]$. Avtorji te naloge so bili res izčrpani, saj so upoštevali tudi temperaturno odvisnost hitrosti reakcije in rezultate normalizirali na sobno temperaturo.

Tretja naloga v tem delu je bila analiza mineralnih vod, s katerimi je Slovaška res bogata. Najvišjo koncentra-



Jedilni list.



Kutná Hora.

cijo mineralov ima vrelec Solivar (292 g L^{-1}), najvišjo koncentracijo H_2S vrelec Smrdáky (292 g L^{-1}), največ CO_2 pa Korytnica ($3,8 \text{ g L}^{-1}$). Dijaki so med drugim izvedli kompleksometrično analizo z EDTA, in na koncu ugotovili, katera mineralna voda izmed 11 možnosti je bila njihov vzorec.

Mentorji smo se po dveh dneh preselili v Prago, kjer smo prevajali najprej praktične naloge, potem pa še teoretične. Vsako od obeh prevajanj traja ves dan, pri tem pa je treba biti zelo precizen, saj ne sme priti do napak. Dijaki imajo sicer možnost vpogleda tudi v angleško verzijo testa, vendar se počutijo mnogo bolj suverene, če lahko naloge prebirajo v svojem jeziku.

Praktični test pomeni 40% končnega rezultata, in teoretični 60%. Nasploh je bila ekipa letos v laboratoriju nekaj manj uspešna kot lani, vendar moram povedati, da so bile naloge časovno zahtevne, in prostor na pultu zelo omejen.

Preden smo začeli s prevajanjem teoretičnih nalog, smo si mentorji seveda ogledali Prago. To mesto kar kipi, saj v njem poleg turistov in domačinov srečate tudi veliko študentov, ki so prišli sem študirat. Obvezen je obisk Karlovega mostu, pa praškega gradu, ki je največje grajsko področje na svetu. Ponoči je lepo osvetljen, za kar gre zasluga rock ansamblu Rolling Stones, ki je pokril vse stroške zunanje razsvetljave na gradu. Tukaj je močno sled pustil tudi naš arhitekt Jože Plečnik, o čemer vam bodo Čehi pripovedovali z velikim spoštovanjem.

Na programu je bila tudi čudovita pot z ladjo po Vltavi, kjer se lahko navdušujete nad lepimi vedutami mesta. Obvezen je seveda obisk Švejkove pivnice. Čehi pridelajo (in popijejo) res veliko najrazličnejšega piva, in nekaj od tega smo izkusili tudi sami. Pivska zgodba je sploh zanimiva; pred stoletji je bila namreč poraba piva na osebo tudi desetkrat večja kot danes, saj je bila kvaliteta vode slaba. Pred težaškim delom so ljudje zjutraj pojedli kruh in toplo pivo; služabnikom na dvoru sta naprimer pripadala dva litra piva dnevno, poleg nekaj vina seveda. Navada je osta-

la, in tako je danes pivo tudi sestavina raznih jedi, od pivskih juh pa vse do slastnih omak in slaščic. Najbolj znana piva so Staropramen, pa Kozel, Budweiser iz mesta České Budějovice in tako naprej. Večino lahko danes dobite tudi v Sloveniji.

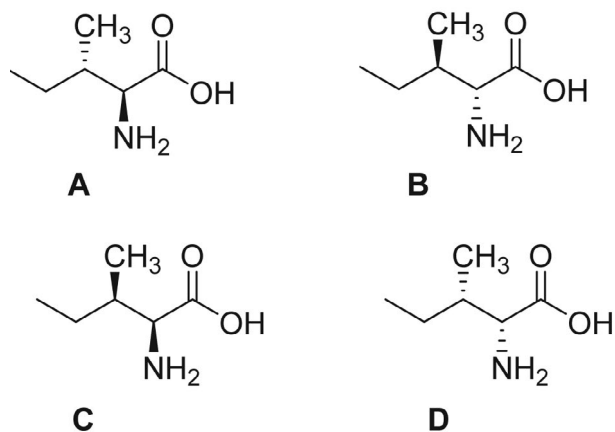
Mentorji smo obiskali tudi mesto Kutná Hora, zakladnico čeških kraljev, saj so bila tukaj bogata najdišča srebra. Mesto je bilo zato od trinajstega stoletja dalje eno najpomembnejših v državi. Impozantna je katedrala Sv. Barbare, posvečena zaščitnici rudarjev. V precej bizarni podzemni kapeli na mestnem pokopališču pa lahko vidite kosti več kot 40 000 ljudi, iz katerih so pri obnovah pred več kot sto leti naredili »dekoracije«, naprimer ogromni lestenec in vaze.

Vse to so organizatorji uporabili tudi pri teoretičnih nalogah na olimpijadi, ki jih bom opisal v nadaljevanju. Vse informacije v zvezi z olimpijado najdete na spletni strani organizatorja (<https://50icho.eu/>), in v naši spletni učilnici Kemljub, kjer so na voljo tudi druge vsebine (<https://skupnost.sio.si/course/view.php?id=150>).

Prva teoretična naloga je bila na temo DNK. Dijaki so morali analizirati termodinamiko nastanka dvojne vijajnice DNK iz posameznih verig ter njeno odvisnost od temperature. Izračunali so konstanto ravnotežja za asociacijo enojnih verig za nepalindromno in za palindromno DNK. Iz podatkov za spremembo proste entalpije asociacije in temperaturnih odvisnosti so izračunali še standardno spremembo entalpije ΔH° in standardno spremembo entropije ΔS° asociacije.

Druga naloga je bila na temo kosti vladarja Lotharja III, ki je umrl leta 1136 na poti iz juga Italije domov. Da bi med transportom ohranili truplo, so zgodovinarji predpostavili, da so njegovi vojaki truplo skuhalo; to hipotezo pa je bilo možno potrditi šele v dvajsetem stoletju z uporabo kemijske kinetike. Datiranje je osnovano na razmerju optičnih izomerov aminokislin. Po smrti se začne racemizacija L-aminokislin, dokler ne pride do ravnotežja med L- in D-obliko. Na ta način lahko določijo starost fosilov

ali kosti do 40 000 let. Pogoj je, da se temperatura ne spreminja dosti, vpliva pa seveda tudi vlaga. Nalogo so avtorji sestavili na primeru L-izoleucina, dijaki pa so morali najprej določiti konfiguracijo in iz termodinamskih podatkov izračunati prosto entalpijo vsakega stereoizomera.



Nato so naredili izračune koncentracij L- in D-oblike, ki sta prisotni po 1943 urah kuhanja pri 374K. Na koncu so iz podobnih podatkov za arginin izračunali še, da so morali truplo Lotharja III kuhati 6 ur.

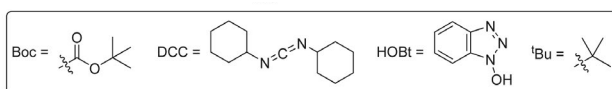
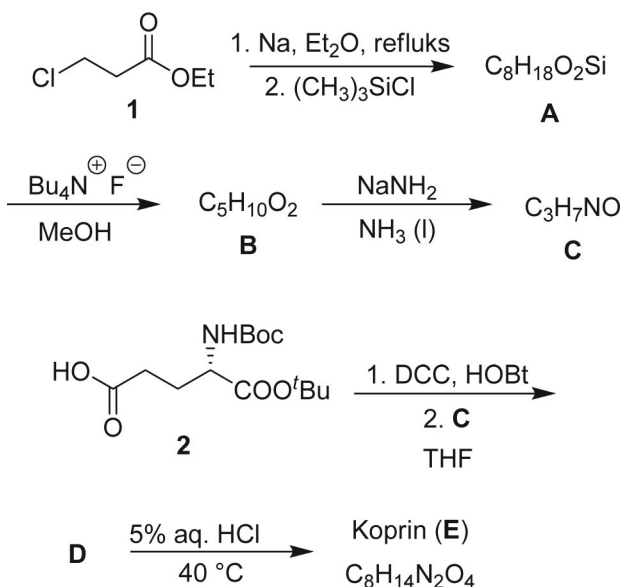
Tretja naloga je bila na temo elektromobilnosti. Gorivne celice predstavljajo način, kako povečati izkoristek motorjev v bodočnosti. To lahko dosežemo z gorivnimi celicami na osnovi vodika. Dijaki so morali najprej iz standardnih tvorbenih entalpij izračunati vrednosti specifičnih sežignih entalpij čistega tekočega izooctana in čistega plinastega vodika. Nato so s pomočjo entropij izračunali napetost vodikove gorivne celice, in njen termodinamski izkoristek. Alternativa tem so lahko gorivne celice na osnovi hidrazina (N_2H_4). Dopolniti so morali Latimerjev diagram z oblikami hidrazina in amonijaka, ki prevladujejo pri danih pogojih. Na koncu pa so za primerjavo izračunali še energijsko gostoto (v kWh kg^{-1}) modelne litij-ionske baterije.

Tema četrte naloge je bila pozitronska emisijska tomografija, ki se uporablja za diagnozo raka. Razen fluorovih in ogljikovih radioizotopov se v tej tehniki lahko uporablja tudi ^{64}Cu . Naloga 4 je obsegala pripravo tega izotopa iz ^{64}Zn , ki ga obstreljujejo z devterijem. Takšno aktivirano tarčo raztopimo v koncentrirani raztopini klorovodikove kisline (HCl (aq)), pri čemer nastane zmes, ki vsebuje Cu^{2+} in Zn^{2+} ione in njihove kloridne komplekse. Dijaki so morali s pomočjo konstante kompleksacije določiti deleža obeh. To zmes so nato ločili z anionskim izmenjevalcem. Z uporabo povprečnih masnih distribucijskih koeficientov D_g ($D_g(Cu \text{ delci}) = 17.4 \text{ cm}^3 \text{ g}^{-1}$, $D_g(Zn \text{ delci}) = 78.5 \text{ cm}^3 \text{ g}^{-1}$) so morali izračunati retencijski volumen V_R v cm^3 za bakrove in cinkove delce in ugotoviti, ali so se ločili.

Peta naloga je bila posvečena češkemu granatu (pirop), ki je cenjen poldrag kamen med izdelovalci nakita. Sestava češkega granata je $Mg_3Al_2(SiO_4)_3$, rdečo barvo tega

granata pa povzročajo primesi kroma. Granati imajo kuubično osnovno celico. Dijaki so morali iz podatkov za osnovno celico izračunati gostoto granata, ter narisati in ovrednotiti diagram razcepa d orbital. Razen tega so morali ugotoviti, kateri absorpcijski spekter je značilen za posamezen mineral izmed štirih možnosti: rdeč češki granat, zelen uvarovit, moder safir in rumeno-oranžen citrin. Na koncu pa so morali za sintetični granat YAG (itrijev aluminijev granat, $Y_3Al_5O_{12}$), ki se uporablja v optoelektroniki, ugotavljati strukturo, če je dopiran z ioni redkih zemelj, in ugotoviti, kakšna bi bila svetloba laserja, narejenega iz teh materialov.

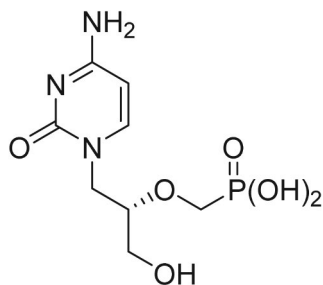
Šesta teoretična naloga je bila v zvezi z gobarjenjem, ki je tudi v teh državah zelo popularna aktivnost. Prava tintovka (*Coprinopsis atramentaria*) velja za užitno specialiteto. Vsebuje naravno snov koprin (E), ki ga lahko sintetiziramo iz etil 3-kloropropanoata (1) po shemi spodaj.



Dijaki so morali narisati formule spojin A–E in prikazati stereokemijo. V telesu koprin hidrolizira do L-glutaminske kisline in naprej do spojine, ki je odgovorna za škodljiv stranski učinek koprina, saj inhibira encim acetaldehid dehidrogenazo, ki sodeluje v presnovi alkohola. Po inhibiciji encima nastaja acetaldehid, ki se nabira v telesu in povzroči močne simptome podobne mačku (takoimenovani antabusni sindrom). Ta sindrom je dobil ime po antabusu, ki je najbolj znano zdravilo za zdravljenje odvisnosti od alkohola. Dijaki so morali dopolniti reakcijske sheme za omenjene reakcije. Na koncu pa so obravnavali še gobo pomladanski hrček (*Gyromitra esculenta*), ki je, čeprav je veljala za užitno, zaradi giromitrina strupena, in terja posebno pripravo. Dopolnili so reakcijske sheme za

sintezo te spojine, ter za njeno hidrolizo, ki se začne takoj, ko pride v stik s kislim okoljem želodca. Iz podatkov za nihanje vezi C-N so izračunali še kinetični izotopski efekt za hidrolizo pri telesni temperaturi.

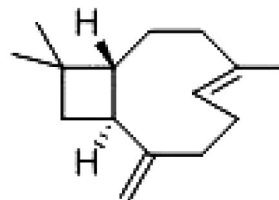
Sedma naloga je bila posvečena cidofovirju (1), ki ga je pripravil profesor Holý iz bivše Čehoslovaške. Gre za analog nukleotida s protivirusnim delovanjem, uporablja pa se za zdravljenje virusnih infekcij, predvsem pri pacientih, ki imajo AIDS. Več kot polovica pacientov, inficiranih z HIV ali hepatitisom B, se zdravi z zdravili, ki jih je razvil ta znanstvenik.



Cidofovir (1)

Dijaki so morali dopolniti reakcijsko shemo za sintezo te spojine, ki vključuje več vmesnih produktov, in vključiti povsod še stereokemijo.

Zadnja, osma naloga, je bila na temo β -kariofilena, ki se nahaja v klinčkih, baziliki, rožmarinu in kanabisu, najdemo pa ga tudi v nekaterih tradicionalnih čeških in slovaških rastlinah, kot sta hmelj ali lipovec.



V naravi ga vedno najdemo skupaj z izomerom. Dijaki so dopolnili reakcijsko shemo za sintezo β -kariofilena, ter proučevali različno reaktivnost dvojnih vezi v tej spojinu ter v izomeru.

Pri nalogah na olimpijadi sta najbolj zastopani fizikalna in organska kemija, skupaj skoraj 70%, zato je tudi na pripravah največ poudarka na teh dveh.

Naslednja mednarodna kemijska olimpijada bo v Parizu.

Vabljeni in vabljeni!

KOLENDAR VAŽNEJŠIH ZNANSTVENIH SREČANJ S PODROČJA KEMIJE IN KEMIJSKE TEHNOLOGIJE

SCIENTIFIC MEETINGS – CHEMISTRY AND CHEMICAL ENGINEERING

2018

October 2018

- 1 – 3 INTERNATIONAL SYMPOSIUM ON CATALYSIS AND SPECIALITY CHEMICALS IS CSC
2018
Tlemcen, Algeri
Information: <https://iscsc2018.univ-tlemcen.dz/>
- 3 – 5 10TH ECNP INTERNATIONAL CONFERENCE ON NANOSTRUCTURED POLYMERS
AND NANOCOMPOSITES
San Sebastian, Spain
Information: <http://www.rsc.org/events/detail/31234/10th-ecnp-international-conference-on-nanostructured-polymers-and-nanocomposites>
- 4 – 5 2ND SYMPOSIUM ON ORGANIC AND INORGANIC CHEMISTRY, SOUTHERN AFRICA
Gaborone, Botswana
Information: https://www.chalmers.se/en/conference/Organic_Inorganic_Chemistry
- 4 – 5 INTERNATIONAL SUSTAINABLE PRODUCTION AND CONSUMPTION CONFERENCE
Manchester, UK
Information: <http://www.icheme.org/ispcc>
- 7 – 10 SPICA 2018 – 17TH INTERNATIONAL SYMPOSIUM ON PREPARATIVE AND
INDUSTRIAL CHROMATOGRAPHY AND ALLIED TECHNIQUES
Darmstadt, Germany
Information: <https://www.spica2018.org/>
- 7 – 12 27TH EUCHEMS CONFERENCE ON MOLTEN SALTS AND IONIC LIQUIDS
(EUCHEMSIL2018)
Lisboa, Portugal
Information: <http://www.euchemsil2018.org/>
- 10 – 12 EAST-WEST CHEMISTRY CONFERENCE 2018 (EWCC2018)
Lviv, Ukraine
Information: <http://ewcc2018.org/>
- 14 – 17 4TH INTERNATIONAL CONFERENCE ON BIOINSPIRED AND BIOBASED CHEMISTRY
& MATERIALS
Nice, France
Information: <http://www.unice.fr/nice-conference/>
- 14 – 18 14TH IUPAC INTERNATIONAL CONGRESS OF PESTICIDE CHEMISTRY
Rio de Janeiro, Brazil
Information: <https://iupac.org/event/14th-iupac-international-congress-of-pesticide-chemistry/>
- 16 – 19 IBERO AMERICAN CHEMISTRY CONGRESS
Lima, Peru
Information: <http://sqperu.org.pe/congreso-2018/>

- 17 – 19 8TH INTERNATIONAL SYMPOSIUM ON DNA-ENCODED CHEMICAL LIBRARIES
Chengdu, China
Information: <http://www.dnaencodedlibrary.com/>
- 18 – 19 INTERNATIONAL WORKSHOP ON ENERGETIC MATERIALS
Istanbul, Turkey
Information: <http://iwem2018.istanbul.edu.tr>
- 19 – 20 13TH WORLD CONFERENCE ON APPLIED SCIENCE, ENGINEERING AND TECHNOLOGY
Bangkok, Thailand
Information: <http://wcaset.co/index.php>
- 19 – 21 3RD INTERNATIONAL CONGRESS OF CHEMISTS AND CHEMICAL ENGINEERS OF BOSNIA AND HERZEGOVINA
Sarajevo, Bosnia and Herzegovina
Information: <http://www.pmf.unsa.ba/hemija/kongres/index.php/en>
- 21 – 24 15TH INTERNATIONAL CONFERENCE ON MICROREACTION TECHNOLOGY
Karlsruhe, Germany
Information: <http://dechema.de/en/IMRET2018.html>
- 24 – 25 IES2018 – 25TH SEMINAR AND SYMPOSIUM ON INFORMATION AND EXPERT SYSTEMS IN THE PROCESS INDUSTRIES
Belgrade, Serbia
Information: <http://bg.ac.rs/en/members/faculties/FTM.php>
- 28 – 31 XXIX INTERAMERICAN CONGRESS OF CHEMICAL ENGINEERING INCORPORATING THE 68TH CANADIAN CHEMICAL ENGINEERING CONFERENCE
Toronto, Canada
Information: <http://www.csche2018.ca/>

November 2018

- 4 – 7 2018 – SUSTAINABLE INDUSTRIAL PROCESSING SUMMIT
Rio de Janeiro, Brazil
Information: <https://www.flogen.org/sips2018/>
- 4 – 8 EMERGING POLYMER TECHNOLOGIES SUMMIT
Hanoi, Vietnam
Information: <http://emts18.org/index.html>
- 5 – 7 MicrobiotaMi 2018
Milano, Italy
Information: <https://microbiotami.com/>
- 5 – 9 XXIII INTERNATIONAL CONFERENCE ON CHEMICAL REACTORS
Ghent, Belgium
Information: http://conf.nsc.ru/CR_23/en/
- 7 – 9 14TH INTERNATIONAL CONFERENCE ON POLYSACCHARIDES-GLYCOSCIENCE (14TH ICPG)
Praha, Czech Republic
Information: <http://www.polysaccharides.csch.cz/index.html>
- 11 – 17 FOURTH INTERNATIONAL CONFERENCE ON APPLICATION OF RADIOTRACERS AND ENERGETIC BEAMS IN SCIENCES (ARCEBS-2018)
Kolkata, India
Information: <https://indico.cern.ch/event/674510/>
- 19 – 20 INTERNATIONAL CONFERENCE ON MOLECULAR BIOLOGY & STEM CELLS
Paris, France
Information: <http://molecularbiology.alliedacademies.com/>

20 – 22 2ND INTERNATIONAL CONFERENCE ON FUNCTIONAL MATERIALS AND CHEMICAL ENGINEERING(ICFMCE 2018)
Abu Dhabi,UAE, United Arab Emirates
Information: <http://www.icfmce.org/>

25 – 29 30TH INTERNATIONAL SYMPOSIUM ON THE CHEMISTRY OF NATURAL PRODUCTS AND THE 10TH INTERNATIONAL CONGRESS ON BIODIVERSITY
Athens, Greece
Information: <http://www.iscnp30-icob10.org/>

December 2018

19 – 20 THE INTERNATIONAL CONFERENCE ON ADVANCED AND APPLIED PETROLEUM, PETROCHEMICALS, AND POLYMERS (ICAPPP2018)
Bangkok, Thailand
Information: <http://www.icappp2018.com/>

2019

January 2019

18 – 20 2ND INTERNATIONAL JOINT CONFERENCE ON MATERIALS SCIENCE AND MECHANICAL ENGINEERING (CMSME 2019)
Phuket, Thailand
Information: <http://www.cmsme.net/>

29 IYPT2019 OPENING CEREMONY
Paris, France
Information: <http://www.iypt2019.org/>

February 2019

12 EMPOWERING WOMEN IN CHEMISTRY: A GLOBAL NETWORKING EVENT
Online
Information: <https://iupac.org/100/global-breakfast/>

21 – 24 3RD INTERNATIONAL CONFERENCE ON ENGINEERING PHYSICS AND OPTOELECTRONIC ENGINEERING (ICEPOE 2019)
Kuala Lumpur, Malaysia
Information: <http://www.icepoe.org/>

March 2019

11 – 13 2ND INTERNATIONAL CONFERENCE ON MATERIALS SCIENCE AND ENGINEERING (ICMSE-2)
Giza /Cairo , Egypt
Information: <https://icmse-egypt2019.org/>

11 – 15 6TH INTERNATIONAL CONFERENCE ON MULTIFUNCTIONAL, HYBRID AND NANOMATERIALS
Sitges, Spain
Information: <https://www.elsevier.com/events/conferences/international-conference-on-multifunctional-hybrid-and-nanomaterials>

24 – 28 1ST GHI WORLD CONGRESS ON FOOD SAFETY AND SECURITY (GHI2019)
Leiden, The Netherlands
Information: <https://ghiworlworldcongress.org/>

31 – Apr. 4 AIChE SPRING MEETING 2019 AND 15TH GLOBAL CONGRESS ON PROCESS SAFETY
New Orleans, USA
Information: <https://www.aiche.org/conferences/aiche-spring-meeting-and-global-congress-on-process-safety/2019>

April 2019

9 – 12 26TH CROATIAN MEETING OF CHEMISTS AND CHEMICAL ENGINEERS (26HSKIKI)
Šibenik, Croatia
Information: <http://www.26hskiki.org/en/>

May 2019

19 – 24 14TH IUPAC INTERNATIONAL CONGRESS OF CROP PROTECTION CHEMISTRY
Ghent, Belgium
Information: <https://www.iupac2019.be>

June 2019

2 – 6 14TH INTERNATIONAL SYMPOSIUM ON MACROCYCLIC AND SUPRAMOLECULAR
CHEMISTRY
Lecce, Italy
Information: <https://ismsc2019.eu/>

11 – 13 23RD GREEN CHEMISTRY & ENGINEERING CONFERENCE AND 9TH INTERNATIONAL
CONFERENCE ON GREEN AND SUSTAINABLE CHEMISTRY
Reston, Virginia, United States
Information: <http://www.gcande.org/>

16 – 19 9TH INTERNATIONAL COLLOIDS CONFERENCE
Sitges, Spain
Information: <https://www.elsevier.com/events/conferences/international-colloids-conference>

16 – 19 LOSS PREVENTION 2019
Delft, The Netherlands
Information: <http://lossprevention2019.org/>

16 – 20 17TH INTERNATIONAL CONFERENCE ON CHEMISTRY AND THE ENVIRONMENT
– ICCE2019
Thessaloniki, Greece
Information: <http://www.euchems.eu/events/17th-international-conference-chemistry-environment-icce2019/>

16 – 20 12TH IWA INTERNATIONAL CONFERENCE ON WATER RECLAMATION AND REUSE
Berlin, Germany
Information: <http://efce.info/IWA+Conference+2019.html>

26 – 28 THERMODYNAMICS 2019
Huelva, Spain
Information: <http://efce.info/Thermodynamics+2019.html>

26 – 30 6TH EUROPEAN CONFERENCE ON ENVIRONMENTAL APPLICATIONS OF
ADVANCED OXIDATION PROCESSES (EAAOP-6)
Portorož, Slovenia
Information: <http://eaaop6.ki.si/>

July 2019

1 – 3 CONGRESS ON NUMERICAL METHODS IN ENGINEERING
Guimarães, Portugal
Information: www.cmn2019.pt

5 – 12 IUPAC 2019 PARIS FRANCE
Paris, France
Information: <https://www.iupac2019.org/>

21 – 26 THE 18TH INTERNATIONAL SYMPOSIUM ON NOVEL AROMATIC COMPOUNDS
(ISNA-18)
Sapporo City, Japan
Information: <https://iupac.org/event/18th-international-symposium-novel-aromatic-compounds-isna-18/>

- 26 – 28 MENDELEEV 150: 4TH INTERNATIONAL CONFERENCE ON THE PERIODIC TABLE
ENDORSED BY IUPAC
Saint Petersburg, Russian Federation
Information: <http://mendeleev150.ifmo.ru/>
- 30 – Aug. 1 8TH INTERNATIONAL CONFERENCE FOR NETWORK FOR INTER-ASIAN CHEMISTRY
EDUCATORS (NICE)
Taipei, Taiwan
Information: <https://iupac.org/event/8th-international-conference-network-inter-asian-chemistry-educators/>

August 2019

- 4 – 8 36TH INTERNATIONAL CONFERENCE OF SOLUTION CHEMISTRY
Xining China
Information: <http://icsc2019.csp.escience.cn/>
- 25 – 30 6TH INTERNATIONAL CONFERENCE ON THE CHEMISTRY AND PHYSICS OF THE
TRANSACTINIDE ELEMENTS (TAN 19)
Wilhelmshaven, Germany
Information: <https://www-win.gsi.de/tan19/>

September 2019

- 1 – 5 EFMC-ASMC'19 – EFMC INTERNATIONAL SYMPOSIUM ON ADVANCES IN
SYNTHETIC AND MEDICINAL CHEMISTRY
Athens, Greece
Information: <https://www.efmc-asmc.org/>
- 2 – 6 1ST INTERNATIONAL CONFERENCE ON NONCOVALENT INTERACTIONS (ICNI)
Lisbon, Portugal
Information: <http://icni2019.eventos.chemistry.pt/>
- 8 – 13 INTERNATIONAL SYMPOSIUM ON IONIC POLYMERIZATION – IP '19
Beijing, China
Information: <https://iupac.org/event/international-symposium-on-ionic-polymerization-ip-19/>
- 15 – 19 11TH EUROPEAN CONGRESS OF CHEMICAL ENGINEERING – ECCE11 &
4TH EUROPEAN CONGRESS OF APPLIED BIOTECHNOLOGY – ECAB5
Florence, Italy
Information: http://efce.info/ECCE12_ECAB5-p-112545.html
- 25 – 27 SLOVENIAN CHEMICAL SOCIETY ANNUAL MEETING 2019
Maribor, Slovenia
Information: <http://chem-soc.si/slovenski-kemijski-dnevi-2019>

2020**July 2020**

- 5 – 9 48TH WORLD POLYMER CONGRESS – MACRO2020
Jeju Island, Korea
Information: <http://www.macro2020.org/>

August 2020

- 16 – 21 12TH TRIENNIAL CONGRESS OF THE WORLD ASSOCIATION OF THEORETICAL AND
COMPUTATIONAL CHEMISTS
Vancouver, Canada
Information: <http://watoc2020.ca/>
- 30 – Sept. 3 ECC8 – 8TH EuChemS CHEMISTRY CONGRESS
Lisbon, Portugal
Information: <http://www.euchems.eu/events/ecc8-8th-euchems-chemistry-congress/>

Acta Chimica Slovenica

Author Guidelines

Submissions

Submission to ACSi is made with the implicit understanding that neither the manuscript nor the essence of its content has been published in whole or in part and that it is not being considered for publication elsewhere. All the listed authors should have agreed on the content and the corresponding (submitting) author is responsible for having ensured that this agreement has been reached. The acceptance of an article is based entirely on its scientific merit, as judged by peer review. There are no page charges for publishing articles in ACSi. The authors are asked to read the Author Guidelines carefully to gain an overview and assess if their manuscript is suitable for ACSi.

Additional information

- Citing spectral and analytical data
- Depositing X-ray data

Submission material

Typical submission consists of:

- full manuscript (PDF file, with title, authors, abstract, keywords, figures and tables embedded, and references)
- supplementary files
 - **Full manuscript** (original Word file)
 - **Statement of novelty** (Word file)
 - **List of suggested reviewers** (Word file)
 - **ZIP file containing graphics** (figures, illustrations, images, photographs)
 - **Graphical abstract** (single graphics file)
 - **Proposed cover picture** (optional, single graphics file)
 - **Appendices** (optional, Word files, graphics files)

Incomplete or not properly prepared submissions will be rejected.

Submission process

Before submission, authors should go through the checklist at the bottom of the page and prepare for submission.

Submission process consists of 5 steps.

Step 1: Starting the submission

- Choose one of the journal sections.
- Confirm all the requirements of the **checklist**.
- Additional plain text comments for the editor can be provided in the relevant text field.

Step 2: Upload submission

- Upload full manuscript in the form of a Word file (with title, authors, abstract, keywords, figures and tables embedded, and references).

Step 3: Enter metadata

- First name, last name, contact email and affiliation for all authors, in relevant order, must be provided. Corresponding author has to be selected. Full postal address and phone number of the corresponding author has to be provided.

- **Title and abstract** must be provided in plain text.
- Keywords must be provided (max. 6, separated by semicolons).
- Data about contributors and supporting agencies may be entered.
- **References** in plain text must be provided in the relevant text filed.

Step 4: Upload supplementary files

- Original Word file (original of the PDF uploaded in the step 2)
- **Statement of novelty** in a Word file must be uploaded
- All **graphics** have to be uploaded in a single ZIP file. Graphics should be named Figure 1.jpg, Figure 2.eps, etc.
- **Graphical abstract image** must be uploaded separately
- **Proposed cover picture** (optional) should be uploaded separately.
- Any additional **appendices** (optional) to the paper may be uploaded. Appendices may be published as a supplementary material to the paper, if accepted.
- For each uploaded file the author is asked for additional metadata which may be provided. Depending of the type of the file please provide the relevant title (Statement of novelty, List of suggested reviewers, Figures, Graphical abstract, Proposed cover picture, Appendix).

Step 5: Confirmation

- Final confirmation is required.

Article Types

Feature Articles are contributions that are written on editor's invitation. They should be clear and concise summaries of the most recent activity of the author and his/her research group written with the broad scope of ACSi in mind. They are intended to be general overviews of the authors' subfield of research but should be written in a way that engages and informs scientists in other areas. They should contain the following (see also general directions for article structure in ACSi below): (1) an introduction that acquaints readers with the authors' research field and outlines the important questions to which answers are being sought; (2) interesting, new, and recent contributions of the author(s) to the field; and (3) a summary that presents possible future directions. Manuscripts normally should not exceed 40 pages of one column format (letter size 12, 33 lines per page). Generally, experts in a field who have made important contribution to a specific topic in recent years will be invited by an editor to contribute such an **Invited Feature Article**. Individuals may, however, send a proposal (one-page maximum) for an Invited Feature Article to the Editor-in-Chief for consideration.

Scientific articles should report significant and innovative achievements in chemistry and related sciences and should exhibit a high level of originality. They

should have the following structure:

1. Title (max. 150 characters),
2. Authors and affiliations,
3. Abstract (max. 1000 characters),
4. Keywords (max. 6),
5. Introduction,
6. Experimental,
7. Results and Discussion,
8. Conclusions,
9. Acknowledgements,

10. References.

The sections should be arranged in the sequence generally accepted for publications in the respective fields and should be successively numbered.

Short communications generally follow the same order of sections as Scientific articles, but should be short (max. 2500 words) and report a significant aspect of research work meriting separate publication. Editors may decide that a Scientific paper is categorized as a Short Communication if its length is short.

Technical articles report applications of an already described innovation. Typically, technical articles are not based on new experiments.

Preparation of Submissions

Text of the submitted articles must be prepared with Microsoft Word. Normal style set to single column, 1.5 line spacing, and 12 pt Times New Roman font is recommended. Line numbering (continuous, for the whole document) must be enabled to simplify the reviewing process. For any other format, please consult the editor. Articles should be written in English. Correct spelling and grammar are the sole responsibility of the author(s). Papers should be written in a concise and succinct manner. The authors shall respect the ISO 80000 standard [1], and IUPAC Green Book [2] rules on the names and symbols of quantities and units. The Système International d'Unités (SI) must be used for all dimensional quantities.

Graphics (figures, graphs, illustrations, digital images, photographs) should be inserted in the text where appropriate. The captions should be self-explanatory. Lettering should be readable (suggested 8 point Arial font) with equal size in all figures. Use common programs such as MS Excel or similar to prepare figures (graphs) and ChemDraw to prepare structures in their final size. Width of graphs in the manuscript should be 8 cm. Only in special cases (in case of numerous data, visibility issues) graphs can be 17 cm wide. All graphs in the manuscript should be inserted in relevant places and **aligned left**. The same graphs should be provided separately as images of appropriate resolution (see below) and submitted together in a ZIP file (Graphics ZIP). Please do not submit figures as a Word file. In **graphs**, only the graph area determined by both axes should be in the frame, while a frame around the whole graph should be omitted. The graph area should be white. The legend should be inside the graph area. The style of all graphs should be the same. **Figures and illustrations** should be of sufficient quality for the printed version, i.e. 300 dpi minimum. **Digital images and photographs** should be of high quality (minimum 250 dpi resolution). On submission, figures should be of good enough resolution to be assessed by the referees, ideally as JPEGs. High-resolution figures (in JPEG,

TIFF, or EPS format) might be required if the paper is accepted for publication.

Tables should be prepared in the Word file of the paper as usual Word tables. The captions should appear above the table and should be self-explanatory.

References should be numbered and ordered sequentially as they appear in the text, likewise methods, tables, figure captions. When cited in the text, reference numbers should be superscripted, following punctuation marks. It is the sole responsibility of authors to cite articles that have been submitted to a journal or were in print at the time of submission to ACSi. Formatting of references to published work should follow the journal style; please also consult a recent issue:

1. J. W. Smith, A. G. White, *Acta Chim. Slov.* **2008**, *55*, 1055–1059.
2. M. F. Kemmere, T. F. Keurentjes, in: S. P. Nunes, K. V. Peinemann (Ed.): *Membrane Technology in the Chemical Industry*, Wiley-VCH, Weinheim, Germany, **2008**, pp. 229–255.
3. J. Levec, Arrangement and process for oxidizing an aqueous medium, US Patent Number 5,928,521, date of patent July 27, **1999**.
4. L. A. Bursill, J. M. Thomas, in: R. Sersale, C. Collela, R. Aiello (Eds.), *Recent Progress Report and Discussions: 5th International Zeolite Conference*, Naples, Italy, 1980, Gianini, Naples, **1981**, pp. 25–30.
5. J. Szegezdi, F. Cszimadia, Prediction of dissociation using microconstants, http://www.chemaxon.com/conf/Prediction_of_dissociation_constant_using_microconstants.pdf, (assessed: March 31, 2008)

Titles of journals should be abbreviated according to Chemical Abstracts Service Source Index (CASSI).

Special Notes

- Complete characterization, **including crystal structure**, should be given when the synthesis of new compounds in crystal form is reported.
- Numerical **data should be reported with the number of significant digits corresponding to the magnitude** of experimental uncertainty.
- **The SI system of units and IUPAC recommendations** for nomenclature, symbols and abbreviations should be followed closely. Additionally, the authors should follow the general guidelines when citing spectral and analytical data, and depositing crystallographic data.
- **Characters** should be correctly represented throughout the manuscript: for example, 1 (one) and l (ell), 0 (zero) and O (oh), x (ex), D7 (times sign), B0 (degree sign). Use Symbol font for all Greek letters and mathematical symbols.
- The rules and recommendations of the **IUBMB** and the **International Union of Pure and Applied Chemistry (IUPAC)** should be used for abbreviation of chemical names, nomenclature of chemical compounds, enzyme nomenclature, isotopic compounds, optically active isomers, and spectroscopic data.
- **A conflict of interest** occurs when an individual (author, reviewer, editor) or its organization is involved in multiple interests, one of which could possibly corrupt the motivation for an act in the

other. Financial relationships are the most easily identifiable conflicts of interest, while conflicts can occur also as personal relationships, academic competition, etc. **The Editors** will make effort to ensure that conflicts of interest will not compromise the evaluation process; potential editors and reviewers will be asked to exempt themselves from review process when such conflict of interest exists. When the manuscript is submitted for publication, **the authors** are expected to disclose any relationships that might pose potential conflict of interest with respect to results reported in that manuscript. In the Acknowledgement section the source of funding support should be mentioned. The statement of disclosure must be provided as Comments to Editor during the submission process.

- **Published statement of Informed Consent.** Research described in papers submitted to ACSi must adhere to the principles of the Declaration of Helsinki (<http://www.wma.net/e/policy/b3.htm>). These studies must be approved by an appropriate institutional review board or committee, and informed consent must be obtained from subjects. The Methods section of the paper must include: 1) a statement of protocol approval from an institutional review board or committee and 2), a statement that informed consent was obtained from the human subjects or their representatives.
- **Published Statement of Human and Animal Rights.** When reporting experiments on human subjects, authors should indicate whether the procedures followed were in accordance with the ethical standards of the responsible committee on human experimentation (institutional and national) and with the Helsinki Declaration of 1975, as revised in 2008. If doubt exists whether the research was conducted in accordance with the Helsinki Declaration, the authors must explain the rationale for their approach and demonstrate that the institutional review body explicitly approved the doubtful aspects of the study. When reporting experiments on animals, authors should indicate whether the institutional and national guide for the care and use of laboratory animals was followed.
- To avoid conflict of interest between authors and referees we expect that not more than one referee is from the same country as the corresponding author(s), however, not from the same institution.
- Contributions authored by **Slovenian scientists** are evaluated by non-Slovenian referees.
- Papers describing **microwave-assisted reactions** performed in domestic microwave ovens are not considered for publication in *Acta Chimica Slovenica*.
- *Manuscripts that are **not prepared and submitted** in accord with the instructions for authors are not considered for publication.*

Appendices

Authors are encouraged to make use of supporting information for publication, which is supplementary material (appendices) that is submitted at the same time as the manuscript. It is made available on the Journal's web site and is linked to the article in the

Journal's Web edition. The use of supporting information is particularly appropriate for presenting additional graphs, spectra, tables and discussion and is more likely to be of interest to specialists than to general readers. When preparing supporting information, authors should keep in mind that the supporting information files will not be edited by the editorial staff. In addition, the files should be not too large (upper limit 10 MB) and should be provided in common widely known file formats to be accessible to readers without difficulty. All files of supplementary materials are loaded separately during the submission process as supplementary files.

Proposed Cover Picture and Graphical Abstract Image

Graphical content: an ideally full-colour illustration of resolution 300 dpi from the manuscript must be proposed with the submission. Graphical abstract pictures are printed in size 6.5 x 4 cm (hence minimal resolution of 770 x 470 pixels). Cover picture is printed in size 11 x 9.5 cm (hence minimal resolution of 1300 x 1130 pixels)

Authors are encouraged to submit illustrations as candidates for the journal Cover Picture*. The illustration must be related to the subject matter of the paper. Usually both proposed cover picture and graphical abstract are the same, but authors may provide different pictures as well.

* The authors will be asked to contribute to the costs of the cover picture production.

Statement of novelty

Statement of novelty is provided in a Word file and submitted as a supplementary file in step 4 of submission process. Authors should in no more than 100 words emphasize the scientific novelty of the presented research. Do not repeat for this purpose the content of your abstract.

List of suggested reviewers

List of suggested reviewers is a Word file submitted as a supplementary file in step 4 of submission process. Authors should propose the names, full affiliation (department, institution, city and country) and e-mail addresses of three potential referees. Field of expertise and at least two references relevant to the scientific field of the submitted manuscript must be provided for each of the suggested reviewers. The referees should be knowledgeable about the subject but have no close connection with any of the authors. In addition, referees should be from institutions other than (and preferably countries other than) those of any of the authors.

How to Submit

Users registered in the role of author can start submission by choosing USER HOME link on the top of the page, then choosing the role of the Author and follow the relevant link for starting the submission process. Prior to submission we strongly recommend that you familiarize yourself with the ACSi style by browsing the journal, particularly if you have not submitted to the ACSi before or recently.

Correspondence

All correspondence with the ACSi editor regarding the paper goes through this web site and emails. Emails are sent and recorded in the web site database. In the correspondence with the editorial office please provide ID number of your manuscript. All emails you receive from the system contain relevant links. **Please do not answer the emails directly but use the embedded links in the emails for carrying out relevant actions.** Alternatively, you can carry out all the actions and correspondence through the online system by logging in and selecting relevant options.

Proofs

Proofs will be dispatched via e-mail and corrections should be returned to the editor by e-mail as quickly as possible, normally within 48 hours of receipt. Typing errors should be corrected; other changes of contents will be treated as new submissions.

Submission Preparation Checklist

As part of the submission process, authors are required to check off their submission's compliance with all of the following items, and submissions may be returned to authors that do not adhere to these guidelines.

1. The submission has not been previously published, nor is it under consideration for publication in any other journal (or an explanation has been provided in Comments to the Editor).
2. All the listed authors have agreed on the content and the corresponding (submitting) author is responsible for having ensured that this agreement has been reached.
3. The submission files are in the correct format: manuscript is created in MS Word but will be **submitted in PDF** (for reviewers) as well as in original MS Word format (as a supplementary file for technical editing); diagrams and graphs are created in Excel and saved in one of the file formats: TIFF, EPS or JPG; illustrations are also saved in one of these formats. The preferred position of graphic files in a document is to embed them close to the place where they are mentioned in the text (See **Author guidelines** for details).
4. The manuscript has been examined for spelling and grammar (spell checked).
5. The **title** (maximum 150 characters) briefly explains the contents of the manuscript.
6. Full names (first and last) of all authors together with the affiliation address are provided. Name of author(s) denoted as the corresponding author(s), together with their e-mail address, full postal address and telephone/fax numbers are given.
7. The **abstract** states the objective and conclusions of the research concisely in no more than 150 words.
8. Keywords (minimum three, maximum six) are provided.
9. **Statement of novelty** (maximum 100 words) clearly explaining new findings reported in the manuscript should be prepared as a separate Word file.
10. The text adheres to the stylistic and bibliographic requirements outlined in the **Author guidelines**.
11. Text in normal style is set to single column, 1.5 line spacing, and 12 pt. Times New Roman font is

recommended. All tables, figures and illustrations have appropriate captions and are placed within the text at the appropriate points.

12. Mathematical and chemical equations are provided in separate lines and numbered (Arabic numbers) consecutively in parenthesis at the end of the line. All equation numbers are (if necessary) appropriately included in the text. Corresponding numbers are checked.
13. Tables, Figures, illustrations, are prepared in correct format and resolution (see **Author guidelines**).
14. The lettering used in the figures and graphs do not vary greatly in size. The recommended lettering size is 8 point Arial.
15. Separate files for each figure and illustration are prepared. The names (numbers) of the separate files are the same as they appear in the text. All the figure files are packed for uploading in a single ZIP file.
16. Authors have read **special notes** and have accordingly prepared their manuscript (if necessary).
17. References in the text and in the References are correctly cited. (see **Author guidelines**). All references mentioned in the Reference list are cited in the text, and vice versa.
18. Permission has been obtained for use of copyrighted material from other sources (including the Web).
19. The names, full affiliation (department, institution, city and country), e-mail addresses and references of three potential referees from institutions other than (and preferably countries other than) those of any of the authors are prepared in the word file. At least two relevant references (important papers with high impact factor, head positions of departments, labs, research groups, etc.) for each suggested reviewer must be provided.
20. Full-colour illustration or graph from the manuscript is proposed for graphical abstract.
21. **Appendices** (if appropriate) as supplementary material are prepared and will be submitted at the same time as the manuscript.

Privacy Statement

The names and email addresses entered in this journal site will be used exclusively for the stated purposes of this journal and will not be made available for any other purpose or to any other party.

ISSN: 1580-3155

Koristni naslovi

Slovensko kemijsko društvo
Slovenian Chemical Society



Slovensko kemijsko društvo

www.chem-soc.si

e-mail: chem.soc@ki.si



Wessex Institute of Technology

www.wessex.ac.uk



SETAC

www.setac.org



European Water Association

<http://www.ewa-online.eu/>



European Science Foundation

www.esf.org



European Federation of Chemical Engineering

<https://efce.info/>



IUPAC

INTERNATIONAL UNION OF
PURE AND APPLIED CHEMISTRY

International Union of Pure and Applied Chemistry

<https://iupac.org/>

Novice evropske zveze kemijskih društev (EuCheMS) najdete na:



EuCheMS: Brussels News Updates

<http://www.euchems.eu/newsletters/>



Donau Lab d.o.o., Ljubljana
Tbilisjska 85
SI-1000 Ljubljana
www.donaulab.si
office-si@donaulab.com



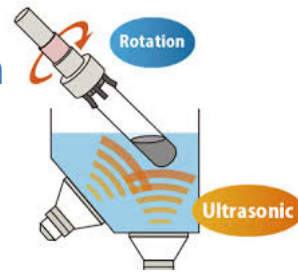
THINKY

Nano PREMIXER PR-1

Uniformna disperzija in deaglomeracija
nanomaterialov (CNT, Graphene, drugi)

Dual-Sonic ultrazvočni sistem

Aktivno hlajenje kopeli



BODITE NEUSTAVLJIVI

MAGNEZIJ Krka 300



Granulat za pripravo napitka vsebuje magnezijev citrat in vitamin B₂.



Magnezij in vitamin B₂ prispevata k zmanjšanju utrujenosti in izčrpanosti ter normalnemu delovanju živčnega sistema.



Magnezij prispeva tudi k delovanju mišic.



www.magnezijkrka.si

- ✔ Okus po pomaranči in limeti. ✔ Brez konzervansov.
- ✔ Brez umetnih barvil, arom in sladil. ✔ Ena vrečka na dan.

Prehransko dopolnilo ni nadomestilo za uravnoteženo in raznovrstno prehrano. Skrbite tudi za zdrav življenjski slog.

NOVO

 KRKA

Acta Chimica Slovenica

Acta Chimica Slovenica

Aurivillius phase $\text{Bi}_2\text{Ti}_3\text{O}_{12}$ plates, grown in the molten salt, represent an appropriate template for the synthesis of SrTiO_3 plates through topochemical conversion, which is a unique approach to the preparation of asymmetrically shaped particles of perovskites with a symmetrical crystal structure. (see page 630)



Year 2018, Vol. 65, No. 3

